ORNL
MASTER COPY

ORNL-3193
UC-34 – Physics
TID-4500 (16th ed. Rev.)

NEUTRON PHYSICS DIVISION

ANNUAL PROGRESS REPORT

FOR PERIOD ENDING SEPTEMBER 1, 1961

OAK RIDGE NATIONAL LABORATORY
operated by
UNION CARBIDE CORPORATION
for the
U.S. ATOMIC ENERGY COMMISSION

Printed in USA. Price $4.50. Available from the
Office of Technical Services
Department of Commerce
Washington 25, D. C.

LEGAL NOTICE

This report was prepared as an account of Government sponsored work. Neither the United States, nor the Commission, nor any person acting on behalf of the Commission:

A. Makes any warranty or representation, expressed or implied, with respect to the accuracy, completeness, or usefulness of the information contained in this report, or that the use of any information, apparatus, method, or process disclosed in this report may not infringe privately owned rights; or

B. Assumes any liabilities with respect to the use of, or for damages resulting from the use of any information, apparatus, method, or process disclosed in this report.

As used in the above, "person acting on behalf of the Commission" includes any employee or contractor of the Commission, or employee of such contractor, to the extent that such employee or contractor of the Commission, or employee of such contractor prepares, disseminates, or provides access to, any information pursuant to his employment or contract with the Commission, or his employment with such contractor.

ORNL-3193
UC-34 – Physics
TID-4500 (16th ed., Rev.)

Contract No. W-7405-eng-26

NEUTRON PHYSICS DIVISION
ANNUAL PROGRESS REPORT
for Period Ending September 1, 1961

E. P. Blizard, Director
A. D. Callihan, Associate Director
F. C. Maienschein, Associate Director
A. Simon,* Associate Director

DATE ISSUED

OCT 31 1961

OAK RIDGE NATIONAL LABORATORY
Oak Ridge, Tennessee
operated by
UNION CARBIDE CORPORATION
for the
U. S. ATOMIC ENERGY COMMISSION

*Now at General Atomic.

TABLE OF CONTENTS AND SUMMARY

1. RESEARCH FOR LIGHT-WATER-MODERATED REACTORS

1.1. THE REACTIVITY EFFECT ON AN AIR-FILLED CAVITY WITHIN A POOL CRITICAL ASSEMBLY CORE

E. B. Johnson 3

The existence of positive void coefficients of reactivity in the over-moderated rod well of a Bulk Shielding Reactor I control-rod element, centrally located in a critical core in the Pool Critical Assembly, has been experimentally verified. The method of an earlier experiment, which employed an air-filled aluminum box to define the void, was improved by using a Lucite box, which did not alter the metal-to-water ratio within the core.

1.2. CENTER LINE ATTENUATION MEASUREMENTS OF RADIATION FROM A BERYLLIUM-REFLECTED POOL CRITICAL ASSEMBLY

E. B. Johnson 4

Thermal-neutron fluxes and gamma-ray dose rates were measured behind configurations consisting of successive thicknesses of beryllium, water, and iron, using Loading No. 33 of the Pool Critical Assembly. The data is intended to assist in predicting the performance of nuclear instrumentation located outside the pressure shell of the High Flux Isotope Reactor.

1.3. TOWER SHIELDING REACTOR II OPERATION AND CALIBRATION

L. B. Holland, D. R. Ward, J. Lewin, V. R. Cain, J. H. Wilson, and J. L. Hull 9

The Tower Shielding Reactor II is being operated at powers to 100 kw (thermal) on a 24 hr per day basis. Various reactor shield configurations have been used during its operation. The accuracy of the measurements obtained has been steadily improved by modifications to instruments and techniques which have led to improved power linearity. A comparison method has been developed to determine the absolute reactor power at a relatively low level. Continuing studies of cooling water flow have resulted in improved baffle plate designs providing proper flow in both inner and annular fuel regions for high-power operation.

1.4. IN-AIR MEASUREMENTS OF RADIATION FROM THE TOWER SHIELDING REACTOR II (TSR-II)

F. J. Muckenthaler and L. B. Holland 22

Thermal-neutron fluxes, fast-neutron dose rates, and gamma-ray dose rates were measured in air at various distances from the TSR-II. The normally present shielding on the reactor was augmented by a specially designed shield, Cool-I, to produce desired changes in the leakage spectra. Reactor and detector heights were chosen to minimize contributions due to ground scattering, three 150-ft-high towers being constructed for detector placement at 467, 860, and 1100 ft from the reactor. Experimental dose rates were generally higher by factors of 20% to 50% than those predicted for infinite air media by calculations.

2. RADIATION DETECTOR STUDIES

2.1. THE FITTING OF INTERPOLATION FUNCTIONS TO SCINTILLATION SPECTROMETER PULSE-HEIGHT SPECTRA

R. W. Peelle, R. O. Chester, and F. C. Maienschein 29

A method of nonlinear least-squares estimation has been applied to the problem of interpolating between pulse-height spectra of monoenergetic gamma-ray sources to determine the details of the responses of pair, Compton, and single-crystal gamma-ray spectrometers. The method developed is quantitative and fully objective and permits the assignment of valid error estimates. Application to Compton spectrometer data resulted in essentially unique sets of parameters describing the amplitude and pulse-height dependence of the observation. Suggestions for reducing the cost of the procedure in manpower and computer time are given.

2.2. *UNSCRAMBLING OF SCINTILLATION SPECTRA*

W. R. Burrus 44

A study has been made of the problem of interpreting data from a scintillation spectrometer. A statistical confidence interval cannot be found for the differential energy flux of the incident particles, i.e., the average number of incident particles in an infinitesimal energy interval per unit energy. However, a statistical confidence interval can usually be found for the average number of incident particles in any finite width energy interval, or for physically significant quantities such as dose. It is shown that the problem of finding the best statistical confidence interval (the narrowest possible interval) is equivalent to solving a certain minimization problem. A FORTRAN computer program has been written to obtain the best statistical confidence interval for any linear function of the differential energy spectrum, but it has not been completely checked out.

2.3. *EXPERIMENTAL DETERMINATION OF FLUX DEPRESSION AND OTHER CORRECTIONS FOR GOLD FOILS EXPOSED IN WATER*

W. Zobel 52

The total correction required for the determination of the unperturbed thermal-neutron flux in light water by the use of gold foils has been evaluated. Flux depression factors obtained from experimental measurements with both square foils and circular foils have been compared to several theoretically derived recipes. Good agreement has been achieved with two of the theoretical methods.

2.4. *THE MODEL IV GAMMA-RAY SPECTROMETER: STATUS REPORT*

G. T. Chapman and K. M. Henry 55

The development of the Model IV "total-absorption" gamma-ray spectrometer has continued. After nearly nine months of use the composite NaI(Tl) crystal in the spectrometer shows no signs of deterioration of the cemented interface. A thorough study of backgrounds associated with the spectrometer has indicated that major contributions result from cosmic-ray interactions with the components of the spectrometer shield and from long-lived activity from isotopic impurities in the shield materials.

2.5. *SOLID-STATE FISSION DETECTORS*

T. A. Love and K. M. Henry 58

Experiments hopefully leading to the development of a small solid-state fission detector are in progress. The device is basically a silicon surface-barrier diode modified by the addition of a U^{235} foil. The sample devices first procured exhibited instabilities with total exposures of $\sim 10^8$ thermal neutrons. Efforts to improve reliability have resulted in satisfactory operation to integrated exposures of $\sim 10^{12}$ thermal neutrons. Various evidences of recovery of diodes made unstable by irradiation to high levels have been observed.

2.6. *SCINTILLATION RESPONSE OF ACTIVATED INORGANIC CRYSTALS TO VARIOUS CHARGED PARTICLES*

R. B. Murray and A. Meyer 62

This paper is an abstract of a paper published in *The Physical Review*.

2.7. *INTRINSIC LINE BROADENING IN NaI(Tl) GAMMA-RAY SPECTROMETERS*

C. D. Zerby, A. Meyer, and R. B. Murray 63

This paper consists of an abstract of a paper published in *Nuclear Instruments and Methods*.

2.8. *STUDIES OF THE SCINTILLATION PROCESS IN CsI(Tl)*

R. Gwin and R. B. Murray 63

The scintillation response of several CsI(Tl) crystals of varying thallium content to monoenergetic gamma rays and protons has been investigated. Particular attention was given to the effect of the pulse clipping time. An analysis of the data shows that the pulse height per unit energy is a function of the particle energy over the range of the experiments. The data provide a test of the theoretical model of the scintillation process in thallium-activated alkali halides proposed by Meyer and Murray.

2.9. *EFFECT OF DELTA RAYS ON RESPONSE OF INORGANIC SCINTILLATORS TO HEAVY IONS*

A. Meyer and R. B. Murray 74

Experiments with heavy ions indicate that the scintillation efficiency in activated alkali iodides is not a function of dE/dx alone, as was assumed in a model recently proposed, but instead is composed of a set of functions, one for each ion type. A calculation is described which considers the effect of delta rays produced by the primary particle. Preliminary results show qualitative agreement with experiment and predict the discrete nature of the scintillation efficiency for various particles.

2.10. *THERMAL-NEUTRON DENSITY PERTURBATIONS BY FOILS IN WATER*

S. A. Hasnain, T. Mustafa, and T. V. Blosser 78

A foil perturbation factor, defined as the ratio of the specific activation actually induced in a foil placed in a thermal-neutron flux to that which would be induced in an ideal, infinitely thin foil in the same location, has been experimentally determined. Factors are given for foils of gold, indium, enriched uranium, and copper over a wide range of thicknesses. All exposures were made in the thermal column of the ORNL Graphite Reactor. Two simple formulas to compute foil perturbation factors have been derived from the experimental data.

2.11. *DETERMINATION OF SMALL URANIUM CONTENT IN FOILS BY MEASURING INTENSITY OF NATURAL RADIATIONS*

S. A. Hasnain, T. Mustafa, and T. V. Blosser 95

A method has been developed which employs the natural gamma and X radiations emitted by uranium to give quick, accurate, and nondestructive measurements of the uranium content of small samples, such as foils, strips, and wires. It consists essentially in counting the natural radiation from a sample of unknown weight in a scintillation counter which has previously been calibrated against foils of known uranium content. Tests have indicated that the relative uranium content of a number of samples can be determined with an accuracy better than 1%; absolute weights depend on the accuracy with which the weights of the calibration sources are known.

2.12. *NEUTRON DISTRIBUTION IN A REACTOR FUEL PLATE*

S. A. Hasnain and E. B. Johnson 100

The neutron distribution through a PCA fuel plate and in the water spaces surrounding it has been studied by a fission-foil technique. A stack of ten 2-mil-thick foils rolled from fuel material and enclosed in 20-mil-thick aluminum cladding was inserted into a hole cut in a fuel plate, and other foils were placed in the adjacent water spaces. The reactor was run at low power for 1 hr, after which the foils were removed and counted for fission-product activity. The flux depression observed in the center of the fuel plate was somewhat greater than had been predicted by calculations.

2.13. *CALIBRATION OF A BF_3 PROPORTIONAL COUNTER IN WATER AND IN AIR*

T. Mustafa and T. V. Blosser 102

A highly sensitive BF_3 proportional counter, intended for use in studies of radiation leakage through biological shields of large reactors, has been calibrated in the thermal column of the ORNL Graphite Reactor. The accuracy of calibration was ensured by the use of parallel but independent methods insofar as possible. The calibrated value obtained for the counter in water is 275 counts/min per unit flux. The value obtained in air is 355 counts/min per unit flux. The difference is readily explained as the result of the different perturbations by the counter itself in the two media.

2.14. *DEVELOPMENT OF A LOW-LEVEL GAMMA-RAY DOSIMETER USING AN ANTHRACENE CRYSTAL*

T. Mustafa and T. V. Blosser 110

A gamma-ray dosimeter capable of measuring very low-level gamma-ray doses in a field of mixed radiation has been developed. The detector employed is a 1-in.-dia, ½-in.-thick anthracene crystal enclosed in Lucite which helps to balance electron loss due to leakage. A special pulse-counting technique is employed in conjunction with a transistorized integrator. The dosimeter can readily measure first-collision dose rate in tissue to within ±20% over a gamma-ray energy range from ~100 kev to 5 Mev. Neutron sensitivity is only about 2%. Dose rates as low as 0.03 mrad/hr can be measured.

2.15. *FAST-NEUTRON SPECTROSCOPY WITH SILICON SURFACE-BARRIER COUNTERS*
T. A. Love and K. M. Henry 116

Development of a neutron-sensitive semiconductor detector consisting of a thin layer of Li^6F sandwiched between two silicon-gold diodes for use in neutron spectroscopy has continued with current emphasis on developing methods for subtracting neutron-induced backgrounds. In the method which appears most promising, the barrier depths of Li^6F-coated and uncoated diodes, whose difference in response yields the background, are made equal by adjusting the bias voltage across the diodes to account for the difference in their resistivities. The data thus far indicate that for a fission spectrum the foreground-to-background ratio will be 5:1. The efficiency of the counter remains low (3×10^{-3} for thermal neutrons); however, measurements with 14.7-Mev neutrons show that for this energy the efficiency is improved approximately 100% when the plane of Li^6F is parallel rather than normal to the beam.

2.16. *THE DISTRIBUTION IN ENERGY OF ALPHA-TRITON PAIRS RESULTING FROM NEUTRON BOMBARDMENT OF LITHIUM FLUORIDE*
F. S. Alsmiller 119

The use of paired silicon-gold surface-barrier counters, with an intervening Li^6F layer, as fast-neutron spectrometers is discussed in the preceding paper. The problem of calculating the shape and width of the distribution in total energy of the alpha-triton pairs produced in a $Li^6(n, \alpha)T$ reaction and reaching the silicon was considered in a previous calculation. The analysis has now been generalized in two respects: first, the neutrons are not restricted to normal incidence, and second, the variation of the stopping power with energy over the path length of each particle is taken into account. The mathematical development is completed; numerical computations for a range of energies and angles of incidence are in progress.

2.17. *DETERMINATION OF SELF-SHIELDING FACTOR BY USING MULTIPLY STACKED FOILS*
S. A. Hasnain, T. Mustafa, and T. V. Blosser 123

Tight stacks of thin foils of gold and indium have been exposed to thermal-neutron fluxes in water and air in the thermal column of the ORNL Graphite Reactor. After exposure the stacks were separated and the foils individually counted, thus obtaining the specific activity of each foil as a function of its position in the stack and a measure of the self-shielding factor for the stack. Although the interpretation of the results has not been completed, the raw data is presented as tables and graphs.

3. CRITICAL EXPERIMENTS

3.1. *HOMOGENEOUS CRITICAL ASSEMBLIES OF 3% U^{235}-ENRICHED UF_4 IN PARAFFIN*
J. T. Mihalczo and J. J. Lynn 131

Critical parameters have been measured for a mixture of UF_4, enriched to 3 wt % in U^{235}, and paraffin, with a $H:U^{235}$ ratio of 133. Critical heights of rectangular, square-based parallelepipeds, both bare and reflected, are given as functions of the length of a side of the base. From these data the minimum critical volume for a bare sphere was determined to be 200 liters and for a reflected sphere 121 liters.

3.2. *CRITICAL PARAMETERS OF SOLUTIONS OF U^{235}-ENRICHED URANYL NITRATE IN CYLINDRICAL CONTAINERS*
J. K. Fox 131

Critical parameters have been measured for a solution of 93.15 wt % U^{235}-enriched $UO_2(NO_3)_2$ in a D_2O-H_2O mixture (70.1 wt % D_2O), contained in 40.0- and 50.8-cm-dia aluminum cylinders. For the 40.0-cm-dia cylinder, data are given for two conditions of lateral reflection as well as for the nominally unreflected case. Critical dimensions have also been obtained for a solution of 92.6 wt % U^{235}-enriched $UO_2(NO_3)_2$ in H_2O. This solution was contained in aluminum cylinders ranging in diameter from 24.1 to 38.1 cm, all nominally unreflected.

3.3. NUCLEAR SAFETY TESTS OF THE HIGH FLUX ISOTOPE REACTOR FUEL ELEMENT

J. K. Fox 133

A series of nuclear safety tests on the fuel element for the High Flux Isotope Reactor Critical Experiment No. 2 has been completed. The results show that handling the element, even in the presence of water, is safe. An investigation of the effects of voids introduced into the target region surrounded by the element was also carried out, yielding the critical height of water moderator and reflector for void fractions from 0.34 to 0.97.

3.4. HIGH FLUX ISOTOPE REACTOR CRITICAL EXPERIMENT NO. 2

D. W. Magnuson 136

A second series of critical experiments has been performed in support of the design of the High Flux Isotope Reactor (HFIR). The experimental assembly consisted of a mockup of the reactor, including its two cylindrical fuel annuli, central target region, water moderator and coolant, beryllium reflector, cylindrical control plates, and three beam tubes. A simulated nuclear target was also used. The experiments included control plate calibrations; measurements of the coefficients of reactivity for the temperature, fuel, and voids; and power and flux distribution measurements throughout the system.

3.5. CRITICAL ARRAYS OF NEUTRON-INTERACTING UNITS

L. W. Gilley, D. F. Cronin, J. K. Fox, and J. T. Thomas 159

Critical experiments have been performed with solutions of 92.6 wt % U^{235}-enriched $UO_2(NO_3)_2$ in water, at an average concentration of 410 g of U per liter. The solution containers consisted of two types of polyethylene bottles, having nominal volumes of 13 and 15 liters, respectively, and aluminum cylinders. The variables studied were volume content of the container, surface-to-surface spacing between containers, and the geometric pattern (square, linear, or triangular) within an array of containers. Other experiments evaluated effects of moderation and partial reflection or simulated environmental conditions of interest to nuclear safety. Results are presented as both tables and graphs.

3.6. NEW CRITICAL EXPERIMENT MACHINES

E. R. Rohrer, W. C. Tunnell, and D. W. Magnuson 168

Two newly built devices utilizing the split-table technique for combining subcritical amounts of fissionable material into critical assemblies are described. The first is a vertically operating device, while the second operates in a horizontal plane. Schematics and characteristic scram performance curves are given for both machines.

3.7. EQUIPMENT FOR TIME-DEPENDENT NEUTRON STUDIES AT THE CRITICAL EXPERIMENT FACILITY

D. W. Magnuson and J. T. Mihalczo 173

The Critical Experiment Facility has acquired a 150-kv positive-ion accelerator which is being used to produce 14-Mev neutrons by the $T(d, n)He^4$ reaction for use in time-dependent neutron studies. Burst widths of 1 to 10^4 μsec, with repetition rates of from 10 to 10^5 cycles/sec, are available with one method of operation, while a second method produces neutron bursts as short as 0.7 and 0.06 μsec. Background is less than 0.0001 of the rate when the beam is on target.

3.8. CRITICAL EXPERIMENTS AND CALCULATIONS ON THE ORNL FAST BURST REACTOR

W. E. Kinney and J. T. Mihalczo 174

This paper consists of an abstract of a paper which has previously been issued as a Laboratory memorandum (ORNL-CF-61-8-71).

4. EXPERIMENTAL NUCLEAR PHYSICS

4.1. NEUTRON CAPTURE CROSS SECTION OF GOLD AT 30 AND 64 kev

L. W. Weston and W. S. Lyon 177

This paper consists of an abstract of a paper published in *The Physical Review.*

4.2. NEUTRON RADIATIVE CAPTURE MEASUREMENTS

R. C. Block, F. C. VonderLage, and L. W. Weston 177

This paper consists of an abstract of a paper which has previously been issued as a Laboratory report (ORNL-3085).

4.3. THE MEASUREMENT OF α AS A FUNCTION OF ENERGY

G. de Saussure, L. W. Weston, J. D. Kington, R. D. Smiddie, and W. S. Lyon 177

Preliminary experiments leading toward a precise measurement of α, the capture cross section to fission cross section ratio, as a function of neutron energy have been completed. Determinations of α will be attempted at 30 kev, 65 kev, and over the range from 1 ev to 150 kev for the principal fissionable isotopes. A special fission chamber has been designed and tested, and various problems involving background radiation and counting techniques have been investigated. Special electronic circuitry has also been designed, built, and tested.

4.4. DEVELOPMENT OF A HIGH-EFFICIENCY FAST-NEUTRON DETECTOR

L. Weston and R. D. Smiddie 186

A high-efficiency, low-background, fast-neutron detector has been constructed. It is basically a proton-recoil detector using a 2-in.-dia, 2-in.-thick trans-stilbene crystal and a pulse-shape discrimination circuit. Tests indicate a detection efficiency of ~30% for fission spectrum neutrons with a discrimination against gamma rays of $\sim 10^4$.

4.5. SELECTION OF A LIQUID ORGANIC SCINTILLATOR FOR AN EXPERIMENTAL DETERMINATION OF α

L. Weston, W. S. Lyon, and J. D. Kington 187

Eleven organic scintillator solutions were tested by comparing relative pulse-height response to the 1.1-Mev gamma ray from Zn^{65}. The solution which appeared most promising for use in the experiments to measure α was triple-distilled xylene containing 4.0 g of *p*-terphenyl per liter, 0.3 g of POPOP per liter, 1 wt % gadolinium 2-ethyl hexoate, and 1 vol % ethyl alcohol.

4.6. FISSION GAMMA-RAY ENERGY RELEASE AS A FUNCTION OF TIME AFTER FISSION

F. C. Maienschein 189

Existing experimental and calculated fission gamma-ray energy release data are summarized and plotted as fission gamma-ray release per unit time, integrated over gamma-ray energy, as a function of time after fission.

4.7. USE OF 4π HIGH-PRESSURE IONIZATION CHAMBERS AS SECONDARY STANDARDS FOR CALIBRATION OF GAMMA-RAY SOURCES

R. W. Peelle 191

The efficiencies of the Compton and pair spectrometers used in a previously described measurement of the spectrum of prompt gamma rays from U^{235} fission are to be determined by the use of known-strength radioactive sources. The strengths of these sources were determined by measurement in two 4π high-pressure ionization chambers. Calibration of the absolute efficiences of these chambers was performed in a novel manner which permitted detailed estimates of precision to be assigned.

4.8. COLLIMATOR OPTIMIZATION FOR REACTOR GAMMA-RAY SPECTRA MEASUREMENTS

G. T. Chapman 197

A long, thin core of BSR-I fuel elements has been used to evaluate the influence of collimator design on gamma-ray spectra measured by the BSF Model IV spectrometer. A satisfactory optimization appears to be a relatively long lead collimator preceded by a 2- to 5-ft-long air-filled aluminum cone. With this arrangement the spectrometer can be successfully used at distances as short as 140 cm from the reactor. The cone is designed to include only the collimator solid angle.

5. EXPERIMENTAL REACTOR PHYSICS

5.1. *AN EXPERIMENTAL DETERMINATION OF THE AGE OF U^{233} FISSION NEUTRONS IN WATER*

T. V. Blosser and D. K. Trubey 203

The age to indium resonance energy (1.45 ev) of U^{233} fission neutrons in water has been experimentally determined. Methods and procedures followed those of previously reported U^{235} measurements. A preliminary value of the age, to which only geometric corrections have been applied, is 26.4 cm^2.

5.2. *CALCULATION OF THE TRANSMISSION FUNCTION FOR A NEUTRON CHOPPER*

V. V. Verbinski and J. D. Jarrard 204

Equations have been developed to describe the average transmission per burst and the pulse shape of a burst of neutrons for a neutron chopper consisting of a rotating wheel with slits. An IBM-7090 computer program was written to solve the equations numerically. The method is applicable to any slit shape which can be described in piecewise segments by simple mathematical expressions. A comparison with a previous analytic calculation for a special case showed agreement to better than ±0.1%.

5.3. *PULSED-NEUTRON MEASUREMENTS IN BERYLLIUM*

E. G. Silver and G. deSaussure 215

An attempt has been made to extend previously reported measurements of neutron diffusion parameters in beryllium to temperature regions between 25°C and −100°C, in order to verify published theoretical calculations predicting large changes in this region. It was found that previously unrecognized effects retard establishment of an equilibrium spectrum, thus changing the neutron decay from a single exponential to a decay with continuously changing slope. The present situation prohibits an assignment of unambiguous values to diffusion parameters under these conditions. Improvements to the time base analyzer used have permitted the determination of better values of previously reported room-temperature constants. An existing disagreement between Livermore and ORNL values of the diffusion cooling parameter remains unchanged after experiments with Livermore beryllium.

5.4. *A NOTE ON MEASUREMENTS OF DIFFUSION PARAMETERS BY THE PULSED-NEUTRON SOURCE TECHNIQUE*

G. deSaussure 223

A possible cause for the discrepancies between various measurements of the neutron diffusion cooling constant by the pulsed-neutron technique is presented. The diffusion cooling constant must be determined from the measurement of the asymptotic decay constant of the neutron population in small moderating assemblies. It is shown that under certain conditions this asymptotic decay constant may not be measurable. The effect is investigated in some detail for the case of beryllium.

5.5. *AN APPLICATION OF PILE NOISE ANALYSIS TO MEASUREMENTS OF KINETIC PARAMETERS OF A POOL-TYPE REACTOR*

M. N. Alam, A. Colomb, and K. M. Henry 228

An experiment to measure reactor kinetic parameters such as neutron generation time, temperature and void coefficients, etc. in a pool-type research reactor is in progress. The plan is to utilize the random neutron density fluctuations within the core as reactivity input signals and from them to deduce the reactor transfer function. Assembly, construction, and test of apparatus are essentially completed. No data have been taken.

6. NUCLEAR THEORY AND REACTOR PHYSICS CALCULATIONS

6.1. *A NONLOCAL POTENTIAL MODEL FOR THE SCATTERING OF NEUTRONS BY NUCLEI*

F. G. J. Perey and B. Buck 237

An energy-independent nonlocal optical potential model for the elastic scattering of neutrons from nuclei is proposed and solved numerically in its full integro-differential form. The parameters of the potential, obtained solely from the fitting of the experimental differential cross sections for lead at 7 and 14.5 Mev, were used unchanged to calculate the elastic differential cross sections, total and reaction cross sections, and polarizations on

elements ranging from aluminum to lead at various energies from 0.4 to 24 Mev. The same parameters were used to calculate the S-wave strength function and the effective scattering radius R'. In the usual notation the parameters are real potential V, 71 Mev; r, 1.22 fermi; a, 0.65 fermi; surface imaginary potential W, 15 Mev; a, 0.47 fermi; nonlocality β, 0.85 fermi; spin-orbit potential, using the nucleon mass in the Thomas form, U_{so}, 1300 Mev. Calculations were compared to experiment over the whole energy range, and the agreement was found to be comparable to to published energy-dependent local-potential results.

6.2. *AN AUTOMATIC PARAMETER SEARCH CODE FOR NUCLEAR REACTION CALCULATIONS*

F. G. J. Perey and B. Buck 250

The investigation of the applicability of any phenomenological model of a nuclear reaction depends to a large degree on the ability to find that region of parameter space which will give the best agreement with experimental data. As models become more complex or are extended to cover a wider range of experimental data, the increase in the number of parameters precludes a systematic investigation of the parameter space. A flexible, automatic parameter search code has been written for the IBM-7090 computer which will automatically adjust any combination of up to 15 parameters simultaneously to achieve the best agreement, in the least-squares sense, with the experimental data. The code has been applied successfully to the calculations described in Sections 6.1 and 6.2 of this report. An example of such an application is given.

6.3. *THE CALCULATION OF INELASTIC SCATTERING CROSS SECTIONS*

B. Buck 254

It has become evident in recent years that many inelastic scattering processes cannot be explained satisfactorily on the basis of the compound nucleus theory. The Distorted-Wave Born Approximation, a direct interaction theory approach, gives a good account of many inelastic reactions but breaks down when the interaction strength is not small. A strong-coupling theory has therefore been examined by construction of a pilot calculation to investigate the strong coupling of two nuclear levels, specifically, a ground state 0^+ and a first excited state 2^+. Coded for the IBM-7090 computer, the calculation gives the total absorption cross section, the total inelastic cross section, and the elastic and inelastic differential cross sections. If the incident particles are neutrons, the total nuclear and total elastic cross sections are also obtained. The code is operating successfully, and the results obtained to date appear to show good agreement with available comparison data.

6.4. *THE TDC PERTURBATION CODE*

W. E. Kinney and G. E. Whitesides 258

A Fortran code has been written to compute material replacement coefficients of reactivity and neutron lifetimes by perturbation theory. Fluxes from TDC, a two-dimensional, cylindrical (r, z) geometry, transport theory code, are used. The equation for the fractional change in the multiplication constant is given, input parameters are detailed, available output options are noted, and a sample page of output is shown. Finally, a graphical comparison of code results with experiment is shown, and a neutron lifetime computed by the code is compared with an experimentally determined lifetime in a similar but not identical fast assembly.

6.5. *ISOPERIMETRIC AND OTHER INEQUALITIES IN THE THEORY OF NEUTRON TRANSPORT*

L. Dresner 261

Some isoperimetric and other inequalities related to the one-velocity theory of neutron transport have been derived.

6.6. *SOME REMARKS ON THE EFFECT OF A NONUNIFORM TEMPERATURE DISTRIBUTION ON THE TEMPERATURE DEPENDENCE OF RESONANCE ABSORPTION*

L. Dresner 261

The influence of a nonuniform temperature distribution on the absorption of neutrons in a purely absorbing resonance of an isolated lump has been studied. It is shown that in practical situations the absorption depends only on the average temperature in the lump. (Abstract only)

6.7. *NUMERICAL CALCULATION OF THE EVAPORATION OF PARTICLES FROM EXCITED COMPOUND NUCLEI*

L. Dresner 262

A Monte Carlo program for the IBM-7090 has been written to analyze the evaporation of various nuclear fragments from highly excited compound nuclei. Only the emission of neutrons, protons, deuterons, tritons, He^3 nuclei, and alpha particles is considered.

7. REACTOR SHIELDING RESEARCH

7.1. *ENERGY AND ANGULAR DISTRIBUTIONS OF NEUTRONS PENETRATING SLABS OF DIFFUSING MEDIA. PART I: ENERGY SPECTRA*

V. V. Verbinski 265

Measurements of the spectra of neutrons through a medium of lithium hydride have included the following: leakage spectra from a slab of the material as a function of slab thickness and angle of escape, scalar flux spectra within the slab as a function of position, and spectra of the forward-directed component of neutron flux from the bottom of a re-entrant hole as a function of the material thickness. The energy range of the measurements was from about 0.01 ev to several hundred electron volts. The resulting experimental energy spectra in general agree with NIOBE calculations above 0.08 ev, the disagreement below this energy being attributed to the use of free-atom cross sections in the calculations; they also agree with O5R calculations except that the calculated curve rises above the measured curve below about 10 ev. Both the experiments and the calculations show that the neutron flux attains low-energy spectral equilibrium in a poisoned, hydrogenous medium after remarkably small penetration depths. In addition to the direct comparison of the calculations and experiments, the flux gradients from the NIOBE calculations have been used to relate the neutron flux leaking from a re-entrant hole in lithium hydride to the scalar flux at the bottom of the hole by a recently derived expression.

7.2. *ENERGY AND ANGULAR DISTRIBUTIONS OF NEUTRONS PENETRATING SLABS OF DIFFUSING MEDIA. PART II: ANGULAR DISTRIBUTIONS*

V. V. Verbinski 278

Angular distributions of low-energy neutrons emerging from slabs have been measured for the following media: (1) a non-slowing-down medium without capture (lead), (2) a non-slowing-down medium with capture (lead poisoned with B_4C), (3) a slowing-down medium with weak capture (water), (4) a slowing-down medium with intermediate capture (boric acid solution), and (5) slowing-down media with strong capture (methyl borate + methanol and lithium hydride). The results for media 1 and 2 agree with an analytical expression given by Case, de Hoffman, and Placzek, and those for media 3 and 4 with an expression derived by Fermi. The results for media 5 have been found to agree with a NIOBE code calculation except in the region below 0.1 ev where the free-atom cross sections used in the calculation are invalid. Both the measurements and the calculations indicate that the emergent angular distributions of low-energy neutrons attain equilibrium after a few centimeters of penetration for a hydrogenous medium with intermediate or strong capture.

7.3. *MONTE CARLO CALCULATION OF NEUTRON REFLECTION FROM WATER*

D. K. Trubey 288

Neutron histories generated by the O5R code have been processed to yield values of both the number and the energy reflection coefficients (albedos) for a 10-in.-dia monoenergetic beam of neutrons incident on a 42-in.-dia, 6-ft-long cylinder of water. Five source energies, ranging from 0.5 to 8 Mev, were considered and calculations were made both by statistical estimation and by analog methods. The results show good agreement with previously reported calculations utilizing similar assumptions concerning cross sections.

7.4. *THE CONDITIONAL MONTE CARLO METHOD APPLIED TO NEUTRON SCATTERING IN AIR*

W. E. Kinney and R. R. Coveyou 295

The applicability of the conditional Monte Carlo method to the calculation of neutron scattering in air has been evaluated by comparison with analog Monte Carlo age theory, and "moments" method calculations. Three forms of the function $f_n(\rho)$, which appears in the weighting factor for the conditional method, were tried — a collision age form, a group age form, and an exponential form. Computations of collision density as a function of radius by the various methods show a general failure of the conditional Monte Carlo method as higher orders of collision are approached. Analog Monte Carlo results, on the other hand, appear to agree with moments method calculations to distances of $\sim$8 mean free paths, and age theory results become valid after about 12 collisions.

7.5. MOMENTS METHOD AND NIOBE CALCULATIONS OF NEUTRON PENETRATION IN Be, BeO, LiH, AND OTHER MATERIALS

H. Goldstein 299

A study of neutron penetration in various reactor and shield materials has been carried out by NDA on subcontract with the Laboratory. The program consisted of extensive Renupak (moments method) and NIOBE code calculations for Be, BeO, and LiH and some additional calculations for D_2O, Fe, H_2O, and C. In addition, a few computations were carried out for specific shield configurations. Although the analyses are incomplete, it is expected that the data on Be and BeO, which includes information on ages, fast effects, flux spectra, and neutron dose, will provide a definitive picture of the neutron penetration in these materials. The calculated ages for Be and BeO are 69 cm^2 and 89 cm^2, respectively.

7.6. A RECALCULATION OF THE GAMMA-RAY ENERGY SPECTRUM OF THE BULK SHIELDING REACTOR I

G. T. Chapman 304

Newly available capture gamma-ray data and a more complete prompt-fission gamma-ray spectrum have been utilized to recalculate the gamma-ray spectrum of the BSR-I. In general the procedure followed that of previous calculations. The results of the calculation show essential agreement with previous estimates and a strong disagreement with experimental measurements, although the resemblance in shape is improved.

7.7. EXPERIMENTAL VERIFICATION OF A GEOMETRICAL SHIELDING TRANSFORMATION

L. Jung, F. J. Muckenthaler, J. M. Miller, and J. K. Grant 310

The geometrical transformation enabling dose rate due to a large disk to be inferred from data obtained with a smaller disk is being experimentally tested at the LTSF. Thermal-neutron fluxes from source disks with diameters of 7, 9.33, 14, and 19.80 in., which were simulated by cadmium irises placed adjacent to the 28-in.-dia LTSF source plate, are being measured and compared to predictions based on standard transformations. The experimental work is complete, and the analysis is in progress.

7.8. A GENERAL-PURPOSE MONTE CARLO GAMMA-RAY CODE

S. K. Penny 314

A general Monte Carlo code is being written for the purpose of studying the transport of gamma rays. It is presently being "debugged" on the IBM-7090 computer.

7.9. THE DIFFERENTIAL ENERGY AND ANGULAR SPECTRA OF NEUTRONS FROM A POINT ISOTROPIC SOURCE IN INFINITE GEOMETRY

H. E. Stern, R. E. Maerker, and D. K. Trubey 314

The Monte Carlo technique of statistical estimation has been applied to the calculation of differential energy and angular spectra, angular collided dose rates, and total dose rates from a point isotropic 8-Mev source of neutrons in an infinite medium of hydrogen of density 0.111 g/cm^3. A comparison of the results with moments method data shows reasonable agreement for source-detector separation distances of up to 60 cm.

7.10. DESIGN OF A WINDOW FOR A HOT CELL

J. M. Miller and F. J. Muckenthaler 318

Preliminary experiments leading to the design of a hot cell window for the Transuranium Processing Facility have been completed at the Lid Tank Shielding Facility (LTSF). Neutron removal cross sections were measured for two commercially available glasses and compared to calculations based on analyses of the glasses. The commercial glasses were mocked up with ordinary plate glass and lead slabs to give an equivalent neutron removal cross section, and these mockups were then used in various configurations with water in order to optimize the design of the window. Oil will be used instead of water in the actual window. A full-scale mockup of the design resulting from the preliminary experiments is now being tested at the LTSF.

8. SHIELDING AGAINST HIGH-ENERGY RADIATIONS

8.1. *INTRANUCLEAR CASCADE CALCULATION*

H. Bertini 323

The completion of a previously described Monte Carlo program intended to calculate the types, energies, and direction cosines of the cascade particles resulting from the interactions of high-energy particles incident on complex nuclei has been delayed by various difficulties due to machine changes, etc. A new sampling technique has been substituted for the scheme originally used, eliminating a need for using estimated average cross sections. Some preliminary problems, encompassing incident proton energies of from 82 to 426 Mev, have been run and are compared with available experimental data.

8.2. *EXPERIMENTAL SPACE VEHICLE SHIELDING PROGRAM*

W. A. Gibson, W. R. Burrus, and T. A. Love 325

In order to investigate the problems involved in shielding a space vehicle from the protons found in the Van Allen belts and solar emissions, an experimental program has been initiated to study the secondary particles emerging from shields bombarded by high-energy protons from cyclotrons. Intensity, angular distribution, and spectral measurements will be undertaken on the secondary neutrons, protons, and gamma rays. Dosimeter measurements will also be made. The instrumentation for the neutron measurements is discussed. In order to cover the energy range from 50 to 700 Mev, cyclotrons at different laboratories will be used.

8.3. *ELECTRON-PHOTON CASCADE SHOWERS*

C. D. Zerby and H. S. Moran 329

A general-purpose electron-photon cascade calculation, using the Monte Carlo technique, has been programmed for the IBM-7090 computer. The calculation is designed to investigate cascade showers in the energy range from 6.5 Mev to 50 Gev and yields information on track length, flux, probability of finding n particles at various depths, and energy deposition. Thus far, some data on copper, water, iron, and lead are available.

8.4. *TRANSVERSE SHIELDING CALCULATION FOR A 45-Bev ELECTRON ACCELERATOR*

R. G. Alsmiller, Jr., and F. S. Alsmiller 339

An approximate cascade calculation is being carried out to provide a check on other estimates of the thickness of earth shielding required for the accelerator tube of the proposed 45-Bev Stanford electron accelerator. A straight-ahead approximation results in a set of coupled integrodifferential transport equations which give the neutron, proton, charged pion and muon fluxes as functions of energy and distance. Because of the limited experimental information available concerning high-energy interactions, major reliance has been placed upon cosmic-ray data. An IBM-7090 code has been written to solve the transport equations numerically. The equations and the code are not uniquely restricted to the Stanford problem, and are expected to be of value in the solution of other high-energy shielding problems.

9. PLASMA PHYSICS THEORY

9.1. *INSTABILITIES IN A HOMOGENEOUS, ANISOTROPIC PLASMA*

Y. Shima 345

This paper consists of an abstract of a paper which has previously been issued as a Laboratory memorandum (ORNL-CF-61-7-69).

9.2. *A RECALCULATION OF THE H^3 BREEDING RATIO IN A STELLARATOR BLANKET*

W. E. Kinney 345

This paper consists of an abstract of a paper which has previously been issued as a Laboratory memorandum (ORNL-CF-61-6-63).

9.3. *PLASMA STABILITY ANALYSIS EMPLOYING EQUILIBRIUM CONSTANTS OF MOTION*

T. K. Fowler 345

This paper consists of an abstract of a paper which has previously been issued as a Laboratory report (ORNL-3123).

9.4. "NEGATIVE MASS" INSTABILITY IN DCX-1

T. K. Fowler 346

This paper consists of an abstract of a paper which has previously been issued as a Laboratory memorandum (ORNL-CF-61-7-1).

9.5. ENERGY DISTRIBUTIONS OF PARTICLES IN DCX

T. K. Fowler and M. Rankin 346

This paper consists of an abstract of a paper which has previously been issued as a Laboratory report (ORNL-3161).

9.6. EFFECT OF ENERGY DEGRADATION ON THE CRITICAL CURRENT IN AN OGRA-TYPE DEVICE

T. K. Fowler 346

This paper consists of an abstract of a paper which has previously been issued as a Laboratory report (ORNL-3037).

9.7. STABILITY OF PLASMAS AGAINST ELECTROSTATIC PERTURBATIONS

T. K. Fowler 347

This paper consists of an abstract of a paper which has previously been issued as a Laboratory report (ORNL-3162).

9.8. DISSOCIATION OF THE H_2^+ MOLECULE BY ELECTRONS AND PROTONS

R. G. Alsmiller, Jr. 347

A formalism introduced by M. Gryzinski for calculating the ionization and excitation of atomic systems by charged-particle impact has been used to calculate the total cross section for the dissociation of the H_2^+ molecule by electrons and protons. The results are compared with Born approximation results.

9.9. FOKKER-PLANCK COEFFICIENTS FOR A PLASMA INCLUDING CYCLOTRON RADIATION

A. Simon and N. Rostoker 349

Previous derivations of the Fokker-Planck equation from the Liouville equation have been extended to include the complete electromagnetic field and a constant magnetic field. The rate of cyclotron radiation predicted in the limit of low plasma density, that is, in the limit $k \gg \omega_p/c$, agrees with the vacuum radiation formula of Trubnikov.

9.10. CONCERNING A POSSIBLE APPROACH TO THE MODE I–MODE II TRANSITION PROBLEM

G. Guest and A. Simon 350

An attempt has been made, following the method of Kadomtsev and Nedospasov, to analyze the Mode I–Mode II instability in terms of a simple model of the gaseous arc discharge in a uniform longitudinal magnetic field. The essential features of the model are the inclusion of streaming effects to the end walls as utilized by Simon and the neglect of lower order terms in the transverse motion of charged particles due to electrostatic fields.

9.11. ELECTROSTATIC ION-CYCLOTRON PLASMA INSTABILITIES IN A TWO-FLUID HYDRODYNAMIC THEORY

H. K. Wimmel 350

This paper consists of an abstract of a paper which has previously been issued as a Laboratory report (ORNL-3170).

Part 1

RESEARCH FOR LIGHT-WATER-MODERATED REACTORS

1.1. THE REACTIVITY EFFECT OF AN AIR-FILLED CAVITY WITHIN A POOL CRITICAL ASSEMBLY CORE

E. B. Johnson

A previous investigation[1] of the effect of air voids on the reactivity of pool-type reactors indicated that positive void coefficients existed in the over-moderated rod well of a Bulk Shielding Reactor I control-rod element centrally located in a critical core. In these measurements the air volume was defined by an aluminum box attached to an aluminum positioning tube. Since the presence of the aluminum changed the metal-to-water ratio in the core, the measurements have now been extended to include reactivity effects of an air volume defined by a Lucite (methyl methacrylate) box.

For these measurements, an array of BSR-I fuel elements similar to that used in the earlier work was loaded in the Pool Critical Assembly (PCA) as shown in Fig. 1.1.1. The test cell was a standard control-rod element located in grid position D-~~6~~ 35, essentially in the center of the core. A Lucite box enclosing an air volume of 5 in.^{3} (4 in. long, 2 in. wide, and $\frac{5}{8}$ in. thick) was positioned at various locations above and below the horizontal midplane of the fuel by a Lucite rod. The vertical traverses were made with the plastic box filled with air and again with the box filled with water. The changes in reactivity observed during each of these traverses are plotted as functions of the position of the center line of the box relative to the center line of the fuel in Fig. 1.1.2. Also shown is the difference curve representing the effect of the air volume alone. For comparison, the difference curve obtained during the earlier experiment is also shown. Although the two curves differ in magnitude, both indicate the existence of a positive void coefficient of

[1] K. M. Henry, E. B. Johnson, and J. D. Kington, *Applied Nuclear Phys. Ann. Prog. Rep., Sept. 10, 1956*, ORNL-2081, p. 10.

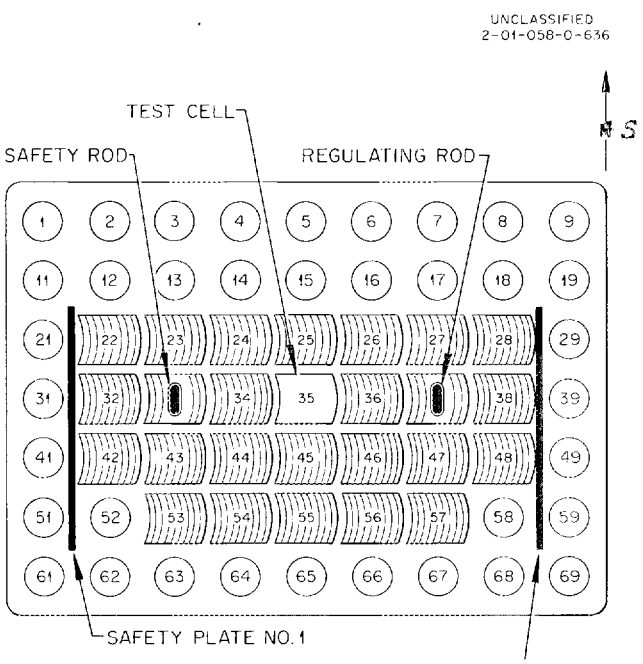

Fig. 1.1.1. Pool Critical Assembly Loading No. 36 (BSR-I). (BSR-I ELEMENTS)

Add note below title as follows:

Note: The curvature of the fuel elements shown in this figure is incorrect. The elements should be rotated 90 deg to the left.

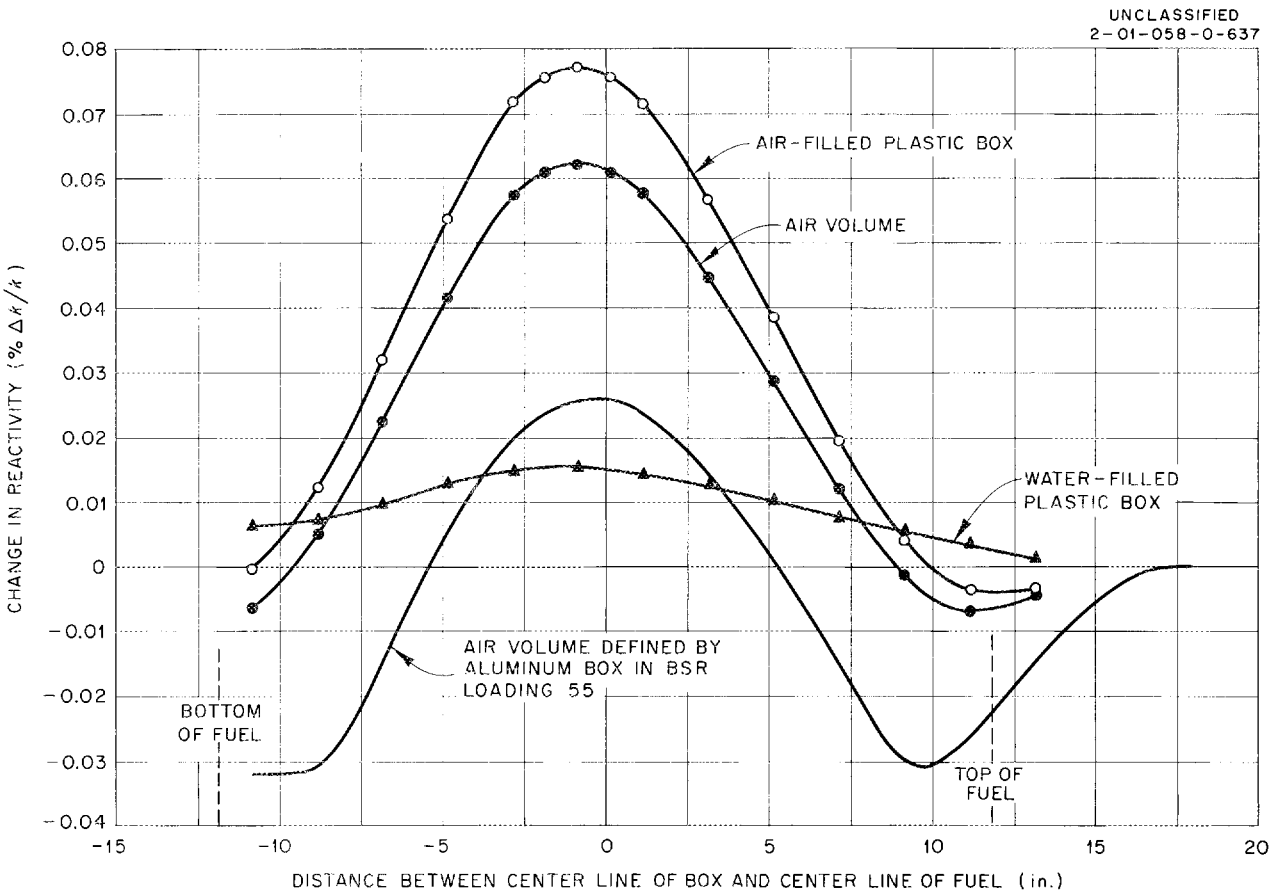

Fig. 1.1.2. Reactivity Changes Produced by the Presence of an Air-Filled and Water-Filled Lucite Box at Various Positions in the Rod Well of a BSR-I Control Rod Element.

reactivity around the reactor center line in the control-rod well. The disagreement in shape between the two difference curves, however, is not readily explainable.

The largest single source of uncertainty in these data is that due to the error in the delayed-neutron data of Keepin[2] used in the inhour equation to compute reactivity. This error is given as ±3.2%. Random errors in period measurements (±2%) and the uncertainty in the appropriate effective delayed-neutron fraction (±2.5%) result in a probable cumulated error of ~ ±5% in the present measurements.

[2]G. R. Keepin, T. F. Wimett, and R. K. Ziegler, *J. Nuclear Eng.* **6**, 1 (1958).

1.2. CENTER LINE ATTENUATION MEASUREMENTS OF RADIATION FROM A BERYLLIUM-REFLECTED POOL CRITICAL ASSEMBLY

E. B. Johnson

The ORNL High Flux Isotope Reactor (HFIR), a beryllium-reflected, water-moderated plate-type reactor, is to be enclosed in a water-filled steel pressure shell, and the major portion of the nuclear in-

strumentation will be located outside the shell.[1] In order to assist the Instrument and Controls Division in predicting the performance of instrumentation in such a location, measurements of the attenuation of thermal neutrons and gamma rays from the Pool Critical Assembly (PCA) by successive thicknesses of beryllium, water, and iron have been completed.

The reactor configurations which were used are shown in Fig. 1.2.1. The fuel elements were arranged in as close an approximation to the proposed cylindrical geometry of the HFIR as was possible with BSR-type elements in a critical array. Beryllium oxide reflector elements were used on two sides of the fuel

[1] T. E. Cole, *High Flux Isotope Reactor – A General Description*, ORNL-CF-60-33-33 (March 15, 1960).

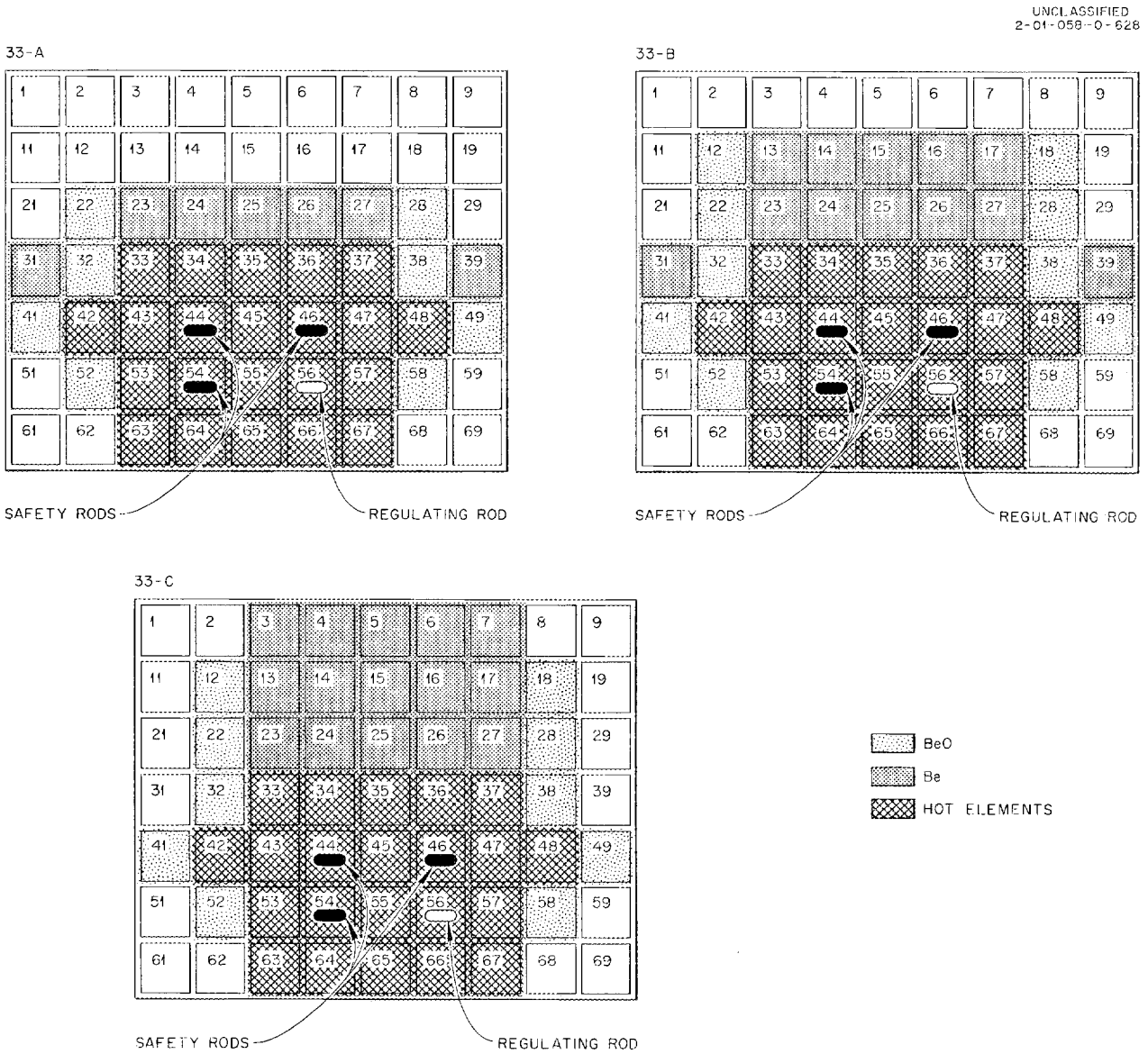

Fig. 1.2.1. Loadings Nos. 33A, 33B, and 33C of the Pool Critical Assembly.

region to prevent direct radiation from the core from reaching the detectors. Three different thicknesses of beryllium reflector were used across the south face of the fuel region. The primary interest was in Loading No. 33C, which had three rows (~9 in.) of beryllium, since this was the thickness specified for the HFIR reflector; however, in order to determine the effect of the beryllium thickness on thermal-neutron and gamma-ray attenuation, measurements were also made with two rows (Loading 33B) and one row (Loading 33A) of beryllium. Thermal-neutron flux and gamma-ray dose-rate measurements were made in the pool water behind each of these configurations. In addition, the thermal-neutron flux was measured through the beryllium layer and into the fuel region with calibrated gold foils. Following the completion of the water attenuation curves, an iron slab 3 in. thick and 4 ft by 3.5 ft in area was positioned 25.75 in. from the south face of the beryllium of Loadings 33B and 33C in order to determine the effect of the presence of the HFIR pressure shell on radiation levels. All measurements were made along the north-south center line of the reactor.

The thermal-neutron flux in water was measured with a small spiral U^{235} fission chamber. The resulting curve was normalized to the flux measured at three positions with thin U^{235} foils, which were prepared and calibrated by T. V. Blosser.[2] Since it was considered unnecessary to determine the integrated power level of the reactor, all measurements were arbitrarily adjusted to $\phi_{th} = 1.0$ at the fuel-reflector interface.

The gamma-ray dose rate was measured with a calibrated 50-cc spherical ionization chamber[3] which was positioned at known distances from the reactor. Because of the relatively high gamma-ray background, it was necessary to measure the background attenuation curve for each reflector configuration with the reactor shut down and to subtract this curve from that obtained with the reactor critical.

The thermal-neutron flux is plotted in Fig. 1.2.2 as a function of distance from the fuel-reflector interface. The slope of the curves became progressively smaller as the beryllium thickness was reduced, approaching that of the curve measured from a BSR water-reflected loading.[4] The neutron flux measured behind the iron slab showed a moderate increase over that measured without the slab and a somewhat steeper slope.

The errors associated with these data are primarily due to an uncertainty of about ±5% in the thermal-neutron flux at the core-reflector interface. The probable error in the flux measured with the thin U^{235} foils, to which the fission chamber data was normalized, is not greater than ±2%.

It should be noted that the ~5% uncertainty in the thermal-neutron flux in effect simply shifts all data upward or downward. The internal consistency of the measurements, however, is essentially good; thus the shapes of the curves are reliable within narrow limits.

The gamma-ray dose rate is plotted in Fig. 1.2.3 as a function of distance from the fuel-reflector interface. These curves were normalized by the same factor as that required for the corresponding thermal-neutron attenuation curves. The gamma-ray attenuation from a water-reflected reactor[4] (BSR Loading No.

[2] T. V. Blosser, unpublished work.

[3] J. D. Kington and R. K. Abele, *Appl. Nuclear Phys. Ann. Prog. Rep., Sept. 1, 1957*, ORNL-2389, p. 260.

[4] F. C. Maienschein *et al.*, *Attenuation in Water of Radiation from the Bulk Shielding Reactor: Measurements of the Gamma-Ray Dose Rate Fast-Neutron Dose Rate and Thermal-Neutron Flux*, ORNL-2518 (July 7, 1958).

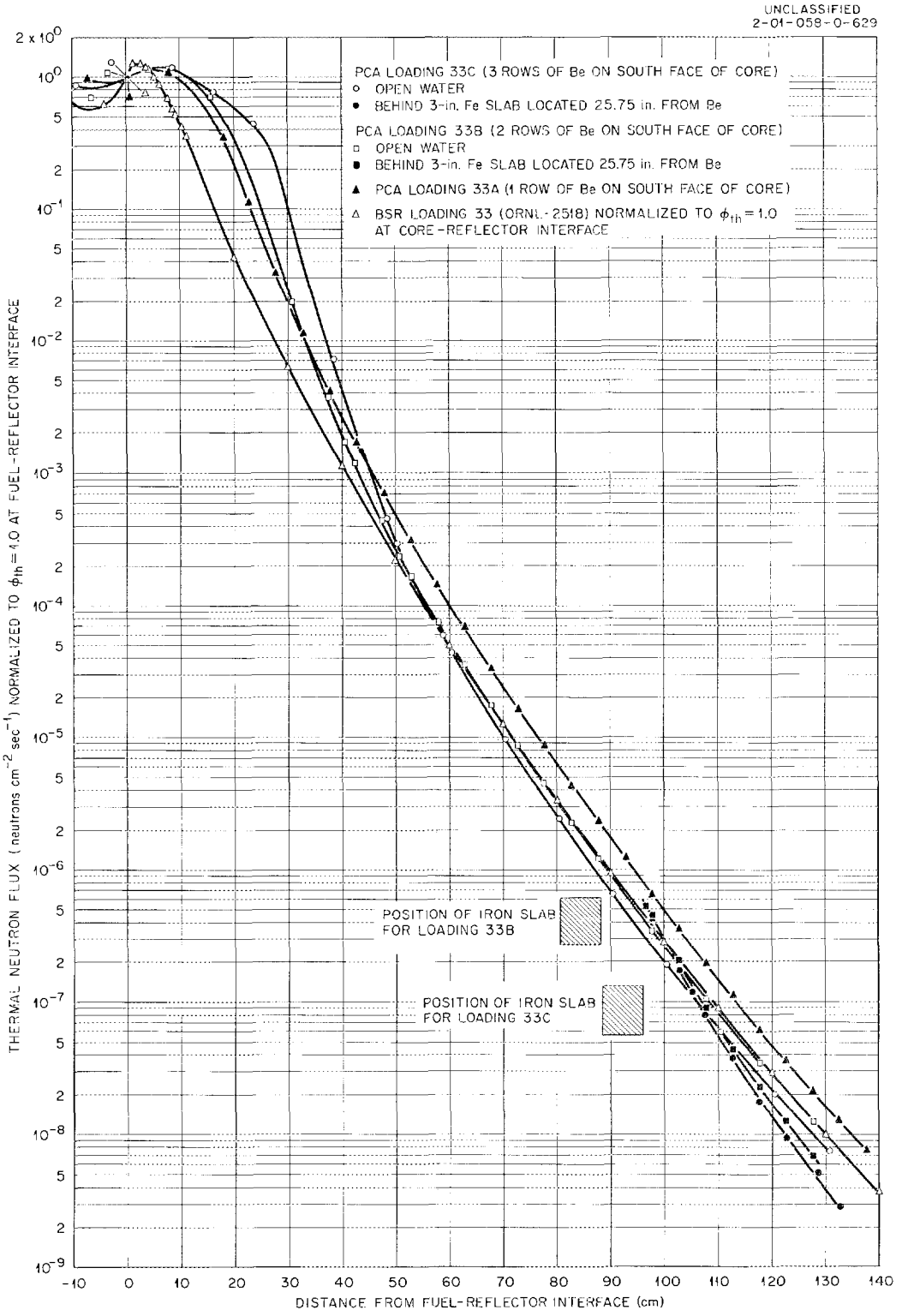

Fig. 1.2.2. Thermal-Neutron Flux as a Function of Distance from the Fuel-Reflector Interface.

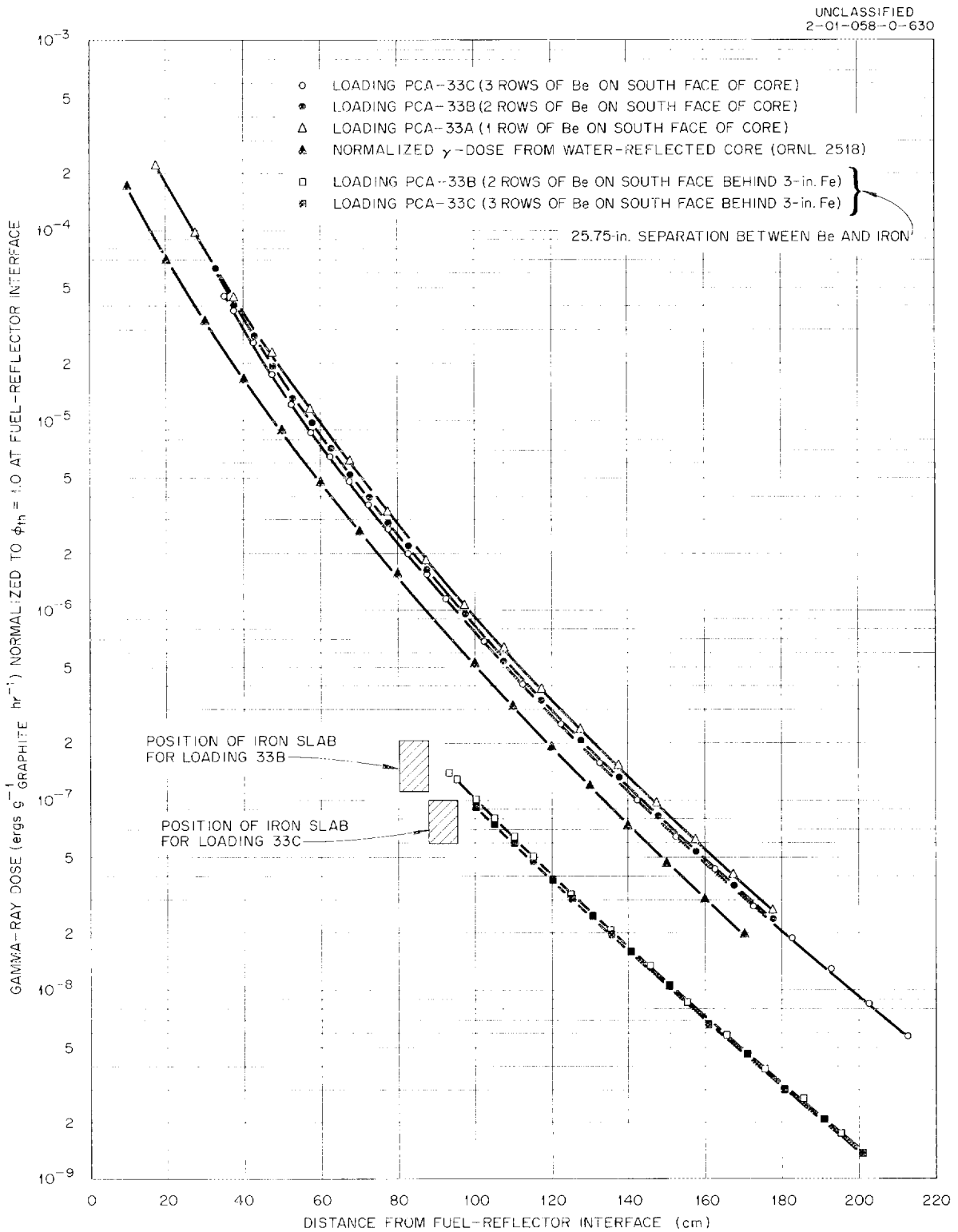

Fig. 1.2.3. Gamma-Ray Dose Rate as a Function of Distance from the Fuel-Reflector Interface.

33) is also shown for reference. It will be noted that the slopes of these curves are essentially the same and that the magnitudes increased slightly as the beryllium reflector thickness was reduced. The introduction of the iron slab resulted in a reduction in dose by a factor of about 7.5 at 120 cm and a slight hardening of the spectrum behind the iron.

The errors associated with these data are due to the previously noted uncertainty of about 5% in the thermal-neutron flux at the fuel-reflector interface and to a probable error of about ±5% in the measured dose.

The fact that the magnitudes of the measured doses from the water-reflected core (BSR Loading 33) and the beryllium-reflected loadings are different is not surprising because the leakage flux from the two cores was obviously not the same.

1.3. TOWER SHIELDING REACTOR II OPERATION AND CALIBRATION

L. B. Holland D. R. Ward J. Lewin
V. R. Cain J. H. Wilson[1] J. L. Hull

Preliminary experiments with the Tower Shielding Reactor II (TSR-II) have previously been described.[2] During the past year the completely assembled reactor, including control systems and cooling systems, has been checked out, and the reactor is being operated at powers to 100 kw (thermal) on a 24 hr per day basis. The reactor has been used with no shield external to the pressure vessel, with an asymmetric shield for measurements required by the now-abandoned Aircraft Nuclear Propulsion program, and with two nesting, lead-water shields (designated as COOL-I and COOL-II) designed to provide spectrum changes for experiments reported elsewhere.[3]

During the operation of the reactor, power linearity has been improved, a comparison technique has been developed to measure absolute reactor power, and studies leading to improved coolant circulation have been carried out.

Power Linearity

For a reactor system which is to be used as a source for shielding studies, it is important that the relation between the actual power generated within the reactor to the power reported by the reactor instrumentation be linear over the entire range of useful powers. Three aspects of this problem have been studied during operation of the TSR-II. They are separately discussed below.

Regulating Rod Position. – The power level in the TSR-II is routinely held at a predetermined value by manual or servo rod adjustments based on the current output of neutron-sensitive ionization chambers located within the pressure vessel. Because of their location, these chambers cannot be calibrated. Other

[1]On loan from Lockheed Aircraft Company, Marietta, Georgia.

[2]L. B. Holland *et al.*, *Neutron Phys. Ann. Prog. Rep., Sept. 1, 1960*, ORNL-3016, p. 42.

[3]Section 1.4 of this report.

calibrated ionization chambers are positioned at a fixed distance from the reactor and monitor the leakage radiation from the reactor shield. During the first series of experiments performed with the TSR-II, variations in leakage were noted from run to run, even though the reactor was supposedly at the same power. Measurements were then made of the leakage radiation as a function of regulating rod position, with the results shown in Fig. 1.3.1. In obtaining these data the reactor power was maintained at a nominal 10 kw by shim rod adjustment as the regulating rod position was changed. A total of 0.178 in. movement of the shim rods was required for a change in the regulating rod position of 1.6 in. The evident strong influence of regulating rod position on leakage flux stems from the rod location within the reactor, since it depresses the flux in the core region nearest the ionization chambers which set the reactor power level. Variation in shim rod position should not produce such effects. Therefore, while data is being taken, the regulating rod is now routinely held in the range of 0.9 to 1.1 in. withdrawn from the core. This confines the variation in leakage to ± 1.0%.

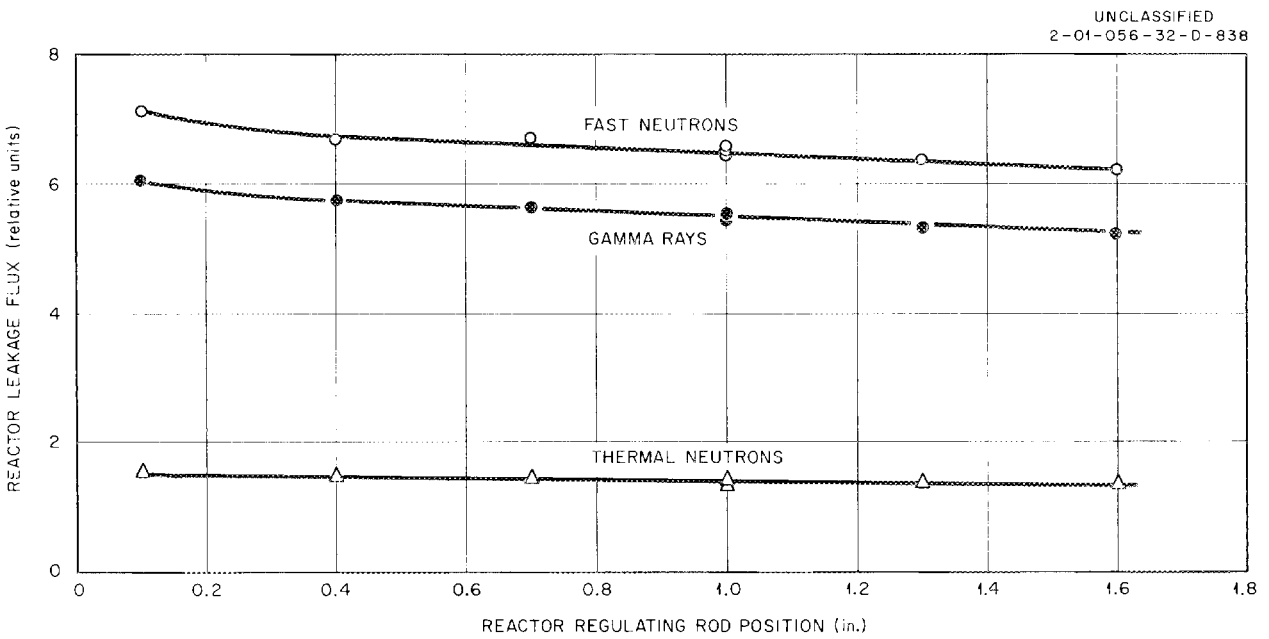

Fig. 1.3.1. Leakage Flux from the TSR-II in Cool-II Shield as a Function of Regulating Rod Position.

Instrument Modification. – A second source of difficulty in obtaining power linearity was also discovered in early experiments with the TSR-II. This difficulty was due to the nonlinear response of the micromicroammeter in the instrumentation channel controlling the reactor power. Variations of the order of ±5.5% were observed. The manufacturer's specification had claimed an accuracy of ±2% on ranges above 10^{-7} amperes and ±4% on lower ranges, both values being somewhat high for satisfactory use in the present application. Modifications have been made to this instrument which have resulted in reducing the nonlinearity error to less than ± 1%. The performance of the instrument before and after modification is compared in Fig. 1.3.2.

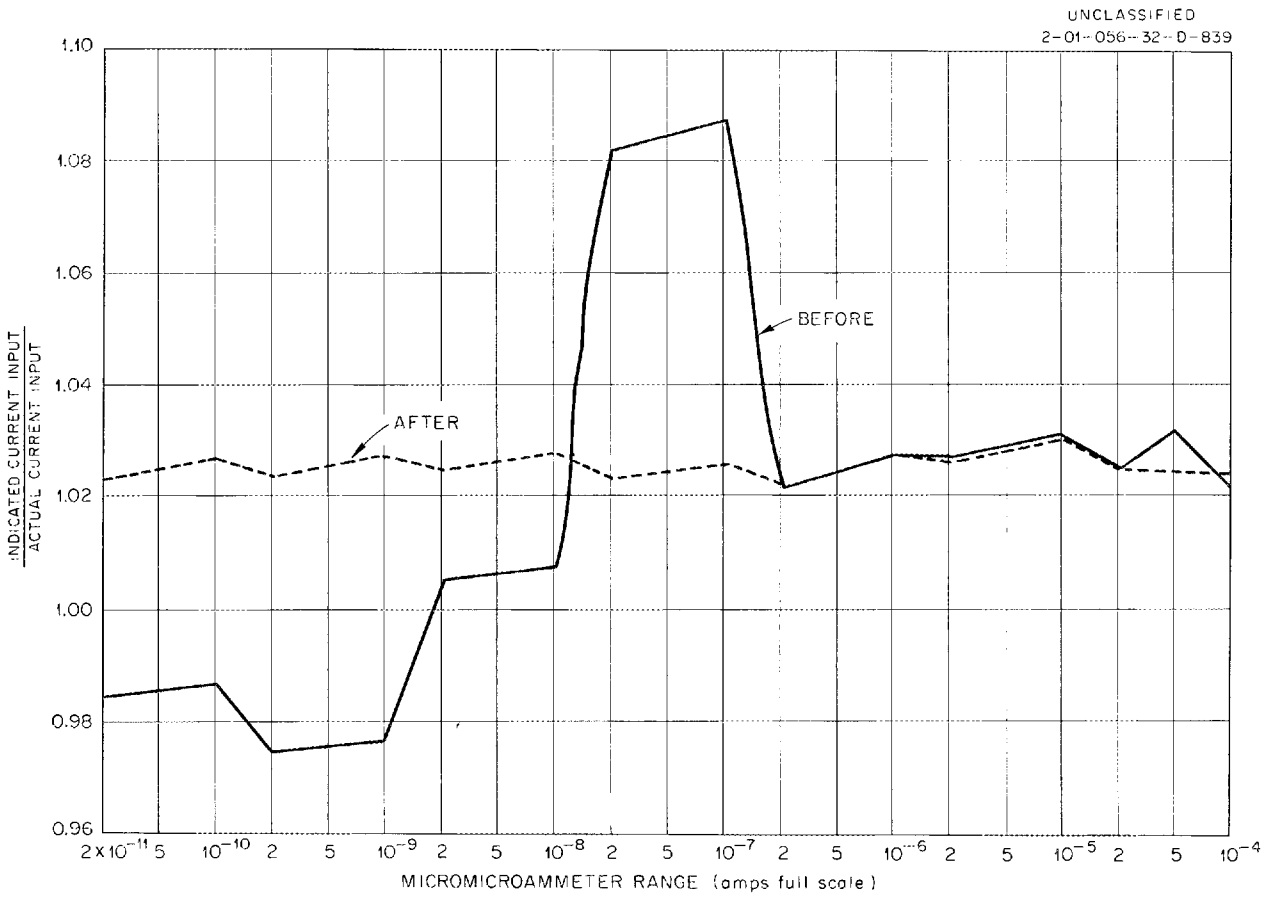

Fig. 1.3.2. Ratio of Indicated Current to Actual Current on Keithley Model 411 Micromicroammeter as a Function of Range Setting: Comparison of As-Received Performance with Performance after Modification.

Gamma-Ray Compensation of Ionization Chambers. – For a fission source the gamma-ray decay at reactor shutdown differs from the neutron decay. It is therefore important that the ionization chambers which control the reactor power level be insensitive to changing gamma-ray fields. In the TSR-II the effect of gamma rays is reduced by the placement of 12 in. of lead between the core and the chambers. The gamma-ray compensation of the chambers was checked by placing detectors to monitor the leakage radiation from the reactor and increasing the reactor power in steps from 2 watts to 100 kw, then returning it to 2 watts in similar steps. Had any significant gamma-ray effect existed, the monitors would have shown a difference in the leakage level observed for any pair of up versus down steps. Since the levels remained the same, it is concluded that the 12-in. lead protection is adequate for operation at powers below 100 kw.

Power Calibration

Principle of Calibration. – The absolute power determination for the TSR-II at its design power of 5 Mw will employ the conventional method of measuring the rate of cooling water flow and its temperature rise as it flows through the reactor. Heat losses can be calculated and the power determined from

the corrected data. The present operation of the TSR-II at powers less than 100 kw, however, does not lend itself to the above method. A technique was therefore developed in which the rate of heating of the water in the pressure vessel at a nominal reactor power of 40 kw is compared to the rate of heating by an electric heater rated at 40 kw. The electric power input to the heater can be measured accurately, and if losses are minimal the change in system temperature as a function of time is directly related to the power input by $P_h = K\, dT/dt$. Since the system constants, except for losses, are essentially the same for heating by the reactor, the reactor power is related to the heater power by

$$\frac{P_r}{P_h} = \frac{(dT/dt)_r}{(dT/dt)_h},$$

where the subscripts r and h identify reactor and heater terms.

In practice, if environmental conditions are held identical for the two heatings, the only losses which need be considered are electrical line loss and heat loss from the water as it moves from the electric heater to the reactor core. Line loss can be calculated, and heat loss can be minimized by proper choice of water flow rates. To further reduce possible error, the comparison between temperature changes in the system due to electric and reactor heat, respectively, is made at the temperature where the heat gain from pumping power is equal to the heat loss from the system.

Physical Arrangement. – The physical arrangement for the calibration is diagrammed in Fig. 1.3.3. The water cooling system and the shim pump lines are disconnected from the reactor. A gasoline motor-driven pump is connected so that it will take water from the reactor outlet at a rate of 200 gpm and circulate it through a 440-v, three-phase electric heater rated at 40 kw and thence into the reactor pressure vessel. A portion of the discharge from this pump is also fed to two Roth turbine pumps, connected in parallel, which supply high-pressure water to operate the shim-safety rods. Copper-constantan thermocouples are placed in the reactor exit lines and in any shields placed around the reactor. Ammeters, voltmeters, and wattmeters, all standardized, are connected to measure the power input to the heater, and a recording wattmeter is included to detect possible power changes occurring between readings on the standardized instruments.

Procedure. – Water, usually taken from the reactor pool, is first flushed through the modified system until a desired temperature, well below ambient, is reached. The exit standpipe valve is then opened and the water allowed to drain to the level of the valve, a procedure which ensures that exactly the same volume of water is contained in the system for all calibrations. The valve is then closed.

The water is then electrically heated, with both circulating pump and shim pumps running, until an equilibrium temperature is found such that the heat input from the pumps equals the losses from the system. This temperature is noted, and the system drained and refilled with cool water to begin the calibration run.

Before starting a heater or reactor run, pumping is begun and measurements are made of the water temperature as a function of time, in order to verify that the heat input from the pumps is approximately correct. Then the heater is turned on, the electrical power input to the heater is monitored, and thermocouple readings are made as a function of time. When the water temperature exceeds the previously noted equilibrium

temperature by ~ 10°F, the heater is shut off and the heat loss from the system is followed as a function of time long enough to detect any abnormalities.

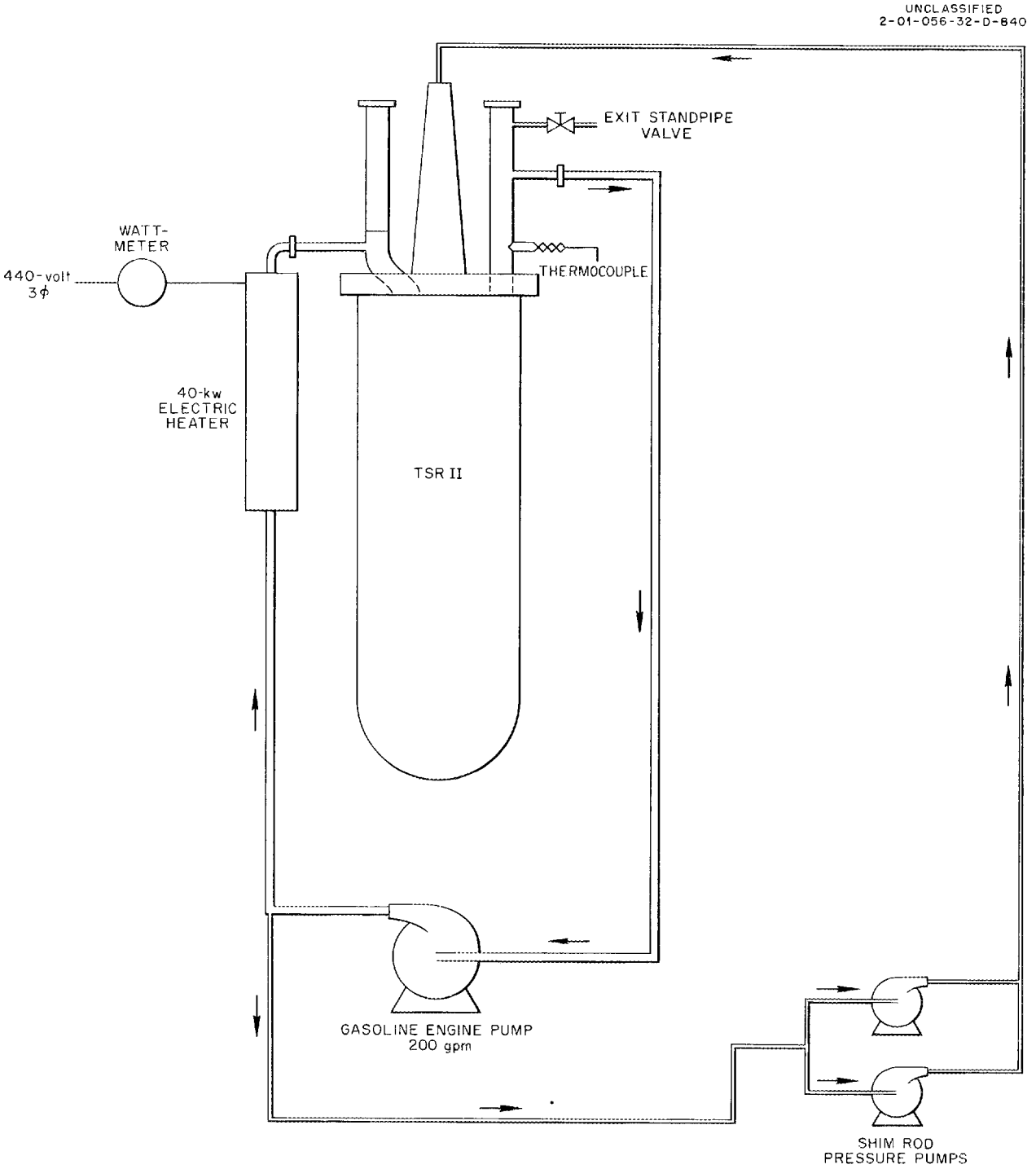

Fig. 1.3.3. Functional Arrangement for Heat Power Calibration of the TSR-II at Low Powers.

The system is then flushed and the run repeated with the reactor operating. During the reactor run the regulating rod is held in the range from 0.9 to 1.1 in. to minimize the effect of variations in its position on reactor power, as discussed previously. The reactor normally is suspended 6 ft above the ground. Calibrated ionization chambers are placed at a fixed distance from the reactor to observe the change in radiation leakage as the temperature of the water in the system increases.

The nominal power of the reactor may differ from the actual power determined by the calibration run. An adjustment is then made upon the demand setting of the servo amplifier to give the desired power, with the change in leakage observed by the monitors being noted to ensure that the change is made correctly.

The reactor power is calibrated in the above manner at the beginning and near the end of a particular experiment or whenever the reactor shield is changed. The power may be checked at any time by replacing the reactor in the position where the calibration runs were made and checking the leakage radiation with the monitor chambers.

The neutron leakage decreases linearly with system temperature increase during a calibration run, as shown in Fig. 1.3.4. Because of decreased water density, an increase in temperature permits a greater number of thermal neutrons to reach the ionization chambers controlling the reactor power, an effect which can be calculated. Since the per cent change in leakage is the same as the per cent change in the calculated number of thermal neutrons reaching the ionization chamber, the observed leakage change can be assumed to reflect an actual power change. The curve of Fig. 1.3.4 can therefore be used to correct the power readings when the reactor is operated at temperatures other than the calibration temperature.

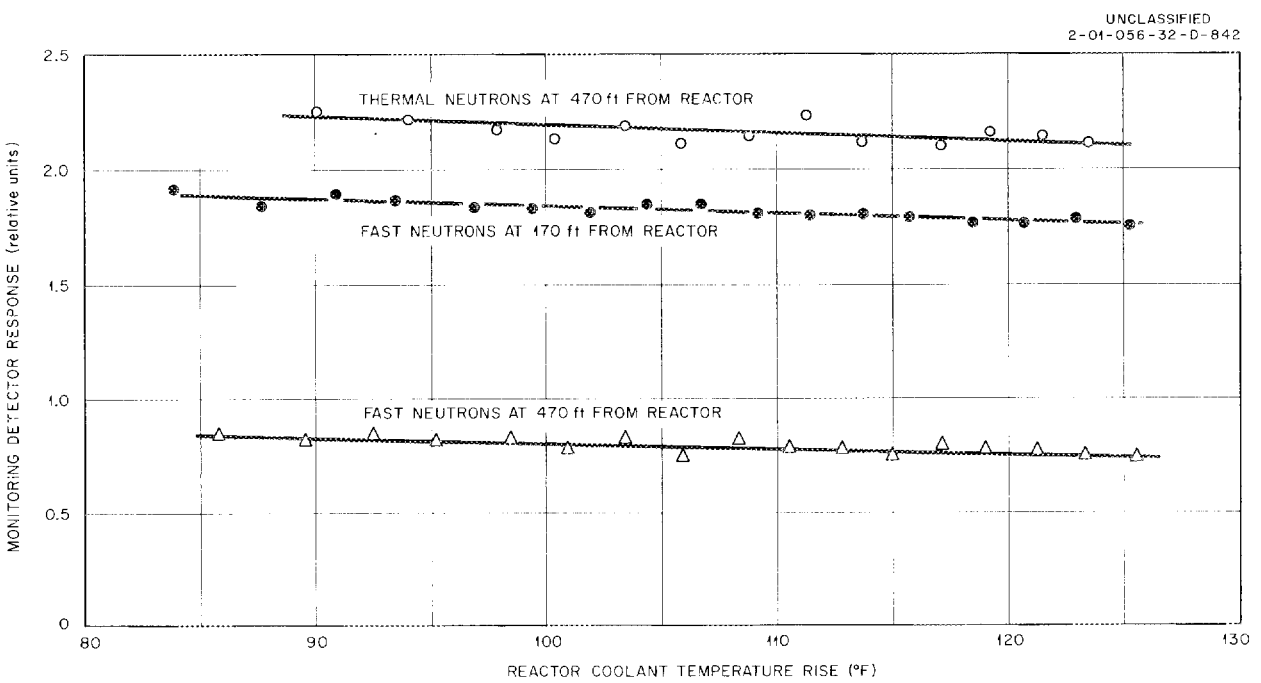

Fig. 1.3.4. Neutron Leakage from the TSR-II in Cool-II Shield as a Function of Coolant Temperature.

The system temperature can be maintained at a selected temperature by a servo system, so that there will be no power variations due to temperature change during a run.

Results. – Figure 1.3.5 presents typical results from a calibration run with the TSR-II placed within the Cool-II shield.[3] The thermocouple readings, in millivolts, are plotted as a function of time for both heater and reactor runs. Tangents have been drawn to both curves at the pump-heat–heat-loss equilibrium temperature (~ 1.8 mv) and show that the slopes of both curves (dT/dt) are essentially the same. Usually two or more reactor runs are required to determine the reactor power demand setting that will result in such close agreement in the slopes of the reactor run and heater run curves. Once the demand setting has been fixed, however, repeated runs agree within ±2%. In the calibration run shown, the heater power found by electrical measurements was 34.4 kw. Since the ratio of $(dT/dt)_h$ and $(dT/dt)_r$ in this example was unity, the reactor power was also 34.4 kw at the equilibrium temperature of 112°F.

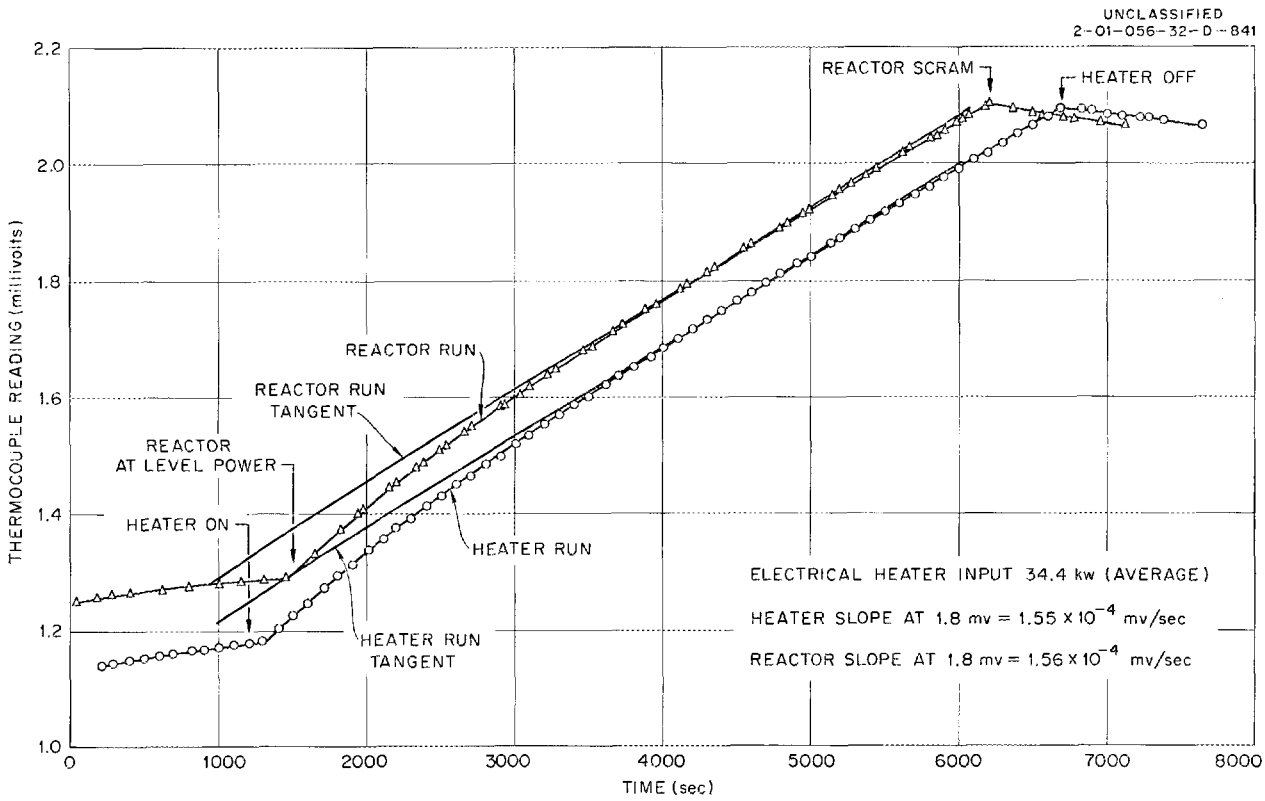

Fig. 1.3.5. Temperature of Water in the TSR-II as a Function of Time During Heat Power Calibration with Cool-II Shield.

Errors. – The optimum arrangement for the comparison method of measurement would be to replace the fuel elements with the heater and run under identical conditions for both the heater and the reactor. Since this is obviously impossible, the heater is connected as close to the core as practical, and runs are then made under conditions of temperature, wind, time of day, etc., as nearly the same as possible.

The slopes of the temperature versus time curves are measured at that temperature where the heat input from the pumps equals the heat losses from the system. Therefore, no losses need be considered except heat loss between the electric heater and the reactor. This loss is minor, since the 200-gpm flow rate and the 35-kw operating power combine to raise the temperature of the water passing through the heater less than 2°F above the system temperature. Nevertheless, the piping between the heater and the core is well insulated as a precautionary measure. Measurements of the electrical power input to the heater are made with instruments having an accuracy of $\frac{1}{4}$% of full scale. Considering the accuracy of the measurements and the possible heat losses, the heat input to the system is probably known to better than ±0.5%.

Since the important quantity is the slope of the temperature versus time curve, it is not necessary that the accuracy of individual thermocouple readings be better than ±0.5%. The thermocouples are calibrated at 32°F and 212°F before each run. Experience has shown that the slope of the temperature versus time curve can be determined to ±2% with the number of readings usually taken.

After taking into consideration the possible error in power level resulting from regulating rod positioning (± 1%), the accumulated error in the power calibration at equilibrium temperature is less than ±3%.

During routine reactor operation the reactor power may vary an additional ± 1% due to the previously discussed error in linearity of the electronics. Thus for normal operations the reactor power level is probably known to better than ±5%. The level can be checked routinely with calibrated ionization chamber monitors which are accurate to within ± 5%.

Coolant Flow Studies

In the TSR-II there are four fuel regions in which coolant flow distribution must be considered. These regions are the upper fuel, the fuel-loaded cover plates on the control mechanism housing, and the lower fuel, all cooled by the "first pass" of the coolant, and the annular fuel, cooled by the "second pass" of the coolant.

The coolant flow distribution among the channels of the upper fuel region and the channels of the lower fuel region, both included in the first pass of the coolant, was studied in a specially constructed test rig. The rig consists of a full-sized reproduction of the central cylinder of the reactor. Complete upper or lower fuel assemblies (unfueled plates) were installed in the rig, with actual entrance and exit conditions fully reproduced, and water flowed through them at rates identical with those to be used in the reactor.

The velocity of the water flowing through the channels was measured by the conductivity probe method, with the probes being inserted through the Plexiglas end cap of the rig and extending into a fuel element channel. The conductivity probe method essentially involves the injection of a salt solution into the water flowing through the channel under test and measuring the time required for the solution to pass two probes which sense the change in resistivity of the water. It is sensitive to such variables as salt injection location and velocity, probe location relative to the channel walls, and turbulence in the fluid stream. To reduce the probability of serious error, therefore, at least 20 readings were made of each velocity and an average velocity used, provided that agreement between the 20 readings was good.

The velocities obtained by this method can be regarded neither as average velocities nor as peak velocities, and therefore cannot be used as absolute values. They are, however, an excellent indication of predominant relative velocities and are used as a basis for calculation of average velocities in the fuel element coolant channels.

Upper Section of Central Fuel. – The upper fuel region of the TSR-II is located immediately below the ionization chamber guide assembly lead-water shield can[4] at the beginning of the first pass region. The shield can is penetrated by 133 helical tubes through which all cooling water must flow to make the first pass of the core. A screen had been developed to flatten the velocity profile at the inlet to the first pass.[5] It was found, however, that the screen did not produce a uniform velocity at the exit of the upper section of the first pass (bottom of the upper fuel element). It is here and at the entrance to the lower fuel unit that the highest heat flux exists, and therefore these regions have the most stringent flow requirements.[6] After an extensive series of trials involving various designs, a tapered thickness baffle plate with drilled holes was substituted for the original screen at the entrance to the first pass region. Its location is shown in Fig. 1.3.6.

The flow distributions obtained by the use of the tapered thickness baffle plate are shown in Figs. 1.3.7 and 1.3.8. Figure 1.3.7 gives the results of three sets of measurements, two at 800 gpm and another

[4]L. B. Holland and C. E. Clifford, *Description of the Tower Shielding Reactor II and Proposed Preliminary Experiments*, ORNL-2747 (1959).

[5]W. R. Gambill, *TSR-II Fluid Flow Studies*, ORNL-CF-59-10-104 (1959).

[6]L. B. Holland *et al.*, *Neutron Phys. Ann. Prog. Rep., Sept. 1, 1960*, ORNL-3016, p. 50.

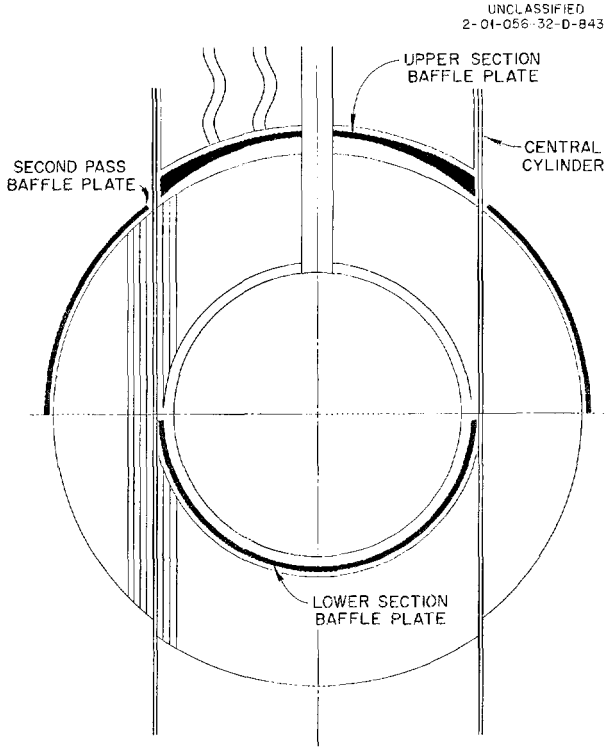

Fig. 1.3.6. Location of Baffle Plates Relative to the TSR-II Core.

at 400 gpm in one quadrant of the upper fuel element. Figure 1.3.8 shows results of single sets of measurements in each of the other three quadrants of the upper fuel element, all at 800 gpm. Each point represents the arithmetic average of 20 readings at the same location. The spread of the readings is shown by the "error bars" on the points of Fig. 1.3.8, where the upper and lower limits are the two extreme readings made during the test.

It is obvious from Fig. 1.3.7 that test results do not make possible the assignment of one definite velocity to the flow through a given channel. Careful examination of the data does seem to justify the conclusions that the flow is properly distributed and adequate for proper cooling of the fuel plates.

The differences in velocities measured in an individual channel may be ascribed to current eddies in the water which cause the injected salt to approach the probes at angles other than zero degrees. This explanation is based on two observations: first, the obvious eddies seen directly in the water through the Plexiglas end plates; and second, the nonrepetition of the negative velocities observed in some channels. It will be seen in Figs. 1.3.7 and 1.3.8 that the negative readings did not reappear when the test was repeated, usually after reassembly of the rig or change of the probes.

The pressure drop through the improved baffle remained approximately the same as in previous tests and is 7 psi at 850 gpm for water at 77°F.

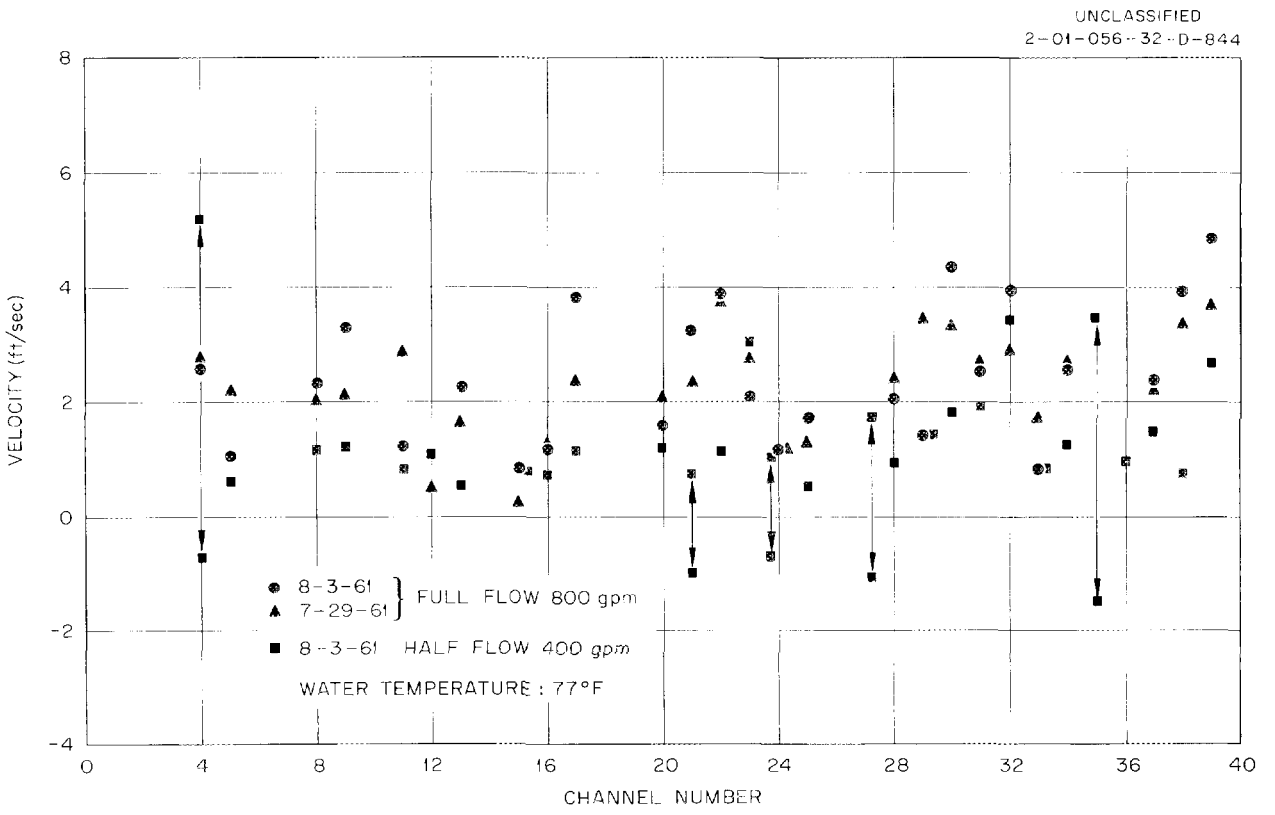

Fig. 1.3.7. Cooling-Water Flow Distribution in Quadrant No. 2 of the TSR-II Upper Fuel.

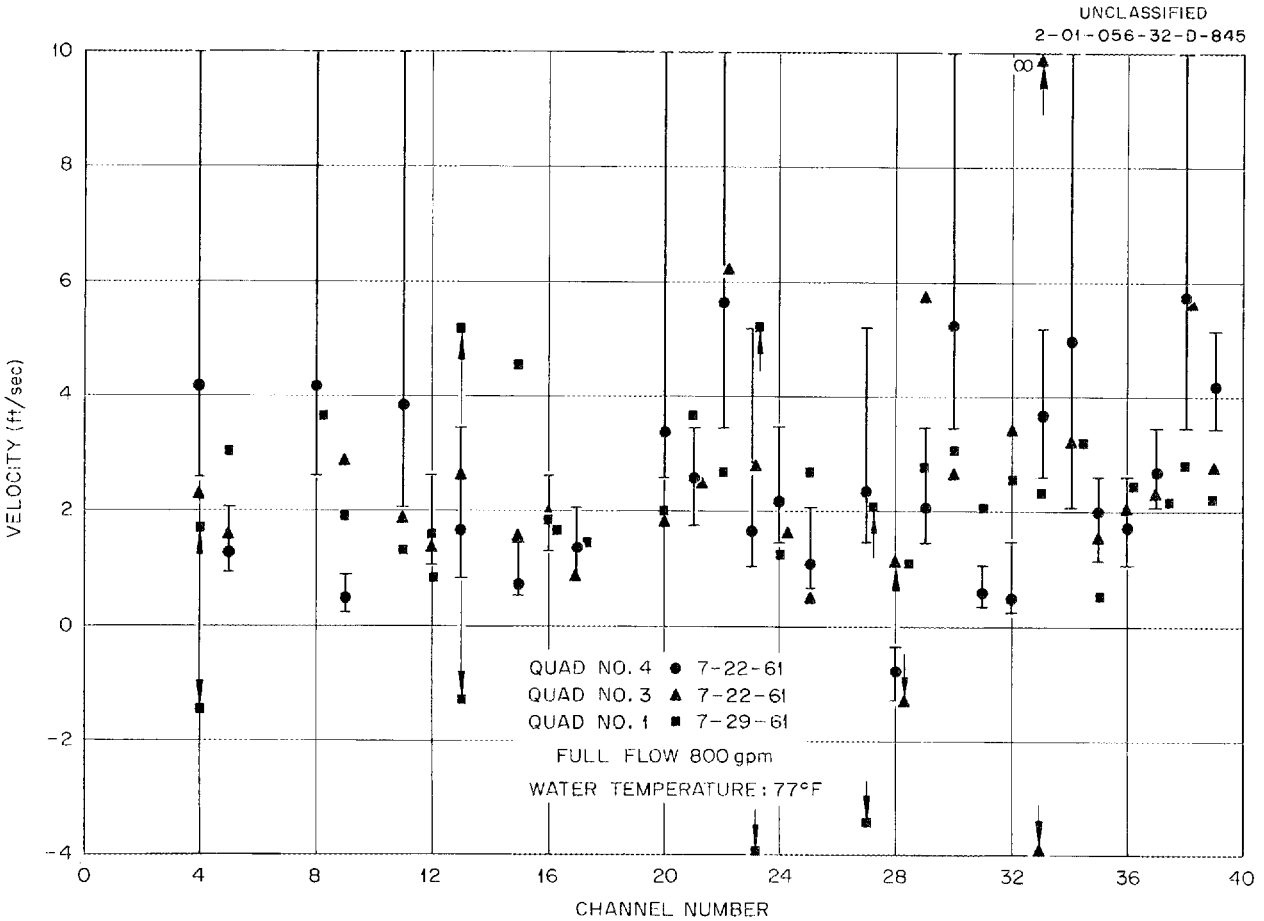

Fig. 1.3.8. Cooling-Water Flow Distribution in Quadrants Nos. 1, 3, and 4 of TSR-II Upper Fuel.

Lower Section of Central Fuel. – A satisfactory flow distribution through the lower section of the central fuel was achieved by using a hemispherical baffle, located as shown in Fig. 1.3.6. Development followed the same pattern as that discussed for the upper baffle. The flow velocity distribution obtained is shown in Fig. 1.3.9.

Annular Fuel Region. – The annular fuel elements are cooled by the "second pass" of the coolant after it has reversed direction and is directed toward the cooling water outlet. Tests with a Plexiglas model of the second pass region were reported previously.[7] When the reactor core was being assembled for the first critical experiments, the conductivity probe method was used to test the flow distribution in the annular elements after they were fully assembled in the pressure vessel. A specially made "cap," simulating the inner surface of the lead-boral region and providing fittings for probe mounting, was fabricated for the test. Velocities in at least some channels of eight of the annular elements were measured.

[7]L. B. Holland *et al.*, *Neutron Phys. Ann. Prog. Rep., Sept. 1, 1959*, ORNL-2842, p. 49.

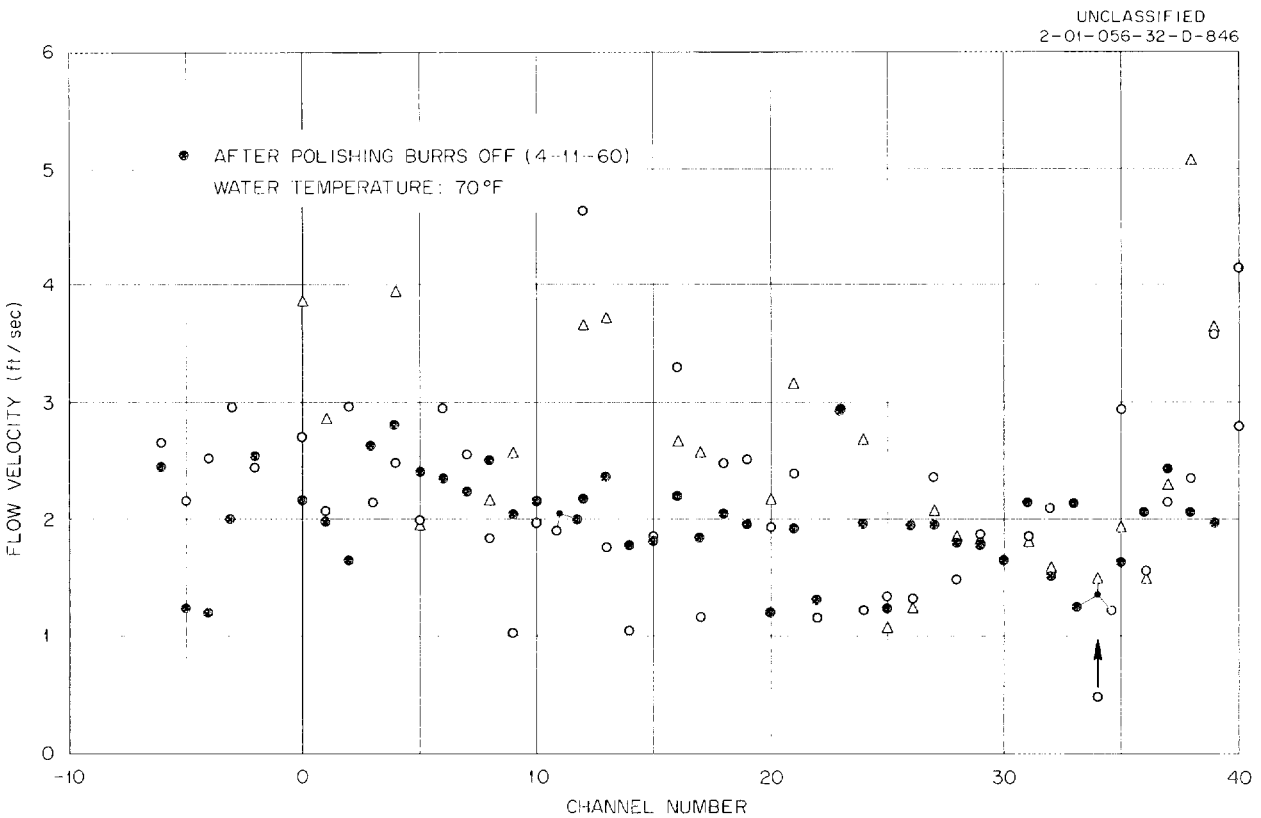

Fig. 1.3.9. Cooling-Water Flow Distribution in Lower Fuel of the TSR-II.

The tests showed that the flow distribution was very sensitive to proper sealing of the equator of the annular fuel elements, i.e., if any water was allowed to leak around the elements instead of going through them, the flow distribution deteriorated seriously. A lead gasket was therefore developed for this seal. Velocity distributions obtained in the tests were generally satisfactory and in good agreement with the Plexiglas model tests. The experimentally obtained velocities are compared to the calculated velocities required to maintain saturation temperatures at the fuel plate surfaces in Fig. 1.3.10.

Tests on the fully assembled TSR-II have shown that the coolant pump is capable of maintaining a flow rate of 800 gpm with the baffle plates installed.

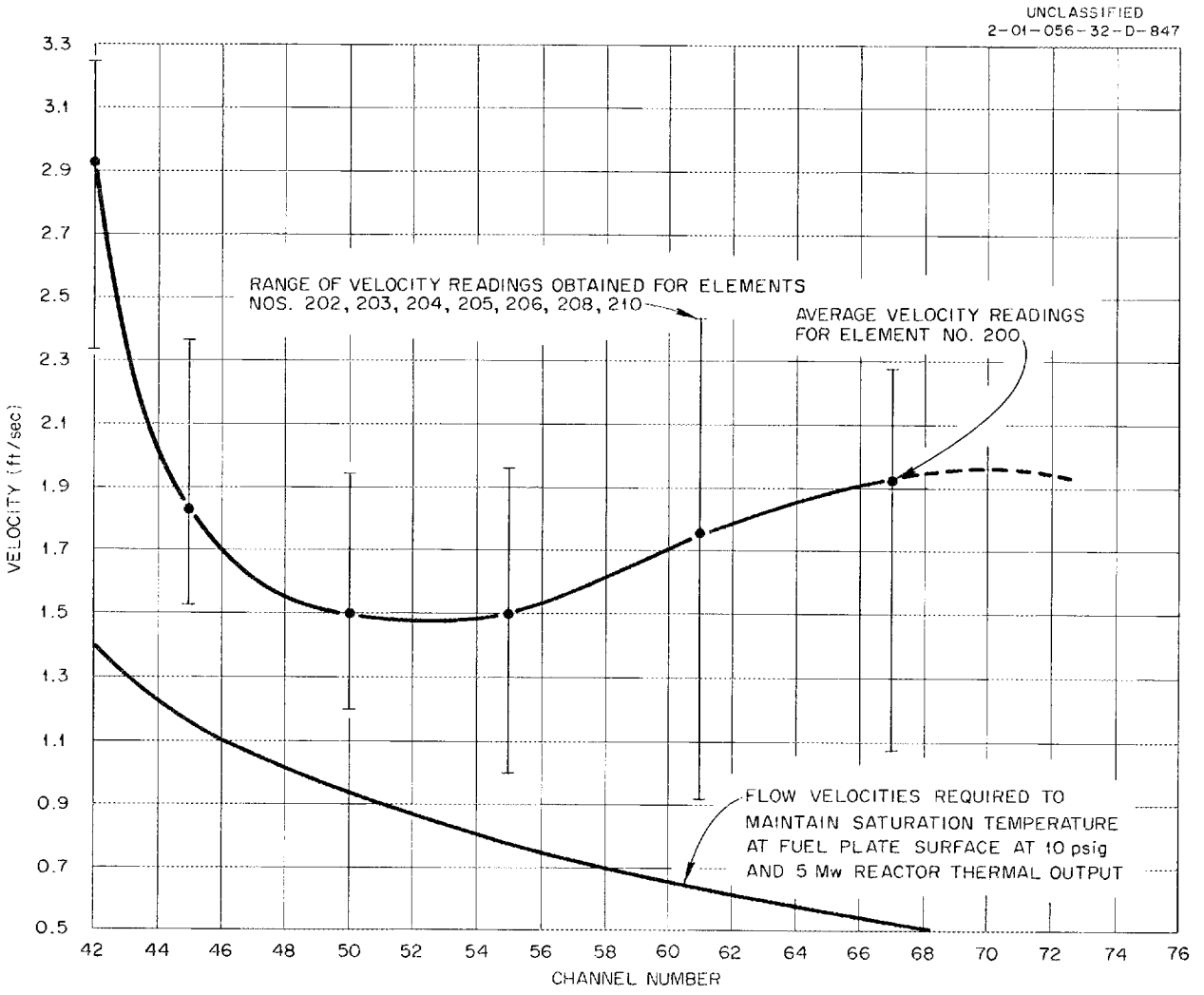

Fig. 1.3.10. Cooling-Water Flow Distribution in the TSR-II Annular Fuel Element.

1.4. IN-AIR MEASUREMENTS OF RADIATION FROM THE TOWER SHIELDING REACTOR II (TSR-II)

F. J. Muckenthaler and L. B. Holland

An extensive program of "free-field" mapping of radiation from the Tower Shielding Reactor II (TSR-II) is in progress at the Tower Shielding Facility (TSF). The term "free field" is here used to describe radiation measurements taken in air at various distances from the reactor, with minimal interference or bias caused by ground scattering, structures, equipment, etc. The measurements include thermal-neutron fluxes, gamma-ray dose rates, and fast-neutron dose rates as functions of reactor-detector distance and detector height above ground level for two reactor heights and two reactor shields. A general description of the purpose and scope of this work has been published elsewhere.[1]

Reactor Shields

As normally constituted the TSR-II embodies a lead, boral, and water shield. For the purposes of these tests the permanent shield was augmented by two specially built shields, Cool-I and Cool-II, which were intended to produce certain specific modifications in the leakage spectrum. It was intended that the two shields would differ only in the relative hardness of their fast-neutron leakage spectra, and that they would have identical fast-neutron–gamma-ray dose rate ratios, thermal-neutron–gamma-ray flux ratios, and the same relative air-capture gamma-ray spectra. The goal was only approximately achieved, since the actual fast-neutron–gamma-ray dose rate ratio is about 3 for Cool-I at distances of a few hundred yards and is only about 2 for Cool-II under similar conditions.

At the present time only the measurements with the Cool-I shield have been completed. Sufficient data will be taken with the Cool-II shield to establish any significant differences between the two not included in a leakage normalization factor.

Detector Stations

A plan view of the TSF site showing the locations of detector stations is shown in Fig. 1.4.1. Test Stations I and II (modified) are located on the concrete apron of the TSF. Measurements at Test Stations I and II were made only at a detector height of 40 in. Detectors at Station II (modified) were suspended below a crew compartment shield which could be raised or lowered with the TSF hoist equipment. Special towers 150 ft high were erected at Stations III, IV, and V for the purpose of elevating the detectors to various heights above the ground. For most measurements several detectors were located at each tower station, the detectors being positioned so that there was no detector shadowing of the direct beam.

In addition to the stations, a traversing mechanism was developed to position detectors uniformly 24.66 ft from the reactor center. This mechanism was used in combination with reactor rotation to measure fast-neutron and gamma-ray dose rates and thermal-neutron fluxes as functions of azimuthal and polar angles with the reactor at a height of 150 ft. From these data the degree of anisotropy of the radiation leakage could be deduced.

---

[1] S. C. Dominey, *Data Plan for Ordnance Corps Tests at ORNL-TSF*, FZK-126 (Dec. 15, 1960).

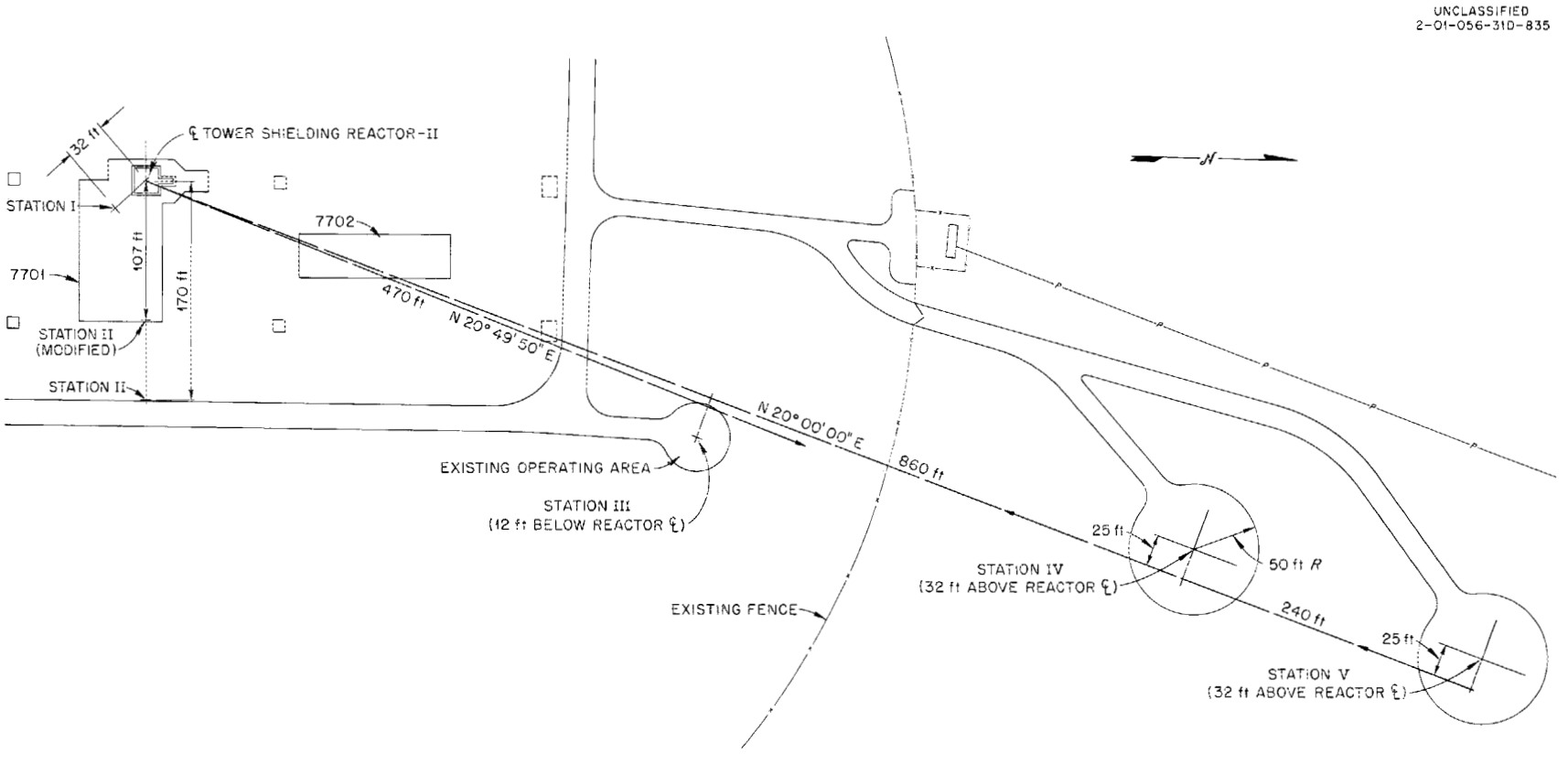

Fig. 1.4.1. Location of Detector Stations for In-Air Measurements at TSF.

Detectors

Gold foils, bare and cadmium covered, were used to map the thermal-neutron flux in air outside Cool-I. A total of 14 pairs were exposed at 10-ft intervals, starting at a point 5.33 ft from the reactor shield surface. The reactor was at a height of 175 ft, and the foils were mounted on cards attached to a cable extending from the reactor center line to a point on one of the tower legs 145 ft above the ground. Sulfur pellets were placed at the same locations as the foils to measure the fast-neutron flux above the sulfur threshold energy of 2.9 Mev. At the reactor and foil heights given, the gold foil activities were assumed to be unaffected by ground effects.

The thermal-neutron flux at each detector station was measured with a BF_3 chamber with one exception. Because of the extreme sensitivity of the BF_3 chamber, a U^{235} fission counter was used to map the shield leakage at a point 24.66 ft from the center of the reactor.

Gamma-ray dose rates were measured with an anthracene crystal scintillation counter using a 5819 photomultiplier tube. Gamma-ray spectra were also obtained with a NaI(Tl) crystal scintillation spectrometer, but these results have not yet been analyzed.

Fast-neutron dose-rate measurements employed a Hurst-type proportional counter. Fast-neutron leakage spectra were measured with photographic emulsions, but again the data has not been analyzed.

The error of measurement for all of the detectors used is estimated as ±5%. However, because of difficulties in maintaining reproducible power levels in the TSR-II, the over-all accuracy of all measurements is estimated at ±10%.

Results

The experimental values of the fast-neutron leakage from Cool-I as a function of slant range, obtained at a detector height of 145 ft above the ground and a reactor height of 175 ft, are approximately 20% higher than the values calculated by Stokes[2] and Maerker[3] for an infinite air medium. In Fig. 1.4.2 the experimental fast-neutron dose-rate values have been multiplied by $4\pi R^2$ and plotted as a function of R, the slant range from the reactor. After the initial buildup that peaks in the vicinity of $R = 200$ ft, the relaxation length for Cool-I neutrons in air is approximately 190 yd.

The agreement between the experimental and predicted values of the gamma-ray dose rate is somewhat poorer, the experimental values being about 50% higher than the predicted values. In Fig. 1.4.3 the gamma-ray dose rate, multiplied by $4\pi R^2$, is plotted as a function of slant range. The relaxation length for Cool-I gamma rays in air is approximately 260 yd at distances greater than 1000 ft.

---

[2] J. R. Stokes and W. C. Farries, *Preanalysis of Ordnance Corps Tests at ORNL-TSF*, FZK-132 (June 30, 1961).

[3] R. E. Maerker, *Preanalysis on Testing of Main Battle Tank Test Pod at the Tower Shielding Facility*, ORNL-3173 (Aug. 17, 1961).

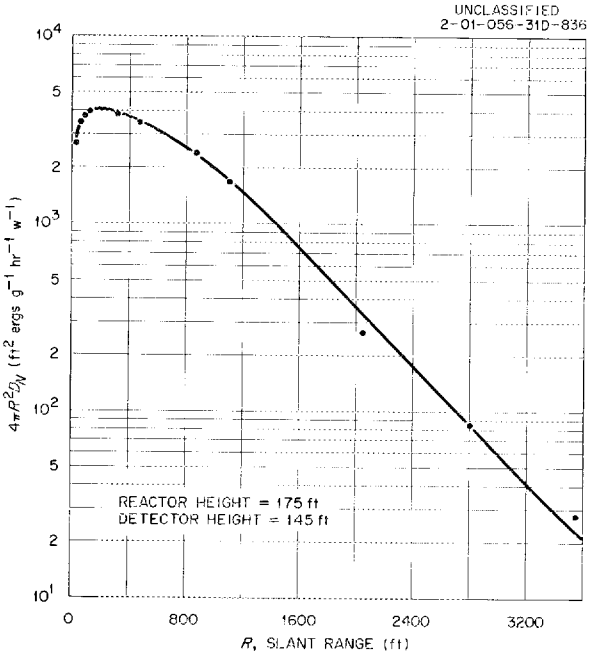

Fig. 1.4.2. Fast-Neutron Dose Rate from Cool-I as a Function of Slant Range.

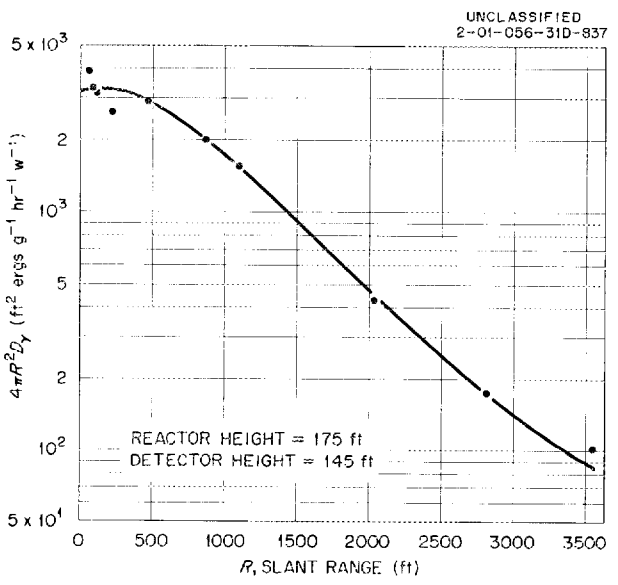

Fig. 1.4.3. Gamma-Ray Dose Rate from Cool-I as a Function of Slant Range.

Part 2

RADIATION DETECTOR STUDIES

2.1. THE FITTING OF INTERPOLATION FUNCTIONS TO SCINTILLATION SPECTROMETER PULSE-HEIGHT SPECTRA

R. W. Peelle, R. O. Chester,[1] and F. C. Maienschein

In order to determine the spectrum of prompt gamma rays from thermal-neutron fission of U^{235} from the existing pulse-height spectra obtained with scintillation spectrometers, it is necessary to have available the details of the response of the spectrometer. In the unscrambling technique described by Burrus,[2] for instance, it is required to know the expected count in each pulse-height channel or bin per gamma ray emitted by the source as a function of the source energy. Any other technique would require equivalent information. Thus, once the spectrometer has been "calibrated" by measuring the pulse-height spectra from a number of monoenergetic gamma-ray sources of known disintegration rate, a difficult interpolation task is required before the "unscrambling" work itself can be started. This must be true unless calibration sources are available at closely spaced intervals throughout the energy range of interest, a condition difficult or impossible to achieve.

This need for carefully determining the response of each type of spectrometer used (in this case pair, Compton, and single-crystal) as a function of both pulse height, p (kev), and gamma-ray energy, e (kev), and for having reliable estimates of the errors in these parameters has led to the use of methods more complex than those previously described[3] for the pair spectrometer. Further, the earlier methods did not yield the shape of the "peak" of the response.

Other workers[4] have interpolated between measured distributions for similar purposes, but as far as is known only in the earlier work of Chester was the interpolation done with the aid of quantitative and fully objective methods allowing valid error estimates. In the present work, as in the work of Hartley,[5] the method of nonlinear least-squares estimation is employed to determine the desired parameters.

Let $f(p,e)\,\delta p$ be the number of pulses observed in the energy increment δp per photon of energy e emitted by the source of radiation under study. [δp is not written as a differential because the discrete nature of the original pulse-height spectra in principle does not allow $f(p,e)$ to be known pointwise. Of course, there is good reason to trust the smoothness of f everywhere except at the x-ray absorption edges, and there the discontinuity is only as a function of energy.] The available calibration data, in the case of the Compton spectrometer, consists of pulse-height spectra for 11 sources of known strength, some of which simultaneously emit two gamma rays. A number of spectra are available in each case so that it is possible to note the degree of consistency in the response of the system. (More so than for a single-crystal spectrometer, the Compton and pair spectrometers have a response dependent upon proper alignment of electronic equipment.) Thus, while the detail in the data as a function of pulse height is quite

---

[1] Instrumentation and Controls Division.

[2] W. R. Burrus, Section 2.2 of this report.

[3] F. C. Maienschein and R. W. Peelle, *Neutron Phys. Ann. Prog. Rep., Sept. 1, 1960*, ORNL-3016, p. 82.

[4] R. O. Chester, paper presented at the Total Absorption Gamma-Ray Spectrometry Symposium, Gatlinburg, Tennessee, May 10–11, 1960; N. H. Lazar, *IRE Trans. on Nuclear Sci.* NS-5, 138 (1958); J. H. Hubbell and N. E. Scofield, *IRE Trans. on Nuclear Sci.* NS-5, 156 (1958).

[5] H. O. Hartley, *Technometrics* 3, 269 (1961).

fine, only a few points are available for the interpolation as a function of energy. The observed count per kev in the ith energy channel of the observed pulse-height spectrum for monoenergetic gamma rays is finally approximated by the relation

$$y_i \cong Qt \int_{(p_i-\Delta p_i)/2}^{(p_i+\Delta p_i)/2} f(p, e; \mathbf{d})\, dp , \tag{1}$$

where

y_i = observed number of counts per kev in ith pulse-height channel from emission from the source of Qt gamma rays of energy e,

p_i = pulse height corresponding to y_i, in energy units,

$\mathbf{d}$ = vector whose components are the set of parameters required to completely describe the spectrometer response.

Since it is difficult to introduce the two-dimensional function and all the data at once, the procedure is actually carried out by considering only the pulse-height spectrum from the source m and writing

$$y_i^m = Qt \int_{(p_i-\Delta p_i)/2}^{(p_i+\Delta p_i)/2} f^m(p; \mathbf{b}^m)\, dp , \tag{2}$$

where now the parameter vector $\mathbf{b}^m$ is only supposed to describe the behavior for the energy e^m of the mth source. If two species of gamma rays are given off by the isotope in question, the observed number of counts per kev, y_i, is approximated essentially by a sum of terms of the type (2). When all the observed y_i's have been fitted in this manner, it is then necessary to interpolate the values of the b_λ's as a function of the energy e in order to determine all the components of $\mathbf{d}$. As we shall see, the two fitting procedures are similar except for the weighting of the corresponding "observations."

The remainder of this report summarizes the fitting methods used, illustrates the degree of success which has so far been obtained, and indicates how the information on the parameters and their uncertainties may be obtained from the combination of the many calibration experiments.

Methods Used to Fit Parameters to Interpolation Formulas. – The first step in the interpolation procedure is the choice of an equation whose shape is believed to be adaptable to the experimental data. As an example, we choose the fitting of the Compton spectrometer pulse-height spectrum from an individual gamma ray of fairly low energy. In generating such formulas, an attempt is made to obey the following "rules":

1. The expression should be the sum of terms, each of which represents an obvious shape feature of the observations when plotted as a function of pulse height.

2. Each term in the sum should be a continuous function of pulse height and should have the form of an amplitude coefficient times a shape function having unit area.

3. For convenience in combining source strength information with information from the fits of counts per kev versus pulse height, a single normalizing constant should appear for the entire expression, representing either the entire area of the fitted function or that of the peak corresponding to the full gamma-ray energy.

4. Whenever possible, the form should be arranged so that the derivatives of the entire expression with respect to the various parameters are reasonably orthogonal to each other.

The example below is a simplification of the expression used for the Compton spectrometer data:

$$f(p\,;\mathbf{b}) = b_3\,\{G(p) + b_1[(1 - b_8)\,T(p) + b_8\,R(p)]\}\,, \tag{3}$$

where the full energy peak is given by

$$G(p) = \frac{1}{b_4\sqrt{\pi}}\exp - \left[\left(\frac{p - b_5}{b_4}\right)^2\right];$$

the main tail function, $T(p)$, by

$$T(p) = \frac{\left[1 - e^{b_6(p-b_7)}\right]^2 e^{b_2 p}}{A(b_6, b_7, b_2)}\,, \qquad \text{if } p \leq b_7\,,$$

$$T(p) = 0\,, \qquad \text{if } p > b_7\,,$$

where $A(b_2, b_6, b_7)$ normalizes $T(p)$ to unit area; and the "low energy rise" by

$$R(p) = \begin{cases} 0\,, & \text{for } p > b_{23}\,, \\ 2(b_{23} - p)/b_{23}^2\,, & \text{for } p \leq b_{23}\,. \end{cases}$$

It can be seen that the expression for $f(p\,;\mathbf{b})$, for each m, is nonlinear in the parameters which determine the shapes of the various features. In practice the parameter b_7 was "frozen" to a stated function of the energy e^m to reduce the number of poorly determined parameters. This technique is arbitrary, but its occasional use with relatively unimportant parameters is considered appropriate.

Because of the form of Eq. 3, and of Eq. 2 for resulting y_i^m's, it was necessary to rely on an iterative method for the solution of the nonlinear least-squares problem. The type of analysis required is reproduced below. No claim of originality is made except perhaps for the application to the present problem.

The method is designed to refine (in the least-squares sense) the approximation of Eq. 2 above, which we now write more simply by redefining f to include the source strength and integration of Eq. 2:

$$y_i \cong f(p_i;\, b_1, \ldots, b_\sigma, \ldots, b_\Sigma) = f(p_i, \mathbf{b})\,, \tag{2'}$$

where the refinement is produced by adjustment of the Σ parameters b_σ to fit the l experimental data points y_i obtained at respective pulse heights labeled p_i. This approximation involves the expected inexactness of the fit, which must "miss" the points if only because of statistical errors in the y_i's. Iteration is performed on the second approximation:

$$f(p_i;\mathbf{b}) \cong f(p_i;\mathbf{b}^0) + \sum_\sigma \beta_\sigma \frac{\partial}{\partial b_\sigma}[f(p_i;\mathbf{b})]_{\mathbf{b}=\mathbf{b}^0}\,. \tag{4}$$

This second approximation involves the truncation after the first order of the above Taylor expansion of f in the Σ differences $\beta_\sigma = b_\sigma - b_\sigma^0$, where the b_σ^0's (in this section only) represent previously estimated values of the components of the parameter vector. More sophisticated techniques have been developed which attempt to use additional terms of the Taylor expansion. The present code uses the method

of weighted least squares to obtain estimates of the correction vector β. The resulting $\mathbf{b} = \mathbf{b}^0 + \beta$ value is immediately used as the $\mathbf{b}^0$ for the next iterative least-squares procedure. The process is concluded when no further reduction in the weighted sum of squared residuals can be obtained. The detailed procedure follows.

For compactness we define a vector of estimates of the data with components $\mathbf{y}_i^0 = f(p_i; \mathbf{b}^0)$, dim $\mathbf{y}^0(I)$, which must be compared to the observations $\mathbf{y}_i$ to obtain an improved estimate. We also define the elements of a derivative matrix

$$F_{i\rho} = \frac{\partial}{\partial b_\rho} [f(p_i; \mathbf{b}^0)] , \qquad \dim F(I, \Sigma) , \tag{5}$$

where the values of the arguments denote the point at which the derivatives are to be evaluated. The dimensional notation dim $F(I, \Sigma)$ indicates the maximum values of the right subscripts of $F_{i\rho}$. It has been found most convenient to compute the derivatives of Eq. 5 numerically.

The least-square equations are

$$\frac{\partial S}{\partial \beta_\rho} = 0 , \qquad \rho = 1, \ldots, \Sigma , \tag{6}$$

where S may be defined in various ways depending on the weighting system to be used. For instance

$$S_0 = \sum_i (y_i - y_i^0 - \sum_\sigma \beta_\sigma F_{i\sigma})^2 , \tag{7}$$

if an unweighted fit is desired. The resulting equations are

$$0 = \sum_i F_{i\rho}(\delta y_i - \sum_\sigma \beta_\sigma F_{i\sigma}) \qquad \rho = 1, \ldots, \Sigma, \tag{8}$$

where

$$\delta y_i = y_i - y_i^0 .$$

It can already be seen that the equations have exactly the same form as for a linear fit to observed values of δy_i. However, because of the Taylor expansion truncation, an iterative process is required.

Equation 8 makes no explicit arrangement for the introduction of the experimental errors of the y_i's into the fit. Since we want such a weighted fit, it is necessary to complicate the equations in the manner prescribed below. In the weighted case, if the input data are uncorrelated,

$$S_w = \sum_i w_i (\delta y_i - \sum_\sigma \beta_\sigma F_{i\sigma})^2 , \tag{7a}$$

where we take

$$w_i = \frac{1}{\text{variance of } y_i} = \frac{1}{\sigma_i^2} .$$

Here we have actually assumed that no correlation exists between the quantities $(y_i - y_i^0 = \delta y_i)$, which amounts to the assumption that the result of the whole process will be a satisfactory fit with no systematic deviations. This is the point at which an evaluation of the effects of systematic lack of fit would have to begin.

The normal equations become

$$\frac{\partial S_w}{\partial \beta_\rho} = 0 = \sum_i w_i F_i (\delta y_i - \sum_\sigma \beta_\sigma F_{i\sigma}) . \tag{8a}$$

To cast this in the form of Eq. 8, we could define

$$y_i' = \frac{y_i}{\sigma_i}; \qquad y_i^{0\,\prime} = \frac{y_i^0}{\sigma_i}; \qquad F_{i\sigma}' = \frac{1}{\sigma_i} F_{i\sigma} .$$

Note that this definition, required if the computing code being used does not include a weighting matrix, has the result that $y_i^{0\,\prime}$ and $F_{i\sigma}'$, estimates which one thinks of as being determined by the estimates b_σ^0 and the values of p_i, also depend upon the experimental uncertainties in the particular set of data under analysis. The program originally used in this work handled weighting in this manner.[6]

It is most general to introduce at once the matrix **W**, dim $W(I, I)$, which is called the weighting matrix. In the case of uncorrelated differences δy_i, **W** is a diagonal and the normal equations reduce to Eq. 8*a* above. It can be shown[7] that an appropriate definition of S in this case is given below, where $\mathbf{W} = \mathbf{V}^{-1}$ and **V** is the error or variance matrix of the input differences δy_i, i.e. $\mathbf{V} = E\{\delta\mathbf{y}\delta\mathbf{y}^T\}$:

$$S_w' = \sum_{ij} (\delta y_i - \sum_\sigma \beta_\sigma F_{i\sigma}) W_{ij} (\delta y_j - \sum_\sigma \beta_\sigma F_{j\sigma}) . \tag{7b}$$

It will be best to go over now to matrix notation. We have already defined the vector quantities

$$\mathbf{y}, \mathbf{y}^0, \mathbf{p}, \text{ dim } (I)$$
$$\mathbf{B}, \text{ dim } (\Sigma)$$
$$\mathbf{F}, \text{ dim } (I, \Sigma) .$$

The superscript T will denote the transpose. Then Eq. 7*b*, above, becomes

$$S_w' = (\delta\mathbf{y} - \mathbf{F}\beta)^T \mathbf{W}(\delta\mathbf{y} - \mathbf{F}\beta) . \tag{7b'}$$

The normal equations are still derived from $(\partial S/\partial \beta_\sigma) = 0$ (Eq. 6). They lead to

$$0 = (\delta\mathbf{y} - \mathbf{F}\beta)^T \mathbf{W}\mathbf{F}_{.\sigma} + (\mathbf{F}_{.\sigma})^T \mathbf{W}(\delta\mathbf{y} - \mathbf{F}\beta) , \qquad \text{for all } \sigma = 1, 2, \ldots \Sigma ,$$

where $\mathbf{F}_{.\sigma}$ is defined as the vector composed of the σth column of **F**.

---

[6] Parkhurst B. Wood, *NLLS, A 704 Program for Fitting Nonlinear Curves by Least Squares*, K-1440 (Jan. 28, 1960).

[7] Henry Scheffe, *The Analysis of Variance*, p. 19, John Wiley and Sons, New York, 1959.

Since W must be symmetric, the two terms above are equal, and since the equation holds for all σ's, we have

$$0 = \mathbf{F}^T\mathbf{W}(\delta\mathbf{y} - \mathbf{F}\beta) ,$$

or

$$\mathbf{F}^T\mathbf{W}\mathbf{F}\beta = \mathbf{F}^T\mathbf{W}\ \delta\mathbf{y} . \tag{8b}$$

We define the "least-squares matrix" $\mathbf{A} = \mathbf{F}^T\mathbf{W}\mathbf{F}$, dim $A(\Sigma, \Sigma)$ and the "least-squares vector" $\mathbf{r} = \mathbf{F}^T\mathbf{W}\ \delta\mathbf{y} = \mathbf{F}^T\mathbf{W}(\mathbf{y} - \mathbf{y}^0)$, dim $r(\Sigma)$. If $\mathbf{A}$ has an inverse, the solution of the improvements β is

$$\beta = \mathbf{A}^{-1}\mathbf{r} . \tag{8b'}$$

Note that Eq. 8b' is just the usual expression of the least-squares solution except for the definitions of $\mathbf{r}$ and β, which here have the estimates of the function and parameters, respectively, subtracted out. Therefore, as long as the truncation of the Taylor expansion is adequate, certainly true in small-error theory, the usual manipulation of errors for least-squares analysis still holds. The only difference is that the final solution for $\mathbf{b}$ must be obtained by iteration.

At each step of the iteration, progress may be assessed in a number of ways. At the converged result, the β's should be very small, so the program used insists that each β_i be a small fraction of the error (see below) in the corresponding parameter $\mathbf{b}_i$ before convergence is assumed. In the program presently used, an adaption of one written by Busing,[8] we also inspect the weighted square of residuals from the calculated function,

$$\chi^2 = \delta\mathbf{y}^T\mathbf{W}\ \delta\mathbf{y} . \tag{9}$$

If the weighting matrix is appropriate,

$$\chi^2 \cong (I - \Sigma) .$$

In addition, it is possible to estimate, assuming the validity of the truncated Taylor expansion, the values S'_w or χ^2 expected to be realized after the current refinement of the parameter estimates. Thus

$$S'_w = (\delta\mathbf{y} - \mathbf{F}\beta)^T\ \mathbf{W}(\delta\mathbf{y} - \mathbf{F}\beta) = \delta\mathbf{y}^T\mathbf{W}\ \delta\mathbf{y} - (\mathbf{F}\beta)^T\ W(\delta\mathbf{y} - \mathbf{F}\beta) - \delta\mathbf{y}^T\mathbf{W}\mathbf{F}\beta .$$

The middle term drops out by application of the equation for the least-squares solution β, and the last term becomes

$$\delta\mathbf{y}^T\mathbf{W}\mathbf{F}\beta = \mathbf{F}^T\mathbf{W}\ \delta\mathbf{y}^T\beta = \mathbf{A}\beta^T\mathbf{B} = \mathbf{B}^T\mathbf{A}\beta ,$$

so that

$$S'_w = \delta\mathbf{y}^T\mathbf{W}\ \delta\mathbf{y} - \beta^T\mathbf{A}\beta , \tag{10}$$

or

$$= \sum_{i,j} W_{ij}\ \delta y_i\ \delta y_j - \sum_{\alpha,\beta} \beta_\alpha\beta_\beta A_{\alpha\beta} . \tag{10a}$$

For iterations to be concluded, the program requires a small difference between the estimated S'_w and χ^2, as well as a small change in χ^2 since the previous iteration. The degree of agreement which should

[8] W. R. Busing, Chemistry Division, private communication.

be required here is uncertain, but once the linearized equations become accurate, convergence is *usually* quite rapid. About 0.01% agreement is presently required.

In recognition that use of the truncated expansion can result in sizable errors when the estimated parameters are far from the final solution, limits are placed on how great a change may be made in any parameter in a single cycle. Such constraints can be applied in any manner which aids final convergence. It is assumed that a unique minimum exists for S'_w, and no evidence of nonuniqueness has come to our attention so far, though convergence has sometimes been difficult to obtain.

Recently the suggestion of Perey[9] and Hartley[5] has been adopted to ensure more reliable convergence. One writes $\mathbf{b} = \mathbf{b}^0 + g\beta$ and allows g to take values different from unity, the value previously assumed; g is chosen to minimize the value of χ^2. A small search is made for such a minimum in the region $0 \leq g \leq gM$, where gM is smaller than 2 and small enough so that the largest value of $|g\beta_i/b_i| = 0.9$. Experience shows this technique to be helpful in a number of cases studied in which a large number of parameters must be determined. In simple cases this "refinement" is not needed when good first estimates are available for the parameters.

An example is presented in Fig. 2.1.1 of the type of fit obtained with the analysis outlined above. An observed spectrum, y_i, is shown for a Na^{24} source which emits gamma rays of 2.754 and 1.368 Mev. The fitted function, $f(p, b_1 \ldots b_{23})$, is also shown with its major components which include from Eq. 3 four Gaussian peaks, $G(p)$; two tail functions, $T(p)$; and one "low-energy" rise, $R(p)$. The physical processes which give rise to the three higher energy peaks are indicated on the figure. The causes of the other features are not uniquely determined but include bremsstrahlung and electron escape from the sodium iodide crystals and various scattering phenomena leading to coincidences between the two scintillators used. The statistical deviations may be judged from the scatter of the points, y_i, and are about average for the calibration spectra used. The quality of fit is indicated by the values of $\chi^2/(I - \Sigma) = S'_w/(I - \Sigma) = 1.01$, an atypically low value. This spectrum represents one of the most complex types which has been fitted.

Parameter Error Matrices and Weighting Procedures in the Interpolation Process

As described by Eq. 1, the goal of the interpolation process is the production of the vector, $\mathbf{d}$, of coefficients capable of describing the pulse-height and energy response of each of the spectrometers. In addition, it is necessary to characterize the first-order error properties among the coefficients of $\mathbf{d}$. The purpose of this section is to indicate how the second objective can be realized. The previous section suggested how the d's might be obtained by fitting the energy dependence of the coefficients b, but completion of this work requires proper weighting, also discussed in this section.

First, we must understand the fluctuations in the b_σ's, the parameters which fit the pulse-height dependence of the observed counts per kev from one experimental calibration. These fluctuations in the b_σ's and any function thereof are produced by fluctuations in the y_i's. If, as we assume, the uncertainties so resulting in the b_σ's are sufficiently small that the first-order Taylor expansion in the fluctuations is adequate, the equations derived in the previous section can be utilized in the analysis of such fluctuations.

[9] F. G. J. Perey, Neutron Physics Division, private communication, 1961.

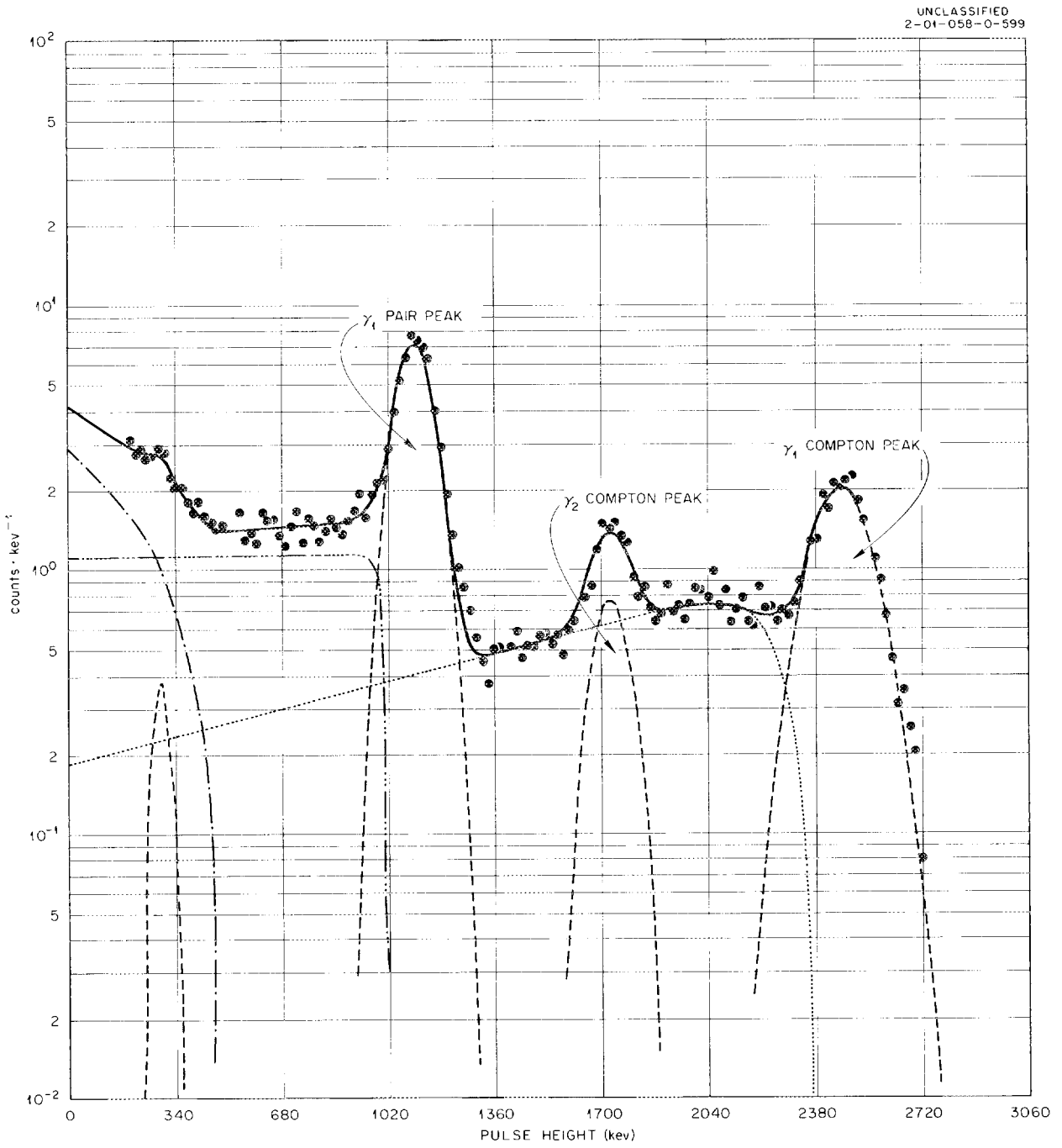

Fig. 2.1.1. Experimental Data, y_i, and Fitted Function, $f(p, b_1, \ldots, b_{23})$, for a Gamma-Ray Spectrum Obtained with a Compton Spectrometer and a Na^{24} Source. The features of the curves are explained in the text.

Let the superscript (0) represent the expectation value of a given quantity, for our purposes the value which would be observed in the mean from an infinite series of experiments equivalent to the one under study. We have assumed that differences between values of **b** calculated for a particular case and $E(\mathbf{b}) = \mathbf{b}^0$ are so small that the first-order Taylor expansion is adequate. In this notation, we automatically have

$$E(\mathbf{y} - \mathbf{y}^0) = 0 \; ; \qquad E(\beta) = 0 \, .$$

The assumption inherent in these simultaneous statements is discussed later.

First it is necessary to compute the covariance matrix of **b**, which gives the variances of the elements of **b** on its diagonal and the covariances between them in the remaining terms. Let $\mathbf{V}(\mathbf{b})$ be this matrix:

$$\mathbf{V}(\mathbf{b}) = E\{(\mathbf{b} - \mathbf{b}^0)(\mathbf{b} - \mathbf{b}^0)^T\} = E\{\beta\beta^T\} \, , \tag{11}$$

where it is understood that the $\mathbf{b}_\sigma^0$'s are unknown. Note that in this section β represents differences between converged parameters and their expectation value. By using the least-squares equations, Eqs. 8, which lead to the establishment of the b_σ's,

$$\mathbf{V}(\mathbf{b}) = \mathbf{E}\{\mathbf{A}^{-1}\mathbf{F}^T\mathbf{W}\,\delta\mathbf{y}[\mathbf{A}^{-1}\mathbf{F}^T\mathbf{W}\,\delta\mathbf{y}]^T\} \, .$$

Since **A**, **F**, and **W** are not affected by the averaging process, $\mathbf{A}^{-1}$ is symmetric, and since we have chosen $\mathbf{W}^{-1} = \mathbf{V}(\delta\mathbf{y}) = E\{\delta\mathbf{y}\;\delta\mathbf{y}^T\}$, we quickly obtain

$$\mathbf{V}(\mathbf{b}) = \mathbf{A}^{-1} = (\mathbf{F}^T\mathbf{W}\mathbf{F})^{-1} \, . \tag{12}$$

This is the usual result for least-squares analyses, yielding experimental errors in the parameters which are determined by the weighting matrix of the input data. The observed residuals between the fitted curve and the data points have not entered. This result stems from the assumption that the correlations and variances of the fluctuations among the I differences δy_i are fully taken into account by the weighting matrix. This will usually require the unrealistic assumption leading to Eq. 12 that $E(\mathbf{b})$ inserted into the chosen "perfect" fitting function will yield $E(\mathbf{y})$. In our problem it is not expected that enough parameters have been properly incorporated into the chosen fitting function to perfectly match the expectation value of any particular response curve, so the statistically "best" sets of data should not fit well by a χ^2 criterion, though, as seen above, the fits obtained are good even in this sense.

For the usual case of a diagonal weighting matrix, a standard procedure is available for sidestepping this difficulty, probably applicable if the systematic errors are not too large. The method is based on the observation that $\chi^2/(I - \Sigma)$ is an *empirical* estimate of the average value of any diagonal element of $\mathbf{W}\mathbf{V}(\delta\mathbf{y})$. The rather conservative standard procedure can be summarized as follows:

1. If $\chi^2/(I - \Sigma)$ is less than unity, use the errors from Eq. 12 based on the input weights.
2. If $\chi^2/(I - \Sigma)$ is significantly greater than unity, adjust the experimental weights by the scale factor needed to make it unity. Propagated through the matrices defined for the least-squares fit, this leads to a new value of $\mathbf{A}^{-1}$ in Eq. 12.

Though this procedure is widely used, it is considered reasonably valid only when random errors in the input data may well be greater than those estimated. For our pulse-height distributions, input errors can be well estimated from Poisson statistics, so this method will not be used. Instead, in cases of fits

to raw data, we ignore the lack of fit and use the computed error matrix. Essentially this assumes that components of the data which are systematically not fit are unimportant to the problem.

In similar cases involving weighted averages of fitting parameters, lack of agreement within the random error presumably implies a lack of reproducibility in the spectrometer. Such difficulties are assumed not to affect directly the covariance terms between averaged parameters which are induced by the input data. However, the variances of averaged parameters are increased to cover the scatter observed among the various runs.

From 2 to 16 calibration spectra were obtained for a given isotope during the course of the experiments. Though in some cases the less significant data can be ignored, it is usually necessary to obtain a set of averaged parameters b_λ^m by combining the information from several experimental runs using isotope m. Reasonable averaged weights for the parameters are essentially proportional to the relative number of counts per kev (in every energy interval) in the various spectra. Values of the diagonal elements of the least-squares matrix, $A_{\lambda\lambda}$, were actually used for the relative weight of b_λ except in the case of b_3, the normalization constant. Combining values of this parameter to give spectrometer efficiency involves the strengths of the calibration sources, and so a least-squares average is performed, taking into account the rather important correlations among the various source strengths determined.

Parameters obtained by the above averaging process were used to calculate the Compton spectrometer response functions shown in Fig. 2.1.2. A curve is shown at the energy of each available calibration source, but for sources emitting two photons, only the response to the higher-energy photon is shown. The increase in importance with increasing gamma-ray energy may be seen for the tail function, the pair peak, and the "low-energy rise." The Compton spectrometer was used from ~300 to 2300 kev and was the only instrument available from 800 to 1400 kev. The tail is relatively less important for the pair spectrometer.

An integral under a pulse-height distribution shown in Fig. 2.1.2 corresponds to b_3/Qt, the peak efficiency of the Compton spectrometer. Data, shown in Fig. 2.1.3 for individual spectral measurements rather than for the average, are self-consistent within the errors (not shown), except for the Mn^{54} points. The decrease in efficiency at high energy is due to the diminishing cross section for Compton scattering. The decrease at low energy follows from the fact that pulses arising from the Compton-scattered gamma rays have insufficient energy to overcome the pulse-height bias on the "side" crystal.

Ignoring the problem of the b_3's, it was found possible to estimate the error matrix of averaged parameters by combining the least-squares matrices of all the runs L of the same type as follows:

$$\text{Covariance matrix of averaged parameters} = [\sum_L \mathbf{A}_L']^{-1} , \tag{13}$$

where $\mathbf{A}_L'$ is a slightly modified least-squares matrix to take account of having performed original fits on data not divided by the number of source disintegrations Qt.

By analogy with Eq. 12, it is clear that if the full parameter vector $\mathbf{d}$ can be obtained at the output of a least-squares fitting procedure, the inverse of the corresponding least-squares matrix will give the error

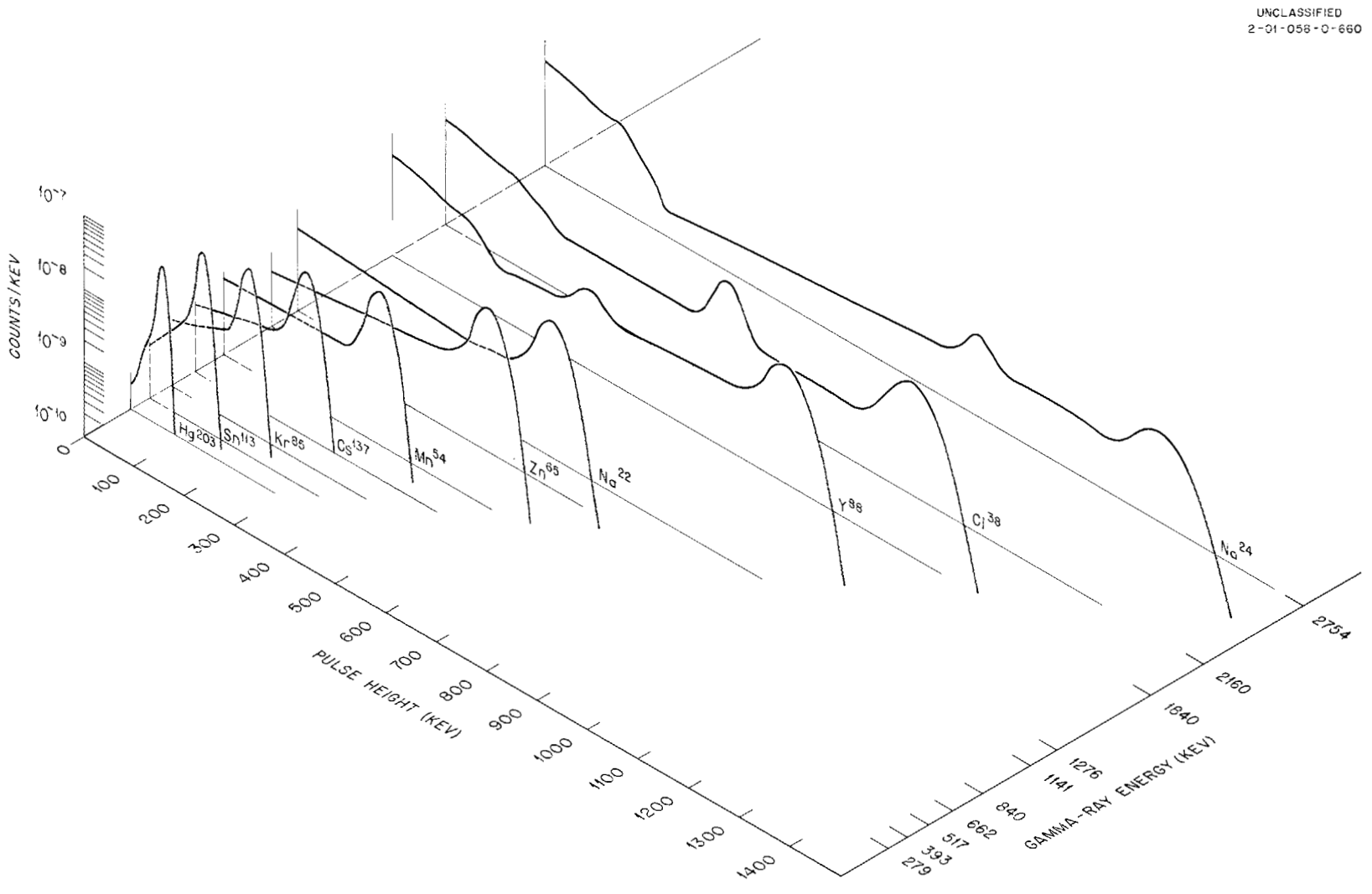

Fig. 2.1.2. Response of the Two-Crystal Compton Spectrometer to Various Monoenergetic Gamma-Ray Sources. The logarithm of the number of counts per unit energy interval is plotted versus pulse height for one photon of the indicated energy emitted at the source position, about 22 cm from the face of the center crystal of the spectrometer.

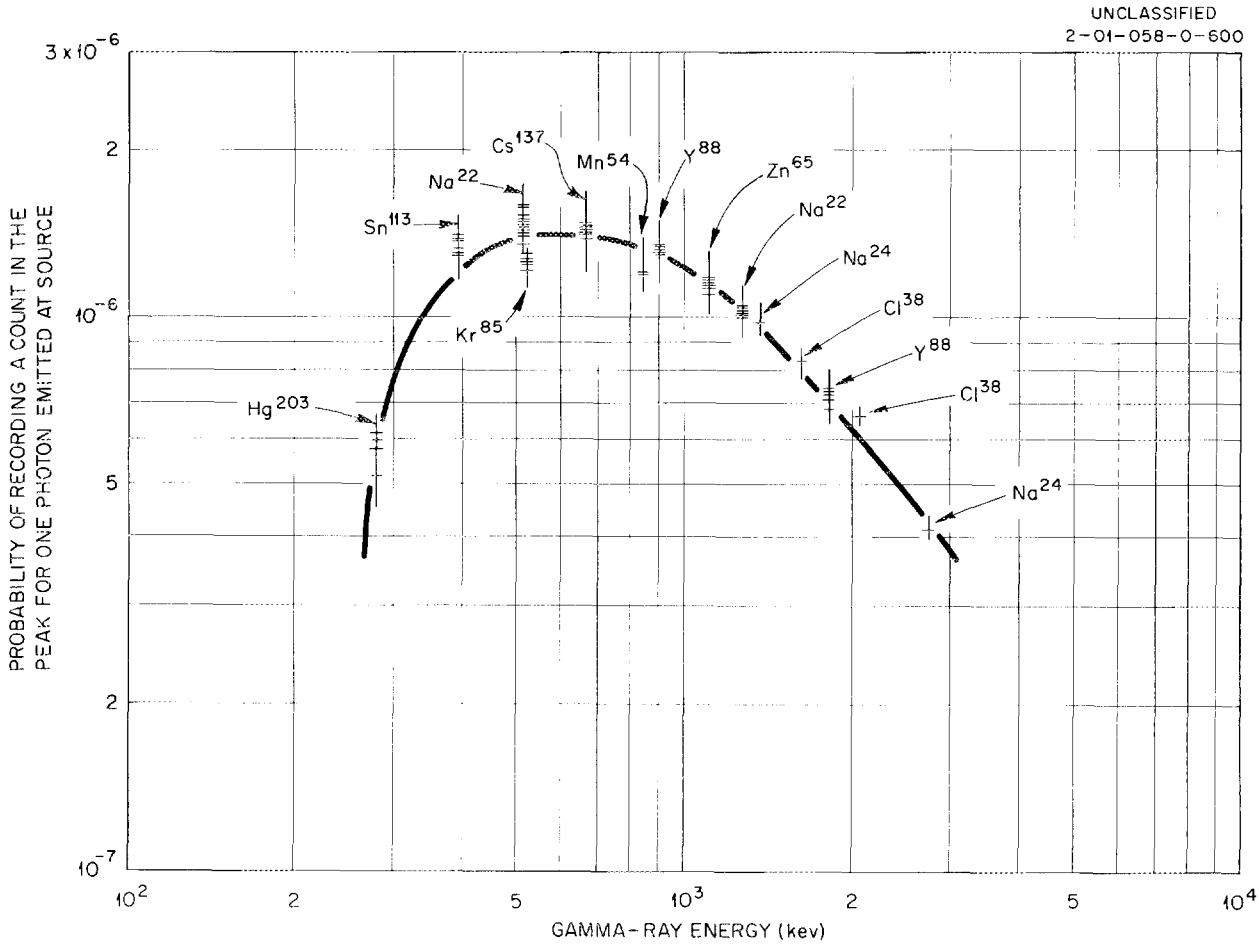

Fig. 2.1.3. Peak Efficiency of the Compton Spectrometer as a Function of Gamma-Ray Energy. Each horizontal bar represents the result of a spectral measurement with a gamma ray of the energy indicated by the vertical line. The efficiency values were determined by dividing the area under the peaks of the fitted response curves by the known source strengths, with appropriate corrections for random backgrounds, count losses, etc. Efficiency errors range from 2 to 4% except for the Cl^{38} source, where the error is roughly a factor of two greater. The curve is drawn by eye, since the weighted least-squares fit was not available when the drawing was made.

matrix **V**(d) which will complete the solution. The remainder of this section describes how such a solution for d and **V**(d) can be expected to be obtained.

The result of the above work is a series of fitted functions $f^m(p\,;\mathbf{b}^m)$ involving averaged sets of parameters $\mathbf{b}^m$. In order to study the behavior of each b_λ as a function of e, one must obtain from Eq. 13 the weights to assign to the b_λ^m for all m. The following simplifying assumptions are made to avoid sticky details:

1. One set of averaged parameters $\mathbf{b}^m$ and the corresponding $\mathbf{V}(\mathbf{b}^m)$'s represent the pulse-height distributions obtained from each isotope used.

2. A variance matrix exists for the Ω_m's, the peak efficiencies obtained as b_3/Qt. Covariance terms between the components of Ω and of the $\mathbf{b}_m$'s will be ignored because the largest part of the efficiency uncertainty originates in the source strengths.

3. Problems involved with inconsistent pulse-height spectra have been resolved.

4. Parameters to be chosen on physical grounds, such as "escape peak" positions, have been cleared away from the indexing system, and some solution has been attained for completing the separation of the pulse-height distributions from sources giving off two gamma rays. Resulting are the coefficients $c_{m\lambda}$ obtained by these modifications on the b_λ^m's, where, for instance, $c_{m3} = \Omega^m$, $c_{m4} = b_4^m$, etc.

5. Equations can be found which "fit" the e-dependence of the $\mathbf{c}_{m\lambda}$'s for all m's.

With these assumptions, let us approach the interpolation as a function of e. We want to minimize the appropriately weighted sum of squares of all the quantities of the form

$$c_{m\lambda} - g_\lambda(e_m; \mathbf{d}_\lambda) , \tag{14}$$

since we hope to "fit" the quantities $c_{m\lambda}$ with the functions g_λ. Note that we accept here that each of the original parameters for fitting pulse-height distributions, represented by different λ's, may require different functional forms g_λ, and that we assign the parameters of the vector $\mathbf{d}_\lambda$ to fit the c's for a given λ. The number of parameters $d_{\lambda a}$ required for a given λ is $A(\lambda)$.

For each λ we have

$$g_\lambda(e_m; \mathbf{d}_\lambda) \cong g_\lambda(e_m; \mathbf{d}_\lambda^0) + \Sigma_\sigma \delta_{\lambda\sigma} \left[\frac{\partial}{\partial d_{\lambda\sigma}} g_\lambda(e_m; \mathbf{d}_\lambda) \right]_{d=d^0} . \tag{15}$$

For convenience, we define as before

$$c_{m\lambda}^0 \equiv g_\lambda(e_m; \mathbf{d}_\lambda^0) \tag{16}$$

and

$$G_{\lambda,m\sigma} \equiv \frac{\partial}{\partial d_{\lambda\sigma}} g_\lambda(e_m; \mathbf{d}_\lambda^0) . \tag{17}$$

A weighted solution is required using the weights implied by assumption 2 above. The following error matrices are available to provide these weights:

1. $\mathbf{V}(\mathbf{c}_{.3})$, the covariance matrix of the average peak efficiencies, from the result of the least-squares averaging procedure including the correlations between observed source intensities.

2. $\mathbf{V}(\mathbf{c}_m)$ for each m, giving the variances and covariances established by averaging the shapes of the pulse-height distributions for a given source isotope m.

3. $\mathbf{V}(\mathbf{c}_m, \mathbf{c}_{m'})$ for each m and m', corresponding to gamma-ray energies from the same isotope, giving the covariances coupling the parameters describing the distributions for the two different energies.

In order to perform the L fits implied in Eq. 14, one must know $\mathbf{V}(\mathbf{c}_{.\lambda})$ for each λ. The nonzero terms could be extracted from the above and individual fits performed for each λ. Such a procedure would allow no ready means for estimating the important correlations between the $d_{\lambda\sigma}$'s for different λ's. In practice, it is necessary to perform the independent fitting procedures, but as a final step to obtain a plausible set of variances and correlations, it is necessary to perform simultaneously all of the L fits. The process may be analyzed by breaking up all the large matrices which appear in the "macro" least-squares formulation into submatrices corresponding to a given λ.

We already have the "micro" parameter vectors $\mathbf{d}_\lambda$. These can be combined into a macrovector $\mathbf{d}$, dim $\mathbf{d}(P)$, where $P = \Sigma_\lambda A(\lambda)$:

$$\mathbf{d} = \begin{pmatrix} d_1 \\ \vdots \\ d_\rho \\ \vdots \\ d_P \end{pmatrix} = \begin{pmatrix} (\mathbf{d}_1) \\ (\mathbf{d}_2) \\ (\mathbf{d}_\lambda) \\ (\mathbf{d}_L) \end{pmatrix} . \tag{18}$$

Here we have written $\mathbf{d}_\lambda$ for $\mathbf{d}_{.\lambda}$.

Next we identify the appropriate macro c-vector:

$$\mathbf{c} = \begin{pmatrix} (\mathbf{c}_{.1}) \\ (\mathbf{c}_{.2}) \\ \vdots \\ (\mathbf{c}_{.\lambda}) \\ (\mathbf{c}_{.L}) \end{pmatrix} = \begin{pmatrix} c_1 \\ c_2 \\ \\ c_n \\ c_N \end{pmatrix} , \tag{19}$$

where dim $\mathbf{c}(N)$, where $N = M \times L$, and dim $\mathbf{c}_{.\lambda}(M)$, letting $\mathbf{c}_{.\lambda} = \mathbf{c}_\lambda$. Equation 17 gives the information necessary to form the macro derivative matrix $\mathbf{G}$, dim $G(N, P)$,

$$\mathbf{G} = \begin{pmatrix} (\mathbf{G}_{11}) & 0 & 0 & 0 \\ 0 & (\mathbf{G}_{22}) & 0 & 0 \\ & \ddots & & \\ 0 & 0 & (\mathbf{G}_{\lambda\lambda}) & 0 \\ & & \ddots & \\ 0 & 0 & 0 & (\mathbf{G}_{LL}) \end{pmatrix} . \tag{20}$$

The elements of the above are given as

$$(\mathbf{G}_{\lambda\lambda})_{m\sigma} = \frac{\partial}{\partial d_{\lambda\sigma}} g_\lambda(e_m ; \mathbf{d}_\lambda) , \qquad \dim \mathbf{G}_{\lambda\lambda}[M, A(\lambda)] . \tag{21}$$

The over-all least-squares equation whose solution we desire is, of course,

$$(\mathbf{G}^T \mathbf{W} \mathbf{G})\, \delta = \mathbf{G}^T \mathbf{W}\, \Delta\mathbf{c} . \tag{22}$$

Here δ and $\Delta\mathbf{c}$ are the usual differences from previous estimates (or, for error analysis, expectation values):

$$\delta = \mathbf{d} - \mathbf{d}^0$$

$$\Delta\mathbf{c} = \mathbf{c} - \mathbf{c}^0 .$$

Only the weight matrix $\mathbf{W} = \mathbf{V}^{-1}(\mathbf{c})$ has not been described in detail, though the input error matrices listed above are adequate to determine it. By appropriate rearrangement of indices, $\mathbf{V}(\mathbf{c})$ takes the form of submatrices along the diagonal, the inverse of each submatrix being the least-squares matrix from an earlier part of the problem. Following this evaluation of W, it, too, can be broken into L^2M by M submatrices, $\mathbf{W}_{\mu\nu}$, most of which are diagonal.

Solution of Eq. 22 becomes tractable when the matrices have been broken down into the $M \times M$ submatrices. The intermediate results are

$$\mathbf{G}^T\mathbf{W}\,\Delta\mathbf{c} = \begin{pmatrix} \mathbf{G}_{11} & \sum\limits_{\lambda} & \mathbf{W}_{1\lambda} & \Delta\mathbf{c}_{\lambda} \\ & \vdots & & \\ \mathbf{G}_{\nu\nu} & \sum\limits_{\lambda} & \mathbf{W}_{\nu\lambda} & \Delta\mathbf{c}_{\lambda} \\ & \vdots & & \\ \mathbf{G}_{LL} & \sum\limits_{\lambda} & \mathbf{W}_{L\lambda} & \Delta\mathbf{c}_{\lambda} \end{pmatrix} \tag{23}$$

$$\mathbf{G}^T\mathbf{W}\mathbf{G} = \begin{pmatrix} (\mathbf{G}_{11}^T & \mathbf{W}_{11} & \mathbf{G}_{11}) & \dots & (\mathbf{G}_{11}^T & \mathbf{W}_{1L} & \mathbf{G}_{LL}) \\ \vdots & & & & & & \\ (\mathbf{G}_{LL}^T & \mathbf{W}_{L1} & \mathbf{G}_{11}) & \dots & (\mathbf{G}_{LL}^T & \mathbf{W}_{LL} & \mathbf{G}_{LL}) \end{pmatrix} . \tag{24}$$

The inverse of this latter matrix is the desired $\mathbf{V}(\mathbf{d})$. The off-diagonal submatrices of $\mathbf{G}^T\mathbf{W}\mathbf{G}$, for $\lambda \neq 3$, have elements

$$(\mathbf{G}_{\lambda\lambda}^T\mathbf{W}_{\lambda\lambda'}\mathbf{G}_{\lambda'\lambda'})_{\sigma\tau} = \sum_{m=1}^{M} (\mathbf{G}_{\lambda\lambda})_{m\sigma}(\mathbf{G}_{\lambda'\lambda'})_{m\tau} A_{\lambda\lambda'}^{m} , \tag{24a}$$

where $A_{\lambda\lambda'}^{m}$ is an element of the weighting matrix from Eq. 12.

While this breakdown into submatrices may not prove necessary for machine calculations, it appears helpful to an understanding of the problem. While the inverse of Eq. 24 is the best available estimate of $\mathbf{V}(\mathbf{d})$, for numerical reasons it may occur that values of d_λ from the many individual fits are more reliable.

Conclusions

From the empirical results and the methods presented above, we can draw the following conclusions at the present time:

1. It is possible to fit the pulse-height calibration spectra from the Compton spectrometer with essentially unique sets of parameters describing the amplitude and pulse-height dependence of the observations. The combination of a series of such results is sufficiently difficult that methods of averaging comparable raw calibration data prior to fitting might have been worth while.

2. Parameters averaged over a series of comparable runs adequately fit all the data obtained, though a perfect fit is not attained.

3. The parameters obtained for a series of energies e^m can be made to behave reasonably as a function of e, depending on the cleverness of choice of the interpolation formula to which the data are fit.

4. A procedure of the type used is expensive in both manpower and computer time, though both types of expense can apparently be controlled by (a) reducing the amount of input data for a given isotope – quite possible for workers using a spectrometer whose response can be shown to be time-independent; (b) clever choices of interpolation formulas to ensure smooth energy dependence of the "features" of the spectrum and use of a fitting program which avoids divergence problems; (c) carefully assuring that early formulations of the fitting methods to be used will smoothly go over into the more complete formulations to be needed later, which can appreciably reduce "debugging" time and repeated production costs as the various complications are introduced.

5. It is possible to establish a plausible error matrix of the many parameters required for the description of the response of the spectrometers used.

2.2. UNSCRAMBLING OF SCINTILLATION SPECTRA

W. R. Burrus

In scintillation spectroscopy, the aim is to estimate the spectrum of a source of radiation (or, more generally, to estimate some function of the spectrum such as dose, heating, etc.). Instead of measuring the spectrum directly, however, a set of numbers is observed which represents the accumulated number of counts in the "bins" of a multichannel pulse-height analyzer. Thus an "unscrambling" problem results which is the problem of estimating the desired spectrum or quantities from the observed count data.

The principal aim in developing a new unscrambling method is to avoid the necessity for making any subjective assumptions. In the method discussed here, this aim has been accomplished, and all results follow directly from the observational data. In essence, the problem of estimating any linear function of the spectrum (including the spectrum itself) is formulated as a problem of minimizing a certain "objective function" subject to certain inequality constraints. The solution to the problem is obtained by "mathematical programming"[1] (not to be confused with the "programming" of digital computers). The resulting estimates are obtained in the form of confidence intervals for the desired linear function of the spectrum. The method produces the "best," in the sense of the narrowest, confidence interval for the estimate which can be obtained from the observational data. The method is not a panacea, since if the experimenter asks for an estimate of an unreasonable quantity the confidence interval may be so wide as to be useless. But this is the fault of the questioner or the spectrometer and not of the method. Unfortunately, estimates for the spectrum, $g(e)$, usually turn out to be trivial (i.e., $0 \leqq g(e') \leqq \infty$ for any e'), but meaningful estimates may be obtained for a partially unscrambled spectrum or for quantities such as dose, etc.

[1] Vera Riley and S. I. Gass, *Linear Programming and Associated Techniques, A Comprehensive Bibliography*, Operations Research Office, Johns Hopkins University, Chevy Chase, Maryland, 1958.

The Problem

In scintillation spectroscopy, particles (e.g., photons, beta rays, neutrons, etc.) interact with a light-producing "scintillator." The intensity of the resulting scintillation is approximately proportional to the net energy deposited in the scintillator. A photomultiplier then converts the light flashes into electrical pulses which are amplified and sorted according to amplitude by a pulse-height analyzer.

In an ideal scintillation spectrometer, source particles of energy e would give rise to electrical pulses of a definite amplitude v. But practical spectrometers produce a spread of pulse heights, which can be denoted by $K(v,e)$, and in most applications the source particles are distributed in energy. The resulting pulse-height distribution is thus given by

$$f(v) = \int_0^\infty g(e)\, K(v,e)\, de\ , \tag{1}$$

where

$f(v)\, dv$ = average number of pulses which have amplitudes between v and $v + dv$,

$g(e)\, de$ = average number of "source particles" which have energies between e and $e + de$,

$K(v,e)\, dv$ = probability that a "source particle" of energy e will result in a pulse with amplitude between v and $v + dv$.

The function $f(v)$ is not really observed, however, because of the finite number of bins of a multichannel pulse-height analyzer and because of the statistical fluctuations in the number of pulses which are counted in a particular bin. If the pulse-height analyzer has m bins corresponding to m equal pulse-height intervals, then the average number of pulses counted in the ith bin is given by

$$\bar{c}_i = \int_{(i-1)\Delta}^{i\Delta} f(v)\, dv\ , \qquad i = 1, 2, \ldots, m\ , \tag{2}$$

where $\bar{c}_i$ is the average number of pulses counted in the ith bin, and Δ is the channel width.

Under conditions which usually (but not always) prevail in scintillation spectroscopy, the number of counts observed, $\hat{c}_i$, have approximately independent Poisson statistical distributions, with average values given by Eq. 2, and standard deviations, or dispersions, given by

$$\sigma_i \approx \sqrt{\hat{c}_i}\ , \qquad i = 1, 2, \ldots, m\ . \tag{3}$$

The average number of counts, $\bar{c}_i$, may be expressed directly in terms of the spectral distribution function, $g(e)$, by combining Eqs. 1 and 2 to give

$$\bar{c}_i = \int_0^\infty K_i(e)\, g(e)\, de\ , \tag{4}$$

where

$$K_i(e) = \int_{(i-1)\Delta}^{i\Delta} K(v,e)\, dv\ , \qquad i = 1, 2, \ldots, m \tag{5}$$

is the probability that a "source" particle of energy e will result in a count in the ith bin.

As stated above, "unscrambling" a spectrum means estimating the value of a linear function of the spectrum. For generality the form of the quantities to be estimated can be taken to be an inner product of the spectral distribution function $g(e)$ and a window function $w(e)$. Thus

$$\psi = \int_0^\infty w(e)\, g(e)\, de \,, \tag{6}$$

where ψ is the unknown quantity to be estimated and $w(e)$ is the window function which relates ψ to $g(e)$.

Even though estimates of several quantities of the above form may be desired, there is no loss of generality in considering them one at a time. Notice that this class of quantities includes the spectrum itself, since $\psi = g(e')$ if $w(e) = \delta(e - e')$, and also such quantities as dose which are related to the spectral distribution function by a cross section. The function $w(e)$ is called a "window function" for the estimate ψ, since the influence of $g(e)$ on the value of ψ is controlled by the value of $w(e)$. [The term "window function" is sometimes used differently to denote the response function of the spectrometer, $K(v,e)$, which occurred in Eq. 1, but here "response function" will be used for this meaning.]

As mentioned previously, sometimes a partially unscrambled spectral function is of interest, since the estimation of the actual spectral function, $g(e)$, leads to a trivial estimate with $0 \leqq g(e') \leqq \infty$ for any e'. A partially unscrambled spectral function, $g^*(e')$, may be obtained by correcting for only a portion of the instrumental smearing introduced by $K(v,e)$ and allowing a residual smearing $K^*(v,e)$ to remain. Thus, the partially unscrambled spectral function to be estimated is given by

$$g^*(e') = \int_0^\infty K^*(e',e)\, g(e)\, de \,, \tag{7}$$

where $g^*(e')$ is the partially unscrambled spectral distribution function and $K^*(e',e)$ is the residual smearing that is allowed to remain.

Usually any unsymmetric portion of the instrumental smearing should be removed and a small amount of symmetric residual smearing left. The amount of residual smearing is to be chosen so that the precision of the resulting estimates for $g^*(e')$ is satisfactory. Equation 7 is of the form of an inner product of $g(e)$ times a window function $K^*(e',e)$, so that the general theory may be used to estimate $g^*(e')$ also. The concept of residual smearing is certainly not new, having been used by A. Sommerfeld in 1891 (ref 2), but its application for improving the accuracy of spectral estimates in scintillation spectroscopy is believed to be new.

Since $K(v,e)$ is allowed to contain all contributions to the nonideal spread of $f(v)$, $K_i(e)$ must usually be determined partly by experiment using known "sources." Thus, $K_i(e)$ will have a statistical uncertainty associated with it. It has been shown, however, that small statistical uncertainties in $K_i(e)$ can be

[2] A. Sommerfeld, *Die Wilkurlichen Functionen in der Mathematischen Physik*, Ph.D. Dissertation, Konigsberg University, 1891.

taken into account by increasing the effective variance of the observed counts, $\hat{c}_i$, above the value given by Eq. 3 (ref 3). In this paper it is assumed that the response functions $K_i(e)$ are known exactly.

In summary, the unscrambling problem, with the above assumption, can be completely stated as follows: Given

$$\left.\begin{aligned} &\hat{c}_i,\ \sigma_i,\ K_i(e)\ ,\ \text{and}\ w(e)\ , && i = 1, 2, \ldots, m\ , \\ &\text{and knowing that} \\ &\bar{c}_i = \int_0^\infty K_i(e)\, g(e)\, de\ , && i = 1, 2, \ldots, m\ , \\ &\text{find} \\ &\psi = \int_0^\infty w(e)\, g(e)\, de\ . \end{aligned}\right\} \quad (8)$$

The Estimation Method

In this section, a new solution to Problem 8 is obtained. Ideally, on the basis of the data alone, without additional assumptions, it is desired to make the "best" probability statement possible of the type

$$\Pr[\hat{\psi}^- \leqq \psi \leqq \hat{\psi}^+] = \alpha\ , \quad (9)$$

where

ψ = true value of the quantity to be determined,

$\hat{\psi}^-, \hat{\psi}^+$ = random variables used as upper and lower estimates of ψ,

α = confidence coefficient.

Thus, if an experiment were repeated a large number of times under the same conditions, the experimentally obtained estimates $\hat{\psi}^-$ and $\hat{\psi}^+$, for $\alpha = 0.95$, would bracket the true value in 95% of the experiments and miss the true value in 5% of the experiments. "Best" is used in the sense that no narrower confidence interval could be found for a particular value of α.

Upon further examination, it is found that values of $\hat{\psi}^-$ and $\hat{\psi}^+$ which will satisfy Eq. 9 cannot be obtained from the observational data. The explanation lies in the finite number of bins which are used to accumulate the counts. Even if the spectrometer had no other source of pulse-height broadening and the true average count distribution were known, the width of the bins would make it impossible to experimentally distinguish fine detail in a spectrum which occurred within the width of a bin. Thus, there are an infinite number of physically possible spectra which will yield exactly the same average accumulated count distribution. But not all these spectra would result in the same value of ψ. The approach taken is to consider the whole class of spectra which are consistent with the observational data and to pick one which yields the largest possible value of ψ and one which yields the smallest possible value of ψ. These can be called "nature's most adverse spectra." Then no matter what the actual spectra happen to be, the

[3] Walter R. Burrus, *The Theory of Corrections for Instrumental Scrambling of Spectra*, (Preliminary copy of dissertation), to be submitted to Ohio State University; also to be published as an ORNL memorandum.

true value of ψ will be somewhere between the largest possible and smallest possible. This technique of interval estimation can be thought of as an extension of the minimax method of statistical estimation.

There are two major difficulties with the above approach. First, the true count distribution can never be found. Rather only a statistical sample from a random population is observed. Thus, it is difficult to define the class of spectra which are consistent with the observational data. Second, since "nature's most adverse spectra" might have any number of discrete components as well as a continuous component, these spectra would be difficult to find. In the following development, both these difficulties are bypassed by treating an equivalent problem formulated in terms of a finite number of components, $u_1, u_2, \ldots u_m$. The problem formulated in terms of the u's is said to be "dual" to the original (or "primal") problem. Once the solution to the dual problem has been obtained the primal problem can be solved.

The idea of the dual formulation is to find a combination of response functions, $\sum_{i=1}^{n} u_i^+ K_i(e)$, which lies entirely above the window function and another combination, $\sum_{i=1}^{n} u_i^- K_i(e)$, which lies entirely below the window function as shown in Fig. 2.2.1. Then

$$\sum_{i=1}^{n} u_i^- K_i(e) \leqq w(e) \leqq \sum_{i=1}^{n} u_i^+ K_i(e) .$$

UNCLASSIFIED
2-01-058-01-653

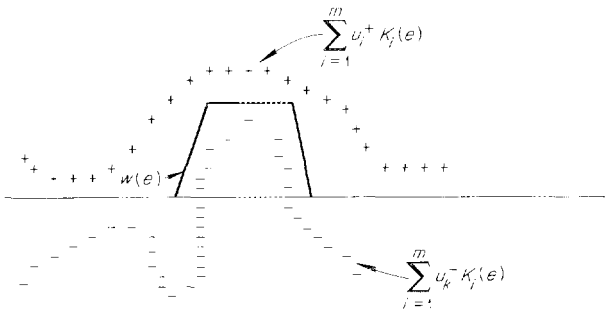

Fig. 2.2.1. The Upper and Lower Bounds for a Window Function in Terms of Response Functions.

Now since $g(e)$ is nonnegative, the terms in the above inequality may be multiplied by $g(e)$ and an integration over e may be made without affecting the inequality. Then

$$\sum_{i=1}^{m} u_i^- \int_0^\infty K_i(e)\, g(e)\, de \leqq \int_0^\infty w(e)\, g(e)\, de \leqq \sum_{i=1}^{m} u_i^+ \int_0^\infty K_i(e)\, g(e)\, de . \tag{10}$$

Now by using Eq. 4 and Eq. 6,

$$\sum_{i=1}^{m} u_i^- \bar{c}_i \leqq \psi \leqq \sum_{i=1}^{m} u_i^+ \bar{c}_i . \tag{11}$$

In order to obtain the best possible estimate of ψ, u_i^+ must be chosen so that the right side of Eq. 11 is as small as possible and u_i^- must be chosen so that the left side is as large as possible. Thus upper and lower bounds for $w(e)$ would be found which would hug $w(e)$ closest in the most important regions, perhaps at the expense of a close fit in regions which are not so important. If there were no uncertainty in the true average counts, the problem of choosing u_i^+ and u_i^- could be concisely stated as follows:

$$\left.\begin{array}{l}\text{Find numbers } u_1^+, u_2^+, \ldots, u_m^+ \text{ which minimize } \sum_{i=1}^{m} u_i^+ \bar{c}_i \text{ subject} \\ \text{to the restrictions that } \sum_{i=1}^{m} u_i^+ K_j(e) \geqq w(e) \text{ for all } e\,.\end{array}\right\} \quad (12)$$

$$\left.\begin{array}{l}\text{Find numbers } u_1^-, u_2^-, \ldots, u_m^- \text{ which maximize } \sum_{i=1}^{m} u_i^- \bar{c}_i \text{ subject} \\ \text{to the restrictions that } \sum_{i=1}^{m} u_i^+ K_j(e) \leqq w(e) \text{ for all } e\,.\end{array}\right\} \quad (13)$$

A basic theorem in mathematical programming asserts that these two problems are equivalent to the following problems:

$$\left.\begin{array}{ll}\text{Find a nonnegative function } g^+(e) \text{ which maximizes} \int_0^\infty g^+(e)\, w(e)\, de & \\ \text{subject to the restrictions} \int_0^\infty K_i(e)\, g^+(e)\, de = \bar{c}_i\,, & i = 1, 2, \ldots, m\,.\end{array}\right\} \quad (12')$$

$$\left.\begin{array}{ll}\text{Find a nonnegative function } g^-(e) \text{ which minimizes} \int_0^\infty g^-(e)\, w(e)\, de & \\ \text{subject to the restrictions} \int_0^\infty K(e)\, g^-(e)\, de = \bar{c}_i\,, & i = 1, 2, \ldots, m\,.\end{array}\right\} \quad (13')$$

Furthermore,

$$\min \sum_{i=1}^{m} u_i^+ \bar{c}_i = \max \int_0^\infty g^+(e)\, w(e)\, de\,,$$

and (14)

$$\max \sum_{i=1}^{m} u_i^- \bar{c}_i = \min \int_0^\infty g^-(e)\, w(e)\, de\,.$$

It can also be shown that the two most adverse spectra, $g^+(e)$ and $g^-(e)$, need have at most m discrete components.

Now when the statistical errors in the observational counts $\hat{c}_1, \hat{c}_2, \ldots, \hat{c}_m$ are considered, the statistical distribution of $\left(\sum_{i=1}^{m} u_i^- \hat{c}_i\right)$ and $\left(\sum_{i=1}^{m} u_i^+ \hat{c}_i\right)$ which would appear in Eq. 11 should be considered. Assuming that $\hat{c}_1, \hat{c}_2, \ldots, \hat{c}_m$ are normally distributed with standard deviations $\sigma_1, \sigma_2, \ldots, \sigma_n$ $\left(\sum_{i=1}^{m} u_i^+ c_i\right)$ will be normally distributed with standard deviation, given by the usual rule for combination o errors, of

$$s^+ = \left(\sum_{i=1}^{m} u_i^{+2} \sigma_i^2\right)^{1/2} . \tag{15}$$

Similarly $\left(\sum_{i=1}^{m} u_i^- \hat{c}_i\right)$ will be normally distributed with standard deviation

$$s^- = \left(\sum_{i=1}^{m} u_i^{-2} \sigma_i^2\right)^{1/2} . \tag{16}$$

If Problems 12 and 13 are solved by using $\hat{c}_i$ instead of $\bar{c}_i$, it may be found that some coefficients, u_i^+ or u_i^-, of large magnitudes (positive or negative) will be required to obtain the best upper and lower bounds. These coefficients will result in large standard deviations, s^+ or s^-. Thus, Problems 12 and 13 should be modified to take into account the statistical distribution of $\hat{c}_1, \hat{c}_2, \ldots, \hat{c}_m$.

It has been shown[3] that for the estimators $\hat{\psi}^- = \sum_{i=1}^{m} u_i^- \hat{c}_i - \kappa s^-$ and $\hat{\psi}^+ = \sum_{i=1}^{m} u_i^+ \hat{c}_i + \kappa s^+$,

$$\Pr[\hat{\psi}^- \leq \psi \leq \hat{\psi}^+] \geq \begin{cases} 0.6827 \text{ for } \kappa = 1 , \\ 0.9545 \text{ for } \kappa = 2 , \\ 0.9973 \text{ for } \kappa = 3 . \end{cases} \tag{17}$$

An inequality rather than an equality occurs because a slight approximation is made by assuming that the most unfavorable correlation exists between $\left(\sum_{i=1}^{m} u_i^- c_i\right)$ and $\left(\sum_{i=1}^{m} u_i^+ c_i\right)$ and, more importantly, because there is an inequality in Eq. 11 which was used in deriving the result. Equation 17 should be compared with Eq. 9. Equation 17, with $\kappa = 2$, implies that if an experiment is repeated a large number of times under the same conditions, in at least 95% of the experiments $\hat{\psi}^-$ and $\hat{\psi}^+$ will bracket the true value of ψ, but in favorable cases (depending on the true spectra), the fraction may be much higher than 0.95.

When the statistical fluctuations in $\hat{c}_1, \hat{c}_2, \ldots, \hat{c}_m$ are considered, Eq. 17 suggests that the best estimates of ψ would be obtained by minimizing the interval from $\hat{\psi}^-$ to $\hat{\psi}^+$ for some value of κ which depends upon the confidence level desired. Then the resulting upper and lower bounds for $w(e)$ will represent a compromise between a close fit and one which can be obtained using small coefficients u_i^- and u_i^+.

To summarize, the problem of choosing u_i^- and u_i^+, when statistical fluctuations in the data are considered, can be stated as follows:

Find numbers $u_1^+, u_2^+, \ldots, u_m^+$ which minimize

$$\left.\hat{\psi}^+ = \sum_{i=1}^{m} u_i^+ c_i + \kappa \sqrt{\sum_{i=1}^{m} u_i^{+2} \sigma_i^2} \quad \text{subject to} \quad \sum_{i=1}^{m} u_i^+ K_i(e) \geqq w(e) \right\} \tag{18}$$

for all e. Find numbers $u_1^-, u_2^-, \ldots, u_m^-$ which maximize

$$\left.\hat{\psi}^- = \sum_{i=1}^{m} u_i^- c_i - \kappa \sqrt{\sum_{i=1}^{m} u_i^{-2} \sigma_i^2} \quad \text{subject to} \quad \sum_{i=1}^{m} u_i^- K_i(e) \leqq w(e) \right\} \tag{19}$$

for all e.

It is possible to solve Problems 18 and 19 by standard linear programming methods if the functions ψ^+ and ψ^- are approximated by linear functions of the c's and σ's. A FORTRAN code has been written for this problem using the Simplex linear programming method but has not yet been completely checked out.

Conclusions

A statistical estimation technique based on mathematical programming has been developed for estimating the solutions to the integral equations resulting from a scintillation spectrometer (and from many other instruments as well). The technique is based on expressing the quantity for which an estimate is desired in terms of a window function, and, by proper choice of the window function, estimating a partially unscrambled spectrum with some residual smearing or any linear function of the spectrum. Generally, estimates of the actual spectrum are trivial.

The result of the estimation method is a confidence interval for the desired quantity which is based on "nature's most adverse spectra," consistent with the observational data; consequently the confidence interval is nearly always conservative (i.e., too wide). The reduction of the mathematical problem to a numerical problem is also done in such a way that the numerical approximation due to a finite number of breakpoints also gives a conservative result.

An attractive feature of the method is its ability to use all the statistical information about the observational data. Another characteristic, which is pleasantly opposed to some methods, is that the results never become worse when the number of response functions is increased. If the inclusion of the new response functions would worsen the answer, the method automatically ignores the function.

By replacing the continuous variables by discrete variables, the same method may be used to estimate the solution to a poorly conditioned matrix equation whose solution is known to be positive but is obscured by errors in the constant vector or matrix. The improvement over regular matrix inversion is due to the incorporation into the problem of the nonnegativity of the solution. Thus spurious oscillatory solutions which would result in a negative value can not occur.

2.3. EXPERIMENTAL DETERMINATION OF FLUX DEPRESSION AND OTHER CORRECTIONS FOR GOLD FOILS EXPOSED IN WATER

W. Zobel

An investigation leading to an accurate evaluation of the total correction required for the determination of the unperturbed thermal-neutron flux in light water by the use of gold foils has recently been completed. The design of the experiment, experimental materials, and experimental arrangement were detailed in previous reports and some preliminary values were given.[1] In the paragraphs below some additional results and a final analysis of all the experimental data are presented.

Normalization of Data

Since the several runs making up this experiment were rather widely separated in time, it was necessary to normalize the data from different runs in order to compare the results. Two normalizations must be considered. The first takes account of the small short-term fluctuations in the source power during a run; the second corrects for possible long-term drifts between runs.

The short-term correction for changes in source power is based on the output of a boron-lined ionization chamber which monitored the neutron flux incident upon the Lid Tank Shielding Facility source plate. While it is known that the output of the chamber is not quite linear over a large change in reactor power, e.g., from 1700 to 3400 kw, the fluctuations to be expected during a run will not exceed 100 kw, and over that interval the linearity of the instrument is adequate.

The long-term normalization, in the case of square foils, was accomplished by using the average of the normalization factors obtained from the ratios of the saturated activities per unit mass of 0.001-in.-thick and 0.003-in.-thick foils in the different runs. In the case of the circular foils the normalization was based on the comparison of 1-cm-square, 0.002-in.-thick foils exposed during each run for this purpose.

Experimental Results

The results of the foil activations for the square foils are presented in Figs. 2.3.1 and 2.3.2. Saturated activity per unit mass is plotted as a function of foil thickness. Each point shown is the average of from four to eight determinations.

[1] W. Zobel, *Neutron Phys. Ann. Prog. Rep., Sept. 1, 1960*, ORNL-3016, p. 267; W. Zobel, *Neutron Phys. Ann. Prog. Rep., Sept. 1, 1959*, ORNL-2842, p. 202.

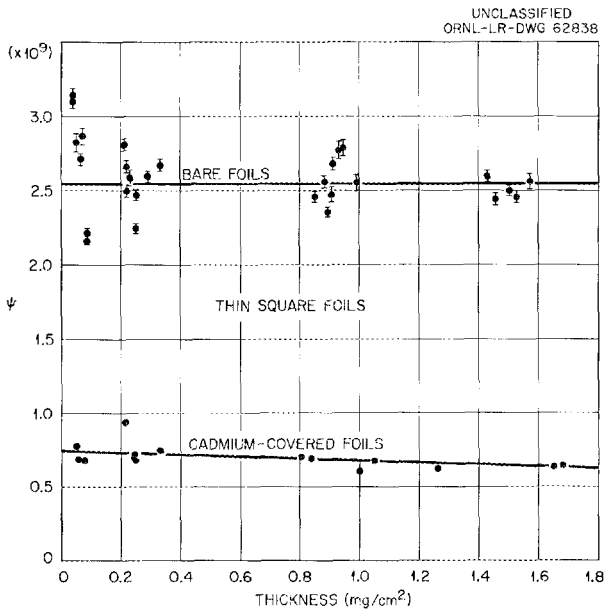

Fig. 2.3.1. Saturated Activity per Unit Mass as a Function of Thickness for Thin Square Gold Foils.

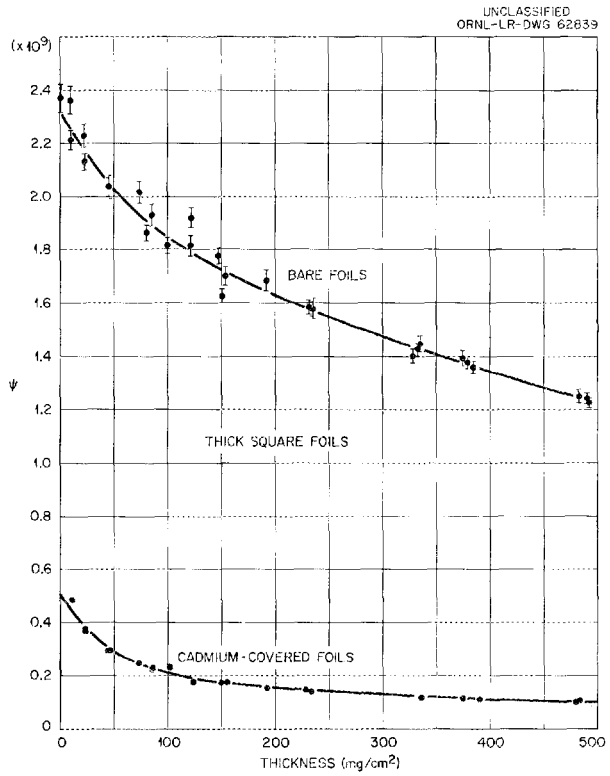

Fig. 2.3.2. Saturated Activity per Unit Mass as a Function of Thickness for Thick Square Gold Foils.

In order to compute the "flux depression factor," the value by which an experimentally measured flux must be multiplied to obtain an unperturbed flux, it is necessary to determine the value of the unperturbed flux in the present measurements. This value can be obtained by extrapolation of the finite-thickness foil data to zero foil thickness, since such a foil should not affect the flux. To permit this extrapolation, straight lines were fitted to the thin foil data by the method of least squares, using an IBM-7090 program. The thick foil data was fitted with exponential functions, again using a least-squares program for the IBM-7090.[2] The function chosen was the simplest smooth function which appeared to fit the data.

The subtraction of the cadmium-covered activities from the bare activities was facilitated by additional IBM-7090 computations of the value of the function at certain predetermined points chosen to be the theoretical masses of the foils for the thicknesses used. Subtraction of these points should eliminate errors due to small fluctuations in the masses of foils with the same nominal thickness. For the very thin foils, arbitrary masses were chosen at convenient intervals. The errors on these computed points were determined from the errors of the individual points from which the curve was determined and the scatter of the points about the curve.

The flux depression factor for each foil thickness was calculated by using the cadmium difference activities per unit mass. The factor was taken to be the saturated activity per unit mass for a foil of

[2]Some of the programs of R. W. Peelle and R. O. Chester were used in this work.

the finite thickness involved divided by the saturated activity per unit mass for a foil of zero thickness. These factors are plotted in Fig. 2.3.3. Also shown on this figure are theoretical curves computed according to several different recipes.[3-6] For these comparisons, the foils were assumed to be circular but to have the same area as the square foils.

The data obtained for circular foils of different diameters were treated in the same way as those for the square foils, except that the value for the unperturbed flux was taken to be the same as that obtained for the square foils and not redetermined for each diameter. The data are shown in Figs. 2.3.4 through 2.3.7.

[3]W. Bothe, *Z. Physik* **120**, 437 (1943).

[4]T. H. R. Skyrme, *Reduction in Neutron Density Caused by an Absorbing Disc*, MS-91 (n.d.).

[5]R. H. Ritchie and H. B. Eldridge, *Nuclear Sci. and Eng.* **8**, 300 (1960).

[6]G. R. Dalton and R. K. Osborne, *Nuclear Sci. and Eng.* **9**, 198 (1961).

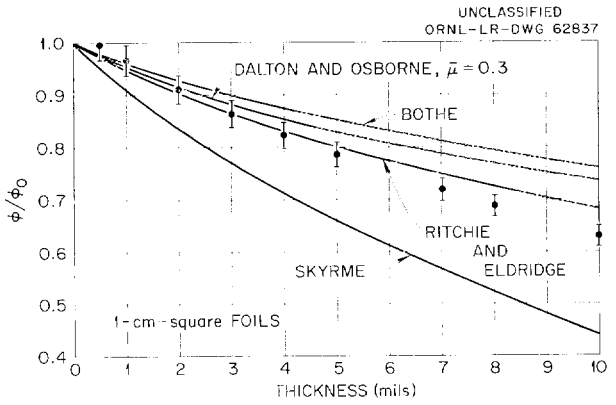

Fig. 2.3.3. Flux Depression Factor, ϕ/ϕ_0, as a Function of Thickness for 1-cm-square Gold Foils.

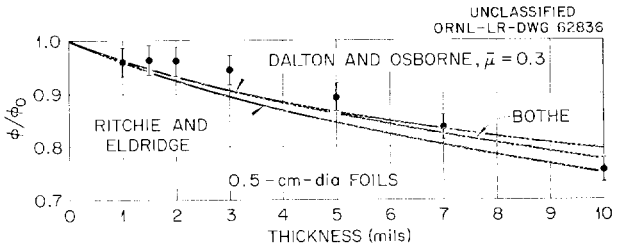

Fig. 2.3.4. Flux Depression Factor, ϕ/ϕ_0, as a Function of Thickness for 0.5-cm-dia Circular Gold Foils.

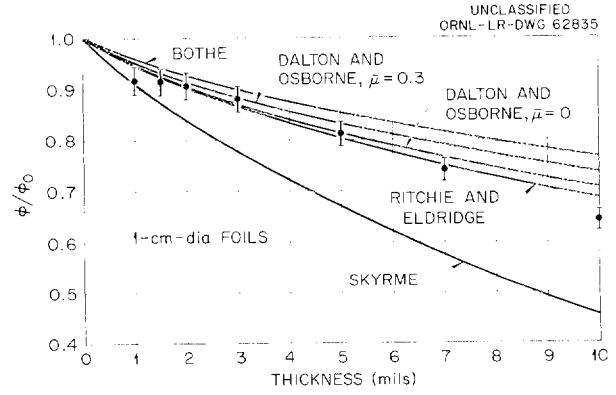

Fig. 2.3.5. Flux Depression Factor, ϕ/ϕ_0, as a Function of Thickness for 1-cm-dia Circular Gold Foils.

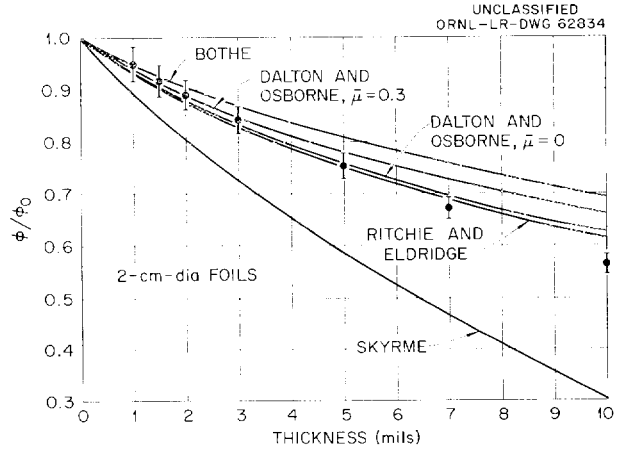

Fig. 2.3.6. Flux Depression Factor, ϕ/ϕ_0, as a Function of Thickness for 2-cm-dia Circular Gold Foils.

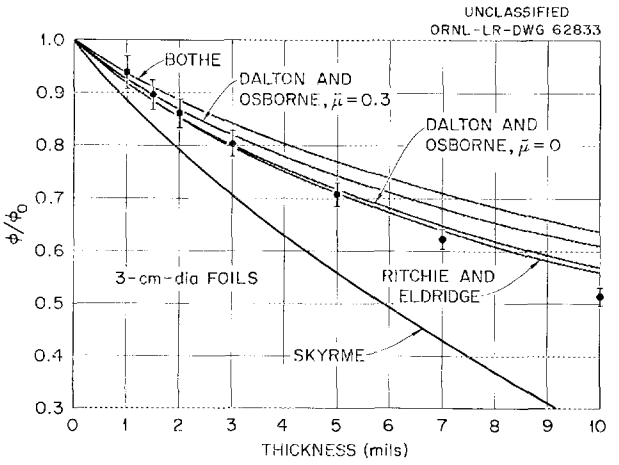

Fig. 2.3.7. Flux Depression Factor, ϕ/ϕ_0, as a Function of Thickness for 3-cm-dia Circular Gold Foils.

Conclusions

It is obvious from Figs. 2.3.3 through 2.3.7 that the best agreement is obtained with the calculations of Ritchie and Eldridge[5] and those of Dalton and Osborne[6] using isotropic scattering.

The discrepancies apparent for thick foils may be due to the absorption of the 411-kev gamma ray in the foil itself. This effect is included in the experimental results, but as yet no correction has been made to the theoretical calculations. Further work along this line is in progress.

Calculations are being performed in cooperation with Dalton to include the effect of higher harmonics on his results. It is expected that this may lead to a reduction of the present discrepancy for thick (>0.005 in.) foils.

An apparent shape discrepancy also exists between experiment and calculation for foil thicknesses <0.0015 in. and diameters of 0.5 and 1 cm. This is due to the model chosen to fit the experimental data. Since the model was chosen as the simplest fit to the data, it is probably not correct in detail.

2.4. THE MODEL IV GAMMA-RAY SPECTROMETER: STATUS REPORT

G. T. Chapman and K. M. Henry

The development of the Model IV "total-absorption" gamma-ray spectrometer has continued. The 9-in.-dia, 12-in.-long NaI(Tl) crystal described previously[1] has now been in almost constant use for about nine months without any noticeable deterioration of the cemented interface. Figure 2.4.1 shows a recent determination of the response of the spectrometer to collimated gamma rays ranging in energy from 0.511 to 2.754 Mev.

A complete study of the background associated with the Model IV spectrometer has indicated that the major contribution to the high-energy region (>4 Mev) may come from cosmic-ray interactions with the components of the spectrometer shield. This was implied when measurements made with the spectrometer

[1] G. T. Chapman, *Neutron Phys. Ann. Prog. Rep., Sept. 1, 1960*, ORNL-3016, p. 264.

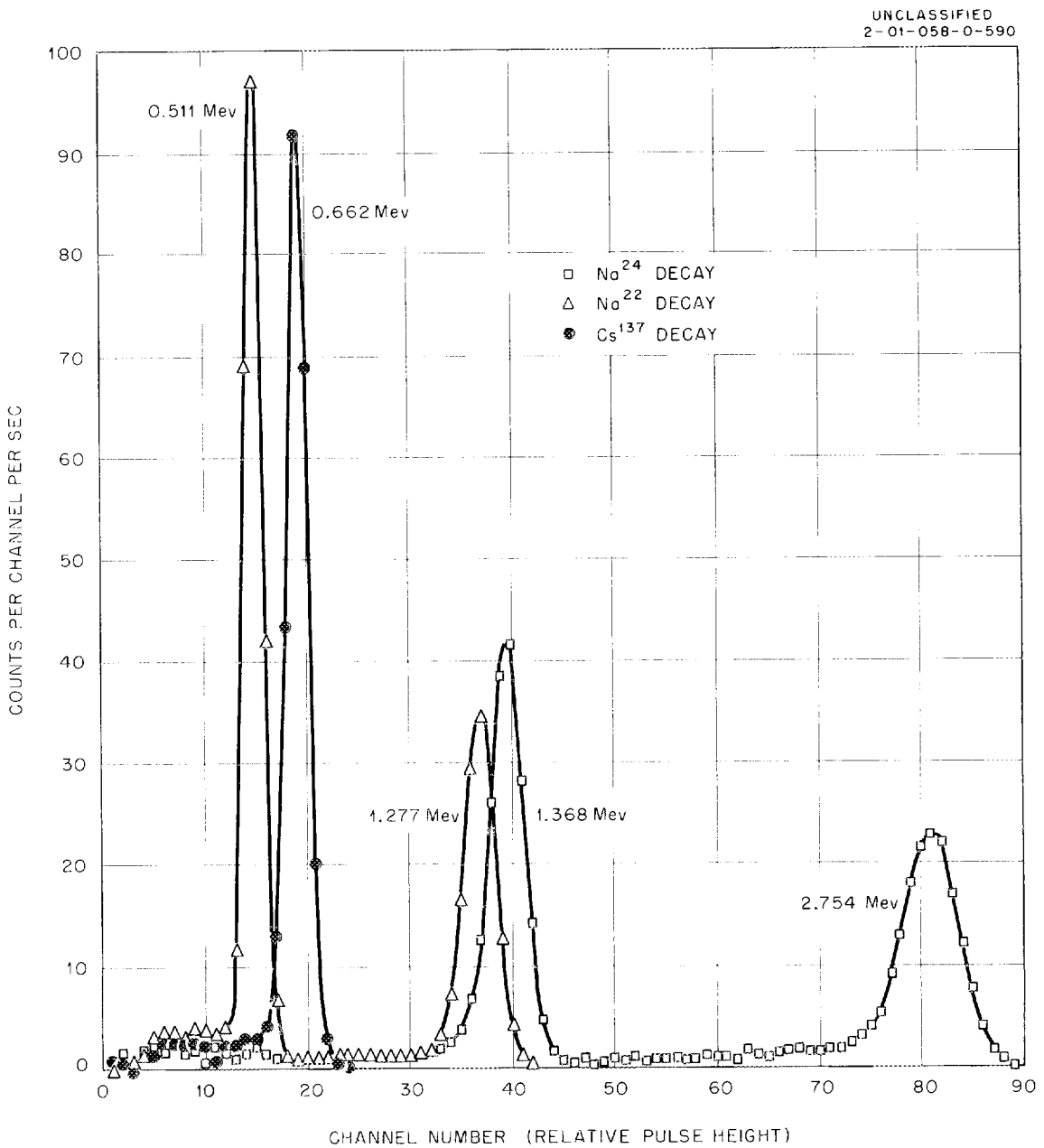

Fig. 2.4.1. Response of the Composite 9-in.-dia, 12-in.-long NaI(Tl) Crystal to Collimated Gamma Rays.

covered with 19 ft of water showed a decrease of ~30% in the magnitude of the high-energy background. As shown in Fig. 2.4.2, there are peaks in the distribution up to 116 Mev.

Below 4 Mev the background counts appear to arise largely from the long-lived activity of impurities in the spectrometer shield. Measurements made with the reactor operating at a power of 2 watts and with the spectrometer located ~6 ft from the reactor surface resulted in spectra unchanged from the spectrum observed at the same point but with the reactor shut down. It is therefore reasonable to conclude that

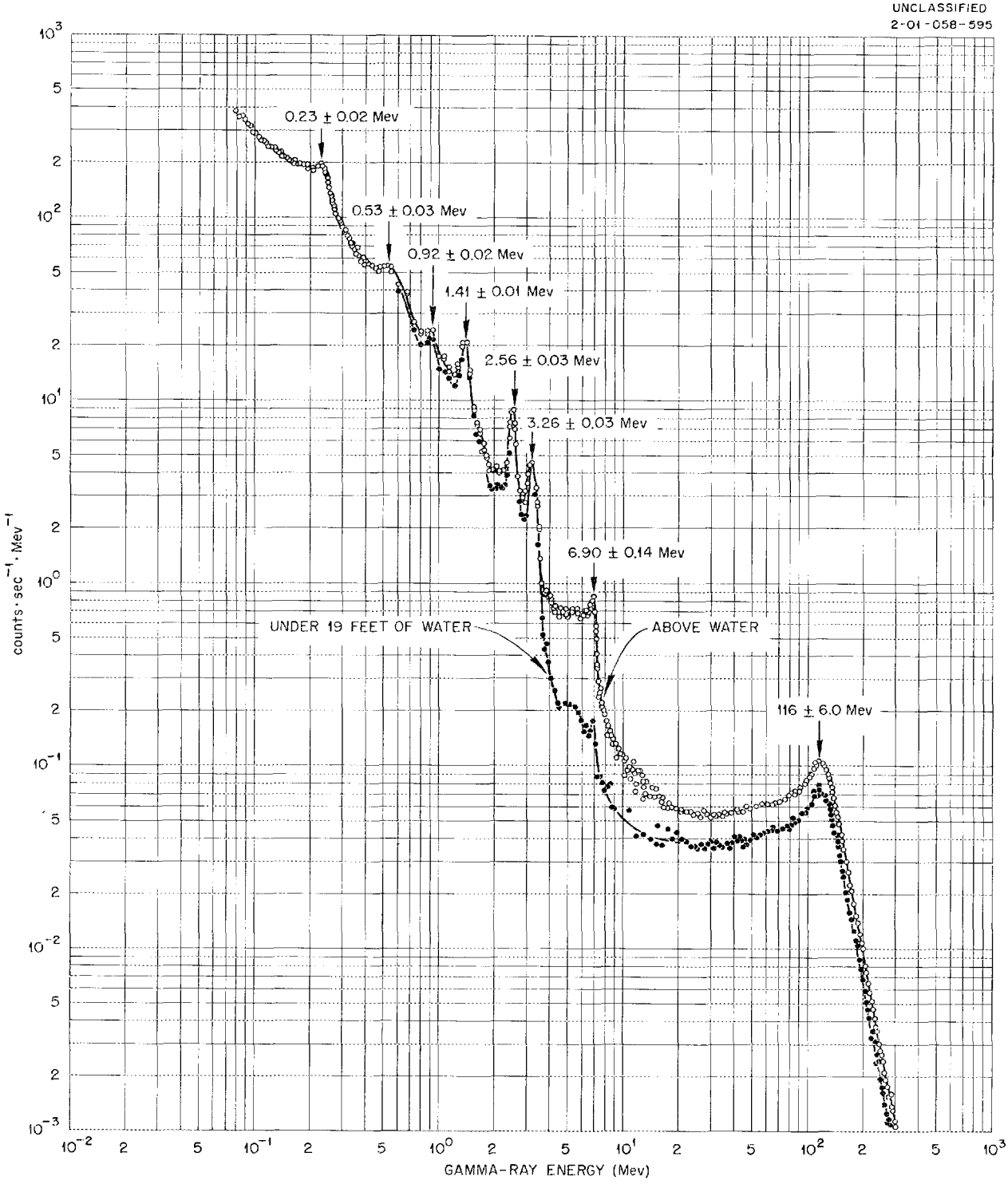

Fig. 2.4.2. Background Associated with the Model IV Gamma-Ray Spectrometer.

under the circumstances of the measurement, at least, capture gamma rays resulting from reactor neutron interactions in the shield are negligible. A second measurement, made 72 hr after exposure of the shield to reactor neutrons, failed to show any time-dependent decay of the peaks, indicating that the peaks could not logically be associated with neutron activation of any isotope expected in the spectrometer.

The energies shown for the peaks in Fig. 2.4.2 were obtained by comparison with the energies of known gamma-ray sources up to 3.26 Mev; the energies above this point were assigned by an extrapolation based on the linearity of the system as determined by a standard pulser.

Although the structure of the curve has not yet been completely explained, the measurements indicate that backgrounds due to high-energy particles or photons may become a serious problem when large scintillation detectors are used, even if the detector is completely shielded with a very massive shield such as that of the Mark IV spectrometer. The data shown indicate the minimum to which the background in this spectrometer may be reduced.

2.5. SOLID-STATE FISSION DETECTORS

T. A. Love and K. M. Henry

Silicon-gold surface barrier diodes have been successfully used as particle detectors and spectrometers in many situations. The general concept and methods of fabrication have been described elsewhere.[1] The properties of such diodes suggested that they might be adapted for use as fission particle detectors, specifically for employment in the small water spaces between the fuel plates of MTR-type reactor fuel elements. A number of probes incorporating surface barrier diodes in conjunction with U^{235} films were therefore fabricated,[2] and three were obtained for testing at the Bulk Shielding Facility. Since no particular difficulty was anticipated in the proposed application of surface barrier diodes, a detailed series of tests was not originally scheduled, and the somewhat random nature of the experiments to be described is primarily due to the surprisingly bad results observed in the first tests.

Experimental Materials

The three probes originally obtained utilized surface barrier diodes made in conventional fashion. The starting material was low-resistance (150 $\Omega \cdot$cm) silicon, in the form of a 0.2-in. square, 0.050 in. thick. The thickness was reduced to 0.030 in. by lapping before evaporation of the gold barrier. The diode was cast in a plastic mold, and a 1-mg/cm^2 U^{235} film evaporated on aluminum foil was mounted close to but not in contact with the gold surface. The arrangement was fitted at the bottom of a thin aluminum tube,

[1] T. A. Love *et al.*, *Neutron Phys. Ann. Prog. Rep., Sept. 1, 1960*, ORNL-3016, p. 280, incl. references; also, G. Dearnley and A. B. Whitehead, *The Semiconductor Surface Barrier for Nuclear Particle Detectors*, AERE-R-3662 (Feb., 1961); see also Sec. 2.15, this report.

[2] All diodes were prepared under the supervision of R. E. Zeller, Instrumentation and Controls Division.

26 in. long, 0.75 in. wide, and 0.10 in. thick. The space remaining in the tube was filled with Lucite, so that the reactor would not "see" a void when the probe was introduced.

Original Tests and Results

The first diode probe to be tested was connected to a suitable preamplifier and a DD-2 amplifier with a 100-v diode supply. The PHS circuit of the DD-2 amplifier and a scaler were used to obtain a curve of the response to alpha particles, which was used to set the PHS to discriminate against the alpha particles. The unit was then inserted into a critical array of BSR-I fuel elements in the Pool Critical Assembly operating with a flux of $\sim 10^6$ neutrons·cm^{-2}·sec^{-1}. The resulting fission particle response curve was completely unreproducible. The electronic system, including the diode supply, and the reactor power were checked and found to be stable. The probe was then withdrawn from the reactor and again tested for its response to alpha particles. The response was both unstable and decreasing, and it was tentatively diagnosed that moisture due to water leakage into the probe was causing the difficulty.

A second probe was then prepared with particular care being taken to ensure complete waterproofing. When tested in the same fashion, the behavior of this second probe was the same as the first, thus proving that the cause of the difficulty was not moisture. Subsequent dismantling of the first probe showed no indication of attack by water.

To test the speculation that damage might be resulting from the fast-neutron flux in the reactor, the third probe was exposed in the thermal column of the ORNL Graphite Reactor without electrical connections of any kind. Measurements made after removal showed a large change in resistivity of the material, and a check of the response to alpha particles showed that it was unsteady.

At the end of these tests all three diodes had been exposed to a large number of alpha particles from the U^{235} foil, to between 10^7 and 10^8 thermal neutrons, and to relatively low gamma-ray fields. In addition, the first two diodes tested had been exposed to 10^7 and 10^8 epicadmium neutrons. All the results were inconclusive and additional investigation was clearly required.

Additional Tests and Results

Preliminary to further tests with the diodes, the behavior of the base material was scrutinized. Two silicon wafers, a bare one used as a monitor and another with a U^{235} foil attached, were exposed to $\sim 10^8$ thermal neutrons in order to determine the probable depth of additional impurity centers produced by fission products impinging on the silicon. The electrical resistance of the bare wafer did not change as a result of the exposure, but the resistance of the wafer to which the U^{235} foil was attached decreased tremendously off scale at the low end of the meter used. The change was obviously due to fission-product accumulation, and lapping was begun on the surface of the contaminated piece to determine the probable depth of penetration. The first lapping restored the original resistivity, indicating only surface contamination by fission products.

An original and basic criterion for the use of surface barrier diodes as fission particle detectors was that the diode must remain stable in response until a sufficient number of counts above the alpha-particle

cutoff could be obtained to completely map the flux in a reactor core. Thus primary attention was placed on accumulated count rather than total dosage, although the latter should also be known. The experiments which followed were intended to further investigate stability.

Since fabrication of additional probes was clearly premature at this stage of experimentation, the remainder of the work to be described utilized conventionally sized and packaged "stock" diodes, similar to those described by Love.[3]

A fresh start was made with an arrangement consisting of a low-resistance ($\sim$200-Ω) diode, a U^{235} foil, a preamplifier and DD-2 amplifier, and a 256-channel analyzer. The diode was selected only on the basis that it was to operate with an applied bias of 100 v, no other conditions being imposed. With the rapid failure of the first three diodes in mind, testing was begun at a slow pace, using D-T neutrons from the BSF particle accelerator. The sequence of operations was as follows: D beam off, alpha check; beam on, accumulate 1000 counts; beam off, alpha check and comparison; beam on . . . etc. Some 3×10^4 counts, at a rate of 2 counts/sec, were accumulated in this manner with no evidence of shift of fission spectrum or change in position of alpha peak.

Since no apparent progress was being made, the diode was then shifted to a position near the BSR-I reactor for a series of runs with the reactor at 2 watts. A total of 2×10^6 fission counts was thus accumulated. The reactor power was then incrementally increased to 33 watts, at which level the "dead time" for the 256-channel analyzer was 25% of the run time. Beyond this power level, therefore, irradiations and counts were extrapolated on the basis of the reactor power. Small, random gain shifts (<1%) had been observed, and the alpha peak appeared somewhat broadened as if from gamma-ray smearing. A total of 2×10^7 counts of energy >6 Mev, corresponding to a total count of 1.4×10^{12} neutrons, had been accumulated. An increase in reactor power to 330 watts for 2300 sec, corresponding to 1.5×10^{13} neutrons, jammed all the counting equipment and terminated the run.

Postirradiation tests of the diode indicated a capacitance reduction (apparent gain increase) of 6% immediately, then 8%, 24%, and 24% at half-hour intervals. One day later the shift had decreased to 18% above the original value, and small changes were observed in the alpha-particle response distribution.

A later run, amounting to an integrated power of 3.3×10^5 watt-sec, resulted in 10% terminal, 18% maximum, and 0% long-term capacitance reductions. These values were repeated in additional runs.

The diode had at this time survived an exposure to 3.6×10^{13} thermal neutrons. An additional exposure to 1×10^{14} neutrons (reactor power level at 4 kw for 1300 sec) produced a capacitance reduction which required 4 hr for recovery. The alpha peak became a smear and then partially recovered.

Since no particular account had been taken of diode temperature during the above runs, it was of interest to determine, in grossly qualitative fashion, the effect of temperature changes. Immediately following the above run, therefore, the detector in its container was plunged into water at $\sim$75°C. The result, as shown in Fig. 2.5.1, was a rapid and large gain shift in the direction of diode capacity increase. Removal from the hot water and immersion in liquid nitrogen produced an immediate and dramatic gain shift in the opposite direction. The time scale of these data was greatly influenced by poor heat transfer.

[3] T. A. Love *et al.*, *op. cit.*, p. 281.

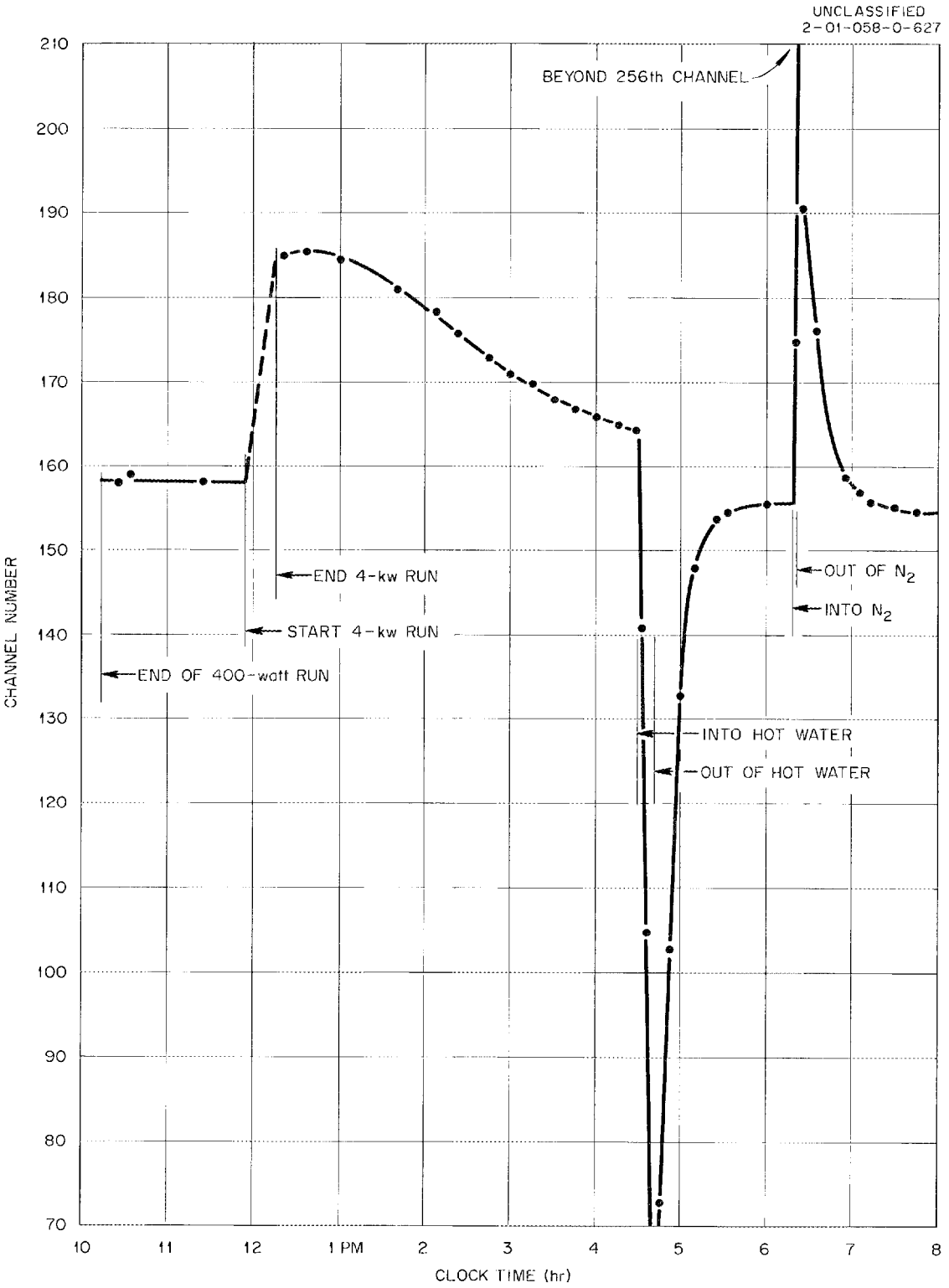

Fig. 2.5.1. Gain Change of a Low-Resistance Silicon Diode Particle Detector Under Abrupt Temperature Variations. Output amplitude for a constant charge input is plotted as a function of time.

As the alpha-particle response curve was recovering from the above treatment, a run at a reactor power of 40 watts was terminated at 300 sec when an apparent breakdown of the diode occurred. Total exposures in this run were: 1.4×10^{14} thermal neutrons, 2×10^{13} fast neutrons, and $>5 \times 10^{8}$ alpha particles.

Two weeks later the alpha-particle response curve for this diode indicated a large amount of recovery. Four more exposures of $\sim 1 \times 10^{14}$ thermal neutrons each resulted in smeared alpha peaks, with diminishing amounts of recovery after each run. A fifth exposure of $\sim 1 \times 10^{14}$ thermal neutrons resulted in little evidence of recovery after four days. A potential of 150 volts was then applied to the diode and for a short time appeared to somewhat accelerate recovery, but it may also have contributed to the complete failure due to breakdown which occurred shortly thereafter.

The experiments reported above have all been performed with low-resistance diodes. A high-resistance diode (1500 $\Omega \cdot$ cm) was also exposed to the BSR-I in the same fashion. The results were opposite in sense; that is, the gain shifts in the high-resistance diode were in the direction of increased capacitance. Small gain shifts and alpha-peak distortions occurred for exposures up to $\sim 10^{13}$ neutrons; relatively large shifts and small recoveries at exposures $>3 \times 10^{13}$ neutrons.

Conclusions

Neutron-induced gamma-ray activities in the diodes and mounting structures could account for some of the alpha-peak distortions and subsequent recovery but would not account for the observed gain shifts. This was verified by exposing diodes to the high residual gamma-ray field of the shut-down reactor. Therefore, most, if not all, of the observed effects must result from diode structure changes. A future experiment will use two identical diodes operated at 10 and 100 volts bias, respectively, to test the hypothesis that bias voltage has a strong influence upon diode life and stability.

2.6. SCINTILLATION RESPONSE OF ACTIVATED INORGANIC CRYSTALS TO VARIOUS CHARGED PARTICLES[1]

R. B. Murray and A. Meyer

Experimental studies of the response of activated ionic crystals such as NaI(Tl) and CsI(Tl) to heavy charged particles indicate decreasing scintillation efficiency with increasing particle mass and a nonlinearity in pulse height versus energy for heavier particles. Recent experiments indicate that the scintillation efficiency to electrons, however, is less than that to protons. In an attempt to account for these effects, this paper presents a calculation based on a model of the process of energy transfer from the incoming particle to the activator sites. In this model, the energy carriers are taken to be excitons resulting from recombination of electron-hole pairs in the wake of the particle. The migration of carriers to

[1]Abstract of published paper: *Phys. Rev.* 122, 815 (1961).

activator sites is described by a one-velocity diffusion equation in which the density of unoccupied activator sites, N_a, is a function of space and time. The diffusion equation is coupled with a second differential equation describing the time dependence of N_a. The solution to these equations indicates that the depletion of available activator sites by a particle with high dE/dx can account for observed saturation effects. This model further contains the activator concentration as a parameter and permits a prediction of scintillation efficiency as a function of both dE/dx and concentration. The low scintillation efficiency to electrons is predicted as a consequence of the smaller recombination probability for particles of very low dE/dx. Finally, for a low-dE/dx particle in a crystal of 0.1-mole % activator concentration, the diffusion length of energy carriers is found to be of order 20 A.

2.7. INTRINSIC LINE BROADENING IN NaI(Tl) GAMMA-RAY SPECTROMETERS[1]

C. D. Zerby, A. Meyer, and R. B. Murray

Previous experimental studies of the response of NaI(Tl) to gamma rays have indicated that the pulse height is not strictly proportional to the energy of the absorbed gamma ray. It is the purpose of this paper to point out that the nonproportional response to gamma rays implies a nonproportional response to electrons, which results in an intrinsic broadening of the full-energy peak in the pulse-height distribution from a monoenergetic gamma ray. The magnitude of this effect is such that it results in a significant contribution to the total line width for scintillation crystals of typical dimensions. The work reported here is based on Monte Carlo calculations using the nonproportional response of NaI(Tl) to electrons, an energy-dependent function which was deduced from previous experimental work with gamma rays. Results of calculations for a 2.5-in.-dia by 2-in.-high crystal indicate a distinct broadening in the total absorption line in the case of Compton and pair-production events. The calculated fractional line width from this effect alone is negligible for energies below about 0.1 Mev and amounts to 2.6% at 0.15 Mev, 5.0% at 0.4 Mev, and 1.5% at 2.5 Mev. The dependence of this effect on the crystal size and source geometry is discussed.

[1]Abstract of published paper: Nuclear Instr. & Methods 12, 115 (1961).

2.8. STUDIES OF THE SCINTILLATION PROCESS IN CsI(Tl)

R. Gwin and R. B. Murray

A phenomenological theory of the scintillation process in thallium-activated alkali iodides, based on a description of energy transport from the incident charged particle to the luminescence centers, has recently been proposed.[1] This model leads to several specific predictions of the behavior of scintillation

[1]R. B. Murray and A. Meyer, *Phys. Rev.* 122, 315 (1961).

efficiency as a function of thallium concentration of the crystal and as a function of the specific energy loss of the incident particle. These predictions, which are subject to experimental investigation as a test of the validity of the proposed model, constitute the primary motivation for the program reviewed here. The experimental program to be described encompasses a study of the scintillation response of several CsI(Tl) crystals of varying thallium content to monoenergetic gamma rays and protons, with attention to effects dependent upon the scintillation-pulse clipping time.

Scintillation Response of CsI(Tl) to Gamma Rays

The results of experiments on the scintillation response of a particular crystal of CsI(Tl) to gamma rays were reported in the preceding annual progress report.[2] These experiments have been extended to include a total of three CsI(Tl) crystals whose thallium contents have been determined as follows: Crystal 1, 0.0041 mole %; Crystal 2, 0.046 mole %; and Crystal 3, 0.18 mole %. The experimental method employed in determining the scintillation response of these crystals to gamma rays has been indicated previously.[2] Briefly stated, the pulse height L corresponding to a gamma ray of energy E_γ is measured *relative to* the pulse height corresponding to a "standard" gamma-ray line which was chosen to be the 662-kev gamma ray of Cs^{137}. With this method the results do not depend upon such factors as the linearity of the amplifier and pulse-height analyzer, the long-time stability of the gain of the electronic system, or a knowledge of the zero of the pulse-height analyzer.

In all experiments preformed to date with gamma rays, the scintillation pulse was amplified in a DD-2 amplifier which had been modified by the substitution of 7-μsec delay lines in place of the standard 1.2-μsec delay lines. Pulse-height analysis was then performed in a 20-channel analyzer which was equipped with a long-pulse adapter. Thus analysis of a scintillation pulse occurred 7 μsec after the gamma ray was absorbed in the crystal. This is a significant feature of the present work, as the long clipping time guarantees collection of all light from the fast luminescent component (decay time about $\frac{1}{2}$ μsec) plus collection of some light from a slower luminescent component (decay time of the order of several microseconds).

In the analysis of data points for which the pulse height is very small (viz., low-energy gamma rays on the low-thallium content crystal), it is necessary to take into account the deviation of the peak of the gamma-ray spectrum from the mean. The asymmetry of the observed peak occurs when a small number of electrons are emitted, on the average, from the photocathode of the photomultiplier tube. A theoretical calculation of this asymmetry has been made by G. T. Wright[3] and served as the basis for the corrections applied in this work. The average number of electrons reaching the first dynode was measured by using U^{233} alpha particles (4.8 Mev) to produce the light pulses in the crystal. This was done by disconnecting all of the tube elements except the photocathode, the first dynode, and the focusing electrode, and measuring the current flowing out of the first dynode while other physical conditions were the same as during the normal scintillation experiments. The maximum value of this correction was 4% for the Ba^{137} (32.88-

[2] R. Gwin and R. B. Murray, *Neutron Phys. Div. Ann. Prog. Rep. Sept. 1, 1960*, ORNL-3016, p. 293.

[3] G. T. Wright, *J. Sci. Instr.* 31, 377 (1954).

kev) K x ray for the CsI(Tl) crystal having a thallium concentration of 0.0041 mole %. An uncertainty of ±25% was placed upon this correction.

Data resulting from gamma-ray experiments on the individual crystals are shown in Figs. 2.8.1–2.8.3 and are shown superimposed in Fig. 2.8.4. It was not possible to obtain data below 30 kev in Crystal 1 as a consequence of the very low pulse heights. The error limits shown include contributions arising from the reproducibility of the individual experiments, uncertainty of the K x ray energies, low pulse-height asymmetry corrections, and uncertainties in corrections for K escape peaks. The uncertainties involved in comparing the curves are shown in Fig. 2.8.4 and are reduced essentially to the uncertainty in the measurements. The ordinates on Figs. 2.8.1–2.8.3 are fixed relative to the value of L/E_γ for 662-kev gamma rays on Crystal 2; L/E_γ for this point is arbitrarily assigned a value of 1.00. With this value fixed, the light output for Crystals 1 and 3 relative to that for Crystal 2 was determined in a separate experiment which will be described below.

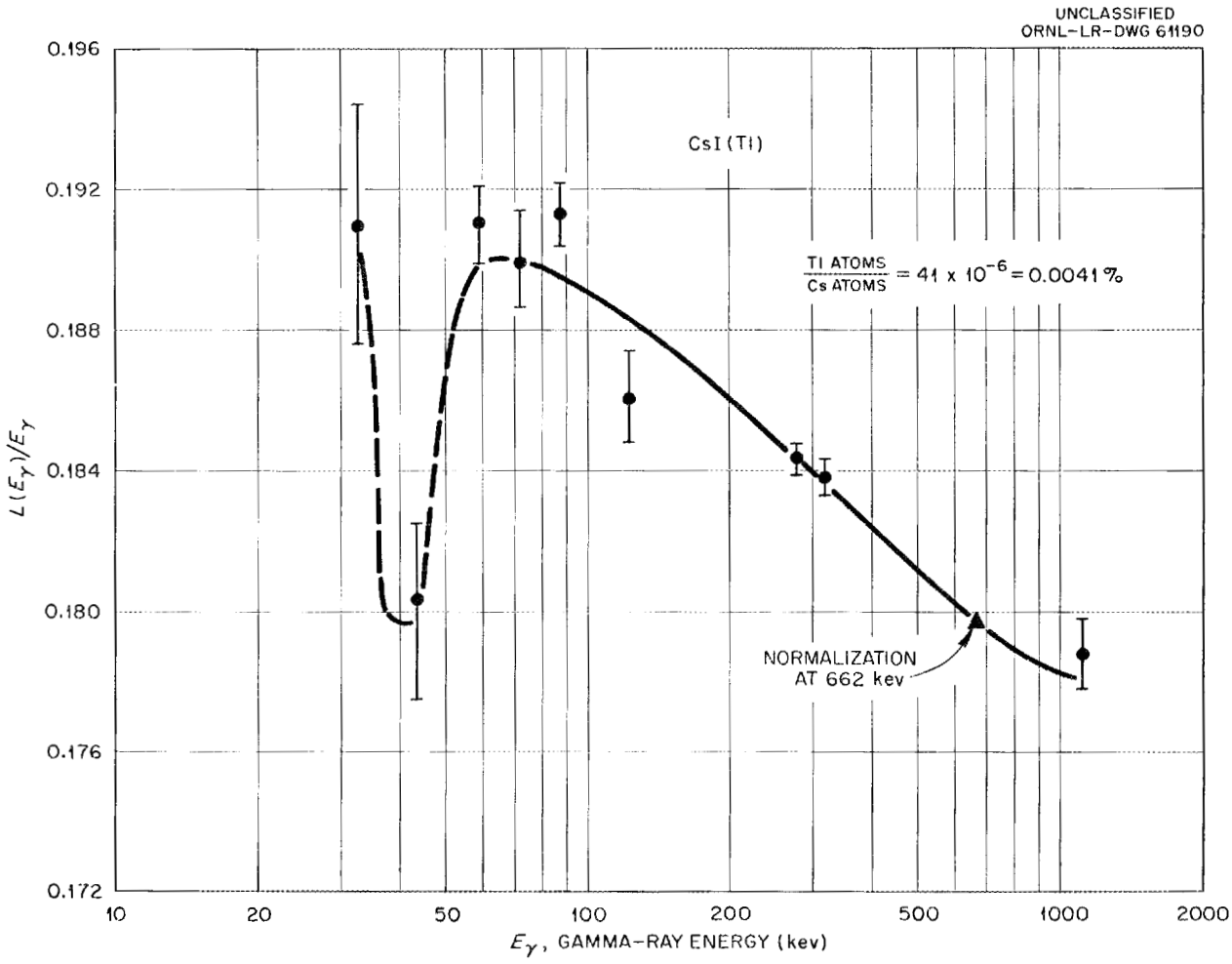

Fig. 2.8.1. Relative Light Output per Unit Energy of CsI(Tl) (0.0041 mole % Tl) for Gamma Rays.

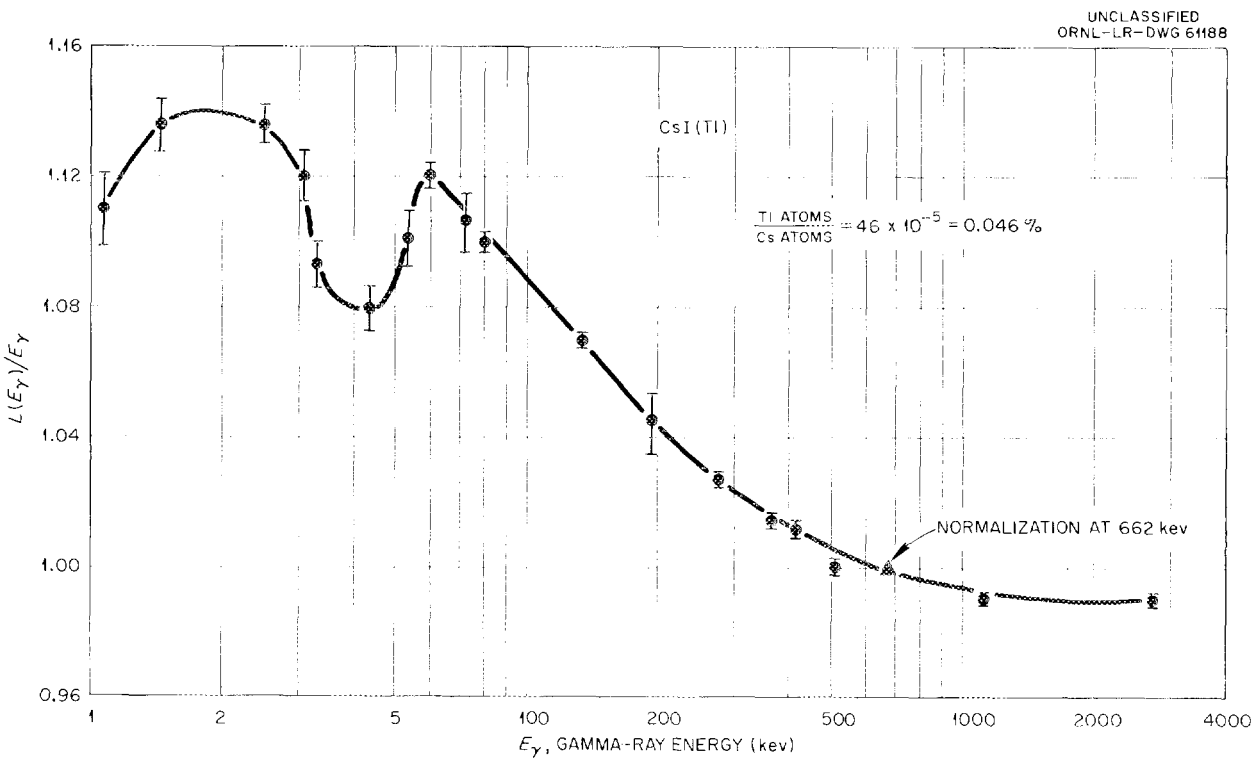

Fig. 2.8.2. Relative Light Output per Unit Energy of CsI(Tl) (0.046 mole % Tl) for Gamma Rays.

It is to be noted in connection with Figs. 2.8.1–2.8.4 that all three crystals exhibit L/E_γ response functions which are basically similar. The L/E_γ functions indicate a distinct nonproportional relation between pulse height and gamma-ray energy. Further, the scintillation response of these crystals to gamma rays is very nearly the same as that observed at other laboratories in NaI(Tl).[4]

[4]For references to work on NaI(Tl), see C. Zerby, A. Meyer, and R. B. Murray, *Nuclear Instr. & Methods* 12, 115 (1961).

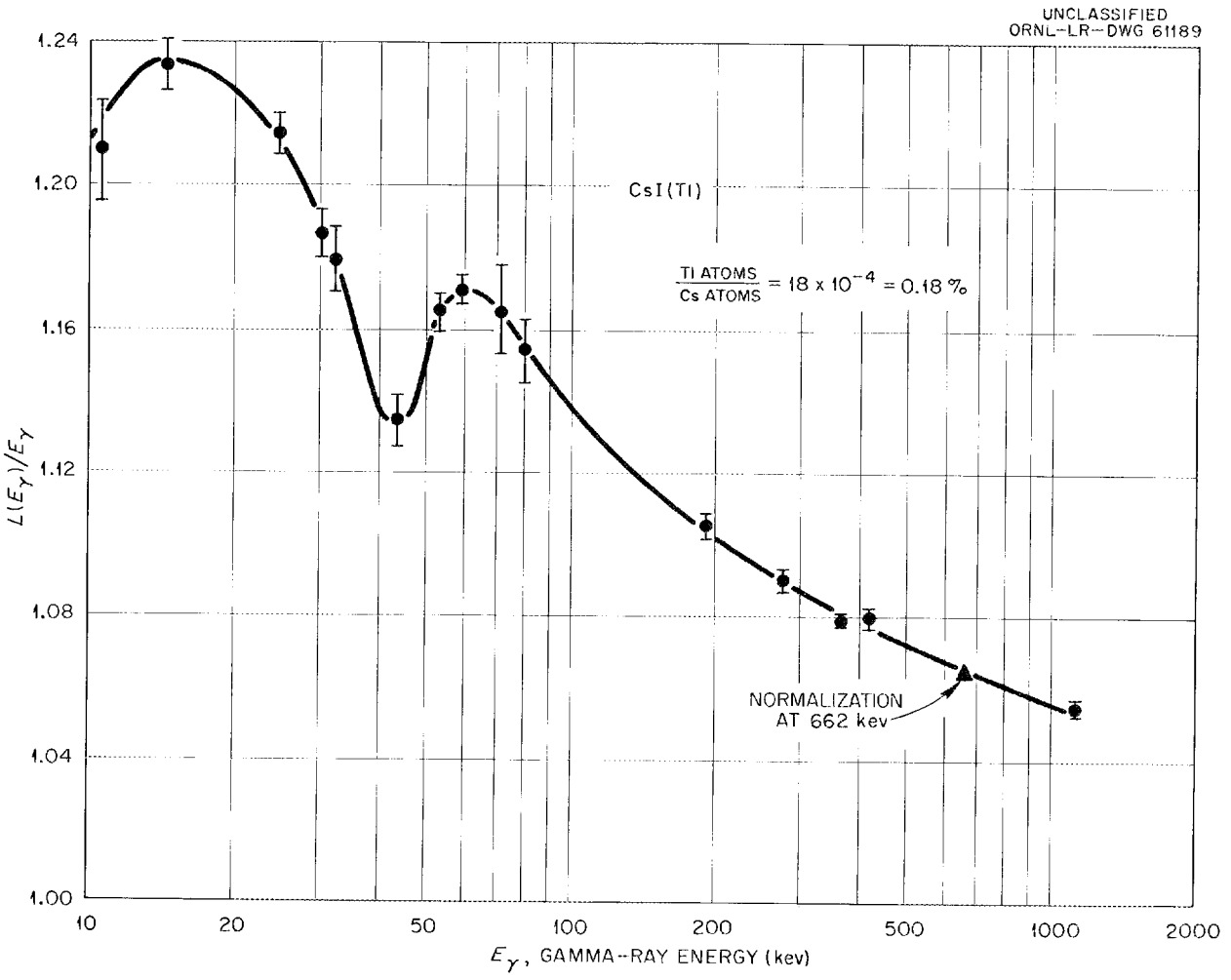

Fig. 2.8.3. Relative Light Output per Unit Energy of CsI(Tl) (0.18 mole % Tl) for Gamma Rays.

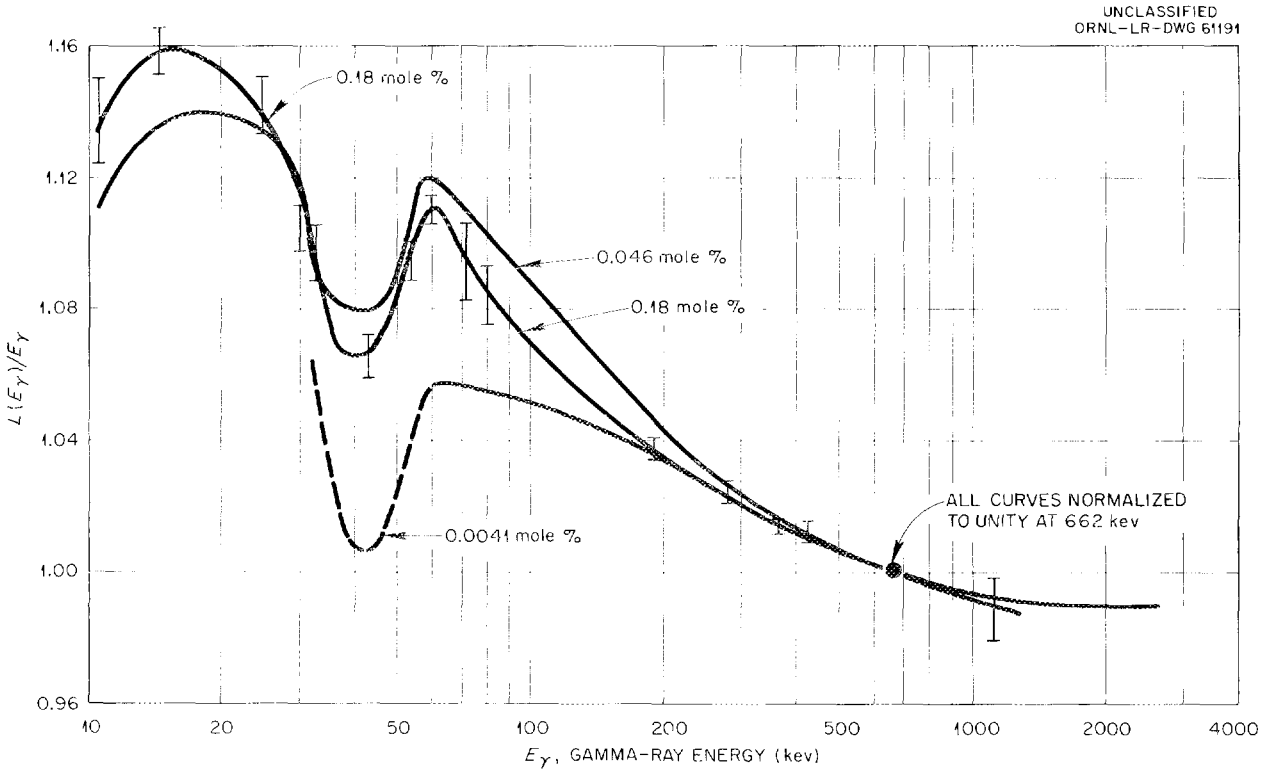

Fig. 2.8.4. Comparison of the Dependence of Light Output per Unit Energy on Thallium Concentration in Various CsI(Tl) Crystals.

Scintillation Response of CsI(Tl) to Electrons

It is not possible to compare the results of Figs. 2.8.1–2.8.4 directly with the predictions of the scintillation model,[1] as the experimental results refer to the interaction of *gamma rays* with the crystal, whereas the model describes the interaction of *electrons* with the crystal. It is thus necessary to obtain the electron response functions from the experimental results with gamma rays. The analytical methods necessary to perform this operation have been described elsewhere in conjunction with studies of NaI(Tl).[4]

The only difference introduced in CsI(Tl) is that both iodine and cesium have K absorption energies which must be considered and this complicates the electron spectrum arising from gamma-ray absorptions. The pulse height per unit energy, L/E_e, for electrons has been obtained in the energy region below 70 kev for the three different thallium concentrations. This derived curve for L/E_e as a function of the electron energy E_e is shown in Fig. 2.8.5 for the 0.046 mole % thallium crystal. From this curve the gamma-ray response of the crystal can be calculated and is shown in Fig. 2.8.6 along with the experimental points. The agreement between the derived curve and the experimental points is considered good. The fact that the curves as shown in Figs. 2.8.1–2.8.4 show a decrease below 60 kev means that another decrease in the gamma-ray curve will occur at about 20 kev. This behavior is shown by the experiments and gives increased confidence in the precision of the experiments.

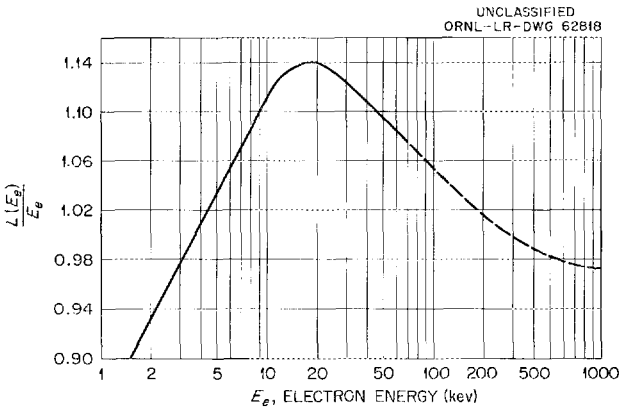

Fig. 2.8.5. Relative Light Output per Unit Energy of CsI(Tl) (0.046 mole % Tl) by Electrons (Deduced from Gamma-Ray Data).

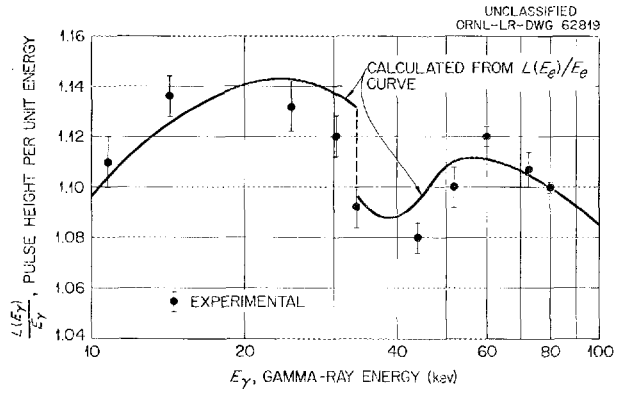

Fig. 2.8.6. Relative Light Output per Unit Energy of CsI(Tl) (0.046 mole % Tl) for Gamma Rays: Comparison of Experimental and Calculated Data.

Pulse Height as a Function of Thallium Concentration

In the formulation of the scintillation process model, the relation between scintillation efficiency and the thallium concentration enters in a very basic way. It is thus of considerable interest to measure the relative pulse height as a function of the thallium concentration for a series of CsI(Tl) crystals. Accordingly, a number of CsI(Tl) crystals of varying thallium content were obtained, both from Harshaw Chemical Company and by growing at this Laboratory. A slice 3 mm in thickness was obtained from each ingot, and the pulse height corresponding to 662-kev gamma rays was recorded for each sample. Pulse heights were determined with a test pulse generator and precision potentiometer as described previously.[2] Care was taken to ensure that the optical coupling between the crystal and the light guide was the same for every crystal. Uniformity of optical coupling was indicated by the fact that any given crystal system could be disassembled and remounted with a change in pulse height amounting to 3% at most. The pulse height associated with any one crystal was determined several times.

Two sets of measurements of pulse height versus concentration were performed. In the first set, pulses were amplified with the DD-2 amplifier and analyzed at 7 μsec as indicated above. In the second set of measurements, pulses were amplified and analyzed in a Nuclear Data 256-channel analyzer. The clipping time of the internal amplifier (hence the time at which analysis occurs) in this system was 1.25 μsec, in contrast with the 7-μsec clipping time in the first set of experiments. The shorter clipping time permits collection of most of the light from the fast scintillation component and has the advantage of excluding all but an insignificant amount of light from the longer component. The data are shown in Figs. 2.8.7 and 2.8.8.

The experimental data was fitted to a Johnson and Williams[5] function,

$$L \sim \frac{c(1-c)^z}{c + \sigma_l/\sigma_a\,(1-c)}\,,$$

[5]P. D. Johnson and F. E. Williams, *J. Chem. Phys.* 18, 1477 (1950).

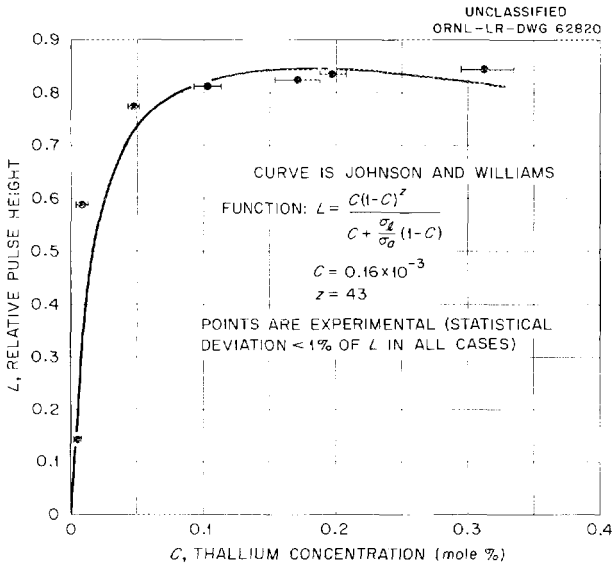

Fig. 2.8.7. Relative Pulse Height as a Function of Thallium Concentration in a CsI(Tl) Crystal (7-μsec Pulse Analysis).

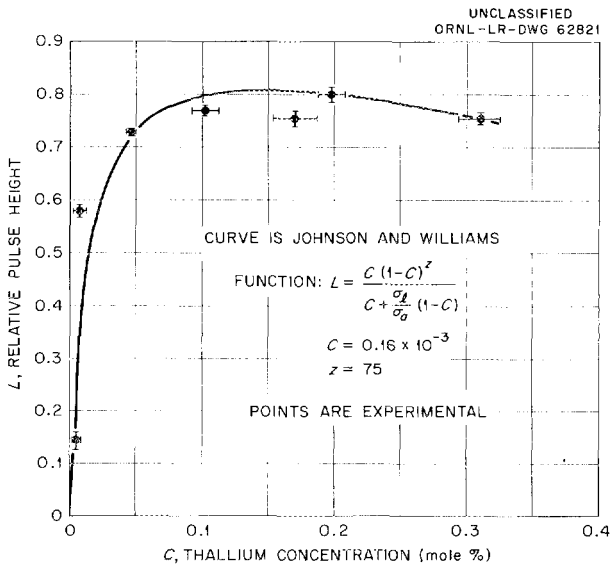

Fig. 2.8.8. Relative Pulse Height as a Function of Thallium Concentration in a CsI(Tl) Crystal (1.25-μsec Pulse Analysis).

where c is the mole fraction of thallium, σ_l and σ_a are the cross sections for capture at a trapping site and an activator site, respectively, and z is the effective number of lattice sites surrounding a given activator site such that concentration quenching will occur if another activator atom is contained within z. The two curves are normalized with respect to each other at the low thallium concentration point. A z of 75 was obtained for the 1.25-μsec pulse analysis and 43.5 for the 7-μsec pulse analysis.

The behaviors of the curves at the 1.25-μsec and 7-μsec pulse analysis differ from each other considerably. Note that there is no evidence from the data at 7 μsec to say that there is a maximum in the pulse height versus concentration relation. The difference in the two curves can be explained qualitatively by suggesting that a second luminescent site is present in the crystal which increases in density as the activator concentration increases and which has a longer decay time than the other luminescent site. One such site could be two thallium ions associated with each other in the lattice.

The maximum in the pulse height versus thallium concentration for the 1.25-μsec pulse analysis occurs between 0.12 and 0.16 mole % thallium. This is in disagreement with the work of Tsirlin *et al.*[6] who conclude that the maximum occurs at about 0.02 mole % thallium. This conclusion does not seem to be borne out by their published data.

Scintillation Response of CsI(Tl) to Protons

The scintillation response of Crystals 1, 2, and 3 to monoenergetic protons was examined over the proton energy range from 0.2 to 5.5 Mev. Monoenergetic protons in this energy region were obtained by

[6] Iu. A. Tsirlin, S. N. Komnik, and L. M. Soifer, *Optics and Spectroscopy (U.S.S.R.)* **6**, 265 (1959).

accelerating protons in the ORNL 5.5-Mev Van de Graaff generator. The primary proton beam was scattered from a thick tantalum foil; the scattered beam was then analyzed in a 60-deg charged-particle analyzing magnet. The CsI(Tl) crystal was placed immediately beyond the focus of the analyzing magnet. The energy of the proton beam striking the crystal was well known from a magnet calibration which was performed immediately before starting the series of scintillation response experiments.

The experimental method in determining the response to protons was very similar to that in the gamma-ray experiments. In all cases the pulse height L corresponding to monoenergetic protons of energy E_p was determined *relative to* the pulse height associated with 662-kev gamma rays. A gamma-ray calibration point was obtained in conjunction with *each* proton point. In the series of proton experiments, data were obtained both with a 7-μsec clipping time and with a 1-μsec clipping time (using an A-8 amplifier and a Nuclear Data analyzer).

The results for Crystal 2 are shown in Fig. 2.8.9 (7-μsec clipping time) and in Fig. 2.8.10 (1-μsec clipping time). The ordinate on each figure is pulse height per unit energy, arbitrarily normalized to unity for 662-kev gamma rays. Results from Crystals 1 and 3 exhibit qualitatively similar features and are not shown here. There are two significant features in Figs. 2.8.9 and 2.8.10 to be noted. First, with the 7-μsec clipping time (Fig. 2.8.9) the pulse height per unit energy at 662 kev is significantly *smaller* for protons than for gamma rays. With a 1-μsec clipping time, however, the pulse height per unit energy for protons is *greater* than that for gamma rays. This latter behavior has been previously observed in several alkali iodide scintillations (see Ref. 1 for summary). The significant difference in pulse height per unit energy relative to gamma rays which is observed in Figs. 2.8.9 and 2.8.10 is a reflection of the fact that in CsI(Tl) the pulse shape depends on the specific energy loss of the incident particle.[5] It is this property of CsI(Tl) which permits discrimination between charged particles by suitable electronic inspection of the pulse shape. The fact that the L/E_p may be greater or less than L/E_γ at 662 kev, depending on the time of analysis, is a consequence of the detailed nature of the pulse shape from CsI(Tl). In the

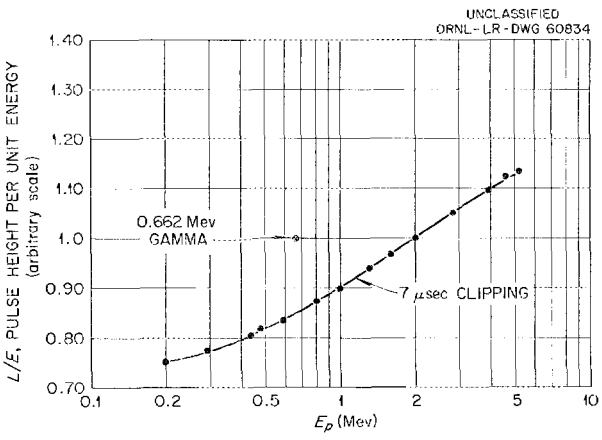

Fig. 2.8.9. Relative Light Output per Unit Energy of CsI(Tl) (0.046 mole % Tl) for Protons (7-μsec Pulse Analysis).

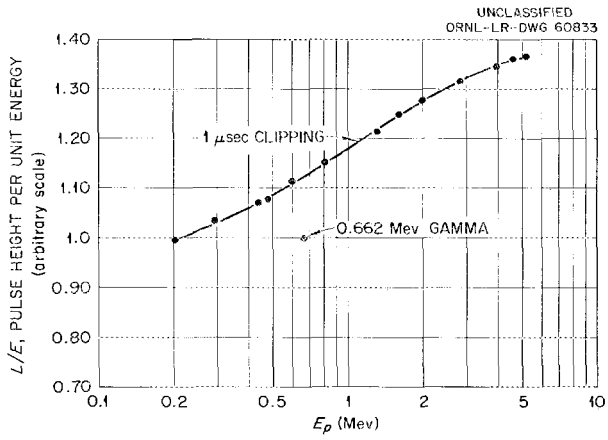

Fig. 2.8.10. Relative Light Output per Unit Energy of CsI(Tl) (0.046 mole % Tl) for Protons (1-μsec Pulse Analysis).

series of proton experiments it was possible to observe simultaneously the amplified pulses from both 662-kev protons and gamma rays. The proton pulse was observed to have a faster initial rise than the gamma-ray pulse, such that L/E_p is *greater* than L/E_γ at 1 μsec. At longer times, the proton pulse becomes relatively flat and crosses the increasing gamma-ray pulse, such that L/E_p is *less* than L/E_γ at 7 μsec. It is to be noted that this particular situation holds at 662 kev. The ratio of $(L/E_p)/(L/E_\gamma)$ will be reversed at lower energies for the 1-μsec clipping time and at higher energies for the 7-μsec clipping time since both L/E_p and L/E_γ are energy-dependent functions. The detailed nature of the relative proton and gamma-ray responses is thus a rather complicated function of energy, analysis time, and, to a smaller extent, thallium concentration.

The second feature to be noted in connection with Figs. 2.8.9 and 2.8.10 is the fact that L/E_p is a function of E_p throughout the energy range of the present experiments. This means that the relation between pulse height L and proton energy E_p is nonproportional; i.e., $L \neq AE_p$, where A is a constant. A plot of L versus E_p (Fig. 2.8.11), taken from the data of Fig. 2.8.10, demonstrates this nonproportionality. From a pulse height versus energy plot, as in Fig. 2.8.11, it appears that the data above 1 Mev can be well fitted by a straight line which intersects the energy axis at about 0.2 Mev (see Fig. 2.8.11). This "linear" relation, however, is illusory; the straight line is simply a good approximation to an energy-dependent function. This fact emphasizes the relative crudeness of a pulse height versus energy plot and illustrates the necessity of interpreting the data in terms of pulse height per unit energy.

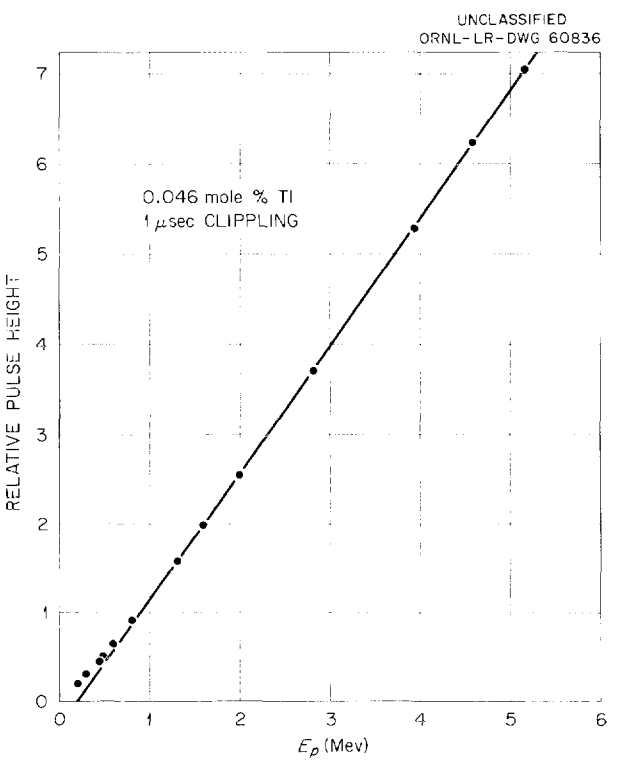

Fig. 2.8.11. Relative Light Output of CsI(Tl) (0.046 mole % Tl) for Protons (1-μsec Pulse Analysis): Demonstration of Nonproportionality.

Scintillation Efficiency as a Function of Specific Energy Loss

The data presented above can be expressed in terms of scintillation efficiency as a function of specific energy loss of the incident particle. Scintillation efficiency is defined as dL/dE, the slope of the pulse height versus energy curve. The specific energy loss, dE/dx, for protons was obtained from curves calculated by Murray and Meyer for CsI.[1]

A graph of dL/dE for protons as a function of dE/dx is shown in Fig. 2.8.12 for the three CsI(Tl) crystals used. The behavior of the dL/dE versus dE/dx follows the predictions of Murray and Meyer[1] in a qualitative manner. This curve is quite steep and has a maximum where previous data have indicated that the pulse height as a function of energy was constant and, therefore, dL/dE was constant. The curve dL/dE versus dE/dx for electrons also exhibits a maximum and in the same dE/dx range in which the proton maximum occurs. This occurrence of a maximum for the scintillation efficiency as a function of dE/dx is predicted by the model of Murray and Meyer.[1]

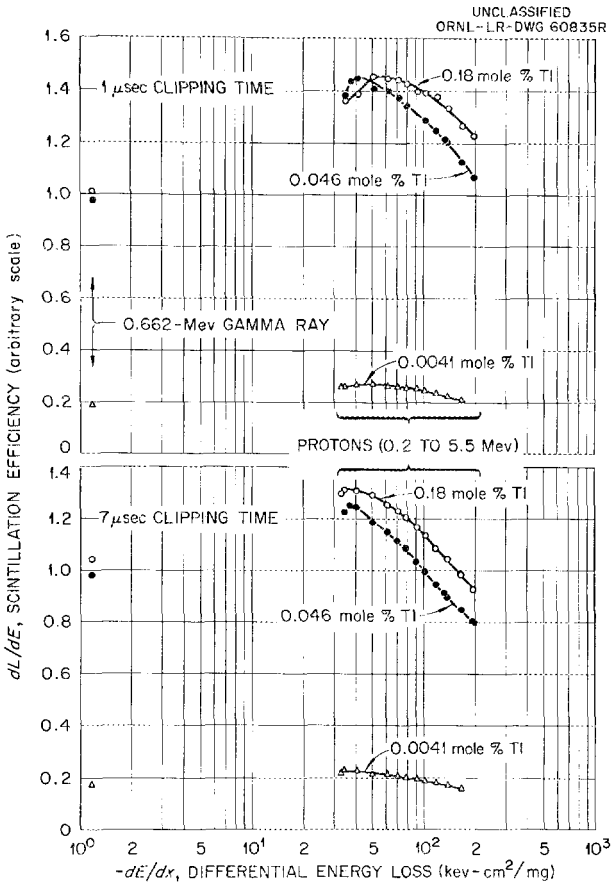

Fig. 2.8.12. Scintillation Efficiency of Various CsI(Tl) Crystals for 0.2- to 5.5-Mev Protons and 0.662-Mev Gamma Rays.

Discussion

The experimental program to date neither conclusively confirms nor denies the validity of the scintillation model of Murray and Meyer.[1] The difference in response of the photomultiplier system to light emitted by CsI(Tl) for excitation by different particles must be investigated in order to interpret the above

data. Hrehuss[7] has measured a difference in the emission spectrum of CsI(Tl) for excitation by electrons, deuterons, and alpha particles.

Storey *et al.*[8] have shown that the shape of a scintillation pulse in CsI(Tl) is different for various exciting particles. Robertson and Lynch[9] have performed experiments which indicate that the shape of the scintillation pulse is a function of the thallium concentration in CsI(Tl) for certain particles (5.3-Mev alpha particles and 3.14-Mev protons). These experiments indicate the necessity of investigating the emission spectrum as a function of the thallium concentration in order to make a valid comparison of theory and experiment. In addition, the variation of the pulse shape and emission spectrum from one particle to another suggests that two or more luminescent centers may be present in the crystal and that the theoretical model may have to be extended to include this possibility.

[7]G. Hrehuss, *Nuclear Instr. & Methods* 8, 344 (1960).

[8]R. S. Storey, W. Jack, and A. Ward, *Proc. Phys. Soc. (London)* 72, 1 (1958).

[9]J. C. Robertson and J. D. Lynch, *Proc. Phys. Soc. (London)* 77, 751 (1961).

2.9. EFFECT OF DELTA RAYS ON RESPONSE OF INORGANIC SCINTILLATORS TO HEAVY IONS

A. Meyer and R. B. Murray

Preliminary results have been obtained in a study of the effect of delta rays (energetic secondary electrons) on the response of activated inorganic scintillators to heavy ions.

A semiempirical model of the scintillation process proposed by the authors in a recent paper[1] accounts for the major features of the scintillation response of thallium-activated alkali iodides to charged particles. These features are the nonproportional response to electrons and the reduced efficiency in response to heavy ions relative to protons. Figure 2.9.1 illustrates the behavior of the scintillation efficiency of NaI(Tl) to various charged particles whose specific energy loss (dE/dx) varies over four orders of magnitude. The data points and dashed curves are experimental results. Attention is especially called to the dashed curves, which correspond to heavy ions ranging from B^{10} to Ne^{20}. The smooth curve of Fig. 2.9.1 is a theoretical curve based on the model of Ref. 1. It may be noted in the figure that the response function for these crystals is a discontinuous, multivalued function. The present study is an attempt to modify the earlier model to account for this behavior. To this end we calculate the light produced external to the primary ionization column by delta rays formed as the incident particle slows down and stops in the crystal. The light produced within the primary column, assumed to be described by the original model, exhibits saturation of the luminescence centers for particles of high dE/dx. The over-all scintillation efficiency is the weighted average of the primary column and delta-ray efficiencies. Such a calculation has been carried out and the results indicate that a discontinuous behavior as illustrated in

[1]R. B. Murray and A. Meyer, *Phys. Rev.* 122, 815 (1961).

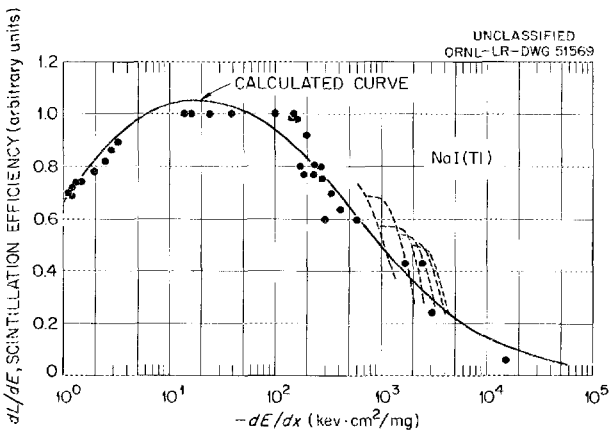

Fig. 2.9.1. Scintillation Efficiency vs. Stopping Power for NaI(Tl). Experimental data are shown as points and dashed curves; the solid curve is calculated from the model of Ref. 1.

Fig. 2.9.1 for heavy ions can arise through the action of delta rays. These delta rays significantly change the over-all response because of the high scintillation efficiency of NaI(Tl) to electrons.

Much of the present calculation is devoted to ascertaining the fraction of energy lost by the incident particle, in a small thickness of crystal, which goes into delta-ray formation and is subsequently deposited outside of the primary ionization column. In order to make an estimate of this fraction, several items of input information are necessary. These include knowledge of (1) an approximate range-energy relation for electrons in the scintillator, (2) an assumed spatial distribution of electrons diffusing from a line source in an absorbing medium, (3) an average energy distribution characteristic of delta rays created along the particle track, (4) an estimated radius of the primary ionization column, and (5) the total stopping power of heavy ions in the scintillator.

For present purposes it is useful to assume for electrons from about 500 ev to 20 kev that the range R_0 can be described accurately enough by a single relation:

$$R_0 = aE^n \,, \tag{1}$$

where E is the initial electron energy and a and n are constants which were obtained from the current literature.

The second item involves the spatial distribution of electrons diffusing from a line source in an absorbing medium. This is unknown for such extremely low-energy electrons. We assume for simplicity that the number of electrons per square centimeter arising from a point isotropic source and reaching radius R decreases as $[1 - (R/R_0)]$ for values of R removed from the origin. Under this assumption, a transformation to cylindrical geometry can be effected by methods well known in neutron diffusion theory. This results in an expression for the differential number of electrons stopped between y and $y + dy$:

$$dn \sim y \ln \frac{1 + \sqrt{1 - y^2}}{1 - \sqrt{1 - y^2}} \, dy \,, \tag{2}$$

where y is the ratio R/R_0.

In connection with item 3, it is assumed that the Rutherford energy distribution applies, so that the contribution to the specific energy loss arising from delta rays of energy ϵ to $\epsilon + d\epsilon$ is

$$\frac{dE}{dx} = \frac{2\pi e^4 z^2 Z N_A}{m v^2 A} \frac{d\epsilon}{\epsilon} , \tag{3}$$

where the symbols are the conventional ones encountered in stopping power theory.

The radius of the primary ionization column, item 4, was taken to be that radius containing one-half of those initial energy carriers which were captured either at luminescent centers or trapping sites. This radius was calculated on the basis of the solutions to the diffusion equation described in Ref. 1.

Calculation of the specific energy loss of heavy ions in NaI(Tl), item 5, was performed with reference to recent measurements of dE/dx for heavy ions in various stopping media. This calculation is similar to that outlined by Newman and Steigert,[2] but in addition includes K- and L-shell correction terms.

Starting from this input information, it can be shown that the ratio of energy deposited by delta rays outside the primary column to the total energy lost by the incident particle in a small thickness of crystal is

$$F = \frac{2\pi e^4 z^2 Z N_A}{(dE/dx)_T m v^2 A} \int_0^{\epsilon_0} \frac{d\epsilon}{\epsilon} \int_{\chi(\epsilon)}^1 \left[1 - \frac{\chi(\epsilon)}{y}\right]^{1/n} y \ln \left[\frac{1 + \sqrt{1 - y^2}}{1 - \sqrt{1 - y^2}}\right] dy , \tag{4}$$

where ϵ_0 is the maximum delta-ray energy and $\chi(\epsilon)$ is the ratio of primary column radius to the range of an electron of energy ϵ.

The over-all scintillation efficiency, $(dL/dE)_T$, can be shown to be related to F of Eq. 4 and to the efficiencies for delta rays and the primary column by the equation

$$\left(\frac{dL}{dE}\right)_T = F\left(\frac{dL}{dE}\right)_\delta + (1 - F)\left(\frac{dL}{dE}\right)_p . \tag{5}$$

In calculating $(dL/dE)_T$ from Eq. 5 it is assumed that $(dL/dE)_\delta = 1$; an iterative procedure is required by the slight interdependence of F and $(dL/dE)_p$.

The results reported here are preliminary in the sense that the methods for choosing the values of certain parameters in the input information are not the best available. We are presently engaged in efforts to improve this information. For this reason the detailed methods for calculating these quantities will not be shown here. On the other hand, the results of an improved calculation cannot be very different from our current values and for this reason these results should have qualitative validity.

Figure 2.9.2 shows the Eby and Jentschke[3] results for alpha particles and those of Newman and Steigert[2] for heavy ions B^{10} through Ne^{20}. These can be compared with the results of the preliminary

[2]E. Newman and F. E. Steigert, *Phys. Rev.* **118**, 1575 (1960).

[3]F. S. Eby and W. K. Jentschke, *Phys. Rev.* **96**, 911 (1954).

calculations for the same particles shown in Fig. 2.9.3. For further comparison, the primary response curve obtained previously is also shown in Fig. 2.9.3. This indicates that delta rays *can* account for separation of the response curves for individual ions. These figures also point up the similarities in the experimental and calculated efficiencies to heavy ions, in attaining higher values and in declining with steeper slopes than predicted by the earlier model. These effects all derive from the fact that delta rays deposit outside the primary column about 25% of the energy lost by the highest velocity particle considered and this fraction diminishes rapidly to zero as the particle velocity decreases. For this reason the separation between the over-all and the primary response curves is greatest at the highest energy (low dE/dx). The separation diminishes with decreasing energy until the two curves merge at low energy (high dE/dx).

Another aspect of the response behavior reflects this decreasing importance of delta rays with increasing stopping power. Figure 2.9.4 shows the differential light output dL/dx plotted against dE/dx for

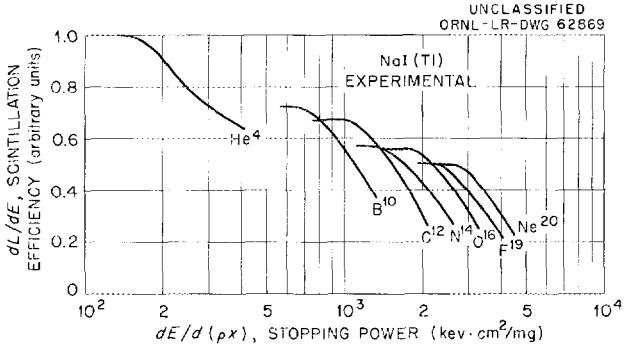

Fig. 2.9.2. Scintillation Efficiency vs. Stopping Power: Observed in NaI(Tl) for Alpha Particles by Eby and Jentschke and for Heavy Ions B^{10} Through Ne^{20} by Newman and Steigert.

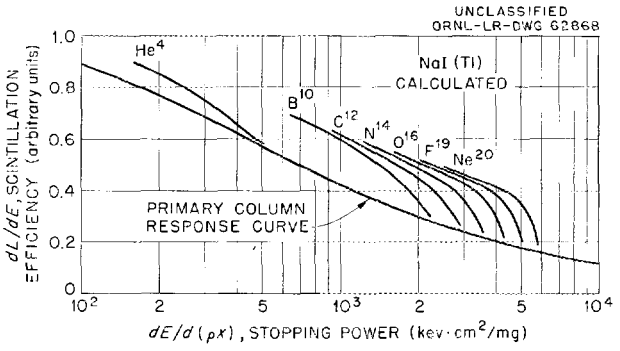

Fig. 2.9.3. Calculated Scintillation Efficiency vs. Stopping Power for Heavy Ions in NaI(Tl). The individual curves merge with the primary response base line at the high-(dE/dx) end of each curve.

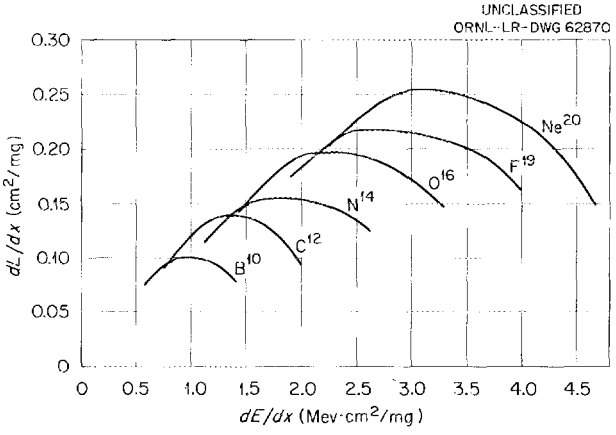

Fig. 2.9.4. Light Output, dL/dx, vs. Stopping Power for Heavy Ions B^{10} Through Ne^{20}, from Newman and Steigert.

the Newman and Steigert results already quoted. This exhibits the unusual behavior that dL/dx declines with increase in stopping power above a certain value. This, in turn, implies that the light output from a slice of crystal along the particle track actually decreases as more energy is dissipated there. This can

be traced directly to delta rays. A high-velocity particle converts much of its energy into energetic delta rays which produce light with high efficiency. On the other hand, a low-velocity particle loses a larger amount of energy, to be sure, but this energy is dissipated within the primary column where the scintillation efficiency is very low owing to the saturation of activator centers. The light produced by delta rays at low dE/dx is thus responsible for the maximum occurring in the over-all dL/dx for each individual particle. The dL/dx curve for the light from the primary ionization column is a curve without a maximum, and, owing to the decreasing importance of delta rays for high dE/dx, the over-all dL/dx and the primary column dL/dx also merge at high dE/dx.

A more complete description of this work will be given upon completion of the calculation now in progress.

2.10. THERMAL-NEUTRON DENSITY PERTURBATIONS BY FOILS IN WATER

S. A. Hasnain,[1] T. Mustafa,[2] and T. V. Blosser

A standard method for tracing neutron flux within a medium is to measure the gamma-ray activity induced in suitable fission or activation foils exposed in the medium. To convert measured foil activity to neutron density or flux, it is necessary to know, among other quantities, the perturbation of the neutron density caused by the presence of the foil. This perturbation is most readily defined when the flux consists of thermal neutrons only. In this case the activation cross sections usually vary as $1/v$ and the activation at any point of the foil is proportional to the neutron density at that point. The perturbation can then be defined as the ratio of specific activity actually induced to that which would be induced were there no perturbation, i.e., if the foil were infinitely thin.

Although considerable experimental data exists for perturbations by foils exposed in a graphite medium,[3] there is a scarcity of information from water experiments. Water as a medium is interesting because, in addition to the lowering of the flux inside a foil due to self-shielding, there is a considerable depression of the flux outside the foil. It is here that differences between various theories of foil perturbation appear.[4]

The work reported here differs from similar measurements reported elsewhere largely in the use of an effectively "pure" thermal-neutron source, which eliminated the need for the familiar cadmium-difference measurements generally used, as well as in the extension to materials other than gold.

[1] Present address: Pakistan Atomic Energy Commission, Karachi, Pakistan.

[2] Present Address: c/o Third Secretary, Embassy of Pakistan, Washington, D.C.

[3] A. Sola, *Nucleonics* 18, 78 (1960).

[4] R. H. Ritchie and H. B. Eldridge, *Nuclear Sci. and Eng.* 8, 300 (1960).

Experimental Procedure

In work described here the perturbations due to the presence of an absorbing foil were studied by means of a series of exposures made in the water thermal column of the ORNL Graphite Reactor, using sets of gold, indium, copper, and uranium foils. Gold and indium were chosen because they are among the materials commonly used for foil activation measurements; copper is an example of a material with a low absorption cross section, and uranium exemplifies a material with a high absorption cross section. In each set there were about a dozen foils of the same substance, all having the same diameter but different thicknesses. By exposing the foils singly to the same flux it was possible to evaluate the activity per unit weight as a function of the thickness of the foil. Extrapolation to zero thickness and renormalization then yielded the desired neutron perturbation factors.

The thermal column of the ORNL Graphite Reactor is a 5-ft × 5-ft × 6-ft-deep, ¼-in.-thick-walled aluminum tank, filled with water and resting with its ½-in.-thick aluminum base on the top of 7 ft of graphite. Below the graphite is an 8-in.-thick layer of bismuth bricks, lying on top of the reactor proper, which attenuates the gamma-ray flux. The neutrons in the tank are thus well thermalized. The cadmium ratio at the base of the tank has been measured to be about 3000 for indium and 5000 for gold.[5]

At a reactor power of 3400 kw, the magnitude of the thermal-neutron flux in the water is given by

$$\phi(x, y, z) = 9.2 \times 10^6 \cos(0.018x) \cos(0.018y) e^{-0.36z} \text{ n/cm}^2 \cdot \text{sec} ,$$

where x and y are the horizontal coordinate distances from the center of the tank, in centimeters, and z is the vertical distance from the base of the water tank, in centimeters. For a given reactor power the thermal-neutron flux remains fairly constant in a horizontal plane over a central area of some 20 × 20 in. There were small variations from one foil exposure to another due either to off-center positioning of the foil or to the movement of control rods or the insertion of core experiments in the reactor. These variations were taken care of by placing a gold monitor foil in the same mount as the foil to be exposed, but at a fixed distance of several centimeters below the test foil.

Since the neutron flux in the thermal column has a relaxation length of about 2.7 cm, it is not isotropic. However, as far as the perturbing effects of foils are concerned, the small anisotropy in the flux is unimportant. This was verified by comparison of three sets of data which are shown in Fig. 2.10.1. The first set consists of data from 1.11-cm-dia gold foils exposed in the thermal column. The second set consists of results from exposure of similar 1.11-cm-dia gold foils in the ORNL Lid Tank Shielding Facility (LTSF) at a point in the tank where the thermal-neutron flux is essentially isotropic. The third set of data is that of Zobel,[6] who exposed 1-cm-square foils in the LTSF at the point at which the flux is isotropic. The comparison indicates that within the assigned errors the small nonisotropy of flux in the thermal column does not make a significant difference.

---

[5] R. O. Bagley *et al.*, *MIT Practice School Memorandum*, EPS-X-269 (1956).

[6] Section 2.3, this report.

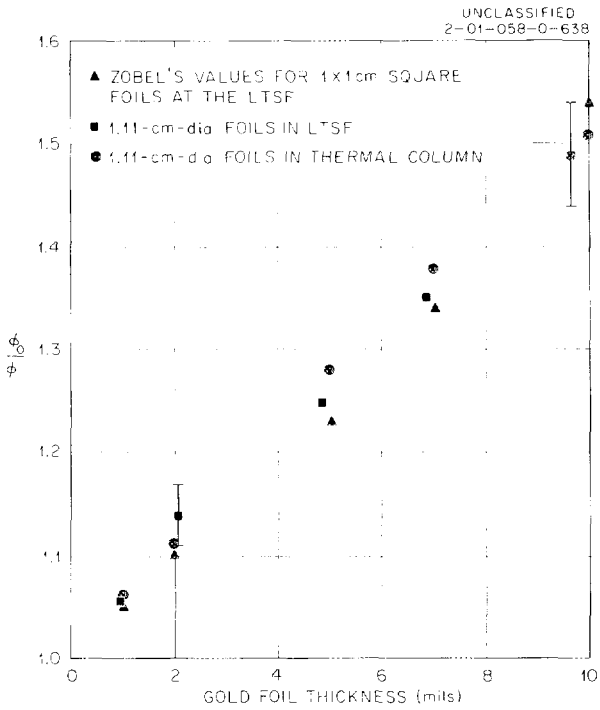

Fig. 2.10.1. Comparison of Thermal Column Data with Lid Tank Data.

Foil Preparation. -- The thicknesses of foils used ranged from roughly 1602 mg/cm^2 (copper) down to about 45 μg/cm^2 (gold). Thicker foils were prepared by normal rolling mill techniques and were weighed on a conventional microbalance. The very thin foils, however, were made by evaporating gold or indium on a 0.25-mil-thick Mylar sheet. Weights of these extremely thin films were determined by chemical analysis. The accuracy of the analyses, unfortunately, was only of the order of ±3%, causing appreciable scatter in the data points.

In order to circumvent the uncertainties in the chemical weights, an activation analysis technique was tried in which the 8-in.-dia steel beam tube described by Mustafa and Blosser[7] was used to provide a beam of thermal neutrons in air. The saturated activity induced in the extremely thin gold films when placed in this beam was compared to the saturated activity induced in a 0.25-mil-thick gold foil placed in the same location. The thicker foil could be accurately weighed on a microbalance. The comparison of the thin foil activity with that of the thicker foil then gave the weight of the thin foil. Since the only important perturbation arises from the self-shielding in the foil, a correction for this effect could readily be made for the beam geometry used. For a unidirectional thermal-neutron beam, the self-shielding is given by

$$\frac{1}{\Sigma_a t} \quad 1 - e^{-\Sigma_a t} \quad ,$$

where

Σ_a = macroscopic absorption cross section, cm^{-1},
t = thickness of the foil, cm.

[7] Section 2.13, this report.

The product $\Sigma_a t$ also gives the foil thickness in terms of mean free paths of thermal neutrons in the foil material.

By using the activation weights, more consistency and less scatter were obtained. However, the extrapolated value at zero thickness was essentially the same with either activation or chemical weights.

The difficulty encountered with the activation method lay in obtaining a monodirectional thermal-neutron beam of sufficient intensity to yield good counting statistics. At the mouth of the beam tube where the beam is sensibly unidirectional, the intensity was low; close to the bottom of the tube where the intensity was usefully high, neutrons are entering from many directions.

The very thin uranium foils were made by evaporating uranium on ¼-mil Mylar film or on ⅓-mil copper. In the latter case the copper activity was subtracted from the total count to obtain the activity of the uranium alone.

The parameters assigned to the various materials in this experiment were as follows: Au density = 19.32 g/cm^3, Σ_{a2200} = 5.83 cm^{-1}; In density = 7.28 g/cm^3, Σ_{a2200} = 7.30 cm^{-1}; Cu density = 8.94 g/cm^3, Σ_{a2200} = 0.326 cm^{-1}; and U (93.18 wt% U^{235}) density = 18.7 g/cm^3, Σ_{a2200} = 31 cm^{-1}.

Foil Mounts. – The sketch of the Lucite foil mount shown as Fig. 2.10.2 is self-explanatory. After the foil was placed in position it was covered with Lucite disks, with the top disk sealed with Vaseline to make it watertight. The distance of the detector foil from the monitor foil was held constant for any single set of foils, but was varied for foils of widely different activation cross sections.

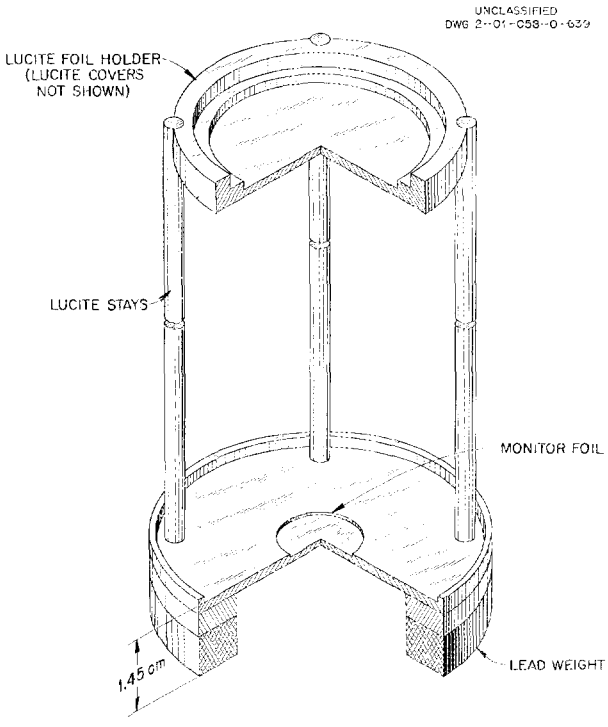

Fig. 2.10.2. Foil Holder Used for Thermal Column Irradiations.

Gamma-Ray Counting. – The gamma-ray activity induced in the foils was observed with the two-crystal NaI(Tl) scintillation counter previously described by Blosser and Trubey.[8] The two-crystal arrangement provided an approximate 4π geometry, and foil placement was excellently reproducible. Pulse-height discriminator settings used were 0.314 Mev for gold, indium, and uranium, and 0.419 Mev for copper.

An important factor which must be taken into account in the use of this or similar counters is the counting loss correction. The counting loss suffered at high count rates is a function of the counter electronics and must be checked each time any element is replaced or any alteration made to time constants. In determining the counting loss as a function of count rate, a sample of the material is strongly activated by thermal neutrons and counted until its activity has decayed to well below the stage where any count loss exists. The correction factor then is simply the ratio of the true activity, extrapolated back on the basis of the known decay rate, to the observed activity. A typical curve of counting loss correction as a function of count rate, in this case for indium, is shown in Fig. 2.10.3. The threshold for counting loss appears to be at about 4×10^4 counts/min when the X1 switch is used, and at about 6×10^4 counts/min when the X10 switch, which brings in a Burroughs tube circuit, is used. Counting loss increases with increasing count rate in a roughly linear manner.

Variation of Counter Response with Foil Thickness. – Two effects exist which tend to make the observed activity per unit weight of a foil different from the true activity induced by the neutron flux. Both increase with foil thickness. The first is the geometry effect, which in effect considers the variation in the way the detector "sees" various thicknesses of foil. This effect is minimized in the double-crystal arrangement of the counter used.

The second effect is due to the attenuation of the gamma rays originating within the foil by the outer layers of the foil. This is the more important of the two. The combined effect, however, may be considered to be a variation of counter efficiency with foil thickness. A correction must therefore be applied to convert the observed count rate to that which would be observed in an infinitely thin foil. Such a correction factor was determined experimentally for each of the materials studied. Several foils of a given material were exposed to neutrons and counted, first singly and then in combinations simulating thicker foils. The saturated activity per unit weight (in the case of uranium, the activity after a 30-min wait time) was calculated. The ratio of the average activity of the single foils to the activity in combinations was then plotted against the combination weights, so that the value of unity corresponded to the weight of a single foil. An extrapolation of the resulting curve to zero weight gave a normalization factor by which all values were divided. The normalized curve then gave the correction factors by which the observed count rate per unit weight for a foil of given weight must be multiplied to give the activity of an ideal foil. These factors, called counter factors, are plotted in Fig. 2.10.4 for gold, copper, and uranium. Interestingly, for indium foils not more than 10 mils thick, the factor is unity; in other words, no self-absorption or geometry effect was observed when indium foils were counted separately and as a stack.

[8] T. V. Blosser and D. K. Trubey, *Neutron Phys. Ann. Prog. Rep., Sept. 1, 1960*, ORNL-3016, p. 142.

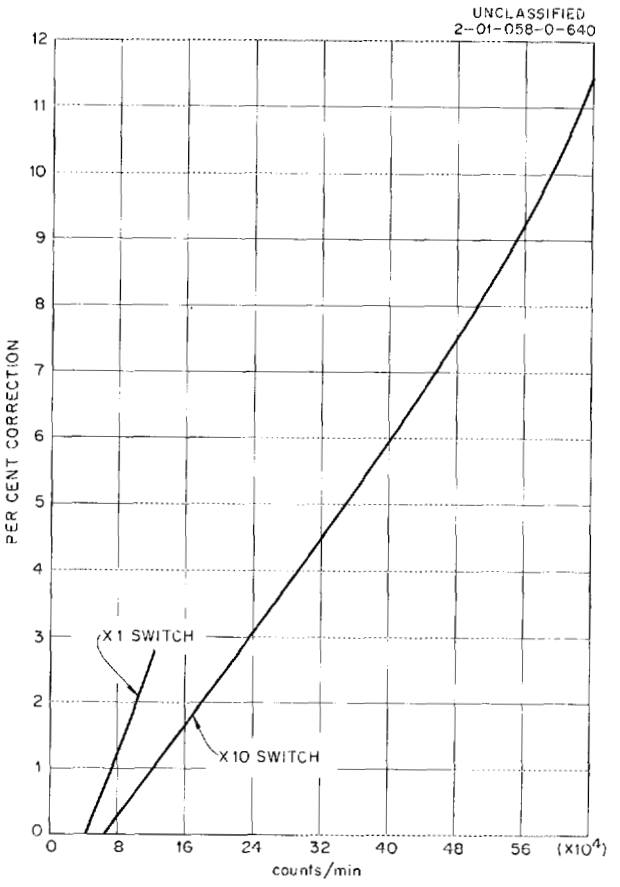

Fig. 2.10.3. Typical Counting Loss Correction Curve (Indium).

The factors appear to be practically independent of foil diameter within the limits of the foil dimensions used.

Decay of Uranium Activity. – The activity exhibited by a uranium foil after exposure to thermal neutrons is, of course, due to the decay of the fission products formed within it. Thus the shape of the count rate versus time curve for a given counter setting depends upon the time for which the sample was exposed. In order to obtain a standard decay curve for the counter settings and geometry used in the present work, the irradiation time was fixed at 1 hr for all exposures. Foils of the same enrichment but of different weights were separately exposed for the standard 1-hr time and counted. A wait time (delay between exposure and start of counting) of 30 min was arbitrarily chosen to which to normalize all experimental decay curves. The curve for each run was used to calculate a set of values for the ratio of the count rate at a given wait time to the count rate after the arbitrary 30-min wait time. Only those portions of each experimental curve were used where the count rate was low enough so that there was no counting loss yet was at least 100 times the room background. The heavier foils, which were countable only after a wait of several hours, were correlated to the thin foils by the use of data from foils of intermediate thicknesses which overlapped the two extremes. The average of more than a dozen runs was taken as the standard decay curve and is shown in Fig. 2.10.5. The errors on individual points are of the order of 1%.

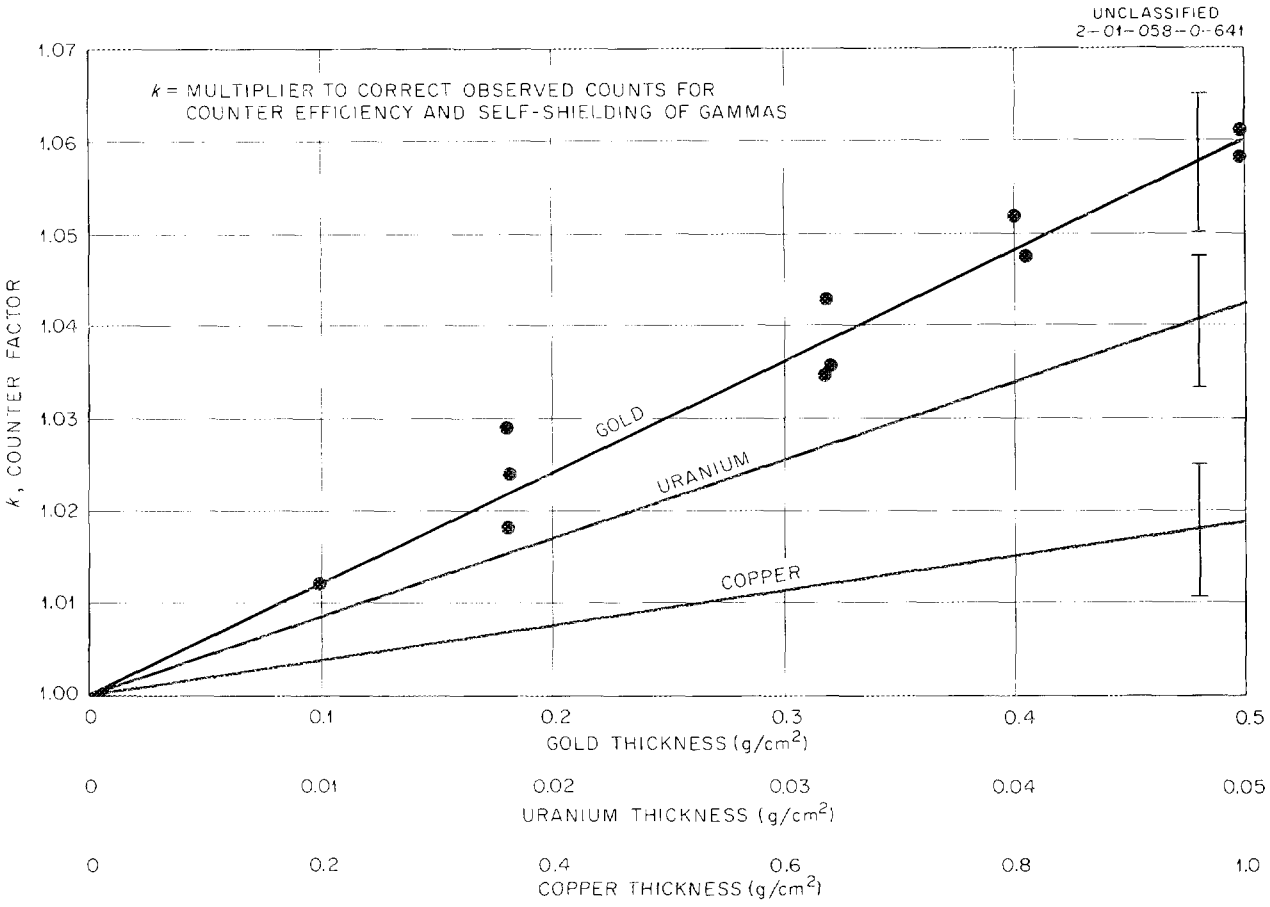

Fig. 2.10.4. Variation of Counter Efficiency with Foil Thickness for Gold, Uranium, and Copper Foils.

The curve is of course valid only for the particular geometry and counter settings used, since the efficiency of counting for gamma rays of different energies depends upon these variables.

Results

The results of the work with gold, indium, copper, and uranium foils are presented in Tables 2.10.1 through 2.10.8. (Not all of the values for thin foils are shown.) The foil perturbation factors are given in two forms, the measured factor, which is to be used for foil activity corrections to data taken under the conditions of geometry and counter efficiency of the present experiments, and a corrected factor. The corrected factor embodies the correction for counter efficiency previously discussed and is the factor to be used for comparison with theories of neutron density depression and self-shielding in foils.

The corrected foil perturbation factors of Tables 2.10.1 through 2.10.8 are plotted in Figs. 2.10.6 to 2.10.9. By presenting the perturbation factor as a multiplier rather than a divisor of the foil activity, it turns out that the plot of perturbation factor as a function of foil thickness is very nearly a straight line, although the points for the thickest foils consistently fall below the line. For very thin foils there

is the theoretical possibility of a complicated shape involving logarithmic functions. Since the straight line is admittedly an approximation and the error is certainly within the experimental error associated with the thin foil points, the differences may be ignored.

Table 2.10.1. Foil Perturbation Factors for Various Thicknesses of 1.11-cm-dia Gold Foils

Foil Thickness (mg/cm^2)	Foil Weight (mg)	Foil Perturbation Factor	
		Measured*	Corrected for Counter Efficiency
488.5	473.6	1.461	1.380
346.8	336.2	1.345	1.291
244.3	236.8	1.240	1.205
102.8	99.7	1.127	1.114
94.7	91.8	1.126	1.114
50.2	48.5	1.037	1.031
48.1	46.6	1.055	1.049
10.9	10.6	1.010	1.009
2.6	2.5	0.983	0.983

*All foils were irradiated at a point 4.3 cm above the aluminum-water boundary of the thermal column.

Table 2.10.2. Foil Perturbation Factors for Various Thicknesses of 1.59-cm-dia Gold Foils

Foil Thickness (mg/cm^2)	Foil Weight (mg)	Foil Perturbation Factor	
		Measured*	Corrected for Counter Efficiency
245	484	1.319	1.281
239	474	1.300	1.263
103	203	1.138	1.125
96.0	190	1.129	1.117
54.7	108	1.070	1.063
12.0	23.7	1.013	1.012
11.1	22.0	1.019	1.018

*All foils were irradiated at a point 4.3 cm above the aluminum-water boundary of the thermal column.

Table 2.10.3. Foil Perturbation Factors for Various Thicknesses of 2.54-cm-dia Gold Foils

Foil Thickness (mg/cm^2)	Foil Weight (mg)	Foil Perturbation Factor	
		Measured*	Corrected for Counter Efficiency
259	1313	1.383	1.341
231	1173	1.340	1.304
126	638	1.179	1.162
576	291.7	1.093	1.085
52.2	264.5	1.082	1.075
11.8	59.7	1.018	1.016
10.7	54.1	1.014	1.012

*All foils were irradiated at a point 4.3 cm above the aluminum-water boundary of the thermal column.

Table 2.10.4. Foil Perturbation Factors for Various Thicknesses of 3.175-cm-dia Gold Foils

Foil Thickness (mg/cm^2)	Foil Weight (mg)	Foil Perturbation Factor	
		Measured*	Corrected for Counter Efficiency
468.1	3706.5	1.693	1.603
362.8	2872.5	1.551	1.486
242.8	1922.3	1.381	1.342
158.4	1254.5	1.261	1.237
102.1	808.2	1.167	1.153
102.0	807.7	1.157	1.143
56.4	446.4	1.092	1.084
11.5	90.7	1.021	1.020
11.2	89.1	1.015	1.014
1.22	9.69	1.001	1.001

*All foils were irradiated at a point 4.3 cm above the aluminum-water boundary of the thermal column.

Table 2.10.5. Foil Perturbation Factors for Various Thicknesses of 1.11-cm-dia Indium Foils

Foil Thickness (mg/cm^2)	Foil Weight (mg)	Foil Perturbation Factor*
184.6	178.7	1.570
101.1	97.9	1.342
94.0	91.0	1.307
61.9	59.9	1.216
39.4	38.1	1.146
21.3	20.6	1.072
15.4	14.9	1.056
13.8	13.4	1.057
12.9	12.5	1.052
10.9	10.6	1.046
10.0	9.7	1.039
2.85	2.76	1.005

*Since the correction for counter efficiency for indium foils is unity, corrected and measured factors are identical. All foils were irradiated at a point 7.5 cm above the aluminum-water boundary of the thermal column.

Table 2.10.6. Foil Perturbation Factors for Various Thicknesses of 3.175-cm-dia Indium Foils

Foil Thickness (mg/cm^2)	Foil Weight (mg)	Foil Perturbation Factor*
188.2	1489.9	1.885
120.2	951.7	1.634
94.1	745.1	1.507
80.5	637.1	1.430
65.0	514.6	1.339
34.4	272.	1.196
17.7	140.4	1.088
11.6	91.6	1.064
2.96	23.4	1.024
1.40	11.05	1.025
0.67	5.29	1.005
0.27	2.11	0.997

*Since the correction for counter efficiency for indium foils is unity, corrected and measured factors are identical. All foils were irradiated at a point 8.7 cm above the aluminum-water boundary of the thermal column.

Table 2.10.7. Foil Perturbation Factors for Various Thicknesses of 3.175-cm-dia Copper Foils

Foil Thickness (mg/cm^2)	Foil Weight (mg)	Foil Perturbation Factor	
		Measured*	Corrected for Counter Efficiency
1602	12687	1.289	1.251
1172	9282	1.221	1.195
854	6758	1.159	1.141
430	3405	1.089	1.080
114	903	1.019	1.017
113	895	1.025	1.023
87.0	689	1.028	1.026
86.5	685	1.015	1.013
69.1	547	1.014	1.013
23.6	187	1.012	1.012
22.4	177	0.999	0.999
7.25	57.4	1.001	1.001

*All foils were irradiated at a point 4.3 cm above the aluminum-water boundary of the thermal column.

Table 2.10.8. Foil Perturbation Factors for Various Thicknesses of 93.18 wt% U^{235}-Enriched Uranium Foils 3.175 cm in Diameter

Foil Thickness (mg/cm^2)	Foil Weight (mg of U)	Foil Perturbation Factor	
		Measured*	Corrected for Counter Efficiency
80.45	637.0	1.589	1.488
52.3	414.3	1.438	1.377
52.3	414.1	1.419	1.359
18.8	148.6	1.158	1.140
9.35	74	1.079	1.070
1.9	15.0	1.041	1.039
1.86	14.7	1.004	1.002
1.44	11.4	1.049	1.047
0.8	6.30	1.023	1.022
0.2	1.72	1.008	1.008
0.2	1.70	0.992	0.992

*All foils were irradiated at a point 4.3 cm above the aluminum-water boundary of the thermal column.

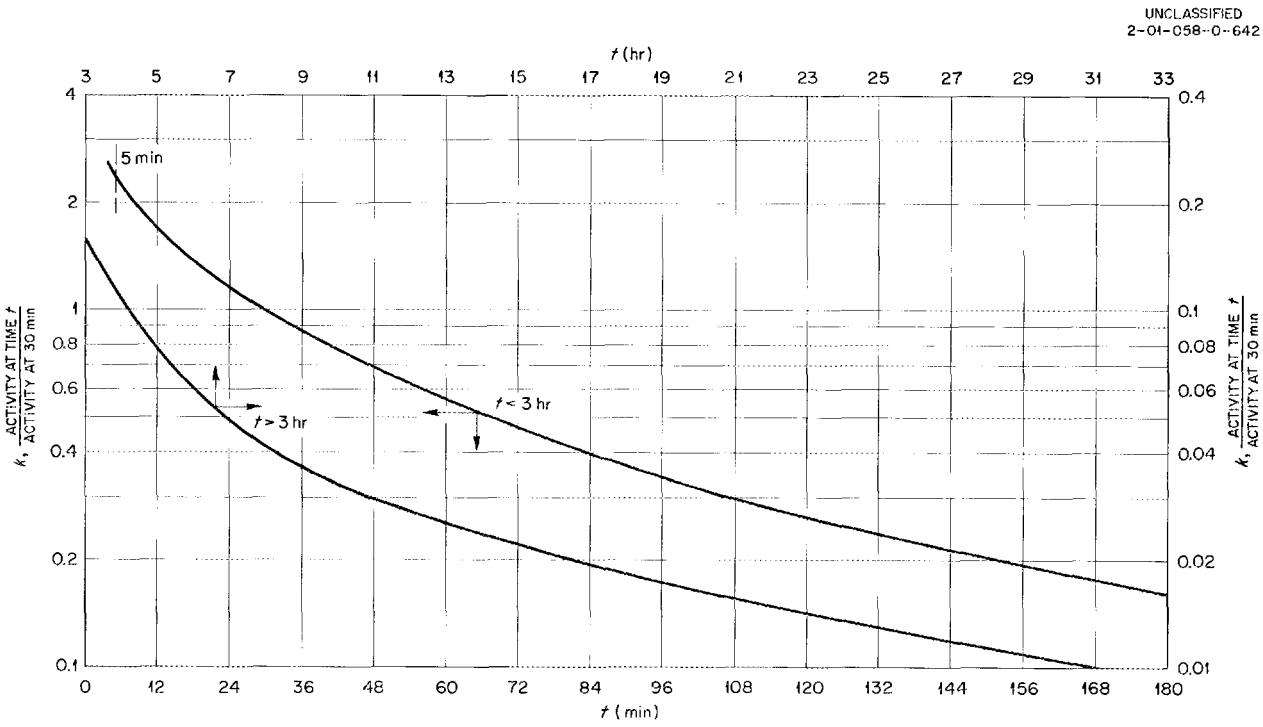

Fig. 2.10.5. Decay Curve for 93.18 wt% U^{235}-Enriched Uranium Exposed for 1 hr in Thermal Column of ORNL Graphite Reactor.

The approximately linear relationship observed leads readily to the development of simple recipe-type formulas. Recalling that the perturbation factor, as defined here, is the ratio of unperturbed neutron density, n_0, to the actual neutron density, n, the straight line is used to derive the value of K in the formula

$$n_0/n = 1 + Km \ , \tag{1}$$

where

m = foil thickness, g/cm^2,

K = slope of line, cm^2/g .

Equation 1 may also be written as

$$n_0/n = 1 + A\tau \tag{2}$$

where

$\tau = \Sigma_0 t$,

Σ_0 = 2200-m/sec absorption cross section, cm^{-1} ,

t = foil thickness, cm .

The dimensionless quantity A is obtained from K by multiplying by the foil density and dividing by Σ_0.

Equations 1 and 2 should not be applied to thick foils with $\tau > 0.1$; otherwise the perturbation factor will be overestimated. Values for K and A are listed in Table 2.10.9.

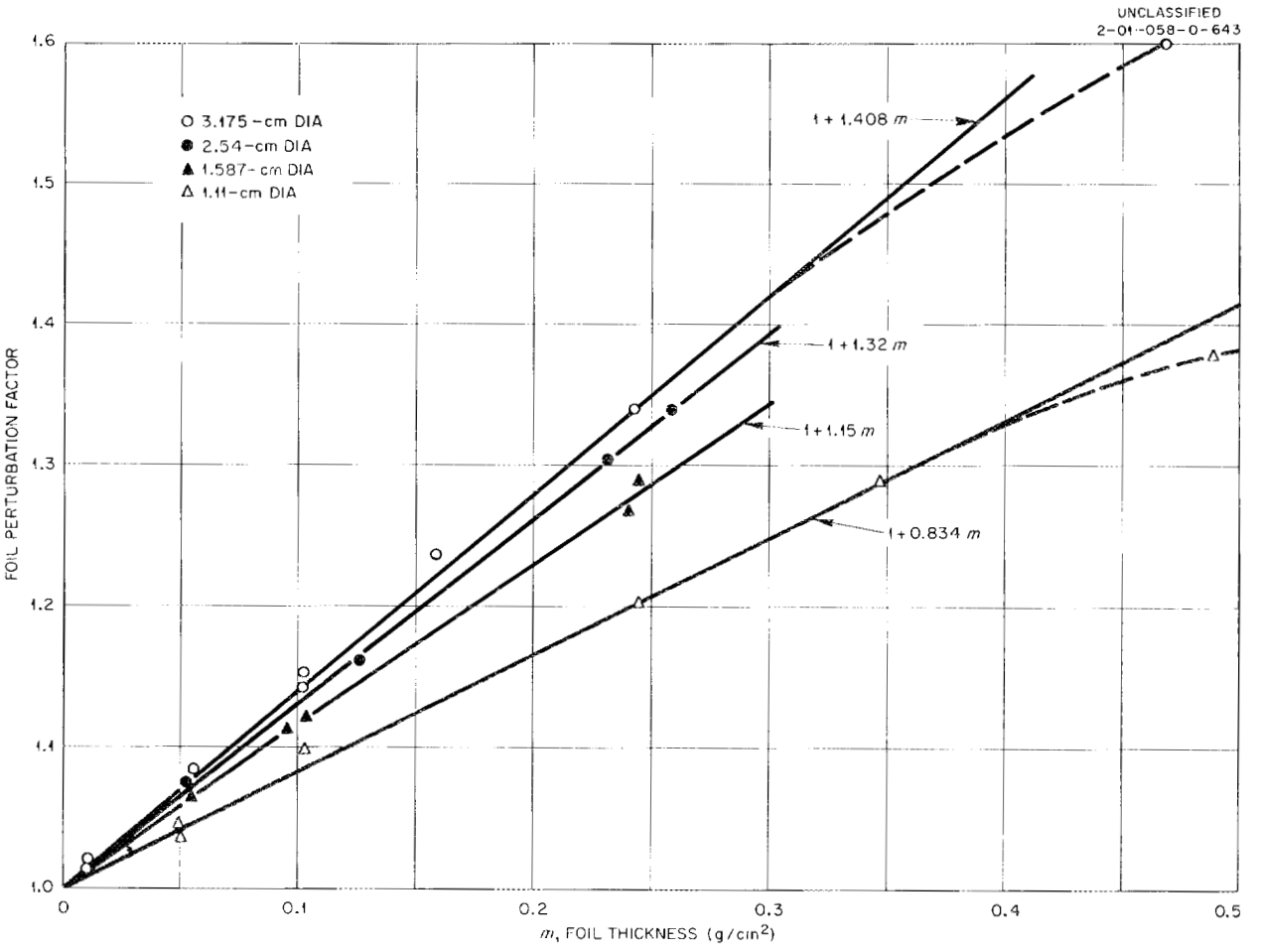

Fig. 2.10.6. Corrected Foil Perturbation Factors for Gold Foils of Various Diameters in Water.

From the values of A in Table 2.10.9, it is apparent that the numbers are similar from one substance to another, particularly in the case of the measured values. The variation from substance to substance may be attributable to neutron scattering in the foil. For no scattering, theory predicts that the perturbation is independent of material if expressed in terms of $\tau = \Sigma_0 t$ (Ref. 9).

The dependence of the foil perturbation on the foil diameter is displayed by the plot of the quantity A of Table 2.10.9 as a function of foil diameter in Fig. 2.10.10. It appears that A increases with foil diameter but tends to reach a limit for large diameters. This is physically reasonable since increasing the diameter should no longer increase the perturbation once a diameter greater than a few mean paths is exceeded. The experimental points appear to fit the empirical equation

$$A = 5.57(1 - e^{-0.86D}) , \tag{3}$$

where D is the foil diameter in centimeters.

[9] G. R. Dalton and R. K. Osborne, *Nuclear Sci. and Eng.* 9, 198 (1961); R. H. Ritchie and H. B. Eldridge, *op. cit.*

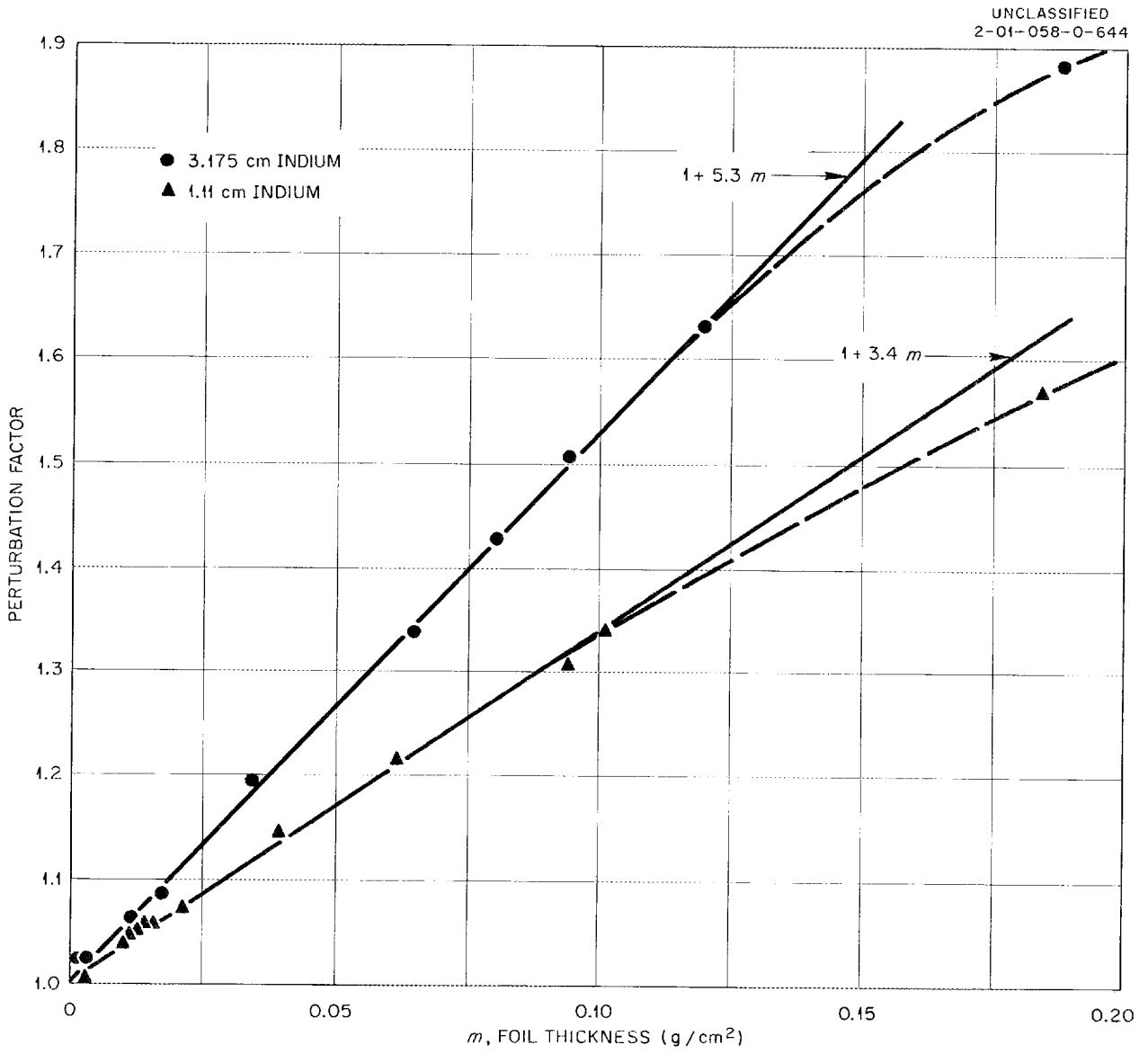

Fig. 2.10.7. Corrected Foil Perturbation Factors for 3.175- and 1.11-cm-dia Indium Foils in Water.

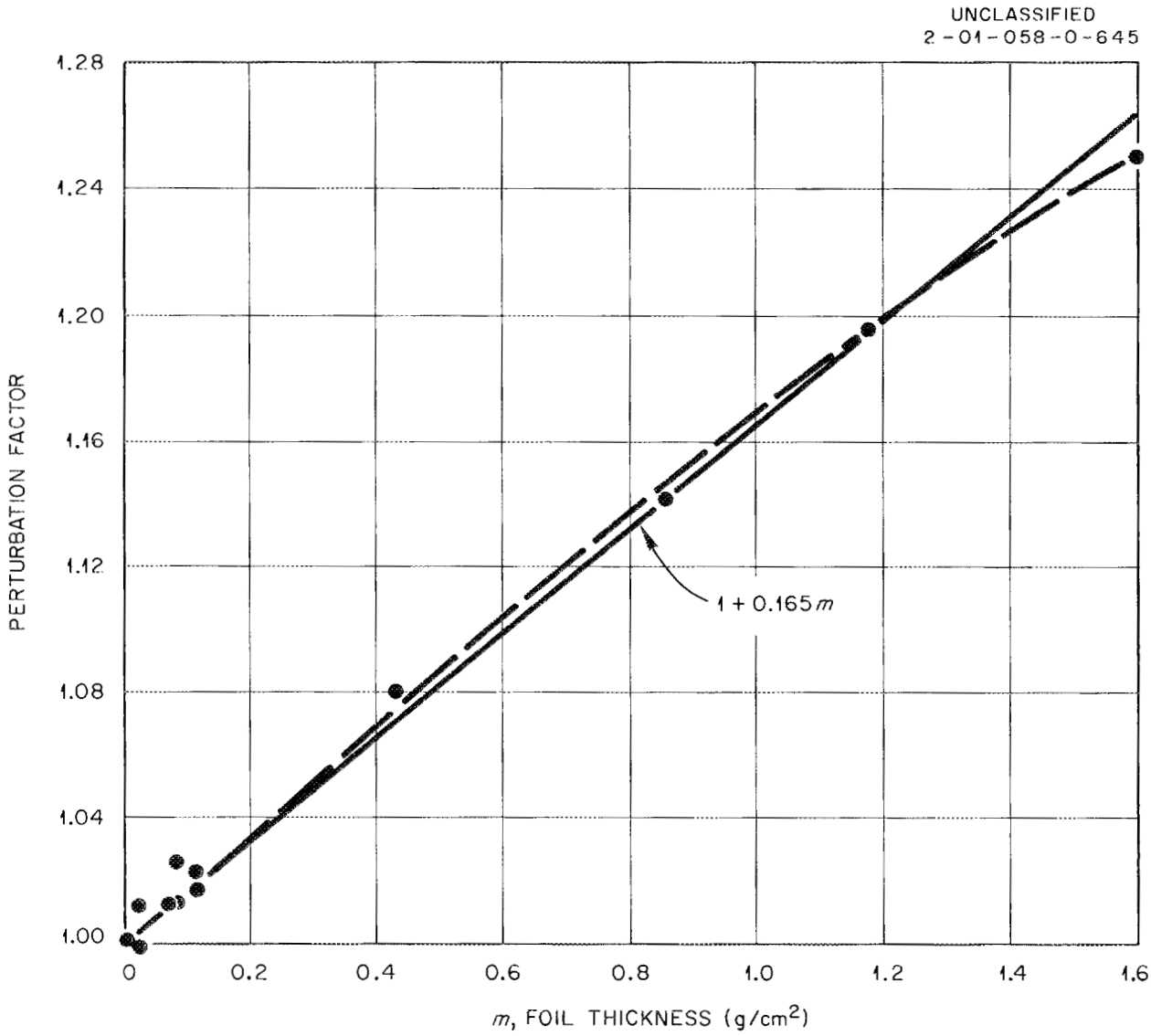

Fig. 2.10.8. Corrected Foil Perturbation Factors for 3.175-cm-dia Copper Foils in Water.

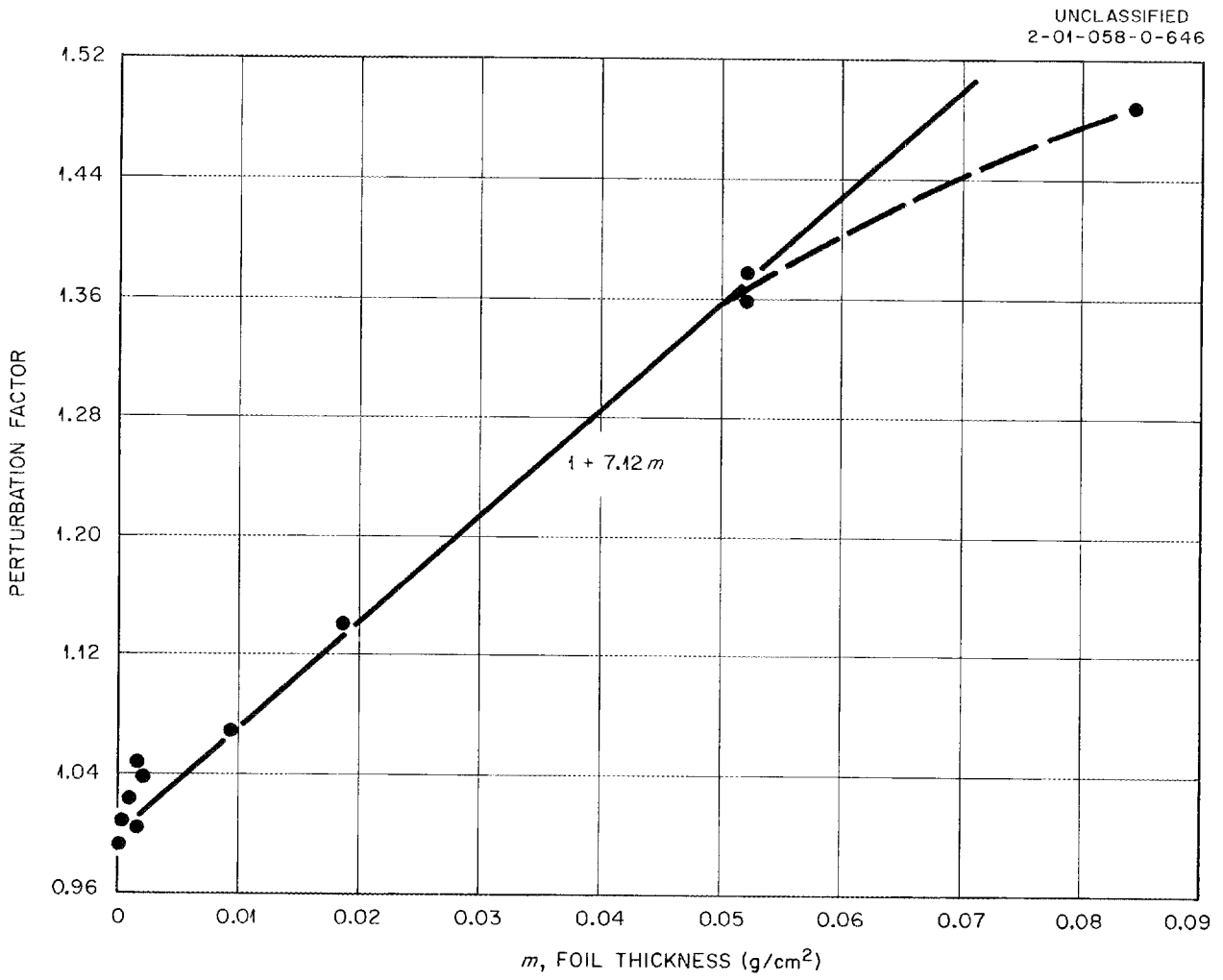

Fig. 2.10.9. Corrected Foil Perturbation Factors for 3.175-cm-dia, 93.18 wt% U^{235}-Enriched Uranium Foils in Water.

Table 2.10.9. Values of K and A for Computation of Flux Perturbation Factors*

Material	Foil Diameter (cm)	K (cm^2/g)		A (dimensionless)	
		Measured	Corrected	Measured	Corrected
Gold	3.175	1.57	1.41	5.20	4.67
	2.54	1.48	1.32	4.90	4.37
	1.5875	1.31	1.15	4.30	3.81
	1.11	0.99	0.83	3.28	2.76
Indium	3.175	5.3	5.3	5.28	5.28
	1.11	3.4	3.4	3.39	3.39
Copper	3.175	0.187	0.165	5.12	4.52
Uranium (93.18 wt% U^{235})	3.175	8.17	7.12	4.93	4.30

*The two columns headed "Corrected" give the values of the constants after correction for counter efficiency and gamma-ray self-shielding.

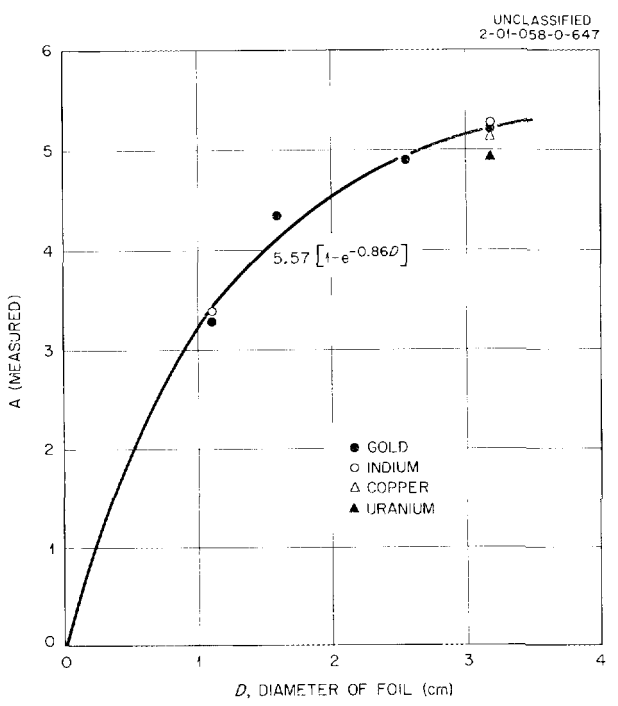

Fig. 2.10.10. Variation of Dimensionless Factor "A" with Foil Diameter.

2.11. DETERMINATION OF SMALL URANIUM CONTENT IN FOILS BY MEASURING INTENSITY OF NATURAL RADIATIONS

S. A. Hasnain,[1] T. Mustafa,[2] and T. V. Blosser

The measurement of the intensity of the natural x and gamma radiations emitted by a sample of uranium provides a quick, accurate, and nondestructive method of measuring the uranium content of small specimens. A procedure has been developed by which such measurements can be made with high accuracy for foils, very thin films, or solutions of uranium. The method has been tested with various samples of known composition.

Experimental Procedure

The experimental procedure consists essentially of counting the gamma and x radiations emitted by the sample of unknown composition in a NaI(Tl) scintillation counter which has previously been calibrated against standard samples of known uranium content. Ideally the sample to be tested should have the same isotopic composition as the calibration standard. This condition can usually be approximated or completely met in practical applications.

Table 2.11.1 gives the energies and intensities of the x and gamma rays emitted by samples of U^{234}, U^{235}, and U^{236} as measured by Bell *et al.*[3] The gamma rays emitted by natural uranium have been given by Heath.[4] The natural uranium spectrum may be considered as essentially due to U^{238}, since only very weak gamma rays at 0.08, 0.18, and 0.34 Mev suggest any contribution from U^{235}. As Bell has shown, the spectrum to be expected from uranium of any given isotopic composition can be obtained by a properly weighted summation of the spectra of the various isotopes. Such a procedure permits identification of peak energies in an experimental spectrum.

The isotopic composition of the highly enriched uranium used in the present measurements was: U^{234}, 0.963 wt%; U^{235}, 93.18 wt%; U^{236}, 0.037 wt%; and U^{238}, 5.53 wt%. Figure 2.11.1 shows an experimental spectrum of this material obtained with a single $1\frac{1}{2} \times 1\frac{1}{2}$ in. NaI(Tl) crystal at a distance of 10 cm in air. The sample was a 1.5-mil-thick disk 0.25 in. in diameter. The 32-kev barium *K* x ray emitted by Cs^{137} was used for the energy calibration of the pulse height. The curve shown has only been corrected for background: no effort has been made to correct for self-absorption of low-energy x rays by the sample or their absorption in the crystal or crystal housing.

The scintillation counter used for the present work is the dual crystal device previously described by Blosser and Trubey.[5] The spectrum of the sample described above as it appears in this counter is shown in Fig. 2.11.2. The smearing evident by comparison with Fig. 2.11.1 is due to the presence of

---

[1]Present address: Pakistan Atomic Energy Commission, Karachi, Pakistan.

[2]Present address: c/o Third Secretary, Embassy of Pakistan, Washington, D.C.

[3]P. R. Bell *et al.*, *Uranium Gamma Spectrum*, AECD-3224 (Aug. 23, 1951).

[4]R. L. Heath, *Scintillation Spectrometry Gamma-Ray Spectrum Catalogue*, IDO-16408 (July 1, 1957).

[5]T. V. Blosser and D. K. Trubey, *Neutron Phys. Ann. Prog. Rep., Sept. 1, 1960*, ORNL-3016, p. 142.

0.25 in. of aluminum between the source and each crystal. For all uranium weighings, the counter was biased at 47 kev.

Weight Calibrations

The counter was calibrated for weight measurements by observing the count rates obtained from various samples which had been accurately weighed on a microbalance. Since the primary goal was to weigh uranium foils of given diameters it would have been best to have calibrated against weighed foils

Table 2.11.1. Principal Gamma Rays Emitted by Samples Containing U^{234}, U^{235}, and U^{236}

(After Bell *et al.*[a])

Sample[b]	Energy (kev)	Relative Intensity
U^{234}	17 ± 2	
	53 ± 2	1.0
	93 ± 2.5	0.11 – 0.31
	118 ± 2	0.42
	181[c]	
U^{235}	17	
	93 ± 2	0.89
	143 ± 3	0.22
	184 ± 3	1.0
	289 ± 5	0.12
	386 ±15	0.049
U^{236}	17	
	51	
	93[c]	
	118[c]	
	143[c]	
	184[c]	
	289[c]	
	386[c]	

[a] P. R. Bell *et al.*, *Uranium Gamma Spectrum*, AECD-3224 (Aug. 23, 1951).

[b] The U^{234} sample contained 94.7 wt% U^{234} and 4.02 wt% U^{235}. The U^{235} sample was 99.9 wt% U^{235} and 0.03 wt% U^{234}. The U^{236} sample contained 95.13 wt% U^{236}, 0.15 wt% U^{234}, and 4.18 wt% U^{235}.

[c] These gamma rays appear to be due to the U^{234} or U^{235} content of the sample.

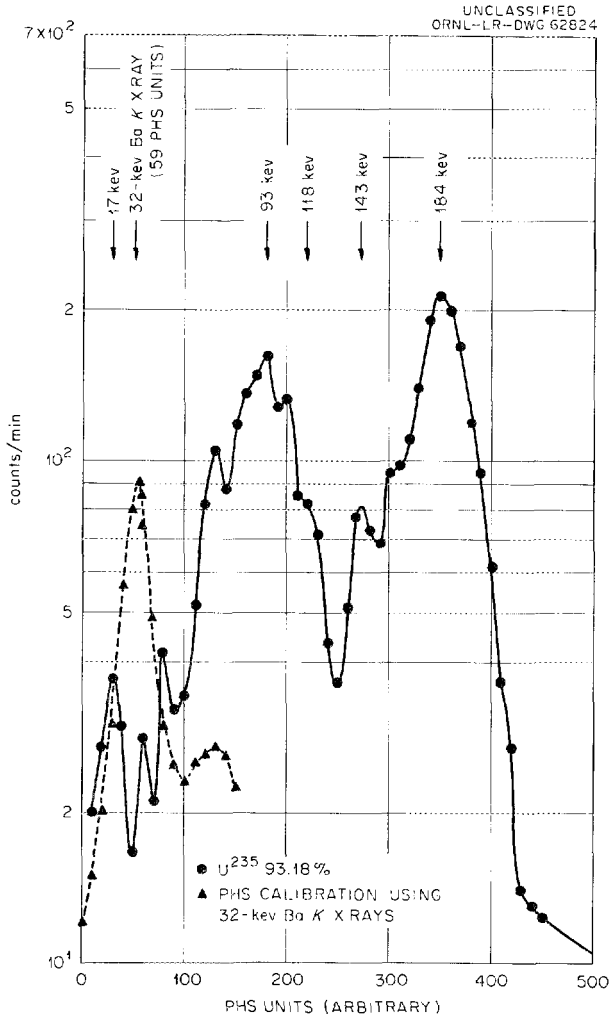

Fig. 2.11.1. Gamma-Ray Spectrum of 93.18 wt% U^{235}-Enriched Uranium Through 10 cm of Air: Single NaI(Tl) Crystal Analyzer.

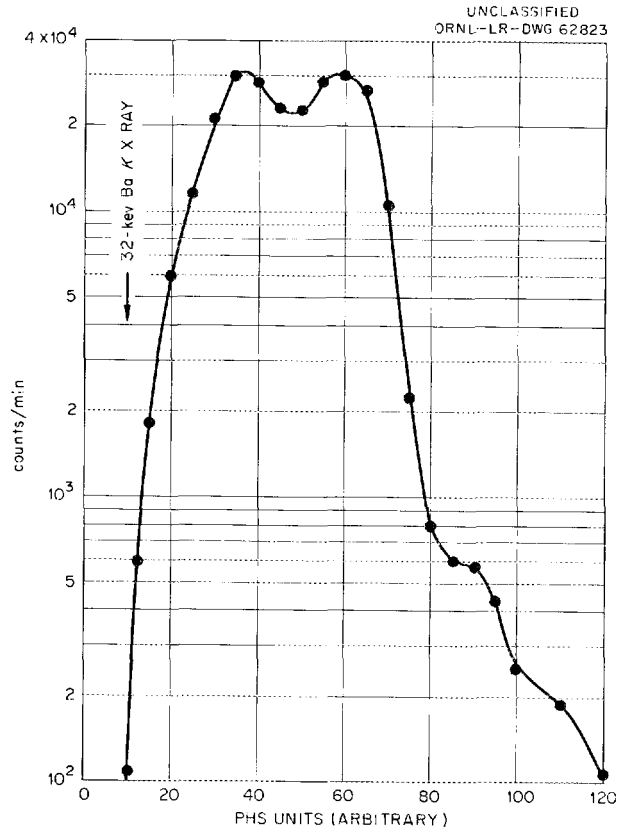

Fig. 2.11.2. Gamma-Ray Spectrum of 93.18 wt% U^{235}-Enriched Uranium Through 0.25 in. of Aluminum: Dual NaI(Tl) Crystal Counter.

of like diameters, since the counter efficiency varies with sample size. However, the accurately weighable foils were cut from 1-mil-thick stock, and for $1\frac{1}{4}$-in.-dia foils containing ~500 mg of uranium the count rate was so high that appreciable counting losses existed. There was no simple way to evaluate these losses. Smaller samples were therefore prepared by cutting strips 3 cm long and from 0.1 to 1 cm wide from the 1-mil-thick stock. These pieces were large enough to ensure accurate weighing, and small enough so that no counting loss occurred. The improved counter efficiency due to better geometry with these strips as opposed to disks was corrected for by a method which will be described below. The calibration data is plotted as counts/min per milligram of uranium as a function of uranium weight and number of counts per minute in Fig. 2.11.3. From this plot a preliminary calibration value of 1434 ± 5 counts/min per milligram of uranium was obtained for thin strips. The shape of the curve clearly indicates where counting losses begin to be seen as samples become larger.

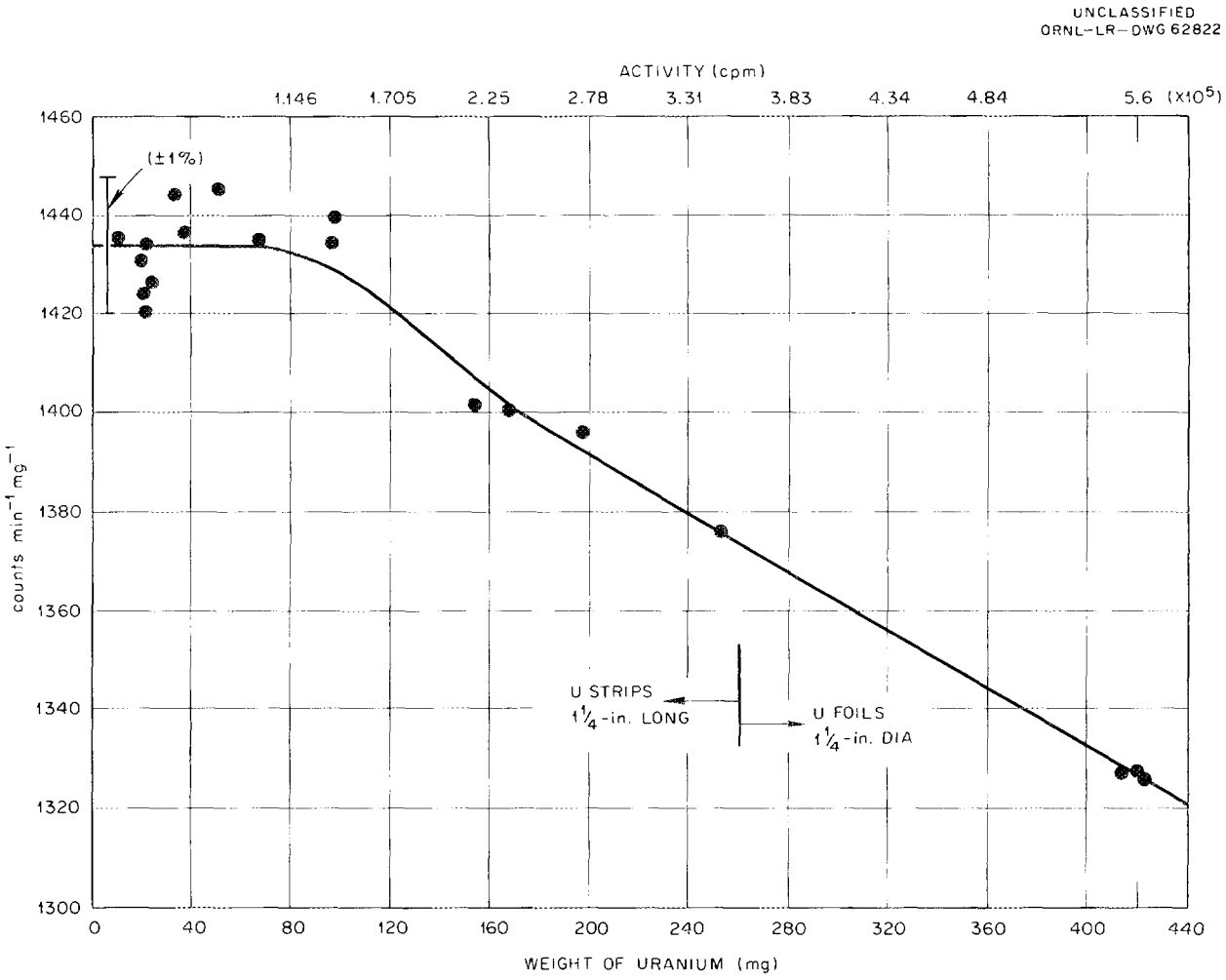

Fig. 2.11.3. Calibration Curve for Weight Determinations on Dual Crystal Counter.

Two methods were used to determine the proper correction to be applied in order to take into account the differences in efficiency due to geometry. In the first, samples of the uranium-aluminum fuel alloy used for BSR-I reactor elements were employed.[6] The samples were in the form of 20-mil-thick, 1¼-in.-dia disks. About 20 of these foils were weighed by counting, after it had been ascertained that the self-shielding due to the aluminum was insignificant. The experimental data are shown in Table 2.11.2. The weights shown in the first two columns were obtained by using the preliminary calibration value of 1434 ± 5 counts/min per milligram of uranium. Also shown in the table are the results of chemical analyses of six of the samples. Although there is some spread evident in the data, with the counter weighings more reproducible than the chemical analyses, it is clear that the chemical analysis consistently is about 4%

[6] These samples were furnished by E. B. Johnson of the Bulk Shielding Facility.

Table 2.11.2. Uranium Content of Uranium-Aluminum Alloys

Sample No.	Uranium Content (%)				Counting-Chemistry Difference (%)[c]
	By Radiation Counting[a]		By Chemical Analysis[b]		
	20-mil Foils	Av. 62-mil Foils	Run 1	Run 2	
B1	13.08	13.12	13.85	13.64	4 – 5.9
B2	13.09	13.10	13.50	13.66	3.1 – 4.4
B3	13.17	13.16	13.65		3.6
B4	12.90	12.94	13.41	13.22	2.2 – 4
B5	13.02	12.96	13.47	13.63	3.5 – 5.2
B6	13.10	13.11	13.56	13.71	3.4 – 4.7
Z1 to Z15 (Average)	13.12				

[a]Using uncorrected calibration value: 1434 counts/min per milligram uranium.
[b]Analytical Chemistry Division, Control Nos. D45382, D46041, and D46174.
[c]Attributable to difference in counter efficiency for disk foils and strips.

higher than the counter results. The correction to be applied to the counter results then is –4%, which results in a final calibration value for $1\frac{1}{4}$-in.-dia circular foils of 1434/1.04, or 1379 counts/min per mg of uranium.

Confirmation of these results was provided by a second experiment, in which the foils weighed by counting consisted of $1\frac{1}{4}$-in.-dia, $\frac{1}{3}$-mil-thick copper, on which uranium had been electroplated to a thickness of the order of 0.1 mg/cm^2. These foils were made by G. S. Pettit,[7] who estimated the thickness of uranium by alpha-particle counting. A comparison of his values with those obtained in the present experiment shows the same 4% difference noted earlier, thus giving the same corrected calibration figure as above.

It may be concluded that although the absolute weights obtained depend upon the accuracy of the chemical analyses, the method described provides a way of obtaining relative uranium weights in foils with an accuracy better than 1%.

[7]ORGDP.

2.12. NEUTRON DISTRIBUTION IN A REACTOR FUEL PLATE

S. A. Hasnain[1] and E. B. Johnson

A traditional method for examining the neutron flux distribution within a BSR-type reactor core depends upon the measurement of the activity induced in thin foils placed in the water gaps between fuel plates. Such placement, however, fails to adequately describe the fission events taking place within the fuel plate itself. The effects of the materials of the fuel plate in depressing the flux are of particular interest, and a knowledge of these effects will become even more important as materials such as stainless steel replace the customarily used aluminum.

Since a number of thin foils rolled from the fuel region of a Pool Critical Assembly fuel plate had been prepared for another experiment and were readily available, they have been used to experimentally measure the neutron distribution through the thickness of a PCA fuel plate and through the water on either side.

Ten 2-mil-thick, $1\frac{1}{4}$-in.-dia uranium-aluminum alloy foils were stacked together to represent the 20-mil-thick fuel region of a PCA fuel plate. A 20-mil-thick, $1\frac{1}{4}$-in.-dia aluminum disk on either side represented the fuel plate cladding. The entire sandwich was inserted in a $1\frac{1}{4}$-in.-dia hole in a test plate of a special fuel element in the PCA. In similar holes in adjacent plates were inserted 20-mil-thick uranium-aluminum alloy foils clad in 20-mil-thick aluminum. Very thin uranium foils, about 0.1 mg/cm^2, encased in Lucite were placed in the water spaces between fuel plates.

After the foils were positioned in the core, the reactor was operated at low power for ~~approximately~~ 1 hr. Immediately following this run, the foils were removed and counted for fission-product activity, sufficient time being allowed before counting to permit the slow-neutron activation of aluminum to decay out. The activity per milligram of uranium after a wait time of 30 min was determined by following the fission-product decay. (A detailed description of the method is given elsewhere in this report.[2]) The aluminum cladding was treated as a catcher foil, its activity being added to that of the uranium foil nearest it. A correction for gamma-ray self-shielding and counter geometry was applied to the 20-mil-thick foil data.[2]

The distribution of the fission-foil response is shown in Fig. 2.12.1. Since the uranium is enriched to 93.18 wt% in U^{235}, the fissions were mostly due to thermal neutrons. If a $1/v$ fission cross section is assumed, the fission-foil response is proportional to the neutron density.

Owing to an uncertainty of $\sim 1\%$ in each experimental point, the details in the shape of the curve are not significant. Some general trends, however, are clearly evident. There is a definite decrease in neutron level outward from the center of the reactor core (left to right in the figure) amounting to 1 or 2% between adjacent fuel plates. Peaking occurs in the water gap between fuel plates, the peak being around 1 or 2% higher than the average level in the fuel plates. Inside the fuel region, as can be seen in the expanded section of Fig. 2.12.1, the neutron level is noticeably depressed at the center. The level at

[1]Present address: Pakistan Atomic Energy Commission, Karachi, Pakistan.

[2]See Section 2.17, this report.

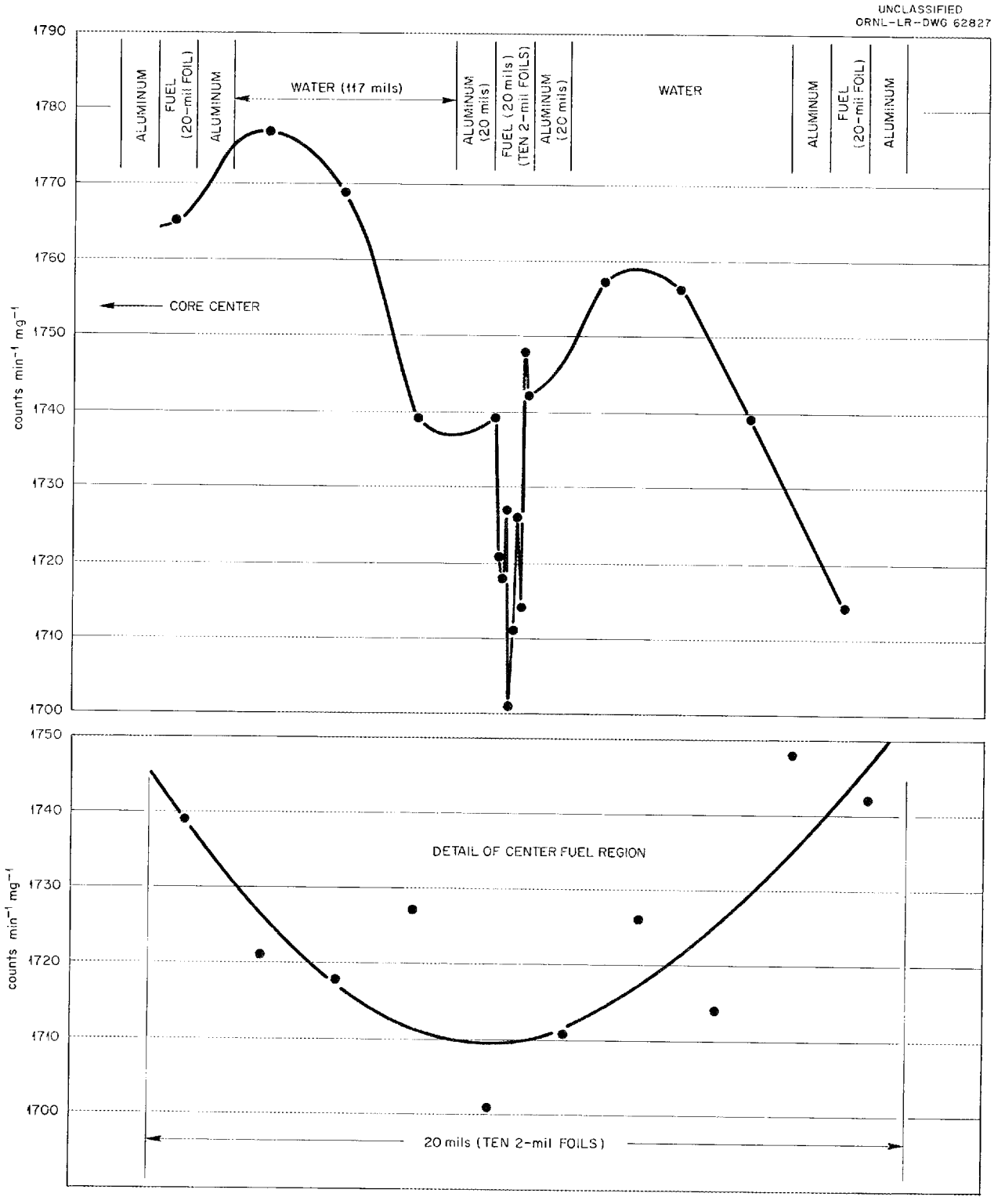

Fig. 2.12.1. Neutron Distribution Through a PCA Fuel Plate and in Adjacent Water Spaces, as Measured with Fission Foils.

the center is at least a percent lower than that at the edges. This is a larger effect than has previously been estimated by calculations.[3]

The precision of the results given above can be improved by two modifications, which are suggested for future experiments. The first lies in the use of thinner foils, say 1 mil thick, and the second would come from the use of reactor power levels higher than those of the present experiment. A proposed study of neutron distributions in the stainless steel BSR-II will attempt to include these modifications.

[3] A. B. Reynolds, Ph.D. Thesis, Massachusetts Institute of Technology (June 1959).

2.13. CALIBRATION OF A BF_3 PROPORTIONAL COUNTER IN WATER AND IN AIR

Tariq Mustafa[1] and T. V. Blosser

In the near future the Neutron Physics Division will make measurements of radiation leakage through the biological shields of a number of large reactors, including the reactor of the nuclear ship "Savannah." Several highly sensitive BF_3 proportional counters[2] have been acquired for this purpose. They will be used to measure thermal-neutron fluxes and will serve as the detecting elements within the "modified long counter" assembly used for measurement of epithermal- and fast-neutron doses. A cross section of a counter tube is shown in Fig. 2.13.1. The fill gas is BF_3, enriched to 96% in B^{10} at a pressure of 76 cm of Hg, essentially 1 atm. Such a pressure, several times that customarily used, not only increases sensitivity but also makes the counter better able to resist accidental damage during field use. Since the tubes are intended to be interchangeable, response identical to within ±1% was a condition of acceptance of the lot. A vacuum tube preamplifier is integrally packaged with the detector, and during the calibrations described below was pressurized to 9 psi with CO_2 to prevent entrance of water. All calibrations were carried out in the vertical thermal column of the ORNL Graphite Reactor, operating at a nominal power of 3800 kw. At this power level the thermal flux at 1 cm from the bottom of the column is approximately 10^7 neutrons·cm^{-2}·sec^{-1}, and the cadmium ratios for indium and gold are ~3000 and ~5000, respectively.

Calibration in Water

The general plan for all calibrations consisted of a comparison of the counting rate of the BF_3 tube with absolute flux measurements made with foils. Initially, vertical traverses were made on the z axis of the thermal column, with the counter lying in the x-y (horizontal) plane. A relaxation length of 2.71 ± 0.03 cm was obtained for the thermal-neutron flux down to a distance of 29 cm from the bottom of the column. At this point, owing to the high sensitivity of the counter, counting losses became appreciable.

[1] Present Address: c/o Third Secretary, Embassy of Pakistan, Washington, D.C.

[2] Purchased from Reuter-Stokes Electronic Components, Inc., No. RSA-42A.

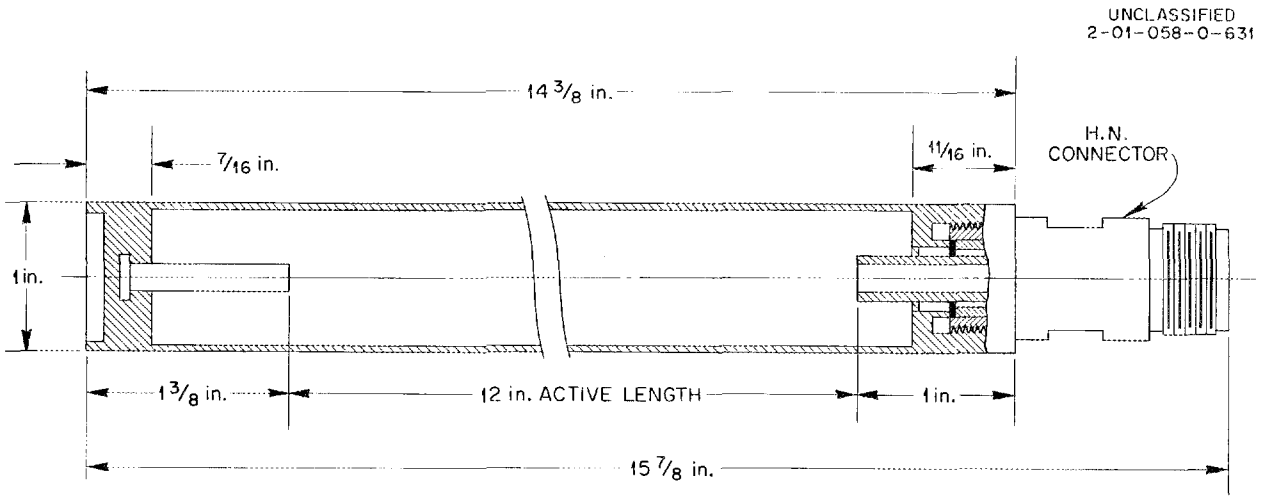

NOTE: BODY MATERIAL: TYPE-1100 ALUMINUM
FILL GAS: BF_3
0.002-in. TUNGSTEN ANODE
INSULATOR MATERIAL: 96-98 % Al_2O_3
CONNECTOR MATERIAL: BRASS

Fig. 2.13.1. Diagram of BF_3 Proportional Counter.

About 95% of the tube surface was then masked with 40-mil-thick cadmium, allowing the traverse to proceed to about 20 cm from the bottom. The relaxation length observed over this region was, within experimental error, identical to the value previously noted. At this point the thermal-neutron flux was estimated to be $\sim 10^4$ neutrons·cm^{-2}·sec^{-1}, giving a count rate almost high enough to jam the counter but too low to obtain a satisfactory measurement of the saturated activity of a gold foil. The use of indium foils at this location was rejected because of the attendant difficulties and uncertainties in translating saturated activity of indium into absolute flux values. Instead, gold foils were exposed in the lower 10 cm of the column, where the flux ranges from $\sim 2 \times 10^5$ to 10^7 neutrons·cm^{-2}·sec^{-1}. These data were then extrapolated to the position of the counter by using the relaxation length of 2.71 cm previously measured. The excellent fit to the data evidenced in Fig. 2.13.2 indicates that the relaxation length remains about the same down to $\sim$1 cm from the bottom of the thermal column.

The determination of absolute flux values from the induced activity in gold foils was carried out by two independent methods. In the first, the gamma-ray activity induced in the foil was counted on a known-efficiency NaI(Tl) scintillation counter. The saturated activity of a gold foil, A_s, can be expressed as $A_s = f\phi\Sigma_{act}$, in which f is the flux perturbation and depression correction, Σ_{act} is the macroscopic activation cross section for gold, and ϕ is the thermal-neutron flux. If C is the count per minute of a scintillation counter with a detection efficiency η, then

$$C = 60 f\phi\overline{\Sigma}_{act}\eta ,$$

and

$$\phi = \frac{C}{60 f\overline{\Sigma}_{act}\eta} . \qquad (1)$$

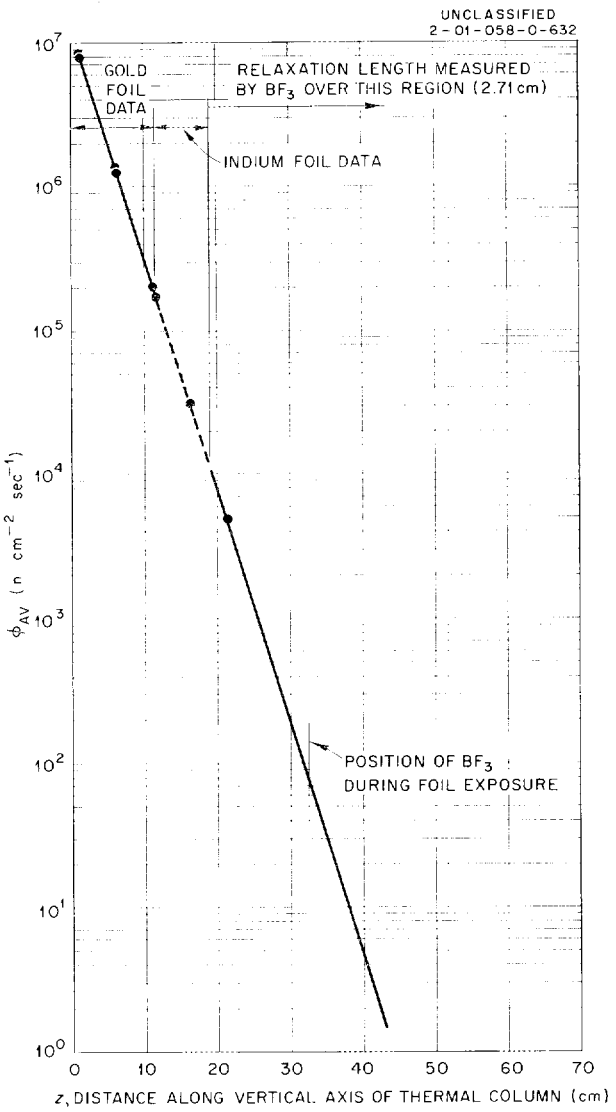

Fig. 2.13.2. Thermal-Neutron Flux Distribution in the Thermal Column of the ORNL Graphite Reactor.

For the 1.11-cm-dia, 5-mil-thick, 0.2368-g foils used, $\overline{\Sigma}_{act} = \frac{96 \pm 10 \text{ barns}}{1.128}$, where 1.128 is the factor required to convert the 2200-m/sec cross section to an average over a Maxwellian distribution. The efficiency, η, was experimentally determined to be 0.093, and the factor f to be 1.24.

The second method for determining the absolute flux value was by direct comparison of the activities induced in a gold foil when it is alternately placed in the unknown flux and in the calibrated flux of slot No. 1 of the ORNL Standard Pile. The comparison was made on a double-crystal NaI(Tl) scintillation counter at the same cutoff bias and amplification.

The results of the flux determinations by both methods are given in Table 2.13.1.

During the 231-min foil irradiations in the thermal column, the BF_3 chamber, which was positioned with its leading edge 31.3 cm above the bottom, was continuously counting. It accumulated a total of 5,055,086 counts in the 231 min at a mean count rate of 21,883 counts/min. Before the extrapolated flux

can be combined with the counting rate of the detector to give a calibration factor, however, some consideration must be given to the position of the center of detection of the counter tube. The most simple approach is to assume that the center of detection coincides with the geometrical axis of the tube. A more sophisticated attack, since the flux varies logarithmically with z, is to assume that the center of detection lies at the logarithmic mean between the leading and trailing edges. In the case of the counter being calibrated, this method places the center of detection at a point 0.4 cm before the geometrical axis.

Such an analysis seems acceptable for a counter tube with square cross section but is questionable for a tube with circular cross section. A numerical method was therefore devised in which the counter was considered to be divided into 20 longitudinal strips. The response of each strip, placed in a 2.71-cm relaxation length field, was then separately evaluated. By this method the center of detection fell at a point only 0.7 cm ahead of the geometrical axis. Results for all three methods are shown in Table 2.13.2. The numerical method seems to be the most physically realistic of the three, and the response of 275 counts·min^{-1}·unit flux^{-1} obtained by its use will be used in practice.

Table 2.13.1. Average Thermal-Neutron Flux at Three Positions in the Thermal Column of the ORNL Graphite Reactor

Distance from Bottom of Thermal Column (cm)	Saturated Activity of Gold Foil (counts/min)	Thermal-Neutron Flux (neutrons·cm^{-2}·sec^{-1})		
		First Method	Second Method	Average
11.2	5.664×10^4	2.07×10^5	2.09×10^5	2.08×10^5
6.2	3.528×10^5	1.28×10^6	1.31×10^6	1.30×10^6
1.2	2.252×10^6	8.19×10^6	8.33×10^6	8.26×10^6

Table 2.13.2. BF_3 Counter Response for Three Assumptions of Center of Detection

Assumed Center of Detection of Counter	Distance of Center Above Bottom of Thermal Column (cm)	Average Flux from Gold Foil Data (neutrons·cm^{-2}·sec^{-1})	Counter Response (cpm per unit flux)
On geometrical axis	32.57	77.5	282
At logarithmic mean of edges	32.2	88.9	246
0.7 cm before geometrical axis*	32.5	79.6	275

*Computed by numerical method described in text.

Calibration in Air

Since the BF_3 counter will often be used in air, an independent calibration was made in a thermal-neutron beam in air. The general method consisted in calibrating the counter against known fluxes determined by comparison of foil activities induced successively by a thermal-neutron beam in air and by the known flux in slot No. 1 of the ORNL Standard Pile.

An 8-ft-long, $7\frac{5}{8}$-in.-ID, $\frac{1}{4}$-in.-thick-walled hollow steel cylinder with closed bottom was placed in the center of the thermal column of the ORNL Graphite Reactor to provide a pure thermal-neutron beam. Four inches of lead was poured in the bottom to reduce the gamma-ray dose to ~15 mr/hr. The device is diagrammed in Fig. 2.13.3. The flux distribution across the beam, measured with indium foils 5 mils thick and either 3.175 cm or 1.11 cm in diameter, is shown in Fig. 2.13.4. It will be noted that the flux is virtually flat to ±1.5% across a central 6-in.-dia zone. Although no significant interaction between foils was expected in such a geometry, the measurements were repeated with 3.175-cm-dia foils spaced 5.08 cm apart. No significant interference effects (> 1%) were noticed.

The measurements with 1.11-cm-dia foils were normalized to the measurements with 3.175-cm-dia foils by multiplying by an experimentally determined factor of 8.97.

The average thermal-neutron flux in slot No. 1 of the ORNL Standard Pile is 1.354×10^4 neutrons·cm^{-2}·sec^{-1}. A 3.175-cm-dia indium foil weighing 0.641 g was exposed in slot No. 1, both bare and within a 30-mil-thick cadmium cover. The saturated activity of the bare foil was 5.94×10^4 counts/min, and that of the cadmium-covered foil was 1.13×10^4 counts/min; thus the activity due to the thermal-neutron flux was 4.81×10^4 counts/min. The ratio of the average thermal-neutron flux to the saturated activity due to thermal neutrons is therefore 1.354/4.81, or 0.2815, for a 3.175-cm-dia indium foil weighing 0.641 g.

UNCLASSIFIED
2-01-058-0-633

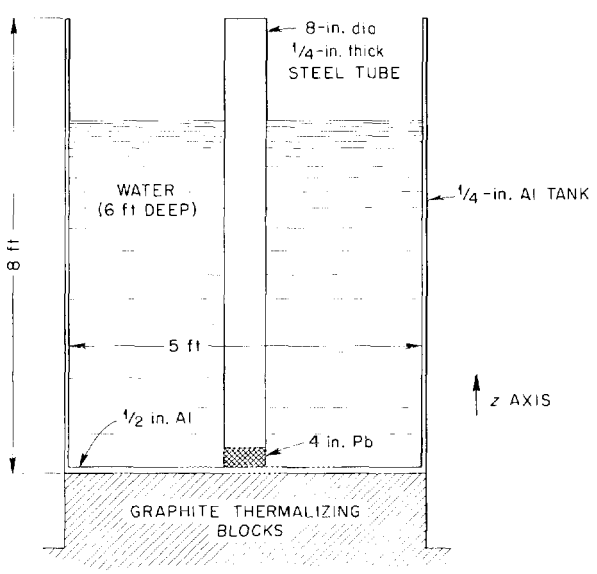

Fig. 2.13.3. Sketch Showing Position of 8-in.-dia Beam Tube in Graphite Reactor Thermal Column.

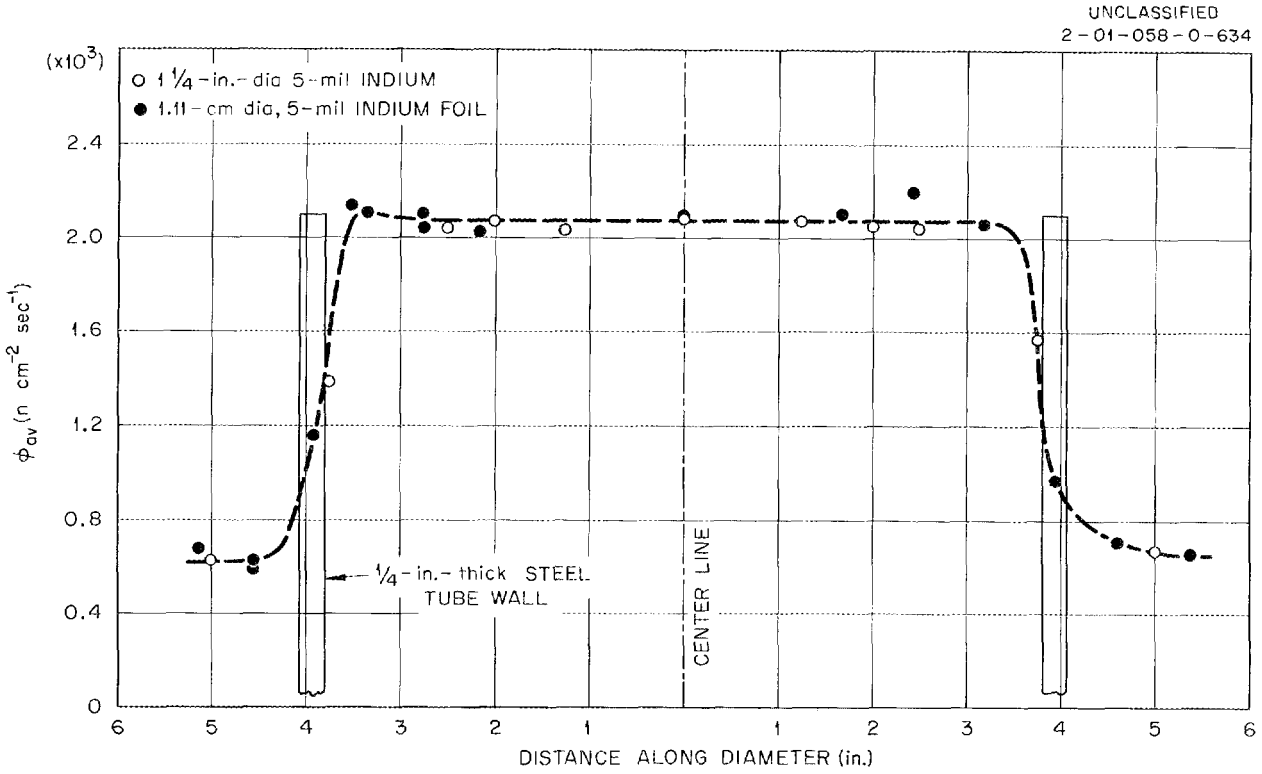

Fig. 2.13.4. Thermal-Neutron Flux Distribution Across Top of 8-in.-dia Beam Tube.

Saturated activities of eight 3.175-cm-dia indium foils placed in the 6-in.-dia central zone of the beam from the steel pipe in the thermal column are listed in Table 2.13.3. The average saturated activity per gram was 11.27×10^3 counts/min. The average thermal-neutron flux over this region then is given by:

$$\bar{\phi} = \frac{(11.27 \times 10^3)\,(0.641)\,(0.2815)\,(0.84)}{f} = \frac{1.71}{f} \text{ neutrons}\cdot\text{cm}^{-2}\cdot\text{sec}^{-1}, \qquad (2)$$

where

0.84 = flux perturbation factor for a 5-mil-thick, 3.175-cm-dia indium foil in graphite,

f = self-protection factor for the foil in beam geometry in air,

and other terms are as identified above. The self-protection factor for an absorbing foil placed in a unidirectional neutron beam is calculated as follows:

Number of neutrons absorbed in thickness element =

$$\phi_0\, e^{-\Sigma_a x}\Sigma_a\, dx\,. \qquad (3)$$

The total number absorbed is the integral of this quantity over the foil thickness:

$$\int_0^t \phi_0\, e^{-\Sigma_a x}\,\Sigma_a\, dx = \bar{\phi}\Sigma_a t\,; \qquad (4)$$

Table 2.13.3. Saturated Activity and Saturated Activity per Gram: Indium Foils in Thermal-Neutron Beam

Foil Weight (g)	Saturated Activity (counts/min)	Specific Activity ($counts \cdot min^{-1} \cdot g^{-1}$)
0.648	7.23×10^3	11.16×10^3
0.642	7.20×10^3	11.21×10^3
0.6333	7.18×10^3	11.35×10^3
0.641	7.13×10^3	11.13×10^3
0.649	7.39×10^3	11.38×10^3
0.641	7.29×10^3	11.37×10^3
0.6333	7.25×10^3	11.45×10^3
0.642	7.11×10^3	11.08×10^3

therefore,

$$\frac{\bar{\phi}}{\phi_0} = \frac{\int_0^t e^{-\Sigma_a x}\,dx}{t} = \frac{1 - e^{-\Sigma_a t}}{\Sigma_a t} \quad . \tag{5}$$

The result of the computation gives a value for the self-protection factor of 0.965 for the indium foils used. The average flux, based on the use of this value in Eq. 2, is thus 1.78×10^3 $neutrons \cdot cm^{-2} \cdot sec^{-1}$.

As a check on this value, the same procedure was carried out with a 3.175-cm-dia, 2-mil-thick gold foil weighing 0.8082 g. The ratio of the average flux to the saturated activity for such a foil in slot No. 1 is quoted as 1.069. The saturated activity per gram for the gold foil was 1.9×10^3 counts/min, giving an average flux seen by the gold of

$$\bar{\phi} = \frac{(1.069)\,(1.9 \times 10^3)\,(0.91)}{f} = \frac{1.85 \times 10^3}{f} \quad . \tag{6}$$

The factor 0.91 is the self-protection factor for the gold foil in graphite. The self-protection factor for the gold foil in the beam was computed according to Eq. 5 to be 0.986. Based on the gold measurement, therefore, $\bar{\phi} = 1.88 \times 10^3$ $neutrons \cdot cm^{-2} \cdot sec^{-1}$.

The average of the gold foil and indium foil determinations is 1.83×10^3 $neutrons \cdot cm^{-2} \cdot sec^{-1}$, which was adopted as the value of the thermal-neutron flux emitted by the thermal column beam tube.

Two methods were used to evaluate the total BF_3 counter response to the thermal column beam. The first is diagrammed in Fig. 2.13.5. The bare counter was placed over the beam and gave a total count rate of 564,300 counts/min.

The area under the flux distribution curve of Fig. 2.13.4, by Simpson's Rule, is 96.4 units over an effective counter length of 9.75 in. The average value of the saturated activity then is 96.4/9.75 = 9.89 counts/min, and the maximum value is 11.3 counts/min. The ratio of maximum to average is 11.3/9.88 = 1.145, meaning that the counter, if placed in a uniform flux equal to that over the flat 6-in. zone, would

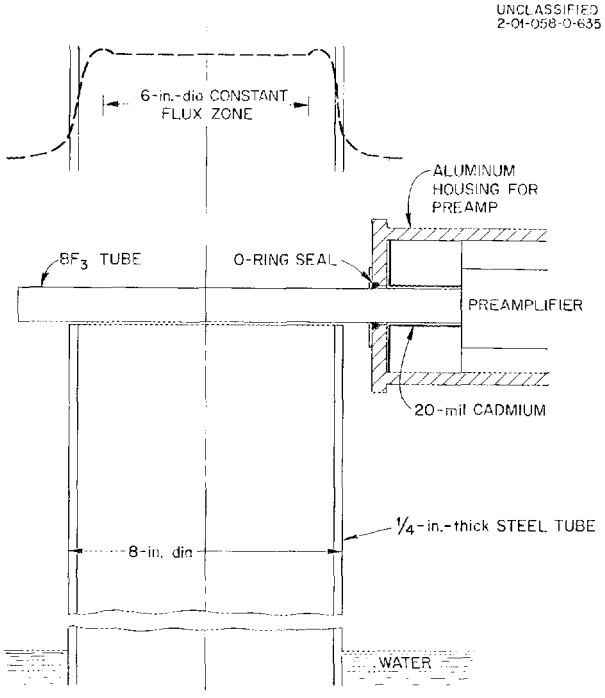

Fig. 2.13.5. Placement of BF_3 Counter with Respect to Beam Tube.

give 1.144 times the number of counts as when placed as shown in Fig. 2.13.5. Therefore the count rate in a uniform flux would have been $5.64 \times 10^5 \times 1.144$, or 6.45×10^5 counts/min.

The second method used to determine the BF_3 counter response to the thermal-neutron beam consisted in dividing the tube into zones by using 40-mil-thick cadmium covers to shield all but a single zone, and placing each zone in turn over the flat portion of the beam. The summed response of all zones was 6.56×10^5 counts/min.

The average of the responses obtained by the methods above is 6.5×10^5 counts/min, and, dividing this by the value of the thermal-neutron flux noted above, the counter response is 355 counts/min per unit average flux.

Conclusions

In air, then, the BF_3 counter response is 355 counts/min per unit flux, while in water it is 275 counts/min per unit flux. The difference may be attributed to the differences in flux perturbations produced by the counter in air and water. When used in air, there is only self-shielding of the sensitive volume, but in water two additional effects show up – buildup of flux, due to displacement of water by the body of the counter, and flux depression in the neighborhood of a BF_3 absorber. Since the latter two effects tend to cancel, the net perturbation in water is only about 30% larger than that in air.

2.14. DEVELOPMENT OF A LOW-LEVEL GAMMA-RAY DOSIMETER USING AN ANTHRACENE CRYSTAL

T. Mustafa[1] and T. V. Blosser

A projected study of the radiation leakage through the biological shield of the N.S. Savannah entails the measurement of total dose rates as low as 0.5 rem/yr (about 0.06 mrem/hr for continuous exposure) from all radiation sources, i.e., gamma rays and fast and slow neutrons. The usual methods of measurement are not suitable for such an application. For example, W. J. Ramm[2] notes that the integrated current ouput method, often used, is capable of dose measurements only to a minimum of 1 mrem/hr with a 1-g anthracene crystal.

A dosimeter has therefore been developed which utilizes an anthracene crystal in conjunction with a special pulse-counting technique. With this combination it appears to be possible to measure tissue dose rates as low as 0.02–0.03 mrad/hr, to observe gamma rays of energies as low as 100 kev, and, in addition, to obtain a good idea of the energy spectrum of radiation striking the detector.

Theory and Principles

If a plot is made of the integral count rate as a function of energy (or pulse height) of the gamma rays impinging on a detector, then the area under the resulting curve will be a measure of the tissue dose rate at the detector, provided that the response of the detector relative to tissue is sensibly constant over the range of energies involved. Carr and Hine[3] have shown that dosage measurements with anthracene crystals show a tissue equivalence for gamma rays from 0.2 to 3.0 Mev. From the plot of the first-collision dose rate as a function of energy shown in Fig. 2.14.1 for tissue and anthracene, it can be seen that the response of anthracene is theoretically tissue equivalent within ±1% from 100 kev to at least 7.0 Mev, provided electron balance can be assured. The present solution to the problem of electron balance is discussed below.

The difficulty inherent in the measuring scheme outlined lies in the fact that for each point where a dose measurement is desired a gamma-ray spectrum must be plotted. This is not necessary, of course, if dose measurements are to be made in a gamma-ray field such that the energy spectrum does not vary appreciably. Under these circumstances the count rate at a fixed energy bias can be related to the area under the spectrum, which in turn is a measure of the dose rate. In the present application, however, the spectrum may not remain constant, since the shield may be penetrated by beam tubes, loops, cooling circuits, etc., may have configuration changes, or may be inhomogeneous.

The pulse-counting method has been made applicable, however, by the development of a small, transistorized integrator,[4] having the equivalent of 80 input channels, which can be mounted within a standard

---

[1] Present Address: c/o Third Secretary, Embassy of Pakistan, Washington, D.C.

[2] *Radiation Dosimetry*, ed. by G. J. Hine and G. L. Brownell, Academic Press, New York, 1956.

[3] R. T. Carr and G. J. Hine, *Nucleonics* **11**, 53 (1953).

[4] Designed by P. T. Perdue, Instrumentation and Controls Division. ~~The integrator has been made the subject of an ORNL Patent Disclosure and will be described in detail in a forthcoming report.~~

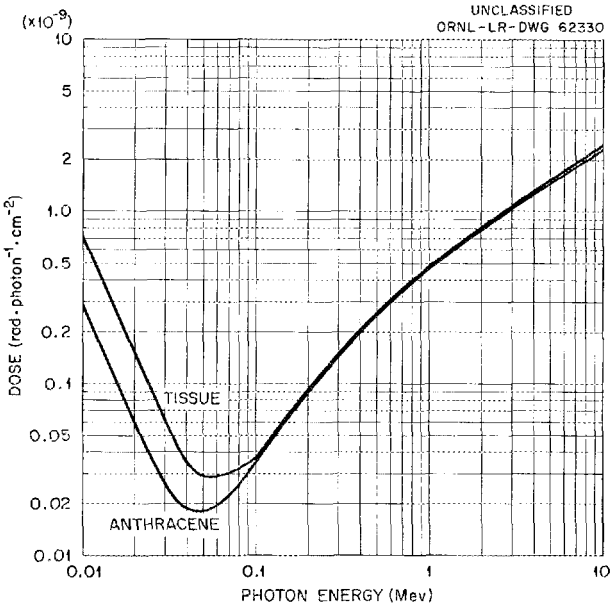

Fig. 2.14.1. First-Collision Dose Rates in Tissue and Anthracene as Functions of Photon Energy.

A1D amplifier and whose response is linear to within ±5% over the entire pulse-height range of interest. The design of the integrator is such that rather high gamma-ray fields can be measured without significant counting losses, the maximum dose rate presently measurable being about 100 mr/hr.

The first-collision dose-rate values for tissue plotted in Fig. 2.14.1 are taken from Appendix 1 of the draft report on "Measurements of Absorbed Dose of Neutrons and of Mixtures of Neutrons and Gamma Rays," by Task Group M-3(1) of the National Bureau of Standards. The anthracene data are based upon the following development.

The first-collision gamma-ray dose, $D_f(E)$, can be written as

$$D_f(E) = 1.602 \times 10^{-8} \left[\sum_i \sigma_i N_i \epsilon_C + \sum_i \tau_i N_i \epsilon_{PE} + \sum_i \kappa_i N_i \epsilon_{PP} \right] , \qquad (1)$$

where σ_i, τ_i, and κ_i are respectively Compton scattering, photoelectric, and pair-production cross sections per atom, N_i is the number of atoms per gram of ith species, and ϵ_C, ϵ_{PE}, ϵ_{PP} is the average energy transferred to the electron undergoing Compton scattering, a photoelectric process, or pair production, respectively. By substituting

$$\sigma_m = \sigma_i N_i (\sigma_a/\sigma_t) , \qquad \tau_m = \tau_i N_i , \qquad \kappa_m = \kappa_i N_i \left(1 - \frac{1.022}{E_\gamma} \right) ,$$

and

$$\mu_m = \sigma_m + \tau_m + \kappa_m ,$$

Eq. 1 reduces to

$$D_f(E) = 1.602 \times 10^{-8} E_\gamma \sum_i \mu_{m_i} .$$

The computed values are tabulated for reference in Table 2.14.1.

Table 2.14.1. First-Collision Dose Rate Values for Tissue and for Anthracene

Photon Energy (Mev)	Dose Rate (rad·photon^{-1}·cm^{-2}·10^{9})		Ratio of Tissue Dose to Anthracene Dose
	Tissue	Anthracene	
0.01	0.702	0.294	2.39
0.02	0.150	0.0614	2.44
0.03	0.063	0.0264	2.39
0.05	0.029	0.0181	1.60
0.07	0.031	0.0231	1.34
0.10	0.038	0.0363	1.047
0.20	0.094	0.0910	1.032
0.30	0.151	0.146	1.034
0.50	0.260	0.251	1.036
0.70	0.357	0.345	1.034
1.0	0.488	0.472	1.034
2.0	0.816	0.791	1.032
3.0	1.07	1.033	1.036
5.0	1.49	1.425	1.046
7.0	1.89	1.793	1.054
10.0	2.43	2.276	1.067

Construction of the Dosimeter

The detecting element consists of a 1-in.-dia, ½-in.-thick anthracene crystal, wrapped in aluminum-coated Mylar reflecting foil 200 $\mu g/cm^2$ thick, in a 3-mm-thick Lucite case and light piper in contact with the cathode of a low-dark-current type RCA 6655 photomultiplier tube. A light-tight, 5-mil-thick aluminum jacket protects the crystal. The entire arrangement is shown in Fig. 2.14.2.

The 3-mm-thick Lucite cover serves to balance the loss in light yield which would result from energetic photoelectrons and Compton electrons leaking out of the anthracene crystal without losing all of their energy in producing the scintillation. The Lucite serves to scatter a portion of the leaking electrons back into the crystal. Since an electron needs to possess an energy greater than 1.4 Mev to penetrate 3 mm of Lucite and 5 mils of aluminum, the balance is complete and the electron loss is fully compensated for at 1.4 Mev, which is the average energy of recoil electrons resulting from 2.6-Mev gamma rays. Electron balance at higher energies could have been accomplished by increasing the thickness of the Lucite case. Such a measure, however, would attenuate low-energy gamma rays excessively and thus

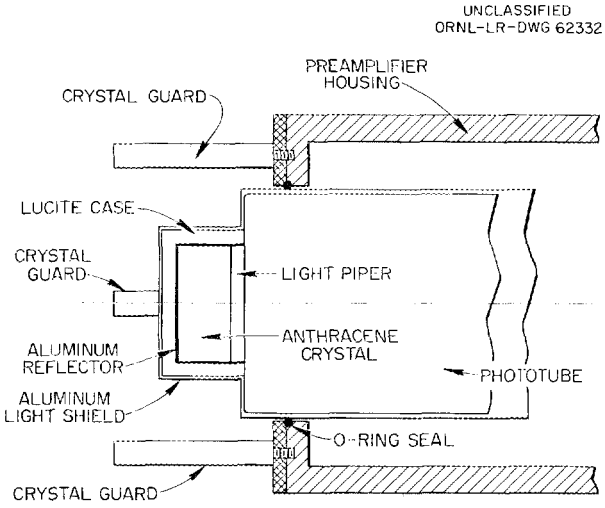

Fig. 2.14.2. Arrangement of the Anthracene Crystal.

misweight the dose rate. The 3-mm thickness is considered a good compromise. Taking into account the thickness of the anthracene crystal, it is estimated that ~30% of the energy of a 6-Mev gamma ray will be lost by leakage.

Calibrations

The initial calibration of the dosimeter was carried out by using known-strength gamma-ray sources of various energies, such as Hg^{203}, Au^{198}, Cs^{137}, Co^{60}, Y^{88}, Na^{24}, and Ra, both singly and in various combinations to give continuous spectra of up to 2.76 Mev. Care was taken to prevent any scattered component from reaching the detector by positioning it at least 8 ft away from the nearest wall, floor, or ceiling. Gamma-ray source strengths were measured to ±3% with a gas ionization chamber which had been previously compared with the calibrated gas ionization chamber of the National Bureau of Standards.

Two quantities were obtained from the exposure of the detector to these sources. The first was the pulse height corresponding to the photopeak. Figure 2.14.3 plots the pulse height corresponding to the photopeak against maximum energy of the recoil electrons. The excellent linearity of the curve shows that over this energy range, at least, the height of the pulse in anthracene is directly proportional to the electron energy. The second quantity of interest, the pulse-height spectrum, was obtained for all of the sources and the area under the integral count rate versus pulse-height curve was obtained by numerical integration. With the source strength and the distance from the source to crystal known, the dose rate can be computed from the relation

$$D = kCE\left(\frac{100}{d}\right)^2 , \tag{2}$$

where

k = dose rate, mrad/hr, at 1 m from a 1-millicurie source,

C = source strength, millicuries,

d = center-to-center source-detector distance, cm,

D = dose rate, mrad/hr.

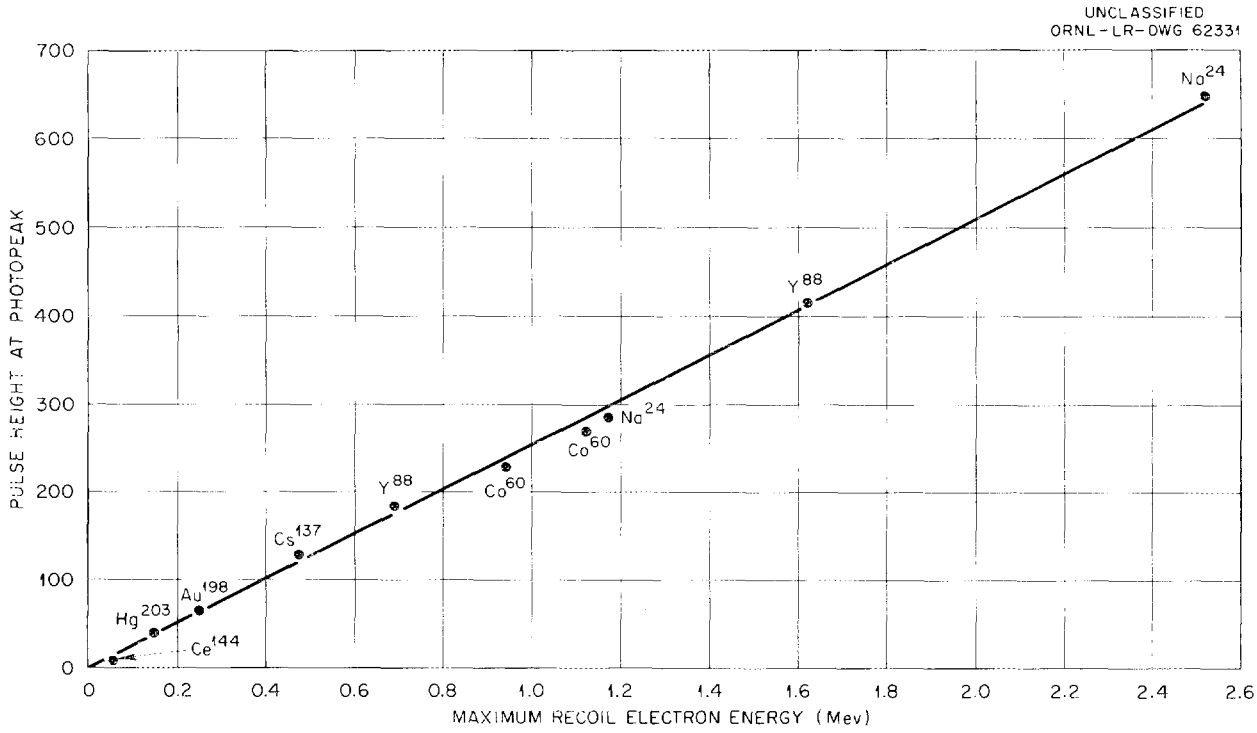

Fig. 2.14.3. Pulse Height at Photopeak as a Function of Maximum Recoil Energy.

Dose rates computed in the above fashion were calculated for each of the sources, and the ratio of dose rate from a particular source to the area under the corresponding pulse-height spectrum was calculated. These data are shown in Table 2.14.2, in which the values are the averages of several runs. It can be seen that with the exception of Hg^{203} all sources give a figure for the dose per unit area which is independent of source energy to within ±5%. The behavior of Hg^{203} is not unexpected, since an appreciable proportion of its dose comes from pulses which are not energetic enough to overcome the discriminator bias, which was set at a pulse-height setting of 10 (1 volt), corresponding to an energy bias of ~50 kev. Below this level the A1D amplifier used is not quite linear and there is also possibility of noise pickup. From the data of Table 2.14.2 the dose in tissue, in mrad/hr, can be expressed as $5.1 \times 10^{-7} A$, where A is the area under a curve of integral counts per minute as a function of pulse-height settings such that the maximum pulse-height dial setting is taken as 1000.

Calibration of the dosimeter and associated electronics is made during operation by means of a Cs^{137} source, which is mounted in an aluminum cap snugly fitting over the crystal housing, thus giving readily reproducible geometry.

The 661-kev photopeak of Cs^{137} is made to correspond to a pulse-height setting of 130, which gives a sensibly linear energy range for the amplifier from ~50 kev to 5 Mev. A pulse larger than 5 Mev then appears to the amplifier just like a 5-Mev pulse with a flat top. In calibrating, counts are taken at pulse-height settings of 130 and 10, respectively, and the A1D amplifier gain is adjusted to bring the counts

Table 2.14.2. Ratio of Computed Dose Rate from Various Gamma-Ray Sources to Area Under Observed Pulse-Height Spectra

Source	Energy (Mev)	Ratio: Dose/Area
Hg^{203}	0.279	6.94×10^{-7}*
Au^{198}	0.412	5.24×10^{-7}
Cs^{137}	0.662	5.30×10^{-7}
Ra	Av. ~1.0	5.04×10^{-7}
Co^{60}	1.17 1.33	4.94×10^{-7}
Na^{24}	1.38 2.76	5.00×10^{-7}
Average		5.1×10^{-7}

*Excluded from average.

into agreement with previously established values. Calibration at two settings not only adjusts the overall gain of the system but insures the linearity of the amplifier, i.e., that the energy bias is directly proportional to the pulse-height setting.

Neutron Sensitivity

A Po-Be neutron source was used to check the response of the dosimeter to fast neutrons. At a distance of 1 m from a Po-Be source of 1.4×10^6 neutrons/sec, the response was equivalent to 0.056 mr/hr, after due allowance had been made for the gamma radiation from Po^{210}. Marion and Fowler[5] give 2 mr/hr as the dose rate to be expected 1 m from a source of 10^6 neutrons/sec, thus the sensitivity of the dosimeter to Po-Be neutrons is only about 2%.

Conclusions

After taking into account all of the uncertainties due variously to the tissue equivalence of anthracene, the electron balance of the detector, and the uncertainties involved in calibration procedures, it is believed that the gamma-ray dosimeter described can readily measure first-collision dose rate in tissue to within ±20% for a more or less continuous gamma-ray spectrum ranging from about 100 kev to 5 Mev, for doses as low as 0.03 mrad/hr in a field of mixed radiation.

It is planned to further check the behavior of the dosimeter against the 6- to 7-Mev N^{16} gamma-ray source provided by coolant water activation in the Bulk Shielding Facility Pool, and also to examine more closely the energy region below 100 kev by means of an x-ray machine.

[5] *Fast Neutron Physics, Part I: Techniques*, ed. by J. B. Marion and J. L. Fowler, Interscience, New York, 1960.

2.15. FAST-NEUTRON SPECTROSCOPY WITH SILICON SURFACE-BARRIER COUNTERS

T. A. Love and K. M. Henry

The possible use of a neutron-sensitive semiconductor detector for neutron spectroscopy has been discussed previously.[1,2] Basically, the detector consists of a thin layer of Li^6F between two silicon-gold surface-barrier counters, the neutrons being detected by observing the $\alpha + T$ pair resulting from the $Li^6(n, \alpha)T$ reaction. The routing of the signal from each detector is shown by the block diagram of the counter and the associated electronics depicted in Fig. 2.15.1. The signal is first fed into a preamplifier which in turn feeds a DD-2 double delay line amplifier[3] with a 0.7-μsec clipping time. The output of the amplifier is fed into a discriminator circuit biased to reject all pulses which represent less than some predetermined energy deposition in the diode (~1.5 Mev in the experiment discussed here). The coincidence circuit rejects all pulses which are separated in time by more than $\sim 10^{-7}$ sec.

UNCLASSIFIED
ORNL-LR-DWG 57795R

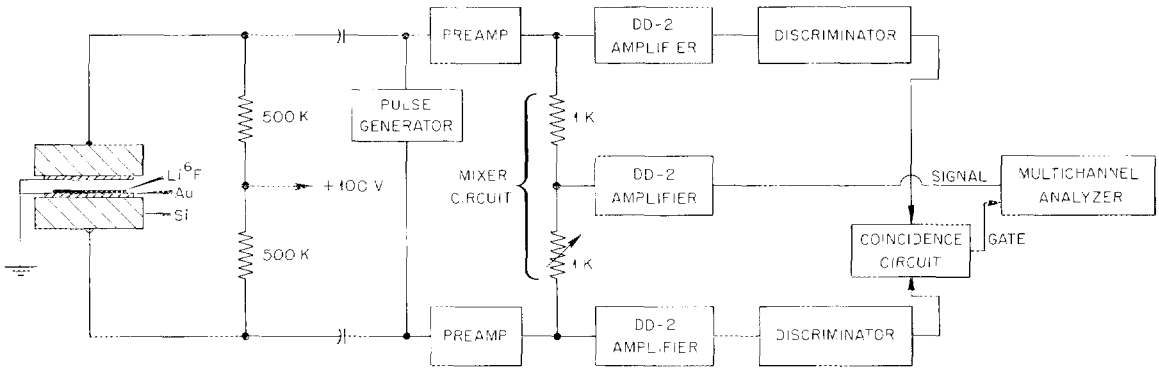

Fig. 2.15.1. Block Diagram of Electronic System for Silicon-Gold Semiconductor Detector.

Since the accuracy of the measurement of a spectrum of fast neutrons always depends to a large extent on whether the gamma-ray- and neutron-induced backgrounds can be subtracted, recent experiments with the detector have been directed toward the understanding of the backgrounds. The gamma-ray-induced background apparently causes little difficulty. The gamma-ray counts are essentially all rejected by the discriminator circuit, since the probability that a gamma ray will produce an electron which will give up at least enough of its energy in one of the counters to trigger the counter discriminator is fairly small, and the probability that the same electron will appear in the other counter with enough energy to trigger

[1] T. A. Love, R. B. Murray, J. J. Manning, and H. A. Todd, *Neutron Phys. Ann. Prog. Rep. Sept. 1, 1960*, ORNL-3016, p. 280.

[2] T. A. Love and R. B. Murray, *IRE Trans. Nuclear Sci.* 8 (1), 91 (1961).

[3] Edward Fairstein, *Rev. Sci. Instr.* 27 (7), 475 (1956).

its discriminator is extremely small. Thus only in very high gamma-ray fields where counts pile up and where the chance rate is high will any gamma-ray background appear. Measurements have been made in gamma-ray fields up to ~200 r with no appreciable background and only small degradation in resolution.

The neutron-induced background is important when the counter is used in a neutron flux where neutrons of energy above a few Mev are present. Whenever neutrons strike one of the counters several reactions may occur which result in the emission of charged particles provided the threshold energy of the reaction is equalled or exceeded by the energy of the incoming neutron. Since the total mass of these counters is composed almost entirely of silicon, essentially all the reactions are of the Si (n, charged particle) type where in every case the reaction is endothermic. For the reaction to produce a background count, however, the energy of the incoming neutron must not only exceed the threshold of the reaction but also impart enough energy to the charged particle to allow sufficient energy deposition in each counter to trigger the discriminator circuits. Thus only neutrons of energy equal to or greater than about 3 Mev plus the threshold energy of the reaction can produce a count. From experiments with these diodes exposed to monoenergetic neutrons where background is clearly defined, a calculation indicates a foreground to background ratio which would be observed in a pulse-height spectrum from fission neutrons. This ratio is about 5:1.

The magnitude of the neutron-induced background has been further investigated by comparing the response of a pair of Li^6F-coated counters to 14.7-Mev neutrons with the response of a pair of uncoated counters. The sensitive area of each counter was ~2 cm^2, and the thickness of Li^6F on the coated pair was ~200 $\mu g/cm^2$.

A pulse generator was used as a reference in order to adjust the gain of the uncoated pair to be the same as the coated pair. A first attempt was made by simply adjusting the electronic gain of the system to give equal pulse-height output for equal charge deposited in each diode. This approach failed because these simple gain adjustments do not take into account the difference in resistivity of the individual diodes. The capacity, C, of the diodes, and in turn the barrier depth, depend on the resistivity according to the equation $C \approx 1/\sqrt{V\rho}$, where V is the bias voltage across the diode and ρ is the resistivity. Clearly, the uncoated diodes must have the same barrier depth, as well as area, if the background measurements are to be meaningful. Thus, a change in voltage is necessary to compensate for the difference in resistivity of the two diodes; in fact, if the individual diodes differ by only a small amount, then gain adjustments (using the pulse generator as a reference) made by varying the bias voltage is all that is necessary.

A comparison of the pulse-height spectra obtained when the coated and uncoated counters were exposed to 14.7-Mev neutrons is shown in Fig. 2.15.2.

In addition to the background measurements, the efficiency of the sandwich-type counters has been investigated. A pair of coated diodes with dimensions the same as those given above was exposed in the ORNL Graphite Thermal Column, and the number of counts under the thermal peak was compared to those from a gold foil exposed the same length of time. This comparison yielded an efficiency of the counter for thermal neutrons of 3×10^{-3}. The calculated efficiency differed by ~15%.

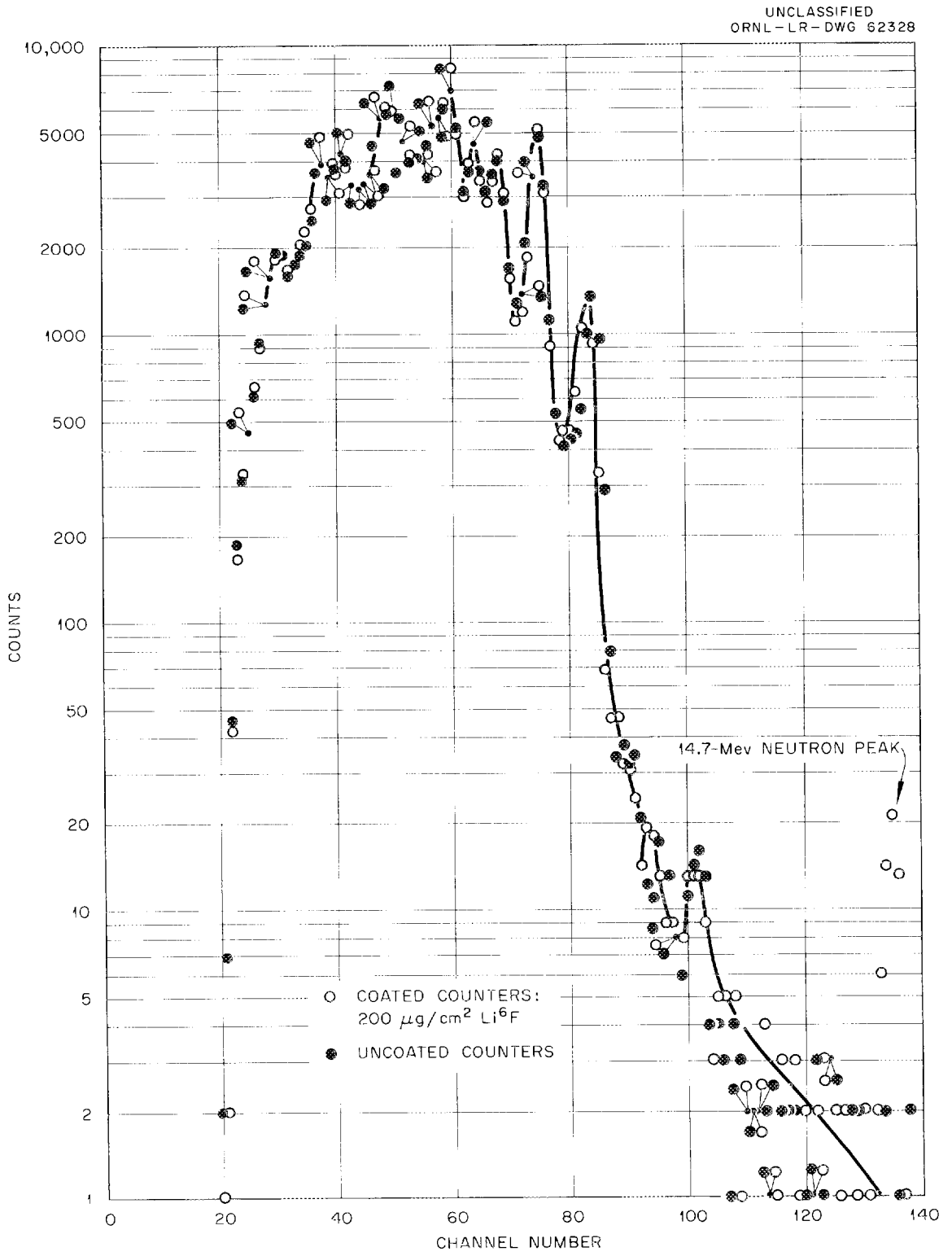

Fig. 2.15.2. Pulse-Height Spectra of Li^6F-Coated and Uncoated Silicon-Gold Semiconductor Detectors.

The efficiency of the diodes was also investigated with 14.7-Mev neutrons, and it was observed that when the plane of Li^6F on the diodes was parallel to the incoming beam, the efficiency was almost twice that realized when the plane of Li^6F was normal to the beam. Thus earlier estimates of losses due to the forward scattering of the alpha particle and the triton are too small.*

From the above measurements it is concluded that neutron spectra may be measured with silicon counters provided proper care is exercised in obtaining the background. Tests for adequacy of the method described above for obtaining backgrounds will be made for monoenergetic neutrons other than 14.7-Mev energy. It is also planned to use the method to determine the spectrum of neutrons leaking from a reactor.

*Attempts have been made to increase the efficiency of the counters by substituting Li^6 metal for Li^6F, but they have been unsucessful thus far because of the high reactivity of the lithium.

2.16. THE DISTRIBUTION IN ENERGY OF ALPHA-TRITON PAIRS RESULTING FROM NEUTRON BOMBARDMENT OF LITHIUM FLUORIDE

F. S. Alsmiller

The use of paired silicon-gold surface barrier counters (with an intervening Li^6F layer) to record the sum of the energies, W, of the triton and alpha particles produced in a $Li^6(n,\alpha)T$ reaction, as a measure of the incident neutron energy, has been described elsewhere.[1]

In this report we consider the problem of calculating the distribution in total energy, $N(W)$, of the pairs reaching the silicon. The analysis has been generalized from that given previously[2] in two respects: first, the neutrons are not restricted to normal incidence, and second, the variation of the stopping power with energy over the path length of each particle is taken into account.

A uniform beam of neutrons of energy E_n is assumed to impinge on a Si-Au-Li^6F-Au-Si sandwich at an arbitrary angle of incidence, ν, with respect with the z axis, which is taken as normal to the plane of the sandwich. The (n,α) reaction takes place at some point z $(0 \leq z \leq T)$ in the LiF layer of thickness T. In the laboratory system, the angles of emergence of the triton relative to the incident neutron velocity vector, $\vec{v}_n$, and to the z-axis are ψ and η, respectively. Similarly, the alpha particle angles relative to $\vec{v}_n$ and to the *negative* z axis are χ and ζ, respectively. Figure 2.16.1 depicts the geometry of the problem.

The particles are assumed to travel in straight-line paths in their initial directions with a continuous rate of energy loss, $-dE/dr = S(E)$. (Subscripts t or α will be used to denote tritons or alpha particles and L or A the stopping materials, LiF or Au.)

[1] T. A. Love, *et al.*, *Neutron Phys. Ann. Prog. Rep., Sept. 1, 1960*, ORNL-3016, p. 280; also, Section 2.15, this report.

[2] F. S. Alsmiller, *Neutron Phys. Ann. Prog. Rep., Sept. 1, 1960*, ORNL-3016, p. 289.

UNCLASSIFIED
2-01-059-644

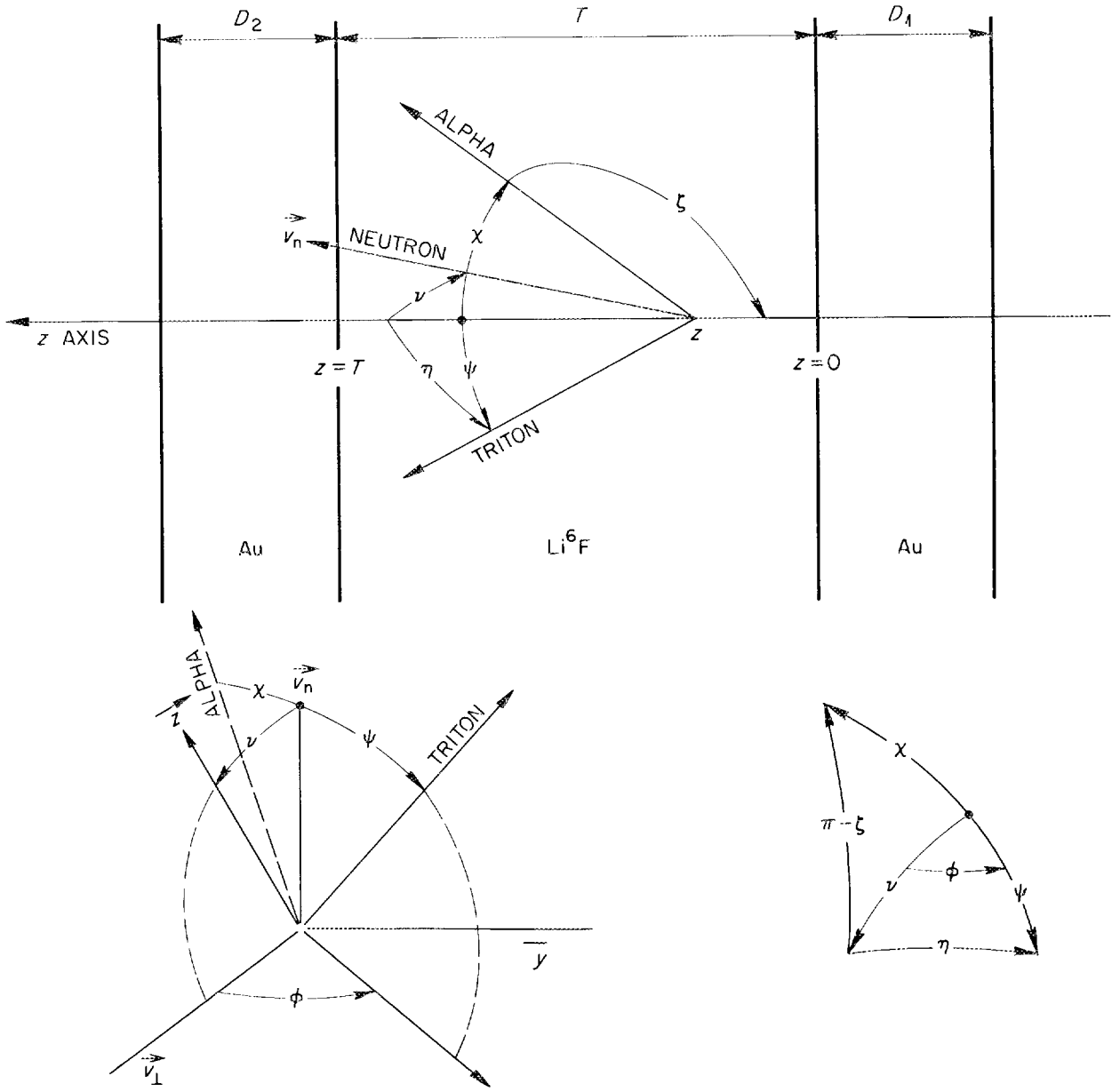

Fig. 2.16.1. Geometry for Calculation of Energy Distribution of Alpha-Triton Pairs Resulting from $Li^6(n,\alpha)T$ Reactions.

The total energy available, E_n plus the reaction Q-value, and the triton scattering angle θ, in the center-of-mass system, determine the angles ψ and χ as well as the initial energies $E_{\alpha_0}(\psi)$ and $E_{t_0}(\psi)$ of the alpha particle and triton.

If

$$x = \left[\frac{M_n M_t}{M_\alpha(M_\alpha + M_T - M_n)}\right]^{1/2} \left[1 + \frac{M_\alpha + M_t}{M_t + M_\alpha - M_n} \quad \frac{Q}{E_n}\right]^{-1/2}, \tag{1}$$

where M_i is the mass of the particular particle or atom denoted by the subscript,

then

$$\frac{\sin(\theta - \psi)}{\sin\psi} = x; \qquad 0 \leq \theta \leq \pi; \qquad 0 \leq \psi \leq \pi, \tag{2}$$

$$\frac{\sin(\theta + \chi)}{\sin\chi} = x; \qquad 0 \leq \chi \leq \pi. \tag{3}$$

Let

$$R = \cos\psi + \frac{\cos(\theta - \psi)}{x}; \tag{4}$$

then

$$E_{t_0}(\psi) = \frac{M_n M_t E_n R^2}{(M_n + M_L)(M_\alpha + M_t)}, \tag{5}$$

$$E_{\alpha_0}(\psi) = E_n + Q - E_{t_0}. \tag{6}$$

The angles ν, ψ, and χ, plus the triton azimuthal angle, ϕ, about $\vec{v}_n$ (in either center-of-mass or laboratory systems) determine the angles η and ζ. These, in turn, with z, T, D_1, and D_2 (the thicknesses of the two gold layers) determine the path lengths traveled in each medium and hence the total energy loss

$$\Delta W = E_n + Q - W, \tag{7}$$

where W is the total energy of the alpha-triton pair when each particle has reached a (different) silicon layer. From Fig. 2.16.1, it is clear that

$$\cos\eta = \cos\nu\cos\chi + \sin\nu\sin\psi\cos\phi, \tag{8}$$

$$\cos\zeta = -\cos\nu\cos\chi + \sin\nu + \sin\chi\cos\phi. \tag{9}$$

The energies of the alpha-triton pair are not recorded unless one particle reaches each silicon layer. Hence, we consider only the two cases:

$$\text{(A)} \qquad 0 \leq \eta \leq \frac{\pi}{2}; \qquad 0 \leq \zeta \leq \frac{\pi}{2}$$

$$\text{(B)} \qquad \frac{\pi}{2} \leq \eta \leq \pi \,; \qquad \frac{\pi}{2} \leq \zeta \leq \pi \,.$$

If X_{t_L}, X_{t_A}, X_{α_L}, and X_{α_A} represent the path lengths of the triton and alpha particle in the LiF and Au media, respectively, the equations for the path lengths are:

	A	B	
	$0 \leq \eta \leq \frac{\pi}{2}$	$\frac{\pi}{2} \leq \eta \leq \pi$	
	$0 \leq \zeta \leq \frac{\pi}{2}$	$\frac{\pi}{2} \leq \zeta \leq \pi$	
$X_{t_L} = \int_{E_{t_I}}^{E_{t_0}(\psi)} \frac{dE}{S_{t_L}(E)}$	$= \frac{T - z}{\cos \eta}$	$= \frac{z}{\lvert \cos \eta \rvert}$	(10)
$X_{t_A} = \int_{E_{t_F}}^{E_{t_I}} \frac{dE}{S_{t_A}(E)}$	$= \frac{D_2}{\cos \eta}$	$= \frac{D_1}{\lvert \cos \eta \rvert}$	(11)
$X_{\alpha_L} = \int_{E_{\alpha_I}}^{E_{\alpha_0}(\psi)} \frac{dE}{S_{\alpha_L}(E)}$	$= \frac{z}{\cos \zeta}$	$= \frac{T - z}{\lvert \cos \zeta \rvert}$	(12)
$X_{\alpha_A} = \int_{W - E_{t_F}}^{E_{\alpha_I}} \frac{dE}{S_{\alpha_A}(E)}$	$= \frac{D_1}{\cos \zeta}$	$= \frac{D_2}{\lvert \cos \zeta \rvert}$	(13)

Here E_{t_I} and E_{α_I} are the intermediate triton and alpha-particle energies upon reaching a gold layer, E_{t_F} is the final triton energy when the triton reaches a silicon layer, and $W - E_{t_F}$ is the final alpha-particle energy.

For a given θ, ϕ, and ν (or ψ, ϕ, and ν), Eqs. 10–13, together with Eqs. 1–9, determine an implicit relation between z and W. Differentiation yields

$$\left.\frac{\partial z}{\partial W}\right)_{\theta, \phi} = \frac{-\cos \eta}{\dfrac{S_{\alpha_L}\left(E_{\alpha_I}\right)}{S_{\alpha_A}\left(E_{\alpha_I}\right)} \dfrac{S_{\alpha_A}\left(W - E_{t_F}\right) \cos \eta}{\cos \zeta} - \dfrac{S_{t_L}\left(E_{t_L}\right) S_{t_A}\left(E_{t_F}\right)}{S_{t_A}\left(E_{t_I}\right)}} \,, \tag{14}$$

which holds when η and ζ are in the same quadrant, i.e., for cases A and B.

The energies E_{α_I}, E_{t_I}, and E_{t_F} (as well as z) are obtained by numerical solution of Eq. 14 for a fixed final energy W and fixed angles θ, ϕ, and ν.

If $\sigma_{CM}(\theta)$ denotes the differential cross section for the $Li^6(n,\alpha)T$ reaction, then

$$\frac{\sigma_{CM}(\theta)}{\sigma_{\text{total}}} \quad d\Omega_{CM} \quad \frac{|dz|}{T}$$

is the probable fraction of alpha-triton pairs which are born in the differential distance interval $|dz|$ and the triton solid angle element $d\Omega_{CM}$. The distribution $N(W)$ $[= N(\Delta W, E_n, \nu)]$ is the probability that a pair will be detected at energy W, per unit energy range, and is given by

$$N(W) = \frac{1}{T}\iint d\Omega_{CM} \frac{\sigma_{CM}(\theta)}{\sigma_{\text{total}}} \left| \left(\frac{\partial z}{\partial W}\right)_{\theta,\phi} \right| H(\theta,\phi) \ , \tag{15}$$

where $H(\theta,\phi)$ is a step function which equals unity when the conditions listed below are satisfied and zero otherwise:

(1) ζ and η are in the same quadrant, i.e., $\cos\zeta \cos\eta \geq 0$.

(2) $0 \leq z \leq T$

(3) $E_{t_F} \geq B$

(4) $W - E_{t_F} \geq B$

(5) $\Delta W \leq E_n + Q - 2B$

Conditions 3–5 reflect the fact that the counter will not record either particle unless its energy upon reaching a silicon layer is at least B (= 1.6 Mev, tentatively).

Numerical computations of $N(W)$ for a range of neutron energies, E_n, and angles of incidence, ν, are in progress.

2.17. DETERMINATION OF SELF-SHIELDING FACTOR BY USING MULTIPLY STACKED FOILS

S. A. Hasnain,[1] T. Mustafa,[2] and T. V. Blosser

A fundamental difficulty inherent in the widespread use of thin foils of indium, gold, and other elements to measure neutron fluxes lies in the lack of exact knowledge of the effects of the foil upon the flux it is measuring. One of these effects, the tendency for each successive layer of the material to shield the layer directly beneath, has been studied in the present work.

---

[1]Present address: Pakistan Atomic Energy Commission, Karachi, Pakistan.

[2]Present address: c/o Third Secretary, Embassy of Pakistan, Washington, D.C.

If several thin foils, all of the same diameter and preferably of the same weight are stacked together leaving no air spaces, the multiple foil stack behaves as a single foil. After an exposure to neutrons the foils may be separated and their activities individually counted. The specific activity of a foil, as a function of its position in the stack, gives a measure of the variation of the neutron density axially inside the stack. From the space variation of specific activity throughout a thick foil, it should be possible to deduce the neutron self-shielding factor. The shape of the curve of specific activity as a function of position should be useful in checking theories of neutron penetration, spectral hardening, etc., in thin foils.[3]

A number of stacks of gold and indium foils have been exposed in the thermal column of the ORNL Graphite Reactor. Although the interpretation of the results to produce numbers applicable to theory has not yet been completed, the raw data is presented for information.

Measurements were made in both water and air media. All water data were taken in a single configuration in which the foils were supported in a horizontal plane about 8 cm from the bottom of the thermal column by a simple Lucite frame.

A variety of arrangements was used to obtain the air data. For convenience they are designated as A, B, C, and D. In configuration A, the foil stacks were held in a horizontal plane about 30 cm from the bottom of an 8-in.-ID aluminum pipe placed in the thermal column.[4]

In configuration B, a monodirectional beam was approximated by using a two-piece cadmium-lined assembly. Each piece consisted of a 15-cm-long, 2.5-cm-ID aluminum tube, lined with cadmium sheet to leave a 2.25-cm-dia air column. The two tubes were placed end to end, with the foil stack between. The edges of the foils were protected from neutrons by cadmium. Ends of the composite were capped, the bottom end with aluminum, the top with cadmium-lined aluminum. When this assembly was lowered vertically into the thermal column, the foils at the middle were exposed to a beam of thermal neutrons which had traversed the 15-cm-long air column of the lower tube.

Configuration C consisted of a long (~ 10-ft) aluminum tube with closed lower end, inserted vertically in the thermal column. The lower 50 cm of the tube was lined with cadmium so as to leave a 5-cm-dia air space. The foils were placed about 25 cm from the bottom of the tube.

Configuration D was identical with A, but for these data the foils were mounted on a Mylar film, which was slowly rotated about a horizontal axis by a motor to approximate an isotropic geometry.

The saturated activity of all foils was measured by counting the induced gamma-ray activity on the two-crystal counter described by Blosser.[5]

Tables 2.17.1 and 2.17.2 give the actual saturated activities observed for each foil of a stack, the number of foils per stack, and the total thickness of the stack, for gold and indium foils. The gold foils were essentially all of the same thickness. Since the indium foils varied somewhat in thickness, the distance of the middle of each foil from the bottom of the stack is given.

---

[3] G. R. Dalton and R. K. Osborne, *Nuclear Sci. and Eng.* 9, 198 (1961); also G. C. Hanna, *The Depression of Thermal Neutron Flux and Density by Absorbing Foils*, to be published.

[4] This is the same apparatus described by Mustafa and Blosser in Section 2.13.

[5] T. V. Blosser and D. K. Trubey, *Neutron Phys. Ann. Prog. Rep., Sept. 1, 1960*, ORNL-3016, p. 142.

To display the shape of the variation of specific activity through the foil stacks, the numbers were normalized to the activity of the bottom foil of a stack. The normalized activity is plotted for various configurations in Figs. 2.17.1 and 2.17.2.

Table 2.17.1. Neutron-Induced Gamma-Ray Activity in Stacks of Gold Foils

Foil Number	Saturated Activity per Milligram (Arbitrary Units)							
	$1\frac{1}{4}$-in.-dia Foils							1.11-cm-dia Foils
	Total = 19.65 mils		Total = 18.68 mils		Total = 11.4 mils	Total = 10 mils		Total = 9.83 mils
	Conf. A*	Conf. D	Water	Conf. A	Conf. B	Water	Conf. A	Water
1	768	1205	1000	1590	167	1912	1657	2080
2	741	1176	977	1554	165	1868	1619	2030
3	723	1151	957	1508	163	1840	1583	2008
4	707	1137	943	1480	161	1821	1559	1985
5	697	1120	931	1444	159	1808	1545	1973
6	682	1112	916	1425	157.2	1799	1526	1963
7	677	1102	913	1406	155.7	1796	1513	1959
8	657	1101	904	1386	154.3	1804	1503	1957
9	659	1094	902	1369	153.1	1820	1500	1971
10	651	1087	895	1360	151.8	1840	1509	2016
11	642	1087	890	1341	150.7			
12	633	1094	890	1333	149.7			
13	628	1096	886	1318	148.8			
14	635	1106	888	1314				
15	628	1107	892	1309				
16	631	1116	895	1311				
17	627	1137	904	1313				
18	629	1145	913	1310				
19	641	1174	929	1323				
20	652	1202	946	1337				

*Configurations are described in text.

Table 2.17.2. Neutron-Induced Gamma-Ray Activity in Stacks of $1\frac{1}{4}$-in.-dia Indium Foils

Distance from Stack Bottom (mils)	Saturated Activity per Milligram (Arbitrary Units)			
	Water	Conf. A*	Conf. B	Conf. C
	20 Foils: Total Thickness = 21.5 mils			
0.7	679		1422	353
2.1	646		1358	343
3.5	632		1344	336
4.7	615		1308	326
5.9	601		1280	315
7.0	594		1244	313
8.0	585		1248	304
8.9	579		1187	299
9.8	577		1206	295
10.6	575		1176	289
11.3	571		1166	283
12.1	575		1134	283
13.0	571		1129	277
13.8	572		1140	274
14.7	572		1117	264
15.7	576		1117	260
16.9	578		1094	256
18.1	583		1100	253
19.4	594		1084	244
20.8	615		1094	238
	10 Foils: Total Thickness = 10 mils			
0.40	600	605		
1.26	587	581		
2.20	571	563		
3.24	561	547		
4.41	558	534		
5.64	557	525		
6.79	558	520		
7.81	563	518		
8.74	573	520		
9.59	584	526		

*Configurations are described in text.

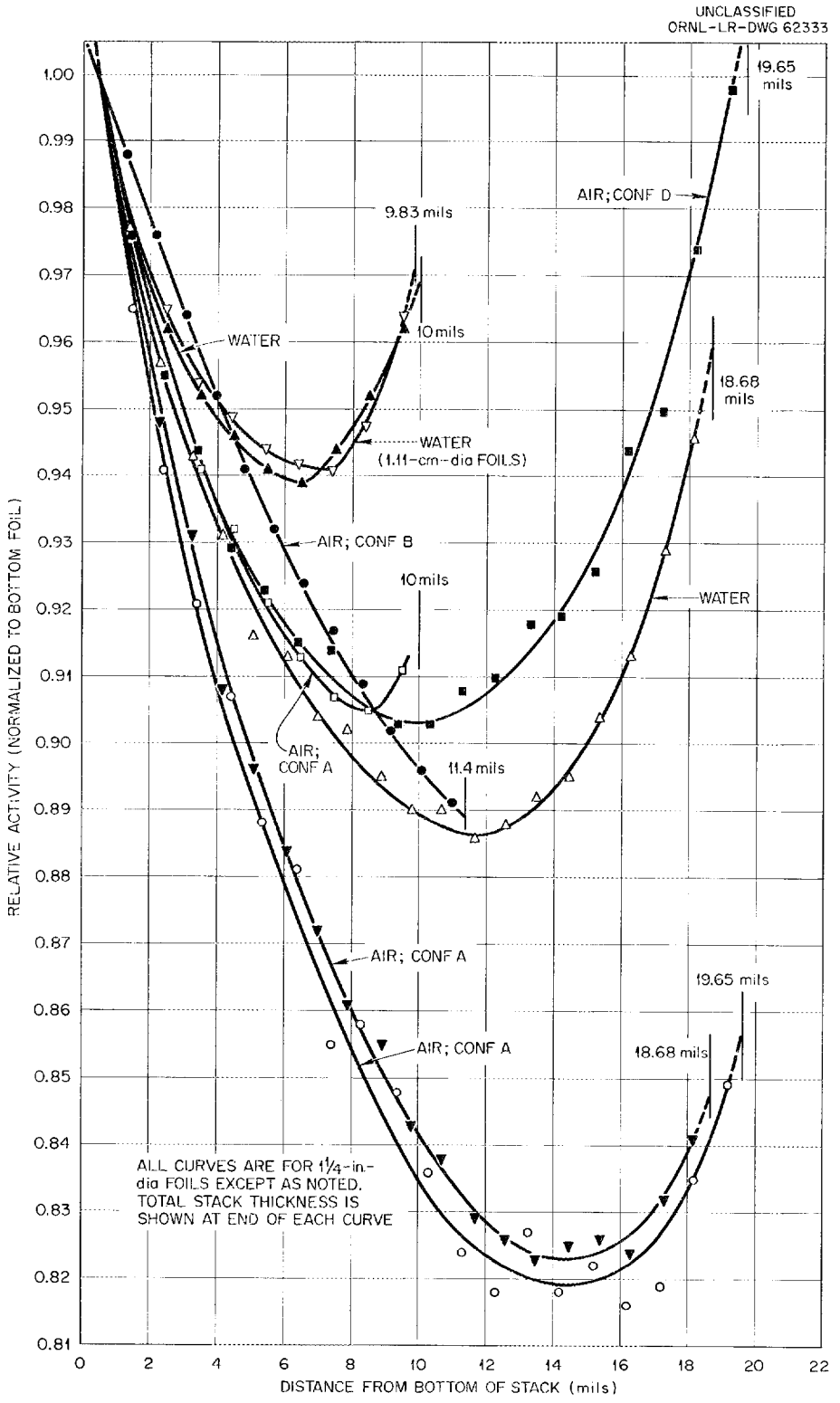

Fig. 2.17.1. Relative Activity (Normalized to Bottom Foil) of Stacked Gold Foils Exposed to Thermal Neutrons in Water and in Air.

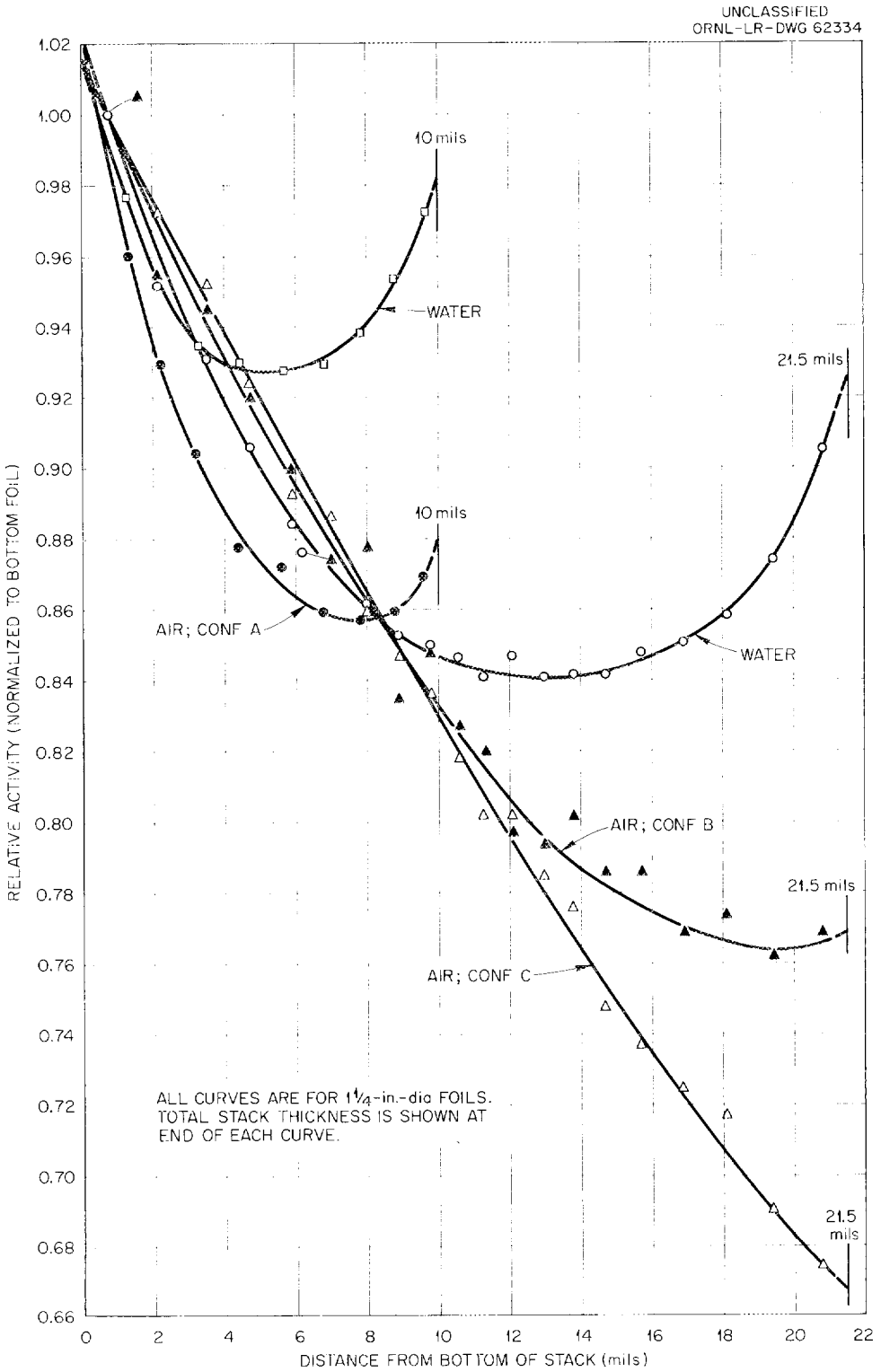

Fig. 2.17.2. Relative Activity (Normalized to Bottom Foil) of Stacked Indium Foils Exposed to Thermal Neutrons in Water and in Air.

Part 3

CRITICAL EXPERIMENTS

3.1. HOMOGENEOUS CRITICAL ASSEMBLIES OF 3% U^{235}-ENRICHED UF_4 IN PARAFFIN

J. T. Mihalczo and J. J. Lynn

The program of critical experiments with homogeneous hydrogen-moderated assemblies of 2 wt% U^{235}-enriched UF_4 in paraffin reported previously[1] has been extended to include a mixture of 3 wt% U^{235}-enriched UF_4 in paraffin with a $H:U^{235}$ ratio of 133. This mixture contains 92 wt% UF_4 and has a uranium density of 3.41 g/cc. The critical height of a rectangular parallelepiped with a square base, as a function of base dimensions, is shown in Fig. 3.1.1. From these data, the minimum critical volumes for bare and reflected spheres are 200 and 121 liters, respectively.

[1] J. T. Mihalczo and J. J. Lynn, *Neutron Phys. Ann. Prog. Rep. Sept. 1, 1960*, ORNL-3016, p. 71.

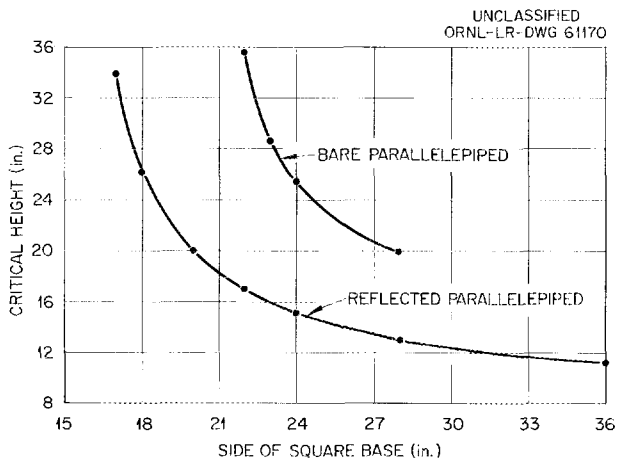

Fig. 3.1.1. Critical Height as a Function of the Base Dimensions of Rectangular, Square-Based Parallelepipeds: 3 wt % U^{235}-Enriched UF_4 in Paraffin.

3.2. CRITICAL PARAMETERS OF SOLUTIONS OF U^{235}-ENRICHED URANYL NITRATE IN CYLINDRICAL CONTAINERS

J. K. Fox

Critical experiments which extend the existing data on fissionable solutions have been performed with solutions of $UO_2(NO_3)_2$ at two U^{235} enrichments. The first material consisted of a solution of $UO_2(NO_3)_2$, enriched to 93.15 wt% in U^{235}, in a D_2O-H_2O mixture containing 70.1 wt% D_2O. The U^{235} concentration in this solution was 105.9 g per liter, the specific gravity 1.226, the $H:U^{235}$ atomic ratio 70.9, and the $D:U^{235}$ atomic ratio 166.3. Experiments with this material were carried out in two types of vessel. The first was a 40.0-cm-ID cylinder originally constructed for the preliminary mockup studies[1] of the ORNL High Flux Isotope Reactor. The outer vessel was constructed of type 6061 aluminum and had a 31.8-mm-thick wall and a 63.5-mm-thick bottom. A 15.24-cm-OD type 1100 aluminum shell was axially located

[1] J. K. Fox, L. W. Gilley, and D. W. Magnuson, *Neutron Phys. Ann. Prog. Rep., Sept. 1, 1960*, ORNL-3016, p. 59.

within the 40-cm-dia main vessel, and surrounding it was an 81.3-cm-dia aluminum shell. The latter shell is believed to have had negligible effect as a reflector, particularly in experiments with lateral liquid reflection. Reflection from the thin bottom of the main vessel was also small, and was ignored in the determination of critical heights. The second vessel was a 50.8-cm-ID, type 3003 aluminum cylinder. Its wall was ~~15.9~~ 1.59 mm thick, and its bottom 1.27 cm thick. The critical height reported for this vessel contains an empirically determined 0.4-cm correction for the effect of the bottom thickness

The experimental data obtained with the described material and containers are summarized in Table 3.2.1.

The second solution studied in this series consisted of $UO_2(NO_3)_2$, enriched to 92.6 wt% in U^{235}, dissolved in H_2O. The U^{235} concentration was 380 g per liter, the specific gravity 1.55, and the $H:U^{235}$ atomic ratio 59.0. Solutions were contained within type 3003 aluminum cylinders having a wall thickness of ~~15.9~~ 1.59 mm and a bottom thickness of 1.27 cm. As before, reported heights contain a 0.4-cm correction for the effect of the bottom. Vessel diameters ranged from 24.1 to 38.1 cm. Critical parameters are shown in Table 3.2.2.

Table 3.2.1. Critical Dimensions of Cylinders Containing 93.15 wt% U^{235}-Enriched $UO_2(NO_3)_2$ Dissolved in a D_2O-H_2O Mixture (70.1 wt% D_2O)

Cylinder Diameter (cm)	Critical Height (cm)	Critical Volume (liters)	Critical Mass (kg of U^{235})
40.0	53.4	67.1	7.11
40.0	34.8*	43.7	4.63
40.0	31.6**	39.7	4.20
50.8	31.8	64.5	6.83

*Lateral reflection by 8-in.-thick solution of 2.35 g of B per liter of D_2O.
**Lateral reflection by 8-in.-thick H_2O.

Table 3.2.2. Critical Dimensions of Cylinders Containing 92.6 wt% U^{235}-Enriched $UO_2(NO_3)_2$ Dissolved in H_2O

Cylinder Diameter (cm)	Critical Height (cm)	Critical Volume (liters)	Critical Mass (kg of U^{235})
24.1	71.7	32.9	12.50
25.4	45.8	23.2	8.82
30.5	25.8	19.6	7.45
38.1	19.7	22.4	8.51

3.3. NUCLEAR SAFETY TESTS OF THE HIGH FLUX ISOTOPE REACTOR FUEL ELEMENT

J. K. Fox

A number of water immersion tests were performed on the fuel element for the High Flux Isotope Reactor Critical Experiment No. 2 (Sec. 3.4) in the absence of the beryllium reflector and prior to installation in the critical experiment equipment in order to establish some measure of its nuclear safety during fabrication and storage. All tests were performed in a large tank which could be filled with water to provide a moderator and an effectively infinite reflector. The element was supported on a 12-in.-high Plexiglas table.

The fuel element is shown in Fig. 3.3.1. It consists of two annular and concentric components, each consisting of two concentric aluminum cylinders between which are mounted aluminum-clad, 93.14 wt% U^{235}-enriched uranium-aluminum fuel plates. The fuel plates are rectangular in profile, with a cross section that is a partial involute of a circle.

The inner annulus, having a 5.067-in. inside diameter and a 10.590-in. outside diameter, contains 171 fuel plates with a total of 2.31 kg of U^{235} and 8.7 g of boron distributed throughout the plates. The volume surrounded by this annulus will be the region of high thermal-neutron flux in the operating reactor and is called the target region. The outer annulus, having a 11.366-in. inside diameter and a 17.125-in. outside diameter, contains 369 fuel plates, with a total of 5.68 kg of U^{235}. The fuel section of the element is 20 in. long.

The first series of experiments was performed using only the outer annulus. Complete submersion of the annulus in water gave no appreciable source neutron multiplication. When the central 11.366-in.-dia region inside the annulus was filled with Styrofoam (polystyrene, density = 0.028 g/cm^3) and the annulus completely flooded, a source neutron multiplication of ~ 2 was observed. The diameter of the Styrofoam was then reduced by small increments, increasing the amount of water between opposite sides of the annulus, but little effect on the multiplication could be seen. Thus it is evident that handling the outer annulus, even in the presence of water, is quite safe.

The second series of tests was performed with the complete element except for 12 removable fuel plates and a 0.050-in.-thick aluminum cylinder which was added at the inner boundary of the outer annulus. The data are summarized in Table 3.3.1. The first entry in the table shows that the complete element, like the outer annulus alone, is subcritical when completely submerged in water; hence the two annuli can be safely handled as a unit. Subsequent experiments showed that the addition of the 12 plates and the cylinder reduced the reactivity by about 1.2 dollars, so that their presence would increase the margin of safety.

For the above measurement with the complete element submerged in water the neutron source was centered on the axis and two BF_3 counters were placed in the reflector about 9 in. from the element and in its midplane. Neutron background was measured with the element replaced by an 8-in.-ID by 11-in.-OD annular aluminum can filled with air.

UNCLASSIFIED
ORNL-LR-DWG 61171

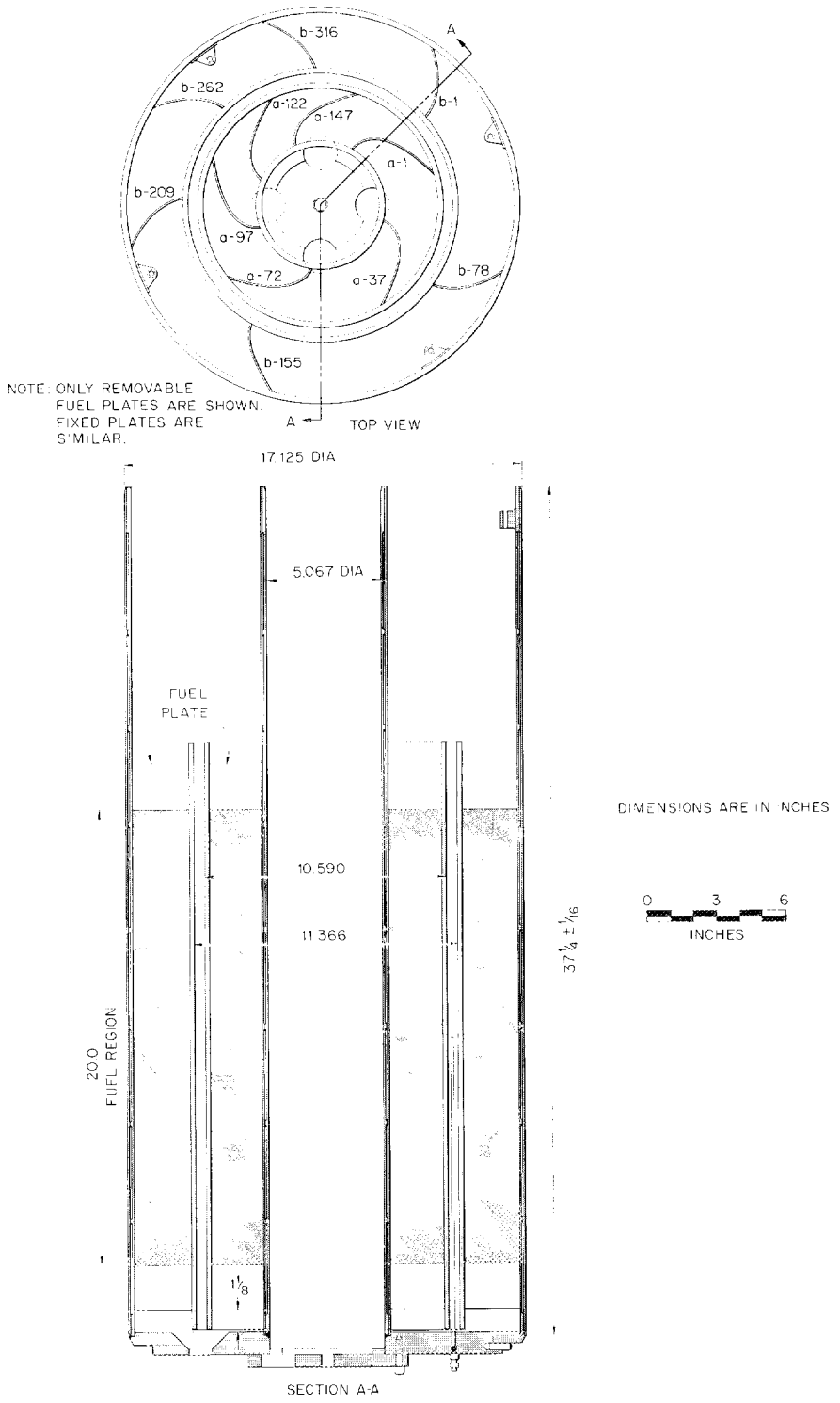

Fig. 3.3.1. Fuel Element for High-Flux Isotope Reactor Critical Experiment No. 2.

Table 3.3.1. Effect of Void in Target Region of Fuel Element of HFIRCE No. 2: Critical Height of Moderator and Reflector Water

Void Fraction in Target Region	Void Diameter (in.)	$\rho/\Delta h$ (cents/in.)	Critical Water Height* (in.)
	Distributed Voids		
0			Not Critical**
0.47		7.9	−0.16
0.56			−0.55
0.64		11.4	−0.83
0.80		11.4	−0.67
	Central Void with Water Annulus		
0.34	4.5		+0.32
0.47	4.0	7.9	−0.43
0.61	3.5	9.8	−0.79
0.77	3.0		−0.59
0.97	5.1		+0.79

*Water height measured from top of fuel; 12 plates and aluminum shell removed.
**Source neutron multiplication > 30 when completely flooded.

The remaining measurements in the second series investigated the effect of removing water from the target region, accomplished by displacing water with Styrofoam. Two methods of adjusting the void fration were used. In the first, voids were effectively "distributed" by inserting in the target region a Styrofoam cylinder through which vertical holes had been drilled. In the second method the voids were formed by axial cylinders of Styrofoam of various diameters. As is evident from the curves of Fig. 3.3.2, the two methods produced somewhat different results. Generally, however, as voids were introduced the reactivity increased, reaching a maximum with a void fraction of between 0.55 and 0.65 of the region volume, depending on the method of introduction of the void. Further increase in void fraction decreased the reactivity. Completely filling the target region with Styrofoam, resulting in a void fraction of 0.97, produced a critical condition with a top water reflector of 0.79 in. thick. In the latter experiment the Styrofoam cylinder was 26 in. long, whereas in all the others the cylinder was 20 in. long and was juxtaposed to the fuel region of the element.

The values of $\rho/\Delta h$, also shown in Table 3.3.1, were obtained from measurements of positive periods. These results make possible an estimate of the reactivity to be expected in the event of complete flooding of the element.

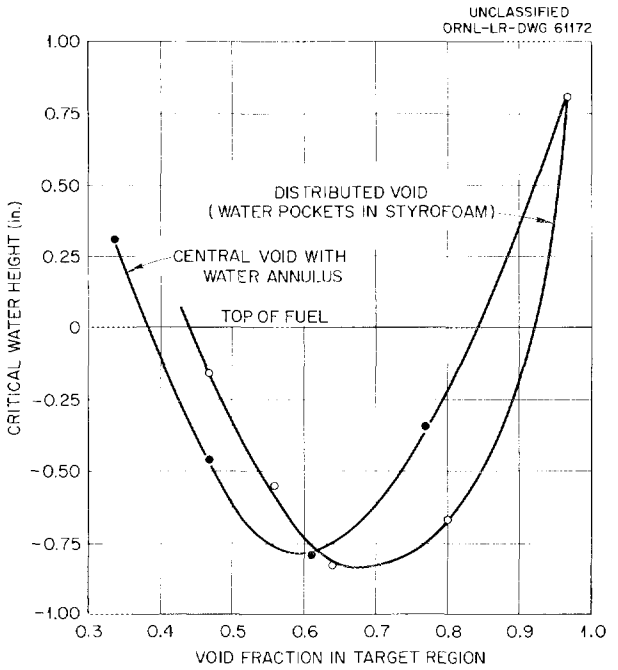

Fig. 3.3.2. Critical Water Height (Above Top of Fuel) as a Function of Void Fraction in Target Region.

3.4. HIGH FLUX ISOTOPE REACTOR CRITICAL EXPERIMENT NO. 2

D. W. Magnuson

The High Flux Isotope Reactor Critical Experiment No. 2 (HFIRCE No. 2) is the second series of measurements made in support of the nuclear design of the High Flux Isotope Reactor (HFIR).[1,2] The HFIR is to be a highly U^{235}-enriched uranium-fueled reactor designed to produce a flux of greater than 10^{15} thermal neutrons for the production of transplutonium nuclides; it will be moderated and cooled by water and reflected by beryllium. The first series of critical experiments supporting its design was completed last year[3,4] and consisted of solution-type experiments in annular geometry. This second series consists of experiments with a mockup more nearly representing the design of the reactor.

Description of the Assembly

The HFIRCE No. 2 assembly consists of mockups of the reactor fuel element, the central target region, a side beryllium reflector, and top and bottom water reflectors. It also includes mockups of a

[1] R. D. Cheverton, *HFIR Preliminary Physics Report*, ORNL-3006 (Oct. 4, 1960).

[2] R. D. Cheverton, *Fuel-Cycle Analysis and Proposed Fuel and Burnable Poison Distribution and Loading for the HFIR and HFCE-2*, ORNL-CF-61-2-36 (Feb. 2, 1961).

[3] J. K. Fox, L. W. Gilley, and D. W. Magnuson, *Neutron Physics Div. Ann. Prog. Rep., Sept. 1, 1960*, ORNL-3016, p. 59.

[4] J. K. Fox, L. W. Gilley, and D. W. Magnuson, *Preliminary Solution Critical Experiments for High Flux Isotope Reactor Parameter Study* (to be published as an ORNL report).

nuclear target, the control plates, and the three beam tubes, referred to as tangential, radial, and through beam tubes.

The fuel element, described in Sec. 3.3, consists of two concentric cylindrical annuli of involute-shaped uranium-aluminum fuel plates. It is surrounded by an annulus of beryllium which is ~12 in. thick at the midplane and is shown being lowered over the fuel element in Fig 3.4.1. (The beryllium was salvaged from another reactor program and remachined for this experiment.) The assembled fuel element and beryllium are shown in Fig. 3.4.2, the two annuli of the element being clearly visible. The interior and exterior walls of the fuel element extend 12 in. above the fuel plates and form the boundaries of the moderator-water system which is separate from the water system that floods the target region and the beryllium. Following the safety tests described in Sec. 3.3, a 0.050-in.-thick aluminum cylinder was placed between the fuel annuli, in contact with the outer annulus, to reduce the water gap thickness in that region. This cylinder, which is not shown in Fig. 3.4.2, reduced the inside diameter of the outer annulus to 11.266 in. and was in position for all the measurements described here unless otherwise specified. In Fig. 3.4.2 the tangential and through beam tubes are also clearly seen, as is the annular slot between the fuel element and the beryllium in which two cylindrical control plates move.

The control plates are vertical coaxial cylinders, the inner cylinder having a 17.8-in. outside diameter and the outer cylinder having an 18.5-in. outside diameter. The inner cylinder is 88 in. long and the outer one 75 in. long. Two of the three roller guides for the outer control plate are visible on top of the beryllium in Fig. 3.4.2, and all the guides, both above and below the beryllium, are apparent in Fig. 3.4.1.

Each control plate is constructed of three $\frac{1}{4}$-in.-thick, 20-in.-long active sections: one of aluminum, a poor thermal-neutron absorber; a central section of nickel, a moderate absorber; and a third section of 23.6% 76.4% ~~86%~~ copper–~~14%~~ silver alloy, a strong absorber. The orientation of the plates is such that the order of the three control materials in one is reversed with respect to the other, aluminum being the upper section of the inner plate and the lower section of the outer plate. Thus, with the inner plate lowered and the outer plate raised both aluminum sections are adjacent to the fuel, while with the plate positions reversed both copper-silver sections are adjacent to the fuel. This arrangement allows symmetric positioning of the absorber sections about the fuel. The sectional construction of the control plates is shown in Fig. 3.4.3. The difference in appearance is due to the fact that the outer plate had been painted with Amercoat 31* for corrosion resistance. Later the inner plate was also painted, but the Amercoat 31* was subsequently removed from the aluminum sections of both control plates because of its undesirable chlorine content.

In Fig. 3.4.4 the outside tank wall is shown being lowered into position on the bottom plate flange, which also supports the control plates in their fully inserted position.

Not shown in any of the photographs is the target mockup that was placed in the central region surrounded by the inner annulus of the fuel element. This target mockup consists of thirty $\frac{3}{8}$-in.-dia vertical

*Amercoat 31 is the trade name for resin base (Bakelite VYHH) paint. The resin is a copolymer of 85% polyvinylchloride and 15% polyvinyl acetate.

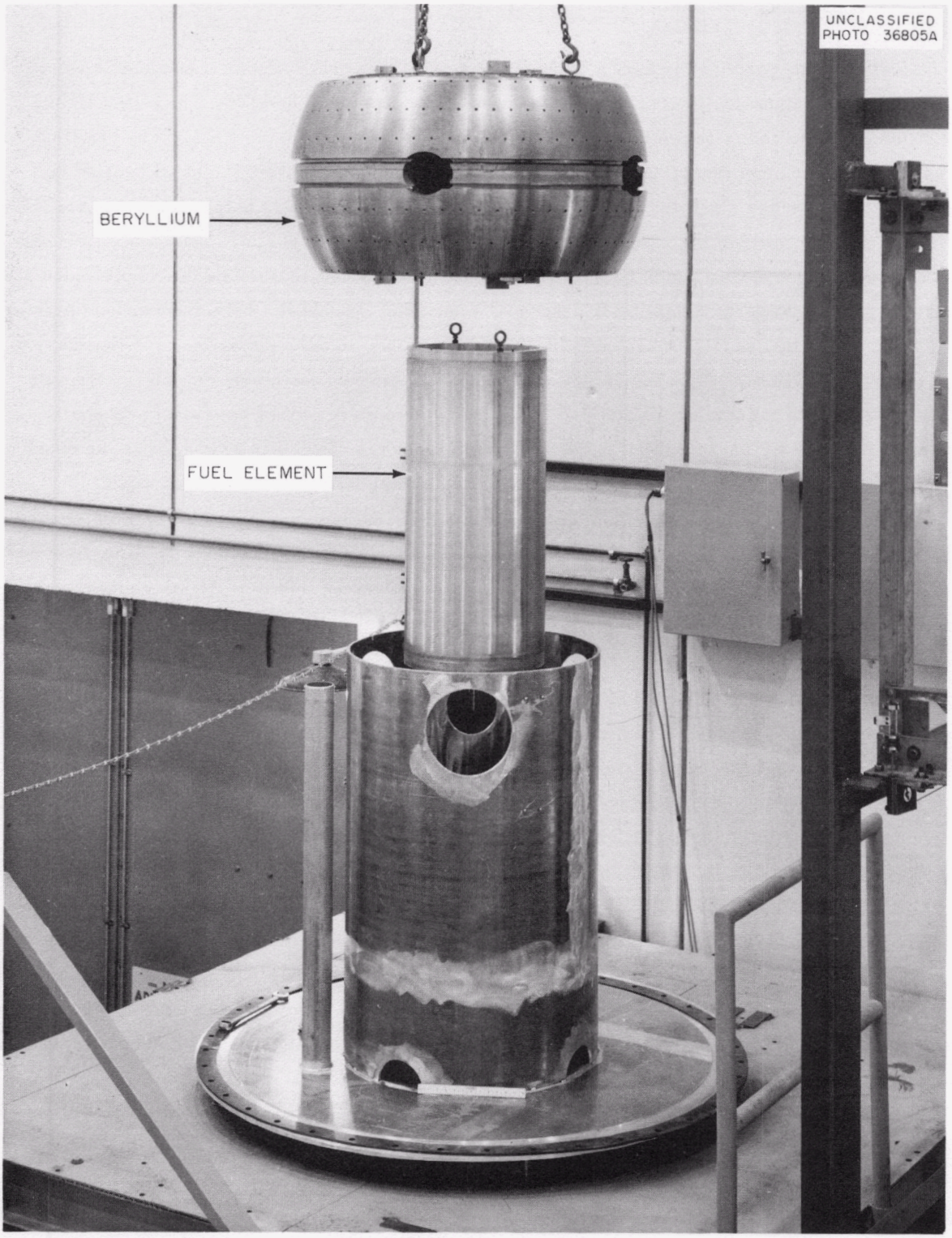

Fig. 3.4.1. Positioning of Beryllium Reflector in HFIRCE No. 2.

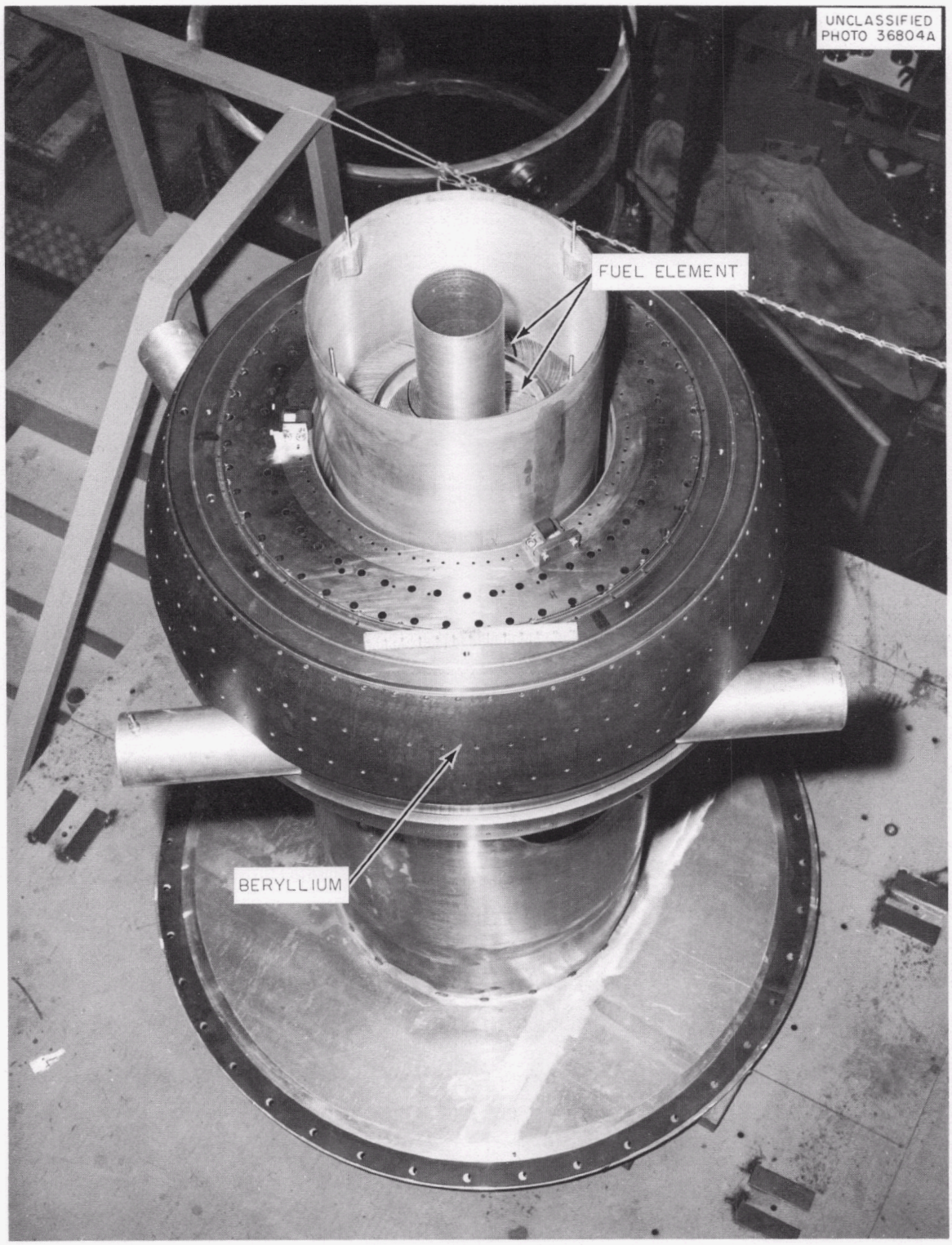

Fig. 3.4.2. Fuel Element and Beryllium Reflector in HFIRCE No. 2.

Fig. 3.4.3. Inner and Outer Control Plate Cylinders for HFIRCE No. 2.

aluminum tubes containing a nuclear mockup of a future HFIR target and seventy-eight $^5/_{16}$-in.-dia aluminum tubes (0.025-in.-thick walls) which could be corked to introduce voids in the target region. The two types of tubes were uniformly distributed in the target region. A cadmium cylinder, encased in stainless steel, could fall between the target and the fuel element as a safety rod for the critical experiment.

A complete design and description memorandum of the HFIRCE No. 2 is being written.[5]

Control Plate Positions at Critical

The critical positions of the control plates with and without the target assembly in position and in the absence of known perturbations such as counters and thermocouple leads in the core are reported in Table 3.4.1. The position with the target inserted is important because it determines how much excess reactivity will be available for the life of the reactor fuel element. Removing the target assembly decreased the reactivity approximately $1.1, based on the limited control plate calibration presently available.

[5] R. E. Hoskins, to be published as an ORNL report.

Fig. 3.4.4. Tank Assembly for HFIRCE No. 2.

Table 3.4.1. Critical Positions of Control Plates

Conditions	Control Plate Positions* (in.)		Nickel or "Grey" Window Height (in.)
	Inner	Outer	
With target installed	17.24	17.24	10.5
Without target	18.69	18.69	13.4

*The position indicator of each control plate was adjusted to 22 in. when the nickel or "grey" sections were symmetrical about the fuel element. An increase in the position indicator reading represents withdrawal of nickel and insertion of aluminum in the control region. A decrease in the reading represents withdrawal of the nickel and insertion of the copper-silver section.

Control Plate Calibration

The outer control plate was calibrated over a limited range by the rod bump method in which the inhour equation yields the reactivity from the positive periods arising from successive plate displacements. It is possible to calibrate two plates simultaneously because the second is used to restore the reactor to critical from the supercritical condition established by the displacement of the first. The results of this calibration are shown in Figs. 3.4.5 and 3.4.6 and were obtained primarily for interpretation of the measurements of the temperature coefficient of reactivity.

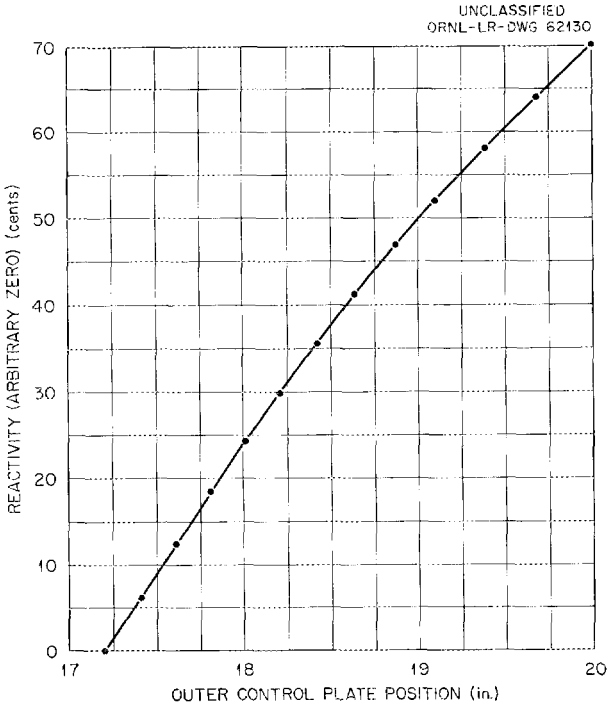

Fig. 3.4.5. Outer Control Plate Calibration: HFIRCE No. 2.

The sensitivity of the outer control plate at various positions was also determined from positive periods and is shown in Fig. 3.4.7 (see also Table 3.4.4 below). An integration under the curve was used to obtain the large increments in reactivity observed during measurements of void coefficients of reactivity.

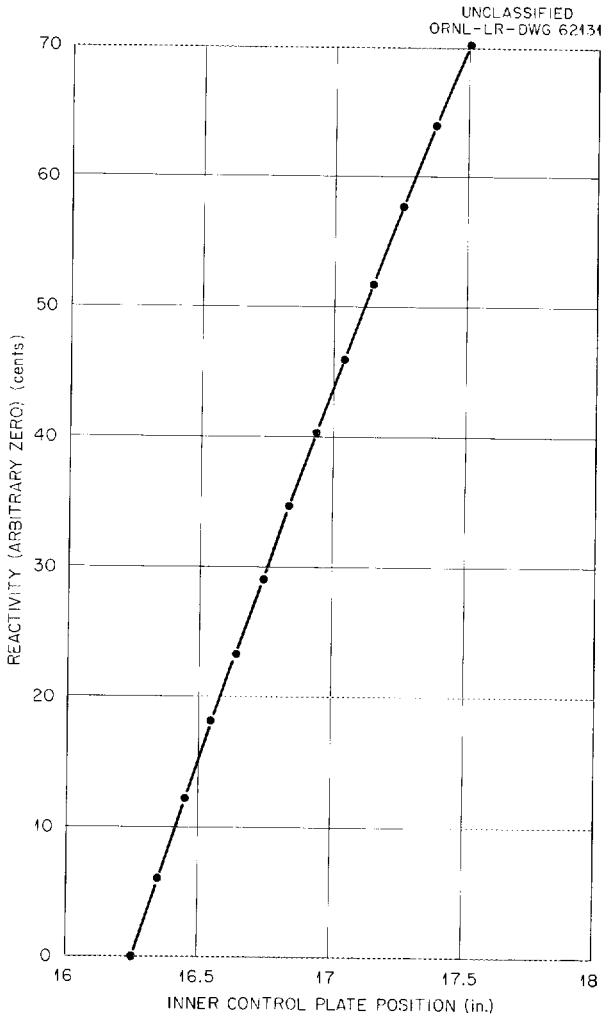

Fig. 3.4.6. Inner Control Plate Calibration: HFIRCE No. 2.

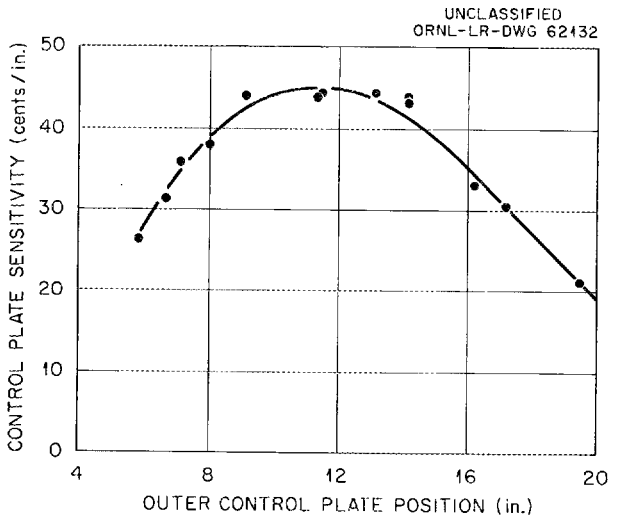

Fig. 3.4.7. Outer Control Plate Sensitivity: HFIRCE No. 2.

The presence of delayed photoneutrons from the beryllium was neglected when estimating reactivity in cents from the stable positive periods.

Temperature Coefficients of Reactivity

The isothermal temperature coefficient of reactivity up to the operating temperature is important because its sign and magnitude influence the amount of control required for the reactor. More important for safety are the sign and magnitude of the fuel temperature coefficient of reactivity since there would not be time to transfer heat from this region during any power transient. Both these coefficients were measured. During the measurements the moderator water was circulated through both a heater and the fuel element in a piping system independent of the system used to circulate water through additional heaters and the target and control regions. Therefore, not only could the temperature throughout the

assembly be altered, but the fuel element temperature could be made 8 to 10°C hotter than the average of the remainder of the system. The water which circulated through the target and control plate regions and through the beryllium could also be cooled by tap water in a heat exchanger. Temperature homogeneity of the water within the tank was improved by a stirrer located adjacent to the beryllium.

Each temperature cycle constituting a series of temperature coefficient measurements extended over 24 to 30 hr because of the time required to heat the large volume of water and for the temperature to equilibrate, and because the quasi-equilibrium temperature differential between fuel and reflector required almost an hour to establish a stable control plate position. The reactivity changes associated with the changes in temperature were followed with the control system, maintaining criticality at constant power. There are reasonable explanations for the control plate movements required to compensate for the reactivity changes during the nonequilibrium temperature periods immediately following changes in heating or cooling.

Two temperature cycles between room temperature and 70°C were made both with and without the target assembly installed. Tables 3.4.2 and 3.4.3 and Fig. 3.4.8 summarize the temperature and reactivity data. The hour of each observation is included in the tables to show the duration of each part of the experiment. The over-all temperature coefficient of reactivity with the target inserted is -3.7×10^{-5}/°C over the range 25 to 70°C. The coefficient without the target exhibits a point of inflection changing from positive to negative over the same temperature range. In Fig. 3.4.9 it can be seen that within the precision of the measurements the fuel-moderator temperature coefficients of reactivity as a

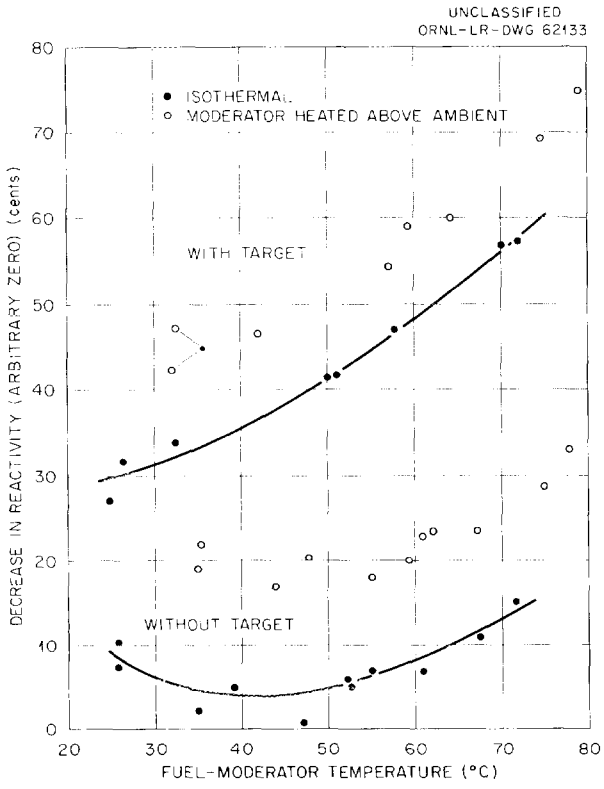

Fig. 3.4.8. Effect of Changes in Fuel-Moderator Temperature on Reactivity in HFIRCE No. 2: With and Without Target in Position.

Table 3.4.2. Temperature Coefficient of Reactivity Data: With Target in Position

Time	Beryllium Temperature, T_1 (°C)	Fuel-Moderator Temperature, T_2 (°C)	Target and Control Region Temperature, T_3 (°C)	$\Delta T = T_2 - T_3$ (°C)	Critical Position of Outer Control Plate* (in.)	Reactivity (Arbitrary Zero) (cents)	Isothermal Reactivity (Corrected to $\Delta T = 0$)	$\frac{\Delta\rho}{\Delta(\Delta T)}$ (cents/°C)
10:05 AM	23.4	24.7	23.5	1.2	18.16	28.5	27.2	
10:45 AM	24.0	35.6	25.7	9.9	18.79	45.0		1.90
7:00 PM	71.0	79.0	72.3	6.7	20.26	74.8		
8:20 PM	72.0	72.0	72.7	−0.7	19.26	55.6	57.4	2.59
11:40 PM	50.0	50.0	50.0	0.0	18.65	41.5	41.5	
12:30 AM	50.9	59.5	52.5	7.0	19.42	59.0		2.50
12:15 PM	25.6	26.4	25.6	0.8	18.33	33.2	31.8	
1:10 PM	27.5	35.6	28.2	7.4	18.79	45.0		1.79
3:45 PM	48.4	51.0	51.2	−0.2	18.64	41.3	41.7	
4:40 PM	50.5	57.1	51.3	5.8	19.20	54.4		2.18
7:00 PM	68.7	70.0	70.8	−0.8	19.22	54.8	56.8	
7:45 PM	69.0	74.6	69.7	4.9	19.94	69.2		2.53
10:15 PM	57.5	57.7	58.3	−0.5	18.82	45.8	47.0	
11:05 PM	58.3	64.2	58.7	5.5	19.47	60.0		2.37
9:10 AM	32.2	32.5	32.1	0.4	18.38	34.6	33.8	
10:15 AM	34.5	42.0	35.2	6.8	18.86	46.7		1.89

*An increase in these values represents a withdrawal of absorber and an increase in reactivity. In these experiments, of course, changes in plate position are balanced by the temperature effects.

Table 3.4.3. Temperature Coefficient of Reactivity Data: Without Target in Position

Time	Beryllium Temperature, T_1 (°C)	Fuel-Moderator Temperature, T_2 (°C)	Target and Control Region Temperature, T_3 (°C)	$\Delta T = T_2 - T_3$ (°C)	Critical Position of Outer Control Plate* (in.)	Reactivity (Arbitrary Zero) (cents)	Isothermal Reactivity (Corrected to $\Delta T = 0$)	$\frac{\Delta\rho}{\Delta(\Delta T)}$ (cents/°C)
9:55 AM	25.6	25.7	25.6	0.1	17.38	10.4	10.3	
10:25 AM	26.4	35.3	27.3	8.0	17.79	21.9		1.46
12:25 PM	38.5	39.1	38.5	0.6	17.24	6.2	5.0	
1:10 PM	38.4	47.6	40.1	7.5	17.74	20.5		2.07
3:15 PM	54.4	55.0	55.3	−0.3	17.24	6.2	7.0	
4:00 PM	55.0	62.1	55.6	6.5	17.85	23.5		2.54
6:10 PM	70.2	71.6	72.3	−0.7	17.48	13.3	15.1	
7:00 PM	71.0	77.8	71.4	6.4	18.14	31.1		2.51
11:30 PM	52.4	52.2	52.2	0.0	17.22	5.7	5.7	
12:10 AM	53.0	59.3	53.7	5.6	17.72	20.0		2.55
10:20 AM	34.1	34.9	34.3	0.6	17.14	3.3	2.2	
11:10 AM	34.9	43.9	35.8	8.1	17.61	17.0		1.83
12:55 PM	46.0	47.0	46.7	0.3	17.08	1.5	0.8	
1:45 PM	47.0	54.9	47.5	7.4	17.66	18.4		2.38
3:35 PM	59.5	61.0	61.4	−0.4	17.22	5.7	6.8	
4:25 PM	60.5	67.2	61.0	6.2	17.85	23.5		2.70
7:00 PM	68.1	67.5	67.7	−0.2	17.37	10.1	10.7	
8:00 PM	68.5	74.9	69.0	5.9	18.05	28.7		3.05
11:00 PM	53.0	52.5	52.5	0.0	17.20	5.0	5.0	
12:00 AM	53.5	60.9	54.1	6.8	17.83	23.0		2.65
2:30 PM	25.0	25.7	25.1	0.6	17.31	8.3	7.4	
3:15 PM	25.7	34.9	26.9	8.0	17.68	19.0		1.45

*An increase in these values represents a withdrawal of absorber and an increase in reactivity. In these experiments, of course, changes in plate position are balanced by the temperature effects.

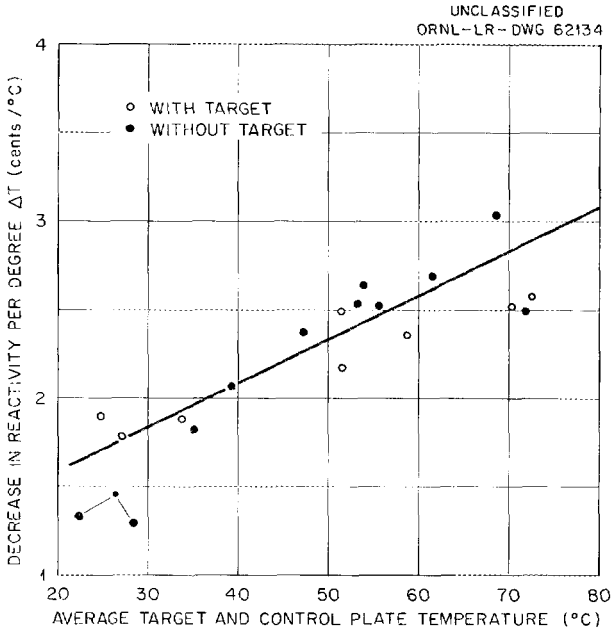

Fig. 3.4.9. Effect of Changes in Target and Control Region Temperature on Reactivity in HFIRCE No. 2: With and Without Target in Position.

function of the average target and control region temperature are not affected by insertion of the target. The straight line in Fig. 3.4.9 is given by the equation $\Delta\rho/\Delta(\Delta T) = [1.1 + 0.025T(°C)]$ cents/°C, yielding a value of -1.8×10^{-4}/°C for the fuel temperature coefficient of reactivity at 70°C and a value of -1.1×10^{-4}/°C at 25°C. The effective delayed neutron fraction was assumed to be 0.0064.

Void Coefficients of Reactivity in Target Region

The void coefficient of reactivity was measured by displacing water from the center of the target region by ½-in.-OD air-filled polystyrene tubes (1/16-in.-thick walls), by Styrofoam* cylinders, and, in some experiments, by air-filled aluminum tubes in the target assembly itself. These data are given in Table 3.4.4 and in Fig. 3.4.10. The maximum positive reactivity, $4.4, was observed with a 70% equivalent void of Styrofoam.

Fuel and Void Coefficients of Reactivity in Fuel Element

The reactivity effects of replacing plates in the fuel element with aluminum and with water were also measured. This was made possible by the fact that the fuel element was constructed with 12 removable fuel plates, six in the inner annulus and six in the outer annulus, primarily for the power distribution measurements described in the following section. Each of the removable plates in the inner annulus contained 13.51 g of U^{235} and each in the outer annulus contained 15.09 g. Both the fuel plates and the aluminum plates with which they were replaced were 0.050 in. thick and 24.00 in. long, although the fuel section was only 20 in. long. The widths of the inner and outer plates were 3.345 and

*A trade name for polystyrene with noninterconnecting air bubbles and having an over-all density of 0.029 g/cm^3.

Table 3.4.4. Void Coefficient of Reactivity Data for Target Region

Number of Air-Filled Aluminum Tubes	Number of Air-Filled Polystyrene Tubes	Diameter of Central Styrofoam Cylinder (in.)	Equivalent Target Region Fractional Area	Critical Control Plate Position* (in.) Inner	Critical Control Plate Position* (in.) Outer	Outer Control Plate Sensitivity (cents/in.)
			With Target			
0	0		0.000	17.50	17.21	30.5
20	0		0.054	17.50	15.92	
39	0		0.105	17.50	14.87	
59	0		0.158	17.50	13.95	
78	0		0.209	17.50	13.19	
0	24		0.158	17.50	14.19	43.8
78	24		0.368	17.50	11.45	44.1
			Without Target			
	0		0.000	20.195	17.21	30.5
	6		0.040	20.195	16.18	33.0
	18		0.119	20.195	14.205	43.2
	36		0.237	20.195	11.47	45.4
	60		0.396	20.195	8.068	38.0
		$4\frac{3}{4}$	0.861	20.195	7.28	35.8
		$4\frac{3}{16}$	0.709	20.195	5.87	26.3
		$3\frac{7}{8}$	0.573	20.195	6.69	31.4
		$3\frac{1}{4}$	0.403	20.195	9.182	43.9
		$2\frac{3}{16}$	0.183	20.195	13.15	45.4

*The position indicator of each control plate was adjusted to 22 in. when the nickel or "grey" sections were symmetrical about the fuel element. An increase in the position indicator reading represents withdrawal of nickel and insertion of aluminum in the control region. A decrease in the reading represents withdrawal of the nickel and insertion of the copper-silver section.

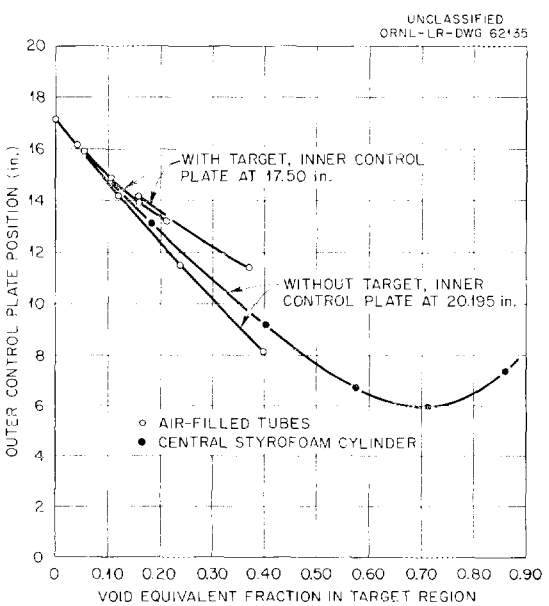

Fig. 3.4.10. Outer Control Plate Position as a Function of Void Fraction in Target Region of HFIRCE No. 2: With and Without Target in Position.

3.010 in., respectively. These experiments are summarized in Table 3.4.5. Substitution of aluminum plates for fuel plates in the inner and outer annulus showed the fuel to be worth 0.342 and 0.204 cents per gram of U^{235}, respectively. When the aluminum plates in the inner and outer annulus were replaced by water, the reactivity was increased 2.38 and 2.25 cents/in.,^{3} respectively. The water displaced outside the 20-in. fuel height was neglected in this calculation. The experiments were performed with the target in place.

The reactivity effect of removing the 0.050-in.-thick aluminum cylinder placed between the fuel annuli was estimated to be $0.80 from the change in the critical position of the outer control plate from 16.82 to 14.55 in. It was necessary to provide a 0.4-in.-wide slot in the lateral surface of the cylinder to permit entry of the neutron source into the original water gap. The result of this experiment shows an increase in reactivity of 2.27 cents/in.^{3} incurred by replacing aluminum by water if the replaced volume is considered to be only that adjacent to the 20-in.-high fuel. This value is in close agreement with those obtained by the removal of aluminum plates from the inner and outer fuel annuli.

Table 3.4.5. Fuel and Void Coefficient of Reactivity Data for Fuel Region

Number of Removable Plates Loaded in Fuel Element		Critical Control Plate Position* (in.)		Outer Control Plate Reactivity** (cents)
Inner Annulus	Outer Annulus	Inner	Outer	
6 Fuel	6 Fuel	16.825	18.000	24.0
0	6 Fuel	16.825	17.335	4.0
6 Aluminum	6 Fuel	16.825	19.075	51.7
6 Fuel	6 Fuel	16.825	17.990	23.7
6 Fuel	0	16.825	17.260	1.7
6 Fuel	6 Aluminum	16.825	18.675	42.2

*The position indicator of each control plate was adjusted to 22 in. when the nickel or "grey" sections were symmetrical about the fuel element. An increase in the position indicator reading represents withdrawal of nickel and insertion of aluminum in the control region. A decrease in the reading represents withdrawal of the nickel and insertion of the copper-silver section.

**Reactivity referred to an arbitrary zero with outer control plate positioned at 17.20 in. as shown in Fig. 3.4.5.

Power and Fission Flux Distribution Measurements

It was pointed out in the preceding paragraph that the fuel element was made with 12 removable fuel plates. In the outer annulus, which contains a total of 369 plates, the first of these removable plates is designated as b-1 and its center line intersects the axis of the radial beam hole. The other removable fuel plate positions are b-78, b-155, b-209, b-262 and b-316, the numbers referring to fuel plate positions in clockwise rotation as viewed from above. Positions b-155 and b-262 are near the through beam hole and the tangent beam hole, respectively. Positions a-1, a-37, a-72, a-97, a-122 and a-147 were designed to be the corresponding azimuthal positions in the inner fuel annulus which contains 171 fuel plates; however, the fuel element was assembled with the inner annulus rotated clockwise approximately 19 deg from the design position.

Small fuel-containing areas ($\frac{1}{8} \times 1\frac{1}{2}$ in.) were punched from a number of the removable plates for use as fission-rate detector foils (see Fig. 3.4.11 for the location of these foils in the fuel plates). The uranium content of these foils was determined[6] by using scintillation counters to compare the 0.18-Mev gamma-ray intensity of the foils with that of a known amount of U^{235}. Corrections were made for the absorption of this gamma ray in the uranium and in the aluminum foils. The content of several foils was verified by chemical analysis.

Foils irradiated in fuel plates occupying eight of the removable plate positions showed the azimuthal variations in the fission density at the outer edge of the outer fuel plates to be no larger than elsewhere within the element. It was concluded, therefore, that, for the positions of the control plates required for the present assembly to be critical, the beam tubes in the beryllium were not perturbing the flux and power distribution. For this reason irradiations were not made in the other available azimuthal positions. In the power distribution determination, fission-product gamma-ray energies greater than 0.5 Mev were counted. The observed activity of the various foils was compared to the simultaneously measured activity of a normalizing foil exposed in an established position. In this manner variations in exposure, from run to run, were compensated for and the data were corrected for the gamma-ray decay.

These relative activities or relative power distributions are given in Table 3.4.6 along with the relative activities per gram of U^{235} in each foil. The latter quantity is proportional to the neutron flux weighted by the fission cross section and averaged over the foil. No significant change was observed in the radial distribution when the water gap between the fuel annuli was increased 0.050 in. by removing the aluminum cylinder described above. One line in the table shows the flux distribution in an outer fuel plate with reversed radial fuel distribution. Figures 3.4.12 through 3.4.15 show the relative power distribution and relative fission flux (relative power per gram of U^{235} in the foil) in both the vertical and radial directions. Also shown in the table and in the figures are the distributions expected in foils containing the design mass of U^{235}.

Flux Measurements in the Reflector and Target Region

A 6-in.-long, $\frac{3}{4}$-in.-dia fission counter* was moved below the assembly to map the flux distribution in the lower water reflector. The axis of this counter was $2\frac{1}{2}$ in. from the axis of the fuel element. Foils were used to normalize this fission counter traverse to fluxes measured in the fuel and in the target regions. One foil was placed 5 in. above the fuel** on the inner cylindrical wall of the fuel element at about the same distance from the fuel element axis as was the fission counter traverse; another foil was placed at the center of an inner annulus fuel plate; and the third one was suspended at the center of the target region. The foil above the fuel established the flux there to be 60.8% of the flux at the center of

[6] D. W. Magnuson, *The U^{235} Content of Foils Punched from HFIR Critical Experiment No. 2 Fuel Plates*, ORNL-CF-61-7-50 (July 20, 1961).

*ORNL Type Q-2609.

**Although the end of the fission counter was 5 in. below the fuel, the center of the counter was $3\frac{3}{8}$ in. lower. Normalization with this foil necessitated, therefore, extrapolation of the counter traverse to a value at 5 in. below the fuel.

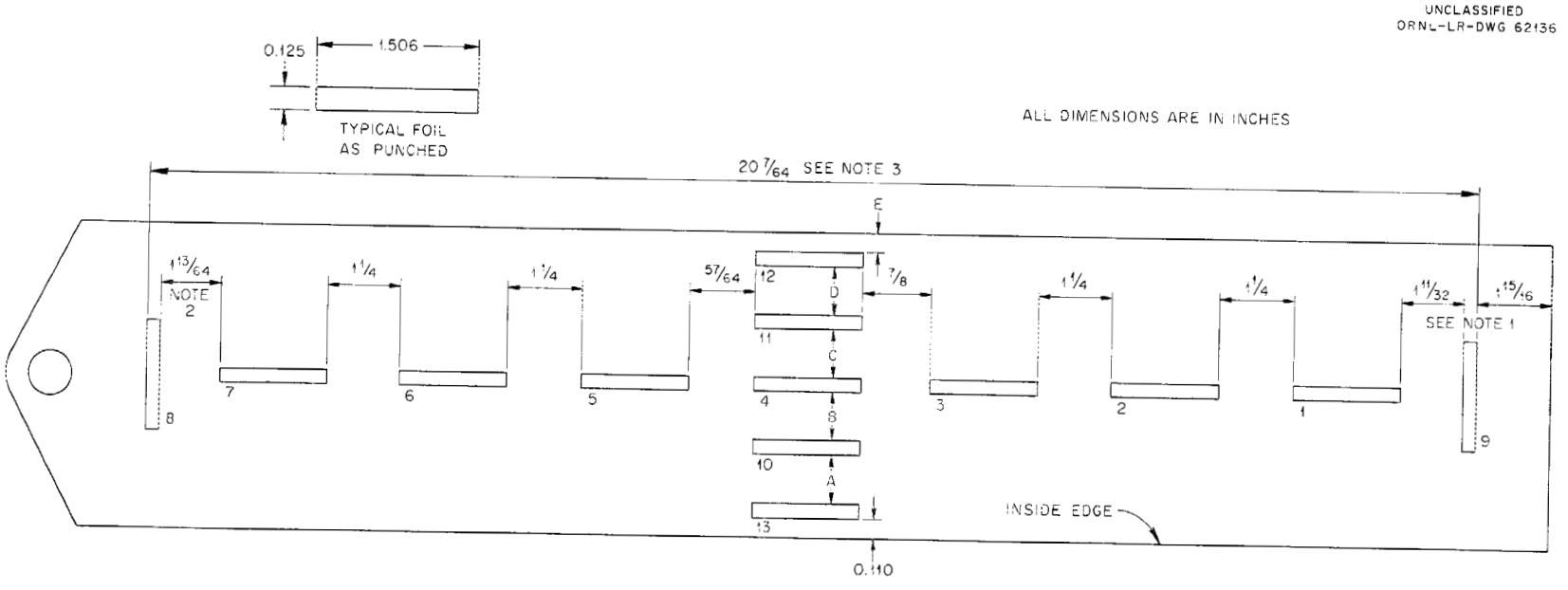

DIMENSIONS AS MEASURED ON DUMMY PLATE (in.)

INNER ANNULUS	OUTER ANNULUS
A = 0.610	A = 0.527
B = 0.610	B = 0.530
C = 0.610	C = 0.580
D = 0.610	D = 0.528
E = 0.170	E = 0.110

NOTE 1: ON PLATES P-1, P-2, F-2, AND F-4, FOIL NO. 9 WAS MOVED $\frac{1}{4}$ IN. TOWARD CENTER OF PLATE AND THESE DIMENSIONS ARE $1\frac{3}{32}$ IN. AND $2\frac{3}{16}$ IN.

NOTE 2: ON PLATES P-1, P-2, F-2, AND F-4, FOIL NO. 8 WAS MOVED $\frac{1}{4}$ IN. TOWARD CENTER OF PLATE AND THIS DIMENSION IS $\frac{61}{64}$ IN.

NOTE 3: AS A RESULT OF MOVING THE TWO END FOILS $\frac{1}{4}$ IN. TOWARD CENTER ON PLATES P-1, P-2, F-2, AND F-4 THIS DIMENSION IS $19\frac{39}{64}$.

Fig. 3.4.11. Location of Foils Punched from Removable Fuel Plates of HFIRCE No. 2.

Table 3.4.6. Relative Power Distributions and Fission Flux Distributions in Inner and Outer Fuel Annuli

Plate Position in Fuel Element	Fuel Plate Number	Foil Number 1	2	3	4	5	6	7	8	9	10	11	12	13
		Relative Activity in Foil (Relative Power Distribution)												
Inner annulus														
a-1	P-2		0.848	0.985	1.083	0.950	0.798	0.559	0.630	0.589	1.041	0.997	0.433	0.990
a-37	P-1	0.591	0.819	0.982	1.000	0.980	0.878	0.552	0.639	0.553	1.103	0.900	0.518	1.044
a-97	T-2[a]				0.939									
a-37	T-2[b]				1.000									
a-72	P-2	0.578	0.815	0.949	1.045	0.952	0.789	0.574	0.588	0.571	1.057	0.986	0.441	0.917
a-97	P-1[c]	0.581	0.813	0.963	0.984[e]	0.965	0.813	0.553	0.605	0.593	1.079	0.890	0.513	1.026
a-37	U-7[d,b]				1.000						0.955	1.095	1.147	0.720
Outer annulus														
b-1	F-4	0.386	0.604		0.797	0.756	0.592	0.401		0.439	0.927	0.652	0.500	1.030
b-78	F-2	0.349	0.550		0.775	0.750	0.578			0.482	0.916	0.670	0.300	1.060
b-155	F-4	0.395	0.618	0.774	0.803	0.747	0.603	0.416	0.523	0.420	0.929	0.671	0.530	1.044
b-209	F-2	0.346	0.543	0.717	0.784	0.768	0.596	0.421	0.509	0.454	0.937	0.657	0.283	1.086
b-78	O-9[d,b]				0.749						0.816	0.636	0.553	1.085
b-78	O-32[g]	0.386	0.588	0.742	0.775	0.733	0.606	0.391	0.562	0.090	0.762	0.781	0.689	0.872
		***Relative Activity per gram of U^{235}* (Relative Fission Flux Distribution)**												
Inner annulus														
a-1	P-2		14.58	17.42	18.29	16.58	14.19	10.25	15.51	14.35	17.51	25.64	50.01	26.97
a-37	P-1	10.60	14.16	16.72	17.73	16.81	15.13	10.65	15.92	14.74	17.83	24.84	47.66	25.44
a-97	T-2				17.69									
a-37	T-2				17.73									
a-72	P-2	10.36	14.03	16.77	17.64	16.62	14.04	10.53	14.47	13.92	17.77	25.36	50.97	24.98
a-97	P-1	10.42	14.05	16.40	17.45	16.55	14.02	10.65	15.08	15.81	17.45	24.56	47.67	24.98
a-37	U-7[f,b]				17.73						24.74	18.05	25.59	48.13
Outer annulus														
b-1	P-4	5.66	8.50		11.45	11.07	8.83	6.20		7.33	13.03	11.63	13.57	21.05
b-78	F-2	5.65	8.72		11.07	10.33	8.44			7.31	12.72	11.71	14.22	20.52
b-155	F-4	5.79	8.71	11.10	11.54	10.94	8.99	6.44	8.28	7.01	13.05	11.97	14.37	21.33
b-209	F-2	5.62	8.61	10.62	11.20	10.58	8.71	6.26	8.44	6.89	13.01	11.49	13.38	21.03
b-78	O-9[f,b]				11.23						12.95	11.45	13.85	22.09
b-78	O-32[g]	5.82	8.63	10.78	11.24	10.63	8.50	6.09	10.69	9.60	13.18	11.54	13.96	21.12
		Relative Activity for Design Mass of U^{235}												
Inner annulus		0.515	0.688	0.813	0.862	0.817	0.735	0.517	0.735	0.681	0.940	0.797	0.766	1.101
Outer annulus		0.332	0.512	0.623	0.650	0.606	0.496	0.367	0.476	0.412	0.766	0.549	0.503	0.849

[a] Foil U-1-1 in foil position 4.
[b] Foil P-1-4 in foil position 4.
[c] Foil U-1-1 in foil position 4.
[d] Values normalized to 1.000 at a-37 position 4.
[e] Foil U-1-1 was used in P-1-4 position; this activity has been corrected for the difference in U^{235} content.
[f] Values normalized to 17.73 at a-37 position 4.
[g] The radial fuel distribution in this plate was reversed.
[h] Water gaps between fuel annuli increased 0.050 in.

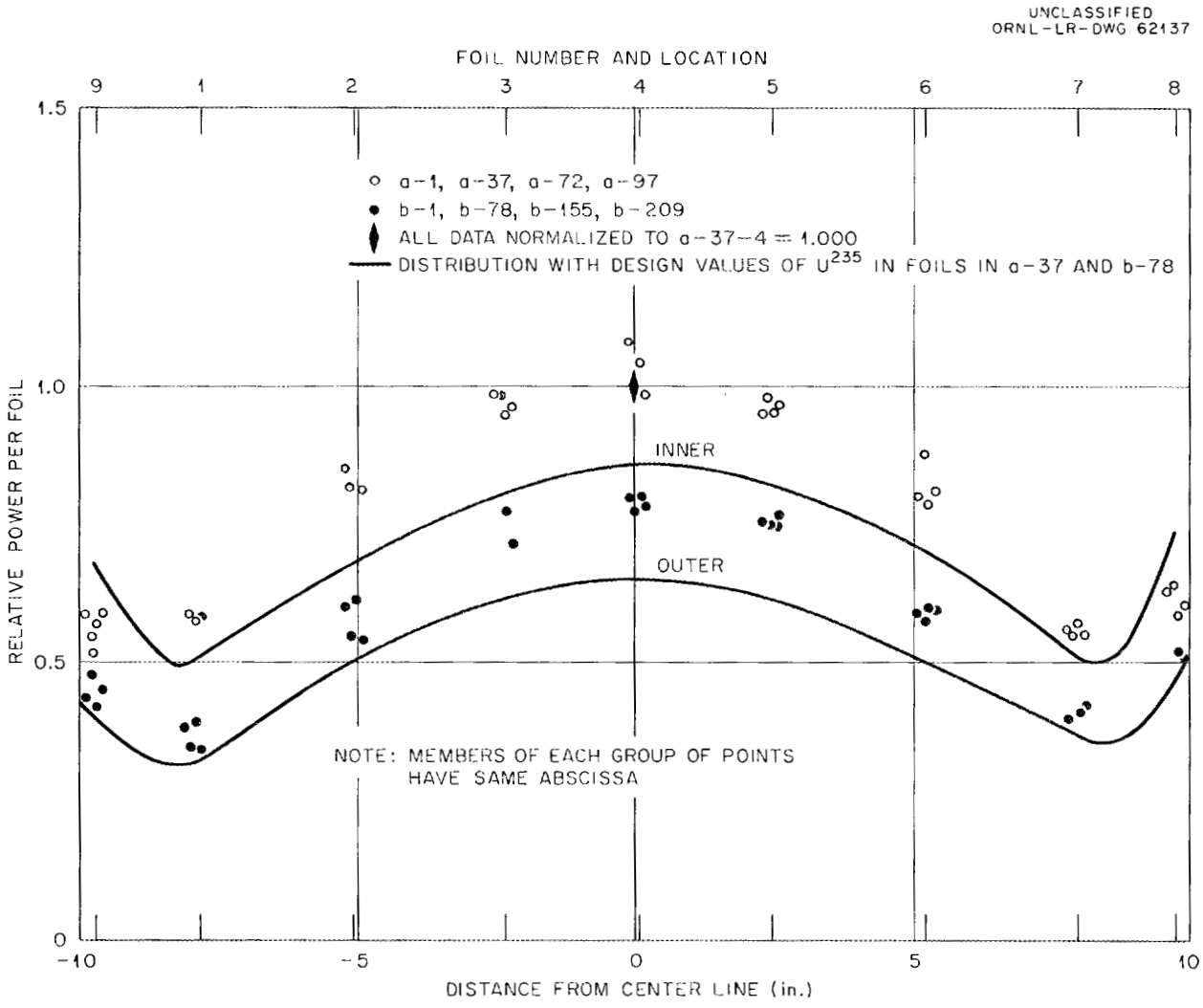

Fig. 3.4.12. Vertical Relative Power Distribution in HFIRCE No. 2.

the inner annulus fuel plate. The data obtained from the fission chamber and normalized by the foil activities are given in Table 3.4.7. In Fig. 3.4.16 this relative fission flux, normalized to unity at the center of the target region, is shown as a function of counter position. Additional foils were activated in the equatorial plane beyond the beryllium to extend the radial traverse into the water reflector. These foil data are given in Table 3.4.8 and are plotted in Fig. 3.4.17, together with the flux contours in the fuel element made with similar foils, and are not corrected for foil self-shielding and flux-depression effects.

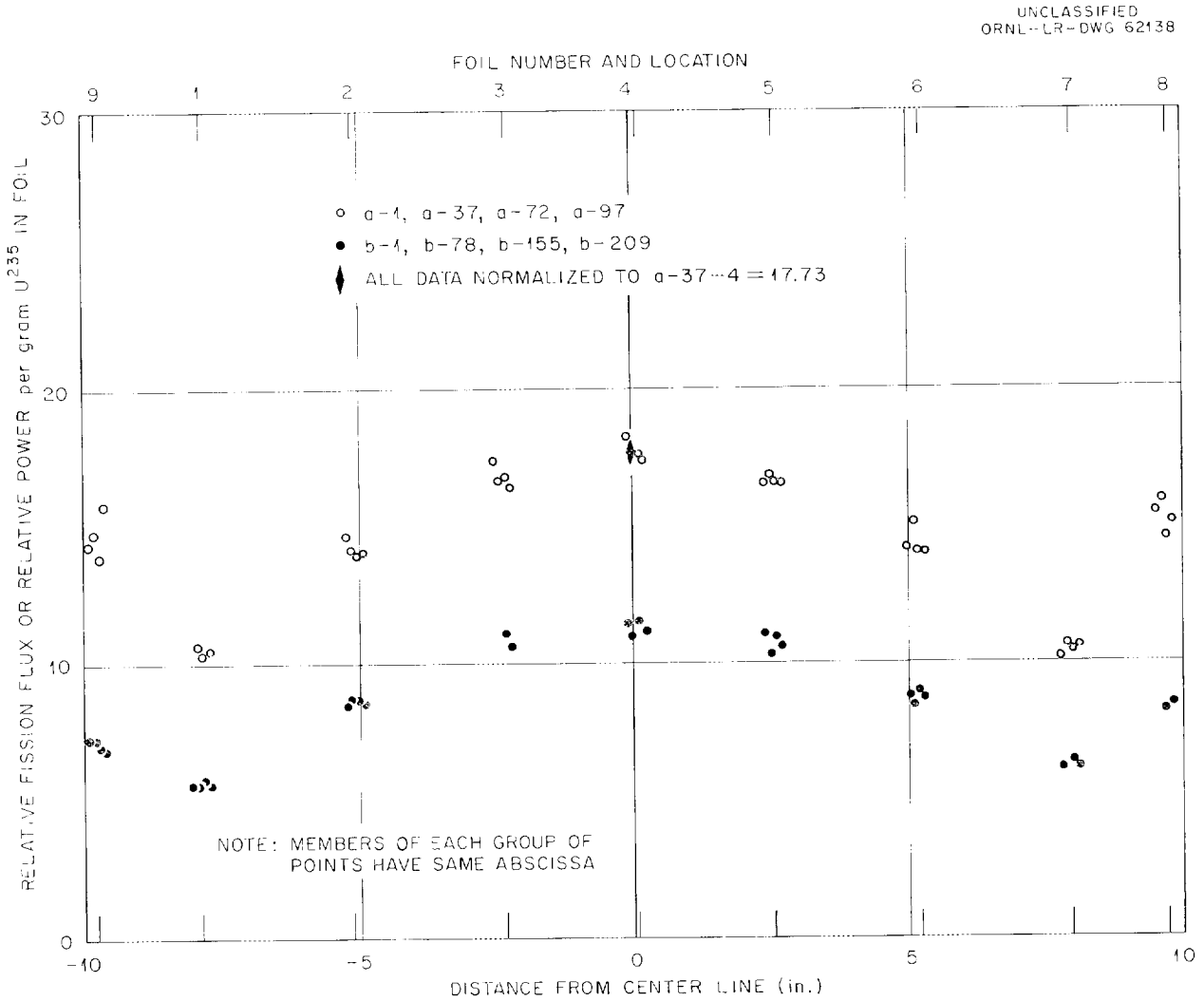

Fig. 3.4.13. Vertical Relative Fission Flux in HFIRCE No. 2.

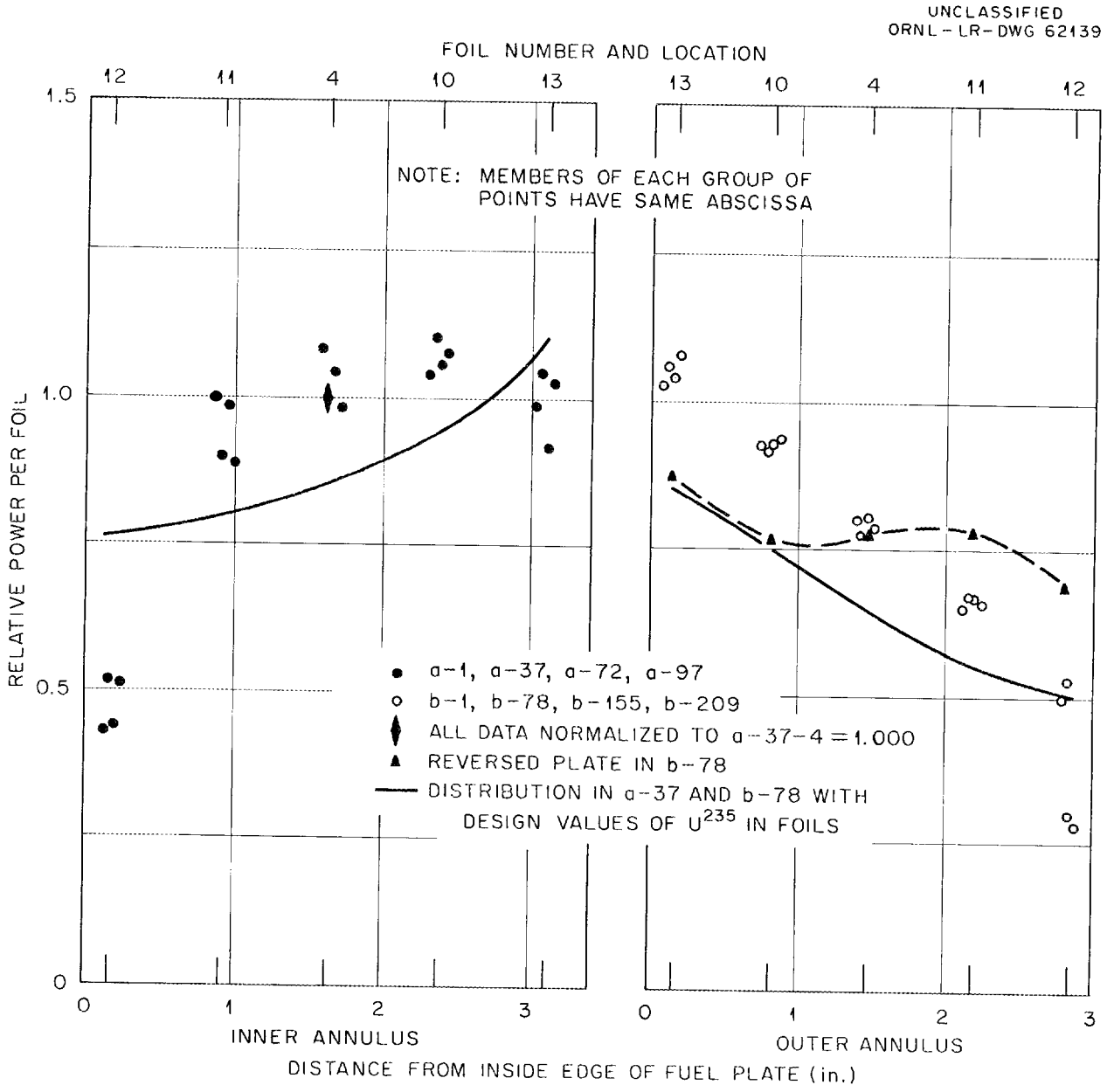

Fig. 3.4.14. Radial Relative Power Distribution in HFIRCE No. 2.

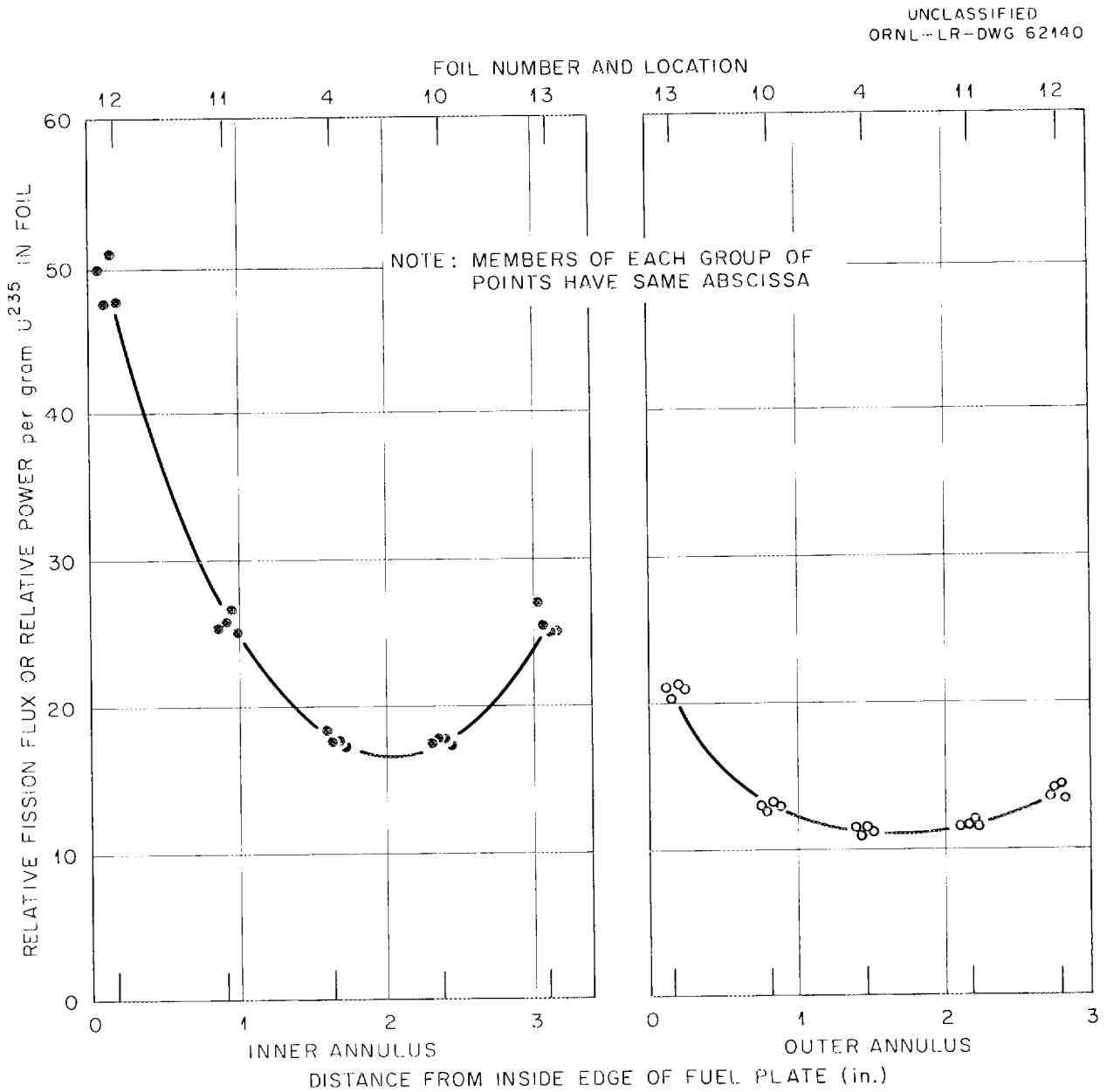

Fig. 3.4.15. Radial Relative Fission Flux in HFIRCE No. 2.

Table 3.4.7. Fission Counter Traverse in Water Reflector Below Fuel Element
(Traverse Displaced $2\frac{1}{2}$ in. from Fuel Element Axis)

Position of Center of Counter Below Fuel (in.)	Relative Count Rate	Count Rate Normalized to 0.608 at 5 in. Below Fuel	Count Rate Normalized to 1.0 at Center of Target
$8\frac{3}{8}$	1.000	0.114	0.0116
$9\frac{3}{8}$	0.628	0.0716	0.00728
$10\frac{3}{8}$	0.370	0.0422	0.00429
$11\frac{3}{8}$	0.230	0.0262	0.00266
$12\frac{3}{8}$	0.138	0.0157	0.00160
$13\frac{3}{8}$	0.0831	0.0095	0.00097
$14\frac{3}{8}$	0.0502	0.0057	0.00058
$15\frac{3}{8}$	0.0309	0.0035	0.00036
$16\frac{3}{8}$	0.0196	0.00223	0.000227
$17\frac{3}{8}$	0.0124	0.00141	0.000143
$18\frac{3}{8}$	0.00815	0.00093	0.000095
$19\frac{3}{8}$	0.00523	0.00060	0.000061
$20\frac{3}{8}$	0.00344	0.00039	0.000040
$21\frac{3}{8}$	0.00230	0.00026	0.000026
$23\frac{3}{8}$	0.00109	0.000124	0.0000126
$24\frac{3}{8}$	0.00077	0.000088	0.0000089
$25\frac{3}{8}$	0.00055	0.000063	0.0000064
$27\frac{3}{8}$	0.00027	0.000031	0.0000032

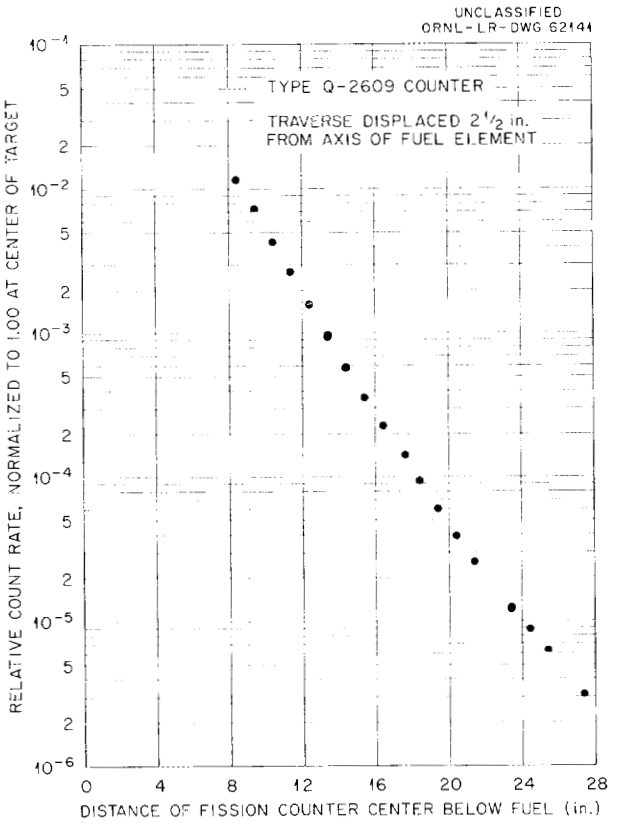

Fig. 3.4.16. Fission Counter Traverse in Water Reflector Below HFIRCE No. 2 Fuel Element.

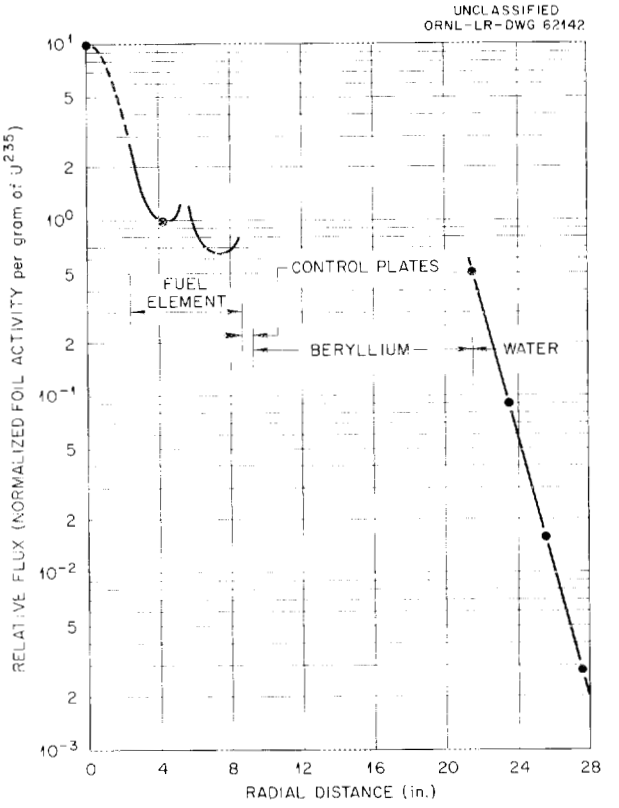

Fig. 3.4.17. Radial Flux Distribution at Midplane of HFIRCE No. 2.

Table 3.4.8. Relative Radial Fluxes from Foil Measurements

Radial Position* (in.)	Relative Flux (Normalized Foil Activity per g of U^{235})	Location
0	9.84	Center of target region
21.2	0.500	In contact with outer beryllium surface at midplane
23.2	0.0896	2 in. beyond beryllium surface at midplane
25.2	0.0158	4 in. beyond beryllium surface at midplane
27.2	0.0028	6 in. beyond beryllium surface at midplane
2.5	0.608	5 in. above the fuel (15 in. above midplane)
~4.2	1.000	Position 4 on an inner fuel plate; normalized to unity

*Measured from fuel element axis.

3.5. CRITICAL ARRAYS OF NEUTRON-INTERACTING UNITS[1]

L. W. Gilley, D. F. Cronin,* J. K. Fox, and J. T. Thomas

A series of experiments using as many as 100 subcritical vessels of U^{235}-enriched uranyl nitrate aqueous solution has been performed. In one group of experiments neither reflector about the arrays nor moderator between the units was present. (The terms "moderator" and "reflector" when used in this text refer to the addition of hydrogenous material between the units or about the array.) In another set the thickness of the moderator and partial reflector was varied to exhibit its maximum effect. Additional experiments simulated various conditions of interest to nuclear safety. A brief description of the materials used is presented, and the results appear in both tabular and graphical form.

Units and Arrays

Each unit consisted of a quantity of 92.6 wt% U^{235}-enriched $UO_2(NO_3)_2$, having an average concentration of 410 g of uranium per liter and a specific gravity of 1.55, contained in one of three different types of vessels. The Type A container was a $5\frac{3}{8}$-in.-OD seamless polyethylene bottle, approximately 48 in. long, which had a $1\frac{1}{2}$-in.-dia capped opening and a nominal capacity of ~13 liters. This container had a wall thickness which varied from 0.45 in. at the bottom to 0.20 in. at the top, resulting in a volume-averaged inside diameter of ~4.67 in. The Type B container was a $5\frac{5}{8}$-in.-OD polyethylene bottle, approximately 48 in. long, which had a wide capped opening, a welded bottom, and a nominal capacity of ~15 liters. The walls had a uniform thickness of 0.25 in. The Type C container was an aluminum cylinder. Seven of the Type C containers had a 6-in. inside diameter, a 72-in. height, and a 0.06-in. wall thickness. An additional 12 Type C containers had a 6-in. outside diameter, a 60-in. height, and a wall thickness of 0.05 in. The 6-in.-ID cylinders could be remotely filled with solution and were those used in previous interaction experiments.[2]

Units in each array were arranged with the vessel axes vertical and their bases in a linear, in a square, or in a triangular pattern. Most of the experiments with unreflected and unmoderated arrays were performed with a single tier of units, that is, with all bases in a common horizontal plane, although in one series two such tiers were arranged, one above the other, with the solution separated vertically. The outer boundary of an array was either square or hexagonal, depending upon whether a square or triangular pattern was used. Figure 3.5.1 is a photograph of a double-tier array containing 98 Type A units. The method of securing the units in the aluminum framework is clearly visible. Each unit in this array contained ~5 kg of U^{235} except for five control units located in the center of the lower tier. Criticality was achieved by remotely filling the five control units.

---

[1] A portion of this work has previously been published in *Trans. Am. Nuclear Soc.* 4, No. 1, 54 (1961).

*Present address: National Lead Company of Ohio, Cincinnati.

[2] J. K. Fox, L. W. Gilley, and A. D. Callihan, *Critical Mass Studies, Part IX, Aqueous U^{235} Solutions*, ORNL-2367 (Feb. 1958).

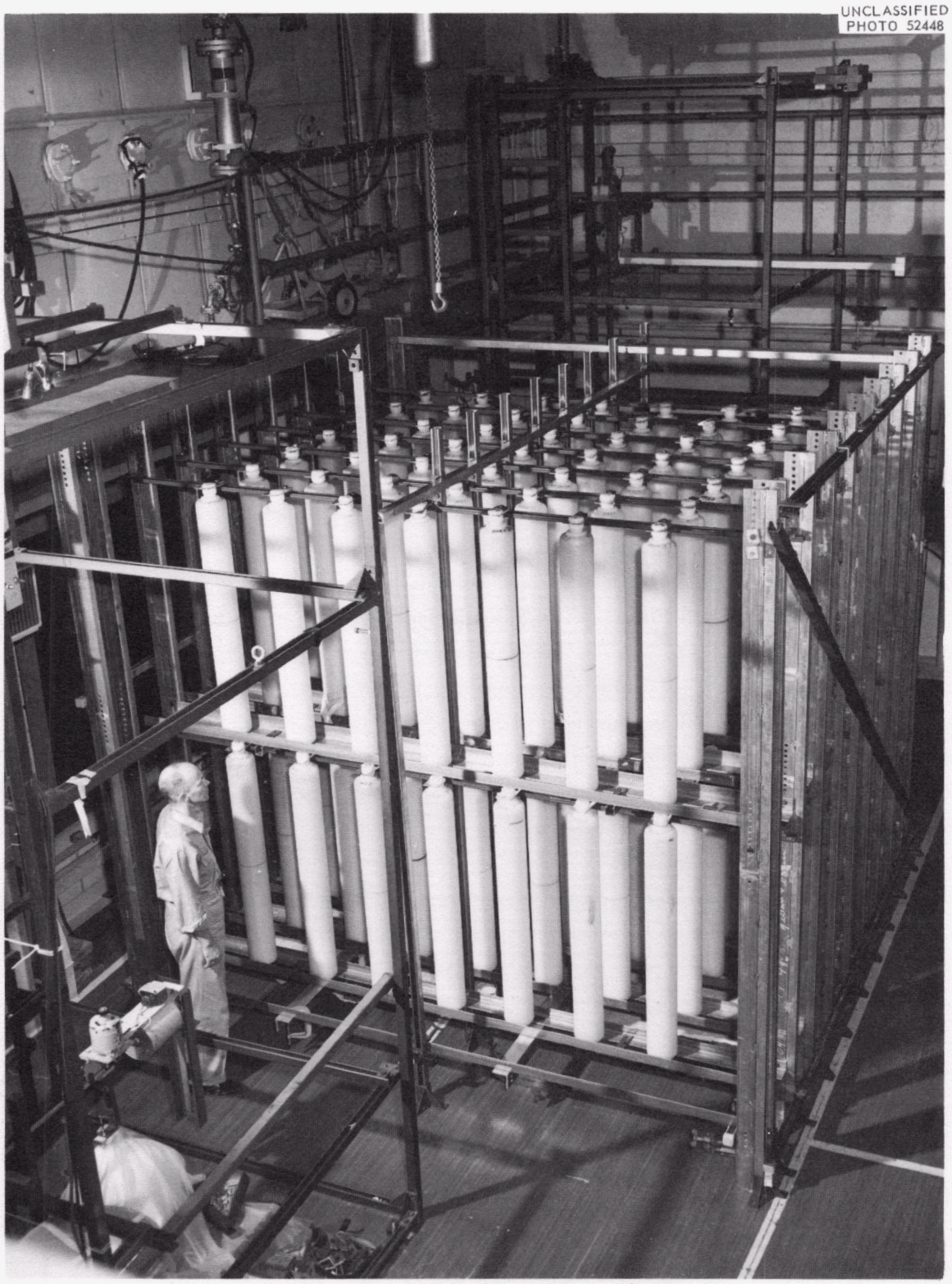

Fig. 3.5.1. Double-Tier Array of Interacting Type A Units.

Experimental Results with Type A Containers

The experiments conducted with Type A units in contact, with no moderator between units and reflector present only in the linear arrays, are summarized in Table 3.5.1. It may be seen that slightly more than 18 units in a linear arrangement against a hydrogenous reflector are required to form a critical array.

Table 3.5.1. Critical Conditions for Type A Units in Contact

Number of Units in Array	Geometry of Array	Solution Height (in.)	Comment
3		44.25	Not critical
4		44.25	Not critical
4		34.56	Critical
5		15.70	Critical
5		44.25	Not critical
19	Linear	44.25	Critical with array against a 6-in.-thick Plexiglas wall; solution height in 5 control units in center of array, 41.70 in.
18	Linear	44.25	Not critical with array against 6-in.-thick Plexiglas wall

In the unreflected and unmoderated arrays in which containers were separated, three different solution heights were used: $22\frac{1}{2}$, $33\frac{3}{8}$, and $44\frac{1}{4}$ in., corresponding to 5.90, 9.30, and 12.76 liters per unit, respectively. Thus, the variables studied were the volume content of the container, the spacing, and the geometric pattern within an array. The number of units in a critical array as a function of their surface-to-surface separation is shown in Fig. 3.5.2 for each of three different solution volumes. The data are also reported in Table 3.5.2. The results from the experiments with the double tier are plotted with ordinate equal to the number of units in one of the tiers, i.e., one half the total number at a particular spacing. In this manner a double tier is shown to have characteristics resembling a single tier but with extended solution height. It is clear that for finite arrays the triangular pattern is more reactive than the square-pattern arrays; i.e., they require a greater surface-to-surface separation.

Experiments were conducted with 16 Type A units that were reflected and moderated with Plexiglas (methyl methacrylate). For these experiments, the vessels were arranged in a 4×4 unit array with each unit containing 12.76 liters of solution. In most of the experiments the Plexiglas formed a matrix of square cells in each of which a unit was centrally located; however, in one experiment the Plexiglas was

in the form of ½-in.-thick cylindrical shells which were placed tightly around each unit in the array. The data are shown in Table 3.5.3. Included in the table, for comparison, are the number of units required to achieve criticality at the same surface-to-surface separation in the absence of Plexiglas, obtained from Fig. 3.5.2. It may be seen that a 1-in. thickness of Plexiglas centered between the units of an array effects the greatest change in the critical number. The first two entries of the table describe arrays with equal quantities of Plexiglas associated with each unit. The Plexiglas is seen to be more effective when

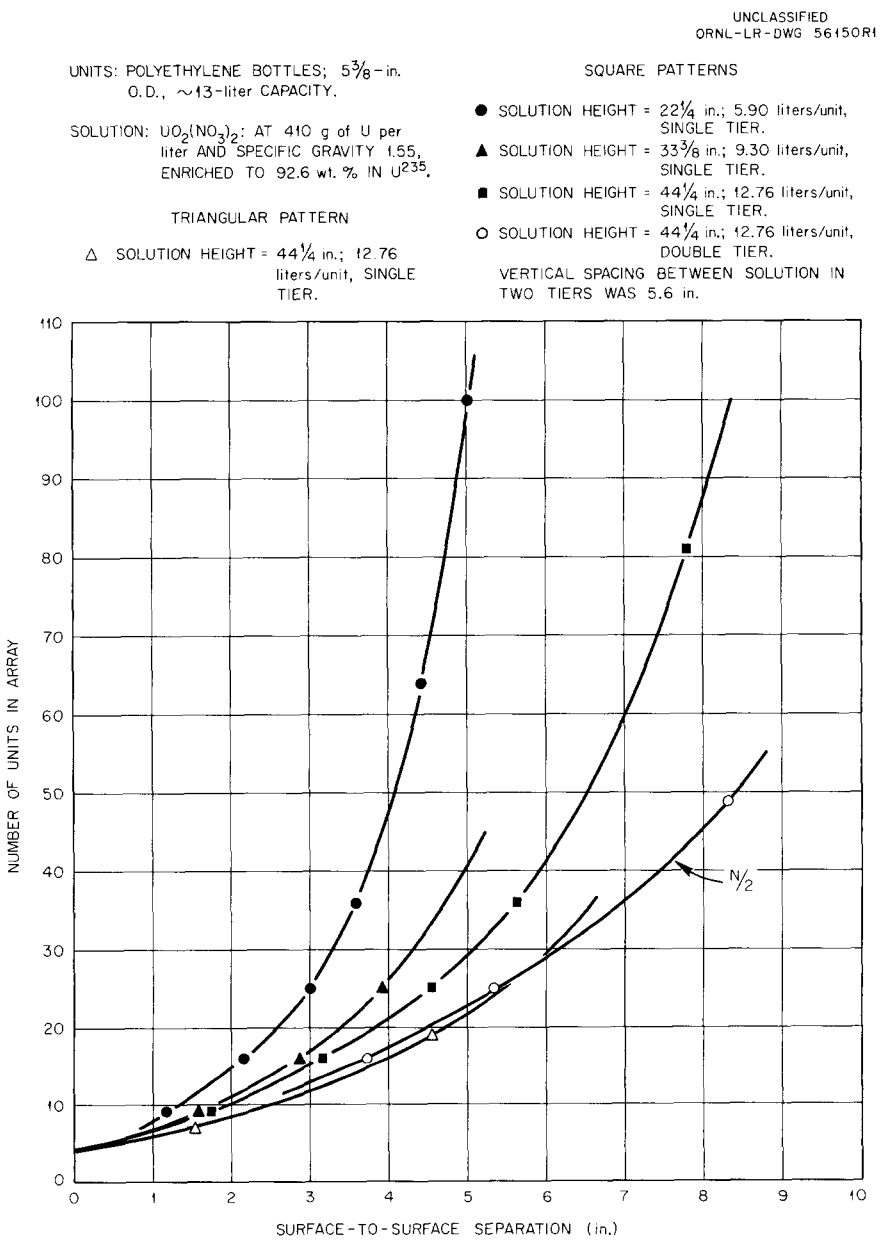

Fig. 3.5.2. Number of Type A Units in a Critical Array as a Function of Surface-to-Surface Spacing.

arranged in a matrix than when the same amount tightly surrounds the units. Later experiments, described by the last two entries in the same table, show that the presence of the ¼-in.-thick reflector is not entirely responsible for this increased reactivity.

An additional series of experiments with Type A containers was conducted in a 9.0-ft-dia by 10-ft-high stainless steel-lined tank into which water could be introduced as a moderator and a reflector. Each unit contained 12.76 liters and a constant surface-to-surface separation of 5.64 in., corresponding to the spacing required for a critical unreflected and unmoderated 6 × 6 array, was maintained. Table 3.5.4

Table 3.5.2. Critical Spacings for Type A Containers

Number of Units in Array	Geometry of Units	Surface-to-Surface Separation (in.)
	5.90 liters per Unit; Single Tier	
9	3 × 3 Square pattern	1.18
16	4 × 4 Square pattern	2.16
25	5 × 5 Square pattern	3.00
36	6 × 6 Square pattern	3.58
64	8 × 8 Square pattern	4.43
100	10 × 10 Square pattern	5.04
	9.30 liters per Unit; Single Tier	
9	3 × 3 Square pattern	1.59
16	4 × 4 Square pattern	2.89
25	5 × 5 Square pattern	3.92
	12.76 liters per Unit; Single Tier	
9	3 × 3 Square pattern	1.75
16	4 × 4 Square pattern	3.32
25	5 × 5 Square pattern	4.55
36	6 × 6 Square pattern	5.64
81	9 × 9 Square pattern	7.79
7	Triangular pattern	1.53
19	Triangular pattern	4.56
	12.76 liters per Unit; Double Tier*	
32	4 × 4 Square pattern	3.72
50	5 × 5 Square pattern	5.35
98	7 × 7 Square pattern	8.33

*Vertical spacing between solution in two tiers was 5.6 in.

Table 3.5.3. Comparison of Plexiglas-Moderated and Unmoderated Arrays of Type A Containers

Sixteen 12.76-liter units in 4 × 4 array

Configuration and Description of Plexiglas	Plexiglas Reflector	Surface-to-Surface Separation (in.)	Number of Units in Unreflected and Unmoderated Array, N'	Ratio: $\frac{N'}{16}$
0.50 in. surrounding each unit	None	(3.72+1)	~~19.2~~ 26.5	~~1.20~~ 1.66
0.50 in. centered in open space	0.25 in.	4.94	28.5	1.78
1.00 in. centered in open space	0.50 in.	5.38	33	2.06
1.50 in. centered in open space	0.75 in.	5.26	31.8	1.99
1.50 in. centered in open space	None	(4.82)*	27.3	1.71

*Interpolated value.

Table 3.5.4. Effect of Water as a Moderator and Reflector on a Critical Array of Type A Units

Surface-to-Surface Separation 5.64 in.

Number of Units in Array	Geometry of Array	Solution Height in 5 Control Units (in.)	Comments
36	6 × 6	44.25	Outside tank; no water reflector or moderator
36	6 × 6	29.03	Inside tank; no water reflector or moderator
30	5 × 6	34.67	Inside tank; bottom reflector only and no moderator
36	6 × 6	44.25	Inside tank; subcritical fully submerged
32.6	5 × 6 + 2.6	39.70	Inside tank; no water reflector or moderator
32	5 × 6 + 2	39.16	Inside tank; water sprayed at 66.8 liters/min

summarized the results. The first three entries indicate that a full array of 36 filled containers in the tank would be supercritical. Although these units are subcritical when submerged at this spacing, interaction between subcritical units has been observed[2] up to distances slightly less than 12 in. The last two entries evaluate the effect of water being sprayed by a nozzle centered about 3 ft above the array. The reactivity value of water being introduced at this rate is less than that of an additional unit.

Experimental Results with Type B Containers

Experiments were performed with the solution in the Type B plastic cylindrical containers at a constant height of 22¼ in., corresponding to 7.41 liters per unit. The units in all arrays were arranged in a square pattern and were unreflected and unmoderated. The number of units in a critical array as a function of surface-to-surface separation is presented in Table 3.5.5 and Fig. 3.5.3. The results of the experiments with Type A units at a solution height of 22¼ in. are reproduced in Fig. 3.5.3 for comparison. The data show that the increased solution content of the Type B units requires an increase in spacing over that for the Type A units for the same uniform solution height. The result of altering the over-all geometry of the array from a square to a rectangle is seen to require a decrease in the surface-to-surface separation, as illustrated by the two cases of 3 × 8 and 3 × 9 arrays. The effect of introducing a plastic liner into the Type B units, thus reducing the inside diameter of the units to ~4.7 in., which approximates the inside diameter of the Type A unit, is to require a decrease in surface-to-surface separation. Although the diameters and heights of the contained solutions were approximately the same, the two arrays are observed not to be equivalent because of the increased amount of plastic among the Type B units and the slightly larger solution volume of the modified Type B units, 6.33 liters per unit compared to 5.90 liters per unit for Type A units.

Table 3.5.5. Critical Spacings for Type B Units

7.41 liters per unit

Number of Units in Array	Geometry of Array	Surface-to-Surface Separation (in.)
9	3 × 3	1.43
16	4 × 4	2.60
36	6 × 6	4.25
64	8 × 8	5.32
27	3 × 9	2.82
24	3 × 8	2.80
16*	4 × 4	2.34

*Plastic liner 0.20 in. thick inside bottle, resulting in a contained volume of 6.33 liters per unit.

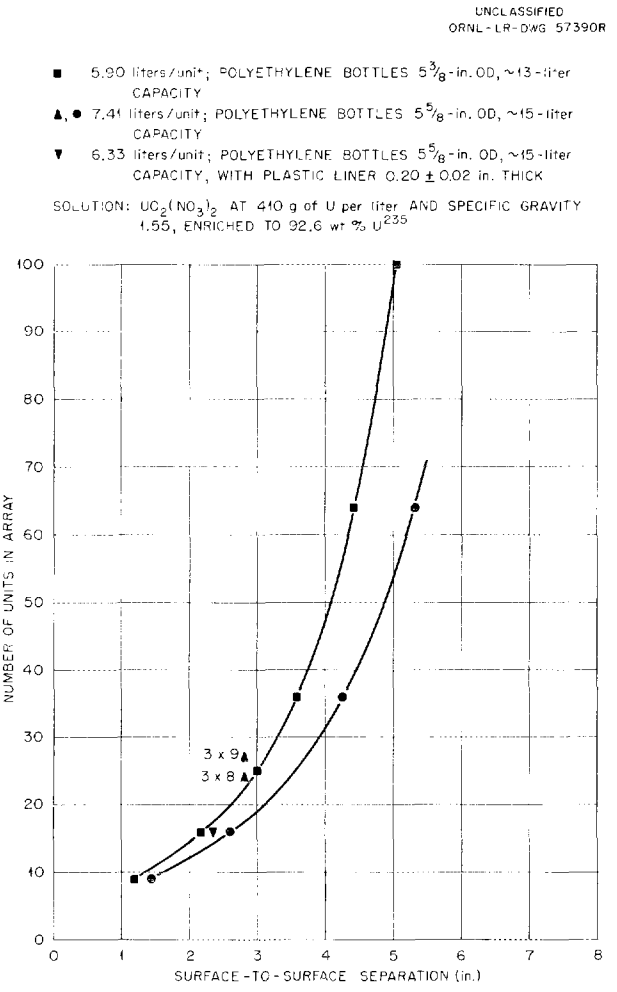

Fig. 3.5.3. Number of Type B Units in a Critical Array as a Function of Surface-to-Surface Spacing.

Experimental Results with Type C Containers

The experimental results obtained with aluminum cylinders are presented in Table 3.5.6. All arrays were unreflected, unmoderated, and single tier only. Both triangular- and square-pattern arrays were assembled. The 6-in.-ID cylinders are more reactive than the 6-in.-OD cylinders, as expected. This was confirmed by experiments which compared two 3 × 3 arrays, containing in one case seven and in the other only three 6-in.-ID cylinders.

Table 3.5.6. Critical Spacings for Type C Units

● = Remotely Filled Units, 6-in.-ID
o = Fixed-Volume Units, 6-in.-OD

Number of Units in Array	Geometry of Array	Uniform Solution Height in Array (in.)	Surface-to-Surface Separation (in.)
4	●● ●●	26.33	0.15
4	● ● ● ●	42.8	0.38
7	●● ●●● ●●	9.76	0.15
		15.40	1.00
		27.47	2.00
		39.16	2.50
19	ooo o●●o o●●●o o●●o ooo	20.00	3.51
		30.00	4.95
		40.00	5.94
		50.00	6.64
9	●●o ●●● o●●	21.67	1.70
		30.65	2.30
		40.01	2.70
		49.60	3.00
9	ooo ●●● ooo	20.26	1.50
16	oooo ●●●● oooo oooo	20.00	2.58
		30.00	3.77
		40.08	4.50
		50.40	5.00

3.6. NEW CRITICAL EXPERIMENT MACHINES

E. R. Rohrer, W. C. Tunnell, and D. W. Magnuson

Two new critical-experiment machines were recently installed and operated in the Oak Ridge Critical Experiment Facility. Both devices utilize the split-table technique for combining subcritical amounts of solid fissionable material into critical assemblies by controls operated in a shielded area.

One of the machines, identified as the Criticality Testing Unit (CTU), was designed for critical experiments on unmoderated metal systems with minimal reflection from the support structure and the room. Existing equipment was not suited to this type of program because of the large mass of the supporting members and the slow speed of separation, especially since the separation of components is the only safety mechanism proposed for the systems to be studied.

The CTU consists primarily of two tables: a fixed table which is manually adjustable in elevation, and a vertically movable platform powered by an air-actuated hydraulic system to bring the parts of an assembly together. The fixed table, which constitutes the upper section of the unit, is a circular stainless steel membrane, 24 in. in diameter, clamped in an aluminum tension ring and set in an aluminum frame supported by vertical legs at the corners of a 4-ft square. Thicknesses of the membranes that have been constructed range from 0.005 to 0.025 in. The table elevation may be varied from 6 to 8 ft above floor level. The movable platform support device is shown schematically in Fig. 3.6.1. The platform itself is an 18-in.-dia by 1-in.-thick circular stainless steel plate attached to the magnet housing. In some experiments the lower section of the critical assembly will rest upon a low-density structure, mounted on this platform, in order to further reduce neutron reflection.

During normal operation the magnet is energized and the platform follows the motion of the hydraulic cylinder piston. Full travel is 24 in., at a maximum lift rate of 34 in. per minute without load. This rate may be decreased by throttling the hydraulic flow, as the table nears its upper limit, to speeds of the order of $\frac{1}{2}$ in. per minute, permitting safe combination of test pieces mounted on the tables. The minimum lowering rate of the platform exceeds the maximum rise rate and is 40 in. per minute. Magnet characteristics limit the permissible load on the movable platform to 500 lb. With this load the maximum rise rate is 16 in. per minute and the lowering rate is 58 in. per minute.

Two safety mechanisms are used in the CTU. When an emergency condition occurs, the magnet is de-energized and the platform drops at least 6 in. under gravity. Separation of the sections of the assembly is also effected by a reversed hydraulic force on the piston, provided by oil under high pressure, which moves the piston through its total downward displacement in less than 2 sec. A characteristic scram performance curve is shown in Fig. 3.6.2. The motion over the first 9 in. of travel is essentially free fall. At the end of this initial interval, contact is made between the platform and the nylon bumper attached to the top of the piston rod, so that ensuing motion is governed by the hydraulic system. Downward motion begins about 35 msec after initiation of the signal to the electrical circuits. This delay depends, of course, upon the load and the magnet current. Minimal release time can be achieved for a particular load by adjusting the magnet current; a value as low as 18 msec has been measured.

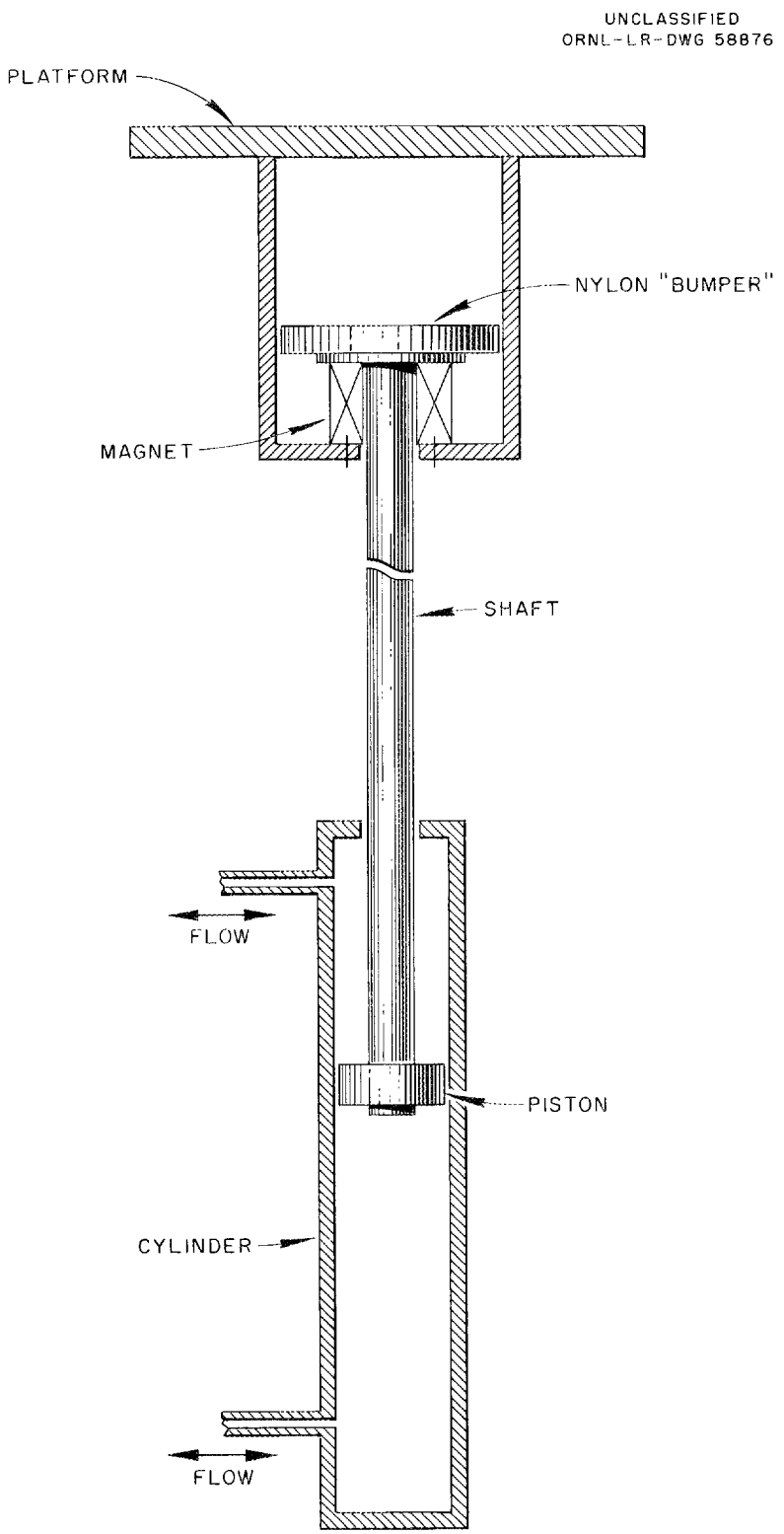

Fig. 3.6.1. Schematic of Criticality Testing Unit Magnetohydraulic Support Device.

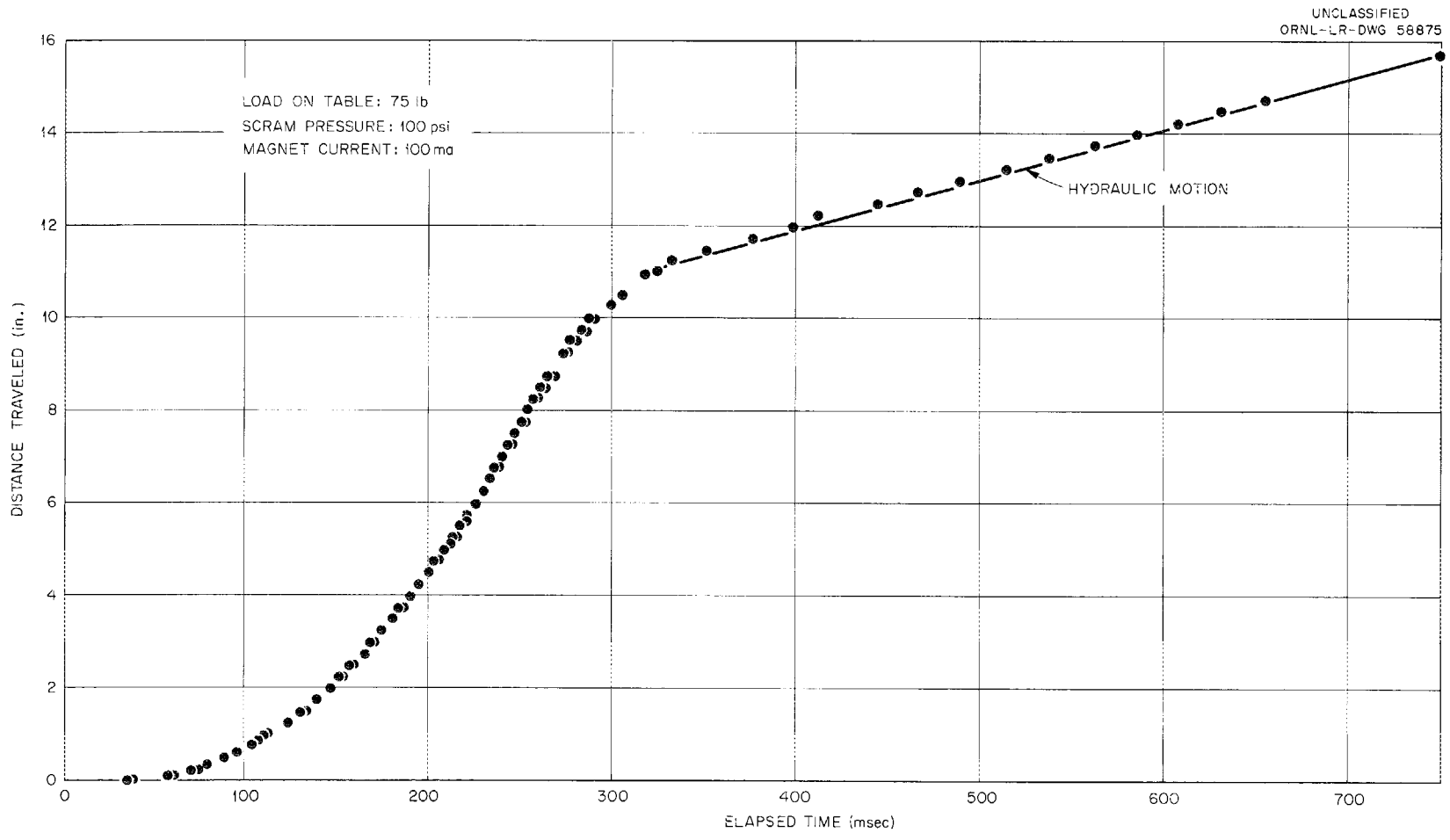

Fig. 3.6.2. Characteristic Scram Performance Curve of the Criticality Testing Unit.

Initial accelerations greater than 1 *g* are possible through the hydraulic action, although in experiments in which the assembly consists of simply stacked components such rapid motion undesirably disturbs the assembly, particularly during the daily test of the safety system.

The second critical-experiment machine, designated as the Split Table Apparatus, consists of two tables, a stationary one, 6 × 6 ft, and a movable one, 4 × 6 ft, both in the same horizontal plane. Each table is designed for a maximum deflection of 0.005 in. under a load of 2000 lb. The maximum table separation is 54 in.

The movable table is firmly fastened to the piston rod of a combination air-hydraulic cylinder which is the prime mover for the complete 54-in. travel. The piston of this cylinder is actuated by low-pressure air during normal motions and its speed is governed primarily by the resistance to flow of the oil in the closed hydraulic system. The cylinder is designed so that the return stroke, even under normal operation, is faster than the forward stroke. High-pressure air, employed during emergency (scram) conditions, effects a much greater speed of component separation.

The rate of forward motion is adjustable, by a manual regulating valve in the hydraulic lines, to a maximum of about 30 in. per minute under the normal operating air pressure of 20 psi. The rate of advance over the final 16 in. of travel to closure is further limited by a retarding block which is moved, in turn, at a continuously decreasing rate by a mechanism similar to that embodied in a "scissors-jack." The mechanism consists of a screw and nut, driven by a constant-speed motor and mounted perpendicularly to the direction of table travel. Translatory motion of the nut is transferred to the retarding block, guided in the direction of table travel, by a linking arm. The speed of the nut and its position on the

UNCLASSIFIED
ORNL-LR-DWG 61173

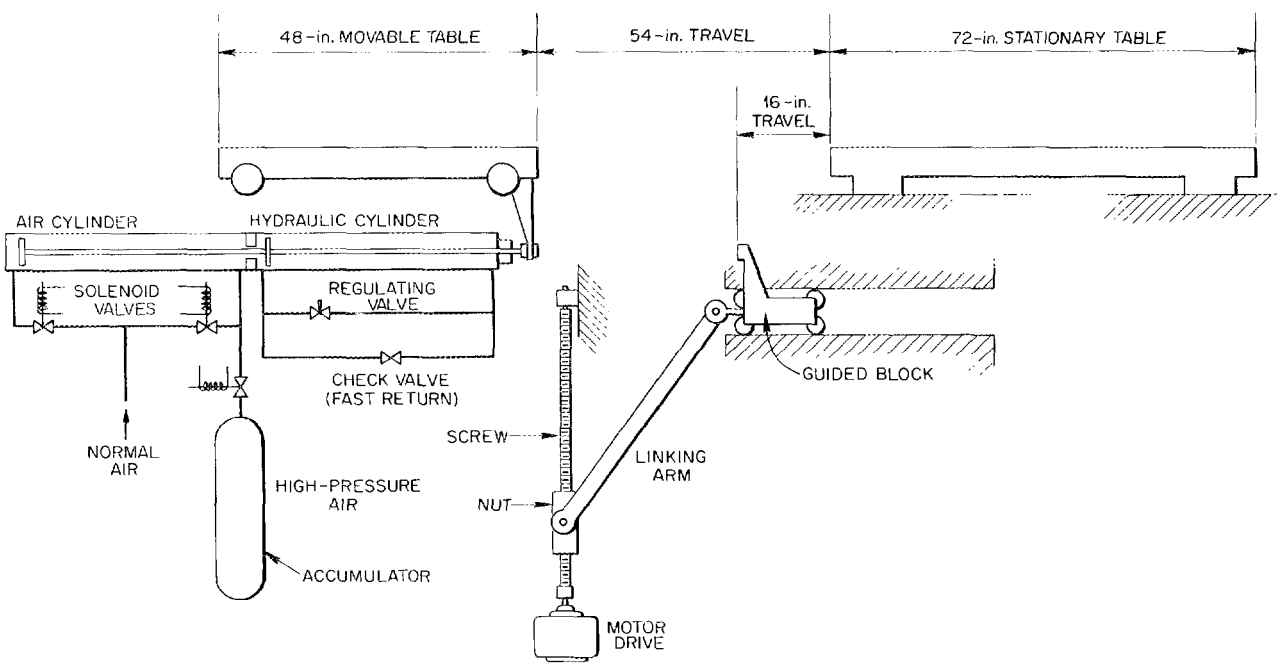

Fig. 3.6.3. Schematic of Drive Arrangement for Split-Table Machine.

screw determine the speed of the block. The maximum speed of the block, 11 in. per minute, occurs when the tables are separated 16 in. and the nut is farthest from the line of motion of the block. As the nut advances, the block speed decreases to 0.44 in. per minute at table closure. About 7 min is required for this displacement. Figure 3.6.3 is a sketch of the drive arrangement, showing the scissors-jack mechanism and linkage.

In operation, the table is moved forward at a fixed rate by the piston rod until it makes contact with the guided block, at which time interlocks allow a motor to rotate the screw. The retarding block and the table, since they are in contact, are allowed to move at a rate dependent on the location of the nut. With this arrangement, the table is held constantly against the block during forward motion but is free to

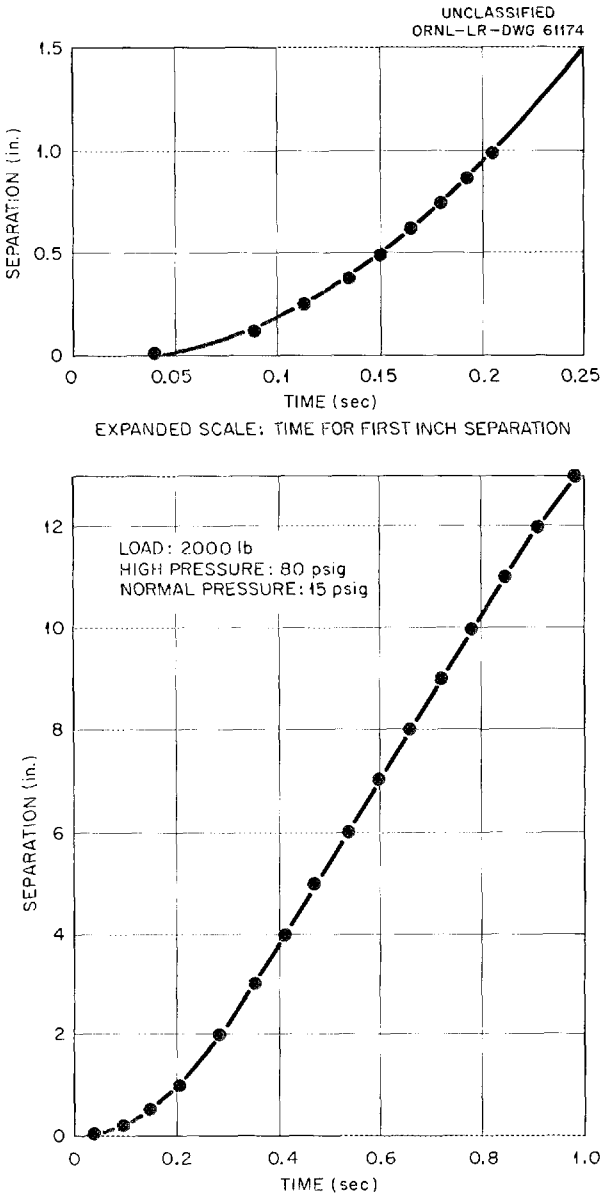

Fig. 3.6.4. Characteristic Scram Performance Curve of Split-Table Machine.

move back from the block and from the fixed table at any time. When it is required to separate the tables quickly, high-pressure air from an accumulator is introduced into the return side of the air cylinder. A typical rate of separation with an 80-psi scram pressure and a 15-psi normal operating pressure, shown on Fig. 3.6.4, was observed with a 2000-lb load on the movable table. Under these conditions the table moved about 1 in. in 200 msec and 13 in. in 1 sec.

3.7. EQUIPMENT FOR TIME-DEPENDENT NEUTRON STUDIES AT THE CRITICAL EXPERIMENT FACILITY

D. W. Magnuson and J. T. Mihalczo

A 150-kv positive-ion accelerator, recently acquired by the Critical Experiment Facility,[1] is being used to produce 14-Mev neutrons by bombarding a thick tritium target with deuterium ions. The maximum yield is at a rate of $\sim 10^{10}$ neutrons/sec. A postacceleration ion beam deflection method is used to produce neutron bursts. Two variations of the method are available. In the first, the burst width and repetition rate vary continuously from 1 to 10^4 μsec and from 10 to 10^5 cycles/sec, respectively. In the second, fixed-frequency (50 and 500 kc) sine wave voltages of various amplitudes are used to produce neutron bursts as short as 0.7 and 0.06 μsec, respectively. A background neutron production rate of less than 10^{-4} of the rate when the beam is on target is achieved by a secondary deflection scheme which bends the pulsed beam onto the target. This scheme became necessary when initial tests showed evidence of an accelerated but neutral beam that was undeflected by the deflection plates. Without secondary deflection there was a background ratio of ~ 0.02.

A Technical Measurement Corp. Model CN-110 multichannel analyzer, with plug-in logic controls for pulse-height analysis and pulsed-neutron time analysis, operates in a time-analysis mode when the varying frequency pulsing method is used. Channel widths are variable from 10 to 2560 μsec. Data printout and punched-tape output are accomplished with a Monroe M-205 coupled to the analyzer.

For the fixed-frequency pulsing, the pulse-height analyzer is used with a time-to-pulse-height converter built by the ORNL Instrument Department according to specification Q-1813-4A.

The equipment will be used for reactivity and buckling studies on geometrically simple assemblies of fissionable materials as well as for studies of reactor mockups such as the High Flux Isotope Reactor Critical Experiment No. 2. Mixtures of UF_4, containing uranium of 2 and 3 wt% U^{235} enrichment, and paraffin are presently being studied with the variable-frequency pulsing system. A typical arrangement is shown in Fig. 3.7.1. The fixed-frequency system was used in conjunction with the Fast Burst Reactor mockup, but modifications to the electronics are necessary to obtain interpretable data.

[1] The accelerator was purchased from Texas Nuclear Corporation, Austin, Texas.

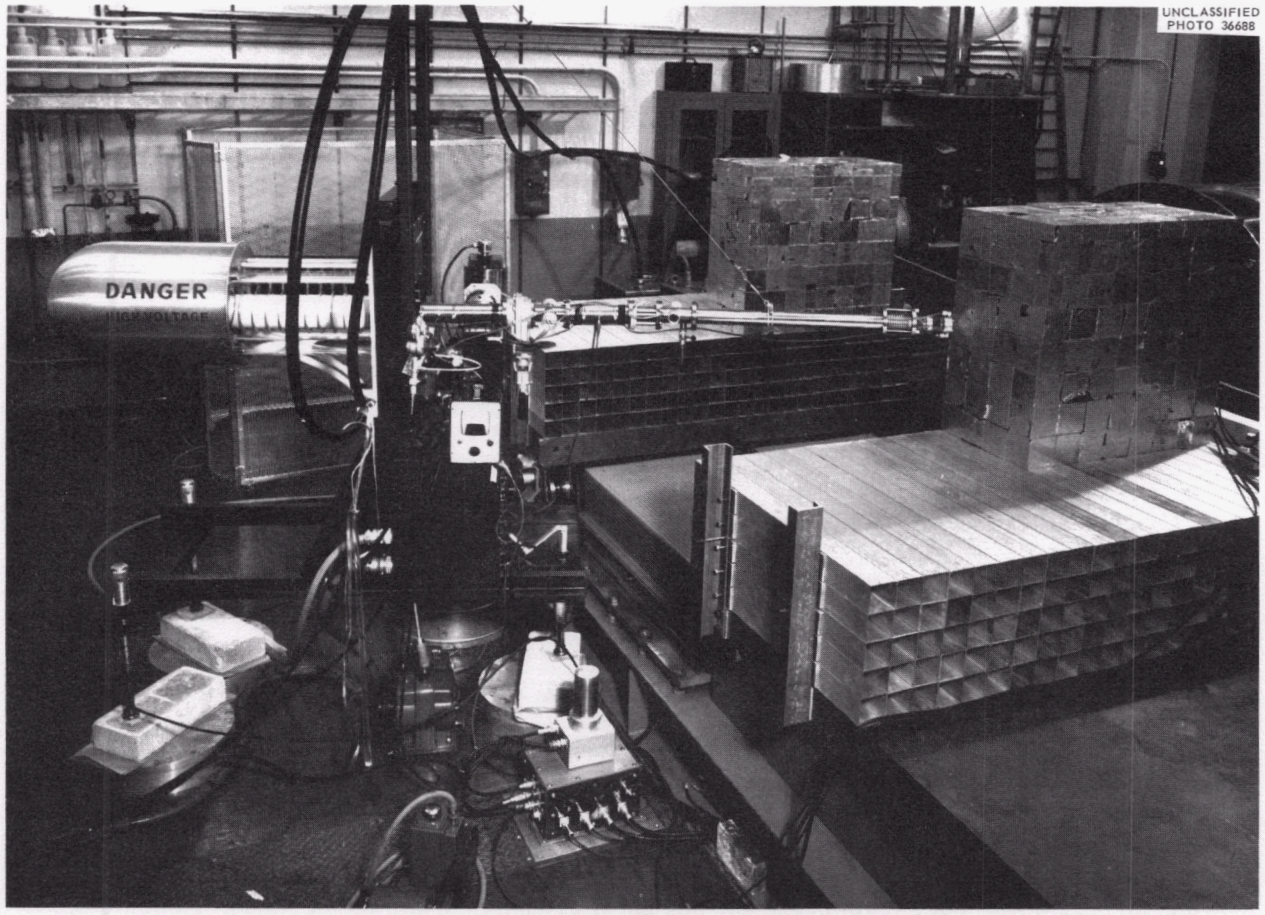

Fig. 3.7.1. Typical Experimental Arrangement for Time-Dependent Neutron Studies.

3.8. CRITICAL EXPERIMENTS AND CALCULATIONS ON THE ORNL FAST BURST REACTOR

W. E. Kinney and J. T. Mihalczo

Critical masses and void coefficients of reactivity of three unmoderated, unreflected assemblies and the critical masses of ten unmoderated, reflected assemblies have been determined at the ORNL Critical Experiment Facility to support the design of the ORNL Fast Burst Reactor, an unmoderated and unreflected research reactor capable of producing intense bursts of fast neutrons. Multigroup and one-group transport theory calculations, as well as perturbation theory calculations, have been performed to predict the results of the experiments with the unreflected assemblies. Details are given elsewhere.[1]

[1] W. E. Kinney and J. T. Mihalczo, *Oak Ridge National Laboratory Fast Burst Reactor: Critical Experiments and Calculations*, ORNL-CF-61-8-71 (in press).

Part 4

EXPERIMENTAL NUCLEAR PHYSICS

4.1. NEUTRON CAPTURE CROSS SECTION OF GOLD AT 30 AND 64 kev

L. W. Weston and W. S. Lyon[1]

The capture cross section of gold has been measured with kinematically collimated neutrons from the $Li^7(p, n)Be^7$ and $T(p, n)He^3$ reactions. The cross sections at 30.2 and 63.9 kev were found to be 0.767 ± 0.060 and 0.456 ± 0.040 barn, respectively. Details have been published elsewhere.[2]

[1]Chemistry Division.
[2]*Phys. Rev.* 123, 3, 948 (1961).

4.2. NEUTRON RADIATIVE CAPTURE MEASUREMENTS

R. C. Block,[1] F. C. VonderLage,[2] and L. W. Weston

Additional radiative capture measurements have been carried out with the 28-in.-dia spherical liquid scintillator installed at the 11.5-m flight station of the ORNL fast chopper. The M1 high-intensity chopper was used for these measurements at a rotor speed of 9500 rpm, resulting in a resolution of 0.17 μsec/m. The elements measured lie in the intermediate to heavy atomic weight range, and the data cover the transition range from low energies, where the capture cross section is almost exclusively due to *s*-wave neutrons, to kev energies, where *p*-wave contributions become important. Details are presented elsewhere.[3]

[1]Physics Division.
[2]Directors Division.
[3]R. C. Block, F. C. VonderLage, and L. W. Weston, *Phys. Div. Ann. Prog. Rep. Feb. 10, 1961*, ORNL-3085, p. 48.

4.3. THE MEASUREMENT OF α AS A FUNCTION OF ENERGY

G. deSaussure, L. W. Weston, J. D. Kington,
R. D. Smiddie, and W. S. Lyon[1]

Introduction

One of the most important parameters of reactor theory is the value of α, the ratio of the capture cross section to the fission cross section. Sufficiently precise values of this quantity now exist for the thermal energy region for the uranium isotopes,[2] and Hopkins and Diven[3] have recently measured α for U^{233}, U^{235},

[1]Chemistry Division.
[2]B. R. Leonard, Jr., *Survey of the Status of Low Energy Cross Sections of Fissile Nuclides*, HW-69342 (1961); G. J. Safford and W. W. Havens, Jr., *Nucleonics* 17 (11), 134 (1959); J. E. Evans and R. G. Fluharty, *Nuclear Sci. and Eng.* 8, 66 (1960).
[3]J. C. Hopkins and B. C. Diven, *Bull. Am. Phys. Soc., Ser. II* 5, 494 (1960).

and Pu^{239} with monoenergetic neutrons at 30 kev, 65 kev, and > 150 kev. In the important energy region from 1 ev to 30 kev, however, no reliable data exist,[4] and a series of experiments intended to accurately measure the value of α for U^{233}, U^{235}, and Pu^{239} over a wide energy range has therefore been initiated. In addition to its primary use in reactor analysis, an accurate value of α of U^{235} in the kev region is expected to assist in normalization of the many existing capture cross-section measurements in this energy range. Present values disagree in absolute magnitude, owing in part to the difficulties of measuring absolute intensities of neutron beams. The fission cross section of U^{235}, however, is well established; thus an accurate value of α of U^{235} will permit a determination of the absorption cross section of U^{235}, to which other capture cross sections can then be normalized. The progress to date in this experiment includes the design and construction of a special fission chamber, a study of suitable experimental methods for various energy regions, and development of suitable detection and counting apparatus.

Experimental Method

The experimental method to be used generally throughout these experiments resembles that of Hopkins and Diven,[3] except that neutron energies will be measured by time-of-flight techniques. The method consists of simultaneously measuring neutron absorptions and neutron-induced fissions within a sample, detecting the absorptions by the resulting gamma rays. If the gamma-ray detector and the fission counter both have efficiencies close to unity, then the ratio of the number of absorptions in anticoincidence with fission to those in coincidence with fission is equal to α, after proper correction for background. Three plans will be followed. In the first, α for U^{235} will be measured at 30 ± 7 kev and at 65 ± 20 kev. The neutron source will be the $Li^7(p,n)$ and $T(p,n)$ reactions near threshold, using protons from a 3.5-Mev Van de Graaff. The detector will be a newly designed multiplate U^{235} fission chamber placed in the center of a 1.2-m-dia tank filled with a liquid scintillator. The second plan proposes to examine the range from ~5 kev to 150 kev for U^{233}, U^{235}, and Pu^{239}. Thick samples will be placed at the center of a 1.2-m-dia tank of liquid scintillator poisoned with gadolinium. The bombarding neutrons will result from the $Li^7(p,n)$ reaction in a thick target, the 3.5-Mev Van de Graaff again being used. Neutron energy will be measured by time of flight. Prompt-fission neutrons will be thermalized in the scintillation tank and subsequently captured in the gadolinium, resulting in a detectable gamma-ray pulse in the scintillator.

Finally, for U^{235}, the energy region from 1 ev to ~20 kev will be explored with neutrons from the Rensselaer Polytechnic Institute Electron Accelerator. A multiplate U^{235} fission chamber at the center of a large tank of liquid scintillator will again be used for these measurements.

Measurements at 30 and 65 kev

Although measurements of α of U^{235} for energies of 30 ± 10 kev and 65 ± 20 kev have been made,[3] an independent measurement, utilizing a different technique to detect fissions, is justified by the importance of these values. The arrangement of the apparatus for the proposed experiments at 30 and 65 kev is shown in Fig. 4.3.1, the electronic arrangement for measuring time spectra in Fig. 4.3.2, and the

[4] J. A. Harvey, *Compilation of Requests for Nuclear Cross Section Measurements*, ORNL-CF-60-11-8 (1960); J. J. Schmidt, *Nuclear Data Requirements for Fast and Intermediate Reactor Calculations* (unpublished); S. Yiftah, D. Okrent, and P. A. Moldauer, *Fast Reactor Cross Sections*, Pergamon Press, New York (1960).

electronics for measuring pulse-height spectra in Fig. 4.3.3. A major source of difficulty inherent in the use of the large volume of liquid scintillator shown lies in the large backgrounds encountered. These backgrounds stem from cosmic rays or other outside sources, from the radioactivity of the sample, from

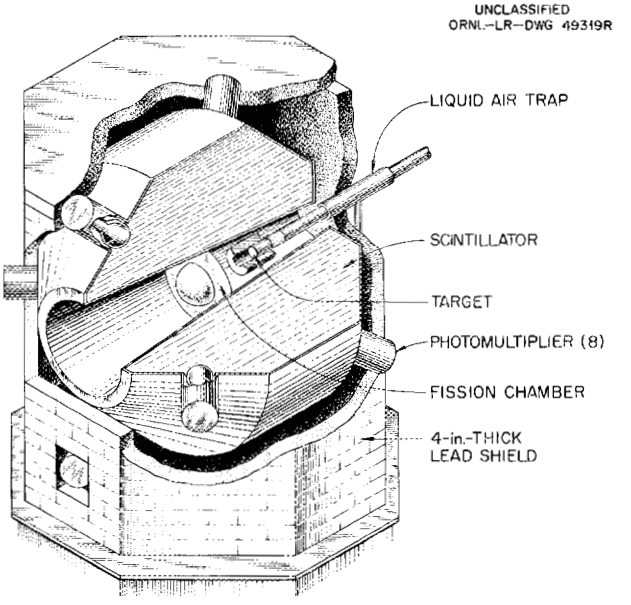

Fig. 4.3.1. Experimental Arrangement for Measurement of α at 30 and 65 kev.

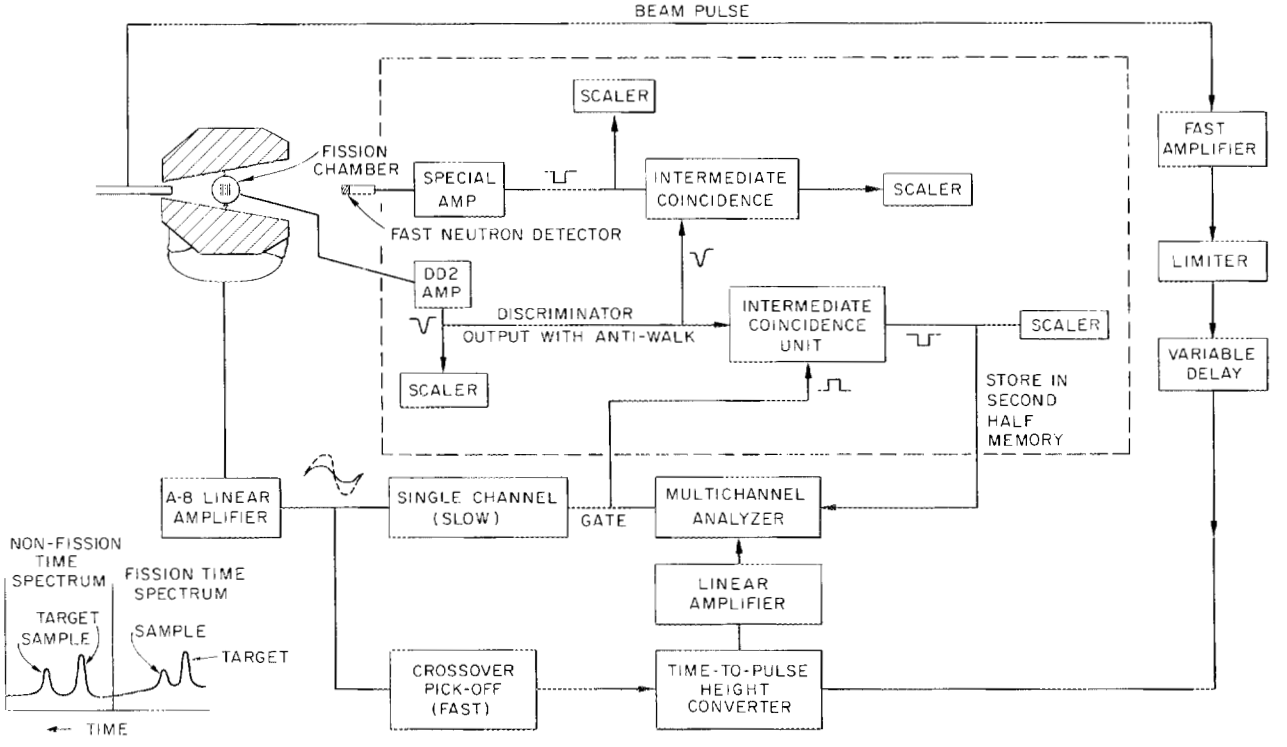

Fig. 4.3.2. Block Diagram of Electronics for Measurement of Time Spectra of Pulses in 30-kev α Experiment.

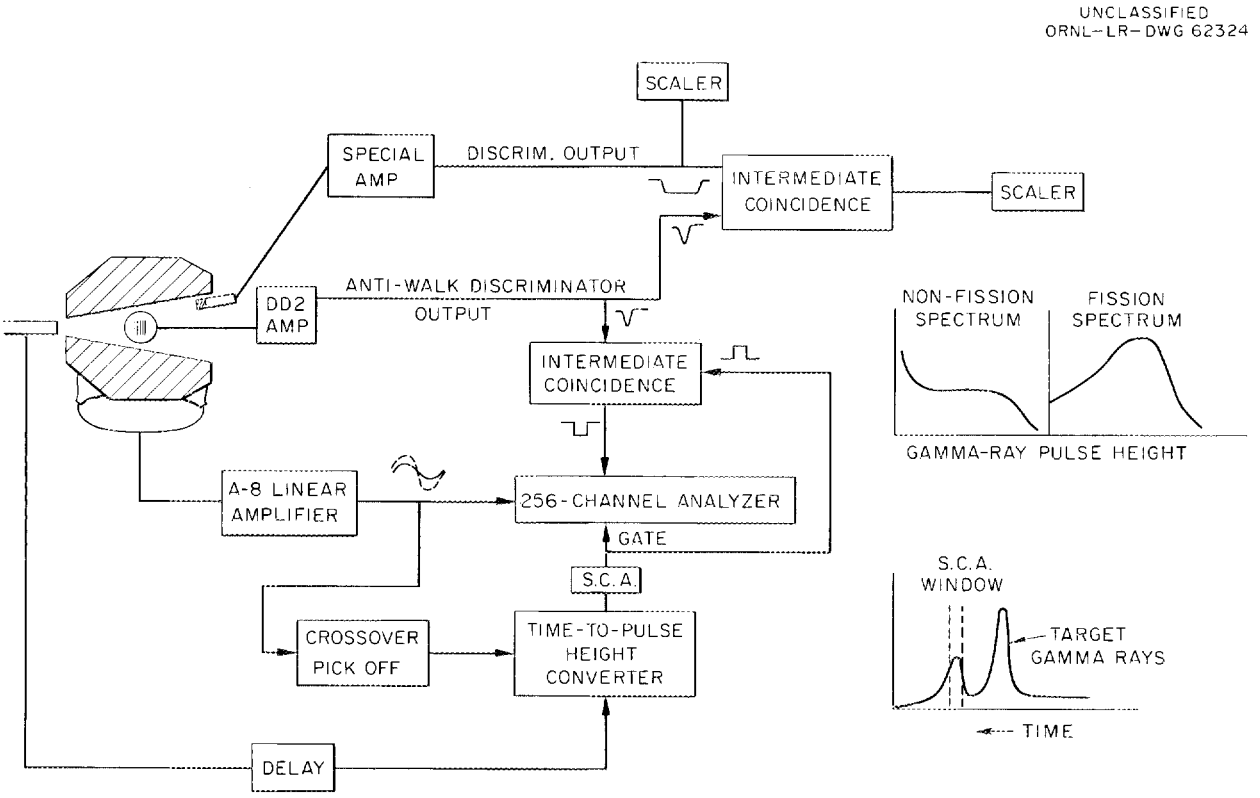

Fig. 4.3.3. Block Diagram of Electronics for Measuring Pulse-Height Spectra in Measurement of α at 30 kev.

gamma radiation born in the Li^7 target, and from capture gamma rays created in the solution, the sample, or the structural materials. From the evidence in Fig. 4.3.4, background from cosmic or other external sources is expected to be large despite the proposed 4-in.-thick lead shielding of the detector, and the addition of boron-loaded paraffin to the top and sides will probably be required. Since only a small sample of U^{235} ($\sim$5 g) will be used, background from sample radioactivity should be small. Since the radiation from the Li^7 target persists only while the proton beam is hitting the target, it will be eliminated by the time-of-flight techniques proposed. Finally, poisoning the scintillator solution with 5 liters of 3-methyl borate, in which the boron is 97 wt% B^{10}, will reduce the capture background by replacing the 2.2-Mev gamma ray from captures in hydrogen by the less bothersome 478-kev gamma ray from the $B^{10}(n,\alpha)$ reaction.[5]

The requirements for the fission chamber for these experiments were rather contradictory. In order to obtain a reasonable counting rate, a maximum quantity of U^{235} was required in the chamber; on the other hand, for time-of-flight discrimination against backgrounds and for time-of-flight neutron energy measurements, the chamber thickness had to be minimized. For high efficiency for detection of fission fragments, the maximum tolerable uranium thickness is only 1 mg/cm^2.

[5] J. H. Gibbons *et al.*, *Phys. Rev.* 122, 182 (1961); B. C. Diven, J. Terrell, and A. Hemmendinger, *Phys. Rev.* 120, 556 (1960).

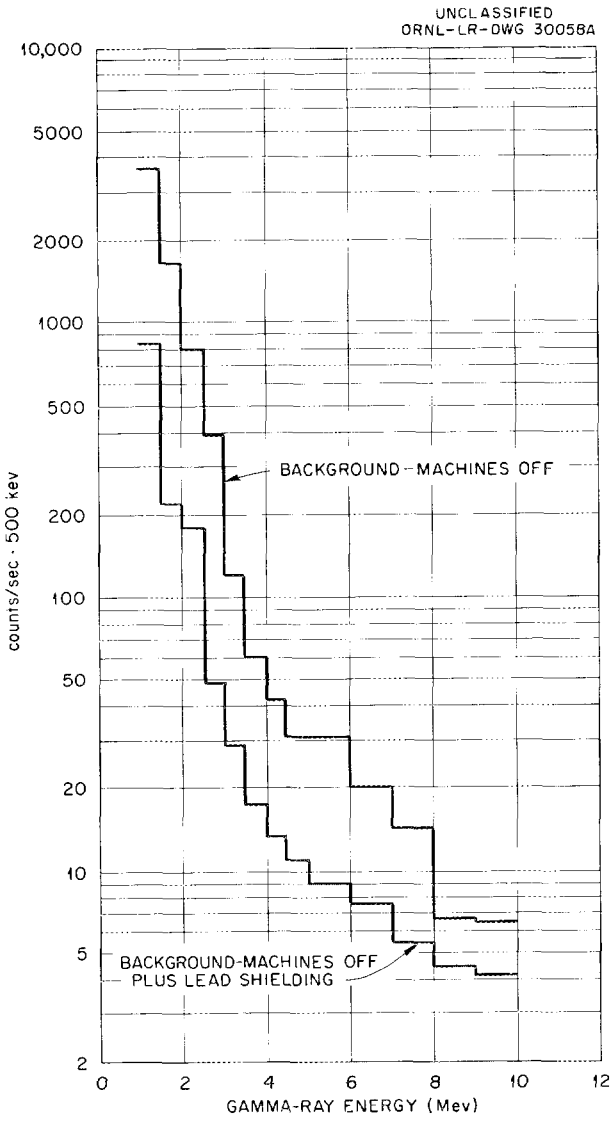

Fig. 4.3.4. Background Counting Rates in a Scintillation Tank, With and Without 4 in. of Lead Shielding on All Sides, Top, and Bottom. (After J. H. Gibbons *et al.*, Ref. 5.)

Much work has been expended on the design of a fission chamber fitting these requirements. For preliminary investigations, a set of U^{235}-coated plates was obtained from the ORNL Isotopes Division. Unfortunately these plates will not be usable for final measurements because of coating inhomogeneities. They were useful, however, in experiments to determine the feasibility of efficiently detecting fission fragments in the high background due to pile-up of alpha-particle pulses. Because of the very large electrical capacitance of the multiplate chamber, pulse-height discrimination was especially difficult. The most satisfactory of many arrangements of the dielectric regions in series and in parallel is shown in Fig. 4.3.5.

Based on this arrangement, pressure in the chamber and interplate voltage were optimized, a special charge-sensitive preamplifier and an amplifier were designed, and the time constants of the preamplifier and amplifier were carefully optimized.[5] Figure 4.3.6 shows a pulse-height spectrum obtained with the chamber

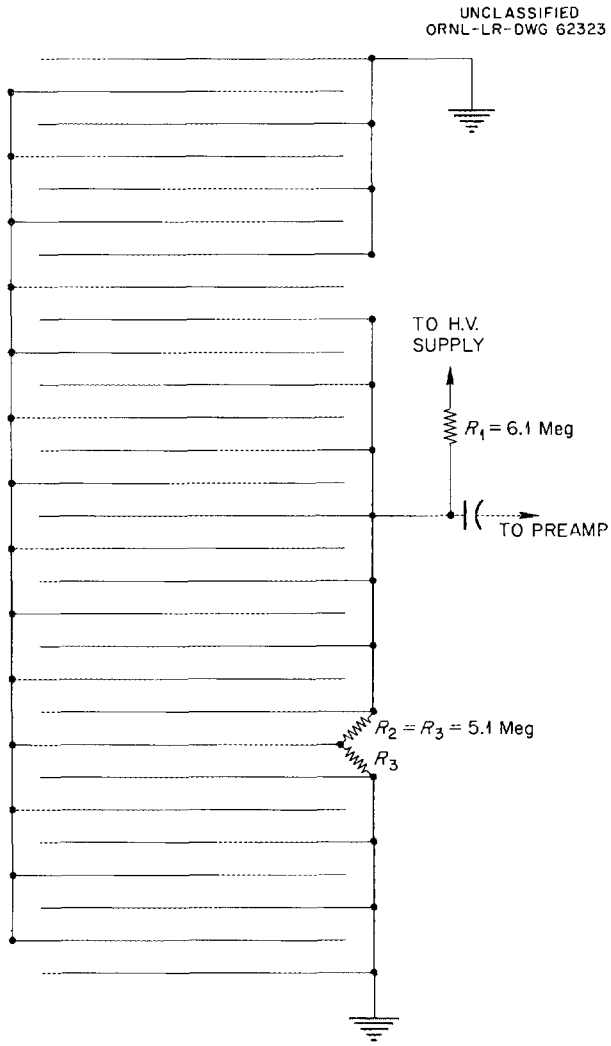

Fig. 4.3.5. Optimum Arrangement of Fission Counter Dielectrics.

in a fast-neutron field compared with the pulse-height spectrum due to the alpha particles. From the comparison it appears that with a judicious setting of the discriminator bias a detection efficiency close to 80% for fission fragments can be obtained with a counting rate due to alpha pile-up less than 10^3 counts per second.

The fission chamber finally constructed is shown in Fig. 4.3.7. It represents a compromise between the conflicting requirements, being 1 in. thick and containing about 5 g of U^{235}. The fissile material is coated on both sides (except for end plates) of 29 plates to a thickness of 1 mg/cm^2. The plates have a 4-in. outside diameter, are about 1 mm apart, and are contained in a spherical $\frac{1}{16}$-in.-thick magnesium shell.

During the series of measurements of α at 30 kev, the efficiency of the fission chamber will be determined by observing coincidences between events detected by the chamber and by the fast-neutron detector described in another part of this report.[6] The arrangement is shown in Figs. 4.3.2 and 4.3.3.

[6]Section 4.4.

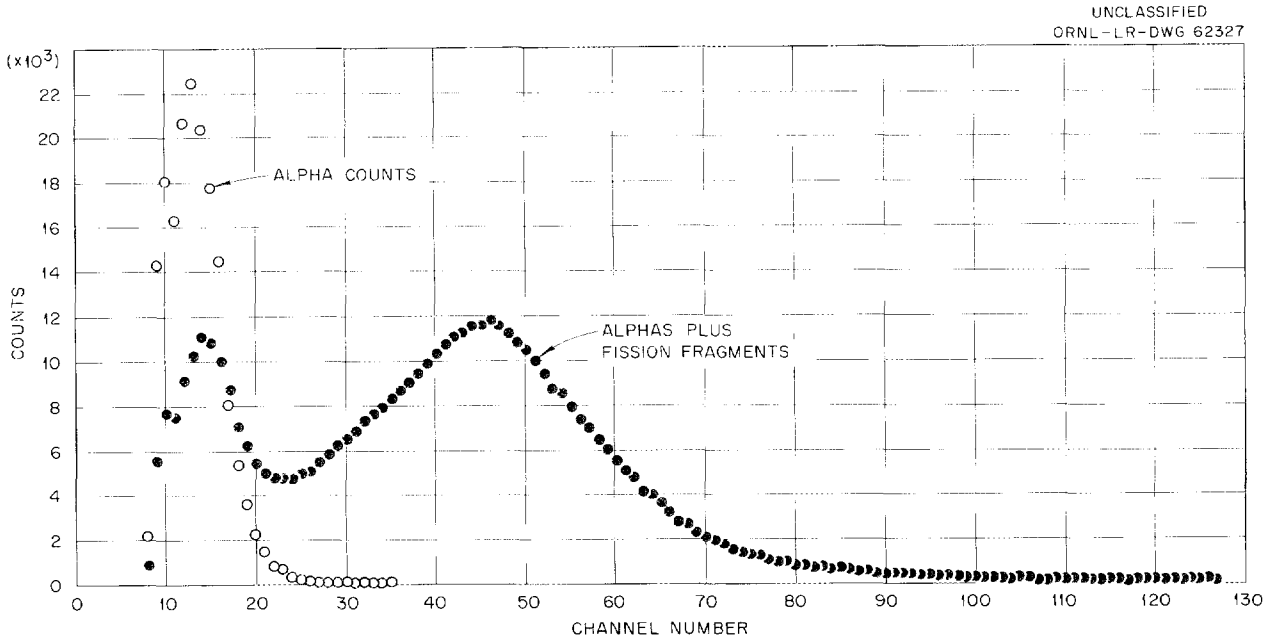

Fig. 4.3.6. Comparison of Pulse-Height Spectrum Due to Alpha Particles with That Due to Both Alphas and Fission Fragments.

The scintillation tank to be used will be that developed by Gibbons *et al.*[5] for capture cross-section measurements. A transistorized time-to-pulse-height circuit to be used is a modification of a design by Bertozzi at MIT and has a time resolution of $< 2 \times 10^{-9}$ sec.

Measurements in the Energy Range 5–150 kev

The general scheme for measurements in the 5- to 150-kev energy range was outlined above. A sketch of the experimental arrangement is shown in Fig. 4.3.8. In connection with this portion of the experiment, some work has been done toward the development of the scintillation tank. Optimization of the scintillator solution is described in a following paper.[7] The solution as finally adopted contains 1 wt% gadolinium. For test purposes, this solution was contained in a 1-ft-dia, 1-ft-high tank accommodating four 5-in.-dia photomultipliers. A small Cf^{252} spontaneous fission chamber was used with this apparatus to prove the feasibility of detecting fissions by the gamma-ray pulse from captures in gadolinium. For the arrangement used, fission neutrons were thermalized in about 8 μsec and had a mean lifetime of 12.5 μsec.

The electronic circuitry required for this method of detection is diagrammed in Fig. 4.3.9. The principle of the method has been described by Hopkins and Diven.[3] In essence, each prompt event in the

[7] Section 4.5.

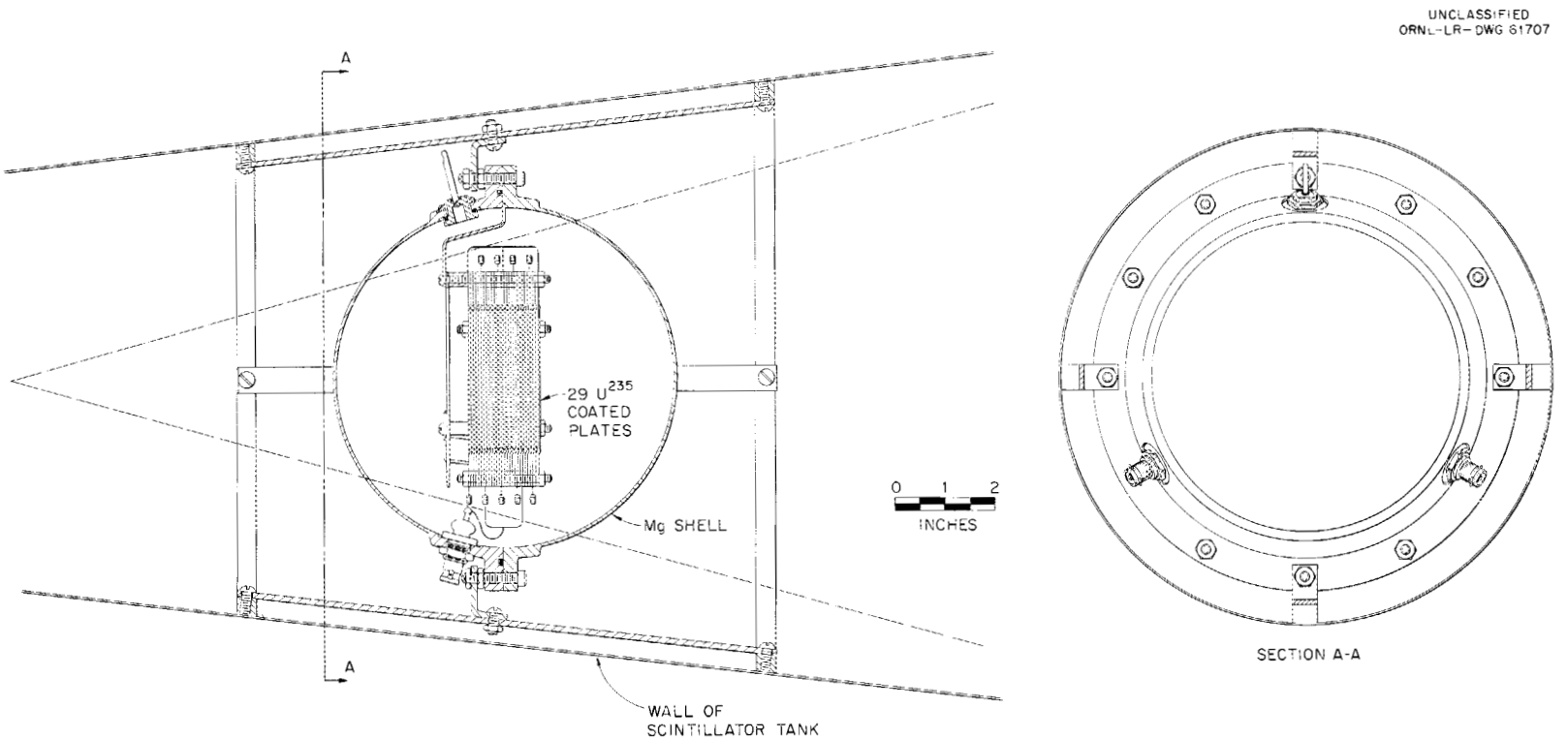

Fig. 4.3.7. Fission Chamber for Measurement of α at 30 and 65 kev.

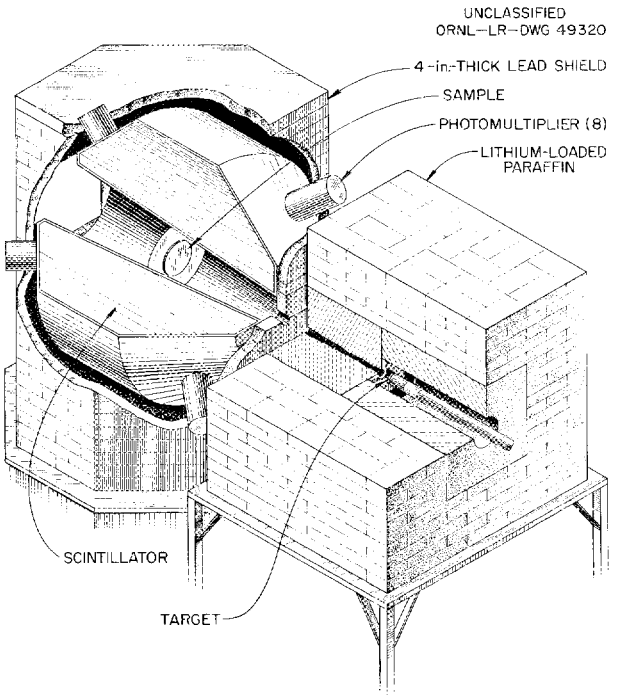

Fig. 4.3.8. Experimental Arrangement for Measurement of $\alpha(E)$ from 5 to 150 kev.

sample generates two gates of about 10 μsec each, the first immediately and the second a random, relatively long time after the event. The second gate thus measures the background in the scintillator. An excess of counts in the first gate over the second is attributed to gadolinium captures and identifies the prompt event as a fission.

Backgrounds due to radioactivity of the sample itself were examined during these preliminary experiments by placing several 1-mil-thick disks of U^{235} in the center of a 1.2-m-dia tank of liquid scintillator. The increase in background due to the disks was negligible. Tests were also made with an ~9-g sample of U^{233}, containing only about 1 part per billion of U^{232}, at the center of a 1-m-dia tank of scintillator. The count rate resulting was within acceptable limits. A suitable sample of Pu^{239} for similar tests is not yet available.

Measurements Using a Linear Accelerator

Measurements over the range from 1 ev to ~20 kev, using neutrons from a linear accelerator, will generally follow the scheme described for the 30- and 65-kev measurements. The time-of-flight technique will be used not only to distinguish against background, however, but also to determine neutron energies. The response of the fission chamber and the scintillator will determine if the scintillator pulse is associated with a fission event or with a capture. Time distributions of capture and fission events will be stored in separate sections of a time analyzer. The ratio of the two spectra, corrected for background and differences in detection efficiency, will be equal to α as a function of time of flight. It is estimated that with a linear accelerator giving an intensity of 10^9 neutrons per pulse, the capture rate in the uranium of the fission chamber will be ~1.5 captures per pulse.

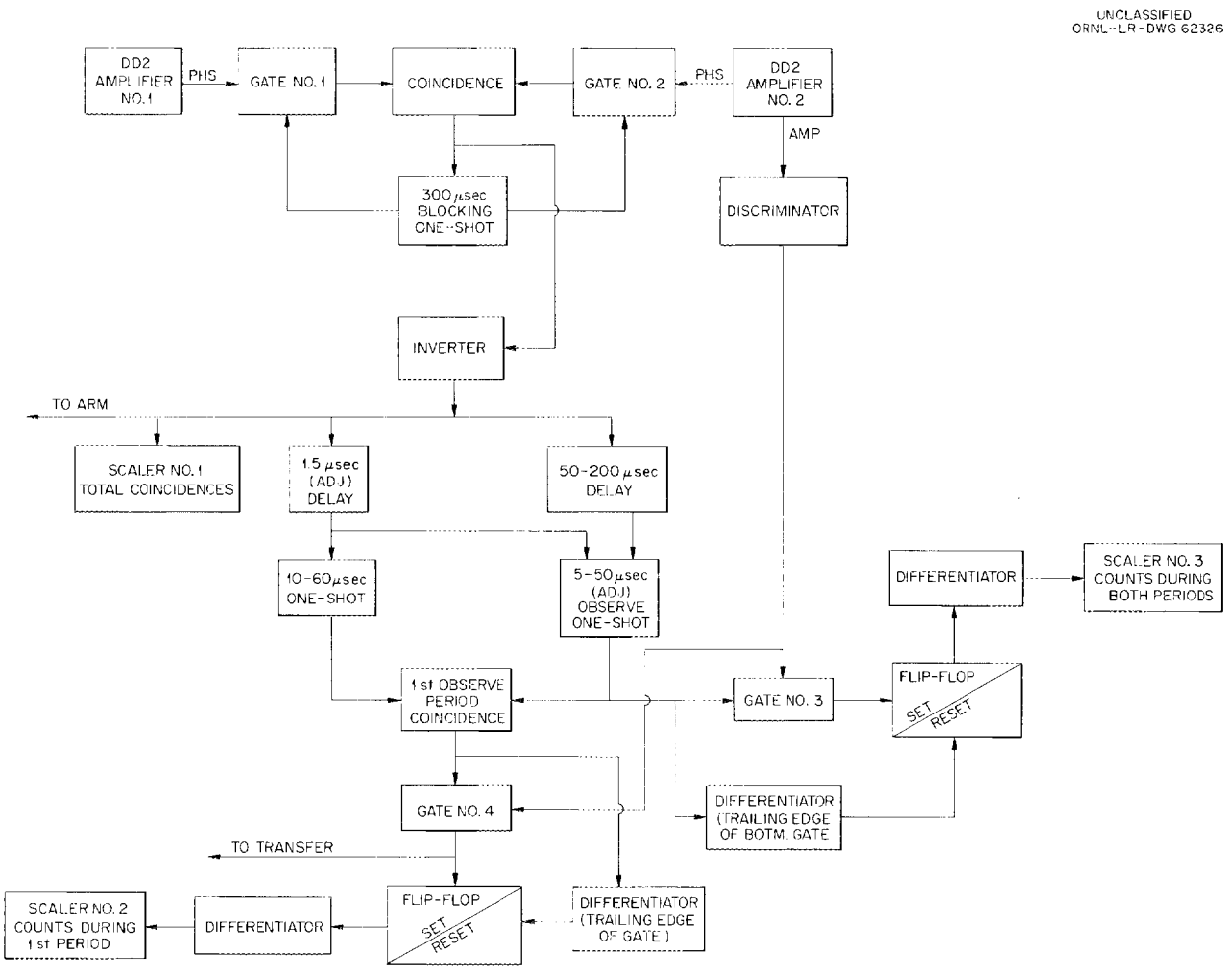

Fig. 4.3.9. Block Diagram of Delayed Coincidence Circuit for Measurement of $\alpha(E)$ from 5 to 150 kev.

4.4. DEVELOPMENT OF A HIGH-EFFICIENCY FAST-NEUTRON DETECTOR

L. Weston R. D. Smiddie[1]

The design of a large U^{235} fission chamber for use in measurements of α of the fissionable isotopes has been described in the preceding paper (Section 4.3). In order to determine the absolute efficiency of this chamber, and also for possible measurements of η of the fissionable isotopes, a high-efficiency, low-background fast-neutron detector which was insensitive to neutrons of energies <100 kev was required. These requirements have been met in the construction of a proton-recoil detector utilizing a 2-in.-dia, 2-in.-thick trans-stilbene crystal and a pulse-shape discrimination circuit.

[1]Instrumentation and Controls Division.

The pulse-shape discrimination circuit chosen was that of Forte,[2] modified for use with a 6810A photomultiplier. The circuit was selected because of its ability to operate in relatively high gamma-ray fields (10^4 counts/sec) with good discrimination between gamma rays and fast neutrons. A trans-stilbene crystal was used because of its superiority for pulse-shape discrimination over the liquid scintillators sometimes used.

Because of the unusual pulse shape, positive for neutrons and negative for gamma rays, from the circuit adopted, a special amplifier, due to Lefevre[3] and having minimum overshoot characteristics for negative pulses, was constructed.

Tests of the completed detector show an efficiency of $\sim$30% for detection of fission neutrons, with a discrimination against gamma rays of $\sim 10^4$.

[2]M. Forte, *Proc. U. N. Intern. Conf. Peaceful Uses Atomic Energy, 2nd, Geneva, 1958*, 14, 300 (1958).
[3]Harlan Lefevre, Dept. of Physics, University of Wisconsin, private communication.

4.5. SELECTION OF A LIQUID ORGANIC SCINTILLATOR FOR AN EXPERIMENTAL DETERMINATION OF α

L. Weston, W. S. Lyon,[1] J. D. Kington

A previous paper (Sec. 4.3) has discussed various plans for an experiment to measure α, the ratio of the capture cross section to the fission cross section, for the principal fissionable isotopes. All of the plans discussed envisage the use of a large tank containing a liquid scintillator suitably poisoned with a neutron-capture agent. In connection with optimization of the scintillation tank, a number of organic solutions have been tested by comparing their relative responses, in terms of pulse height, to the 1.1-Mev gamma ray from Zn^{65}. The midpoint of the Compton edge was taken to be proportional to pulse height.

The solutions tested are shown in Table 4.5.1. Gadolinium, because of its larger cross section for thermal-neutron capture, was chosen over the more commonly used cadmium as a poison. For the initial tests the volume of solution was either 30 ml or 200 ml. The solution container was internally coated with an α-alumina reflector, and a 2-in.-dia photomultiplier having an S-11 response was placed in direct contact with the solution. All solutions were bubbled for 15 min, in order to reduce the quenching effect of dissolved oxygen, before pulse heights were observed. The internal consistency of the data was excellent, being within 3% or better. Since the behavior of scintillator solutions is strongly dependent upon the purity of the ingredients, agreement with published data was not always achieved.

The data show that most of the solvents and solutes commonly used (xylene, toluene, *p*-terphenyl, PPO, PBD, POPOP, α-NPO) do not differ greatly in performance, from the standpoint of pulse height. Triethylbenzene, which is popular as a solvent because of its low flammability, was somewhat disappointing. TS 28M, a petroleum byproduct,[2] seems to offer the same advantages as triethylbenzene at a much reduced

[1]Chemistry Division.
[2]A Shell Oil Co. product; suggested by V. N. Kerr, Los Alamos Scientific Laboratory, private communication.

cost (about that of gasoline). The only purification of the TS 28M was filtration through an alumina column to remove its slightly yellow color. Both TS 28M and triethylbenzene were unsuitable for loading with gadolinium because of the low solubility of gadolinium 2-ethylhexoate in either solvent.

From the results shown in Table 4.5.1 it was concluded that the most promising gadolinium-loaded solution was that of Solution No. 5. The small amount of ethyl alcohol was added because the material tended to be very viscous without some diluent.

In order to test the properties of a larger volume of solution, a tank containing 7 gal of Solution No. 5 was constructed. The behavior of this volume was identical with that observed for smaller volumes. The fast-neutron (fission spectrum) half-life for absorption was measured as 12 μsec.

Three hundred gallons of Solution No. 5 are being prepared for use in the experiments described in Sec. 4.3.

Table 4.5.1. Relative Pulse-Height Response of Various Scintillator Solutions to 1.1-Mev Gamma Rays from Zn^{65}

Solution No.	Solution Composition	Relative Pulse Height
1	Triple-distilled[a] xylene, 4.0 g/liter *p*-terphenyl,[b] 0.3 g/liter POPOP[b]	1.00
2	Triple-distilled xylene, 4.0 g/liter PPO,[b] 0.3 g/liter POPOP	0.90
3	Triple-distilled xylene, 4.0 g/liter PBD,[b] 0.3 g/liter POPOP	1.00
4	Triple-distilled xylene, 4.0 g/liter *p*-terphenyl, 0.1 g/liter α-NPO[b]	0.90
5	Triple-distilled xylene, 4.0 g/liter *p*-terphenyl, 0.3 g/liter POPOP, 1.0 wt% gadolinium 2-ethylhexoate, 1.0 vol% ethyl alcohol	0.95
6	Spectro-quality toluene, 4.0 g/liter *p*-terphenyl, 0.3 g/liter POPOP	0.96
7	Spectro-quality toluene, 4.0 g/liter PPO, 0.3 g/liter POPOP	0.87
8	Single-distilled TEB, 4.0 g/liter PPO, 0.3 g/liter POPOP	0.81
9	TS 28M,[c] 4.0 g/liter PBD, 0.1 g/liter α-NPO	0.73
10	TS 28M,[c] 4.0 g/liter PBD, 0.1 g/liter α-NPO, 6 vol% CH_3BO_3	0.74
11	NE 313[d] (contains 1 wt% gadolinium)	0.56

[a]All distillations over liquid sodium by Chemical-Medical Laboratory, Knoxville, Tennessee.
[b]Purchased from Pilot Chemicals, Inc., Watertown, Massachusetts.
[c]A Shell Oil Co. petroleum byproduct.
[d]Nuclear Enterprises, Ltd. solution.

4.6. FISSION GAMMA-RAY ENERGY RELEASE AS A FUNCTION OF TIME AFTER FISSION

F. C. Maienschein

During the past several years a number of measurements of the energy spectra of gamma rays associated with fission have been reported by Oak Ridge National Laboratory. No additional experiments have been made at this Laboratory, but existing data have been summarized and combined with new and revised results from other laboratories. All of the data except that of Walton pertain to fission of U^{235} by thermal neutrons. Fission gamma-ray energy release per unit time, integrated over gamma-ray energy, is plotted as a function of time after fission in Fig. 4.6.1. At the shortest time interval is shown the yield obtained from the so-called "prompt" fission gamma-ray measurements of Peelle, Maienschein, and Love[1] measured with a resolving time of $\sim 5 \times 10^{-8}$ sec. The actual time required for the fission process is, of course, much less. For the time interval between 6×10^{-8} and 1.1×10^{-6} sec, the "short-lived isomer" data of the above-noted authors are shown.[1] An integration over energy of the previously published spectral data for this time region agrees, to within ±25%, with integral experimental measurements of the time dependence for the energy range above 0.17 Mev. The time-dependent data were obtained with a single NaI(Tl) crystal, and thus the errors in the energy release are large. The factor-of-two limits shown, however, are surely conservative.

The noticeable gap in the data in the interval from 1×10^{-6} to 5×10^{-4} sec after fission results from the breakdown, due to excessive background, of the method used to obtain the data for shorter times. It is hoped that this gap may eventually be filled by an extension of the method of Walton[2] to this region.

For the time range from 5×10^{-4} to ~ 10 sec, new data of Walton[2] are shown. These were obtained with a pulsed gamma-ray source provided by an electron linear accelerator. The measurements were made with a plastic scintillator observing gamma rays following photofission in a U^{238} sample. The plastic scintillator, like the single NaI(Tl) crystal, does not permit a determination of the energy release, since it is a poor gamma-ray spectrometer. In order to calculate the results shown, Walton assumed: (a) that the energy spectra do not vary with time over the time region studied, and (b) that the U^{238} photofission data could be normalized in the 1- to 10-sec time region to that obtained from thermal fission of U^{235}. The detector efficiency was shown to be constant to within ±50% for gamma-ray energies above ~ 0.3 Mev, and Walton estimated that the number of photons per fission per second obtained by normalization should be valid to within a factor of two. If the assumption of a constant spectrum with time is tenable, the value for the energy release would also be valid to within a factor of two.

---

[1] F. C. Maienschein *et al.*, *Proc. U.N. Intern. Conf. Peaceful Uses Atomic Energy, 2nd, Geneva, 1958* **15**, 366 (1959); T. A. Love *et al.*, *Neutron Phys. Ann. Prog. Rep., Sept. 1, 1959*, ORNL-2852, p. 93; R. W. Peelle *et al.*, *Neutron Phys. Ann. Prog. Rep., Sept. 1, 1958*, ORNL-2609, p. 45.

[2] R. B. Walton, *Emission of Gamma Radiation as a Function of Time After Photofission of U^{238}*, AFSWC-TR-61-10 (Feb. 11, 1961).

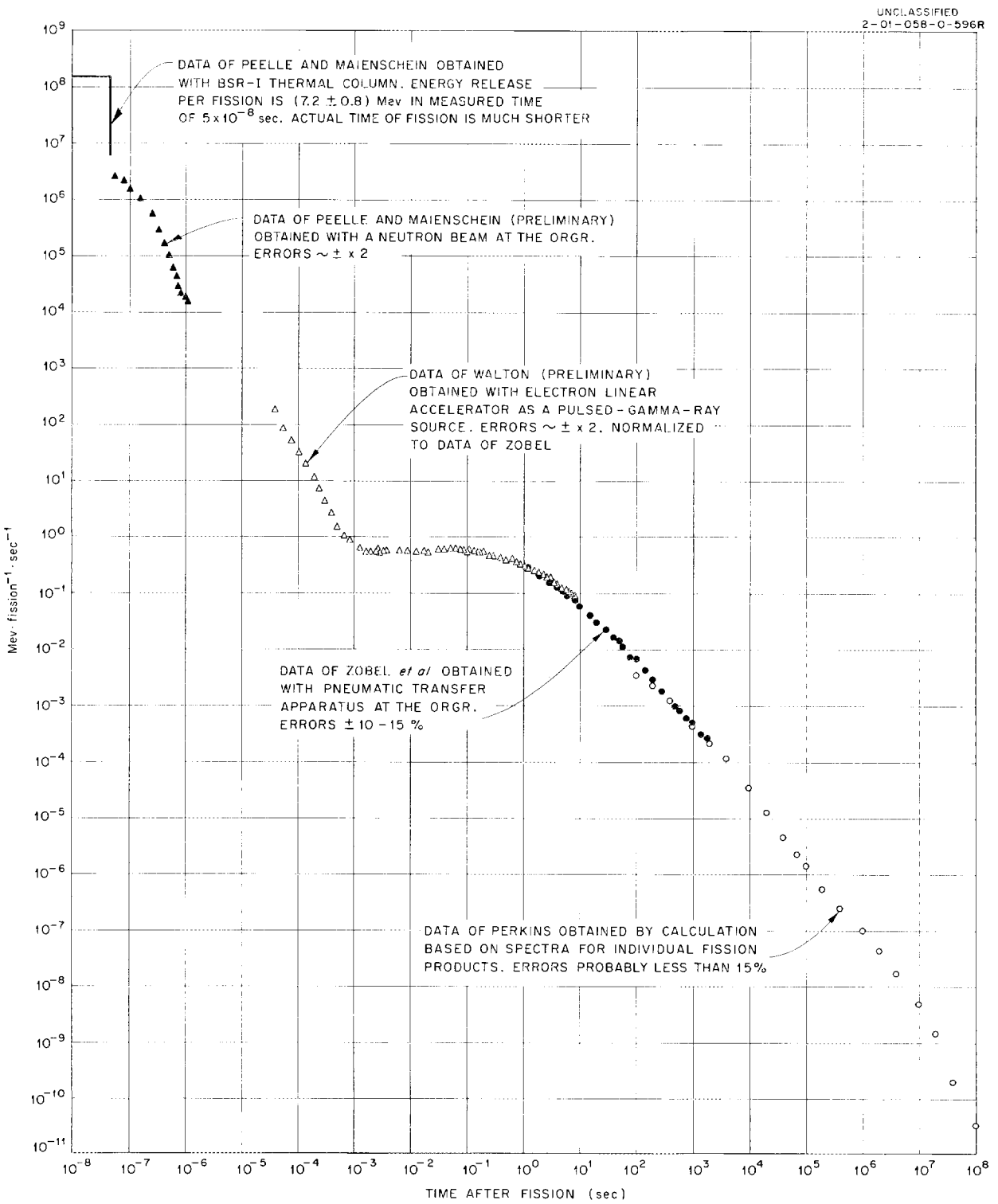

Fig. 4.6.1. Fission Gamma-Ray Energy Release as a Function of Time After Fission.

For times from 1 to 1800 sec after fission, the data of Zobel *et al.* are unchanged from those previously reported.[3]

For times longer than 100 sec, revised data were received from J. F. Perkins, of the George C. Marshall Space Flight Center. Perkins' earlier data[4] were based on fission-product gamma-ray spectra available in July, 1957. His major revisions reflect the work of Johnson, O'Kelley, Eichler, and Lazar, with rubidium and iodine isotopes.[5] The inclusion of spectra for these isotopes results in a larger calculated energy release for times between ~ 100 and 1000 sec after fission, which is now in remarkably good agreement with the experimental data of Zobel *et al.* No normalization has been made.

For all time regions the errors in time determination are insignificant at the scale of the plot.

[3]W. Zobel *et al.*, *Neutron Phys. Ann. Prog. Rep., Sept. 1, 1958*, ORNL-2609, p. 50.

[4]J. F. Perkins and R. W. King, *Nuclear Sci. and Eng.* **3**, 726 (1958).

[5]N. H. Lazar, E. Eichler, and G. D. O'Kelley, *Phys. Rev.* **101**, 727 (1956); G. D. O'Kelley, N. H. Lazar, and E. Eichler, *Phys. Rev.* **102**, 223 (1956); N. R. Johnson and G. D. O'Kelley, *Phys. Rev.* **114**, 279 (1959); G. D. O'Kelley, E. Eichler, and N. R. Johnson, *Proc. U.N. Intern. Conf. Peaceful Used Atomic Energy, 2nd, Geneva, 1958* **15**, 469 (1959).

4.7. USE OF 4π HIGH-PRESSURE IONIZATION CHAMBERS AS SECONDARY STANDARDS FOR CALIBRATION OF GAMMA-RAY SOURCES

R. W. Peelle

Both geometrical complexity and imprecisely known cross sections prevent the computation of the efficiencies of the Compton and pair scintillation spectrometers used in a previously reported measurement of gamma rays associated with fission.[1,2] Efficiency determinations, therefore, depend upon the use of known-strength radioactive sources, with energies ranging from 20 kev to about 3 Mev. At a few energies it was possible to use absolute coincidence counting[3] to determine the strength of a source used to obtain test pulse-height spectra. However, in most cases this direct method was unusable because of timing, intensity, or decay scheme difficulties. A secondary standard was therefore required to determine source disintegration rates.

At the beginning of the experiment the high-pressure 4π solid angle ionization chamber located in Building 3038 was selected as the secondary standard, since its known calibration, presumed simple energy dependence, and presumed low long-term drift seemed to make it ideal for the task. Somewhat later a similar chamber, located in Building 4501, was also used. Each of the important sources was measured in each of these chambers from 1 to 50 times, with five readings per source being typical. Only toward the end of

[1]F. C. Maienschein, R. W. Peelle, W. Zobel, and T. A. Love, *Proc. U.N. Intern. Conf. Peaceful Uses Atomic Energy, 2nd, Geneva, 1958*, **15**, 366 (1959).

[2]R. W. Peelle, F. C. Maienschein, and T. A. Love, *Neutron Phys. Ann. Prog. Rep. Sept. 1, 1958*, ORNL-2609, p. 45; T. A. Love, F. C. Maienschein, and R. W. Peelle, *Neutron Phys. Ann. Prog. Rep. Sept. 1, 1959*, ORNL-2842, p. 93.

[3]R. W. Peelle, *Neutron Phys. Ann. Prog. Rep. Sept. 1, 1960*, ORNL-3016, p. 116.

the 3-yr period spanned by the gamma-ray experiments was the method of data analysis finally developed; thus some of the early measurements did not include as complete information as now seems desirable.

The objective of the work, then, was to obtain accurate, defensible values of the strengths of about 50 sources, representing about 25 radioisotopes. Error estimates on each source strength determination were required so that such errors could be considered in evaluating spectrometer efficiencies and in the final assignment of errors to the measured gamma-ray spectrum.

Drawings showing the design of the ionization chambers are on file in the ORNL Instrumentation and Controls Division. The chambers essentially are heavy-walled iron right-circular cylinders, 12 in. in height and about 10 in. in diameter, filled with argon at a pressure of ~ 40 atm. Along the axis of the cylinder from the top is a re-entrant steel thimble into which the source to be measured is placed, traditionally with glass and plastic layers interposed. The entire chamber is shielded with 4 in. of lead, which reduces the background to $\sim 2 \times 10^{-13}$ amp. The current collected from ionization is observed by measuring the voltage across a chosen resistor (four ranges are available, having 10^8- to 10^{11}-ohm resistors), using a vibrating-reed electrometer to measure the difference in voltage between the unknown voltage and the output of a standard potentiometer.

Lyon[4] and co-workers have calibrated these chambers against standard sources covering the entire range of the instrument up to nearly 10^{-8} amps. Their standard sources were prepared from aliquots of a Co^{60} solution which had been standardized by beta-gamma coincidence techniques. Sets of observed output voltages obtained by the use of these sources have been obtained from time to time, particularly in January, 1957, and September, 1959. These two calibrations differ by from 3 to 7% because of long-term drifts. In addition to these intensity calibrations, Lyon obtained a series of relative efficiency factors, based on counting techniques, which essentially give the ionization produced by one disintegration of a stated isotope relative to that produced by one disintegration of Co^{60}. Others have used a combination of these data to obtain the strength of any unknown source in the appropriate energy range.

For the application toward which the present work is directed, however, a somewhat modified method for ascertaining unknown source strengths was required, particularly since the experimental measurements were spread over a long time.

The method developed for the measurement of unknown source strength in the ionization chambers described makes the following assumptions:

a. The height of the source in the thimble of the chamber does not seriously affect the result. Although a few experiments showed that for the roughly 1-in. variations in the present work the effect was small, better control of this variable might have improved the results.

b. A simplified theory ignoring multiple interactions is adequate to handle self-absorption of gamma rays in the sample capsules. This approximation is good in nearly every case.

c. The calibration of the chamber can most usefully be broken down into a *relative* intensity calibration, based on the data of Lyon, a relative correction based on observed ion-chamber sensitivity drift, and an *absolute* calibration constant for each isotope. This constant takes into account the energy dependence of the ion chamber efficiency.

[4] W. S. Lyon, unpublished (September 1959).

d. Systematic errors >0.5% should be corrected; random errors or systematic errors of unknown magnitude should be estimated at their sources and combined in a proper manner.

e. Data obtained in the present experiment should be used whenever possible, thus making the experiment a self-contained unit.

Implementation of these assumptions involved the following operations on the accumulated data:

a. Each voltage reading was converted to an equivalent "Co^{60} disintegration rate." (The quotation marks indicate that the values were used only in a relative sense.)

b. Each reading was corrected for radioactive decay and for the time-dependent drift of the ion chamber sensitivity.

c. Readings were averaged and corrected for the transmission of the capsule (usually brass) in which the source is contained.

d. These averages, one for each source in each ion chamber, were divided by the respective efficiency factors, yielding the strength of the main gamma ray in the disintegration scheme.

e. At each step in the process, error estimates were propagated.

The manner in which the above steps were taken has been detailed in a previously published memorandum[5] and will be presented at some future date as part of the complete report on the gamma-ray spectral measurements. Since the methods used in general evolved slowly during the course of the experiments and, in the full illumination of hindsight, are not necessarily the best possible, they will not be further discussed. However, the treatment of the absolute efficiency and its energy dependence is believed to be of potential value to other ion chamber users and therefore is outlined below.

It was noted above that for a few sources it was possible to determine strengths by absolute counting techniques. Since most of these sources emit more than one gamma ray it was not possible to plot directly the ion chamber efficiency as a function of energy as is required for the completion of the source strength analysis.

Knowledge of the ion chamber geometry and composition permits the chamber efficiency to be computed using gamma-ray cross-section data. Such a calculation was performed, although uncertainties in the method of calculation, the exact gas pressure, the amount of self-absorption caused by the thimble, etc. prevent this result from being used as a final result. The calculated curve instead was used as a zero-order estimate of the shape of the energy dependence of the ion chamber efficiency, and the absolute source strength determinations were then used to normalize the curve and to determine small changes from the calculated shape.

The energy-dependent efficiency function calculated was $f(E)$, the average fraction of energy deposited in the gas of the ion chamber by a gamma ray of energy E. The number of ion pairs produced by such a gamma ray is then $E\,f(E)/w_{argon}$, where w is the average number of electron volts per ion pair for argon with electrons as the primary radiation. Since only an approximate shape of the curve was required, many simplifications were employed in estimating all of the primary and secondary interactions in the chamber. Over the entire energy range of interest the main contribution to the absorbed energy results from Compton

[5] R. W. Peelle, *Use of 4π High Pressure Ionization Chambers as Secondary Standards for Calibration of Gamma-Ray Sources*, ORNL-CF-61-4-32 (April 17, 1961).

scattering of the primary gamma rays in the argon gas and the subsequent absorption of the Compton recoil electrons. Absorption in the iron, plastic, and glass thimble containing the source produced a cutoff in $f(E)$ at low energy. The exact position of this cutoff was difficult to estimate accurately.

The values resulting from the calculation are plotted in Fig. 4.7.1. The primary characteristic of interest in $f(E)$ is the maximum predicted in the neighborhood of 80 kev, where the curve rises a factor of two above the value at about 1 Mev. Since $f(E)$ is not flat, $E\,f(E)$ is not a straight line, and the ionization per gamma ray is not proportional to gamma-ray energy as might intuitively be supposed. It is evident that the chambers are "thin," absorbing at most 4% of the incident energy. Thus the energy dependence is not a strong function of gas pressure.

The description of the actual ion chamber efficiency as a function of energy can be written as

$$e_I(E) \simeq E\,f(E) + \sum_{\lambda=1}^{L} \alpha_\lambda^I (E - E_0)^{\lambda-1}\, E\,f(E)\,, \tag{1}$$

where

$e_I(E)$ = energy absorbed in the ion chamber from one gamma ray of energy E (Mev),

E_0 = 1.25 Mev (arbitrarily chosen),

α_λ^I = free parameters to be determined by the chamber response to sources of known strength. The superscript implies that the values of each α_λ may be different for the two ion chambers used.

An expansion of three terms ($L = 3$) gave an adequate representation of the data. While Eq. 1 formally gives a corrected energy dependence, it must be adapted to the case of a source emitting gamma rays of more than one energy. Such an isotope, m, yields a series of emitted energies E_k^m with relative emission b_k^m, where $b_1 = 1$ for all m. (The transition for $k = 1$ is arbitrarily called the "ground state" transition.) Then the amount of energy absorbed in ion chamber I per "ground state" gamma-ray emission is

$$e_{Im} = \sum_k b_k^m\, e_I(E_k^m)\,. \tag{2}$$

By substituting the expression for $e_I(E)$ given by Eq. 1, one obtains

$$e_{Im} = e_m^0 + \sum_\lambda G_{m\lambda}\alpha_\lambda^I\,, \tag{3}$$

where

$$e_m^0 = G_{m1}\,,$$

$$G_{m\lambda} = \sum_k b_k^m\, E_k^m (E_k^m - E_0)^{\lambda-1}\, f(E_k^m)\,.$$

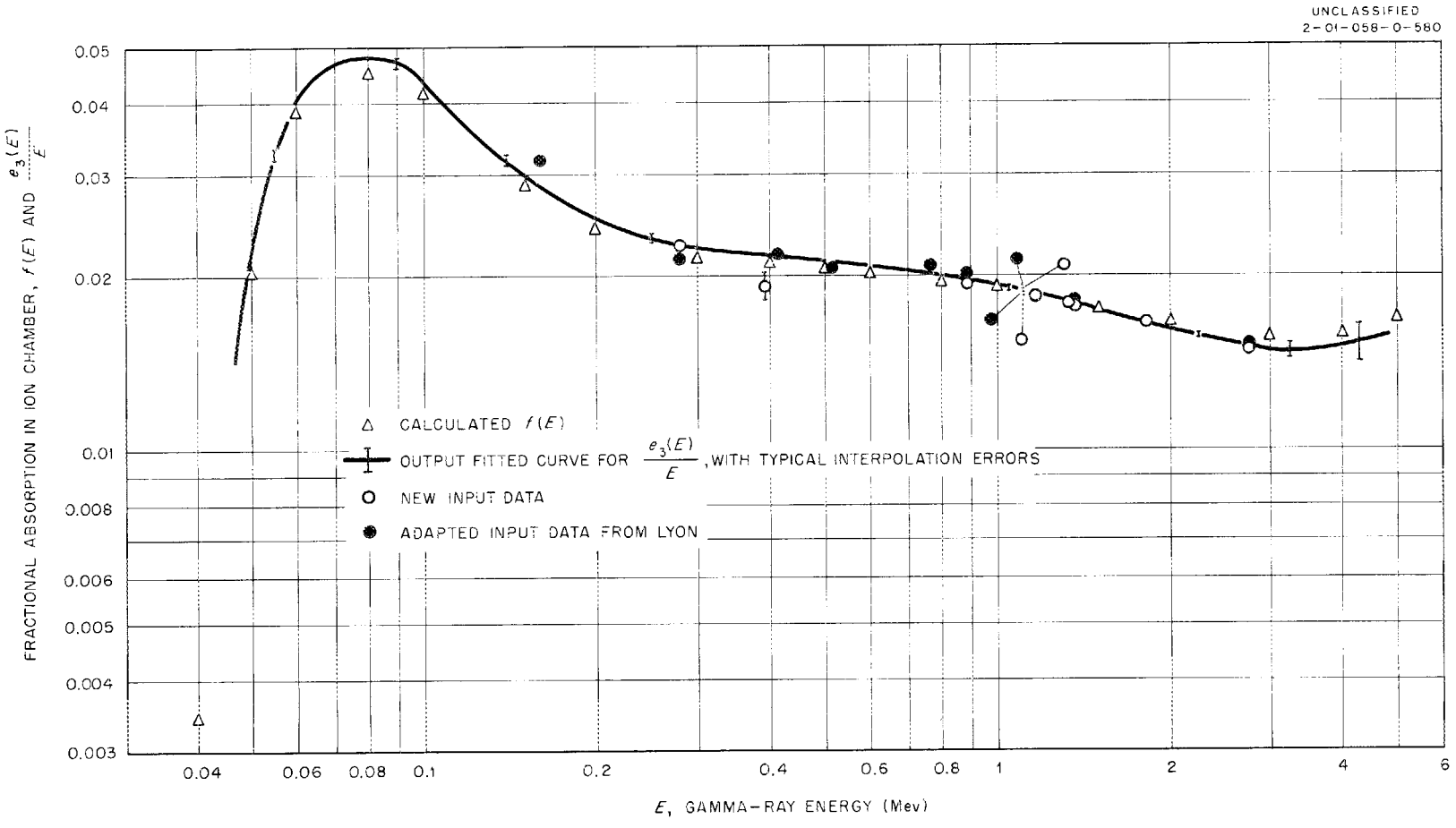

Fig. 4.7.1. Predicted, Experimental, and Interpolated Energy Dependence of the Fractional Energy Absorption in 4π High-Pressure Ionization Chambers.

The use of Eq. 3 permits data from isotopes with complex decay schemes to be employed in determining the α_λ. The numbers $G_{m\lambda}$ are required in the use of the ion chamber calibration as well as in the calibration process. These $G_{m\lambda}$'s will change as decay schemes become better known; for the present work data was obtained from Way's compilation[6] as well as from work performed for this purpose.[7]

If measured values of e_{Im} are available in greater number than the number of α's to be determined, a solution for the α's can be found and values of e_{Im} computed from Eq. 3 for any other source with known decay scheme. Values of $e_I(E)$ will also be known from Eq. 1.

The final values of the α's found in this work are listed in Table 4.7.1.

The solid curve of Fig. 4.7.1 gives the value of $e_3(E) \cdot E$ for the Building 3038 chamber obtained by using the values of Table 4.7.1 in Eq. 1. The curve has nearly the same shape as the calculated $f(E)$, and the deviations were even less for the chamber of Building 4501. Computed interpolation errors are shown at various points on the curve. The input values shown in Fig. 4.7.1 are shown principally to indicate the degree of consistency between output and input and to indicate the region over which input data was available. Since no substantial amount of data was available for energies below 160 kev, the curve which has been extrapolated below that energy may be wrong to a degree in excess of the interpolation errors shown. This point should be noted in making use of the curve, which can be used to estimate the ion chamber efficiency for any gamma-ray source with a known decay scheme.

Table 4.7.1. Values of the Free Parameter, α, Computed for Use in Ion Chamber Efficiency Determinations

Series Index, λ	Free Parameter α_λ	
	Bldg. 3038 Chamber	Bldg. 4501 Chamber
	$\times 10^{-2}$	$\times 10^{-2}$
1	0.17 ± 0.61	1.28 ± 0.75
2	-3.75 ± 0.98	-1.37 ± 1.21
3	0.51 ± 0.96	-0.71 ± 1.18

In applying the results of this work, source strength determinations from the two ion chambers were averaged. In only a few cases did independent values from the two chambers show differences as large as 1.5 standard deviations based on the relative error. Final error estimates took into account the strong mutual dependence of the efficiency factors for the two chambers.

[6] K. Way *et al.*, *Nuclear Data Sheets*, National Academy of Sciences and National Research Council. Data to January, 1960 was used.

[7] R. W. Peelle, *Neutron Phys. Ann. Prog. Rep. Sept. 1, 1960*, ORNL-3016, p. 110; R. W. Peelle and T. A. Love, *Scintillation Spectroscopy Measurements of Gamma-Ray Energies from Sources of* Y^{88}, Mn^{54}, *and* Zn^{65}, ORNL-2790 (1959).

Final quoted errors in the calibrated sources ranged from 1.5 to 3% except for a single case for which the ion-chamber readings were quite inconsistent and two cases in which the decay schemes were poorly known. Table 4.7.2 shows a breakdown on the origins of typical final error estimates (to be summed as squares). It is believed that source strength calibrations resulting from this work are substantially more precise than would otherwise have been possible and are adequately precise for calibration of the Compton and pair spectrometers used in the gamma-ray spectral measurements.

Table 4.7.2. Origins of Typical Final Error Estimates in Source Strength Calibrations

Error In	Range of Percentage Error Including 92% of Cases
Average ion chamber reading	0.2–2.3
Transmission	0–0.6
Interpolation error in e_{Im}	0.6–1.9
Decay scheme error in e_{Im}	0.3–2.5
Ion chamber over-all calibration error	(taken as) 1

4.8. COLLIMATOR OPTIMIZATION FOR REACTOR GAMMA-RAY SPECTRA MEASUREMENTS

G. T. Chapman

A prime purpose of the gamma-ray spectroscopy program at the Bulk Shielding Facility (BSF) is to accurately determine the energy distribution of those gamma rays that are born in the reactor. A total-absorption NaI(Tl) spectrometer[1] has been developed at the BSF and is currently being used for such measurements. The spectra measured with this type of spectrometer may be strongly influenced, especially at low gamma-ray energies, by the collimator used to allow the gamma rays to reach the crystal through the necessarily thick spectrometer shield. In addition, the spectra may be further influenced by gamma rays that penetrate the shield either directly without energy change or as scattered photons which have been degraded in energy by scattering processes in the shielding material and collimator. Since such effects were anticipated, a series of experiments was run at the BSF to determine their magnitudes with the Model IV gamma-ray spectrometer.

[1]G. T. Chapman, *Neutron Phys. Ann. Prog. Rep., Sept. 1, 1960*, ORNL-3016, p. 264.

For this series of experiments a core of "cold" BSR-I fuel elements was assembled in the Pool Critical Assembly.[2] In order to diminish the number of gamma rays scattered or otherwise attenuated by the reactor core before escaping, a loading only three fuel elements thick along the spectrometer-reactor center line was used.

The basic collimator configuration used for one series of variations is shown in Fig. 4.8.1. The "lead shutter section" consisted of a 2-in.-dia hole through an 8-in.-dia lead cylinder which, when rotated 90 deg on the axis shown, blocked the collimator with 6 in. of lead during background measurements.

Initially the front surface of the lead section of the collimator (point *A* in Fig. 4.8.1) was placed 80 cm from the reactor. Choice of this distance was based on earlier work which showed excessive background counts at distances $\leq$50 cm. Part *a* of Fig. 4.8.2 compares "shutter open" and "shutter closed" data from the initial configuration. Background contributions are seen to be large. In an effort to utilize a greater thickness of water between the reactor and the spectrometer shield, a 2-ft-long air-filled cone constructed of very thin aluminum was attached to the front of the lead collimator. The cone was shaped to include only the collimator solid angle. The spectrometer was positioned so that the base of the aluminum cone was 80 cm from the reactor. The "shutter open" and "shutter closed" curves of part *b* of Fig. 4.8.2 demonstrate clearly that the greater thickness of water greatly reduces the number of capture gamma rays created in the collimator and spectrometer shield.

In Fig. 4.8.3 are shown the difference spectra resulting from subtracting the shutter-closed data of Fig. 4.8.2 from the shutter-open data, also from Fig. 4.8.2. The effects of interactions in the collimator and shield when the air cone was not used cre again emphasized. Results obtained with a 5-ft-long cone, which may be more desirable for certain experiments, were the same as those with the 2-ft-long cone.

[2] "Cold" elements are those which have not been used during reactor operations at power levels greater than about 1 watt and have not suffered any considerable amount of fission-product buildup.

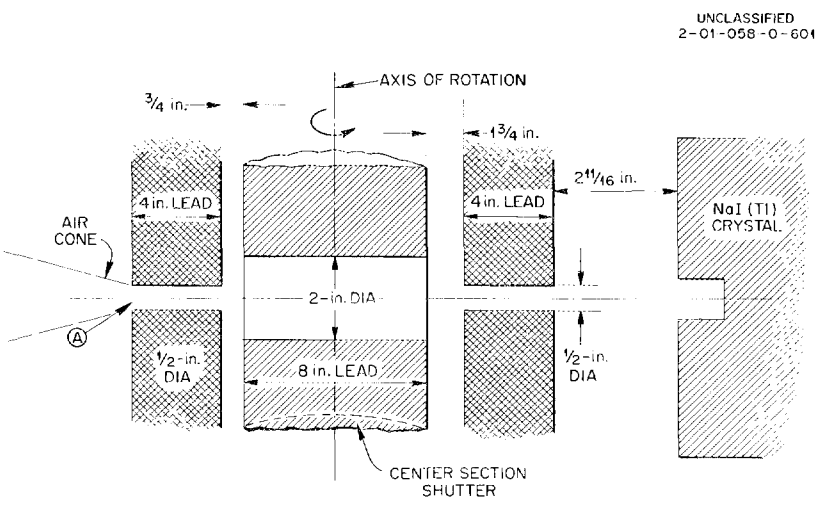

Fig. 4.8.1. Diagram of Collimator Arrangement Used in Spectral Measurements with Model IV Spectrometer.

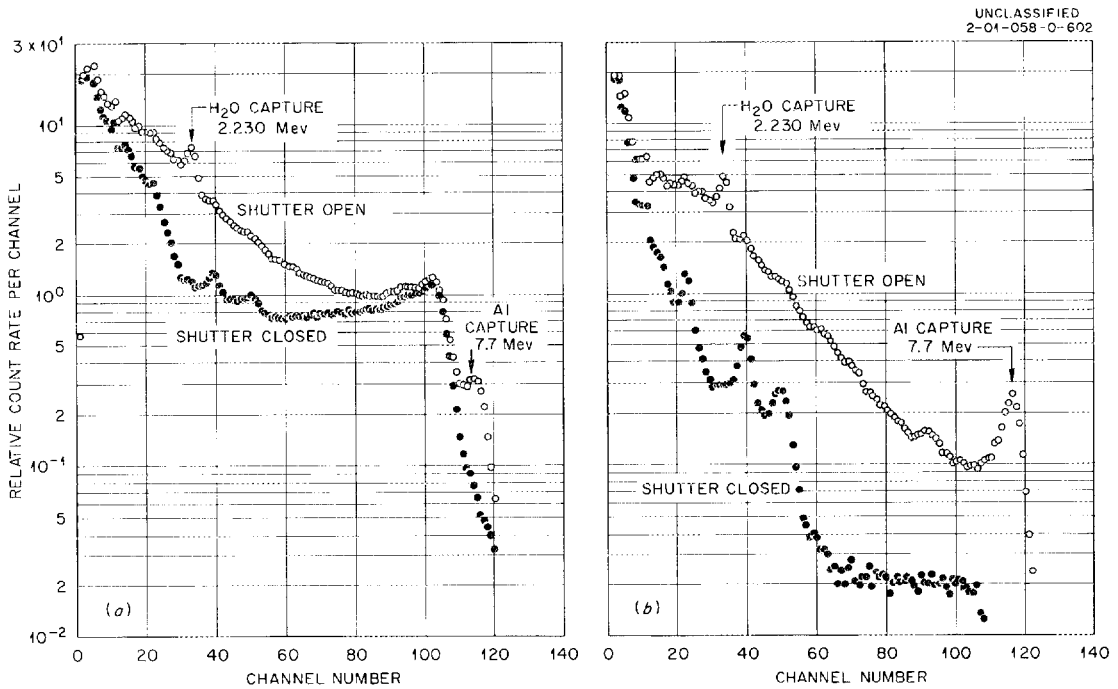

Fig. 4.8.2. Pulse-Height Spectra of a Loading of BSR-1 Elements in the PCA: (a) With a Straight Lead Collimator; (b) With a Straight Lead Collimator Plus an Air-Filled Cone.

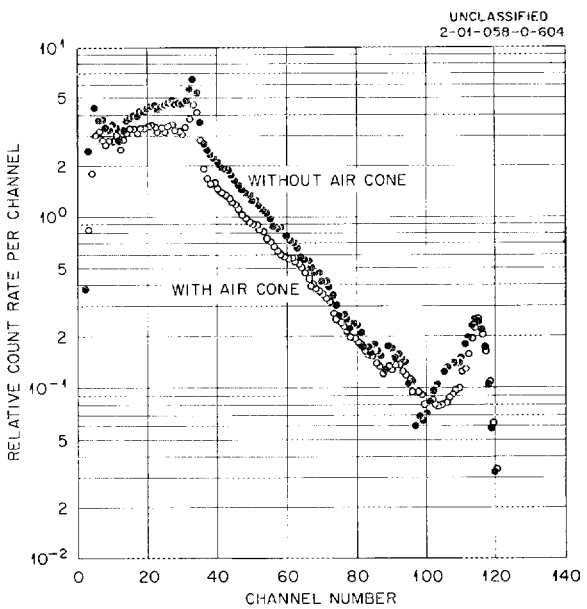

Fig. 4.8.3. Differences in Shutter-Open and Shutter-Closed Distributions Shown in Fig. 4.8.2: (a) Without Air-Filled Cone; (b) With Air-Filled Cone.

Subsequent experimentation, not reported herein, has determined that with the collimator configuration described above background is minimized[3] by a reactor-spectrometer separation distance of not less than 140 cm.

A measurement of the gamma-ray spectrum of the stainless steel Bulk Shielding Reactor II, utilizing the results of the preliminary experiments described above, is now in progress.

[3]Background contributions from causes other than those discussed above are described in Section 2.4.

Part 5

EXPERIMENTAL REACTOR PHYSICS

5.1. AN EXPERIMENTAL DETERMINATION OF THE AGE OF U^{233} FISSION NEUTRONS IN WATER

T. V. Blosser and D. K. Trubey

The strong probability that a successful breeder reactor will be based on U^{233} fission has made an accurate knowledge of all important U^{233} parameters imperative. One important quantity is the age of U^{233} fission neutrons in water, since it will have a bearing upon the losses due to fast-neutron leakage from a U^{233} system.

Faber and Zweifel[1] have calculated the age to indium resonance energy (1.45 ev) of U^{233} fission neutrons in water, using as source terms a Watt spectrum of the form $N(E) = 0.484 \sinh \sqrt{2E}\, e^{-E}$ on the one hand and the experimental spectrum measured by Henry[2] on the other. By the use of the Watt spectrum they arrived at an age to indium resonance of 25.3 cm^2; by using the experimental spectrum the result was 23.0 ± 3 cm^2. They concluded that an experimental measurement must be performed because of the fairly large errors on the experimental U^{233} spectrum, but were able to estimate that the U^{233} age is probably about 8 or 9% lower than the U^{235} age.

An experimental determination of the age to indium resonance of U^{233} fission neutrons in water has been made utilizing the equipment and techniques earlier developed for a similar measurement for U^{235} fission neutrons, which has been extensively discussed in previous reports.[3-5] While the U^{235} work utilized sources and indium detectors of various diameters and thicknesses, however, only one U^{233} source, 3.64 cm in diameter and 0.0635 cm thick, was readily available for the present work. Its dimensions are considerably larger in all respects than those of any of the U^{235} sources used. In order to apply the information gained in the U^{235} measurements to the present work, a supplementary experiment was performed in which the slowing-down distribution from a U^{235} source of the same dimensions (3.64-cm-dia, 0.0635-cm-thick) was measured. This gave a basis for comparison from which the success of the geometric transformations from large disk source to point-to-point detector kernel could be evaluated, as well as a means of estimating the absorption of fission neutrons within the thick source. All measurements were made in the thermal column of the ORNL Graphite Reactor.

As in the U^{235} work, the effects of different thicknesses of cadmium covers on the absorption of neutrons were measured, as well as the effects resulting from displacement of water around the foil by the covers. Within experimental error the results agreed with the previous U^{235} results.

Not all the data has been analyzed, and extrapolation of the age to infinite dilution or zero thickness has not been completed. However, with only geometric corrections applied, an age determined with 5-mil-thick indium foils within 30-mil-thick cadmium covers has been computed to be 26.4 ± 0.5 cm^2. The age measured for a U^{235} source under similar conditions is 26.7 cm^2.

---

[1] M. Faber and P. F. Zweifel, *Nuclear Sci. and Eng.* **6**, 81 (1959).

[2] K. M. Henry, *Appl. Nuclear Phys. Ann. Prog. Rep., Sept. 1, 1957*, ORNL-2389, p. 111.

[3] T. V. Blosser, D. K. Trubey, and E. P. Blizard, *Neutron Phys. Ann. Prog. Rep., Sept. 1, 1958*, ORNL-2609, p. 55.

[4] T. V. Blosser and D. K. Trubey, *Neutron Phys. Ann. Prog. Rep., Sept. 1, 1959*, ORNL-2842, p. 109.

[5] T. V. Blosser and D. K. Trubey, *Neutron Phys. Ann. Prog. Rep., Sept. 1, 1960*, ORNL-3016, p. 142.

5.2. CALCULATION OF THE TRANSMISSION FUNCTION FOR A NEUTRON CHOPPER

V. V. Verbinski and J. D. Jarrard[1]

A neutron chopper used in conjunction with a neutron source such as a reactor produces short bursts of neutrons at controllable intervals and burst durations. If such a burst is allowed to move down an evacuated drift tube, the neutrons become separated as a consequence of their various velocities. A bank of neutron counters placed at the end of the drift tube measures the neutron flux and sends its output pulses to a time-of-flight analyzer, resulting in a time-of-flight spectrum. A procedure for obtaining the neutron energy spectrum from a time-of-flight spectrum has previously been described[2] and depends for success upon an accurate knowledge of the transmission function of the neutrons through the slits of the chopper employed. A numerical method has now been applied to the calculation of the transmission function for a generalized slit chopper.

The Transmission Function

A simplified sketch of the chopper mechanism considered herein is shown in Fig. 5.2.1. It consists of a spinning rotor, penetrated by rows of slits, only a few of which are shown in the sketch. When the rotor slits sweep past the collimator slits, a burst of neutrons is allowed to pass through the chopper mechanism. A neutron having a sufficiently high velocity can pass through the entire length of the rotor slit before it sweeps by a collimator slit. In general, the fraction of neutrons transmitted through the slit will depend on their velocity, or equivalently, on their time of flight, and on the rotor speed.

UNCLASSIFIED
2-01-058-01-648

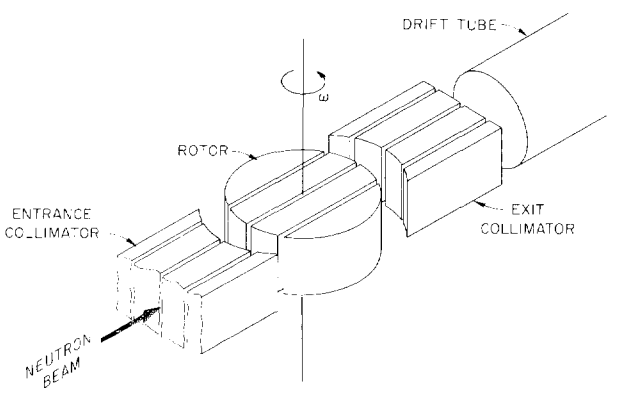

Fig. 5.2.1. Typical Neutron Chopper Geometry.

The action of the rotor on neutrons of a given velocity can be described in the following manner. Consider a beam of monoenergetic neutrons defined by a collimator and incident on a rotor spinning with an angular velocity ω. If the path of a single neutron of velocity V is traced through the rotor (including slit and rotor material), the probability of transmission, P, is given by

$$P(V) = e^{-\Sigma(V)T} , \tag{1}$$

[1] Co-op student from Missouri School of Mines (Rolla, Missouri).
[2] V. V. Verbinski, *Neutron Phys. Ann. Prog. Rep., Sept. 1, 1960*, ORNL-3016, p. 130.

where

Σ = macroscopic total cross section of the rotor material,

T = thickness of rotor material penetrated by the neutron.

The average transmission is obtained by averaging the values of P over all the neutron paths. The chopper transmission function, $C(\omega/V)$, can be determined, point by point, by repeating the averaging for neutrons of other velocities.

It will be noted that the total cross section is used as the removal cross section in Eq. 1. This is a very good approximation, because the very small solid angle usually viewed by the detectors implies that a scattered neutron will be effectively lost from the beam.

Neutron Flight Paths

For the discussion to follow it is convenient to define a laboratory coordinate system centered upon the rotor axis. The x axis is parallel to the source-rotor-detector center line, the y axis at a right angle, and the z axis coincident with the rotor axis. The angle which the entering neutron makes with the x axis is called β. If one considers for the moment that the neutrons enter the slit parallel to the x axis, i.e. at $\beta = 0$, the straight-line equation of the neutron trajectory, $y = H$, can be transformed into rotor coordinates (primed) to get the following parametric equations:

$$x' = x \cos\phi + H \sin\phi \,, \tag{2}$$

$$y' = H \cos\phi - x \sin\phi \,. \tag{3}$$

Physically H is the value of y in the laboratory system at which the neutron passes the center of the rotor. The following relations hold between the remaining parameters in Eqs. 2 and 3:

$$x = V\tau \,, \tag{4}$$

$$\phi = \omega\tau \,, \tag{5}$$

where

V = the velocity of the neutron,

τ = time, taken to be zero when the neutron crosses the midplane of the rotor,

ω = angular velocity of the rotor.

At time τ, according to Eqs. 2 and 3, the axes of the rotor coordinates are parallel with the axes of the laboratory coordinates.

In order to obtain a reasonable degree of resolution, the rotor slit width must be very small compared with its circumference. Thus the angular rotation required for complete cutoff of the neutron beam is also quite small. This fact permits several convenient approximations. By taking $\sin\phi \simeq \phi \simeq \omega\tau$ and $\cos\phi \simeq 1$, good to 1 part in 10^5 for a typical rotor studied, Eqs. 2 and 3 can be written as

$$x' = V\tau + H\omega\tau \,, \tag{6}$$

$$y' = H - V\omega\tau^2 \,. \tag{7}$$

From Eqs. 6 and 7 the parabolic equation describing the trace of the neutron on the rotor grid system is obtained by elimination of the parameter τ:

$$y' = H - \frac{\frac{V}{\omega} x'^2}{\left(\frac{V}{\omega} + H\right)^2} . \tag{8}$$

If the rotor is stopped at the instant each neutron under consideration has reached the rotor midplane, Eq. 8 will describe the neutron trace on the rotor grid but in the laboratory system. By the adoption of this artifice the primed coordinates will henceforth describe events in the laboratory system. Marseguerra and Pauli[3] have derived Eq. 8 for the special case when $H = 0$:

$$y' = -\frac{\omega}{V} x'^2 . \tag{9}$$

The path length of each neutron through the rotor material is obtained by computing the points of intersection of the neutron trace, Eq. 8, and the straight lines defining the slit edges. For a rotor that has been stopped at some angle of rotation $Q = \omega t$, the upper and lower edges of the parallel slit are given by

$$y' \simeq x' \tan Q + (A \pm W)/\cos Q , \tag{10}$$

where

W = half-width of slit,

A = distance from rotor axis to center of slit,

Q = angle of the rotor slits, in the laboratory system, at the time the neutron under consideration reaches the midplane of the rotor.

The plus sign applies to the upper edge, the minus to the lower. The geometry is diagrammed in Fig. 5.2.2.

Simultaneous solution of the path length and slit edge equations yields

$$\frac{-\frac{V}{\omega} x'^2}{\left(\frac{V}{\omega} + H\right)^2} = -x' \tan Q + (A \pm W)(\cos Q + \sin Q \tan Q) - H , \tag{11}$$

in which the $\pm$ sign again indicates upper and lower edges of the slit, respectively.

[3] M. Marseguerra and G. Pauli, *Nuclear Instr. & Methods* 4, 140 (1959).

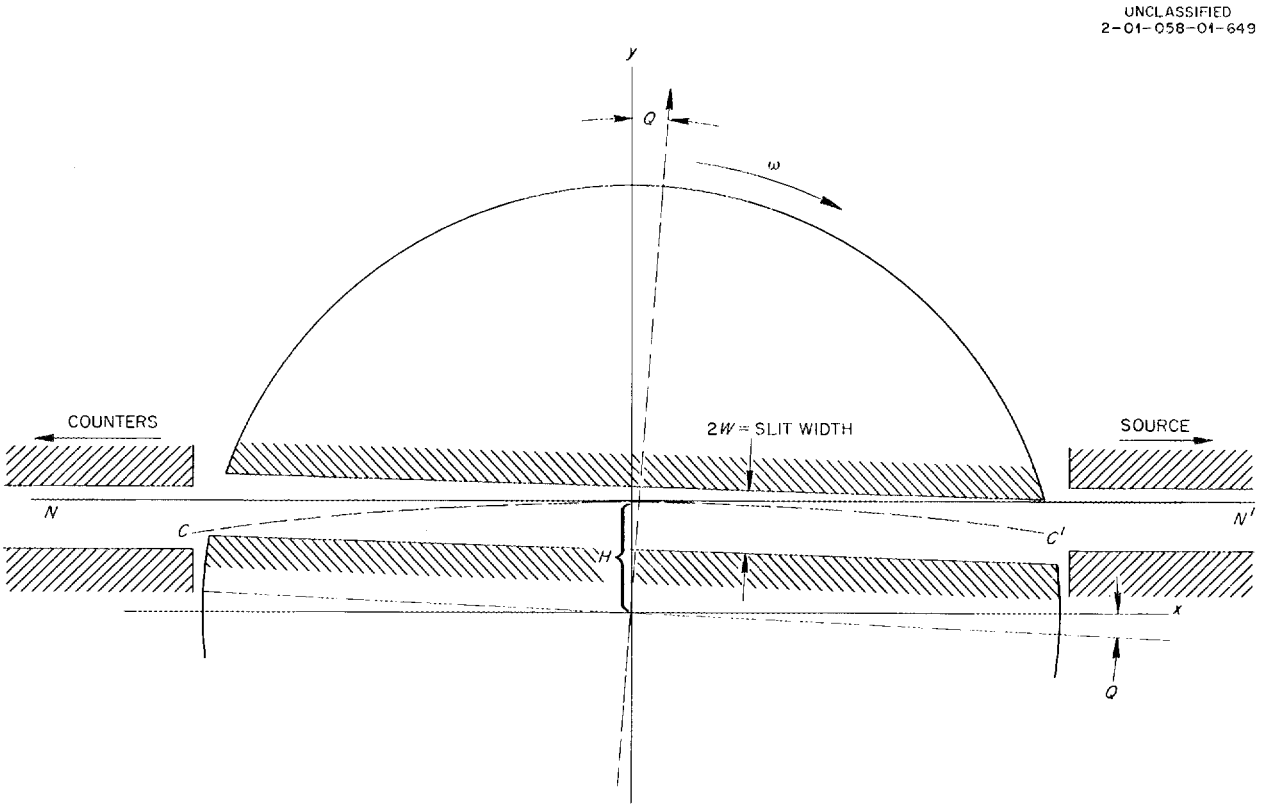

Fig. 5.2.2. Diagram of Chopper Burst Mechanism. The neutron trajectory N-N' in the laboratory coordinate system becomes a relatively flat curve C-C' in the rotating rotor coordinate system associated with the particular neutron in question.

The solution for the edge intercepts is

$$x' = \frac{\tan Q \pm \sqrt{\tan^2 Q - 4\left[\dfrac{V/\omega}{\left(\dfrac{V}{\omega} + H\right)^2}\right][(A \pm W)/\cos Q - H]}}{2\left[\dfrac{V/\omega}{\left(\dfrac{V}{\omega} + H\right)^2}\right]}, \tag{12}$$

where $(A + W)$ is for the upper edge intercepts and $(A - W)$ for the lower.

By using the approximations $\sin Q \simeq \tan Q \simeq Q$, $\cos Q \simeq 1$, and $V \gg H\omega$, Eq. 12 can be reduced to the simple yet accurate expression

$$x' = \frac{Q \pm \sqrt{Q^2 - \frac{4\omega}{V}\left(1 - \frac{2H\omega}{V}\right)[(A \pm H) - H]}}{\frac{2\omega}{V}\left(1 - \frac{2H\omega}{V}\right)}. \tag{13}$$

The neutron velocities involved are sufficiently large compared with the rotor angular velocity to make the neutron trajectories in the rotor coordinate system relatively flat curves. This allows the convenient approximation that the neutron path length in the rotor material, T, is the straight-line distance between the point where the neutron enters the rotor material and the point of exit.

The chopper slit has a breadth many times greater than the slit width $2W$, allowing neutrons to travel at some maximum angle δ with respect to the slit axis. The effective value of δ is limited either by the entrance collimator or by the size of the bank of neutron counters. Its importance lies in increasing the value of x by $(\cos \delta)^{-1} \simeq 1 + (\delta^2/2)$, where $(x\delta^2/2)$ is smaller than the "bin size" to be discussed below. Beam divergence in this direction has therefore been ignored.

Transmission Function Equations

A problem in the the $C(\omega/V)$ analysis is created by the finite length of the entrance and exit collimators, which permits neutrons to enter the rotor slits at values of $\beta \neq 0$, as in Fig. 5.2.3. The limiting magnitude of β is determined by the collimator design and is a function of $|H - A|$, the height of the neutron above or below the longitudinal center line of the slit when it reaches the midplane of the rotor. The

UNCLASSIFIED
2-01-058-01-650

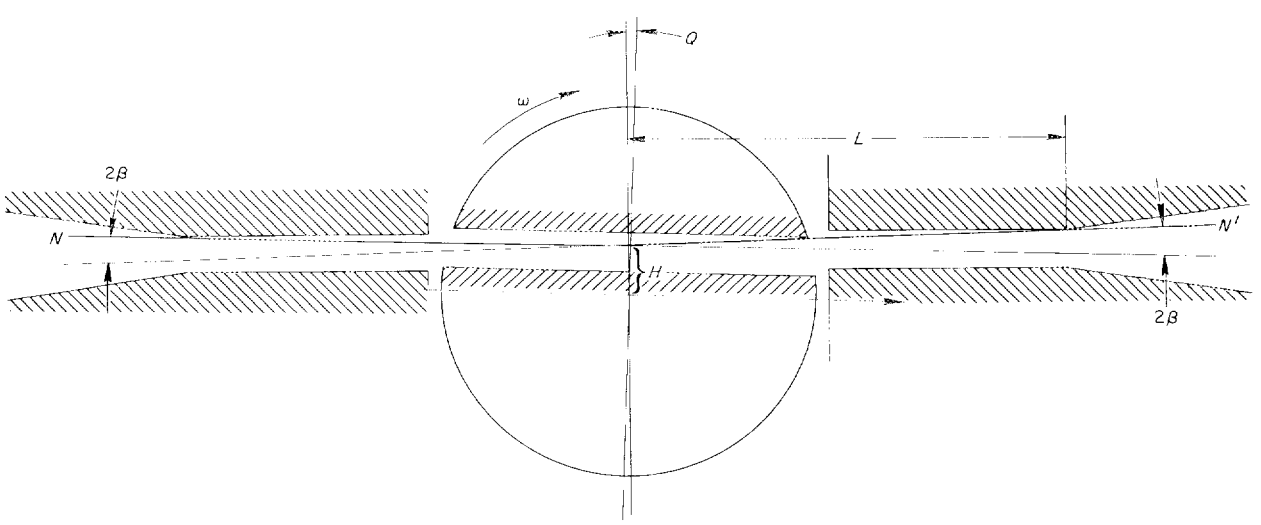

Fig. 5.2.3. Effect of Collimator Geometry on Angle at Which Neutron Can Enter Rotor.

relation between $\Delta\beta$ (the maximum departure from $\beta = 0$) and H is

$$\Delta\beta = \tan \frac{W - |H - A|}{L} \cong \frac{W - |H - A|}{L} , \tag{14}$$

where L is the distance from the center of rotation of the rotor to the effective end of the collimator.

For a fixed rotor speed ω, the transmission function $C(\omega/V)$ for neutrons of velocity V is just the average transmission $P(V)$ of Eq. 1. To obtain this average the neutron trajectories must be sampled by varying β, H, and Q. The proper averaging of $P(V)$ over all neutron trajectories is expressed by

$$C\left(\frac{\omega}{V}\right) = \frac{\displaystyle\int_{Q=-\frac{\pi}{2}}^{\pi/2} \left\{ \int_{H=A-W}^{A+W} \int_{\beta=-\frac{W-|H-A|}{L}}^{+\frac{W-|H-A|}{L}} \exp\left[-\Sigma(V)\, T\left(\frac{\omega}{V}, H, Q+\beta\right)\right] d\beta\, dH \right\} dQ}{\displaystyle\int_{Q=-\frac{\pi}{2}}^{\pi/2} \int_{H=A-W}^{A+W} \int_{\beta=-\frac{W-|H-A|}{L}}^{+\frac{W-|H-A|}{L}} d\beta\, dH\, dQ} . \tag{15}$$

The quantities Σ and T are as defined for Eq. 1. In the treatment below, $C(\omega/V)$ is solved for a series of values of ω/V, holding $\Sigma(V)$ constant for the series. The effective variable is thus ω/V. The equation samples neutrons of velocity V arriving at the center of the slit at all possible times, that is, at all values of Q during the sweep of the slit past the collimator; at all values of H permitted by the collimator; and at all possible β-angles permitted by the collimator.

If the last integration in Eq. 15 is performed over Q ($= \omega t$), the result is the time dependence or burst shape of the transmission. The time $t = 0$ corresponds to the center of the burst.

Equation 15 can be further simplified in the following fashion: Consider a neutron path tilted at an angle β from the x axis and reaching the center of the slit after the rotor has turned through an angle Q. The transmission is identical to that of a $\beta = 0$ neutron reaching the center at the same height H when the rotor has turned through an angle θ ($= Q + \beta$). The relative angle θ then is the angle determining the neutron transmission probability P. As the slit sweeps past the collimator a single burst of neutrons is released over a small range of angle Q. The integral over Q clearly contributes nothing for the larger values of the limits of Q, so that the exact limits on the integral over Q are relatively unimportant provided that they are taken large enough. Also, $C(\omega/V)$ is independent of the time a given neutron is transmitted within the burst. Because of these considerations, a new angular variable θ ($= Q + \beta$) can be introduced, with limits of integration $-[(\pi/2) + \beta_{max}]$ and $[(\pi/2) + \beta_{max}]$, in which $\beta_{max} = W/L$.

After the order of integration is changed, the modified equation is written as

$$C\left(\frac{\omega}{V}\right) = \frac{\displaystyle\int_{H=A-W}^{A+W} \int_{\beta=-\frac{W-|H-A|}{L}}^{\frac{W-|H-A|}{L}} \int_{\theta=-\frac{\pi}{2}+\beta}^{\pi/2+\beta} \exp\left| -\Sigma(V)\, T\left(H, \theta, \frac{\omega}{V}\right)\right| d\theta\, d\beta\, dH}{\displaystyle\int_{H=A-W}^{A+W} \int_{\beta=-\frac{W-|H-A|}{L}}^{\frac{W-|H-A|}{L}} \int_{\theta=-\frac{\pi}{2}+\beta}^{\pi/2+\beta} d\theta\, d\beta\, dH} . \tag{16}$$

Since varying the limits of Q in the above case causes no change in $C(\omega/V)$, the limits can be varied at will, well beyond the burst. These limits then can be considered as not being functions of β. This makes possible an integration first over β. The final simplified equation is

$$C\left(\frac{\omega}{V}\right) = \frac{\displaystyle\int_{H=A-W}^{A+W} \int_{\theta=-\frac{\pi}{2}}^{\pi/2} \frac{W-|H-A|}{L} \exp\left| -\Sigma(V)\, T\left(H, \theta, \frac{\omega}{V}\right)\right| d\theta\, dH}{\displaystyle\int_{H=A-W}^{A+W} \int_{\theta=-\frac{\pi}{2}}^{\pi/2} \frac{W-|H-A|}{L}\, d\theta\, dH} , \tag{17}$$

Equation 15 gives the proper transmission function in practice only when the neutron detector bank uniformly intercepts all the neutrons between $+\beta_{max}$ and $-\beta_{max}$. If it uniformly intercepts only a smaller angle, $+\epsilon$, where $\epsilon = 0$, when $\beta = 0$ (the condition when the detectors are centered on the collimator axis), then the triangular weighting function $(W - |H - A|)/L$ becomes flattened at the top to where $|H - A|/W = \epsilon/\beta_{max}$. Both shape and magnitude of the $C(\omega/V)$ curve will vary with lateral misalignment of either rotor or counter bank with respect to the collimators. The severe requirements for collimator-rotor alignment have led to abandonment of fine collimator slits for low-energy, low-resolution spectrometers. The result is decreased resolution (increased burst width) and higher background. At low energies, however, the background can be decreased by the use of "black" materials such as B^{10} or Li^6. Such spectrometers are called beam sweepers. For a beam sweeper, the weighting function $(W - |H - A|)/L$ is simply deleted from Eq. 17.

Numerical Evaluation of Transmission Function

In Eq. 17 the integration over β is accomplished by weighting with respect to H. From the integration over β it is seen that $\Delta\beta$, the range of β angles that the neutron trajectories can take and still pass through both entrance and exit collimators, is $\pm(W - |H - A|)/L$. This scheme makes it necessary to integrate over only θ and H, which has been done in the numerical evaluations of Eq. 17. The elimination of the integration over β accomplishes a great saving of computing machine time, but at the price of making

access to the burst shape more difficult. The burst shape still can be calculated, however, and the method is described in a later paragraph.

A program to numerically solve Eq. 17 has been written for the IBM-7090 computer.[4] It yields, as a first result, a table giving a path length for each value of H and θ, which is then examined by the computer and developed into a histogram of the number of rays penetrating a given amount of rotor material T, i.e., an $N(T)$ versus T plot.

Rather than compute $e^{-\Sigma T}$ for each mesh point, a neutron encountering an amount of rotor material within a range T_i to $T_i + \Delta T$ is recorded as a count in the ith bin of a histogram. This count, before being placed in the histogram, is weighted by the function correcting for β deviation, $(W - |H - A|/L)$. After all rays are examined, the transmission probability of the entire burst of neutrons of velocity V is given by

$$C\left(\frac{\omega}{V}\right) = \frac{\sum_i N_i(T)\, e^{-\Sigma\left(T_i + \frac{\Delta T}{2}\right)}}{\sum_i N_i(T)}, \tag{18}$$

where

$N_i(T)$ = weighted counts in ith bin,

$T_i + \frac{\Delta T}{2}$ = mean thickness of rotor material encountered by rays of the ith bin,

T = 0 is treated as a special bin.

The histogram is a property of the chopper slit geometry, of the collimator geometry, and of the ratio, ω/V, of the rotor angular velocity to the neutron linear velocity. The construction of 10 to 15 histograms, each for a given value of ω/V, is adequate for construction of a complete $C(\omega/V)$ curve. Once developed the $N_i(T)$ histogram is used in Eq. 18, with the proper value of Σ to take care of the variation of neutron cross sections with energy.

The repeated use of the histogram with several values of Σ accomplishes sizable savings in computer time and saves further time in permitting neglect of all paths beyond a suitably chosen cutoff. For example, in a 200-bin histogram with a bin width of 0.02 in., all neutrons traversing more than 4 in. (200 × 0.02 in.) of rotor material were stored in the last bin, where $N_{200}\, e^{-4\Sigma} \simeq 0$. Once the $N(T)$ curve has been developed for any slit geometry, the remainder of the computer program can be applied almost without modification.

As a check on the utility of the histogram device, the data of the example given above was directly evaluated by taking each individual path length, computing its attenuation, and dividing the sum of the attenuations by the number of paths considered. The agreement, to within 0.1%, validates the method and

[4] W. R. Burrus suggested several of the numerical techniques used and was helpful in guiding the development of the computer program.

indicates that the chosen bin width is sufficiently small, perhaps even excessively small for many problems. The rotor material for the example cited was K Monel.

Transmission Function for Slits Displaced from Rotor Center

A slit at a distance A from the center of a rotor of radius R will not have the same transmission or burst shape as a slit at the center of the rotor because: (1) the slit length is reduced by a factor $\sqrt{1-(A/R)^2}$, and (2) the component of the rotor velocity perpendicular to the slit is also reduced by $\sqrt{1-(A/R)^2}$. The latter change is already included in the derivation of Eq. 9. An investigation of the dependence of the transmission function $C(\omega/V)$ on A shows that the dependence is so weak (a quadratic) that a single value of A could be chosen, corresponding to the proper average of $C(\omega/V)$ over the various values of A.

Construction of $C(\omega/V)$ Curve

The final output of the computer program consists of a series of values of transmission as a function of the total cross section, Σ, of the rotor material and the ratio of rotor versus neutron velocities, ω/V. From this data it is possible to construct a family of parametric curves of transmission versus Σ for each value of ω/V. Such a family of curves is shown in Fig. 5.2.4. These curves make the output data very

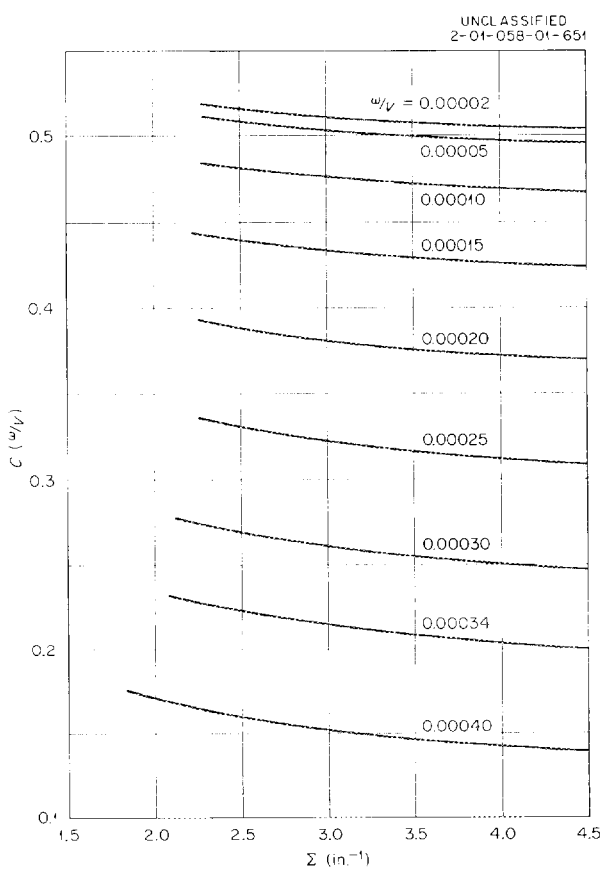

Fig. 5.2.4. A Typical Family of Transmission Function Curves.

flexible, since from them it is easy to develop a transmission function curve for the same rotor geometry and for practically any rotor angular velocity, type of rotor material, or neutron velocity range of interest. The experimenter first chooses a rotor speed, ω. Next a value of neutron velocity, V_1, is chosen such that the ratio of ω/V_1 corresponds to one of the already plotted parametric curves. For a neutron of known energy (or velocity) the total cross section, Σ, is, of course, readily available. These values, ω/V_1 and $\Sigma(V_1)$, fix the value of $C(\omega/V_1)$ in Fig. 5.2.4. The value is plotted, as in Fig. 5.2.4, and the process repeated with V_2, $V_3 \ldots V_i$ until the smooth curve can be drawn. If resonances exist in the cross section of the rotor material, the parametric curves must be more closely spaced in the nonlinear region, as shown near the top of Fig. 5.2.4. Accurate interpolation is then possible for all values of ω.

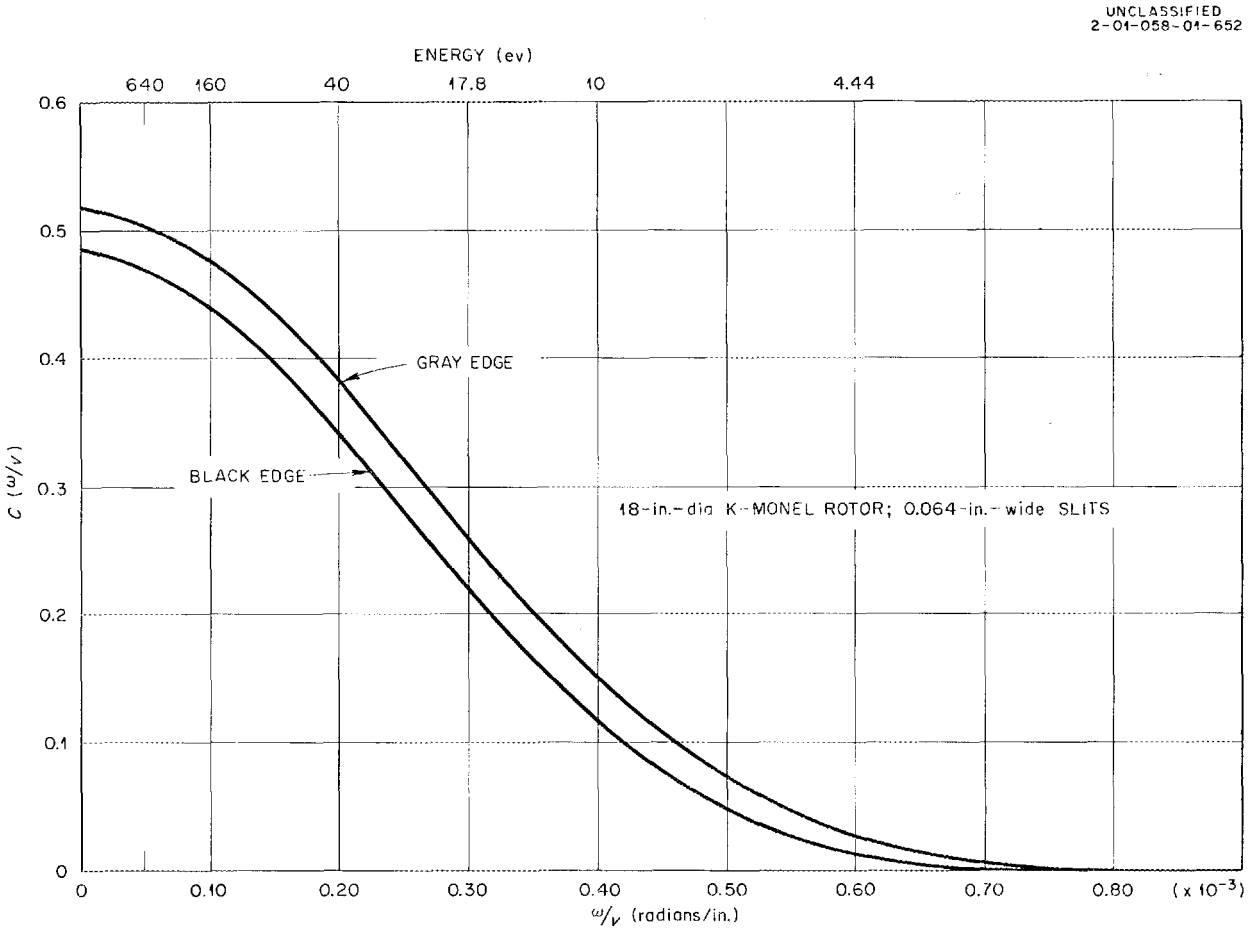

Fig. 5.2.5. Comparison of Transmission Function Curves for Black-Edged and Gray-Edged Rotor Slits.

A comparison of $C(\omega/V)$ curves from black-edged and gray-edged slits is shown in Fig. 5.2.5. The gray slit edges have the effect of distorting the $C(\omega/V)$ curve upward. From the magnitude of the distortion it can be seen that the gray edge considerations are critical in the determination of a neutron spectrum, even with the use of an 18-in.-dia K-Monel rotor.

Burst Shape

It has been noted earlier that the use of a weighting function facilitated computation by eliminating the integration over β. In order to calculate the burst shape, however, β must be factored in from the relation $\theta = Q + \beta$, where the range of β is related to H by $\beta_{max} = \pm(W - |H - A|/L)$. It can be seen that fixing a value of Q generates a diamond-shaped region on the (H,θ) table which is the first output of the computer program. Fixing a value for Q selects for consideration all neutrons arriving at the midplane of the rotor at a time $t = Q/\omega$. By evaluating the transmission of the neutrons whose path lengths are enclosed within the diamond, the transmission of the rotor at time $t = Q/\omega$ thus obtained is a point on the burst-shape curve. A plot of transmission versus time, the burst shape, can thus be obtained by choosing various values of Q and evaluating the corresponding transmissions.

Error Considerations

In any numerical integration the accuracy of the value obtained is essentially a function of the number of increments into which the region under consideration is divided. Several experiments were conducted with the slit transmission program to find the relation between the actual value of $C(\omega/V)$ and that given by the use of a finite number of H and θ increments.

Initially three sets of increments were chosen:

Number of θ Intervals	Number of H Intervals
24	50
48	100
96	200

Since the symmetry of the slit permitted integration over only positive values of θ, the mesh in θ given above is essentially as fine as the corresponding mesh in H.

The pairs of $\Delta\theta$ and ΔH intervals shown above were used to compute the quantity $C(\omega/V)$ for various values of ω/V and Σ. Plots of the resulting $C(\omega/V)$ versus mesh increment were essentially linear. This indicated that the higher terms of the corresponding error polynomial for the relation between $C(\omega/V)$ and the fractional change in mesh increment were small. Extrapolation to zero-increment width yielded the correct value of $C(\omega/V)$ to an estimated accuracy of 0.2%.

By increasing the value of Σ in Eq. 17 to some enormous value, an approximation of a black-edged slit is obtained. This was done for a parallel-edged slit passing through the center of the rotor and a parallel beam of neutrons at $\beta = 0$, in order to compare the results with the transmission function curve analytically obtained by Stone and Slovacek.[5] For the finest mesh used, over-all agreement was better than ±0.1%.

[5] R. S. Stone and R. E. Slovacek, *Reactor Spectrum Measurements Using a Neutron Time-of-Flight Spectrometer*, KAPL-1499 (1959).

Conclusions

From the development earlier it is obvious that the method described can be applied to any shape of slit which can be piecewise described by simple mathematical expressions. Reasonably correct characteristics of a given slit can be obtained with only a few minutes of computer time, making the method a useful tool for empirically adjusting parameters of a chopper system or for investigating the effects of system misalignments.

5.3. PULSED-NEUTRON MEASUREMENTS IN BERYLLIUM

E. G. Silver and G. deSaussure

Measurements of diffusion coefficients in beryllium at temperatures ranging from 20 to 511°C by the pulsed-neutron method have been reported previously.[1] An attempt has now been made to extend this work to the region below 20°C for comparison with calculations by Singwi *et al.*[2] which predict large changes in the diffusion coefficient, D, and the diffusion cooling parameter, C, as the temperature of the material decreases. The apparatus and procedures used in the earlier part of this work were identical with those previously reported; a subsequent modification to a part of the equipment will be described below in introducing the results obtained by its use. In addition to the work noted above, a persisting disagreement in the reported values[1,3,4] of the diffusion cooling parameter, C, in room-temperature beryllium has prompted a careful remeasurement of several beryllium assemblies at room temperature, as well as measurements using two beryllium assemblies sent by another investigator, whose results differed significantly from ours.

Cold Beryllium Measurements

A large number of measurements were made with various sizes of beryllium assemblies at temperatures of 25, 0, −25, −50, −75, and −100°C, in an attempt to determine D and C at low temperatures. A known nonuniformity of channel width in the Bulk Shielding Facility 18-channel time-base analyzer was corrected for in these measurements by applying a weighting factor to the number of counts in each channel. The weighting factor was taken as the inverse of the number of counts recorded in the same channel during a "channel width run" made immediately before or after the data run. During the channel width run, a total of about 10^5 counts from a random, steady-state source was collected in each channel.

About 100 decay-constant measurements were made, over the range of temperatures noted above, in blocks ranging in size from $8 \times 8\frac{5}{8} \times 8\frac{5}{8}$ in. to $20 \times 20\frac{1}{8} \times 20\frac{1}{8}$ in. A careful analysis of the results led,

---

[1] G. deSaussure and E. G. Silver, *Appl. Nuclear Phys. Ann. Prog. Rep., Sept. 1, 1957*, ORNL-2389, p. 119; *Neutron Phys. Ann. Prog. Rep., Sept. 1, 1958*, ORNL-2609, p. 59; *Neutron Phys. Ann. Prog. Rep., Sept. 1, 1959*, ORNL-2842, p. 115.

[2] K. S. Singwi and L. S. Kothari, *Proc. U.N. Intern. Conf. Peaceful Uses Atomic Energy, 2nd, Geneva, 1958*, Paper P/1638; K. S. Singwi, *Arkiv Fysik* 16, 385 (1960).

[3] W. M. Andrews, *Measurement of the Temperature Dependence of Neutron Diffusion Properties in Beryllium Using a Pulsed-Neutron Technique*, UCRL-6083 (1960).

[4] F. A. Kloverstrom and T. T. Komoto, *Trans. Am. Nuclear Soc.* 1(1), 94 (1958).

however, to the conclusion that the decay constants could not be unequivocally understood because of effects which prevent the establishment of an equilibrium spectrum, thereby changing the decay from a single exponential to a decay having a continuously changing slope. These effects, previously not sufficiently understood, are qualitatively discussed in a following section. It is clear that one cannot expect a constant energy spectrum, and therefore cannot expect a single exponential decay. The relative number of longer-lived neutrons, i.e., neutrons of lower energy persisting in a low-energy state, will increase with buckling and with decreasing moderator temperature. This expectation is borne out in these experiments.

Figures 5.3.1 and 5.3.2 give some examples of the relative change in the decay constant as a function of time, in units of the decay periods, for two assembly sizes and two temperatures in each figure. Although the errors in the relative values of the decay constant are rather large compared to the changes involved, the systematic trend is clearly present.

It will be noted that the errors attached to the points increase with increasing slope of the curves. This effect is partly due to the method of analysis, in which deviations from a single exponential decay over the time span of the analysis are treated as experimental errors. Each of the decay-constant measurements in these figures was made over a time of about six decay periods, so that there is a great deal of overlap in the time intervals in which the successive decay constants were measured.

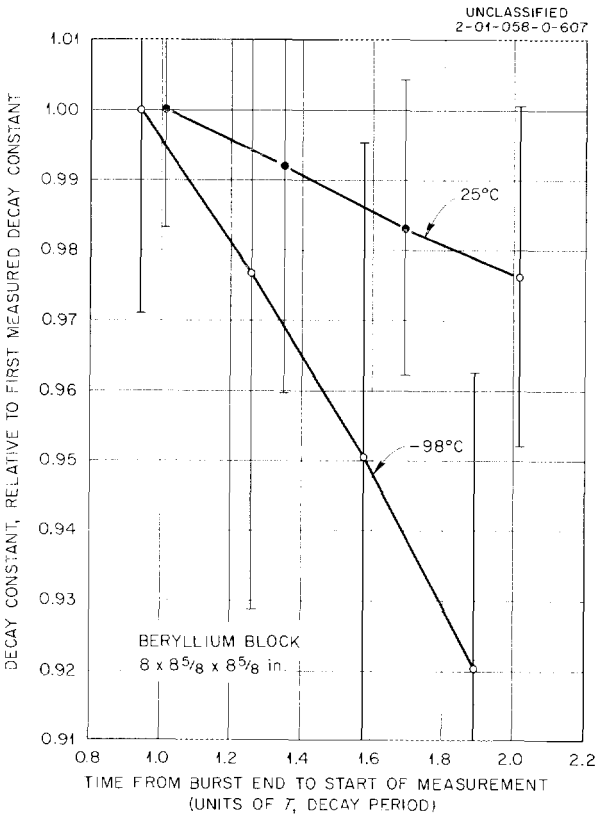

Fig. 5.3.1. Variation in Decay Constant, λ, with Time for an 8 × 8⅝ × 8⅝ in. Beryllium Block at 25 and −98°C.

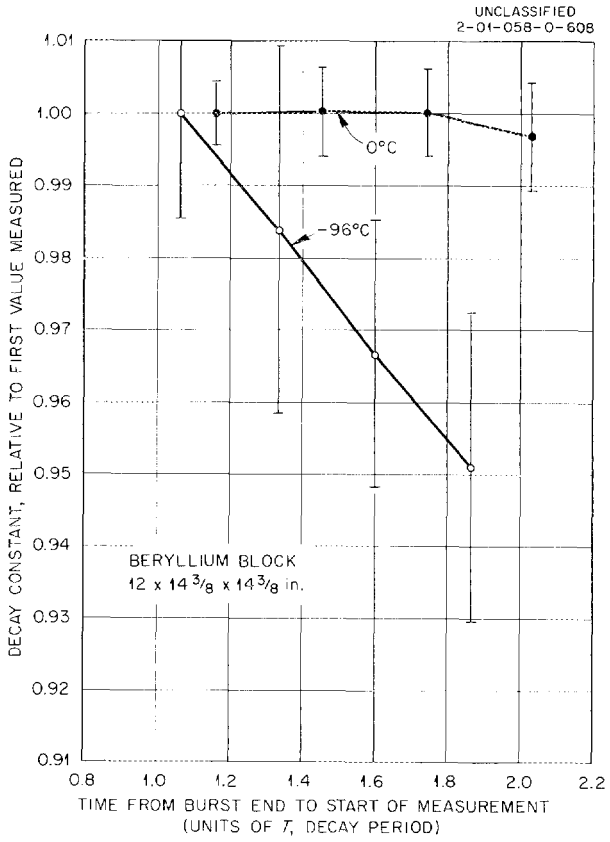

Fig. 5.3.2. Variation in Decay Constant, λ, with Time for a 12 × 14⅜ × 14⅜ in. Beryllium Block at 0 and −96°C.

While the existence of this spectrum-drift effect has so far prevented an accurate determination of D and C as functions of temperature in the temperature range where Singwi predicts large changes, it is clear that the large values of D predicted by the calculations are due to the very few persisting low-energy neutrons. The time needed for establishment of a "pure" population of such neutrons is much too long to be attainable with the available equipment, which possesses but modest source strength and relatively high background, and may be unattainable under any circumstances.

Equipment Improvement

Analysis of the data presented above left open the possibility that better channel-width uniformity might make possible a sufficient increase in waiting time to achieve an equilibrium spectrum, and thus an unambiguous value of the decay constant. This motivated an attempt at improvement. The lack of uniformity in channel width existed from channel to channel at any given time and also from time to time in the same channel. The latter effect was particularly pronounced if the beam-switching tubes in the logic circuit had been replaced in the interim. Figure 5.3.3 shows several channel-width check plots typical of the original equipment. They were obtained by observing random counts from a steady-state source in the

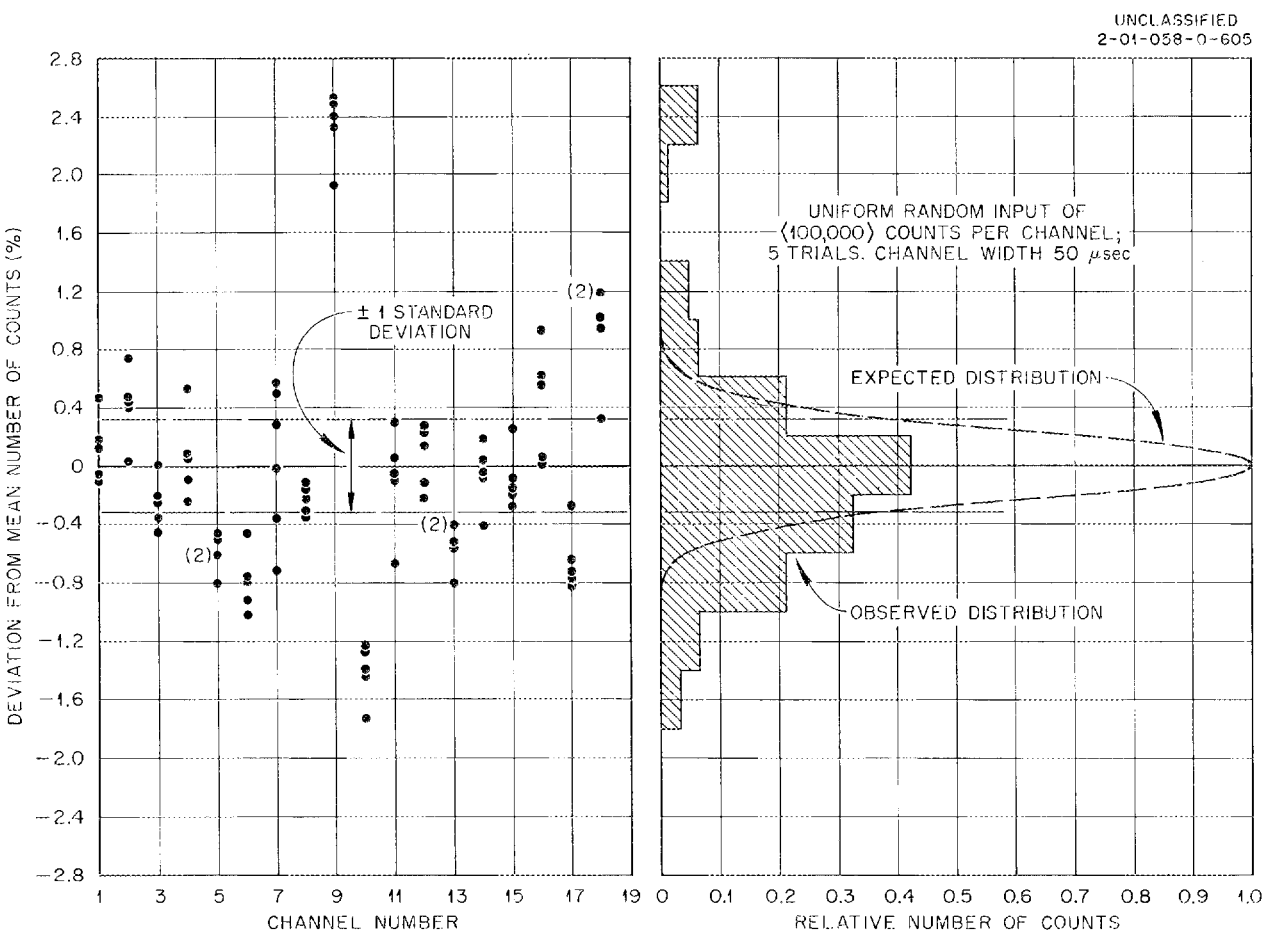

Fig. 5.3.3. Channel-Width Distribution Before Circuit Change.

time analyzer. The right half of the figure is a frequency histogram for these runs, compared with the Gaussian spread to be expected if only statistical variation were involved.

In order to overcome the very obvious channel-width nonuniformity effect, the equipment was modified by the addition of an extra gate circuit which closes 1 μsec before the end of each time channel, remains closed for about 4 μsec, during which time the switch to the next channel occurs, and then reopens.[5] Thus the variable factor of switching time from channel to channel is eliminated. Figure 5.3.4 shows channel-width check plots and a frequency histogram obtained after the circuit was modified. There is little evidence of anything other than statistical factors in the spread of this distribution.

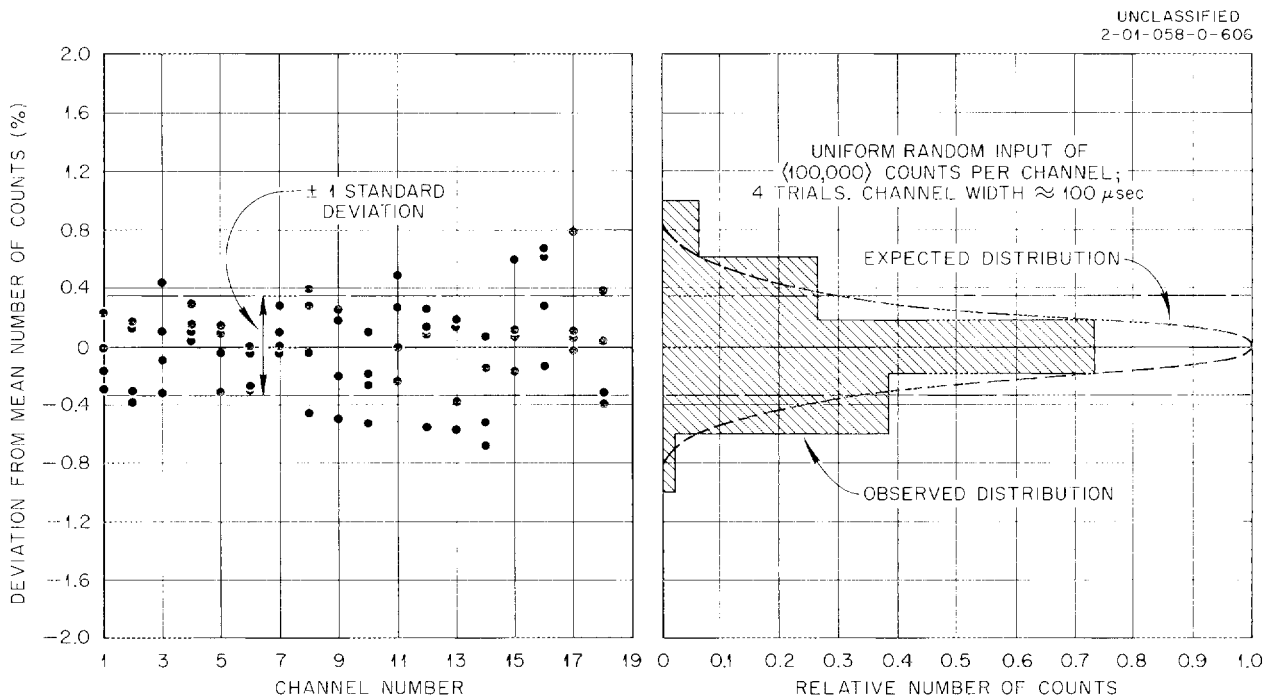

Fig. 5.3.4. Channel-Width Distribution After Circuit Change.

Cold Beryllium Data with Improved Equipment

A number of measurements have been made using the improved circuitry described above, with waiting times extended in some cases far beyond those previously used, to the point where the last time channels were recording almost pure background.

The variations in the decay constant with time observed with the improved system are shown for 25 and −25°C in Figs. 5.3.5 and 5.3.6. While the errors are less than those of previous data, the continuing change in the decay constant persists, and therefore it is still impossible to assign an unambiguous best value to the decay constant, at least as far as small blocks and low temperatures are concerned.

[5]This circuit was designed and installed by J. L. Lovvorn, Instrumentation and Controls Division.

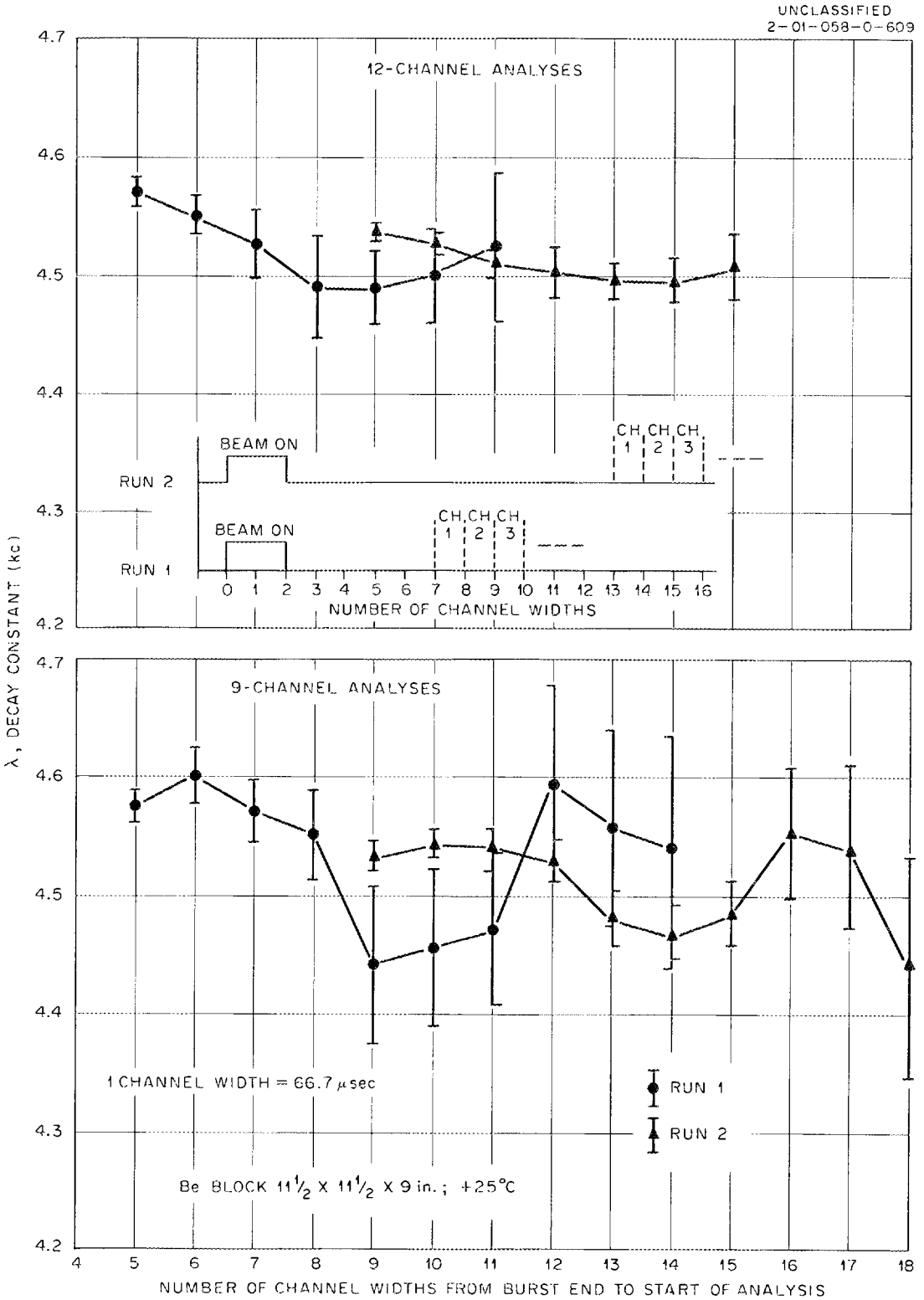

Fig. 5.3.5. Variation in Decay Constant, λ, with Time for an $11\frac{1}{2} \times 11\frac{1}{2} \times 9$ in. Beryllium Block at 25°C (with Improved Circuitry).

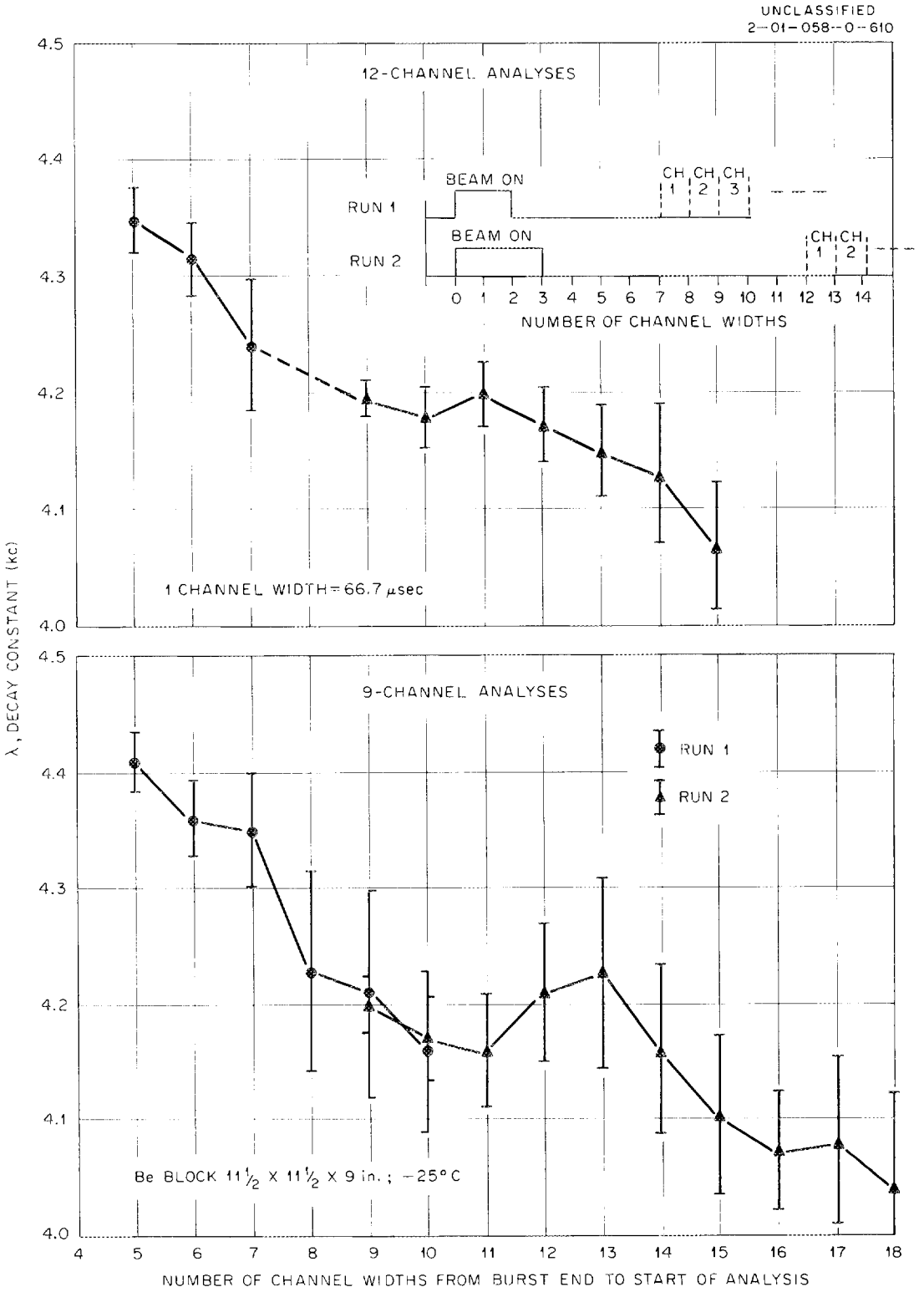

Fig. 5.3.6. Variation in Decay Constant, λ, with Time for an $11\frac{1}{2} \times 11\frac{1}{2} \times 9$ in. Beryllium Block at −25°C (with Improved Circuitry).

Further work toward the solution of these difficulties is projected. There exists the possibility that the method of analysis[6] is introducing spurious variations, and other analytical methods, such as least-squares fitting to the exponential-plus-background model, will be tried to check this possibility. It is also possible that further theoretical consideration may result in a rational scheme for picking a best value of the decay constant for each case.

Room-Temperature Data with Improved Equipment

In order to improve the values of the beryllium diffusion parameters $v\Sigma_a$, D, and C previously reported,[7] two sources of error inherent in the earlier measurements have been reduced. One source lay in the fact that some early work had poor counting statistics and therefore large associated errors. Some of these points have been redetermined by careful remeasurement of the earlier assemblies with the present improved circuitry.

The second source of error resulted from choosing as the best value of the decay constant, λ, that analysis, out of all those performed on each set of data (with various waiting times and spanning various time intervals), which had the smallest associated variance.

As noted above, it is now apparent that even at room temperature there exist continuing variations in the value of λ whose magnitude depends on the assembly size, being most appreciable in the smallest assemblies. The variance in λ determined in any one analysis depends upon the relative background associated with the decay during the time interval spanned by that analysis. This background is a function of burst duration and waiting time to the start of counting. Since these factors are arbitrarily picked, there is a certain amount of arbitrariness in the result of λ. The value of λ, changing with time, will have a lowest variance for some one analysis depending on these arbitrary factors.

In order to remove this difficulty five sets of data taken with the new equipment have been analyzed. For each set an equal value of the "reduced" waiting time, $T' = t/T_d$, where t is the time from the end of the neutron burst to the beginning of the analysis and $T_d = 1/\lambda$, was chosen. Two quite different values of T' were selected and a set of diffusion parameters calculated for each in order to assess the effect of T' on the values. For one analysis T' was in the range $1.5 \rightarrow 1.7$; for the other in the range $2.5 \rightarrow 2.7$. Table 5.3.1 gives the values of the diffusion parameters obtained by these two methods. It will be noted the D is not sensitive to the choice of T'.

[6] R. G. Cornell, *A New Estimation Procedure for Linear Combinations of Exponentials*, ORNL-2120 (June 21, 1956).
[7] G. deSaussure and E. G. Silver, *op. cit.*

Table 5.3.1. Measured Diffusion Parameters in Beryllium for Two Values of T' (Waiting Time Between "Beam Off" and Start of Data Observation)

T', Waiting Time (Units of Decay Periods)	Diffusion Parameters		
	$v\Sigma_a$, Inverse Lifetime (sec^{-1})	D, Diffusion Constant (cm^2/sec)	C, Diffusion Cooling Constant (cm^2)
		$\times 10^6$	
1.5–1.7	288 ± 12	1.250 ± 0.0012	1.42 ± 0.22
2.5–2.7	319 ± 23	1.224 ± 0.0021	1.14 ± 0.33

Measurements with Other Beryllium Samples

In order to make sure that the discrepancies in the value of C reported by various workers were not due to differences in the beryllium material itself, some of the beryllium used by both Kloverstrom[4] and Andrews[3] at Livermore Radiation Laboratory was borrowed for test. Two assemblies, one an 8-in. cube and the other a 9-in. cube, were pulsed with the new equipment. No change in experimental procedure or data analysis was made. Figure 5.3.7 compares a portion of the curve of λ versus B^2 obtained by Andrews with the present results from the same material and with previous results from this Laboratory. It is clear that the differences in the value of C obtained are not due to differences in the beryllium, since the Oak Ridge measurements with the Livermore beryllium are in agreement with the previously measured Oak Ridge data. The source of the disagreement must therefore lie elsewhere.

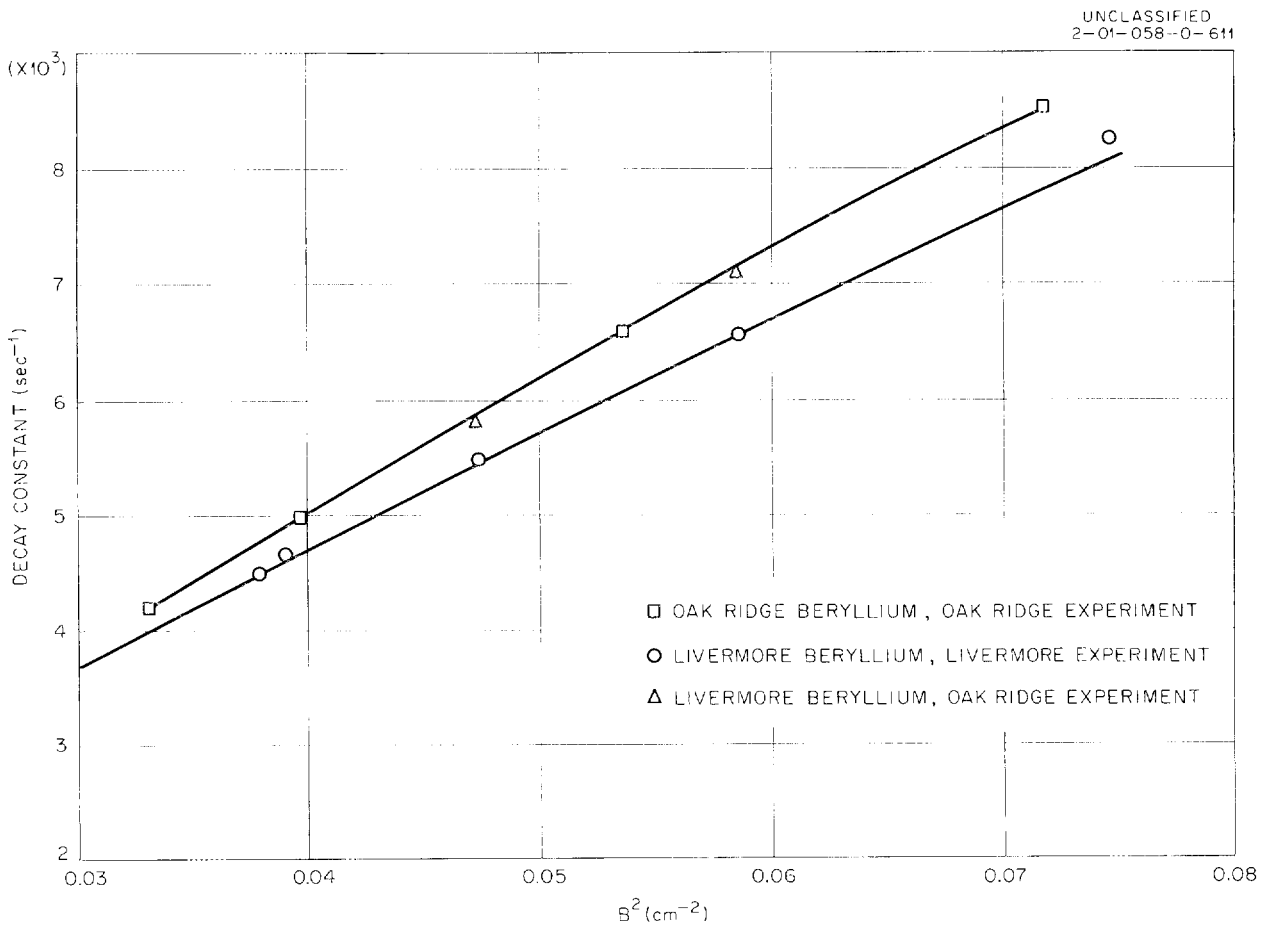

Fig. 5.3.7. Decay Constant, λ, as a Function of B^2, at Room Temperature. Comparison of ORNL results, Livermore results, and ORNL results using Livermore material.

5.4. A NOTE ON MEASUREMENTS OF DIFFUSION PARAMETERS BY THE PULSED-NEUTRON SOURCE TECHNIQUE

G. deSaussure

The pulsed-neutron technique has been extensively used to measure diffusion parameters in a variety of moderators. A description of the technique and an excellent summary of the present status of experiments may be found in a recent review by K. H. Beckurts.[1] It may be seen from Beckurts' review that the values of the absorption cross section and of the diffusion constants obtained by the pulsed-neutron technique for the various moderators are quite consistent. However, some very puzzling discrepancies are observed between various measurements of the diffusion cooling constant, especially for crystalline moderators such as beryllium and graphite.

Beckurts proposes the following possible causes for this discrepancy: (1) the role of B^6 terms, (2) the effect of higher harmonics, and (3) the importance of the data evaluation schemes.

For the case of beryllium, at least, different laboratories measure different decay constants for the same value of the buckling.[2,3] Such discrepancies cannot be blamed on B^6 terms. It is also difficult to see how the effect of spatial harmonics may not be properly accounted for, since, for a small assembly of a moderator with low absorption, the first harmonic decays almost twice as rapidly as the fundamental mode.

The purpose of this note is to propose another possible cause for the observed discrepancies in the measurements of decay constants. It appears that under certain conditions the decay of the neutron population out of a moderating assembly may never be strictly exponential. In this case the "asymptotic decay constant" is not directly measurable and the diffusion cooling constant is not a well-defined concept. The argument will be presented in some detail for the case of beryllium; however, the general conclusions should certainly be valid for crystalline moderators such as graphite and beryllium oxide, and perhaps for other materials as well.

Remarks on the Calculation of the Diffusion Cooling Constant[4,5]

The diffusion cooling effect is obtained by computing the equilibrium neutron-energy spectrum appropriate to a finite diffusing assembly. This equilibrium spectrum is not distorted by diffusion, since the

---

[1] K. H. Beckurts, *Nuclear Instr. & Methods* 11, 144 (1961).

[2] G. deSaussure and E. G. Silver, *Determination of the Neutron Diffusion Parameters in Room-Temperature Beryllium*, ORNL-2641 (1959).

[3] W. M. Andrews, *Measurement of the Temperature Dependence of Neutron Diffusion Properties in Beryllium Using a Pulsed-Neutron Technique*, UCRL-6083 (1960).

[4] G. F. von Dardel, *Kgl. Tek. Högskol. Handl.*, N. 75 (1954).

[5] M. Nelkin, *J. Nuclear Energy* 18, 48 (1958); K. S. Singwi and L. S. Kothari, *J. Nuclear Energy* 18, 59 (1958).

removal of those neutrons that rapidly diffuse out of the assembly is compensated for by the inelastic scattering on the moderator. If the diffusion parameters are properly averaged over this equilibrium spectrum, the decay constant of an assembly of finite size may be computed. From the value of this decay constant the diffusion cooling constant may be obtained. Because of mathematical difficulties the equilibrium spectrum is never computed by using the true transport cross section of the moderator, but what is often used is the incoherent approximation of the transport cross section.[6] It seems in certain cases that if the true transport cross section were to be used, no equilibrium spectrum could be defined, and the decay of the neutron population would never be exponential.

The situation may be illustrated by considering a moderator whose total cross section is due almost entirely to elastic scattering and varies rapidly with energy. If a group of neutrons of various energies is introduced into this moderator, each neutron will diffuse independently, with its own time constant, and it is clear that the spectrum and the "decay constant" will change continuously until the last neutron has left the moderator.

Two-Group Computation of the Decay in a Finite Beryllium Assembly

The elastic transport cross section of beryllium has been computed by Bhandari.[7] This cross section is shown in Fig. 5.4.1. It changes very rapidly with energy and reaches its maximum value where the neutron wavelength is just equal to the distance between parallel planes of Miller's index (1, 0, 1). This corresponds to a neutron energy of 6.85 mv and to a velocity of 1.142×10^5 cm/sec. At this energy the transport cross section is about 18 barns and changes very little with moderator temperature. Below this energy the cross section drops stepwise to a value of 5.5 barns. Above 6.85 mv it is inversely proportional to the square of the neutron energy, up to about 11.6 mv.

[6] K. S. Singwi, *Arkiv Fysik* **16**, 385 (1959).

[7] R. C. Bhandari, *J. Nuclear Energy* **6**, 104 (1957).

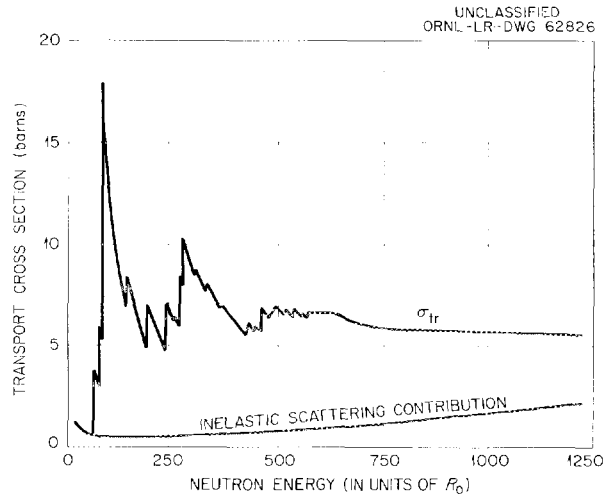

Fig. 5.4.1. The Elastic Transport Cross Section of Beryllium as a Function of Neutron Energy (After Bhandari).

In the energy region around 6.85 mv the inelastic scattering cross section of beryllium is a slowly varying function of energy, but it is strongly temperature dependent; at 300°K it has a value of 0.4 barn, and around this temperature it is proportional to the 7/2 power of the absolute temperature.[8,9]

The neutrons with energies just above 6.85 mv have a very small diffusion coefficient. They also have a very small probability of changing energy, since the scattering is almost entirely elastic. Hence in a small beryllium assembly neutrons of this energy are "trapped" and remain longer than "average" neutrons. In order to compute quantitatively the effect of these trapped neutrons, a two-group neutron diffusion model will be introduced. Group 1 consists of the trapped neutrons; they have a diffusion coefficient D_1 and a probability β_1 of being transferred out of the group. Group 0 consists of those neutrons that are not in group 1; they have a diffusion coefficient D_0 and a transfer probability β_0. Both groups have the same absorption probability α_a. The neutron densities in group 1, n_1, and in group 0, n_0, obey the following coupled differential equations:

$$-\left(D_1 B^2 + \alpha_a + \beta_1 + \frac{\partial}{\partial t}\right) n_1 + \beta_0 n_0 = 0 , \tag{1}$$

$$-\left(D_0 B^2 + \alpha_a + \beta_0 + \frac{\partial}{\partial t}\right) n_0 + \beta_1 n_1 = 0 . \tag{2}$$

The solution of Eqs. 1 and 2 shows that the neutron population of an assembly having buckling B^2 decays according to

$$n = n_1 + n_0 = n^+ e^{-\alpha^+ t} + n^- e^{-\alpha^- t} , \tag{3}$$

where the constants n^+ and n^- must be determined from the initial distribution, and where

$$\alpha^{\pm} = \alpha_a + \frac{D_1 + D_0}{2} B^2 + \frac{\beta_1 + \beta_0}{2} \left\{ 1 \pm \left[1 + 2 \frac{(D_1 - D_0)(\beta_1 - \beta_0)}{(\beta_1 + \beta_0)^2} B^2 + \left(\frac{D_1 - D_0}{\beta_1 + \beta_0}\right)^2 B^4 \right]^{1/2} \right\} . \tag{4}$$

If the energy width of the trap is sufficiently narrow, it follows from the detailed balance condition that $\beta_1 >> \beta_0$. This inequality may be used to simplify Eq. 4:

$$\alpha^{\pm} \cong \alpha_a + \frac{D_1 + D_0}{2} B^2 + \frac{\beta_1}{2} \left\{ 1 \pm \left[1 + \frac{(D_1 - D_0)}{\beta_1} B^2 \right] \right\} , \tag{6}$$

$$\alpha^+ = \alpha_a + D_1 B^2 + \beta_1 ; \quad \alpha^- \cong \alpha_a + D_0 B^2 . \tag{7}$$

---

[8] K. S. Singwi and L. S. Kothari, *Proc. Intern. Conf. Peaceful Uses Atomic Energy, 2nd, Geneva, 1958*, P/1638.
[9] A. Akhizer and I. Pomeranchuck, *J. Exp. Theoret. Phys. USSR* 17, 769 (1947).

This result is not surprising: it shows that the asymptotic decay constant is either the decay constant of the average neutron or the probability of transfer or decay of the trapped neutron, whichever of the two is smaller.

Now we shall evaluate α^+, assuming, somewhat arbitrarily, that the trap consists of those neutrons of energy between 6.85 and 7.40 mv. The absorption probability is energy independent; it has been measured as[2]

$$\alpha_a = 288 \pm 60 \text{ sec}^{-1} . \tag{8}$$

The diffusion coefficient in the trap is

$$D_1 = \frac{v_1}{3N\sigma_{tr}(1)} = \frac{1.142 \times 10^5}{3 \times 0.12 \times 18} = 17600 \text{ cm}^2 \text{ sec}^{-1} , \tag{9}$$

where

v_1 = velocity corresponding to 6.85 mv
= 1.142×10^5 cm/sec,
N = density of beryllium atoms
= 0.12 atom/cm-barn,
$\sigma_{tr}(1)$ = transport cross section at 6.85 mv
= 18 barns,

and

$$\beta_1 \cong v_1 N\sigma_{in} = 1.142 \times 10^5 \times 0.12 \times 0.4 = 5482 \text{ sec}^{-1} \text{ at } 300°\text{K} , \tag{10}$$

where $\sigma_{in} = 0.4$ barn at 300°K is the inelastic cross section at 6.85 mv.

The true transfer probability may be somewhat smaller than the probability of an inelastic scattering, since some of this scattering may keep the neutron inside the trap. However, a smaller transfer probability would make the trap effect even more important. For a buckling of 0.072 cm^{-2}, Eqs. 7, 8, 9, and 10 result in $\alpha^+ = 7037$ sec^{-1}.

For an assembly of 0.072 cm^{-2} buckling, the "asymptotic" decay constant measured is[2] $\alpha = 8500 \pm 300$ sec^{-1}. If reasonable parameters are used for the "average neutrons," including a diffusion cooling effect, this decay constant corresponds approximately to the value of α^- defined in Eq. 7.

Thus this two-group model shows that the decay of the neutron population in an assembly of 0.072 cm^{-2} buckling may be approximately represented as

$$n(t) = n^+ e^{-7037t} + n^- e^{-8500t} \; (t \text{ in sec}) . \tag{3a}$$

The constants n^+ and n^- can be obtained if the initial distribution is known. Assuming that initially the neutrons are in a Maxwellian distribution at 300°K, it turns out that $(n^+/n^-) \simeq 5 \times 10^{-3}$.

Measurement of the Asymptotic Decay Constant in a Finite Beryllium Assembly

It is practically impossible to measure directly the asymptotic decay constant of a population decaying according to Eq. 3*a*. It was shown above that initially the first term of the right-hand side of Eq. 3*a* is about 5×10^{-3} times smaller than the second term. It can easily be computed that these two terms become equal in magnitude when the neutron population has decayed for about 0.0036 sec. At that time the neutron population in the assembly has decayed by a factor of 5×10^{12} and the instantaneous "decay constant," defined as

$$\alpha(t) \equiv \frac{1}{n}\frac{\partial n}{\partial t} , \tag{11}$$

is still more than 10% larger than the asymptotic decay constant. Furthermore, the instantaneous decay constant never changes by more than 1% over an *e*-fold decay of the neutron population. This shows that the asymptotic decay constant cannot be measured directly unless one has available an extremely highly pulsed neutron source and equipment entirely free of background.

Furthermore, the neutron population of a beryllium assembly of 0.072 cm^{-2} buckling does not really decay according to Eq. 3*a*, since Eq. 3*a* was obtained by a simplified two-energy-group treatment. A more realistic model would show the decay to be much more complex, first because there is more than one neutron trap – in fact, the transport cross section of beryllium has a sharp peak every time the neutron wavelength is exactly equal to the distance between two parallel planes of a given Miller index as shown in Fig. 5.4.1 – and second, because within each group the decay constant keeps varying with time, since the cross sections in each group show sharp variations. Nevertheless, it is obvious from physical considerations that some neutrons must decay with the constant $\alpha^+ = 7037$ sec^{-1}, so that the asymptotic decay constant in the assembly considered must be equal to or smaller than that value.

Temperature Dependence of the Trap Effect

It is important to note that the trap effect just described is a very sensitive function of temperature. This is because the inelastic scattering cross section varies so rapidly with temperature. For beryllium above 300°K the trap effect is almost entirely negligible for all bucklings of practical interest, and the usual diffusion cooling calculations performed under the incoherent approximation are probably valid. On the other hand, at a temperature of 273°K the probability of scattering out of the 6.85-mv trap becomes $\beta_1 = 3948$ sec^{-1} (instead of 5482 sec^{-1} at 300°K). The decay constant α^+ (Eq. 7) for a buckling of 0.054 cm^{-2}, appropriate to an 8-in. cube, becomes 5186 sec^{-1}, whereas the experimentally measured value[10] of α^- is 6400 ± 200 sec^{-1}. This shows that, even in this larger assembly, at the lower temperature a true equilibrium spectrum is probably never established.

Conclusions

The development presented above demonstrates that the apparent decay constant of neutrons diffusing in a small beryllium assembly keeps decreasing until most neutrons have left the assembly. A more

[10] E. G. Silver and G. deSaussure, Section 5.3 of this report.

realistic model, taking into account the $1/E^2$ variation of the transport cross section within each neutron trap, would indicate that the decay constant keeps decreasing until the very last neutron has left the assembly and that no true equilibrium neutron-energy spectrum is ever established.

The "asymptotic decay constant" apparently measured in a small assembly is actually a function of the intensity of the pulsed-neutron source available, of the limitations imposed by the background conditions, and of the data evaluation scheme. It must also depend somewhat on such things as the energy of the source and the duration of the pulses, since these factors determine the ratio of the trapped neutron population to the total number of neutrons initially present. It does not appear surprising, then, that as the precision of the measurements is increased, the discrepancy between the "asymptotic decay constants" obtained for the same assembly under different experimental conditions also increases.

Since the determination of the diffusion cooling constant and of terms proportional to B^6 and B^8 must rely upon the measurement of the asymptotic decay constant of a small assembly, a quantity which has been shown above to be not measurable, the concept of the diffusion cooling constant is very questionable.

These considerations, since they are limited to small assemblies, do not greatly affect the measurements of absorption cross sections and diffusion constants by the pulsed-neutron-source method because these parameters can be obtained from measurements on large assemblies, in which a true equilibrium energy distribution can be attained.

5.5. AN APPLICATION OF PILE NOISE ANALYSIS TO MEASUREMENTS OF KINETIC PARAMETERS OF A POOL-TYPE REACTOR

M. N. Alam,[1] A. Colomb,[2] and K. M. Henry

Reactor kinetic parameters such as neutron generation time, temperature coefficients, void coefficients, etc. can be estimated from a study of the variation with frequency of the shape of the reactor transfer function. To measure this transfer function requires that a reactivity input signal be injected into the system. This is not always feasible, especially in a power reactor or a large operation reactor such as the Oak Ridge Research Reactor (ORR), because the injection apparatus is a bulky and delicate piece of equipment. However, it is known that the nuclear processes taking place in a reactor are of random nature and therefore produce random reactivity fluctuations. These fluctuations can be regarded as reactivity input signals, which will be transformed by the reactor transfer characteristics. If the fluctuations in neutron density are analyzed, the transfer function is obtained. The analysis can be carried out by performing a Fourier transformation of the neutron density fluctuation. A transformation from the time domain to the frequency domain yields the spectral density of the neutron density fluctuations.

[1]On loan from Pakistan Atomic Energy Commission.
[2]Operations Division.

The spectral density of random fluctuations is a constant over the whole frequency range, so the spectral density of the neutron level fluctuations will be a measure of the reactor transfer function. Moore[3] has shown that the spectral density of the neutron fluctuations is directly proportional to the square of the amplitude of the transfer function.

The present report outlines the theory upon which an experimental measurement of various kinetic parameters will be based and describes the apparatus which has been developed for the experiments. No data have yet been obtained.

The mathematical model of a thermal reactor, with some simplifying assumptions, is known. The transfer function and the square of its amplitude can therefore be calculated. By comparing a measured spectral density with the calculated square of the transfer function amplitude, it will be possible to determine the values of the parameters used in the reactor mathematical model.

The one-group reactor kinetic equations are

$$\frac{dn}{dt} = \frac{(K_e - 1)(1 - \beta_e) - \beta_e}{\ell} n + \sum_{i=1}^{6} \lambda_i c_i , \tag{1}$$

$$\frac{dc_i}{dt} = \frac{K_e \beta_i}{\ell} n - \lambda_i c_i , \tag{2}$$

where

n = neutron density,

K_e = effective multiplication factor,

β_e = effective delayed-neutron fraction,

ℓ = prompt-neutron lifetime,

λ_i = delayed-neutron fraction of ith group,

c_i = concentration of delayed neutrons of ith group.

We use the notations

$$\text{reactivity, } \rho, = \frac{(K_e - 1)/K_e}{\beta} = \frac{\Delta K/K}{\beta} ,$$

$$\ell^* = \ell/\beta_e ,$$

and assume that (1) diffusion theory applies, (2) space and time variables are separable, (3) slowing-down time is small compared to the diffusion time, and (4) reactivity variation is less than 0.1β. The reactivity variation is considered to be a harmonic function: $\rho(t) = \rho_0 e^{i\omega t}$.

The transfer function, defined as

$$\frac{\text{Laplace transform of } \Delta\rho}{\text{Laplace transform of } \Delta n} ,$$

[3] M. N. Moore, *Nuclear Sci. and Eng.* 3, 387 (1958).

can then be deduced to be

$$K_0(i\omega) = \left\{ i\omega \left[\ell^* + \sum_{i=1}^{6} \frac{\beta_i}{\beta_e(i\omega + \lambda_i)} \right] \right\}^{-1} . \tag{3}$$

The numerical solution of Eq. 3 is obtained by taking its reciprocal and separating the real and imaginary parts:

$$\frac{1}{K_0(i\omega)} = \sum_{i=1}^{6} \frac{\beta_i \omega^2}{\beta_e(\omega^2 + \lambda_i^2)} + i\omega \left[\ell^* + \sum_{i=1}^{6} \frac{\beta_i \lambda_i}{\beta_e(\lambda_i^2 + \omega^2)} \right] . \tag{4}$$

The quantity $\frac{1}{K_0(i\omega)}$ can thus be computed for various values of the angular frequency, ω, and the reciprocals of the computed quantities then give the amplitude of the transfer function $|K_0(i\omega)|$.

It can be seen from Eq. 4 that different values of ℓ^* result in different sets of values of $|K_0(i\omega)|$. Calculations using the values of Keepin, Wimett, and Zeigler[4] for β_i and λ_i have been made for five different values of l^* and the resulting values of $|K_0(i\omega)|$ are plotted in Fig. 5.5.1. Since the value of ℓ^* for the Bulk Shielding Reactor I (BSR-I) has recently been determined to be about 9 msec by Perez-Belles *et al.*,[5] the values chosen for the computation lie around this value.

[4]G. R. Keepin, T. F. Wimett, and R. K. Zeigler, *J. Nuclear Eng.* 6, 1 (1957).
[5]R. Perez-Belles *et al.*, *Neutron Phys. Ann. Prog. Rep., Sept. 1, 1960*, ORNL-3016, p. 12.

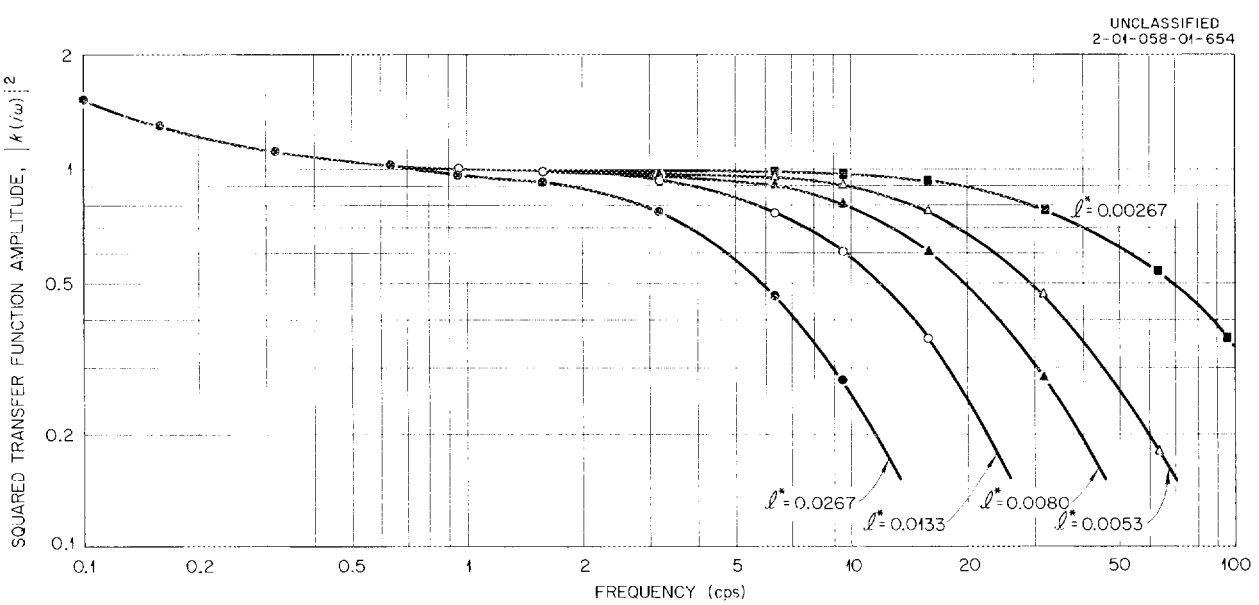

Fig. 5.5.1. The Square of the Reactor Transfer Function Amplitude as a Function of Frequency for Various Values of ℓ^*.

From the curves of Fig. 5.5.1 it is evident that an angular frequency range from about 0.6 to 600 radians per second, equivalent to the frequency range from 0.1 to 100 cycles per second, would be of interest in the present experiments.

The experimental arrangement for the proposed experiments is shown in Fig. 5.5.2. Since it was difficult to obtain a commercially made low-frequency wave analyzer suitable for the present application, an analyzer using analog circuits has been constructed and is shown in Fig. 5.5.3. In it the frequency can be adjusted by changing the effective gain of the two integrators and one amplifier and adjusting the potentiometer P_1. Band width can be adjusted by the potentiometer P_2. A band width of 10% for a voltage attenuation of 3 db, corresponding to a Q-value of 10, is being used for all frequencies.

The equipment has been tested for its frequency response over the required range by feeding a constant-amplitude signal from a sinusoidal function generator into the input of the first d-c filter and measuring the output of the Philbrick amplifier. The response is constant within ±10%, as shown in Fig. 5.5.4.

A photograph of the gamma-ray signal from a Co^{60} source, as displayed on a cathode-ray oscilloscope from the output of the Philbrick amplifier, is shown in Fig. 5.5.5. Figure 5.5.6 is a similar photograph of

UNCLASSIFIED
2-01-058-01-655

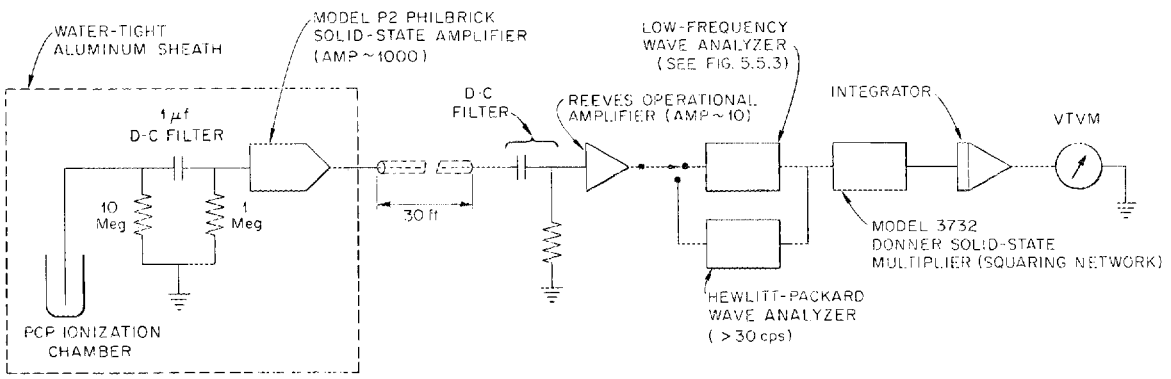

Fig. 5.5.2. Experimental Arrangement for Observing Reactor Reactivity Fluctuations.

UNCLASSIFIED
2-01-058-01-656

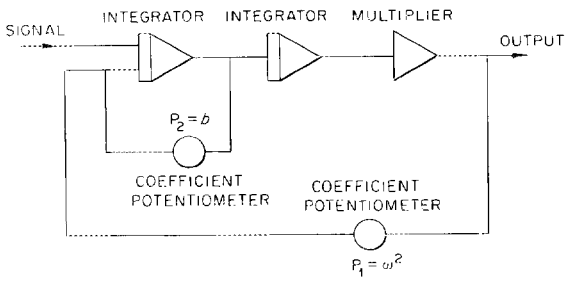

$(\ddot{x} + b\dot{x} + \omega^2 x = A \sin \omega t)$

Fig. 5.5.3. Low-Frequency Wave Analyzer Using Analog Components.

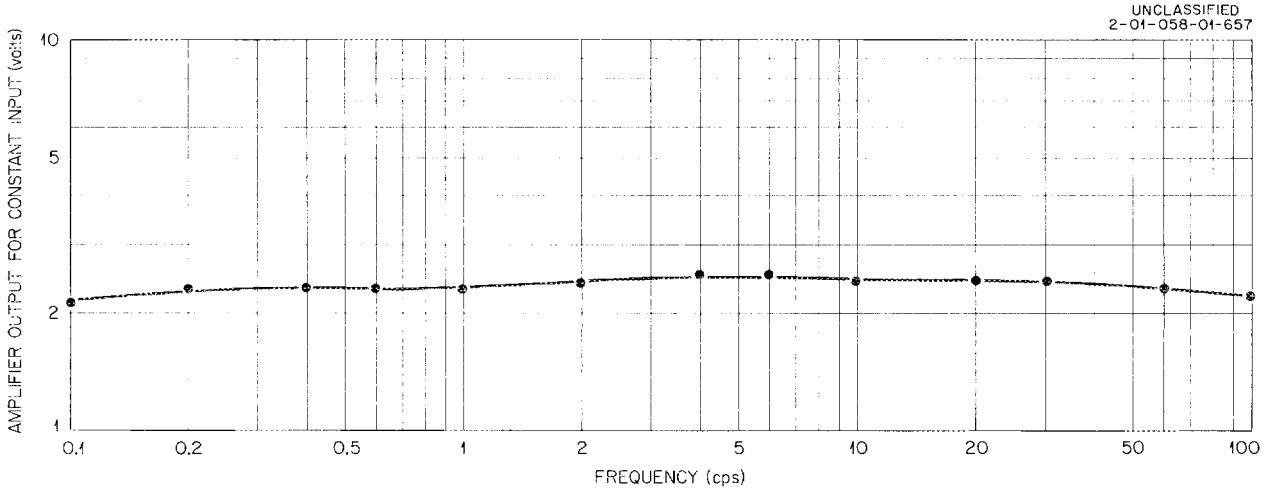

Fig. 5.5.4. Output of the Philbrick Amplifier as a Function of Frequency.

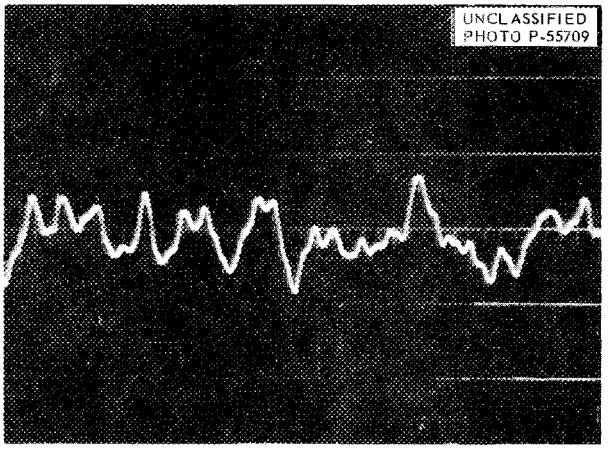

Fig. 5.5.5. Gamma-Ray Signal from a Co^{60} Source.

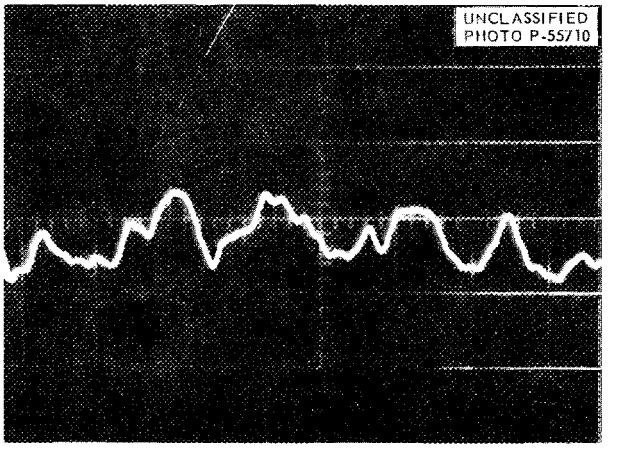

Fig. 5.5.6. Neutron Signal from PCA Core.

the neutron signal obtained when the ionization chamber was exposed to a Pool Critical Assembly (PCA) core.

The last calibration necessary before the equipment can be used to measure the reactor noise spectral density is now in progress. The calibration is based on the principle that the spectral density of the random fluctuation in the decay of a radioisotope is constant with respect to frequency, and therefore the analysis of such fluctuations will yield the frequency response of the instrumentation. The calibration is being made with the PCP chamber located close to a 300-curie Co^{60} source $\sim$15 ft below the surface of the Bulk Shielding Facility pool.

In order to determine an advantageous location for the ionization chamber, a series of flux measurements were made with gold foils at the BSR-I. The data show that a location against the reactor face will be adequate, the flux at this location being only 20% lower than that at the center of the reactor core.

The progress to date indicates that the neutron population fluctuations within a pool-type reactor operating at low powers can be detected and sufficiently amplified to make a frequency analysis possible. Difficulties have been encountered in the reduction of spurious noise but can be overcome by careful grounding and matching of impedances.

The first series of measurements to be made will be that of ℓ^* for comparison with the results of Perez-Belles *et al.*[5] Measurements of the multiplication factor of a subcritical reactor, void coefficients, and temperature coefficients are proposed for future work.

Part 6

NUCLEAR THEORY AND REACTOR PHYSICS CALCULATIONS

6.1. A NONLOCAL POTENTIAL MODEL FOR THE SCATTERING OF NEUTRONS BY NUCLEI

F. G. J. Perey and B. Buck

The empirical (local) optical model potentials introduced to describe the total and differential cross sections for the scattering of nucleons by nuclei have been found to have strengths which vary with bombarding energy. This is to be expected since current theories of the propagation of nucleons through nuclear matter lead to such energy-dependent effective potentials.[1] The energy dependence in general arises in two ways, partly because the effective interaction is nonlocal and partly because of an intrinsic energy dependence.

It is the purpose of the present work to study the consequences of using a nonlocal optical potential and to see how far the energy dependence of the phenomenological local potentials previously used can be accounted for purely in terms of the nonlocality.

In a coordinate representation, a nonlocal potential operating on a wave-function has the form:

$$V\psi(\mathbf{r}) = \int V(\mathbf{r}, \mathbf{r}')\, \psi(\mathbf{r}')\, d\mathbf{r}'. \tag{1}$$

We are now faced with an integrodifferential Schrödinger equation which we solve exactly by numerical integration and iteration.

On physical grounds it is necessary that the kernel function $V(\mathbf{r}, \mathbf{r}')$ be symmetric,[2] i.e.,

$$V(\mathbf{r}, \mathbf{r}') = V(\mathbf{r}', \mathbf{r}) . \tag{2}$$

To facilitate the numerical calculations a separable form was chosen for the nonlocal kernel function:

$$V(\mathbf{r}, \mathbf{r}') = U\left(\frac{\mathbf{r} + \mathbf{r}'}{2}\right) H\left(\frac{\mathbf{r} - \mathbf{r}'}{\beta}\right). \tag{3}$$

Such a form has been suggested before, but only used in the "effective mass" approximation,[3,4,5] which consists of taking only the first nonvanishing term of the expansion of V in powers of $(k\beta)$ where β is the range of the nonlocality and k is the wave-number of the nucleon. Since the empirically determined β is of order 1 fermi, $(k\beta)$ is small only for very low energies, thus throwing doubt on the accuracy of the effective mass approximation. In addition, the effective mass approximation may be misleading in another way in that it gives rise to real potential contributions which are peaked in the region of the nuclear surface. These contributions may be spurious in the sense that the higher terms in the expansion of V greatly reduce their effects. Hence it is of interest to solve the problem in its original integrodifferential form.

---

[1] H. Feshbach, *Ann. Rev. Nuclear Sci.* 8, 49 (1958). The reader is referred to this review article for an extensive bibliography on the optical model.

[2] G. E. Brown and C. T. Dominicis, *Proc. Phys. Soc.* (London) A71, 70 (1958).

[3] W. E. Frahn and R. H. Lemmer, *Nuovo cimento* 5, 523 (1564) (1957).

[4] R. H. Lemmer and A. E. S. Green, *Phys. Rev.* 119, 1043 (1960).

[5] P. J. Wyatt, J. G. Wills, and A. E. S. Green, *Phys. Rev.* 119, 1031 (1960).

In the course of the present work a different type of approximation was discovered. It was originally developed as a guide to the choice of suitable nonlocal parameters for use in the exact calculations; but we found that this approximation gave results very close to those of the accurate treatment. Since the approximation essentially reduces the problem to a local calculation of the usual type, it can be used in conjunction with existing optical model machine codes to give a good imitation of accurate nonlocal calculations.

The Nonlocal Model

The integrodifferential Schrödinger equation is

$$\left[\frac{\hbar^2}{2M}\nabla^2 + E\right]\psi(\mathbf{r}) = -[(U_{so} + W_{so})\, S(r)\mathbf{L}\cdot\sigma]\,\psi(\mathbf{r}) + \int V(\mathbf{r},\mathbf{r}')\,\psi(\mathbf{r}')\,d\mathbf{r}' . \tag{4}$$

In this equation we include a local spin-orbit potential. The problem was actually coded to also include the Coulomb potential due to a charged sphere of radius $R = r_0 A^{1/3}$, but since the Coulomb potential vanishes for neutrons, we drop this term from the equations of this article.

It is assumed that the kernel $V(\mathbf{r},\mathbf{r}')$ is separable and can be written in the form

$$V(\mathbf{r},\mathbf{r}') = U\left(\frac{1}{2}|\mathbf{r}+\mathbf{r}'|\right) H(|\mathbf{r}-\mathbf{r}'|) . \tag{5}$$

Hence $V(\mathbf{r},\mathbf{r}')$ depends on the variables r, r' and $\cos\chi$, where χ is the angle between the vectors $\mathbf{r}$ and $\mathbf{r}'$.

$H(|\mathbf{r}-\mathbf{r}'|)$ was chosen to be a Gaussian function:

$$H(|\mathbf{r}-\mathbf{r}'|) = \frac{\exp\left[-\left(\dfrac{\mathbf{r}-\mathbf{r}'}{\beta}\right)^2\right]}{\pi^{3/2}\beta^3} , \tag{6}$$

which is normalized so that

$$\int H(|\mathbf{r}-\mathbf{r}'|)\,d\mathbf{r}' = 1 . \tag{7}$$

We define

$$p = \frac{1}{2}|\mathbf{r}+\mathbf{r}'| . \tag{8}$$

The form chosen for $U(p)$ in Eq. 5 is similar to those employed in local optical model calculations:

$$-U(p) = [V + iW_I]\, f_S(p) + iW_D f_D(p) , \tag{9}$$

where

$$f_S(p) = \left[1 + \exp\left(\frac{p-R}{a_S}\right)\right]^{-1} , \qquad R = r_0 A^{1/3} , \tag{10}$$

and

$$f_D(p) = 4 \exp\left(\frac{p - R}{a_D}\right)\left[1 + \exp\left(\frac{p - R}{a_D}\right)\right]^{-2} . \tag{11}$$

$f_S(p)$ is the Saxon-Woods form factor while $f_D(p)$ gives a surface absorption term of the Saxon derivative type. Note that the variable is $p = \frac{1}{2}|\mathbf{r} + \mathbf{r}'|$ and not r, as in local calculations.

The spin-orbit function in Eq. 4 is

$$S(r) = \left[\frac{b}{2Mc}\right]^2 \cdot \frac{1}{a_S r} \cdot \frac{\exp\left(\frac{r - R}{a_S}\right)}{\left[1 + \exp\left(\frac{r - R}{a_S}\right)\right]^2} , \tag{12}$$

where M = nucleon mass.

An expansion of $\psi(\mathbf{r})$, $\psi(\mathbf{r}')$, and $V(\mathbf{r}, \mathbf{r}')$ in partial waves and substitution in Eq. 4 results in partial wave equations which were solved exactly to give the scattering phase shifts and hence the theoretical nuclear cross section.

Our first use of the nonlocal model was to investigate its relation to the usual type of local optical potential. We wished to determine whether it was possible to reproduce the predictions of the nonlocal model by using the local calculations. In particular, it was necessary to examine whether the use of a constant set of nonlocal parameters for different neutron energies would imply the observed type of energy variation for the equivalent local parameters.

It was found in every case that there is an energy-dependent local optical potential capable of giving a nearly perfect fit to the nonlocal results. If the nonlocal and the equivalent local results are plotted out, the curves are indistinguishable over the whole angular range.

This success made it plausible that the results predicted by the nonlocal model could always be reproduced by using an equivalent local optical model. Furthermore, it was already evident that one could hope to give a good account of experimental results over a wide energy range with a single fixed set of optical parameters.

We now developed a simple approximate formula relating the parameters defining the nonlocal model and the energy-dependent parameters of the purely local model which reproduced the nonlocal results. This relationship can be written as

$$U_L(r) \exp\left\{\frac{M\beta^2}{2b^2}[E - U_L(r)]\right\} = U_N(r) . \tag{13}$$

On the basis of Eq. 13 and using the experience gained in the preliminary work noted above, we then determined a set of nonlocal parameters required to fit the experimental data available for Pb^{208} at 7 and 14.5 Mev. These parameters are given in Table 6.1.1, and for convenience are designed as Set A.

Table 6.1.1. Nonlocal Optical Potential Parameters Obtained by Fitting the Experimental Differential Cross Section for Lead at 7 and 14.5 Mev: Set A

Parameter	Value
V_N	71 Mev
r_0	1.22 fermi
a_s	0.65 fermi
W_D	15 Mev
a_D	0.47 fermi
U_{so}	1300 Mev
β	0.85 fermi

Nonlocal calculations verified that Set A gave a good account of the data on lead at 7 and 14.5 Mev. As a further check we tried the effects of varying each of these parameters around the values quoted. In each case the results were definitely worse than for Set A except for the spin-orbit depth U_{so}, which could be varied over an appreciable range without much affecting the nonlocal predictions. We emphasize that Set A was decided upon entirely by fitting the lead data at 7 and 14.5 Mev. No attempt had been made at this stage to get detailed nonlocal fits for data on other elements or at other energies; in fact, such attempts turned out to be unnecessary.

We now regarded Set A as our definite nonlocal model and performed the nonlocal calculations for a wide range of elements at 4.1, 7, 14.5, and 24 Mev. The results, together with the experimental data, are presented in Figs. 6.1.1 and 6.1.2. In the 4.1-Mev data of Fig. 6.1.1, the dashed curves are the direct predictions of the nonlocal model, while the corresponding solid curves are results which include theoretical corrections for compound elastic scattering. The criterion for applying such corrections and the details of the method of including compound elastic effects are described later.

It will be observed that the agreement is fair between the theoretical and experimental differential cross sections over this energy range. Indeed, some of the nonlocal model predictions are remarkably good. It was now of interest to examine whether the model gave an equally good account of the total and reaction cross sections. Theoretical values for these were, of course, obtained as a by-product of the calculations described above.

Total and Reaction Cross Sections

In Fig. 6.1.3 we give the theoretical total cross sections, plotted against $A^{1/3}$, together with the available experimental data. The agreement between theory and experiment is fairly good at all four energies. The curves follow the average trend of the data closely except, possibly, at the very highest mass numbers.

The reaction or total nonelastic cross-section theoretical curves and experimental data are plotted in Fig. 6.1.4, also as functions of $A^{1/3}$. The data is somewhat sparse, but the comparison reveals some

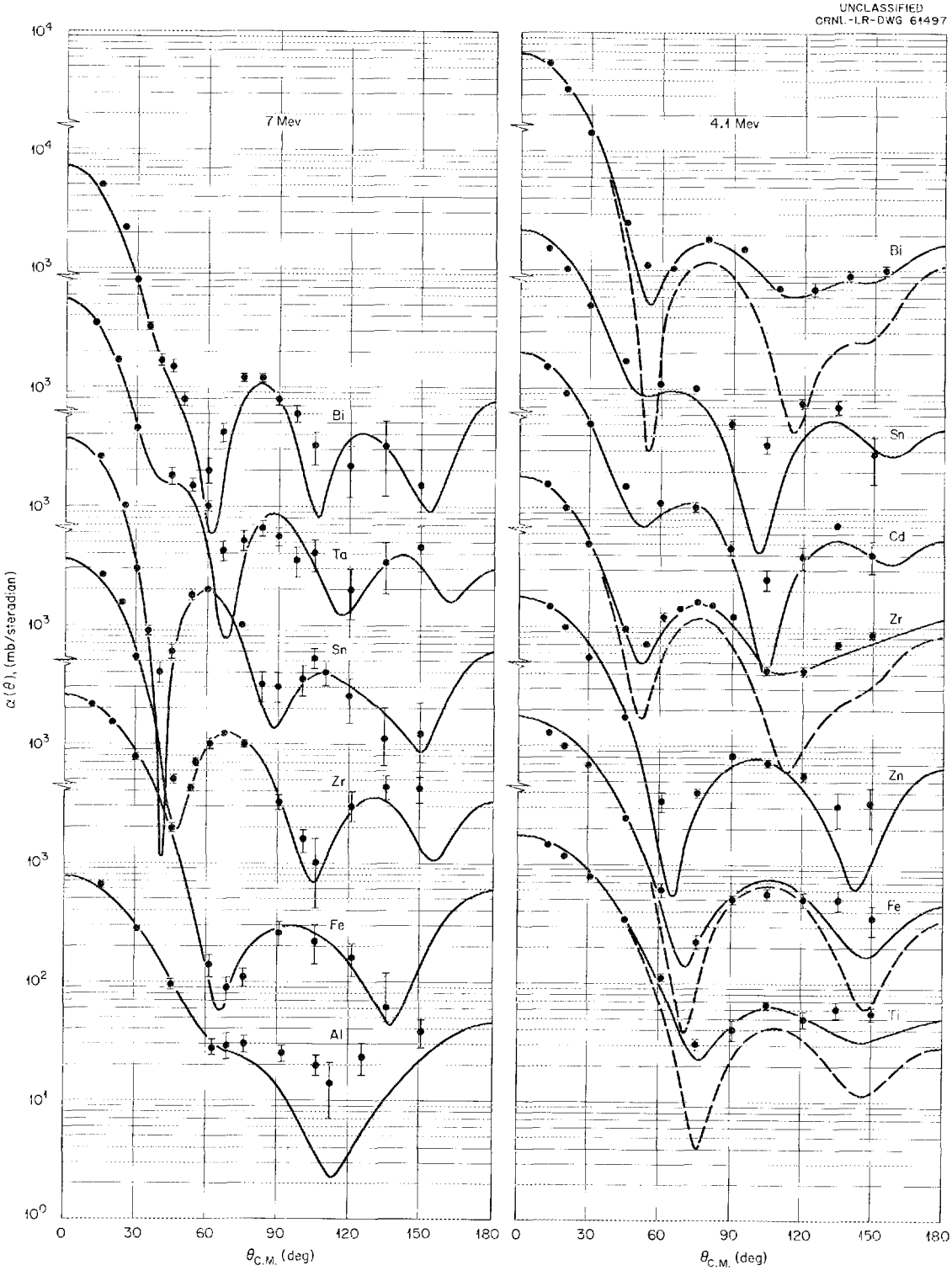

Fig. 6.1.1. Comparison of Predictions of the Energy-Independent Nonlocal Optical Potential Model Calculations with Experimental Values of the Differential Elastic Scattering Cross Sections for 4.1- and 7-Mev Neutrons Incident on Various Elements. Some of the shape-elastic differential cross sections (dashed curves) have been corrected for compound elastic contributions in the manner described in the text to arrive at the solid curves. Parameter Set A.

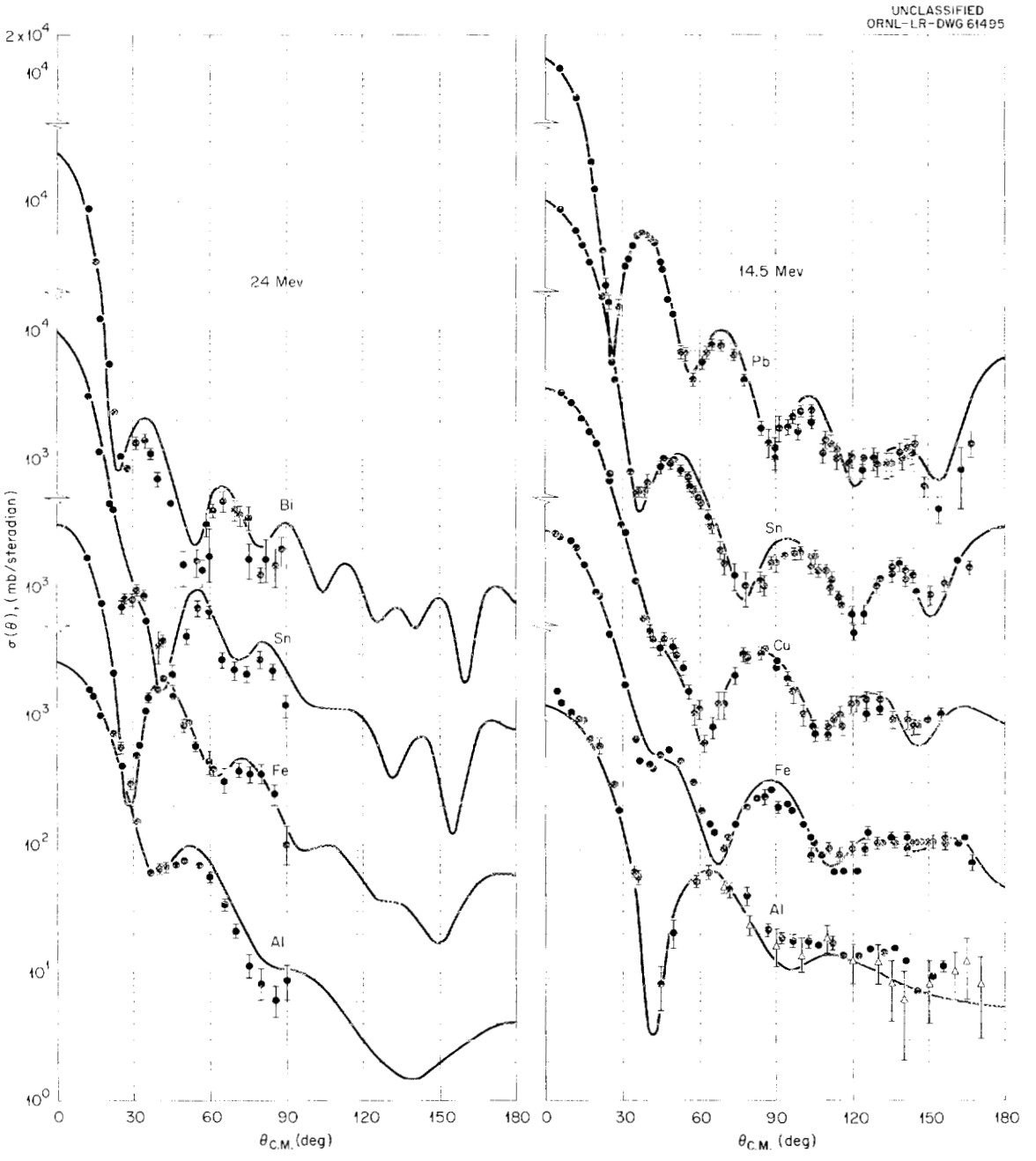

Fig. 6.1.2. Comparison of Predictions of the Energy-Independent Nonlocal Optical Potential Model Calculations with Experimental Values of the Differential Elastic Scattering Cross Section for 14.5- and 24-Mev Neutrons Incident on Various Elements.

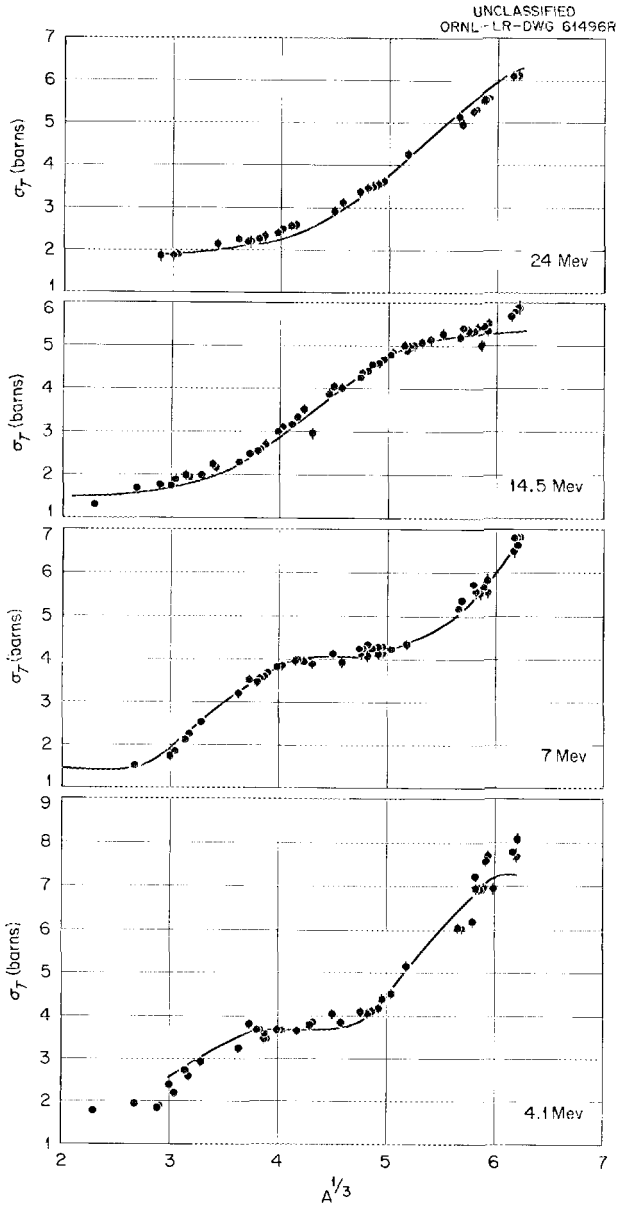

Fig. 6.1.3. Comparison of Calculated versus Experimental Total Cross Sections as a Function of $A^{1/3}$ for Various Neutron Energies.

very interesting features. The theory follows experiment closely at 7, 14, and 24 Mev with several minor discrepancies. However, in the 4-Mev data there are a number of marked deviations from the theoretical curve. In particular, large discrepancies are found at mass numbers corresponding to Pb, Zr, Fe, Ti, and Al. It may be recalled that lead and zirconium are closed-shell nuclei, so we have here a strong indication of shell effects. For elements lighter than copper, the energy 4 Mev is in a transition region for the appearance of disagreement between theoretical and experimental nonelastic cross sections. This will be illustrated in more detail later.

Reference to the angular distribution curves at 4 Mev in Fig. 6.1.1 shows that the direct predictions (dashed curves) of the model for the nuclei mentioned above are also in disagreement with experiment.

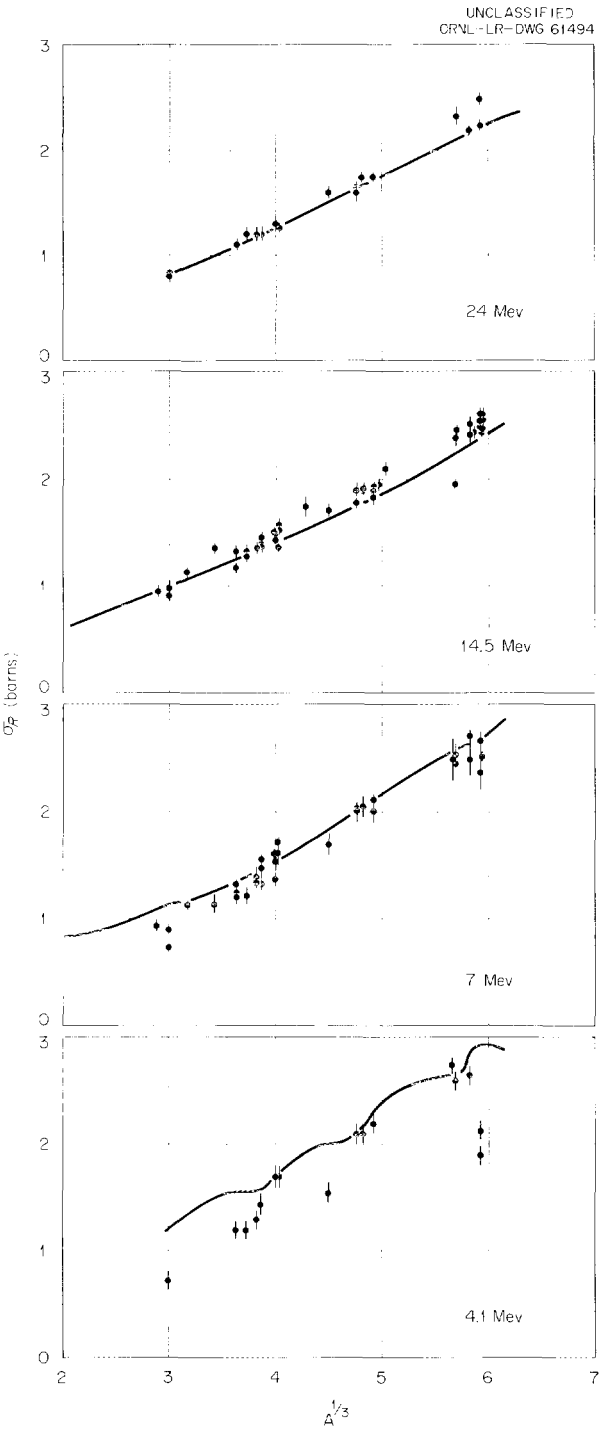

Fig. 6.1.4. Comparison of Calculated versus Experimental Reaction (Total Nonelastic) Cross Sections as a Function of $A^{1/3}$ for Various Neutron Energies.

This correlation is suggestive. More precisely, the above facts in conjunction with the observation that the total cross sections at 4 Mev are in good agreement, indicate that the discrepancies arise from the presence of a considerable amount of compound elastic scattering. Moreover, the consistency of the results provides us with a relatively unambiguous method of correcting for compound elastic effects.

The total cross section σ_T, the shape elastic cross section $\sigma_{S.E.}$, and the reaction cross section σ_R, as predicted by the model, are related by

$$\sigma_T = \sigma_{S.E.} + \sigma_R \,. \tag{14}$$

In our model, σ_R arises mainly from the presence of the imaginary potential W_D, and it includes the cross section, $\sigma_{C.E.}$, for the compound elastic scattering, which in the model is treated as part of the total absorption. Hence, σ_R is the sum of $\sigma_{C.E.}$ and the true reaction or nonelastic cross section $\sigma_{N.E.}$:

$$\sigma_R = \sigma_{C.E.} + \sigma_{N.E.} \,. \tag{15}$$

The experimentally measured quantity is $\sigma_{N.E.}$. The cross sections $\sigma_{S.E.}$ and $\sigma_{C.E.}$ are not as yet experimentally distinguishable, so that the observed elastic cross section σ_{EL} is

$$\sigma_{EL} = \sigma_{S.E.} + \sigma_{C.E.} \,, \tag{16}$$

and the observed differential cross section is

$$\frac{d\sigma_{EL}}{d\Omega} = \frac{d\sigma_{S.E.}}{d\Omega} + \frac{d\sigma_{C.E.}}{d\Omega} \,. \tag{17}$$

Hence, in terms of observed quantities, σ_T is

$$\left.\begin{aligned} \sigma_T &= \sigma_{S.E.} + \sigma_R \\ &= (\sigma_{S.E.} + \sigma_{C.E.}) + (\sigma_R - \sigma_{C.E.}) \\ &= \sigma_{EL} + \sigma_{N.E.} \,. \end{aligned}\right\} \tag{18}$$

The last step follows from Eqs. 15 and 16. Since we know that the observed total cross sections, σ_T, are reproduced very closely by the fixed parameter model, it is highly plausible that we can determine the total compound elastic scattering merely by subtracting the observed nonelastic cross section, $\sigma_{N.E.}$, from the theoretically predicted quantity σ_R. From Eq. 15,

$$\sigma_{C.E.} = \sigma_R - \sigma_{N.E.} \,. \tag{19}$$

Having derived the compound elastic cross section from the nonelastic data, we can use it to correct the nonlocal model predictions for the elastic scattering (see Eq. 17). A slight difficulty remains because we do not know the angular distribution of the compound elastic scattering. We assume that the compound elastic angular distribution is isotropic, giving

$$\frac{d\sigma_{C.E.}}{d\Omega} = \frac{\sigma_{C.E.}}{4\pi} \,. \tag{20}$$

Actually, a slight peaking at forward and backward angles, which is the most probable shape for the angular distribution, would not make much difference to the results. Making the corrections to the 4-Mev

predictions resulted in the solid curves of Fig. 6.1.1 for the nuclei mentioned earlier. Note that these compound elastic corrections were applied *only* when there was a marked discrepancy between the theoretical reaction cross section and the measured nonelastic cross section. Observe, also, that the largest deviations occur for closed-shell nuclei, which have a lower level density and hence fewer possible compound reaction channels than neighboring nuclei at a 4-Mev bombarding energy.

Since we felt that we had a reliable model, we were encouraged to extend the calculations to energies below 4 Mev.

Low-Energy Neutron Scattering

Parameter Set A was then used to calculate cross sections at 3.7, 2.5, 2.1, 0.98, and 0.38 Mev. These energies were chosen since there were data available. For each element we verified that the total cross section was correct and then added to the predicted differential cross sections the amount of compound elastic scattering indicated by the discrepancy between the reaction cross sections. Again, the results gave a reasonable account of the observations.

It was noted previously that the neutron scattering from lighter elements showed some compound elastic contamination at 4 Mev, even away from the closed shells. This becomes more pronounced at lower energies, reflecting the lower level densities of lighter nuclei at bombarding energies up to and beyond 4 Mev. This bears out an earlier remark that 4 Mev is a transition region energy for the appearance of compound elastic effects.

Low-Energy Polarizations

We have also applied the model defined by parameter Set A to the study of neutron polarization. It is well known that the ordinary optical model has hitherto had little success in accounting for these data. Our study was feasible because the model had provided a good way of correcting for compound elastic contaminations.

In an obvious notation, the observed elastic polarization $P_{EL}(\theta)$ at each angle can be represented by

$$P_{EL}(\theta) = \frac{[\sigma^{(+)}_{S.E.}(\theta) + \sigma^{(+)}_{C.E.}(\theta)] - [\sigma^{(-)}_{S.E.}(\theta) + \sigma^{(-)}_{C.E.}(\theta)]}{[\sigma_{S.E.}(\theta) + \sigma_{C.E.}(\theta)]} . \tag{21}$$

The nonlocal model calculations predict what may be called the shape-elastic polarization $P_{S.E.}(\theta)$ which is represented by

$$P_{S.E.}(\theta) = \frac{\sigma^{(+)}_{S.E.}(\theta) - \sigma^{(-)}_{S.E.}(\theta)}{\sigma_{S.E.}(\theta)} . \tag{22}$$

Hence the observed and shape-elastic polarizations should be related as follows:

$$P_{EL}(\theta) = \left[\frac{\sigma_{S.E.}(\theta)}{\sigma_{S.E.}(\theta) + \sigma_{C.E.}(\theta)}\right] P_{S.E.}(\theta) . \tag{23}$$

We see that, in general, the observed polarization is less than the pure shape-elastic polarization.[6]

The neutron polarizations at 2.1, 0.98, and 0.38 Mev have been measured at three scattering angles, 50° or 55°, 90°, and 125° or 130°, for many elements. These results are plotted in Fig. 6.1.5 as functions of the mass number A, along with the shape-elastic predictions of the calculation.[7] It is seen that the observed polarizations show marked fluctuations and that such fluctuations are also indicated by the model curves. However, the theoretical polarization fluctuations at 2.1 and 0.98 Mev have, in general, larger amplitudes than the observed fluctuations since they are as yet uncorrected by the use of Eq. 23.

We also include in Fig. 6.1.5 the theoretically corrected model results for several mass numbers. These correspond to nuclei for which we had reaction cross-section data so that we could derive information about $\sigma_{C.E.}(\theta)$. We see that some of the points which can be corrected in this way are considerably reduced relative to the direct shape-elastic predictions and are now in better agreement with experiment. It seems possible that, if the model curves could be completely corrected, the theory would give approximately the type of curve indicated by experiment, with a few exceptions.

The compound-elastic corrections to the theoretical polarizations, which are required by Eq. 23, are strongly dependent on mass number and angle of observation. The reason for this is that the compound elastic cross-section contributions are only appreciable at the minima of the shape-elastic angular distributions. Since for most nuclei at 2.1 and 0.98 Mev the shape-elastic cross section is peaked forward, the relative contribution of compound elastic scattering is negligible at 50°. Hence little correction is required for this angle of observation.

This is true of the 0.38-Mev data at both 50° and 90°. However, at 130°, for masses in the range $A = 100$ to 130, relatively large corrections would be required, since the 0.38-Mev shape-elastic angular distributions for these nuclei have a minimum near 130°. However, we have no reaction cross-section data at 0.38 Mev to enable us to apply these corrections.

The agreement between experimental polarizations and the compound corrected theory is fair, considering that no attempt has been made to force a fit to the data and that the original parameters of Set A have been used unchanged. It is almost certain that the agreement would be improved if we slightly adjusted the spin-orbit depth U_{so}. Slight changes in U_{so} would not greatly affect any of the other results.

The S-Wave Strength Function

Our final application of the fixed model was to calculate the strength function Γ_n^0/D and the scattering length R' for S-wave neutrons (see reference 1 for details). These calculations were done at 1 kev and the results normalized to 1 ev. The function Γ_n^0/D is given in Fig. 6.1.6 as a function of the mass number, A. Also included are the experimental data.[8]

---

[6] H. Feshbach, *Proc. Intern. Conf. on the Nuclear Optical Model, Florida State University*, Tallahassee (1959).

[7] The polarization data at 0.38 and 0.98 Mev is from J. D. Clement, F. Boreli, S. E. Darden, W. Haeberli, and H. R. Striebel, *Nuclear Phys.* 6, 177 (1958). The polarization data at 2.1 Mev is from L. Cranberg (unpublished). See *Proc. Intern. Symposium on Polarization Phenomena of Nucleons, Basel* (1960), published in *Helvetica Physica Acta, Supl.* 6 (1961).

[8] The compilation of the S-wave strength functions and the scattering lengths R' are due to H. W. Newson and J. H. Gibbons in *Fast Neutron Physics, Vol. II, Sec. V.L.*, Interscience, New York (to be published).

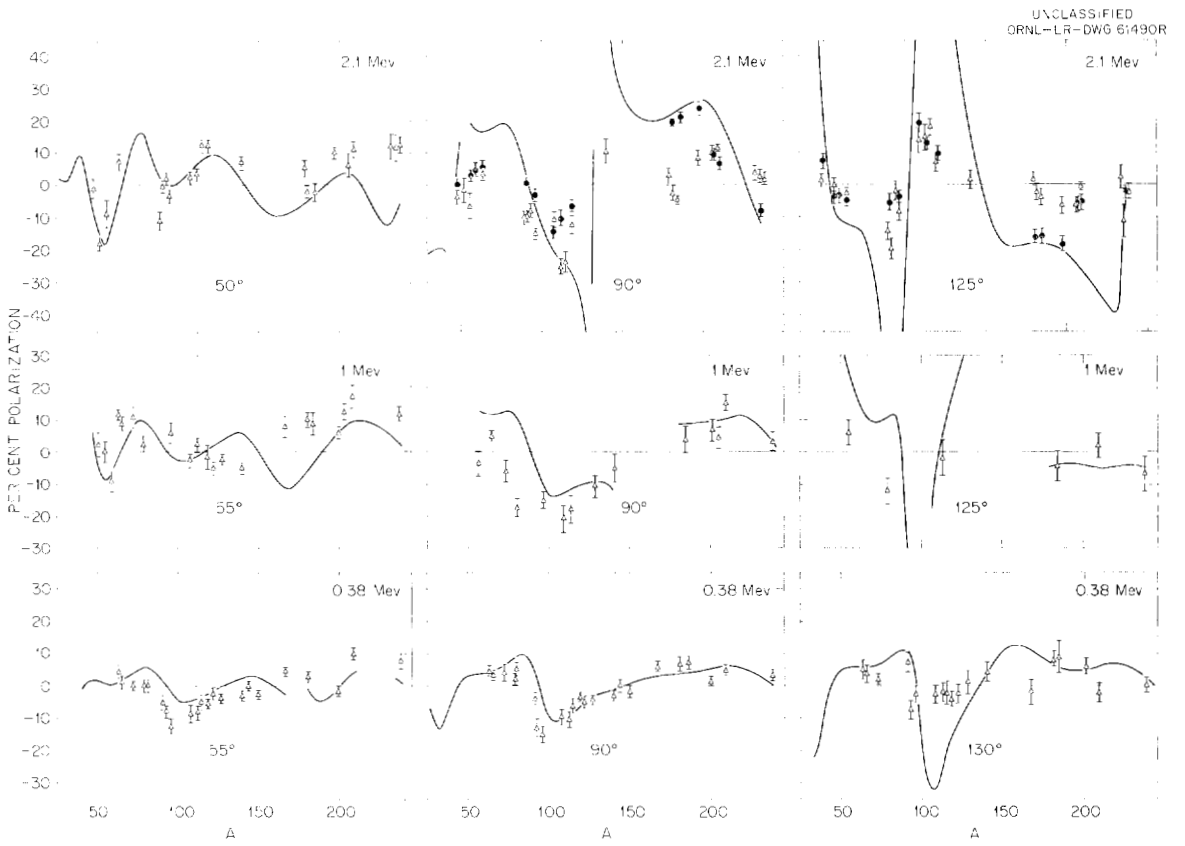

Fig. 6.1.5. Comparison of the Shape Elastic Polarization Predictions of the Nonlocal Optical Potential Model with experimentally Measured Data at 0.38, 0.98, and 2.1 Mev. The solid points at 2.1 Mev are the shape-elastic polarizations corrected for compound elastic scattering.

We see that the nonlocal predictions are not very different from the local optical model results. The experimental values of R' are reproduced approximately by the model; but there are the usual discrepancies in the strength function. In particular, the theoretical curve does not reach very low values near $A = 100$, as would seem to be required by experiment.

Some of the experimental strength functions in the region of $A = 100$ were obtained by analysis of average cross-section shapes. This analysis has been shown[9] to be subject to large errors because of the neglect of P-wave effects, which are quite large in this region. The general effect of the suggested corrections is that the experimental points should be appreciably higher at these mass numbers, i.e., they should be in better agreement with theory.

The model predicts only a single peak in the strength function curve in the vicinity of $A = 160$. Experimentally, there appears to be a double peak in this mass region and it has been accounted for by Chase, Wilets, and Edmonds,[10] in terms of nonspherical distortions of these nuclei. Our calculation does not yet include the effects of nuclear deformation.

[9] P. D. Miller, J. H. Gibbons, and R. L. Macklin, *Bull. Am. Phys. Soc. II* 5, 18 (1960).

[10] D. M. Chase, L. Wilets, and A. R. Edmonds, *Phys. Rev.* 110, 1080 (1958).

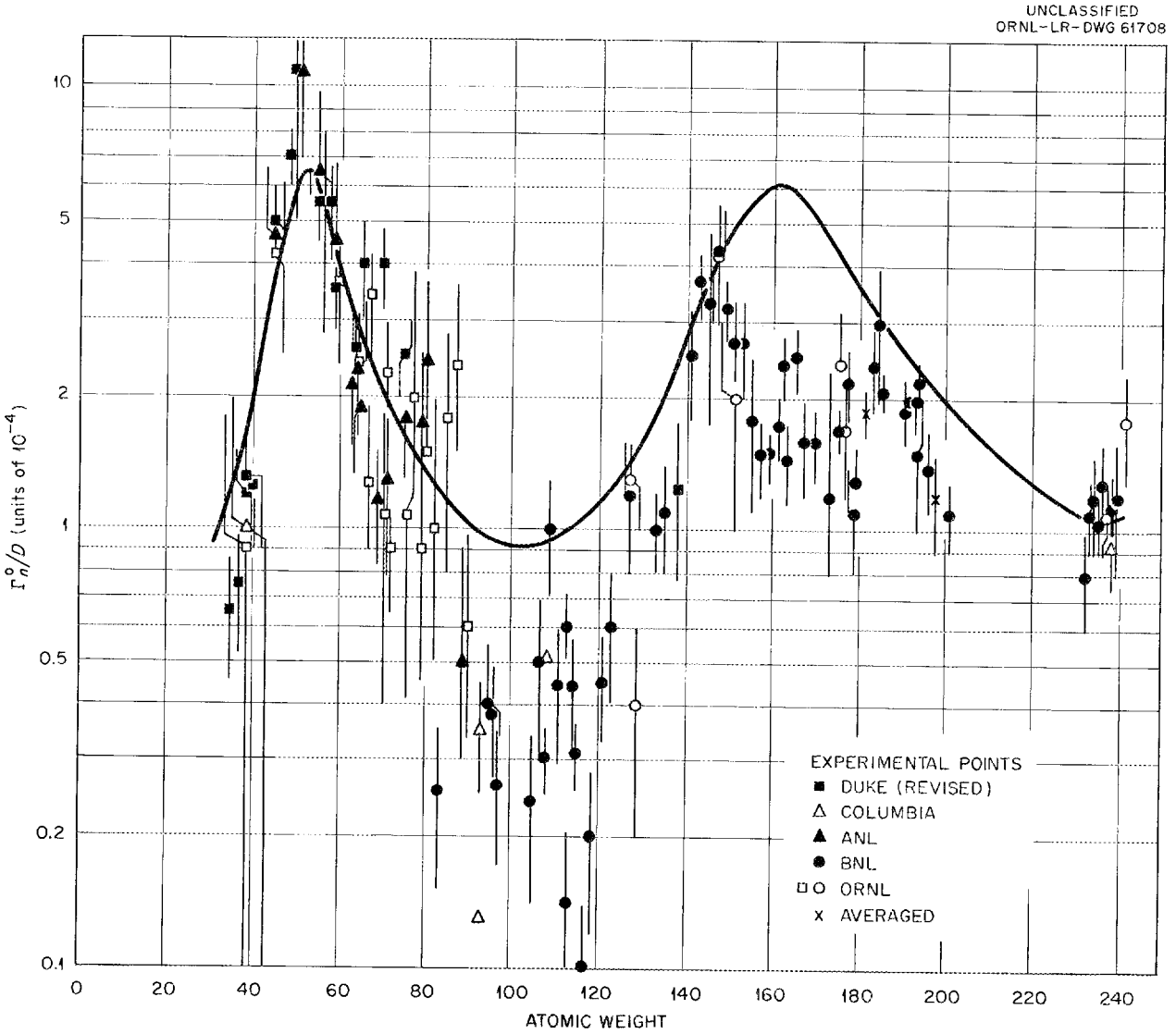

Fig. 6.1.6. Comparison of Predictions of the Nonlocal Optical Potential Model with Experimental Measurements of the *S*-Wave Strength Function.

Summary and Discussion

We have shown that the simple nonlocal optical potential model is able to give a unified account of a variety of experimental data on neutron scattering at energies up to 24 Mev. The nuclei considered range from aluminum to lead. However, it is fairly certain that at energies above 50 Mev a volume absorption term would be required.

The most successful attempt at fitting the neutron experimental data between 4.1 Mev and 14.5 Mev with a local optical potential is the work of Bjorklund and Fernbach.[11] We have purposely, in this energy

[11] F. Bjorklund and S. Fernbach, *Phys. Rev.* 109, 1295 (1958).

range, selected the same elements in order that the comparison between the two models could be easily made. The fixed nonlocal model gives as good a fit to the data as the energy-dependent local model. Comparison with the work of Wyatt, Wills, and Green[5] can also readily be made, and the marked improvement of the full nonlocal calculation over their effective mass treatment is easily seen.

It is stressed that the parameters of Set A are probably not optimum values, since they were fixed by considering only two medium-energy angular distributions (lead at 7 Mev and 14.5 Mev) and without looking at polarization results. It would be difficult to determine the parameters from the low-energy experiments because of the complications introduced by compound elastic scattering. Hence, it seems necessary to fix the model from the medium- or high-energy results where compound scattering is relatively unimportant. We have seen that when the parameters can be fixed at higher energies, the direct extension of the model to low energies enables one to make adequate corrections for compound elastic scattering, but only when measured total nonelastic cross sections are available.

Even with the calculation in its present form, we can confidently predict differential and total cross sections for a large number of elements at energies up to 30 Mev. At energies below about 5 Mev it is necessary to know only the experimental value of the nonelastic cross section so that suitable compound elastic corrections can be estimated and applied.

Work is now in progress to use the model in a study of the elastic scattering and polarization of protons, for which there is a vast amount of experimental data. It will also be of interest to apply the model to the scattering of deuterons, He^3 nuclei, and alpha particles.[12]

[12]We acknowledge many helpful discussions with Dr. G. R. Satchler.

6.2. AN AUTOMATIC PARAMETER SEARCH CODE FOR NUCLEAR REACTION CALCULATIONS

F. G. J. Perey and B. Buck

The investigation of the applicability of any phenomenological model of a nuclear reaction depends to a large degree on the ability to find that region of parameter space which will give the best agreement with experimental data. As models become more complex or are extended to cover a wider range of experimental data, the number of parameters tends to increase and a systematic investigation of the parameter space becomes impracticable. It was found necessary in connection with several calculations reported elsewhere[1,2] to develop a flexible, automatic parameter search code which would vary the parameters until the minimum deviation of the experimental points from the theoretical predictions was obtained. It is the purpose of this report to give the essential details of the code programmed for the IBM-7090 computer.

[1]F. G. J. Perey and B. Buck, Section 6.1, this report.

[2]B. Buck, Section 6.3, this report.

Method Used

The calculations for which the search code was designed predict some of the following quantities:

$\sigma_{el}(\theta)$, the elastic differential cross section;

$\sigma_{in}(\theta)$, the inelastic differential cross section;

$P(\theta)$, the polarization; and

σ_T and σ_R, the total reaction cross sections.

The program is written so that up to 15 parameters may be varied simultaneously to adjust any combination of these quantities to agree, in the least-squares sense, with the experimental data.

For expositional simplicity, let us call A_i the theoretical quantity and B_i the corresponding experimental quantity which has a probable error of ΔB_i. Let there be M such points to be compared to the data and N parameters to be varied by the program. The A_i's are functions of the N parameters x_n which must be varied until the quantity

$$\chi^2 = \sum_{i=1}^{M} \left(\frac{A_i - B_i}{\Delta B_i} \right)^2 \tag{1}$$

is a minimum.

At a central guess $x^c = (x_1^c, x_2^c, \ldots, x_n^c)$ let the A_i's be denoted by A_i^c. We would like to proceed to a new central guess $x^c + \delta x$ so that we have

$$\frac{\partial}{\partial x_n} \left\{ \sum_{i=1}^{M} \frac{1}{\Delta B_i^2} (A_i - B_i)^2 \right\} = 0 .$$

If we let $A_i = A_i^c + \delta A_i$, we have

$$\frac{\partial}{\partial x_n} \left\{ \sum_{i=1}^{M} \frac{1}{\Delta B_i^2} (A_i^c + \delta A_i - B_i)^2 \right\} = \sum_{i=1}^{M} \frac{2}{\Delta B_i^2} (A_i^c + \delta A_i - B_i) \frac{\partial A_i}{\partial x_n} .$$

But

$$\delta A_i = \sum_{s=1}^{N} \frac{\partial A_i^c}{\partial x_s} \delta x_s \tag{2}$$

to first order in the δx's. The following equation results:

$$\sum_{i=1}^{M} \frac{1}{\Delta B_i^2} \frac{\partial A_i^c}{\partial x_n} \sum_{s=1}^{N} \frac{\partial A_i^c}{\partial x_s} \delta x_s = \sum_{i=1}^{M} \frac{1}{\Delta B_i^2} (B_i - A_i^c) \frac{\partial A_i^c}{\partial x_n} . \tag{3}$$

This is the so-called normal equation for the parameter x_n. We have N such normal equations which must be solved for the shift vector $\delta \mathbf{x} = (\delta x_1, \delta x_2, \ldots, \delta x_n)$. One can then proceed to the new central guess and repeat the procedure until the value obtained for χ^2 is stationary. No difficulty is encountered in using this method except when at least one of the parameters varies by more than 10%; Eq. 2 then becomes inaccurate owing to the fact that only first-order terms are kept, and the new central guess predicted is not much better than the original one. In those cases the method is modified to make calculations at two "points" along the predicted shift direction where χ^2 is computed. Then a second degree polynomial in x is computed and the new central guess is taken at the minimum of the polynomial.

Method of Taking Derivatives for the Normal Equations

Before the normal equations are formed, the derivatives of the calculated quantities A_i are required at each central guess. The normal procedure which is used with the strong coupling code[2] is to calculate the A_i^C's first at the central guess and then vary, one at a time, the parameters by 1% and use a difference formula to obtain the derivatives.

In the optical model calculations,[1] it is possible, however, to obtain more accurate first derivatives by an analytical method at the same time as the calculation of A_i at each central guess. Such a method is much faster, particularly in the case of the nonlocal calculation.

Since all the A_i's are only functions of the S-matrix elements, it is only necessary to calculate the derivatives of the S's with respect to the parameters. For simplicity, the derivation will be given for a local optical potential calculation without spin-orbit term. We want to compute the derivative of an S-matrix element with respect to a parameter p. The radial differential equation to be solved is

$$\left[\frac{d^2}{dr^2} + f_l(p) \right] u_l(p) = 0 \tag{4}$$

where

$$f_l(p) = k^2 - \frac{l(l+1)}{r^2} + V_c(p) + V_N(p) ,$$

V_c = Coulomb potential due to a charged sphere,

V_N = complex optical potential.

Equation 4 is solved, starting with some arbitrary value for the slope at $r = 0$, and u is taken out to some radius R where the nuclear potential is negligible. The u's are then matched to the appropriate regular and irregular Coulomb functions to yield the S-matrix elements; the details of the method are explained in Ref. 3.

We have then

$$u_l(R) = A_l[H_l^{(-)}(R) + S_l H_l^{(+)}(R)] , \tag{5}$$

[3] B. Buck, R. N. Maddison, and P. E. Hodgson, *Phil. Mag.* 5, 1181 (1960).

where

A_l = normalization constant, which is, among other things, a function of the parameter p,
$H_l^{(-)}$ = converging spherical wave,
$H_l^{(+)}$ = diverging spherical wave.

In a simplified notation, Eq. 4 becomes

$$\frac{d^2u}{dr^2} + fu = 0 , \tag{6}$$

from which we obtain, by differentiation with respect to p,

$$\frac{d^2}{dr^2}\left(\frac{\partial u}{\partial p}\right) + f\,\frac{\partial u}{\partial p} = -u\,\frac{\partial f}{\partial p} . \tag{7}$$

Combining Eqs. 6 and 7,

$$\frac{\partial u}{\partial p}\,\frac{d^2u}{dr^2} - u\,\frac{d^2}{dr^2}\left(\frac{\partial u}{\partial p}\right) = u^2\,\frac{\partial f}{\partial p} . \tag{8}$$

By integrating Eq. 8 with respect to r from zero to R (the matching radius) and making use of Green's theorem on the left-hand side, we have

$$\left[\frac{\partial u}{\partial p}\,\frac{du}{dr} - u\,\frac{d}{dr}\left(\frac{\partial u}{\partial p}\right)\right]_R = \int_0^R u^2\,\frac{\partial f}{\partial p}\,dr . \tag{9}$$

Substituting for u the expression given by Eq. 5, we have

$$\frac{\partial S_l}{\partial p} = \frac{i}{2k}\,\frac{[H_l^{(-)}(R) + S_l H_l^{(+)}(R)]^2}{u_l^2(R)}\int_0^R u_l^2(r)\,\frac{\partial f_l}{\partial p}\,dr . \tag{10}$$

For the application to a nonlocal optical potential calculation we shall give only the final result. If the radial integrodifferential equation to be solved is written in the following notation:

$$\frac{d^2u_l(r)}{dr^2} + f_l u_l(r) + \int_0^R G_l(r, r', p)\,u_l(r')\,dr' = 0 ,$$

we then have

$$\frac{\partial S_l}{\partial p} = \frac{i}{2k}\,\frac{[H_l^{(-)}(R) + S_l H_l^{(+)}(R)]^2}{u_l^2(R)}\left[\int_0^R u_l^2(r)\,\frac{\partial f_l}{\partial p}\,dr + \int_0^R u_l(r')\int_0^R u_l(r)\,\frac{\partial G_l(r, r', p)}{\partial p}\,dr\,dr'\right] . \tag{11}$$

The above result may not be new, but to our knowledge it has never been published.

The use of Eq. 11 in the nonlocal search code speeds the calculation by a factor of 10.

6.3. THE CALCULATION OF INELASTIC SCATTERING CROSS SECTIONS

B. Buck

It has become evident in recent years that many inelastic scattering processes cannot be explained satisfactorily on the basis of the compound nucleus theory. In particular, it has been necessary to develop an alternative theory for inelastic scattering of nuclear particles which leave the target nucleus in a low excited state, since the observed cross sections for such reactions are much larger than those predicted by the compound nucleus hypothesis. In addition, the angular distributions exhibit marked forward peaking which is explicable only by a radically different type of treatment.

The fundamental idea behind the direct interaction theories is that the incident particle interacts only with a single particle of the target or with some type of collective mode of the target. The most successful formalism based on this hypothesis is the Distorted Wave Born Approximation (DWBA). In this theory, the residual interaction of the incident particle with the target, after the elastic scattering interaction has been subtracted out, is treated as a perturbation. The zeroth-order functions for the first-order reaction matrix element are thus the elastic scattering wave functions, and it is assumed that the residual interaction does not seriously affect the calculation of the elastic scattering. The calculations of this theory are briefly summarized in the following formulas:

$$\frac{d\sigma}{d\Omega} \propto |I|^2 \tag{1}$$

$$I = \left\langle \chi_f^{(-)}(\mathbf{r})\, \psi_f(\xi) \,|V_0 f(\mathbf{r},\xi)|\, \chi_i^{(+)}(\mathbf{r})\, \psi_i(\xi) \right\rangle \quad , \tag{2}$$

where $\mathbf{r}$ denotes the coordinates of the incident particle, ξ signifies the coordinates of the target particles, ψ_i and ψ_f are the initial and final nuclear states, and $\chi_i^{(+)}$ and $\chi_f^{(-)}$ are the initial and final elastic scattering wave functions (distorted waves) of the scattered particle. The quantity $f(\mathbf{r},\xi)$ gives the spatial form of the residual interaction and V_0 is its strength. From Eq. 1 we see that the cross section increases without limit as the square of the interaction strength, and thus the theory is only valid if V_0 is small.

The theory sketched out above gives a remarkably good unified account of many inelastic reactions. But in some processes, the interaction strength is not small and the above treatment breaks down. Hence we must develop a more realistic type of calculation.

The Strong-Coupling Theory

Most even-even nuclei have a first excited state of spin-parity 2^+ and often this is strongly excited by nucleons or other particles (d, He^3, or alpha particles). In particular, the inelastic cross section for the excitation of the 2^+ state at 4.4 Mev in C^{12} is very large. It was decided to construct a pilot calculation to investigate the strong coupling of two nuclear levels, specifically, a ground state 0^+ and a first excited state 2^+. Hence elastic and inelastic cross sections are calculated simultaneously. It is important to note that when the coupling is strong, the presence of inelastic scattering reacts appreciably on the elastic cross sections.

The Schroedinger equation for the system is:

$$[T + V(\mathbf{r},\xi)]\,\psi(\mathbf{r},\xi) = E\,\psi(r,\xi)\,, \tag{3}$$

where T is the kinetic-energy operator, $V(\mathbf{r},\xi)$ is the total interaction energy, $\psi(\mathbf{r},\xi)$ is the complete wave function for the incident particle and the target, and E is the energy of the system. $\psi(\mathbf{r},\xi)$ is expanded in eigenstates of total angular momentum:

$$\psi(\mathbf{r},\xi) = \sum_{JM} a_{JM}\,\psi_J^M(\mathbf{r},\xi)\,. \tag{4}$$

We assume that $\psi_J^M(\mathbf{r},\xi)$ can be adequately described by the superposition of the elastic and inelastic states as follows:

$$\psi_J^M(\mathbf{r},\xi) = \frac{1}{r}\left[f_{0l}^J(r)\,\theta_{0l}^{JM}(\hat{\mathbf{r}},\xi) + \sum_{l'} f_{2l'}^J(r)\,\theta_{2l'}^{JM}(\hat{\mathbf{r}},\xi)\right] \tag{5}$$

where

$$\theta_{Il}^{JM}(\hat{\mathbf{r}},\xi) = \sum_{\lambda} C_{MK\lambda}^{JIl}\left[i^l Y_l^{\lambda}(\hat{\mathbf{r}})\right]\psi_I^K(\xi)\,. \tag{6}$$

The functions $f_{Il}^J(r)$ are the radial wave functions of particles scattered from nuclear states with spin I, partial wave l, and total angular momentum J. The functions $\theta_{Il}^{JM}(\hat{\mathbf{r}},\xi)$ represent the nuclear wave functions vector coupled to the angular part of the incident-particle wave functions. We neglect the spin of the incident particle. Other reaction channels, and hence the rest of the total wave function, are taken into account only in a general way via the introduction of complex optical potentials.

Insertion of the angular momentum eigenfunctions in the Schroedinger equation yields the following set of coupled differential equations for the radial functions $f_{Il}^J(r)$:

$$[T_l + V_{0l:0l}^J(r) - E]\,f_{0l}^J(r) + \sum_{l'} V_{0l:2l'}^J(r)\,f_{2l}^J(r) = 0 \tag{7}$$

$$[T_{l'} + V_{2l':2l'}^{(0)J}(r) - E']\,f_{2l'}^J(r) + V_{2l':0l}^J(r)\,f_{0l}^J(r) + \sum_{l''} V_{2l':2l''}^J(r)\,f_{2l''}^J(r) = 0 \tag{8}$$

where

$$T_l = \frac{\hbar^2}{2M}\left[\frac{l(l+1)}{r^2} - \frac{d^2}{dr^2}\right] \tag{9}$$

and $E' = E - \epsilon$, where ϵ is the energy of the excited state.

For these nuclei of ground state spin zero, $J = l$ always, where l = orbital angular momentum in the entrance channel. In Eq. 7, $l' = l,\ l \pm 2$. Equation 8 represents three equations corresponding to $l' = l,\ l \pm 2$; and the sum in Eq. 8 also goes over $l'' = l,\ l \pm 2$. We assume that only the scalar and quadrupole parts of the interaction are effective, and this leads immediately to the above restrictions on the l values.

For partial waves $l = 0, 1$, some of these equations and parts of the sum drop out because of angular momentum coupling considerations.

Before the coupled equations 7 and 8 can be solved, it is necessary to evaluate the matrix elements $V^J_{l'l':ll}(r)$ of the interaction potential. We have

$$V^J_{l'l':ll}(r) = \left\langle \theta^{JM}_{l'l'}(\hat{\mathbf{r}},\xi) \,\middle|\, V(\mathbf{r},\xi) \,\middle|\, \theta^{JM}_{ll}(\hat{\mathbf{r}},\xi) \right\rangle . \tag{10}$$

The interaction is written as a sum of products of multipole tensor operators:

$$V(\mathbf{r},\xi) = \sum_{Qq} \left\{ i^Q Y^q_Q(\hat{\mathbf{r}}) \right\}^* T^q_Q(r,\xi) . \tag{11}$$

By using the definition of Eq. 6, we can easily evaluate Eq. 10 to give a calculable formula for the potential matrix elements:

$$V^J_{l'l':ll}(r) = -V_{l'l} F_{l'l}(r) (-)^J i^{l-l'} C^{2ll'}_{000} [(2l+1)(2l'+1)]^{1/2} W(lll'l':J2) , \tag{12}$$

where we have assumed that $Q = 2$ (quadrupole interaction). The matrix elements of the scalar component ($Q = 0$) are the usual (complex) optical potentials employed in elastic scattering work. These are taken to be a real Saxon potential plus volume and surface absorption terms, together with a Coulomb interaction. $V_{l'l}$ is the strength of the interaction and $F_{l'l}(r)$ denotes its radial dependence.

Explicit values for $V_{l'l}$ and $F_{l'l}(r)$ can only be found by the use of definite models of the nucleus. For instance, if a single particle excitation model is proposed, they may be calculated in terms of assumed two-body forces. Very simple rotational or vibrational models of the nucleus yield definite ratios for the two coupling strengths V_{02} and V_{22}. On general theoretical grounds, the form factors $F_{02}(r)$ and $F_{22}(r)$ should be zero at $r = 0$ and peaked in the vicinity of the nuclear surface.

In the present calculation we chose a simple parametric form for the coupling functions $F_{l'l}(r)$ which was peaked near the nuclear surface, and left the strengths $V_{l'l}$ as input numbers. Thus various nuclear models could be simulated by altering the strength ratios and the radial form factors.

For a partial wave l, we have in general four coupled equations. We integrate the coupled set four times numerically, each time using different initial values at the origin. The integrations are carried out to the nuclear surface where the optical and coupling potentials eventually become negligible. The four independent solutions for each of the four radial functions are then superposed to yield the true wave functions.

The superposition coefficients are determined by setting up an 8×8 complex matrix equation which matches the internal nuclear functions and their derivatives to the known free-state Coulomb wave functions. The same equation yields immediately the elastic and inelastic scattering matrix elements, from which the corresponding cross sections are easily computed. This is repeated for each partial wave, up from $l = 0$, until the phase shifts are negligible.

The problem was coded for the IBM-7090 computer.[1] For charged incident particles the calculation gives the total absorption cross section, the total inelastic cross section, and the elastic and inelastic differential cross sections. In addition, a subroutine calculates the tensor functions necessary to account for the correlation of the inelastically scattered particles with the decay gamma rays from the excited 2^+ state. If the incident particles are neutrons, we obtain also the total nuclear and the total elastic cross sections.

Results

The code is now operating successfully and has been subjected to a series of exhaustive tests. These were designed to investigate the numerical accuracy and internal consistency of the calculation. Unfortunately, there are no other independent calculations of exactly this type available as yet so that a direct test is impossible. However, when the coupling strengths are small, the calculation reproduces very well the results of the DWBA theory, as it should. The behavior of the results at high coupling strengths conforms to general theoretical expectations and can be tested directly in one or two limiting cases (e.g., the adiabatic approximation when the excitation energy is set to zero).

Several investigations were begun on the scattering of nucleons from various nuclei. For instance, some work has been done on the reaction $C^{12}(p,p')C^{12*}_{4.4}$ in the energy range 14 to 20 Mev and on the reaction $Mg^{24}(p,p')Mg^{24*}_{1.37}$ at 18 Mev. For these cases a typical calculation runs about 20 sec. The work has been facilitated by attaching to the code the automatic parameter search routine described elsewhere[2] so that experimental data can be fitted directly.

If the total inelastic cross section is plotted against coupling strength, several interesting results appear. For low strengths we obtain the same shape as predicted by the DWBA theory, i.e., $\sigma_{IN} \propto V_0^2$. But this relation ceases to be obeyed when the strength reaches reasonable physical values. The strong coupling results eventually level off as V_0 increases and, furthermore, always tend to nearly the same limiting value whatever shape is used for the coupling form factor. Since this limiting value, in the case of $C^{12}(p,p')C^{12*}_{4.4}$, is close to the observed value of the total inelastic cross section, we see that the DWBA treatment is not valid for this reaction.

Unless very large coupling strengths are required (to fit the experimental magnitudes), the inelastic angular distributions given by the code are not very different from those of the DWBA theory. However, the DWBA theory almost invariably overestimates the magnitudes since the observed cross sections for many reactions lie in the region where the DWBA and strong coupling results are already appreciably divergent. Hence the perturbation theory can lead to serious underestimates of coupling strengths, distortion parameters, and the like.

---

[1]The help of D. E. Arnurius, of the Mathematics Panel, in writing the codes is gratefully acknowledged. Many valuable discussions were held with Dr. G. R. Satchler of the Physics Division.

[2]Section 6.2, this report.

The present calculation also demonstrates that strongly coupled excited states react on the elastic scattering, and hence should be taken into account when interpreting elastic scattering data. The main effect is that the coupling can introduce remarkably sharp resonance-type phenomena into some of the elastic partial waves. Thus the elastic cross sections can vary sharply over small energy intervals purely as a result of strong coupling. In addition, the coupling usually makes the elastic angular distribution oscillations more pronounced.

The pilot code described above is really only applicable to the scattering of alpha particles, since the spin is neglected. Indeed, the preliminary investigations show conclusively that it will be necessary to include spin-orbit coupling before we can obtain a satisfactory theory of the above type for the elastic and inelastic scattering of nucleons. Therefore, the pilot code is now being used to study inelastic alpha-particle scattering and the initial results are very encouraging.

The general success of the above theory has stimulated the further development of the code. The program is being modified[3] to calculate cross sections when the incident particle energy is below the threshold of the excited 2^+ state. The presence of this strongly coupled state should have a marked influence on the elastic scattering (resonances).

Work on two further codes is nearing completion. One is along the same lines as the pilot code but includes a second excited state of spin-parity 4^+. This will be used for the theoretical study of various multiple excitation processes. The code is written but has not yet been thoroughly tested. The other code is designed for the study of nucleon inelastic scattering and includes spin-orbit coupling. Work on this is well advanced. In addition to these, another calculation is projected which will treat the simultaneous strong coupling of states of spin-parity 2^+ and 3^- to a ground state 0^+.

[3]By S. K. Penny, ORNL.

6.4. THE TDC PERTURBATION CODE

W. E. Kinney and G. E. Whitesides[1]

Perturbation theory provides the most economical and possibly the most satisfactory method for computing material replacement coefficients of reactivity in a chain-reacting system. For fast-neutron systems, at least, it is the only practical way to compute neutron lifetimes, since the lifetimes are so short. A Fortran code has now been written to perform perturbation theory calculations with fluxes obtained with the TDC Code,[2] a two-dimensional, cylindrical (r,z) geometry, transport theory code. Because it utilizes the TDC fluxes, the new code is identified as the TDC Perturbation Code.

[1]Central Data Processing Group, Oak Ridge Gaseous Diffusion Plant.

[2]B. Carlson, C. Lee, and J. Worlton, *The DSN and TDC Neutron Transport Codes*, LAMS-2346 (1960).

The fractional change in the multiplication constant in the TDC Perturbation Code calculations is given by

$$\frac{\delta k}{k} = \frac{1}{A}\frac{1}{k}\int_{\vec{r}} d\vec{r} \int_0^\infty du\, \chi(u) \int_{\vec{\Omega}} d\vec{\Omega}\phi^+(\vec{r}, u, \vec{\Omega}) \int_0^\infty du'\delta[\nu\Sigma_f(\vec{r}, u')] \int_{\vec{\Omega}'} d\vec{\Omega}'\phi(\vec{r}, u', \vec{\Omega}')$$

$$+\frac{1}{A}\int_{\vec{r}} d\vec{r} \int_0^\infty du \int_{\vec{\Omega}} d\vec{\Omega}\phi^+(\vec{r}, u, \vec{\Omega}) \int_0^u du'\,\delta[\Sigma_s(\vec{r}, u')] \int_{\vec{\Omega}} d\vec{\Omega}'\,K(u'\to u, \vec{\Omega}'\to\vec{\Omega})\phi(\vec{r}, u', \vec{\Omega}')$$

$$-\frac{1}{A}\int_{\vec{r}} d\vec{r} \int_0^\infty du\,\delta[\Sigma_T(\vec{r}, U)] \int_{\vec{\Omega}} d\vec{\Omega}\,\phi^+(r, u, \vec{\Omega})\phi(r, u, \vec{\Omega}) , \qquad (1)$$

where

$$A = \frac{1}{k}\int_{\vec{r}} d\vec{r} \int_0^\infty du\chi(u) \int_{\vec{\Omega}} d\vec{\Omega}\,\phi^+(\vec{r}, u, \vec{\Omega}) \int_0^\infty du'\,\nu\Sigma_f(\vec{r}, u') \int_{\vec{\Omega}} d\vec{\Omega}'\phi(\vec{r}, u', \vec{\Omega}') .$$

Though one is tempted to assume that

$$\int d\vec{\Omega}\,\phi^+(\vec{r}, u, \vec{\Omega})\,\phi(\vec{r}, u, \vec{\Omega}) = \frac{1}{4\pi}\int_{\vec{\Omega}} d\vec{\Omega}\,\phi^+(r, u, \vec{\Omega}) \int_{\vec{\Omega}'} d\vec{\Omega}'\phi(\vec{r}, u, \vec{\Omega}') \qquad (2)$$

in the last term of Eq. 1, such an assumption leads to large errors toward the surface of an assembly where the fluxes are anisotropic.[3]

The code input consists of the change in $\nu\Sigma_f$, Σ_{TT}, Σ_{sT}, and $\Sigma(g'\to g)$, the r and z range over which the changes are made, and the multiplication constant of the unperturbed assembly where

$\nu\Sigma_f = \nu\chi$ fission cross section,
Σ_{TT} = total transport cross section
$= \Sigma_a + \Sigma_{sT}$
Σ_{sT} = scattering transport cross section $= \sum (1 - \bar{\mu}_i)\Sigma_{s_i}$,
$\Sigma(g'\to g)$ = group g' to group g transfer cross section.

The fractional change in multiplication constant may be reported either in each mesh interval of the range or summed over the intervals to give a total change. A typical page of output is shown in Fig. 6.4.1. Running time is about 20 sec per case on the IBM 7090.

The code has been used to compute void coefficients of reactivity for the steel-core assembly of the ORNL Fast Burst Reactor critical experiments;[4] the results are compared to experiment in Fig. 6.4.2. The neutron lifetime for this assembly was 9.31×10^{-9} sec, as calculated by the $\delta k/k$ resulting from

[3] A. F. Henry, *Nuclear Sci. and Eng.* 3, 52 (1958).

[4] W. E. Kinney and J. T. Mihalczo, *Oak Ridge National Laboratory Fast Burst Reactor: Critical Experiments and Calculations*, ORNL-CF-61-8-71 (1961).

the insertion, throughout the system, of an absorber with macroscopic absorption cross section numerically equal to $1/v$. The neutron lifetime measured in an earlier fast system, Godiva I, was 6.23×10^{-9} sec (ref. 5). The difference is believed to be largely due to differences in the materials of the two systems.[6]

---

[5] T. F. Wimett *et al.*, *Nuclear Sci. and Eng.* 8, 691 (1960).

[6] Note added in proof: The neutron lifetime recently computed by perturbation methods for Godiva I is 5.9×10^{-9} sec.

UNCLASSIFIED
ORNL-LR-DWG 61176

```
RADIUS =    2.540000 TO    2.800000        HEIGHT =    0.        TO    0.200000
PICTURE PLOT OF REACTOR
        0000000000
        0000000000
        0000000000
        0000000000
        0000000000
        0000000000
        0000000000
        0000000000
        0000100000
DELTA K OVER K =  0.31151E-03
```

Fig. 6.4.1. A Typical Page of Output from the TDC Perturbation Code.

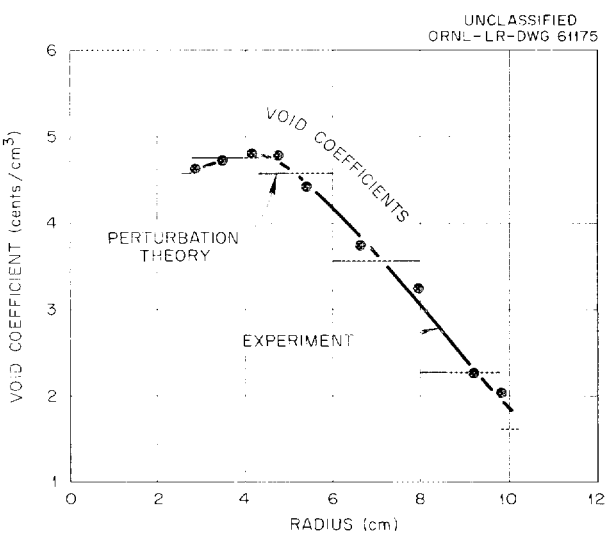

Fig. 6.4.2. Comparison of Void Coefficients Computed by Perturbation Theory with Results of Experiment: ORNL Fast Burst Reactor Critical Experiment.

6.5. ISOPERIMETRIC AND OTHER INEQUALITIES IN THE THEORY OF NEUTRON TRANSPORT

L. Dresner[1]

Some isoperimetric and other inequalities related to the one-velocity theory of neutron transport have been derived. The quantities involved in these inequalities all refer to bare solids and isotropic scattering. They are: the critical multiplication, the first-collision probability of neutrons from a uniform, isotropic source, the nonescape probability of neutrons from a uniform, isotropic source, and the buckling. The inequalities proved provide upper and lower bounds for the quantities considered. Numerous examples of the estimation of these quantities in cases not readily amenable to direct calculation are given in a detailed report published elsewhere.[2]

Recently the author has generalized some of the theorems to the case of linearly anisotropic scattering; a report on this work is being written.

[1]This work was performed while the author was assigned to the Institut für Neutronenphysik und Reaktortechnik, Kernforschungszentrum, Karlsruhe, Germany.

[2]*Kernforschungszentrum, Karlsruhe INR Arbeitsbericht* Nr. 18 (Feb. 27, 1961). Also accepted for publication in the Nov.–Dec., 1961 issue of the *J. Mathematical Phys.*

6.6. SOME REMARKS ON THE EFFECT OF A NONUNIFORM TEMPERATURE DISTRIBUTION ON THE TEMPERATURE DEPENDENCE OF RESONANCE ABSORPTION

L. Dresner[1]

Both the criticality and the initial time behavior of heterogeneous reactors following a large, instantaneous reactivity addition depend to a great extent on the increase in resonance absorption with increasing temperature. The temperature dependence of resonance absorption has been the subject of much previous study, but in all previous work the temperature distribution was assumed uniform in the absorber lump, contrary to the state of affairs in an actual reactor. In the present work the influence of a nonuniform temperature distribution on the absorption of neutrons in a purely absorbing resonance of an isolated lump has been studied.

The results of the study indicate that in practical situations the absorption in the lump depends only on its average temperature and not upon the uniformity of its temperature distribution. Details of the development are published elsewhere.[2]

[1]Work performed while the author was assigned to the Institut für Neutronenphysik und Reaktortechnik, Kernforschungszentrum, Karlsruhe, Germany.

[2]*Kernforschungszentrum, Karlsruhe INR Arbeitsbericht* Nr. 10 (Nov. 9, 1960); also published in *Nuclear Sci. and Eng.* **11**, 39 (1961).

6.7. NUMERICAL CALCULATION OF THE EVAPORATION OF PARTICLES FROM EXCITED COMPOUND NUCLEI

L. Dresner

A Monte Carlo program for the IBM-7090 has been written to analyze the evaporation of various nuclear fragments from highly excited compound nuclei. The program follows the work of Dostrovsky *et al.*[1] very closely. The basis of the analysis is as follows:

1. The emission probabilities are obtained from the statistical theory of Weisskopf.[2]
2. The energy dependence of the nuclear level density is taken to be exp $(2a[U-\delta])^{1/2}$, where a is a constant, U is the nuclear excitation energy, and δ is the pairing energy taken from the work of Cameron.[3]
3. The total binding energy of each nucleus is either obtained from the tables of Wapstra[4] or calculated from the semiempirical formula of Cameron.[5]
4. Only the emission of neutrons, protons, deuterons, tritons, He^3 nuclei, and alpha particles is considered.

The input data consists essentially of the mass and charge numbers of the compound nucleus and its excitation. The output consists of:

1. The number of each kind of fragment evaporated;
2. The energy spectrum of each kind of fragment evaporated; and
3. The number of each kind of final nucleus reached.

At the present time the program is being rewritten to include the emission of particles heavier than the alpha particle.[6]

---

[1] I. Dostrovsky, Z. Fraenkel, and G. Friedlander, *Phys. Rev.* 116, 683 (1959).

[2] V. F. Weisskopf, *Phys. Rev.* 52, 295 (1937).

[3] A. G. W. Cameron, *Can. J. Phys.* 36, 1040 (1958).

[4] A. M. Wapstra, *Physica* 21, 385 (1955).

[5] A. G. W. Cameron, *Can. J. Phys.* 35, 1021 (1957).

[6] I. Dostrovsky, Z. Fraenkel, and G. Friedlander, *Phys. Rev.* 118, 791 (1960).

Part 7

REACTOR SHIELDING RESEARCH

7.1. ENERGY AND ANGULAR DISTRIBUTIONS OF NEUTRONS PENETRATING SLABS OF DIFFUSING MEDIA. PART I: ENERGY SPECTRA[1]

V. V. Verbinski

The initiation of a program for obtaining basic information on the energy and angular distributions of neutrons throughout various shielding materials was reported previously, along with the results of a preliminary experiment for investigating the angular distribution of low-energy neutrons emerging from poisoned hydrogenous slabs.[2] As originally conceived, the over-all purpose of the program was to determine the applicability of several techniques for calculating neutron energies and angular distributions within high-performance materials, specifically LiH. The evaluation of the calculational techniques was to be aided by experimental measurements made with a proposed neutron chopper.[3] Insofar as possible, both the calculated and measured data were to be obtained as energy spectra of neutrons at several points inside the shield, energy spectra of neutrons leaking from the surface of the shield, and angular distributions of the leakage neutrons. Later, however, plans for constructing the neutron chopper facility were cancelled, and the experimental phase of the program was altered to consist of energy spectral measurements at the Linear Accelerator Facility of General Atomic, San Diego, and angular distribution measurements at the Bulk Shielding Facility.

As in the original plans, the calculational methods to be evaluated are the NDA NIOBE (direct numerical integration of the Boltzmann equation) Code, the moments method, and the ORNL O5R Code[4] (a Monte Carlo code used here with biased sampling). Where possible, the same source energies and LiH geometries are used in the calculations and experiments so that direct comparisons of the calculations can be made. The NIOBE Code is set up to handle only spherical geometry, which can consist of multilayered shells; the moments method utilizes only infinite geometry; and the O5R Code can apply to almost any geometry.[5]

Of the three methods, the O5R Code with biased sampling is the least efficient in its present state of development, and it will no doubt remain so. However, it involves a minimum of assumptions and therefore furnishes an excellent check on other calculations at intermediate penetrations. Furthermore, the fact that Monte Carlo codes can be developed for a great variety of geometries makes the O5R Code useful for checking on the geometries used by the other codes, for example, the infinite homogeneous medium and the point-isotropic or isotropic infinite-plane sources assumed for moments method calculations. The O5R Code can also serve to check the validity of the spherical geometry of the NIOBE calculations, and agreement of the three methods would serve as a positive indication that the calculational methods are correct. However, only an experimental check can determine whether correct cross sections have been employed.

---

[1]See Sec. 7.2 for companion paper.

[2]V. V. Verbinski, *Neutron Phys. Ann. Prog. Rep. Sept. 1, 1960*, ORNL-3016, p. 202.

[3]V. V. Verbinski, ORNL-3016, *op. cit.*, p. 130.

[4]R. R. Coveyou and J. G. Sullivan, ORNL-3016, *op. cit.*, p. 193.

[5]The NIOBE and moments method calculations have been performed by the United Nuclear Corporation (formerly Nuclear Development Corporation of America) on subcontract with the Laboratory and are discussed briefly in Sec. 7.5. They will be intercompared and discussed more fully in a paper to be submitted to *Nuclear Science and Engineering*.

It is known that none of the calculations employed the proper cross sections for LiH for neutrons below about 0.1 ev in energy because the scattering law for LiH in this energy region is not known. Free-atom cross sections were used even though it was known that they are not correct in the energy region where molecular bonding and crystal structure become important. The calculations, nevertheless, serve a valuable purpose when compared with experiment. They indicate the degree of departure of the measured spectrum from the free-atom assumption and therefore give a measure of the effects of scattering by bound atoms.

In this and the following paper (Sec. 7.2) the calculations are compared with experiments, this paper dealing with energy spectra and the following paper covering angular distributions. While the calculations cover a wide range of energies, the experimental measurements made thus far are for low energies only. This energy region was chosen for the initial checks because of the interest in two important problems at the time the program was initiated: (1) gamma-ray production by neutron capture within the gamma-ray shielding layers of the composite shield and (2) gamma-ray production by neutron capture in air and other materials near a compact shield. The air-capture problem has received considerable attention, the calculations of Keller, Zerby, and Dunn[6] being complete except for integration over the necessary inputs, which were lacking at the time. These inputs are the energy and angular distributions of leakage neutrons which the present investigation is attempting to supply. Figure 7.1.1, which gives the capture gamma-ray dose in air per unit fractional increment in energy ($\Delta E/E$) for the equilibrium leakage spectrum from LiH, shows that the data for the low energies (a few ev) are the most important.

[6] F. L. Keller, C. D. Zerby, and W. W. Dunn, *Gamma-Ray Dose Rates Resulting from Neutron Captures in Air*, ORNL-2462, p. 21 (Dec. 15, 1958).

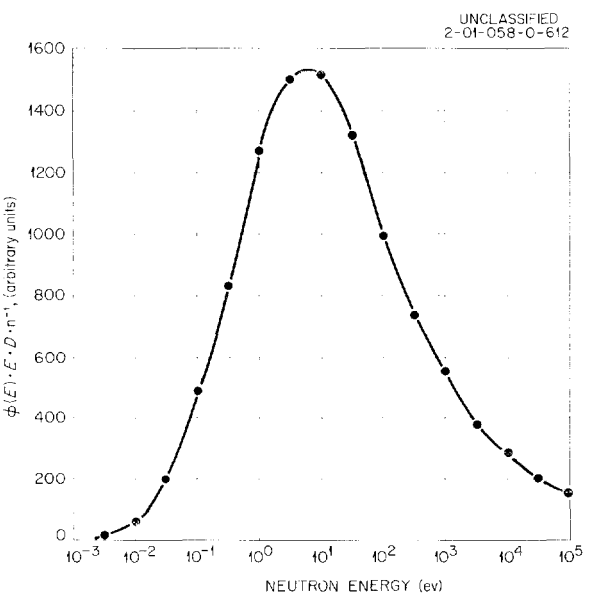

Fig. 7.1.1. Contribution to Gamma-Ray Dose by Neutrons Leaking from a Thick Slab of LiH. $\phi(E)$ = equilibrium leakage spectrum from a thick slab of LiH (fission neutrons); D/neutron = air capture gamma-ray dose[6] from a point isotropic source of energy E and strength of 1 neutron per second at a distance of 50 ft.

Spectral Measurements with LiH

The spectral measurements with LiH are of three different types: (1) leakage spectra from a slab of LiH as a function of slab thickness and angle of escape, (2) scalar flux spectra within LiH as a function of position within a slab, and (3) spectra of the forward-directed component of neutron flux from the bottom of a re-entrant hole as a function of the slab thickness. The energy range of the measurements was from about 0.01 ev to several hundred electron volts.

Leakage Flux Measurements. – Earlier measurements at General Atomic[7] showed that low-energy spectral equilibrium is reached at about 15 cm of penetration of initially fast neutrons in pure polyethylene and at less than 5 cm in lightly poisoned polyethylene, the presence of poison accelerating the attainment of equilibrium in the competing processes of slowing down and capture. These results were used as a guide in designing the LiH experiments and served to reduce the number of spectral measurements required. On the basis of the earlier results, slab thicknesses of 2.5, 5, and 10 cm were chosen for the measurements of the spectra of neutrons leaking normally from a slab of LiH. The 10-cm slab, in which spectral equilibrium would certainly be reached, was then used for measurements of the leakage spectra as a function of angle.

The experimental arrangement used for the leakage flux measurements as a function of angle is shown schematically in Fig. 7.1.2*a*. Five-microsecond bursts of 18-Mev electrons from the GA linear accelerator strike the lead target, producing a bremsstrahlung spectrum of gamma rays which in turn excite the lead nuclei with a resulting boil-off of neutrons that resembles a fission-neutron spectrum. The fast neutrons strike the 45-cm-dia circular LiH slab and are slowed down, in part, by collisions with hydrogen and lithium nuclei. Some of the neutrons escape from the opposite face of the slab at an angle θ (where $\theta = 0°$, 30° and 60°), enter a 1.25-cm-dia precollimator tube which leads into a larger vacuum tube, and reach a bank of $B^{10}F_3$ counters. The angle θ was varied by bodily rotating the LiH slab and lead target about a point which is the intersection of the precollimator axis on the surface of the LiH slab.

The neutron energy is obtained from the transit time required for the 16-m distance to the counters. Two time-of-flight analyzers receive a start pulse from the accelerator and a stop pulse from the $B^{10}F_3$ counters, one analyzer having a 16-μsec interval between time channels and the other a 90-μsec interval. Together they covered the energy range from about 0.01 to 300 ev. After each run a background determination was made by placing a $B_4^{10}C$ block over that portion of the slab "seen" by the precollimator.

Two neutron monitors located in the target room supplied the normalization data between foreground and background runs. The data were processed with codes previously developed and tested by the GA staff. The codes normalized the background counts to the monitor counts; subtracted the background; made corrections for the pulse duration, the mean flight path in the $B^{10}F_3$ stack that varies with energy, and the detector energy sensitivity; and converted the resulting time-of-flight spectra to energy spectra, grouping the data over many channels in the low-energy region to about 10% energy intervals. The statistical uncertainties were hand computed.

---

[7] J. R. Beyster *et al.*, *Measurement of Low Energy Spectra*, GA-1088 (Nov. 13, 1959).

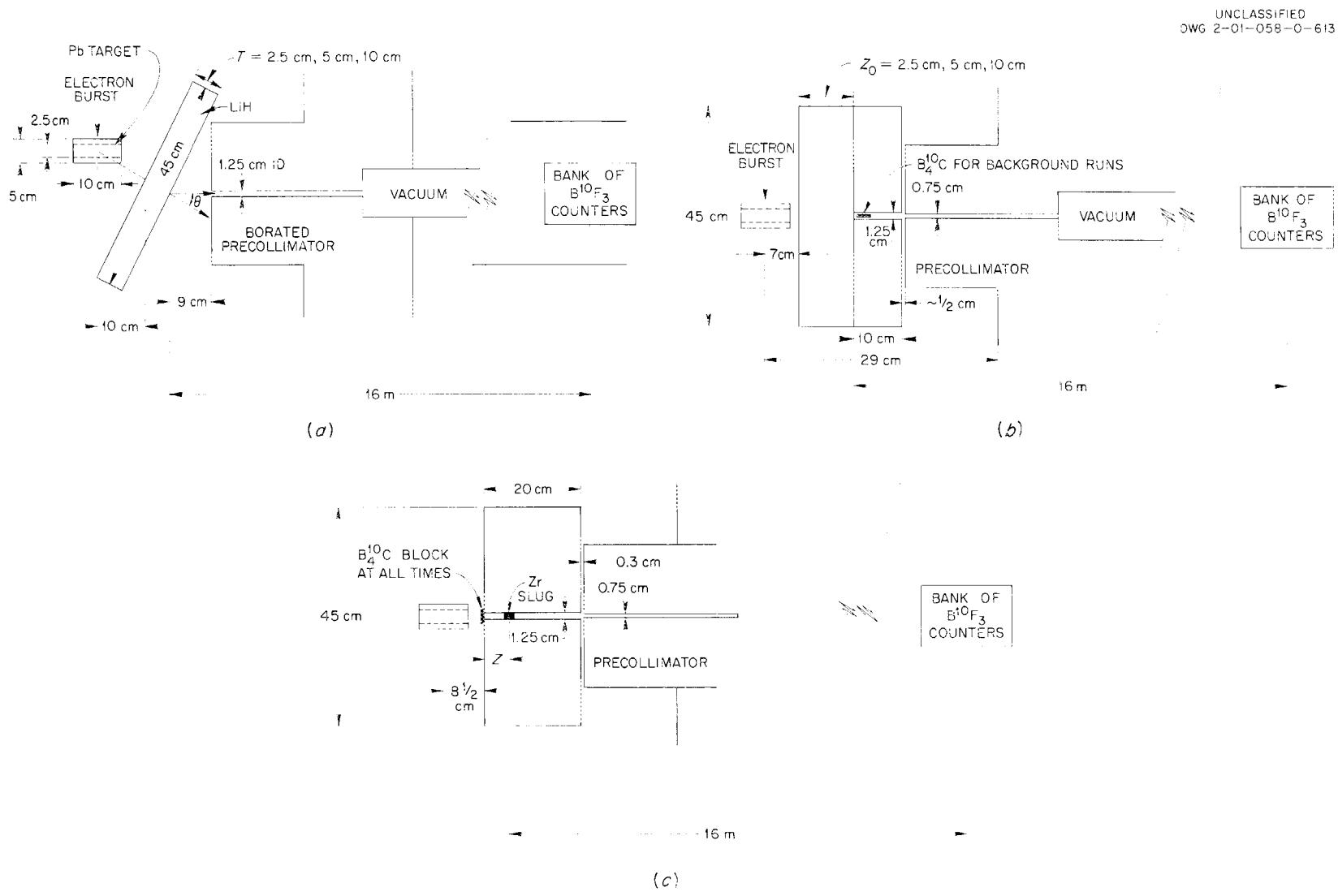

Fig. 7.1.2. Experimental Arrangements for Neutron Energy Spectra Measurements. (*a*) Leakage flux measurements; (*b*) forward-directed flux measurements; (*c*) scalar flux measurements.

The experimental results for the spectra of neutrons leaking normally from 2.5-, 5-, and 10-cm-thick slabs of LiH are compared with the calculations in Figs. 7.1.3, 7.1.4, and 7.1.5, respectively. Similar comparisons for the neutrons leaking at angles of 30 and 60 deg are shown in Figs. 7.1.6 and 7.1.7, respectively. In all the figures the dashed lines represent O5R calculations for a slab geometry and the solid lines represent NIOBE results for a 10-cm-thick spherical shell with a 200-cm inside diameter. The source for the NIOBE calculations was taken to be a 30-cm-dia volume source, the source and LiH shell being separated by vacuum. The statistical uncertainty is given for most of the points at the lower end of the measured spectra. The data below 0.1 ev is being reprocessed to correct for an error in the code which rejects negative numbers before grouping the single-channel data, an error which has been subsequently removed.

The bump apparent in the experimental data for the 2.5-cm-thick slab (Fig. 7.1.3) between 30 and 70 ev was also observed when the slab was removed; thus it does not represent neutrons slowed down in the LiH. A partial bump is also apparent in Figs. 7.1.4 and 7.1.5. It arises partly from the last slow oscillation in voltage in the detector-preamp-amplifier chain that effectively lowers the bias of the discriminator. The oscillation is caused by the burst of bremsstrahlung and fast neutrons that overwhelms the electronics. Note that for the 30- and 60-deg runs the positions of the slab and neutron source are such that the bremsstrahlung and neutron sources are far out of the precollimator's view. The data of these two runs are therefore the most reliable above 30 ev.

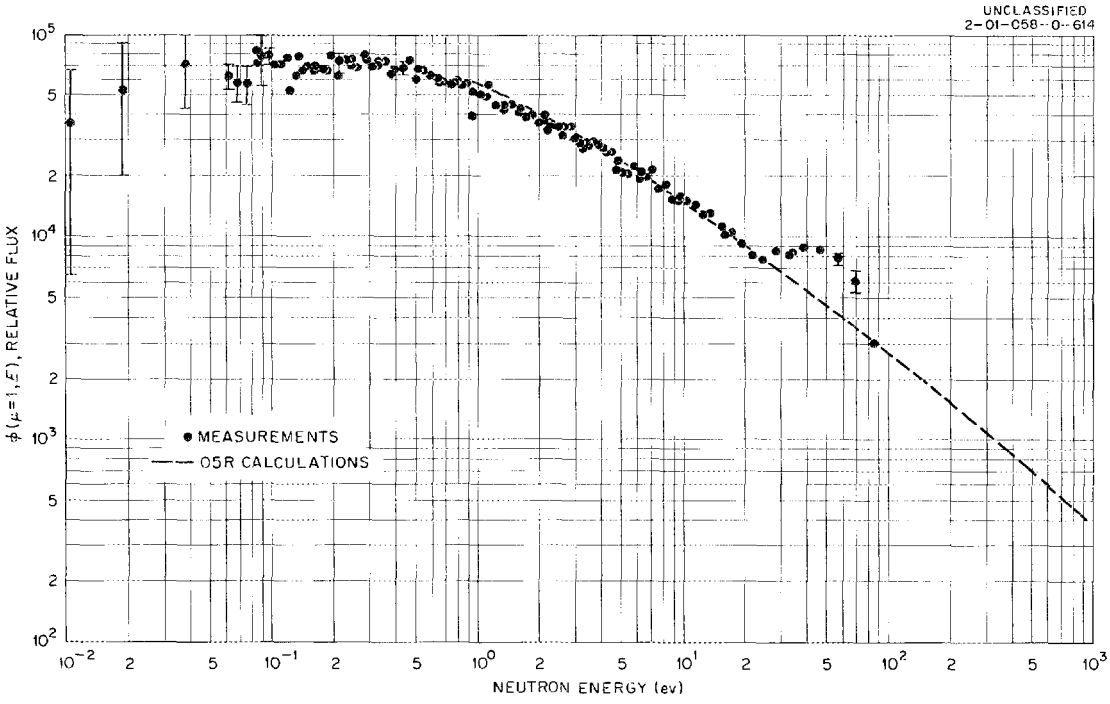

Fig. 7.1.3. Energy Spectrum of Neutrons Leaking Normally from a 2.5-cm-Thick LiH Slab: Comparison of Experiment with O5R Calculations.

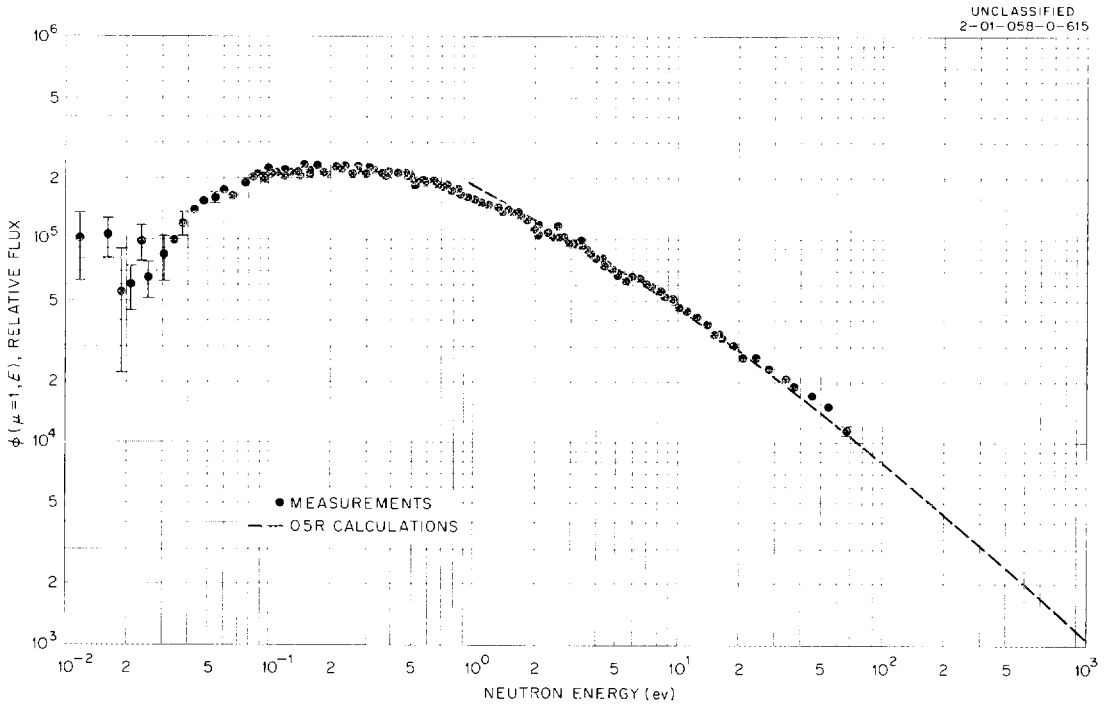

Fig. 7.1.4. Energy Spectrum of Neutrons Leaking Normally from a 5-cm-Thick LiH Slab: Comparison of Experiment with O5R Calculations.

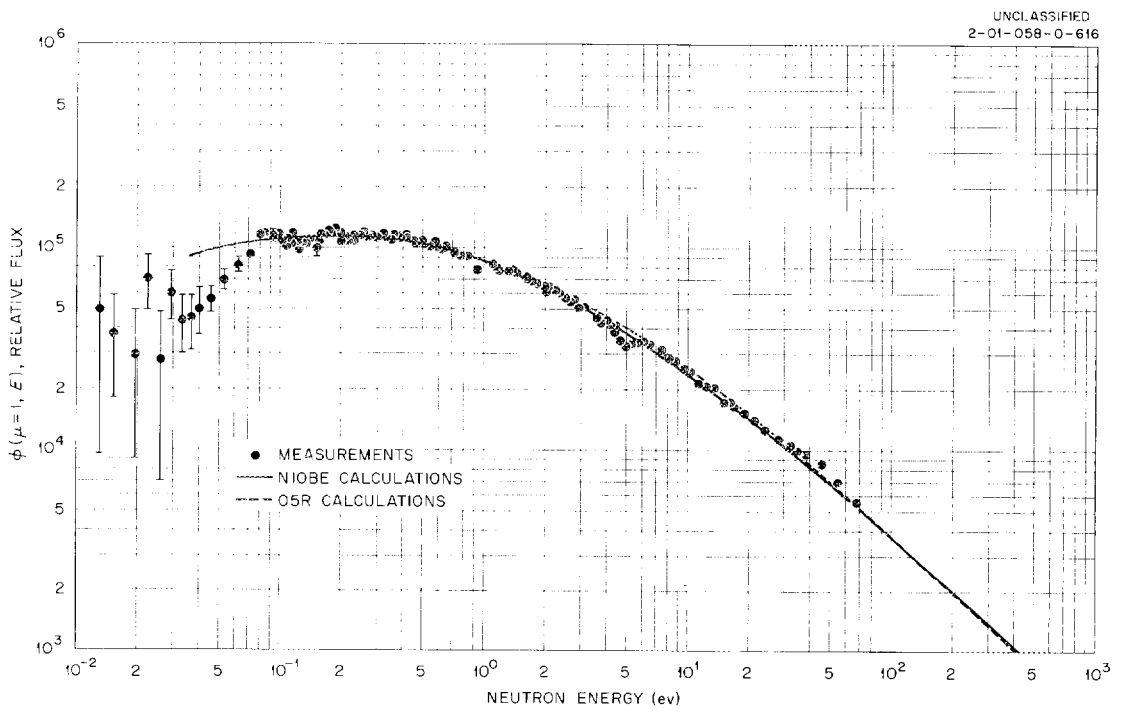

Fig. 7.1.5. Energy Spectrum of Neutrons Leaking Normally from a 10-cm-Thick LiH Slab: Comparison of Experiment with O5R and NIOBE Calculations.

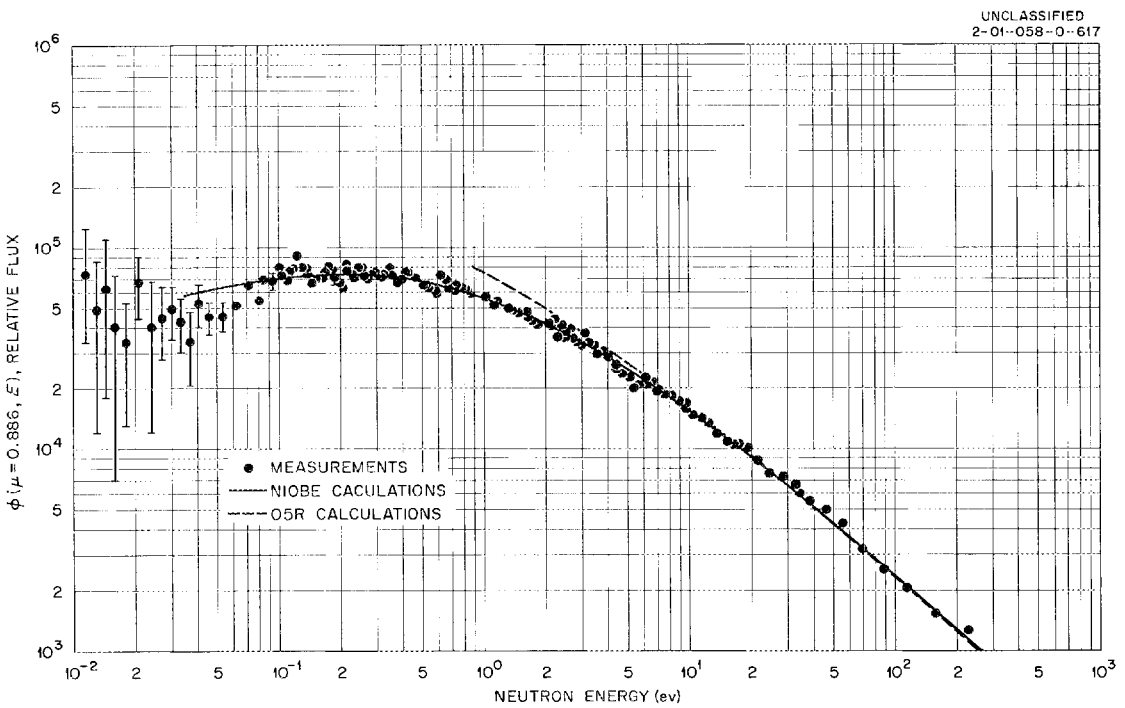

Fig. 7.1.6. Energy Spectrum of Neutrons Leaking at an Angle of 30 deg from a 10-cm-Thick LiH Slab: Comparison of Experiment with O5R and NIOBE Calculations.

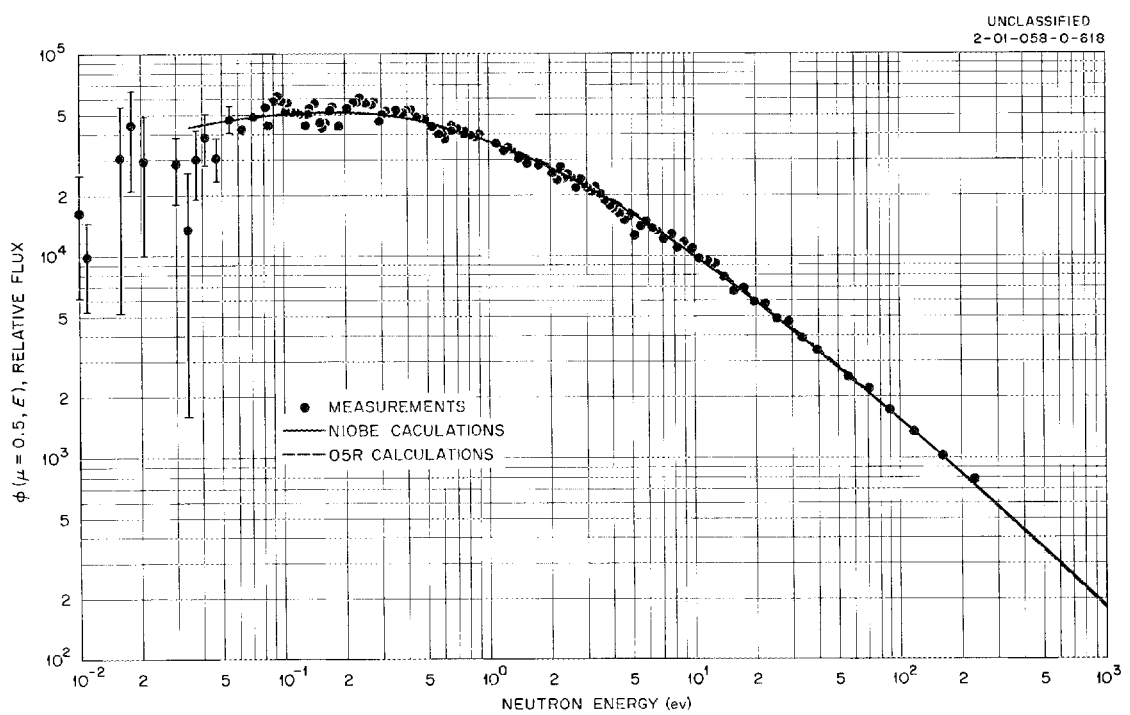

Fig. 7.1.7. Energy Spectrum of Neutrons Leaking at an Angle of 60 deg from a 10-cm-Thick LiH Slab: Comparison of Experiment with O5R and NIOBE Calculations.

There is little doubt that the 5- and 10-cm slabs produce the same spectrum. Spectral equilibrium is therefore definitely realized at penetrations of less than 5 cm. The spectral shapes predicted by the NIOBE calculations are in excellent agreement with the 0-, 30-, and 60-deg measurements for the 10-cm-thick slab from 0.1 to 230 ev. Below 0.1 ev, the measured points drop below the NIOBE results calculated with free-atom cross sections; this drop is the least pronounced for the largest tilt angle (60 deg).

The O5R calculations also agree with experiment except that they tend to be slightly higher than the observed spectrum at a few electron volts. However, the statistics of the O5R calculation are not good in this region.

Forward-Directed and Scalar Flux Measurements. – The experimental arrangements used for the measurements of forward-directed and scalar fluxes are shown in Figs. 7.1.2*b* and *c*, respectively. For the forward-directed flux measurements a 10-cm-thick LiH slab through which a 1.25-cm-dia re-entrant hole had been drilled was aligned with a 0.75-cm-dia precollimator hole leading to the $B^{10}F_3$ counter bank. Another LiH slab with a thickness of 2.5, 5, or 10 cm was positioned adjacent to the drilled slab on the source side. A 2.5-cm-dia hole in the lead target was aligned with the precollimator hole to reduce the effects of the beam flash at the counter bank produced by fast neutrons and bremsstrahlung radiation. Since the re-entrant hole was larger than the precollimator, the precollimator "viewed" only the bottom of the hole and not the sides. Background runs were made with a $B_4^{10}C$ plug inserted to the bottom of the re-entrant hole.

For the scalar flux measurements a 20-cm-thick LiH slab through which a 1.25-cm-dia hole had been drilled was positioned between the lead target and the precollimator. A block of $B_4^{10}C$, black to the energy range of neutrons being measured, was always located at the source end of the through-hole. Scalar flux spectra were then obtained from neutrons scattered by a zirconium slug placed at distances of $z = 2.5$, 5, and 10 cm in the through-hole. Zirconium is a very pure scatterer for neutrons and also has a flat energy dependence up to several hundred electron volts. This technique had been tested earlier at GA[8] by placing the neutron source behind the zirconium, as shown, and also laterally with respect to the zirconium slug. No change of spectra was observed. Background runs were made simply by removing the zirconium slug. This technique slightly overestimates the background since for the background runs the zirconium slug is not in place to attenuate neutrons that leave the sides of the hole between the $B_4^{10}C$ block and the slug, and these neutrons can partly leak through the edges of the precollimator.

The spectra of forward-directed fluxes within the LiH are shown in Figs. 7.1.8 through 7.1.10 for 2.5-, 5-, and 10-cm depths, respectively. As with the leakage flux data, the calculations and measurements agree in spectral shapes. This also holds true for the scalar flux plots in Figs. 7.1.11 through 7.1.13 for the same depths.

[8] J. R. Beyster, General Atomic, San Diego, California, private communication.

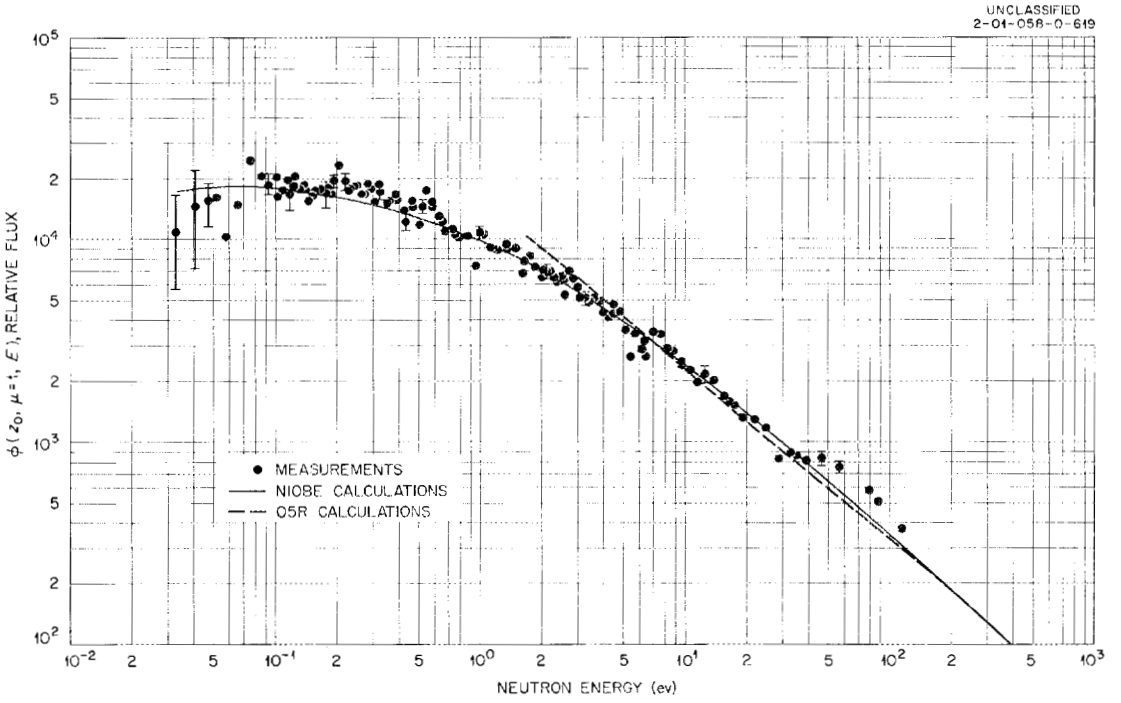

Fig. 7.1.8. Energy Spectrum of Forward-Directed Neutron Flux at a Depth of 2.5 cm in a LiH Slab: Comparison of O5R and NIOBE Calculations.

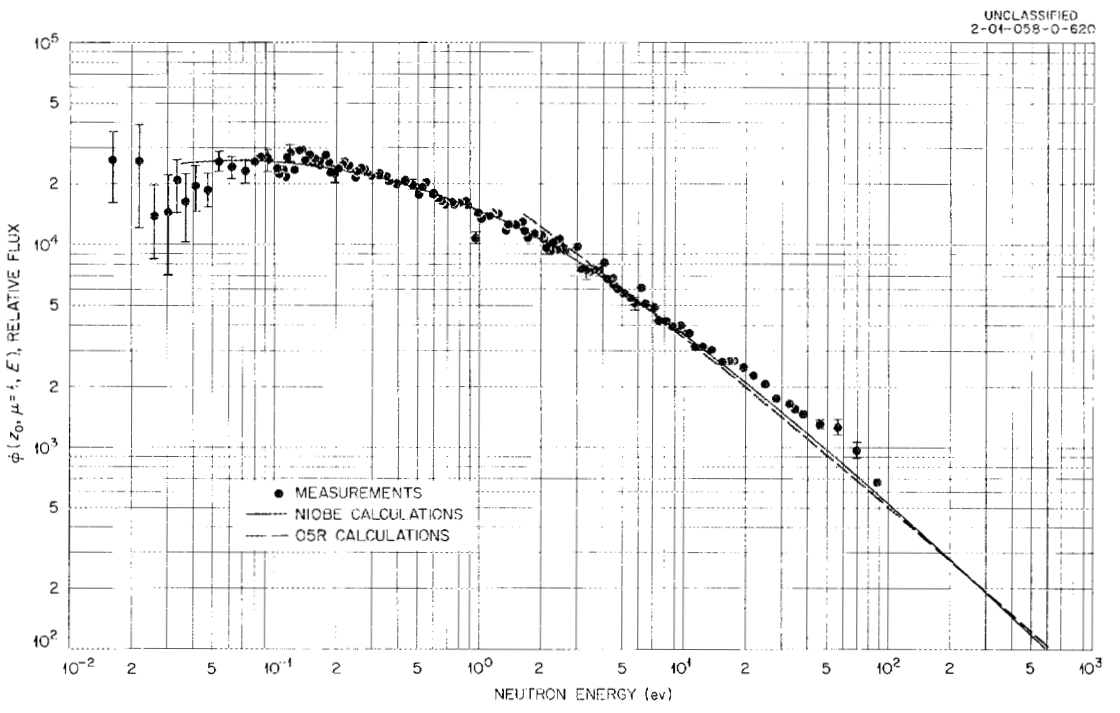

Fig. 7.1.9. Energy Spectrum of Forward-Directed Neutron Flux at a Depth of 5 cm in a LiH Slab: Comparison of O5R and NIOBE Calculations.

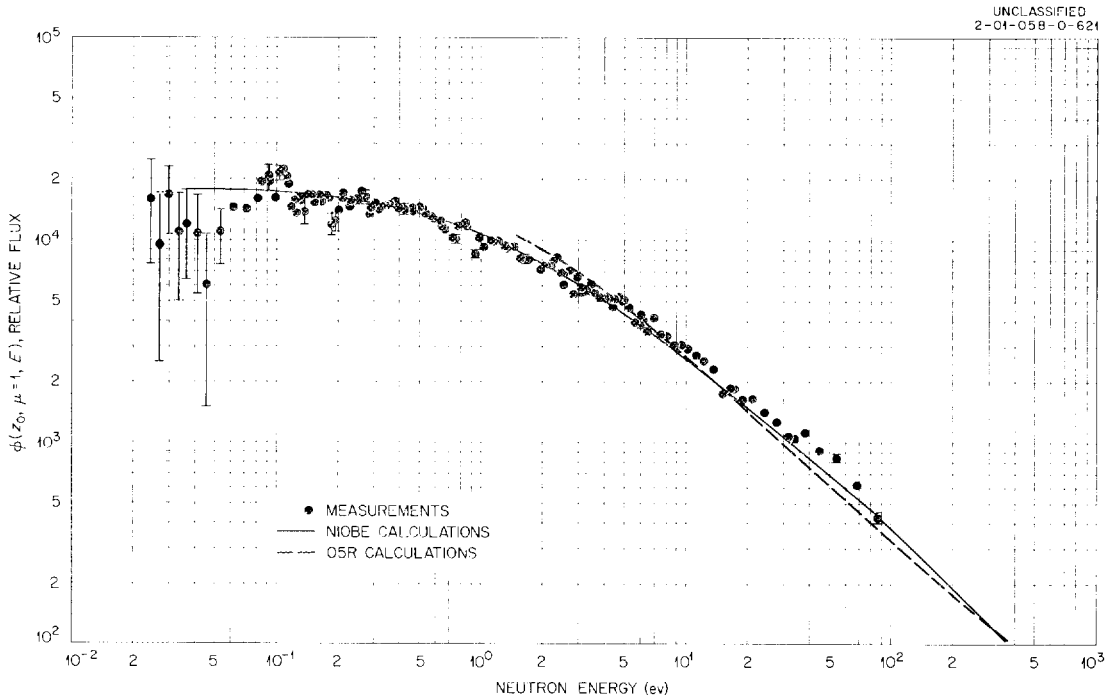

Fig. 7.1.10. Energy Spectrum of Forward-Directed Neutron Flux at a Depth of 10 cm in a LiH Slab: Comparison of O5R and NIOBE Calculations.

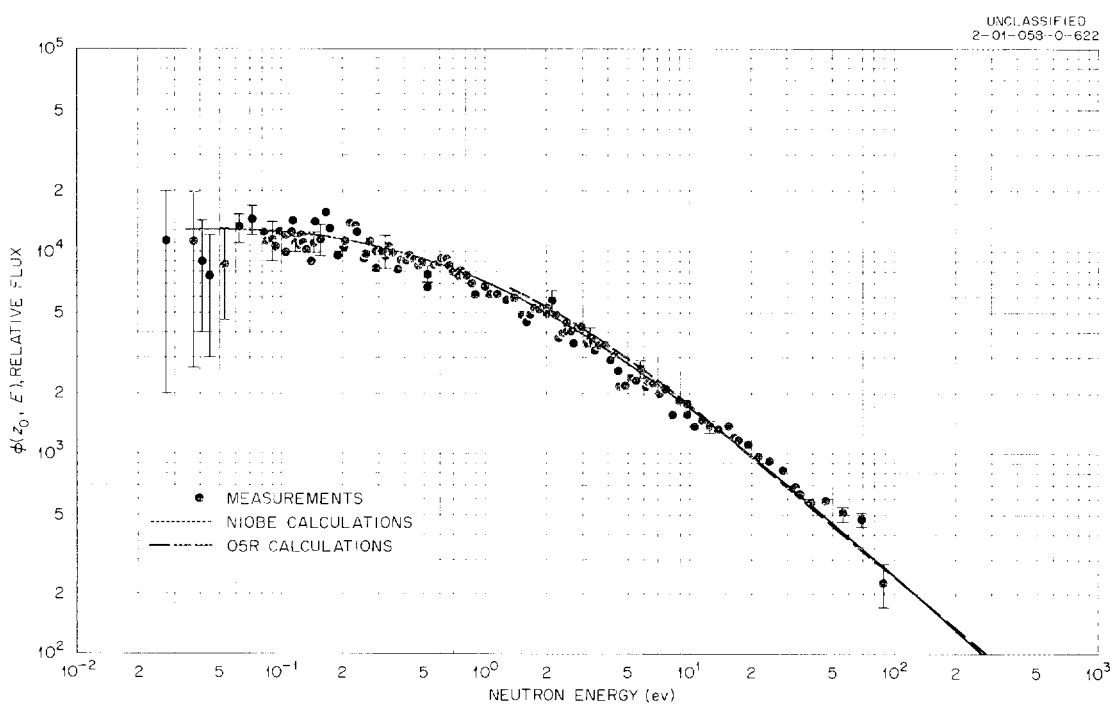

Fig. 7.1.11. Energy Spectrum of Scalar Neutron Flux at a Depth of 2.5 cm in a LiH Slab: Comparison of Experiment with O5R and NIOBE Calculations.

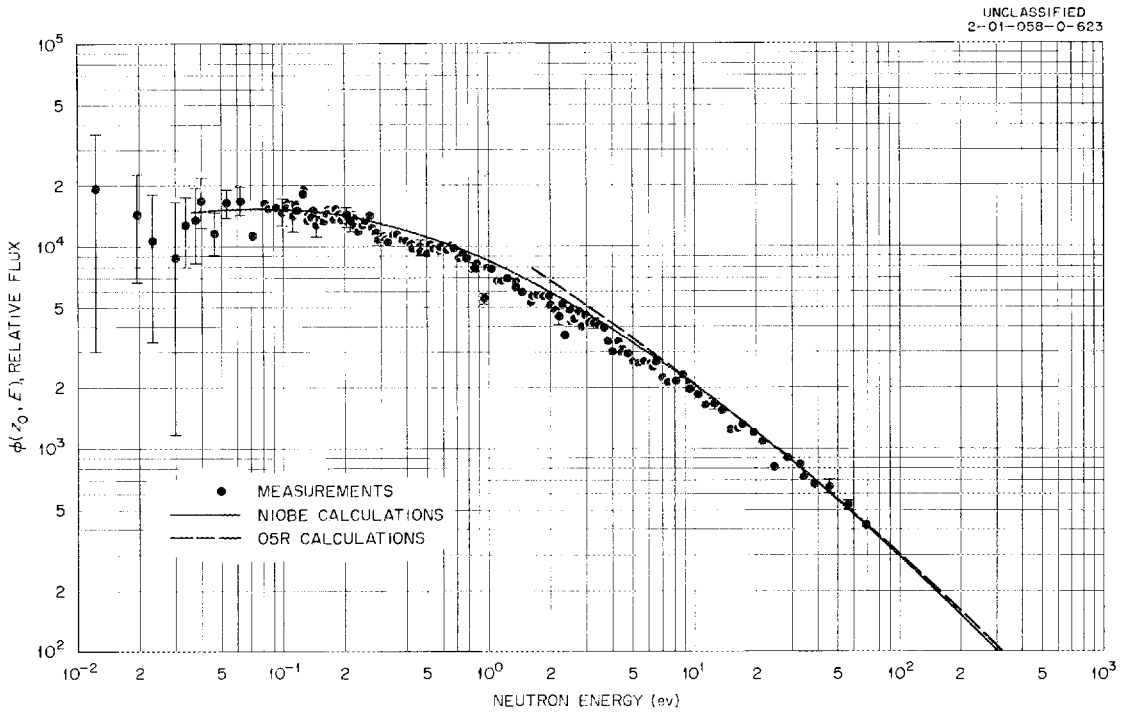

Fig. 7.1.12. Energy Spectrum of Scalar Neutron Flux at a Depth of 5 cm in a LiH Slab: Comparison of Experiment with O5R and NIOBE Calculations.

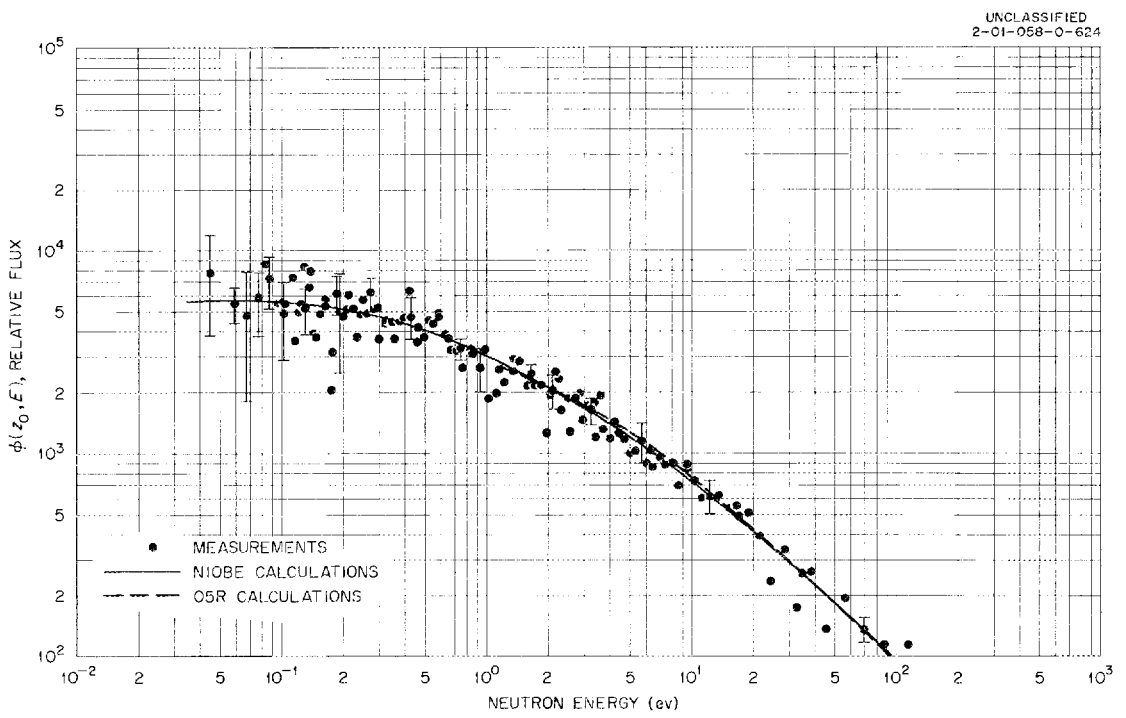

Fig. 7.1.13. Energy Spectrum of Scalar Neutron Flux at a Depth of 10 cm in a LiH Slab: Comparison of Experiment with O5R and NIOBE Calculations.

Several expressions relating the forward-directed flux to the scalar flux have been used, one of which was derived with diffusion theory approximations:[9,10]

$$\phi(z_0, \mu = 1, E) = K\phi(z_0, E) \times \left\{1 - \frac{1}{\Sigma_t}\left[\frac{\phi'(z, E)}{\phi(z, E)}\right]_{z=z_0}\right\},$$

where

$\phi(z_0, \mu = 1, E)$ = forward-directed flux,

$\phi(z, E)$ = scalar flux,

$\phi'(z, E)$ = first derivative of the scalar flux,

z_0 = thickness of LiH between the source and the bottom of the hole,

z = distance from the source side of the LiH slab to a point within the slab,

μ = cos θ, where θ is the angle from the normal,

K = a constant.

This expression is not expected to be valid in a highly poisoned hydrogenous medium where the flux gradients are strong, however, and to cover such cases a more general relationship between the forward-directed and scalar fluxes has been derived by Purohit.[11] Both expressions are compared with the NIOBE calculations in Fig. 7.1.14. The top curve in the figure gives the NIOBE calculations for the scalar flux at a 10-cm penetration and the bottom curve the corresponding forward-directed flux. The latter curve would be obtained from a re-entrant hole in a compressed gas of lithium and hydrogen. Applying Purohit's corrections to the scalar flux curve, with the use of flux gradients given by the NIOBE calculations, moves the curve downward until it is almost on top of the forward-directed flux curve. A correction by the diffusion theory approximation, also using NIOBE flux gradients, completely failed for the LiH in that it moved the scalar flux curve downward only about one-third as much as it should have.

Discussion of Results

As expected, the experimental data show good agreement in shape with NIOBE calculations above about 0.08 ev if the discrepancies due to gamma-ray flash effects sometimes observed at higher energies are ignored. From the behavior of the plots of NIOBE results above 0.08 ev in Fig. 7.1.15 it is observed that the shape of the neutron spectrum does not change with angle of emergence from a 10-cm-thick slab. Also, the internal scalar flux, $\phi(z, E)$, has nearly identical spectra at 2.5-, 5-, and 10-cm slab thicknesses, as does the forward-directed flux. In summary, the neutron flux attains low-energy spatial and spectral equilibrium in a poisoned, hydrogenous medium at remarkably small penetration depths.

---

[9] M. J. Poole, M. S. Nelkin, and R. S. Stone, "Measurement and Theory of Reactor Spectra," *Progress in Nuclear Physics*, Ser. I, Vol. II, pp. 156–7, Pergamon Press (1958).

[10] R. S. Stone and R. E. Slovacek, *Reactor Spectrum Measurements Using a Neutron Time-of-Flight Spectrometer*, KAPL-1499, pp. 15–18 (Mar. 15, 1956).

[11] S. N. Purohit, *Milne Problem with Capture*, ORNL-3005 (Sept. 28, 1960).

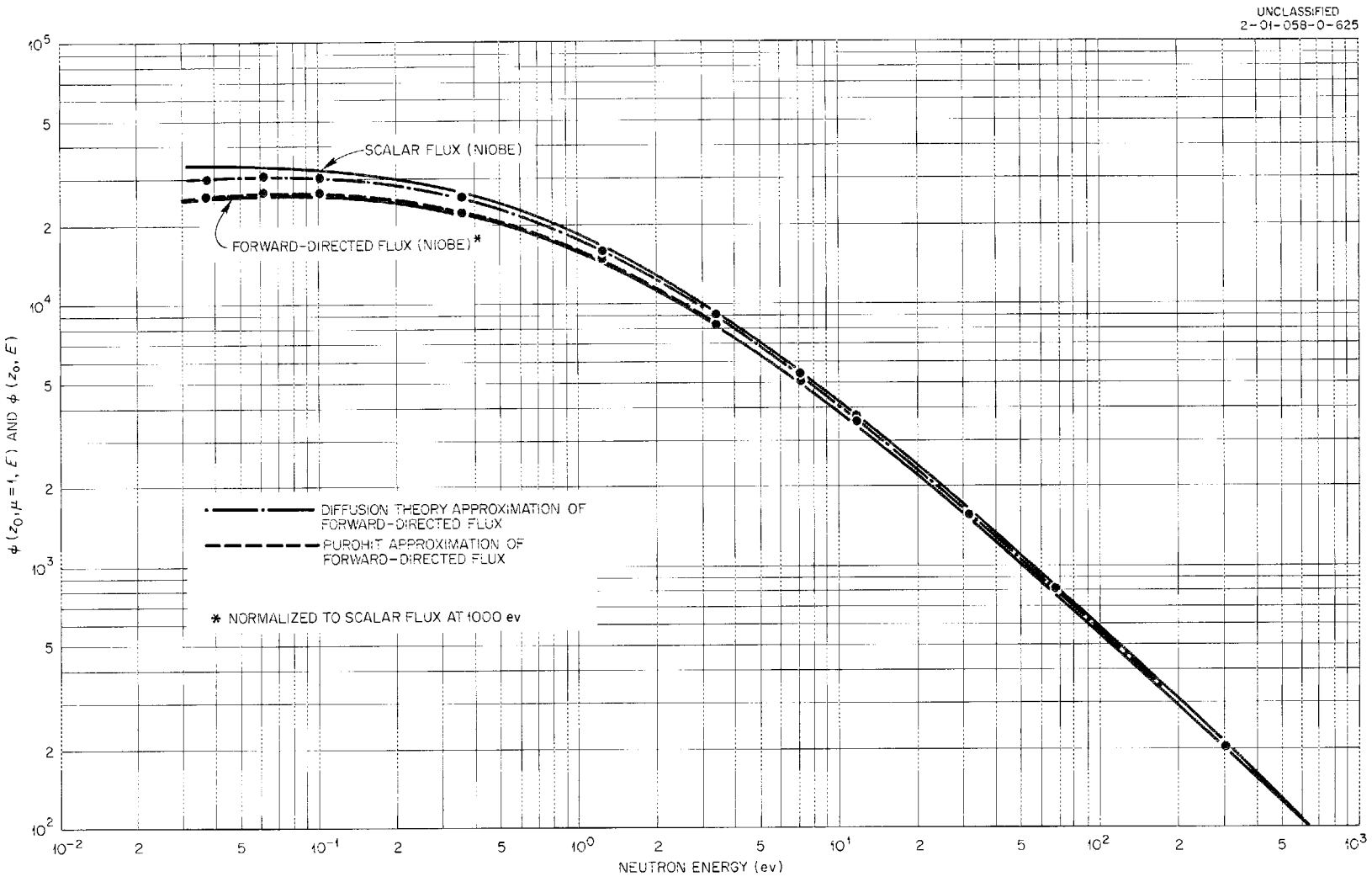

Fig. 7.1.14. Scalar and Forward-Directed Neutron Flux Spectra at a Depth of 10 cm in a LiH Slab: Comparison of Forward-Directed Fluxes Obtained from NIOBE Calculations, Purohit's Derivation, and Diffusion Theory.

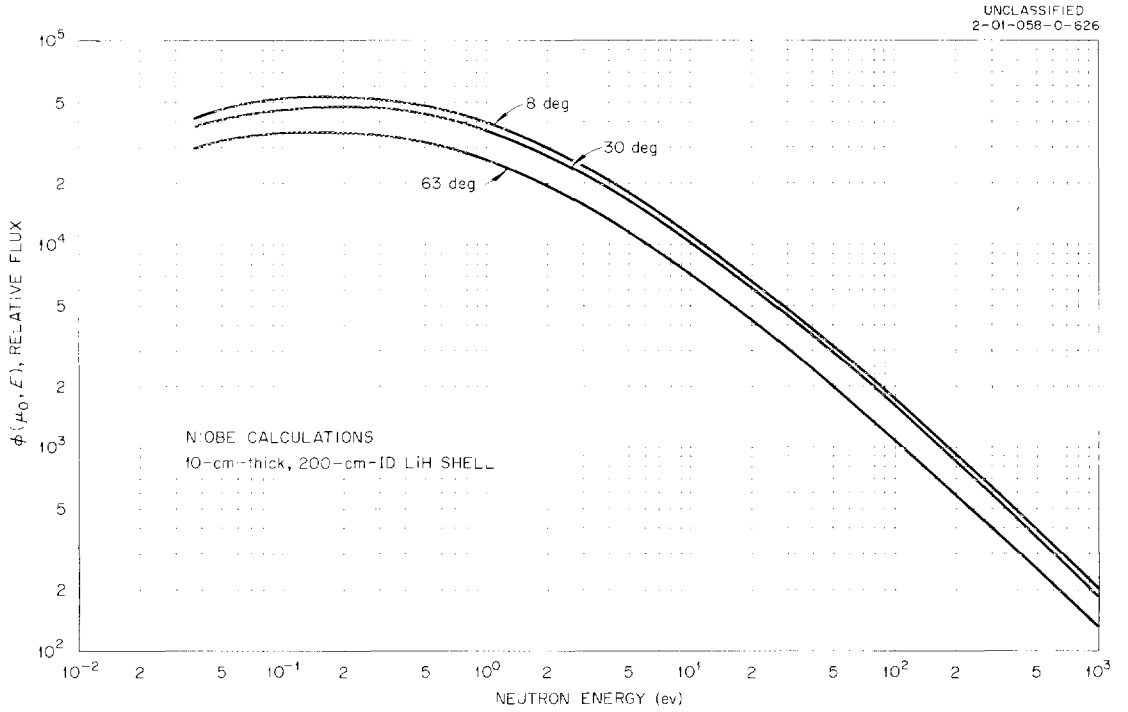

Fig. 7.1.15. Energy Spectra of Neutrons Leaking at Various Angles from a 10-cm-Thick, 200-cm-ID LiH Shell: NIOBE Calculations.

Acknowledgments

The indefatigable efforts of Jack Wood of GA in running the linear accelerator experiments and accumulating and processing the data are gratefully acknowledged. J. R. Beyster has given much perceptive advice for the design of the experiments, and considerable help was received from other members of the GA staff.

7.2. ENERGY AND ANGULAR DISTRIBUTIONS OF NEUTRONS PENETRATING SLABS OF DIFFUSING MEDIA: PART II: ANGULAR DISTRIBUTIONS[1]

V. V. Verbinski

It was pointed out in the preceding paper (Sec. 7.1) that a program is under way which is designed to provide basic data on the energy spectra and angular distributions of neutrons throughout various shielding materials. Wherever possible, experimental data and calculations are compared. It is the purpose of this paper to discuss that portion of the investigation covering the determination of angular distributions.

[1] See Sec. 7.1 for companion paper.

Thus far, the experimental phase of this study has consisted of measurements of the angular distributions of low-energy neutrons emerging from slabs of the following media: (1) a non-slowing-down medium without capture (lead), (2) a non-slowing-down medium with capture (lead poisoned with B_4C), (3) a slowing-down medium with weak capture (water), (4) a slowing-down medium with intermediate capture (boric acid solution), and (5) slowing-down media with strong capture (methyl borate + methanol and lithium hydride).

The calculations which have been compared with the experiments are both analytical and numerical. The analytical calculations, taken from the literature, consist of one performed by Fermi and reported by Bethe[2] for a slowing-down medium without capture and another performed by Case, de Hoffman, and Placzek[3] for a non-slowing-down medium with and without capture. The numerical calculations, performed specifically for this program, consist of two machine computations for a highly poisoned medium by the NDA NIOBE Code (see Sec. 7.5) and the ORNL O5R Code.[4] Since the O5R Code gives poor statistics in the low-energy regions, however, only the NIOBE results are used here. (Note: The O5R results will be more reliable for the higher energies to be reported later.)

To date, only the low-energy regions have been investigated experimentally, all experiments utilizing the apparatus shown in Fig. 7.2.1. Reactor neutrons pass through a rough collimator, the slab of material, an air chamber, blocking foils and collimator tubes until they reach a combination of foils placed at the end of each collimator tube. In order to verify that the angular distribution of the neutrons emerging from the slab does not vary with the angle of incidence of the input neutrons, measurements were also made with the input neutrons incident at 30 deg to the normal. This was effected by placing an air-filled adapter between the shield sample and the 10-in.-dia collimator. Details of the apparatus and the counting and background subtraction techniques have been presented in an earlier report.[5]

Summary of Analytical Calculations

The analytical calculations reported in the literature have used the so-called Milne geometry, which is described as a semi-infinite slab at $z = 0$ and a source at $z = \infty$. It was first used by Fermi, although not identified as such, in his calculations of the angular distribution of thermal and epithermal neutrons emerging from a slowing-down medium (paraffin). Assuming isotropic scattering and a linear flux plot near the $z = 0$ plane, Fermi obtained a distribution[2] of

$$\phi(\mu) = 1 + \sqrt{3}\,\mu ,$$

[2]H. A. Bethe, *Revs. Mod. Phys.* 9, 132-133 (1937).

[3]K. M. Case, F. de Hoffman, and G. Placzek, *Introduction to the Theory of Neutron Diffusion*, p 147, USGPO, Washington 25, D.C., 1953.

[4]R. R. Coveyou and J. G. Sullivan, *Neutron Phys. Ann. Prog. Rep. Sept. 1, 1960*, ORNL-3016, p. 193.

[5]V. V. Verbinski, *Neutron Phys. Ann. Prog. Rep. Sept. 1, 1960*, ORNL-3016, p. 202.

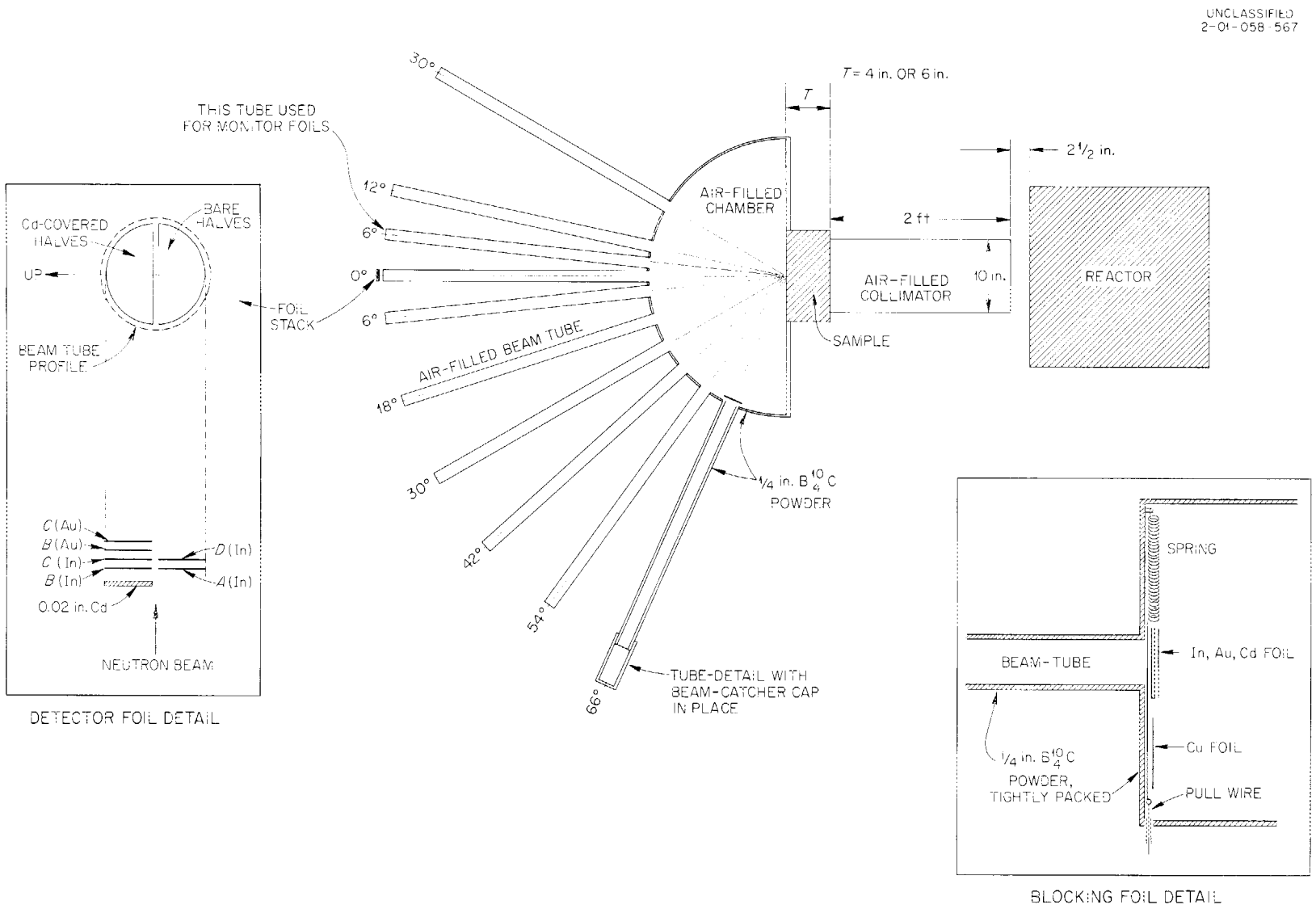

7.2.1. Apparatus for Measuring Angular Distributions of Neutrons Diffusing Through a Plane Parallel Slab of Material.

where μ is the cosine of the scattering angle measured from the normal. Fermi's expression can be derived through the use of a general integral equation such as that given by Purohit[6] for a medium with isotropic scattering and no absorption:

$$\phi(z=0,\mu,E_0)=\frac{1}{2\mu}\int_{z=0}\Sigma_s(E_0)\,\phi(z,E_0)\,e^{-z\Sigma_t/\mu}\,dz\,, \tag{1}$$

where

$\Sigma_s(E_0)\,\phi(z,E_0)\,dz$ = number of scattering events per interval dz at z,

$\exp(-z\Sigma_t/\mu)$ = probability of a scattered neutron of direction μ escaping through a distance z/μ to the surface without further scattering or capture,

$\Sigma_t=\Sigma_a+\Sigma_s$, where Σ_a and Σ_s are absorption and scattering macroscopic cross sections.

If it is assumed that $\phi(z,E_0)=a+bz$ near the boundary, $\phi(0,\mu,E_0)$ would be given by

$$\phi(0,\mu,E_0)\propto 1+\frac{b}{\Sigma_t a}\,\mu=1+\frac{1}{\Sigma_t z_0}\,\mu\,, \tag{2}$$

where, because the scattering is isotropic with no absorption, $\Sigma_t=\Sigma_s=1/\lambda=1/\lambda_t$ (λ_t = transport mean free path). z_0 is the extrapolation distance a/b. From the transport theory relationship[7] the extrapolated distance of the *actual* flux (not to be confused with the *asymptotic* flux) is $z_0=\lambda_t/\sqrt{3}$. Thus, the angular distribution for a medium with no absorption and with isotropic scattering (that is, a heavy medium) becomes

$$\phi(\mu)=1+\frac{\sqrt{3}}{\Sigma_t\lambda_t}\,\mu=1+\sqrt{3}\,\mu\,. \tag{3}$$

This equation may be applicable to a hydrogenous medium by reinterpreting the total macroscopic cross section Σ_t appearing in Eqs. 1 and 3 as the transport cross section $1/\lambda_t$. Equation 3 then agrees with experiment. The use of the transport cross section in Eq. 1 is then the only change made to take into account the forward scattering of neutrons by hydrogen, that is, their "memory" of direction.

The analytical calculations used for comparison with experimental data obtained for a non-slowing-down medium are those performed by Case *et al.*[3] They used the Milne geometry and a hypothetical non-slowing-down medium containing various concentrations of poison. For the case of no poison (no capture), their results agree approximately with the expression given by Eq. 3 above for a heavy scattering medium with no absorption.

Comparison of Experiments with Calculations

Non-Slowing-Down Medium with and without Capture. – The material used in the experiments to mock up a non-slowing-down medium without capture was lead. Since the results were to be compared with the

[6] S. N. Purohit, *Milne Problem with Capture*, ORNL-3005 (Sept. 28, 1960).

[7] S. Glasstone and M. C. Edlund, *The Elements of Nuclear Reactor Theory*, p 403, Van Nostrand, 1958.

Milne geometry calculations of Case *et al.*,[3] it was necessary that a slab thickness be chosen which would properly mock up the semi-infinite Milne geometry. Earlier experiments[5] with a relatively thin lead slab (6 in. of powdered lead, equivalent to a 3-in. solid lead slab) failed in this respect since it was observed that for neutrons incident on the slab 30 deg to normal there was a peaking of the angular distribution of the emerging neutrons at angles of emergence (θ) between 0 and 30 deg and not at precisely 0 deg. This is demonstrated in Fig. 7.2.2 in which the angular distribution of thermal neutrons is given for the thin slab. If the Milne geometry had been correctly mocked up, the experimental data, like the calculations, would have peaked at $\mu = 1$, where $\mu = \cos\theta$. The C value of 0.98 on the figure represents the ratio of the scattering cross section to the total cross section; i.e., $C = \frac{\Sigma_s}{\Sigma_t}$.

In order to ensure that the Milne geometry was correctly mocked up, a 16-in.-thick lead slab was fabricated for these experiments, and the success of the mockup was tested with a 30-deg incident beam. The results for thermal, indium resonance (1.5 ev), and gold resonance (5 ev) neutrons are shown in Figs. 7.2.3, 7.2.4, and 7.2.5, respectively, along with the corresponding calculations of Case *et al.* It can be seen that here the experimental data does peak at $\mu = 1$, so that the Milne geometry is mocked up. It is also observed that the experimental data agree with the calculations. The persistent bump in the curves between $\mu = 1$ and $\mu = 0.866$ represents the uncollided and small-angle scattered flux. This indicates a small degree of failure to mock up the Milne geometry, but it can be ignored in comparing experiment with theory.

The effect of adding poison to a non-slowing-down medium, thus increasing the capture, is demonstrated by one set of measurements taken from the earlier[5] thin-slab experiments and shown in Fig. 7.2.6. The solid and open circles give the experimental data for unpoisoned and poisoned lead, respectively, while the solid and dashed lines show the corresponding calculations. The poisoned lead consists of a mixture of powdered lead and B_4C for which the C value at 0.25 ev neutron energy is 0.59, compared to a

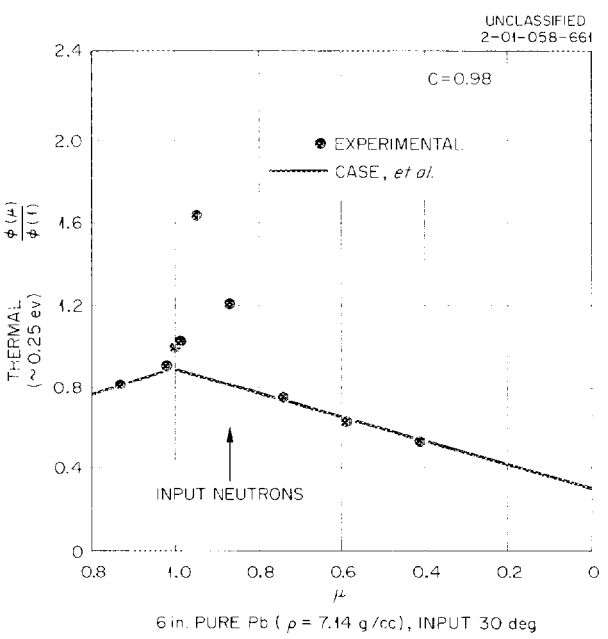

Fig. 7.2.2. Angular Distribution of Thermal Neutrons Emerging from a Thin Lead Slab: 30-deg Incident Neutrons.

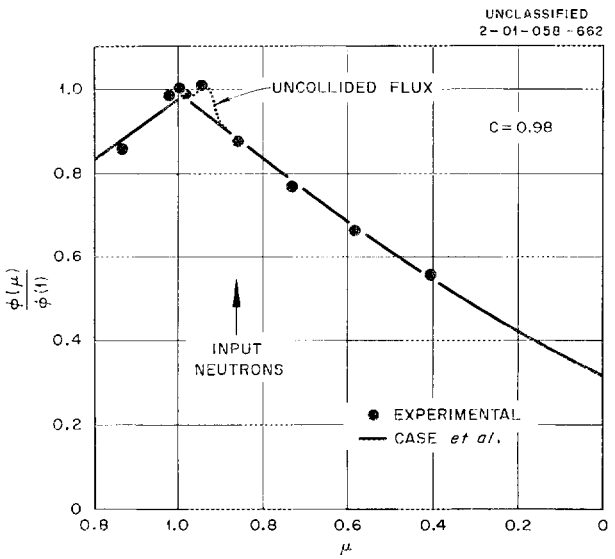

Fig. 7.2.3. Angular Distribution of Thermal Neutrons Emerging from a 16-in.-Thick Lead Slab: 30-deg Incident Neutrons.

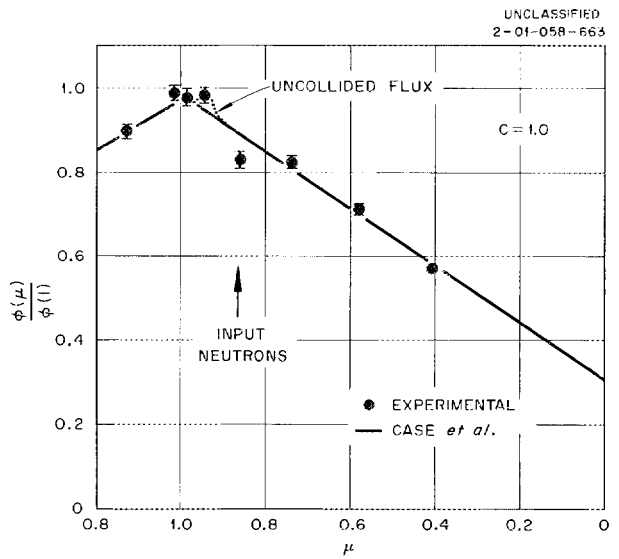

Fig. 7.2.4. Angular Distribution of 1.5-ev Neutrons Emerging from a 16-in.-Thick Lead Slab: 30-deg Incident Neutrons.

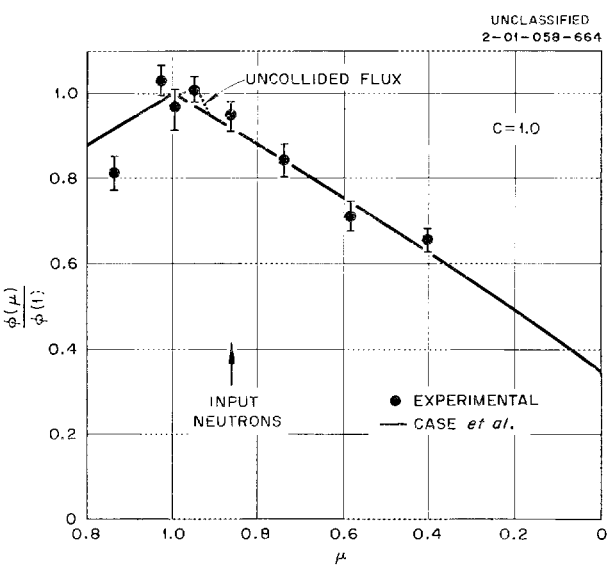

Fig. 7.2.5. Angular Distribution of 5-ev Neutrons Emerging from a 16-in.-Thick Lead Slab: 30-deg Incident Neutrons.

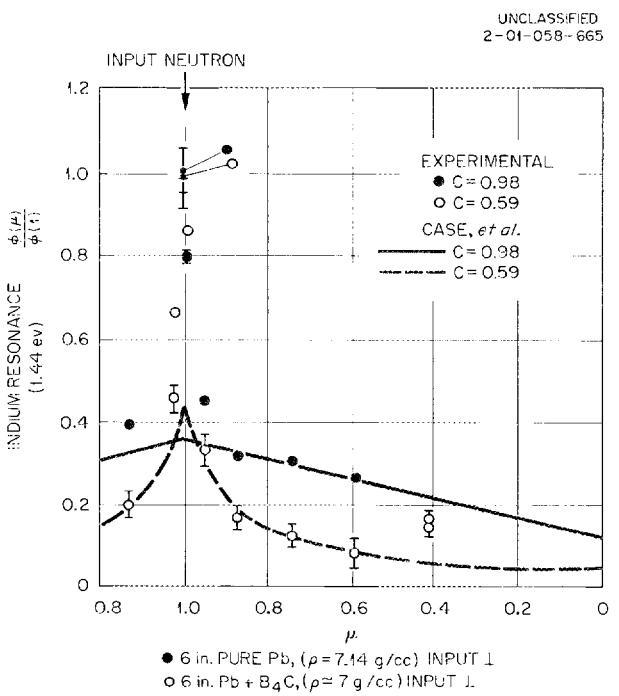

Fig. 7.2.6. Angular Distribution of 1.5-ev Neutrons Emerging from a Thin Lead Slab Poisoned with B_4C: Normally Incident Neutrons.

C value of 0.98 for the unpoisoned lead. Here the input neutrons are normally incident. The increase in forward peaking of the experimental points with added poison is in qualitative agreement with the calculations. The excessive forward peaking in the observed angular distribution is of course due to the small slab thickness employed.

Slowing-Down Medium with Weak Capture. – As mentioned above, the Milne problem for a slowing-down medium (paraffin) was solved by Fermi and reported by Bethe.[2] The experiments performed for comparison with Fermi's calculations consisted of measurements of the angular distribution of low-energy (thermal, 1.5-ev, and 5-ev) neutrons leaking from a 6-in.-thick slab of water, which should be equivalent to paraffin. The results have been reported previously; however, the thermal-neutron data are repeated here in Figs. 7.2.7 and 7.2.8. The fact that the angular distribution did not change when the input neutrons were incident at 30 deg shows that the Milne geometry was properly mocked up by the 6-in. thickness.

Slowing-Down Medium with Intermediate Capture. – The experiments with a slowing-down medium with intermediate capture consisted of measurements with a boric acid solution having a C value of 0.86 at 0.025 ev. The material thickness was 6 in. Since the results agree with an earlier set of measurements,[5] they are not repeated here; however, it is to be pointed out that all the data for 0.025-, 1.5-, and 5-ev neutrons incident both normally and at 30 deg are in rather good agreement with the $\phi(\mu) = 1 + \sqrt{3}\,\mu$ distribution.

Slowing-Down Medium with Strong Capture. – The experiments with a highly poisoned slowing-down medium utilized two materials, a methyl borate + methanol solution and a slab of lithium hydride. The

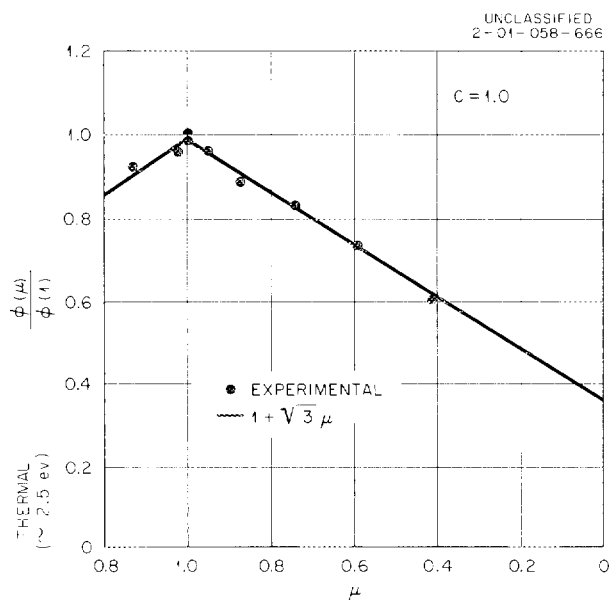

Fig. 7.2.7. Angular Distribution of Thermal Neutrons Emerging from a 6-in.-Thick Water Slab: Normally Incident Neutrons.

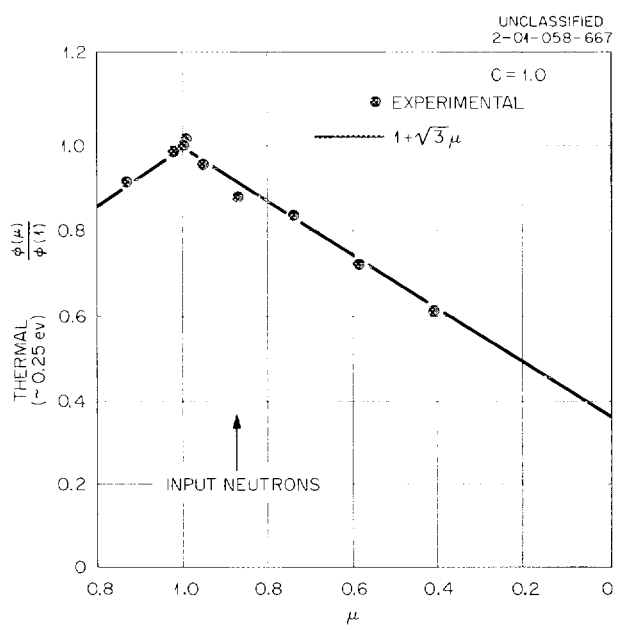

Fig. 7.2.8. Angular Distribution of Thermal Neutrons Emerging from a 6-in.-Thick Water Slab: 30-deg Incident Neutrons.

methyl borate + methanol experiments consisted of measurements of the angular distribution of neutrons emerging from 4- and 6-in. thicknesses of the material. The input neutrons were both normally incident and incident at 30 deg on the 6-in. slab. Only normal incidence was used for the 4-in. slab. Since the angular distribution was the same for the 4-in. slab with normal incidence as it was for the 6-in. slab at both normal and 30-deg incidence, it was assumed that the 4-in. thickness was adequate for a Milne geometry mockup. Note that the angular distribution is apparently constant for shield thickness greater than some minimum thickness.

The measurements for 1.5- and 5-ev neutrons, which have been reported previously,[5] are in approximate agreement with the Fermi expression $[\phi(\mu) = 1 + \sqrt{3}\,\mu]$. The measurements of the subcadmium angular distribution for the 4-in. slab, shown in Fig. 7.2.9, had to be repeated several times and thicker detector foils than those used for the 1.5- and 5-ev measurements had to be employed to improve the statistics. The least-squares fitting gives an angular distribution of $1 + A\mu$ for this data, where $A = 0.78 \pm 0.2$.

The lack of an analytical expression which will accurately describe the angular distribution of neutrons emerging from highly poisoned media such as methyl borate and lithium hydride has necessitated that the angular distributions for such materials be obtained from numerical calculations, and, as mentioned previously, an important phase of the current program is the performance of NIOBE Code calculations (see Sec. 7.5) and their correlation with experimental data. Since lithium hydride is of especial interest for shielding applications, it was the material selected for the study.

Measured angular distributions of neutrons emerging from a 4-in.-thick slab of lithium hydride are compared with NIOBE calculations for a 10-cm-thick, 200-cm-ID spherical lithium hydride shell in Figs. 7.2.10, 7.2.11, and 7.2.12, for subcadmium, indium-resonance, and gold-resonance neutrons, respectively.

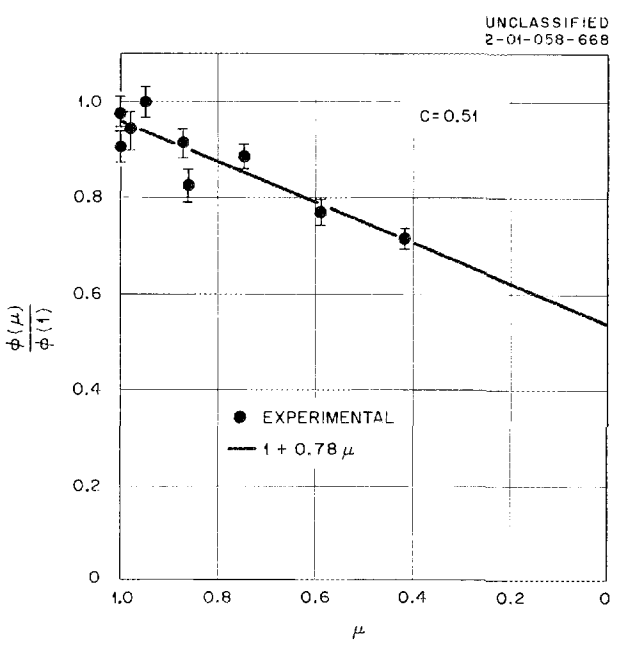

Fig. 7.2.9. Angular Distribution of Subcadmium Neutrons Emerging from a 4-in.-Thick Methyl Borate + Methanol Slab: Normally Incident Neutrons.

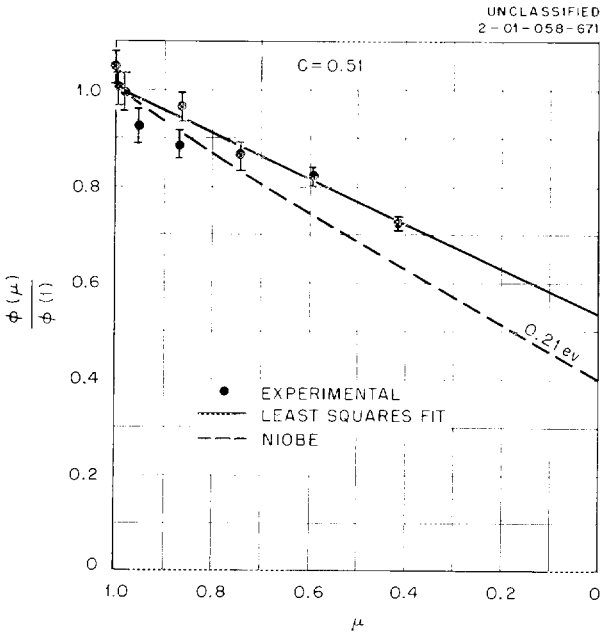

Fig. 7.2.10. Angular Distribution of Subcadmium Neutrons Emerging from a 4-in.-Thick Lithium Hydride Slab: Normally Incident Neutrons.

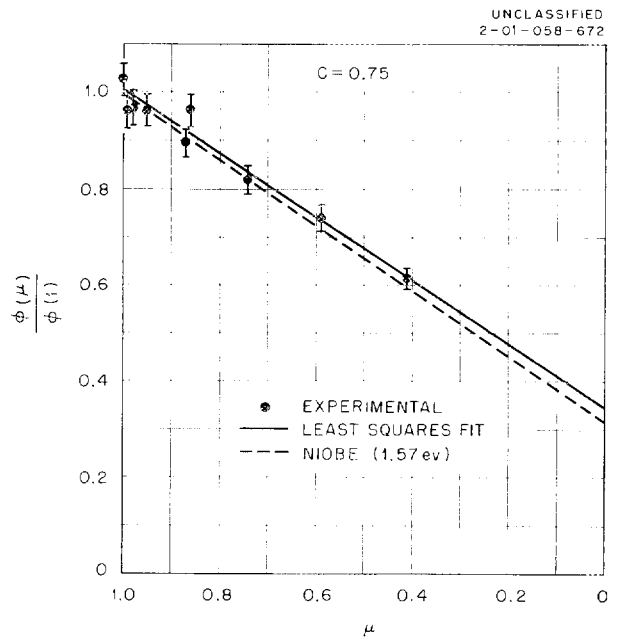

Fig. 7.2.11. Angular Distribution of Indium Resonance Neutrons Emerging from a 4-in.-Thick Lithium Hydride Slab: Normally Incident Neutrons.

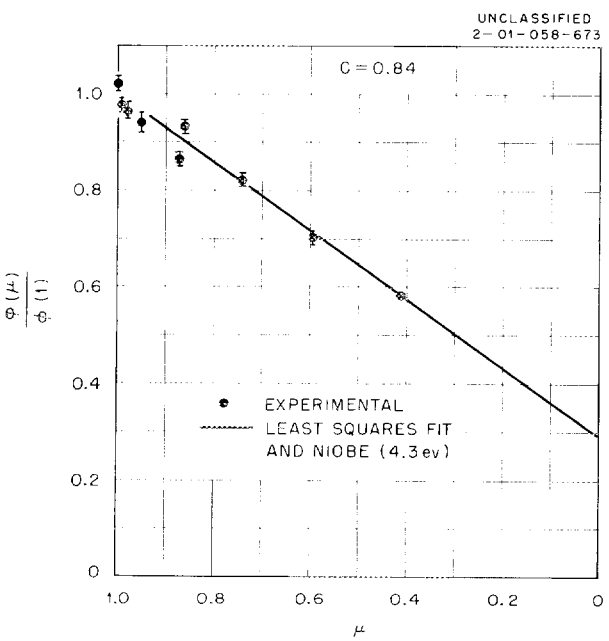

Fig. 7.2.12. Angular Distribution of Gold Resonance Neutrons Emerging from a 4-in.-Thick Lithium Hydride Slab: Normally Incident Neutrons.

Least squares fitting of the experimental data to the form $1 + A\mu$ yielded $A = 0.92$, 1.9, and 2.3, respectively. In the experiment the input neutrons were normally incident; for the calculations the fission source was assumed to be a 30-cm-dia sphere.

The solid lines in the figures represent the least squares fitting to the data and the dashed curves show the NIOBE results for the energy specified. In Figs. 7.2.11 and 7.2.12 the NIOBE calculations fit the data rather well, indicating that the assumption of free-atom cross sections used in the calculations is valid for these energies. For much of the subcadmium region, however, the free-atom assumption is known to be invalid. This is borne out by the fact that the NIOBE calculation for 0.21 ev (the mean energy for activation of indium foils) does not agree with experiment. The disagreement is in the direction expected for molecular binding effects.

Discussion of Results

In summary, it can be concluded that the Milne problem can be experimentally mocked up with a slab whose thickness is several mean free paths for neutrons of a given energy. There is good agreement between measured angular distributions and the one-velocity analytical solution, without capture, as given by Case, de Hoffman, and Placzek,[3] and Fermi's expression would seem to apply for the case of a strong slowing-down medium with weak absorption without exception providing an adequate thickness is used. Since the Milne problem with slowing down and with capture has not been solved analytically, the NIOBE Code of NDA, a semianalytical calculation, must be relied upon. It has produced results that are in agreement with experiment in the epithermal region where the correct cross sections are known.

Experimental results presented previously[5] showed that the angular distribution attains an equilibrium value before 10 cm of penetration, and recent NIOBE calculations with an extended fission-spectrum source indicate that for the energy region below a few kev, spectral equilibrium in lithium hydride is attained before 5 cm of penetration. It should follow that the emergent angular distributions also attain equilibrium values at these smaller penetrations. This being true, shielding calculations need not be extended much more than a few lethargy intervals below source energy for thick hydrogenous shields. For lithium hydride, the calculations need not extend far below the kilovolt region even if the last shielding layer is only about 5 cm thick since the available low-energy spectra can be tacked on where the calculations cut off in energy. Similarly, the angular distributions given by the NIOBE calculations are useful down to about 0.1 ev. Below this the measured subcadmium-neutron angular distribution of Fig. 7.2.10 could be used if it is remembered that this is the angular distribution of neutrons weighted by a $1/\sqrt{E}$ absorber.

7.3. MONTE CARLO CALCULATION OF NEUTRON REFLECTION FROM WATER

D. K. Trubey

In connection with shield design studies for the ORR GCR Loop No. 2,[1] the O5R neutron code[2] was used to generate neutron histories for a 42-in.-dia, 6-ft-long cylinder of water. A monoenergetic 10-in.-dia neutron beam was incident on the end of the cylinder. One of the analysis codes written to process the collisions yielded the albedo energy spectrum which is reported here. Five source energies were considered.

The O5R code generated fast-neutron collisions at all energies from the source energy down to 1 ev, at which point the neutron was considered to be thermalized. The code also generated a thermal history for each neutron. However, since most of the fast-neutron dose rate is due to high-energy neutrons, the code written to process the collision data (written on magnetic tape) considered only neutrons above an arbitrary cutoff which was taken to be 0.0094 Mev. This resulted in a considerable saving in machine time. Statistical estimation[3] was used to calculate the number albedo. In this problem the estimate was taken to be the weight of the neutron multiplied by $\exp[-\Sigma(E)l]$, where $\Sigma(E)$ is the total cross section at the energy of the neutron after a particular collision and l is the path length to the boundary. The energy albedo and energy distribution were also calculated. Since the water cylinder was effectively very large, it was considered to be an infinite slab. Many of the collisions did not give a contribution to the albedo as the neutron was either going in the wrong direction or was below the cutoff energy, as is shown in Table 7.3.1. Only 11% of the collisions generated by the O5R code gave an albedo contribution above 0.0094 Mev.

The computation was done in batches of 400 histories. Four batches per problem were run for all source energies with the exception of the 4-Mev source. The analog albedo was also calculated; that is, each neutron which the O5R code tabulated as leaking was recorded. With each batch considered, an estimate of the answer, the variance, and the standard deviation were computed. The albedos and per cent standard deviation, as computed with both methods, are given in Table 7.3.2. As expected, the statistical estimation variance is generally smaller. The number albedo as a function of energy is shown in Figs. 7.3.1–7.3.5.

It can be seen that the albedo generally decreases as incident neutron energy is increased. This is due to the greater probability for forward scattering at higher energies. The low albedo at $E_0 = 0.5$ Mev is undoubtedly due to the oxygen resonance at 0.43 Mev. (The single-scatter peak observed for other incident energies is not seen for $E_0 = 0.5$ Mev.) The absence of a single-scatter peak in the histogram for $E_0 = 8$ Mev is believed to result from the large anisotropy in the cross section at this energy.

The values in Table 7.3.2 for 1 Mev may be compared to the results of Berger and Cooper.[4] Their results determined from three runs of 3000 histories by the analog method are shown in Table 7.3.3. The

[1] D. K. Trubey, *Neutron Phys. Ann. Prog. Rep., Sept. 1, 1960*, ORNL-3016, p. 219.

[2] R. R. Coveyou and J. G. Sullivan, *Neutron Phys. Ann. Prog. Rep., Sept. 1, 1960*, ORNL-3016, p. 193.

[3] D. W. Drawbaugh, *Nuclear Sci. and Eng.* 9, 185 (1961).

[4] M. J. Berger and J. W. Cooper, *J. Research Nat. Bur. Standards; A. Phys. and Chem* 63A, 2 (1959).

Table 7.3.1. Summary of Collision Data

Source Energy (Mev)	No. of Neutron Histories	No. of Collisions Processed	No. of Collisions Lost	
			Wrong Direction	Below E Cutoff
0.5	1,600	1,858	6,112	20,832
1.0	1,600	3,006	5,383	17,153
2.0	1,600	3,693	6,067	19,520
4.0	800	2,131	3,794	10,747
8.0	1,600	3,568	6,901	16,249
Total	7,200	14,256	28,257	84,501

Table 7.3.2. Number and Energy Albedos for Monoenergetic Neutrons Impinging on Water

Source Energy (Mev)	Residual Energy $\geq$0.0094 Mev		Residual Energy <0.0094 Mev
	Statistical Estimation (%)	Analog Method (%)	Analog Method (%)
		Energy Albedo	
0.5	0.0105 ± 11	0.0099 ± 21	0.0003
1.0	0.1063 ± 6	0.0979 ± 7	0.0001
2.0	0.0430 ± 11	0.0473 ± 13	0.0001
4.0	0.0147 ± 1	0.0131 ± 17	0.0000
8.0	0.0042 ± 9	0.0045 ± 12	0.0000
		Number Albedo	
0.5	0.0498 ± 20	0.0500 ± 27	0.1724 ± 19
1.0	0.2322 ± 6	0.2181 ± 6	0.1293 ± 10
2.0	0.1222 ± 5	0.1281 ± 10	0.1031 ± 12
4.0	0.0695 ± 3	0.0678 ± 2	0.0407 ± 3
8.0	0.0420 ± 10	0.0407 ± 10	0.0333 ± 22

Table 7.3.3. Comparison of Results of Calculations

	Number Albedo	Energy Albedo
Berger calculation	0.370 ± 0.009	0.135
	0.381 ± 0.009	0.148 ± 0.005
	0.361 ± 0.009	0.115
Present calculation	0.361 ± 0.023	0.106 ± 0.007

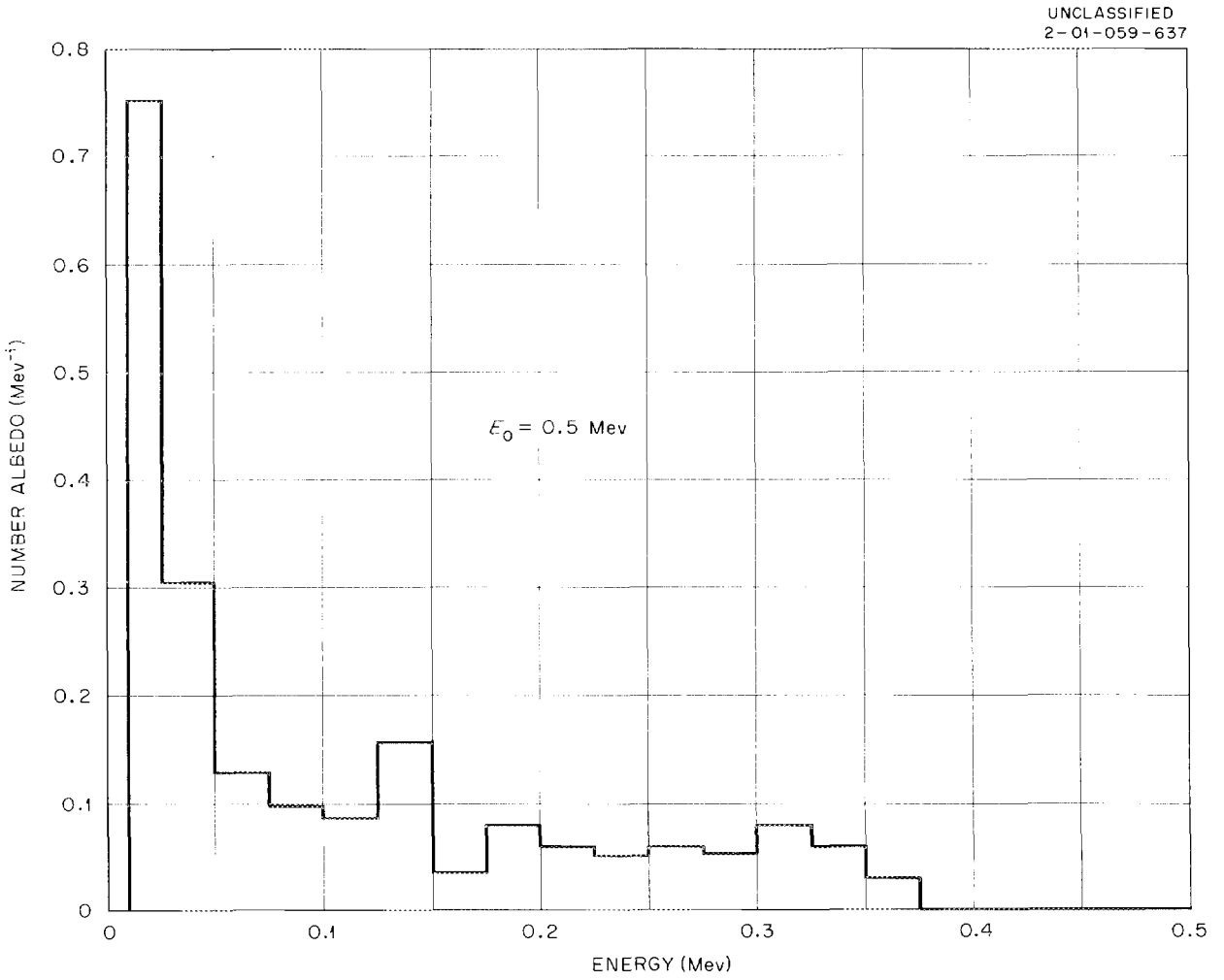

Fig. 7.3.1. Number Albedo for Water as a Function of Energy: E_0 = 0.5 Mev.

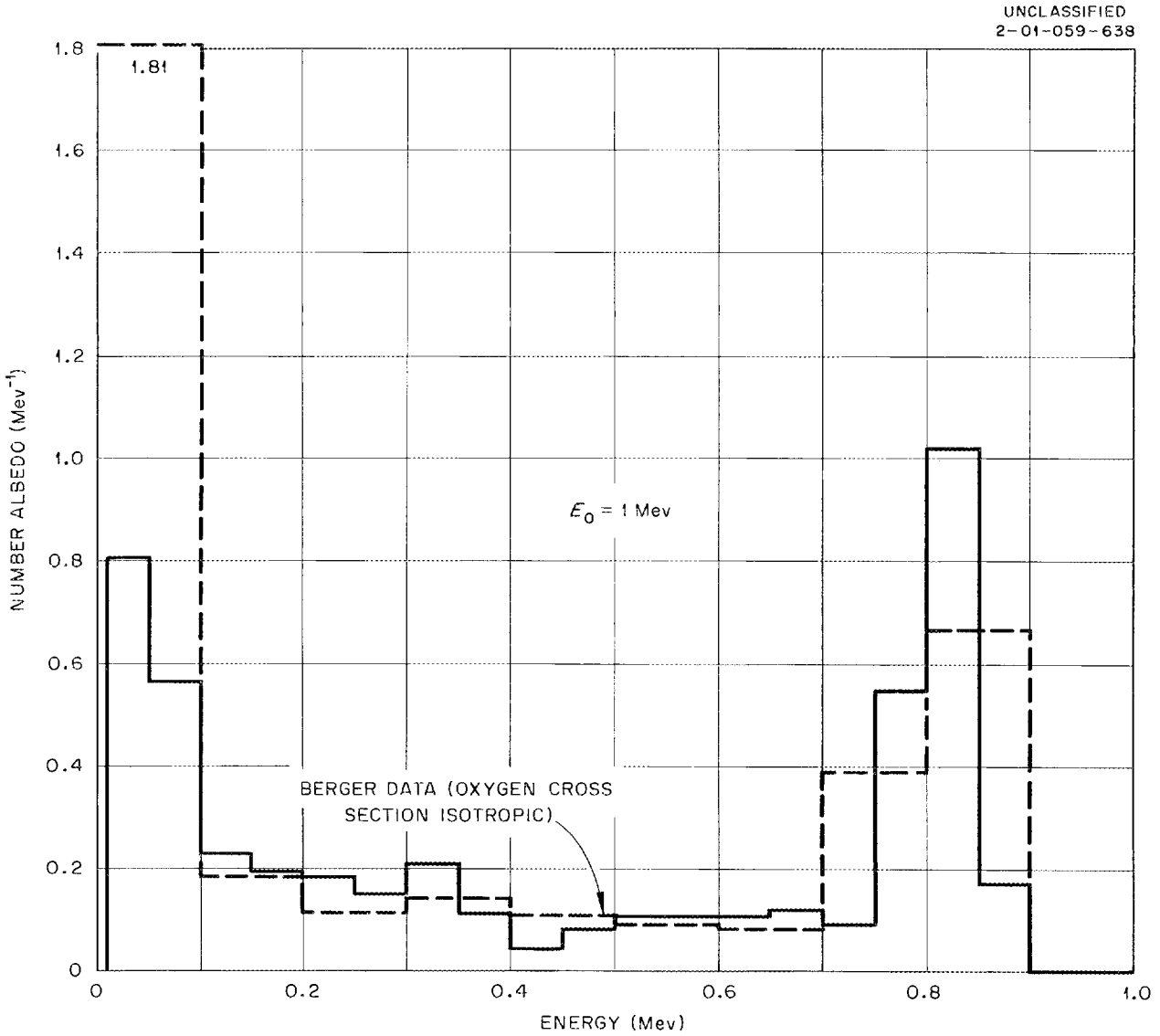

Fig. 7.3.2. Number Albedo for Water as a Function of Energy: E_0 = 1.0 Mev.

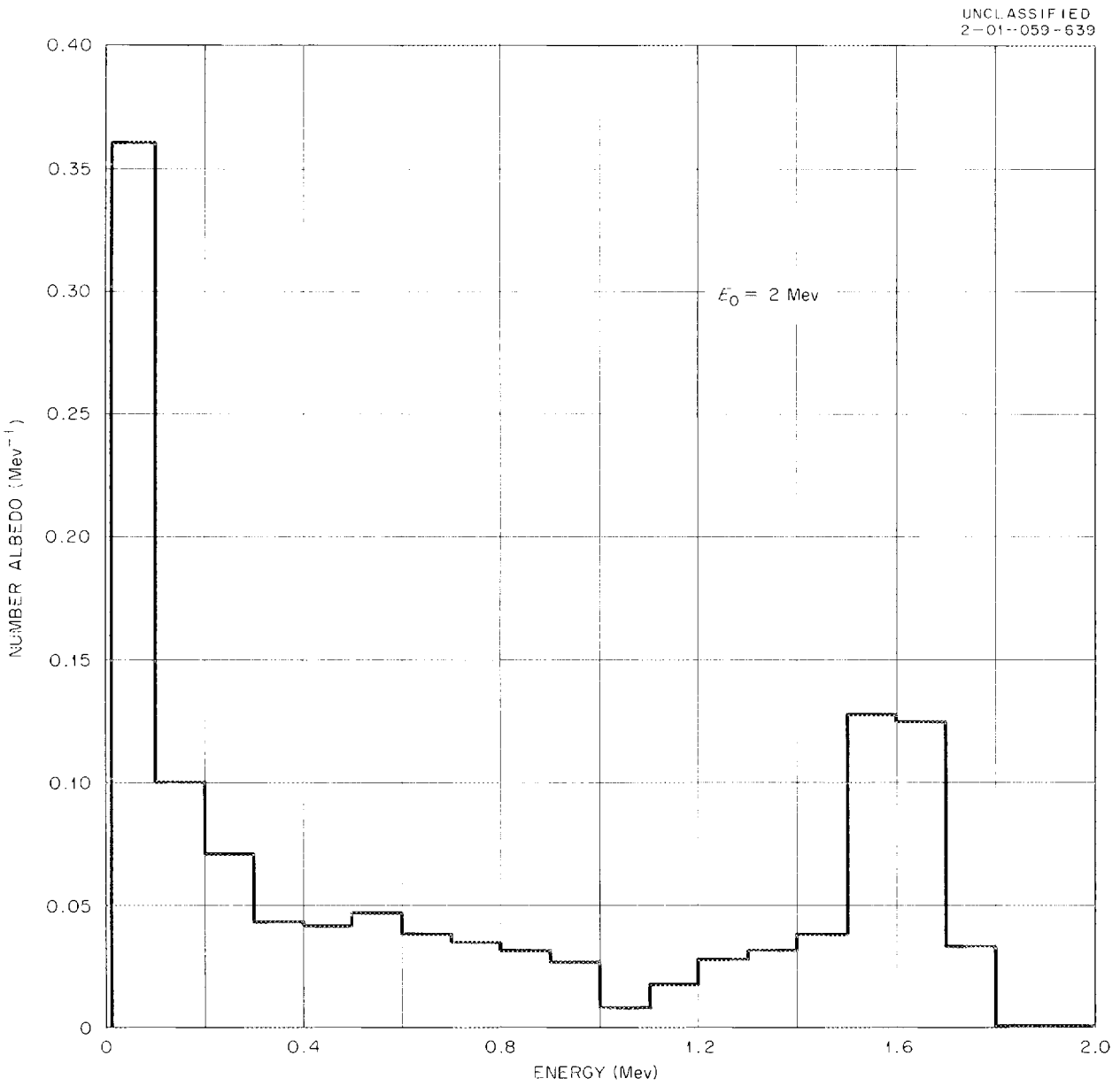

Fig. 7.3.3. Number Albedo for Water as a Function of Energy: E_0 = 2.0 Mev.

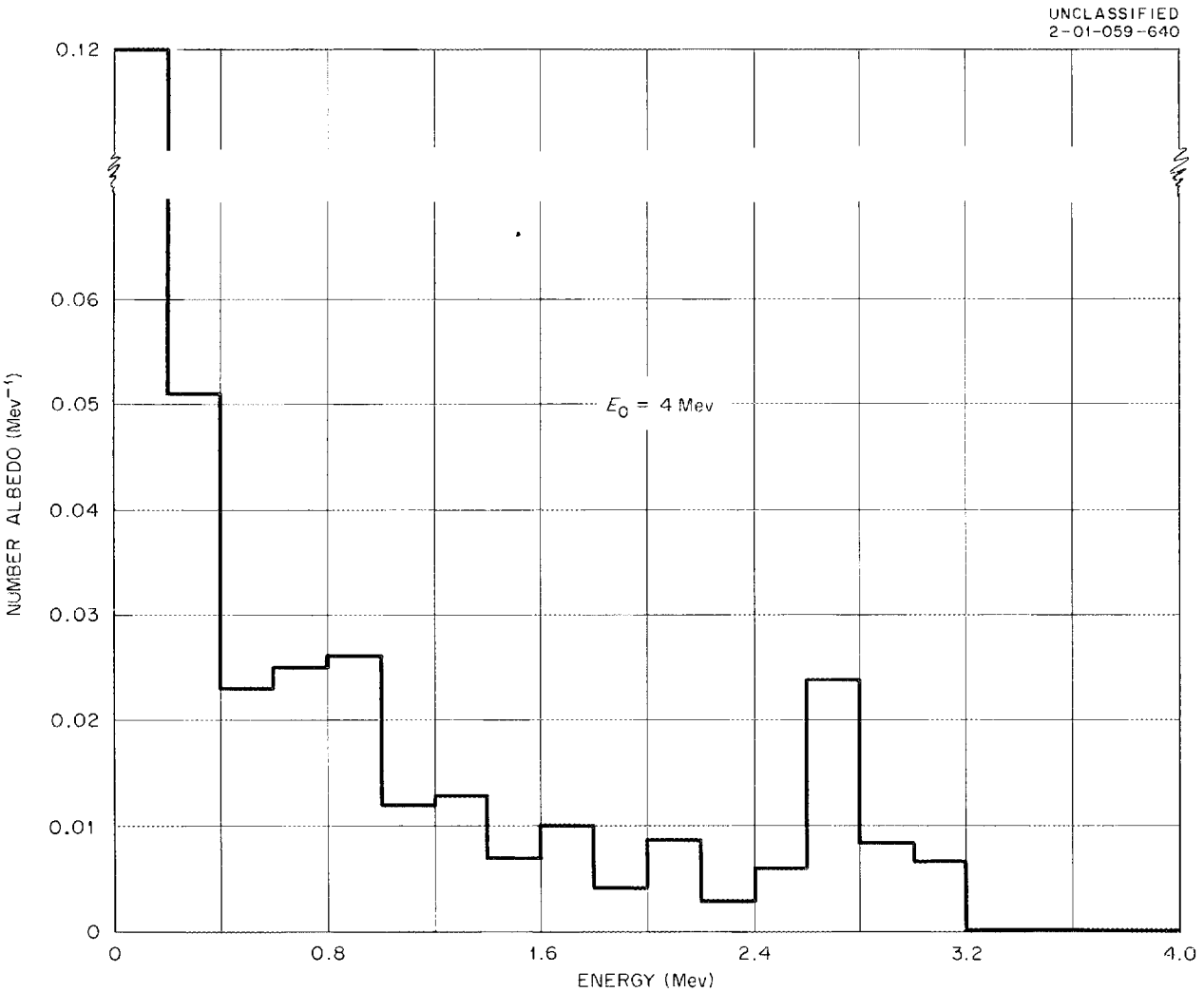

Fig. 7.3.4. Number Albedo for Water as a Function of Energy: $E_0 = 4.0$ Mev.

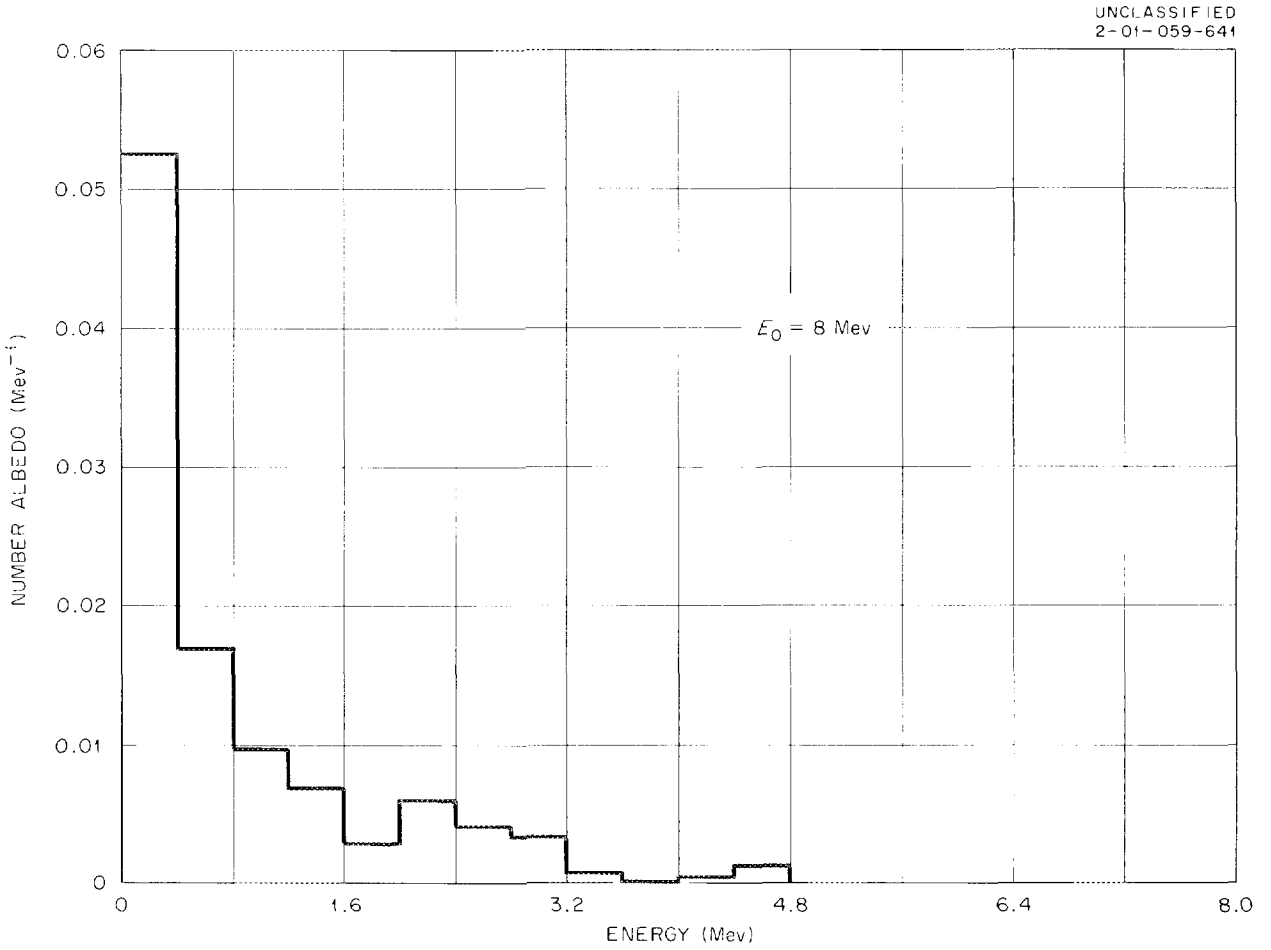

Fig. 7.3.5. Number Albedo for Water as a Function of Energy: $E_0 = 8.0$ Mev.

last of the three Berger values for each albedo are from a calculation which postulated the oxygen cross section to be isotropic in the center-of-mass system. This is equivalent to the assumptions made in the present calculation, since only the f_1 term on the Legendre expansion of the cross section is used by the O5R code and at 1 Mev $f_1 \simeq 0$ (Ref. 5) for oxygen. Thus, there is very good agreement between the calculations.

[5] E. S. Troubetzkoy, *Fast Neutron Cross Sections of Iron, Silicon, Aluminum, and Oxygen*, NDA-2113-3, Vol. C, No. VI (1959).

7.4. THE CONDITIONAL MONTE CARLO METHOD APPLIED TO NEUTRON SCATTERING IN AIR

W. E. Kinney and R. R. Coveyou

A high-energy accelerator beam, by its interaction with the machine structure, produces neutrons which can escape into the air and create a radiation hazard. Thus, neutron scattering in air, the so-called "skyshine," determines the shielding requirements for an accelerator which are consistent with the low tolerance limits specified for the general population.[1] In the past the skyshine problem for accelerators has been treated through simple one-velocity calculations for an infinite air medium;[1,2] however, this treatment is inadequate since the calculational method yields only crude estimates and the problem should be performed for two mediums (air and ground) rather than for an infinite air medium alone.

The analog Monte Carlo method, which gives exact results and can be applied to more than one medium, offers an effective way to deal with the skyshine problem. It was hoped that a variation of the method, the "conditional" Monte Carlo,[3,4] would be even better in that it would require less calculational effort for the same accuracy; however, its applicability, even to the infinite-medium problem, had not been tested. In order to test the method for the infinite-medium case, it has been used to calculate the spatial and energy collision density distributions of the neutron flux in an infinite air medium from a monoenergetic point isotropic source and the results have been compared with the well-known moments method calculations.[5] Further comparisons have been made with analog Monte Carlo and age theory calculations. These comparisons are presented below and are preceded by a brief description of the conditional method.

The conditional Monte Carlo method is supposed to prescribe a way of assigning a probability of achieving an expanded or contracted neutron path identical to the original except that each flight is multiplied by a "stretching factor." Each neutron can thereby be made to contribute to the quantity of interest at any desired distance from the source and so the variance can be reduced.

For these calculations the composition of air was taken to be 79% nitrogen and 21% oxygen with a density of 0.0012 g/cm^3, and the energy of the source was assumed to be 2 Mev. The cross sections of Lustig, Goldstein, and Kalos,[6] and Troubetzkoy[7] were used. The neutron histories were generated by the O5R code[8] stored on tape for later analysis.

---

[1] H. C. DeStaebler, Jr., *A Review of Transverse Shielding Requirements for the Stanford Two-Mile Accelerator*, M-262, Stanford University (April 1961).

[2] S. J. Lindenbaum, "Sky Shine," *Conference on Shielding of High-Energy Accelerators*, TID-7545 (Dec. 6, 1957).

[3] D. W. Drawbaugh, *Nuclear Sci. and Eng.* **9**, 185 (1961).

[4] S. K. Penny and C. D. Zerby, *Nuclear Sci. and Eng.* **10**, 75 (1961).

[5] S. S. Holland, Jr., and P. I. Richards, *J. Applied Phys.* **27**, 1042 (1956).

[6] H. Lustig, H. Goldstein, and M. Kalos, *Appl. Nuclear Phys. Ann. Prog. Rep. Sept. 1, 1957*, ORNL-2389, p. 165.

[7] E. S. Troubetzkoy, *Fast Neutron Cross Sections of Iron, Silicon, Aluminum, and Oxygen*, NDA 2111-3 (Nov. 1, 1959).

[8] R. R. Coveyou and J. G. Sullivan, *Neutron Phys. Ann. Prog. Rep., Sept. 1, 1960*, ORNL-3016, p. 193.

Three forms for the function $f_n(\rho)$, which appears in the weighting factor for the conditional method,[4] were tried:

$$f_n(\rho) = \frac{4\pi\rho^2}{(4\pi\tau_n)^{3/2}} e^{-(\rho^2/4\tau_n)} , \tag{1}$$

the collision age form, where $\tau_n = \frac{1}{6}\langle r^2 \rangle$ for nth collision neutrons;

$$f_n(\rho) = \frac{4\pi\rho^2}{(4\pi\tau_g)^{3/2}} e^{-(\rho^2/4\tau_g)} , \tag{2}$$

the group age form, where $\tau_g = \frac{1}{6}\langle r^2 \rangle$ for neutrons in the gth energy group of the group structure listed in Table 7.4.1; and

$$f_n(\rho) = \frac{1}{\lambda_g} e^{-(\rho/\lambda_g)} ,$$

the exponential form, where $\lambda_g = \langle r \rangle$ for neutrons in the gth energy group.

Table 7.4.1. The Energy Group Structure

Group	Lower Energy (ev)	Upper Energy (ev)
1	1×10^6	2×10^6
2	8×10^5	1×10^6
3	6×10^5	8×10^5
4	4×10^5	6×10^5
5	2×10^5	4×10^5
6	1×10^5	2×10^5
7	5×10^4	1×10^5
8	2×10^4	5×10^4
9	1×10^4	2×10^4
10	5×10^3	1×10^4
11	2×10^3	5×10^3
12	1×10^3	2×10^3
13	5×10^2	1×10^3
14	2×10^2	5×10^2
15	1×10^2	2×10^2
16	5×10^1	1×10^2
17	20	50
18	10	20
19	5	10
20	2	5
21	1	2

Collision densities computed by the use of these three forms are presented as a function of radius for the energy groups 1–2 Mev and 2–5 ev in Fig. 7.4.1. There is no significant difference in the results at high energy and they agree with analog results. The results from the collision and group age forms remain in mutual agreement at all energies; however, at low energy the exponential form leads to results quite different from the other two forms and none agrees with analog results.

Collision densities computed by the conditional Monte Carlo, the analog Monte Carlo, the age theory, and the moments methods are compared in Figs. 7.4.2 through 7.4.6 for several energies. The analog Monte Carlo method used 1000 neutrons, while the conditional Monte Carlo method analyzed 500 neutron histories. There is good agreement between the two methods down to 0.6 Mev. In the energy group from

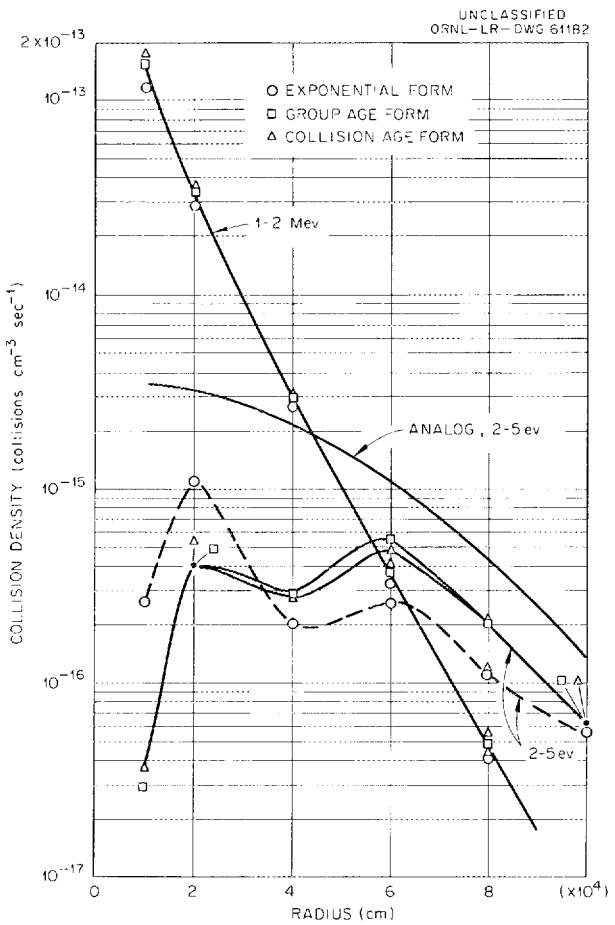

Fig. 7.4.1. Collision Density as a Function of Radius: Comparison of Results from Three Forms of $f_n(\rho)$.

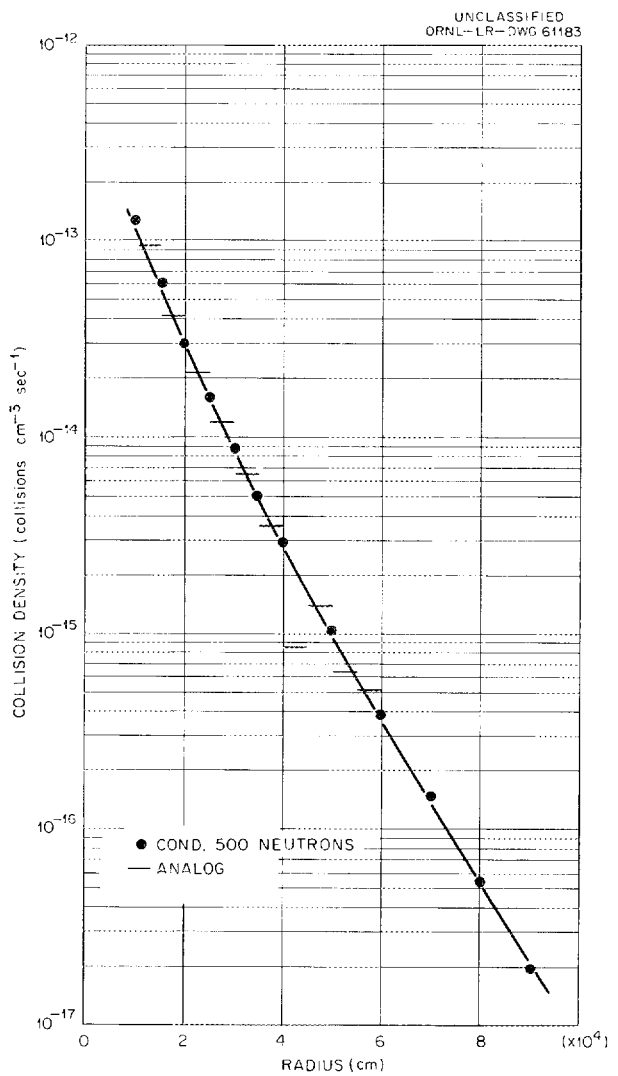

Fig. 7.4.2. Collision Density as a Function of Radius: Comparison of Various Calculational Methods for Energy Range 1–2 Mev.

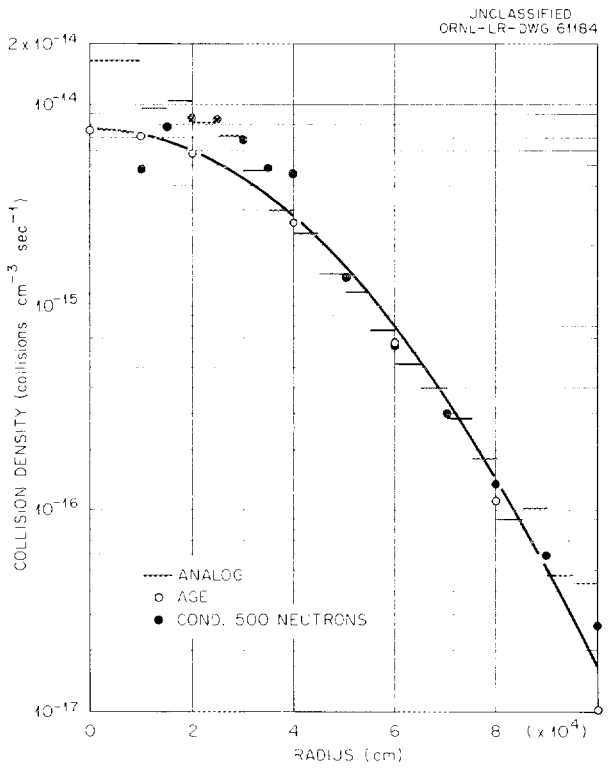

Fig. 7.4.3. Collision Density as a Function of Radius: Comparison of Various Calculational Methods for Energy Range 0.4–0.6 Mev.

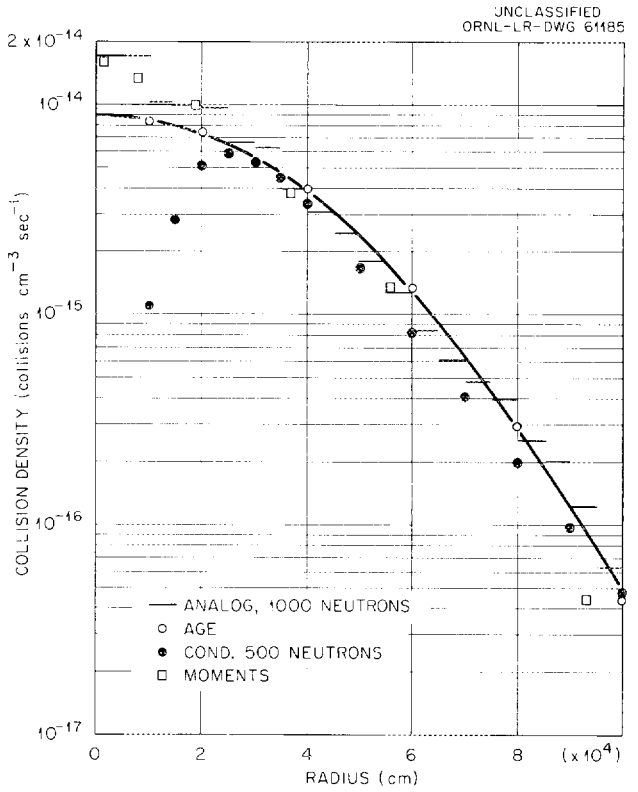

Fig. 7.4.4. Collision Density as a Function of Radius: Comparison of Various Calculational Methods for Energy Range 0.1–0.2 Mev.

0.4 to 0.6 Mev the conditional Monte Carlo results begin to fall below the analog results near the origin, but they are still good from 1 to 8 source mean free paths (1.2×10^4 cm). The conditional results deviate more and more widely from the analog results as the energy is lowered, until in the group from 0.01 to 0.02 Mev there is disagreement everywhere and the conditional Monte Carlo curve becomes somewhat erratic near the origin. The plot of the conditional results becomes even more erratic in the group from 2 to 5 ev. It appears that the volume term, $(r/\rho_n)^{n-1}$, from Eq. 5 of Ref. 4, outweighs the path shrinkage term,

$$\exp - \left\{ \left| 1 - (r/\rho_n) \right| \sum_{i=1}^{n} |Y_i| \, \mu_i \right\},$$

as the paths are shrunk to a point near the origin, but a real understanding of the failure of the conditional method for the high orders of collision has not yet developed.

The age theory results are in reasonable agreement with analog results around 0.4 Mev, which represents approximately 12 collisions. The constants used in each group were obtained from Ratrace,[9] an

[9] D. J. McGoff *et al.*, *Ratrace, A Monte Carlo Code for Characterizing the Slowing Down of Neutrons in an Infinite Homogeneous Medium*, Memorandum EPS-S-389, MIT Engineering Practice School (Nov. 13, 1958).

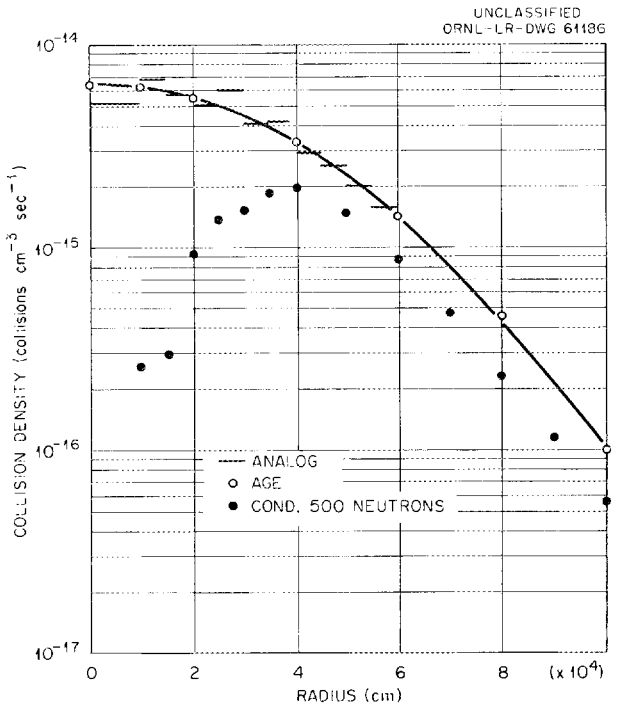

Fig. 7.4.5. Collision Density as a Function of Radius: Comparison of Various Calculational Methods for Energy Range 0.01–0.02 Mev.

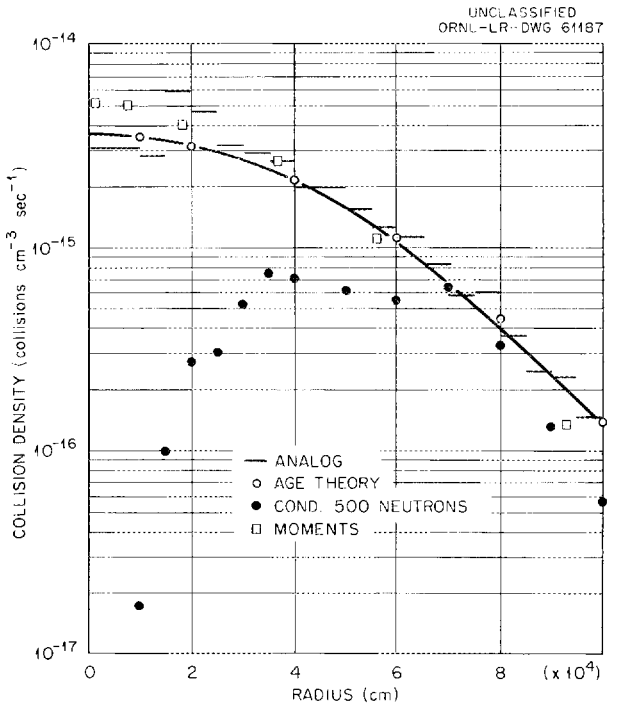

Fig. 7.4.6. Collision Density as a Function of Radius: Comparison of Various Calculational Methods for Energy Range 2–5 ev.

infinite-medium Monte Carlo age code. The analog results are in good agreement with moments method results, except at 10^5 cm, where a factor of 2 is the error in the latter method.[5] It is encouraging to note that the analog results appear to be good out to 8 source mean free paths.

From the above results it appears that the conditional Monte Carlo method has limited applicability to the problem of neutrons diffusing in an infinite medium of air because of its failure as the order of collisions becomes large. The analog Monte Carlo method gives satisfactory collision densities in infinite air out to at least 8 source mean free paths. Age theory becomes valid after about 12 collisions.

7.5. MOMENTS METHOD AND NIOBE CALCULATIONS OF NEUTRON PENETRATION IN Be, BeO, LiH, AND OTHER MATERIALS

H. Goldstein
Nuclear Development Corporation of America

A study of neutron penetration in various reactor and shield materials has been carried out by Nuclear Development Corporation of America on subcontract with the Laboratory. The program consisted of extensive Renupak (moments method) and Niobe Code calculations for Be, BeO, and LiH and some additional

calculations for D_2O, Fe, H_2O, and C. In addition, a few computations were carried out for specific shield configurations.

The Renupak calculations were performed both for a fission source and monoenergetic sources and included variations in the cross sections and the width of the integration interval in lethargy. A catalog of the Renupak problems is given in Table 7.5.1. The Niobe calculations, listed in Table 7.5.2, were all performed for a fission source and spherical geometry.

Although the analyses are incomplete, it is expected that the data on Be and BeO will provide a definitive picture of the neutron penetration in these materials. The Renupak calculations included studies of the effects of changes in the total cross sections, angular distribution of elastic scattering, $(n,2n)$ cross sections, and the spectrum of neutrons emerging from the $(n,2n)$ reaction. Further, enough problems were computed for monoenergetic sources, with the integration interval in lethargy varied from 0.05 to 0.2, to allow any fast-neutron spectrum to be simulated. (A number of the Renupak calculations were repeated when new Be cross-section data became available.) The Niobe calculations for Be included studies of the effects of boundaries, and the angular distributions of the neutron flux were observed. Also, complete simulations were made of the geometry used for measuring removal cross sections.

The Be calculations will yield information on ages, fast effects, flux spectra, and neutron dose. Preliminary results[1] for the indium resonance age of neutrons from a fission source in Be is 69 cm^2, which is definitely in disagreement with the experimental value of 80 ± 2 cm^2 obtained by Nobles and Wallace.[2] The calculated age for BeO is 89 cm^2, in resonable agreement with the experimental value of 93.5 ± 5 cm^2 obtained by Goodjohn and Young.[3]

Lithium hydride also received extensive treatment, particularly with respect to the exit spectra from finite slabs, which is of interest for comparison with current experimental data (see Secs. 7.1 and 7.2). Although the Renupak calculations for this material considered both fission and monoenergetic sources, studies of the sensitivity to changes in the cross sections were not made.

Less extensive investigations were carried out for D_2O, Fe, H_2O, and C. Renupak calculations were performed for D_2O (fission source) by using the best data available and treating the $(n,2n)$ reaction as pure absorption; boundary and geometry effects were studied in two Niobe problems with both sphere and shell configurations. Calculations for iron were made by Renupak for a fission source and by Niobe with several shell thicknesses followed by H_2O to simulate removal cross-section geometry.

The H_2O studies consisted of one Renupak and two Niobe calculations. In the Renupak calculation the angular distributions were assumed to be as close to isotropic as the extremes of existing experimental data will permit, the purpose being to observe the sensitivity of the dose curve to such changes in the angular distribution. The large uncertainties in the angular distributions above 3 Mev precluded any systematic study of H_2O, however, and not until these uncertainties are resolved can definitive calculations

[1] H. Goldstein and A. D. Krumbein, *Trans. Am. Nuclear Soc.* 4 (1), 131 (1961).

[2] R. Nobles and J. Wallace, *The Diffusion Length and Age in Beryllium*, ANL-4076 (1947).

[3] A. J. Goodjohn and J. C. Young, *Trans. Am. Nuclear Soc.* 3(2), 488 (1960).

Table 7.5.1. Catalog of NDA Renupak Moments Method Calculations of Neutron Penetration in Various Materials

Material	Source	Lethargy Interval	Number of Intervals	Problem No.	Comments
Be	Fission	0.1	200	1	
	Fission	0.1	200	2	$(n,2n)$ replaced by elastic scattering
	Fission	0.1	200	3	Reduced $(n,2n)$
	Fission	0.1	200	4	Isotropic elastic scattering
	8.096 Mev	0.1	192	5	
	5.427 Mev	0.1	189	11	
	4.020 Mev	0.1	185	6	
	2.978 Mev	0.1	183	12	
	2.695 Mev	0.1	181	7	
	2.438 Mev	0.1	181	13	
	1.996 Mev	0.1	178	8	
	1.634 Mev	0.1	177	14	
	1.338 Mev	0.1	175	15	
	991.4 kev	0.1	171	9	
	544.0 kev	0.1	166	16	
	Fission	0.2	100	17	
	Fission	0.1	200	18	$(n,2n)$ treated as absorption
	Fission	0.1	200	19	Reduced anisotropy of elastic scattering
	Fission	0.1	100	22a	Changed σ_T (new Be data), incorrect response functions
	Fission	0.1	200	22b	Same as Prob. 22a but correct response functions
	Fission	0.1	200	22c	σ_T nearly new Be data; incorrect σ_{2n}
	Fission	0.05	200	30	New Be data; terminates at 818 ev
	8.096 Mev	0.1	192	31	New Be data
	8.096 Mev	0.1	192	36	New Be data; $(n,2n)$ treated as absorption
	5.427 Mev	0.1	188	32	New Be data
	3.291 Mev	0.1	183	33	New Be data
	2.695 Mev	0.1	181	34	New Be data
	1.996 Mev	0.1	178	35	New Be data
BeO	Fission	0.1	200	10	
	Fission	0.05	200	40	New Be data; terminates at 818 ev
	10.93 Mev	0.1	195	41	New Be data
	2.206 Mev	0.1	179	45	New Be data
	1.479 Mev	0.1	175	46	New Be data
H_2O	Fission	0.1	200	20	Nonstandard (reduced) anisotropy of elastic scattering
D_2O	Fission	0.1	200	21	
	Fission	0.1	200	58	$(n,2n)$ treated as absorption
$D_2O + U^{238}$	999.1 ev	0.02	400	37	Absorption of 66- and 36-ev U^{238} resonances added in proportion; five U^{238} nuclei to one D nucleus

Table 7.5.1 (continued)

Material	Source	Lethargy Interval	Number of Intervals	Problem No.	Comments
$D_2O + U^{238}$	999.1 ev	0.02	400	38	Same as Prob. 37 except one U^{238} nucleus to one D nucleus
	999.1 ev	0.02	400	39	Same as Prob. 37 except one U^{238} nucleus to five D nuclei
Fe	Fission	0.1	100	57	Terminates at 818 ev
LiH	12.08 Mev	0.1	196	24	
	8.096	0.1	192	25	
	5.997	0.1	189	26	
	4.020	0.1	185	27a	Partly incorrect flux reconstitution
	4.020	0.1	185	27b	Same as Prob. 27a except improved flux reconstitution
	2.970 Mev	0.1	182	28	
	1.996 Mev	0.1	178	29	
Swedish Ferroconcrete	Fission	0.1	200	23	

be attempted. The two Niobe calculations were performed primarily so that removal cross sections could be deduced from the beryllium and iron problems; however, other valuable information will also be gained.

The lone Niobe graphite problem was designed to simulate an experiment performed at Fontenay-aux-Roses, in which the exit spectrum in the forward direction through 100 cm of graphite was measured. The spectrum so obtained shows a pronounced dip at about 5 Mev, and the calculations reproduced this behavior in even more striking fashion.

Niobe Problem Nos. XIII, XV, and XVI and Renupak Problem No. 23 represent attempts to calculate the neutron penetration in the Swedish Reactor R-3 Shield and the Windscale Reactor Shield Mockup for comparison with penetration calculations by fast removal and multigroup age-diffusion techniques used in England and Sweden. Unfortunately, the Niobe problems fell short of the accuracy and credibility needed, but it appears that the difficulty can be corrected. The Renupak problem was performed primarily to check out the cross sections used for the concrete in the Swedish Reactor R-3 Shield. Of note was the fact that the calculations did reproduce a "kink" in the dose curve that was observed experimentally.

Renupak Problem Nos. 37–39 were undertaken to investigate a phenomenon observed by P. E. Egelstaff[4] on the D_2O-moderated research reactor at Harwell. With a fast chopper he found that the spectrum near 4 and 7 ev shows definite dips. These are about $\frac{1}{9}$th the energy of two prominent U^{238} resonances, and it was suggested that the dips might be discontinuities in the Placzek functions arising from the "negative" sources caused by the high absorption occurring at the 36- and 66-ev resonances. The calculations were therefore performed in an idealized situation which followed the slowing down of neutrons

[4] P. E. Egelstaff, private communication to H. Goldstein.

Table 7.5.2. Catalog of NDA Niobe Calculations of Neutron Penetration in Various Materials (Spherical Geometry, Fission Source)

Material	Configuration* (from $r = 0$)	Lethargy Interval	Number of Intervals	Cutoff Energy	Number of Angles	Problem No.
Be	2 cm Source + 38 cm Be	0.2	90	0.27 ev	16	I
	2 cm Source + 38 cm Be + 60 cm H_2O	0.2	90	0.27 ev	16	II
	2 cm Source + 20 cm Be	0.2	90	0.27 ev	16	XII
	2 cm Source + 80 cm Be	0.2	45	2.22 kev	16	XI
	15 cm Source + 85 cm Vacuum + 40 cm Be	0.2	90	0.27 ev	16	X
LiH	15 cm Source + 85 cm Vacuum + 10 cm LiH	0.25	80	0.037 ev	16	IV
	15 cm Source + 85 cm Vacuum + 20 cm LiH	0.25	80	0.037 ev	16	III
	15 cm Source + 85 cm Vacuum + 45 cm LiH	0.10	51	109.85 kev	16	V
	15 cm Source + 85 cm Vacuum + 65 cm LiH	0.10	51	109.85 kev	16	VI
	15 cm Source + 85 cm Vacuum + 85 cm LiH	0.10	51	109.85 kev	16	VII
	15 cm Source + 85 cm Vacuum + 105 cm LiH	0.10	51	109.85 kev	16	VIII
	1 cm Source + 84 cm LiH	0.25	80	0.037 ev	16	IX
C	60 cm Source + 340 cm Vacuum + 100 cm C	0.10	80	235 ev	16	XIV
Fe	15 cm Source + 85 cm Vacuum + 12 cm Fe	0.10	90	2.22 kev	16	XXI
	15 cm Source + 85 cm Vacuum + 24 cm Fe	0.10	90	2.22 kev	16	XVII
	15 cm Source + 85 cm Vacuum + 24 cm Fe + 80 cm H_2O	0.10	90	2.22 kev	16	XVIII
H_2O	5 cm Source + 120 cm H_2O	0.20	80	2.02 ev	16	XIX
	15 cm Source + 85 cm Vacuum + 120 cm H_2O	0.20	80	2.02 ev	16	XX
D_2O	4 cm Source + 120 cm D_2O	0.25	80	0.037 ev	16	XXII
	45 cm Source + 255 cm Vacuum + 60 cm D_2O	0.25	80	0.037 ev	16	XXIII
Swedish Reactor R-3 Shield	190 cm D_2O-U^{238} + 30 cm D_2O + 22 cm Fe + 200 cm Ferroconcrete	0.25	24	57.3 kev	8	XIII
Windscale Reactor Shield	100 cm C-U^{238} + 76 cm C + 20.32 cm Fe + 213.68 cm Concrete	0.25	24	57.3 kev	8	XV
	100 cm C-U^{238} + 76 cm C + 20.32 cm Fe + 173.68 cm Concrete	0.25	70	0.452 ev	8	XVI

*Except for Problems XIII, XV, and XVI, the source region is considered to be a vacuum.

in D_2O from a monoenergetic source at 999 ev, using lethargy integration intervals only 0.02 wide. Absorption cross sections were added at 66 ev and 36 ev to the extent that the integral over E corresponded to a fixed percentage of the two U^{238} resonances. The results were completely negative. The Placzek function oscillations from the main source were beautifully portrayed, as was the absorption in the resonances themselves and the changes in the resonance absorption probability. But there were no dips at the energies where they were observed experimentally. On the basis of this calculation, it appears that Egelstaff's observations do not reflect any intrinsic phenomenon but arise from some absorber in his setup.

The calculations performed thus far indicate that the two codes have sufficiently high reliabilities for their application as production programs. Further, final analyses of the data already obtained should resolve a number of heretofore unanswered questions. The results will be prepared as a series of papers which will be submitted to Nuclear Science and Engineering.

7.6. A RECALCULATION OF THE GAMMA-RAY ENERGY SPECTRUM OF THE BULK SHIELDING REACTOR I

G. T. Chapman

The gamma-ray energy spectrum of the Bulk Shielding Reactor I (BSR-I) was experimentally determined in 1953,[1,2] and at least two attempts to theoretically calculate this spectrum have since been made.[3,4] However, although the calculations showed close agreement with each other, the results of both gave a flux which was lower than the measured flux by as much as a factor of three. The magnitude and particularly the direction of the differences were surprising, since the assumptions made for the calculations should have tended to give an overestimate of the flux, especially at lower energies. Although the existence of difficult-to-evaluate experimental errors was recognized, their probable magnitudes did not seem to be sufficient to account for the discrepancy.

Since the performance of the previous calculations, a detailed compilation of capture gamma-ray spectra has become available,[5] and a more complete energy spectrum of prompt-fission gamma rays has been obtained.[6] A new calculation of the BSR-I spectrum has therefore been made, utilizing the most recent information. The result, however, has served only to confirm the results of previous calculations, leaving the disagreement with experiment still unresolved.

---

[1] F. C. Maienschein and T. A. Love, *Spectrum of Gamma Rays Emitted by the Bulk Shielding Reactor*, ORNL-CF-53-10-16 (Oct. 31, 1953).

[2] F. C. Maienschein and T. A. Love, *Nucleonics* 12 (5), 6 (1954).

[3] G. deSaussure, *A Calculation of the Gamma-Ray Spectrum of the Bulk Shielding Reactor*, ORNL-CF-57-7-105 (July 31, 1957).

[4] L. A. Bowman *et al.*, *A Calculation of the Energy Spectrum and Angular Distribution of Gamma Rays at the Surface of the BSR Reactor*, ORNL-CF-58-4-75 (April 15, 1958).

[5] E. Troubetzkoy and H. Goldstein, *A Compilation of Information on Gamma-Ray Spectra Resulting from Thermal-Neutron Capture*, ORNL-2904 (May 17, 1960).

[6] F. C. Maienschein, private communication.

The present calculation follows the method of deSaussure[3] exactly, with the exception of some of the primary gamma-ray source terms. Consequently, only a brief discussion of the method will be presented here.

The assumption is made that the flux at the surface of the reactor is composed of both an uncollided and a Compton-scattered component. The former may be calculated without difficulty, provided the primary gamma-ray sources are known. To facilitate calculating the Compton-scattered component, the gamma rays are assumed to scatter only once in the reactor core, subsequently proceeding to the reactor surface without further attenuation. It is also assumed that the energy distribution of the scattered gamma rays is given by the appropriate Klein-Nishina formula, although the direction of the photon is assumed unchanged by the scattering event.

The energy spectra of the primary gamma-ray sources used for this work are tabulated in Table 7.6.1 and are plotted in Fig. 7.6.1. The distributions for the number of prompt-fission gamma rays [$\nu^f_{25}(\bar{E})$ photons per fission] and the fission-product gamma rays [$\nu^p_{25}(\bar{E})$ photons per fission] were obtained by converting the measured[6,7] energy spectra of these gamma rays into histogram form. The uranium capture gamma-ray spectrum [$\nu^c_{25}(\bar{E})$ photons per fission] was estimated by assuming that these photons are distributed in energy the same as the prompt-fission gamma rays. Consequently, the assumption is made that

$$\nu^c_{25}(\bar{E}) = \frac{\sigma_c}{\sigma_f} \cdot \frac{6.43}{7.45} \nu^f_{25}(\bar{E}) \text{ photons per fission,} \tag{1}$$

[7]R. W. Peelle, W. Zobel, and T. A. Love, *Appl. Nuclear Phys. Ann. Prog. Rep., Sept. 10, 1956*, ORNL-2081, p. 94.

Table 7.6.1. Photon Yield, per Energy Interval, from Primary Gamma-Ray Sources

Energy Limits and Average Energy (Mev)			Photon Yield (photons/fission)					
E_{ak}	E_{bk}	$\bar{E}$	Prompt Fission	Fission Products	U^{235} Capture	Aluminum Capture	Hydrogen Capture	Total
0	1.0	0.5	8.12	4.68	1.29	0.020		14.11
1.0	2.0	1.5	1.69	1.21	0.27	0.124*		3.29
2.0	3.0	2.5	0.47	0.44	0.075	0.028	0.213	1.23
3.0	4.0	3.5	0.16	0.17	0.026	0.022		0.377
4.0	5.0	4.5	0.065	0.047	0.010	0.019		0.141
5.0	6.0	5.5	0.021	0.007	0.003	0.009		0.040
6.0	7.0	6.5	0.007		0.001	0.005		0.013
7.0	8.0	7.5				0.022		0.022

*Includes the Al^{28} beta-decay line.

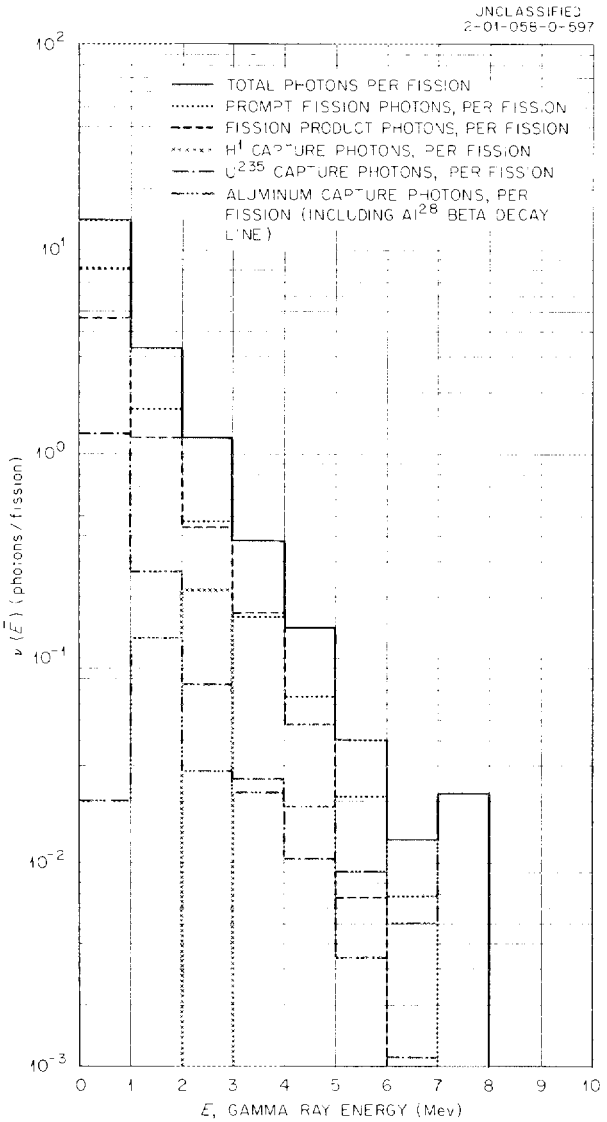

Fig. 7.6.1. Calculated Energy Spectrum of the Primary Gamma-Ray Sources.

where

6.43 = the total photon energy, in Mev, released per U^{235} capture,

7.45 = the total energy, in Mev, released per fission,

σ_c = the cross section for thermal-neutron capture in U^{235} (cm^2),

σ_f = the cross section for thermal-neutron fission in U^{235} (cm^2),

$\nu^f_{25}(\bar{E})$ = the number of prompt-fission photons, per fission, with average energy $\bar{E}$ Mev.

The capture gamma-ray spectra for aluminum and hydrogen were taken from the compilations of Troubetzkoy and Goldstein.[5] The number of photons per fission was calculated by multiplying the number of photons

per neutron capture by the ratio of the macroscopic capture cross section (Σ_a, cm^{-1}) of the aluminum or hydrogen in the core to the macroscopic fission cross section (Σ_f, cm^{-1}) in the core. Thus,

$$\nu_i^c(\bar{E}) = \frac{\Sigma_a^i}{\Sigma_f}\left[\frac{1}{100\bar{E}}\sum_{E_a \leq E' \leq E_b} \lambda(E')\,E'\right] \text{ photons/fission,} \tag{2}$$

where

$\lambda(E')$ = the number of photons with energy E', in Mev, per 100 captures,

E_a, E_b = limiting energies, in Mev, of the energy groups.

Among other sources which may contribute to the total gamma-ray flux are: (1) inelastic scattering of fast neutrons; (2) annihilation radiation; and (3) the decay of radioactive materials other than Al^{28}. However, the contribution of these sources is of little importance at the higher energies where the calculation is expected to give the most accurate results.

The uncollided flux was calculated, as discussed by deSaussure,[3] by using the equation,

$$\Gamma^0(\bar{E}) = K \cdot \nu(\bar{E}) \cdot f(\bar{E}) , \tag{3}$$

where

$\Gamma^0(\bar{E})$ = uncollided flux at the surface of the reactor, in the direction normal to the surface in $cm^{-2} \cdot steradian^{-1} \cdot Mev^{-1} \cdot watt^{-1} \cdot sec^{-1}$,

$$K = (2.7 \times 10^5 \text{ fissions} \cdot \text{sec}^{-1} \cdot \text{watt}^{-1} \cdot \text{cm}^{-3}) \times \frac{L}{4\pi\Delta E}\,\frac{\text{fissions}}{\text{watt} \cdot \text{sec} \cdot \text{cm}^2 \cdot \text{steradian} \cdot \text{Mev}} ,$$

L = length of the reactor core on the center line

= 45 cm,

ΔE = width of the energy group

= 1 Mev,

$\nu(\bar{E})$ = number of photons per fission of energy $\bar{E}$, Mev,

$$f(\bar{E}) = \frac{1 - e^{-\mu(\bar{E})L}}{\mu(\bar{E})L}$$

= dimensionless function describing the attenuation of the radiation in the core,

$$\mu(\bar{E}) = 0.41\mu_{Al}(\bar{E}) + 0.59\mu_{H_2O}(\bar{E})$$

= effective linear absorption coefficient in the core. (The metal-to-water ratio in the BSR is 0.7, and the attenuation by the uranium is neglected.)

On the basis of the assumptions made to govern the scattered flux, only those gamma rays arising from Compton scattering of primary photons originally moving in the direction of the detector were considered. Thus, the total number of photons fulfilling this requirement is obtained by setting $f(\bar{E}) = 1$ in Eq. 3. This number subtracted from the actual uncollided flux is the number of photons that were originally moving in

the required direction but were removed by some interaction in the core material. The portion that was Compton scattered is

$$K\nu(\bar{E})\,[1 - f(\bar{E})]\frac{\mu_c(\bar{E})}{\mu(\bar{E})},$$

where $\mu_c(\bar{E})$ is the linear absorption coefficient for Compton scattering alone.

The probability that a primary photon of energy $\bar{E}_i$ will be scattered into the kth energy group is given by

$$\alpha_{ik} = \frac{1}{\sigma_T(\bar{E}_i)} \int_{E_{ak}}^{E_{bk}} \frac{d\sigma_T(\bar{E}_i)}{dE'}\, dE', \tag{4}$$

where

$\sigma_T(\bar{E}_i)$ = total Compton cross section,

$d\sigma_T/dE'$ = energy distribution of the scattered photons.

Equation 4 was evaluated by taking the values of $\sigma_T(\bar{E}_i)$ from Nelms.[8] The integral is now readily evaluated by expressing the differential cross section in terms of the Compton wave length ($\lambda = mc^2/h\nu$). Thus

$$\alpha_{ik} = \frac{\sigma_0}{\sigma_c} \int_{\lambda_{bk}}^{\lambda_{ak}} f(\lambda_i, \lambda)\, d\lambda, \tag{5}$$

where[9]

$$f(\lambda_i, \lambda) = \frac{3}{8}\left(\frac{\lambda_i}{\lambda}\right)^2 \left[\frac{\lambda_i}{\lambda} + \frac{\lambda}{\lambda_i} - 2(\lambda - \lambda_i) + (\lambda - \lambda_i)^2\right]$$

and σ_0 is the classical Thomson cross section. Thus, the desired probability is

$$\alpha_{ik} = \frac{3}{8}\frac{\sigma_0}{\sigma_T(\bar{E}_i)}\lambda_i^2 \left[\frac{\lambda_i}{2}\left(\frac{1}{\lambda_{bk}^2} - \frac{1}{\lambda_{ak}^2}\right) + \left(\frac{1}{\lambda_i} - 2\lambda_i - 2\right)\ln\frac{\lambda_{ak}}{\lambda_{bk}} - (2\lambda_i + \lambda_i^2)\left(\frac{1}{\lambda_{ak}} - \frac{1}{\lambda_{bk}}\right) + (\lambda_{ak} - \lambda_{bk})\right]. \tag{6}$$

The values of α_{ik} are given for 1-Mev-wide energy groups over a range of 0.5–9.5 Mev in Table 7.6.2. Thus, using the values of Table 7.6.2, the total Compton-scattered flux is obtained by

$$\Gamma^0(\bar{E}) = K\nu(\bar{E})\,[1 - f(\bar{E})]\frac{\mu_c(\bar{E})}{\mu(\bar{E})}\alpha_{ik}. \tag{7}$$

[8] Ann T. Nelms, *Graphs of the Compton Energy-Angle Relationship and the Klein-Nishina Formula from 10 kev to 500 Mev*, NBS Circular 542 (Aug. 28, 1953).

[9] *Ibid*, p. 35.

The results of the present calculation, corrected for the shape of the neutron flux throughout the reactor by the prescription of deSaussure,[3] are shown in Table 7.6.3. A comparison of all calculations with experiment is made in Fig. 7.6.2. Agreement is good among the calculations, but all three give a flux much lower than the experimental flux. The results of the present calculation more accurately approach the shape of the experimental spectrum. The disparity in magnitude, however, has not been effectively decreased or explained by the present work. It may be resolved in possible future experiments.

Table 7.6.2. Probability of Compton Scattering from Initial Energy Group E_i* into Final Energy Group E_k*

Initial Photon Energy, E_i (Mev)	Compton Scattering Probability									
	$E_k = 0.5$ Mev	$E_k = 1.5$ Mev	$E_k = 2.5$ Mev	$E_k = 3.5$ Mev	$E_k = 4.5$ Mev	$E_k = 5.5$ Mev	$E_k = 6.5$ Mev	$E_k = 7.5$ Mev	$E_k = 8.5$ Mev	$E_k = 9.5$ Mev
0.5	1.000									
1.5	0.684	0.316								
2.5	0.611	0.202	0.187							
3.5	0.571	0.172	0.130	0.127						
4.5	0.544	0.159	0.108	0.095	0.094					
5.5	0.524	0.152	0.096	0.080	0.075	0.074				
6.5	0.508	0.147	0.089	0.071	0.064	0.061	0.060			
7.5	0.495	0.143	0.085	0.065	0.057	0.053	0.051	0.050		
8.5	0.484	0.140	0.082	0.062	0.052	0.047	0.045	0.044	0.0437	
9.5	0.475	0.138	0.079	0.059	0.049	0.044	0.041	0.039	0.0384	0.0383

*Energy values represent the midpoint of a 1-Mev-wide group.

Table 7.6.3. Calculated Gamma-Ray Spectrum of the BSR-I

Energy Limits and Average Energy (Mev)			Gamma-Ray Flux* (photons • sec^{-1} • cm^{-2} • Mev^{-1} • watt^{-1} • steradian^{-1})		
E_{ak}	E_{bk}	$\bar{E}$	Uncollided	Compton-Scattered	Total
0	1.0	0.5	3.09×10^6	2.13×10^7	2.44×10^7
1.0	2.0	1.5	1.19×10^6	1.49×10^6	2.68×10^6
2.0	3.0	2.5	5.63×10^5	2.89×10^5	8.52×10^5
3.0	4.0	3.5	1.97×10^5	5.58×10^4	2.54×10^5
4.0	5.0	4.5	7.23×10^4	1.30×10^4	8.53×10^4
5.0	6.0	5.5	2.46×10^4	3.84×10^3	2.84×10^4
6.0	7.0	6.5	8.37×10^3	1.33×10^3	9.71×10^3
7.0	8.0	7.5	1.47×10^4	7.41×10^2	1.55×10^4

*A correction for the thermal-neutron flux shape in the reactor has been applied.

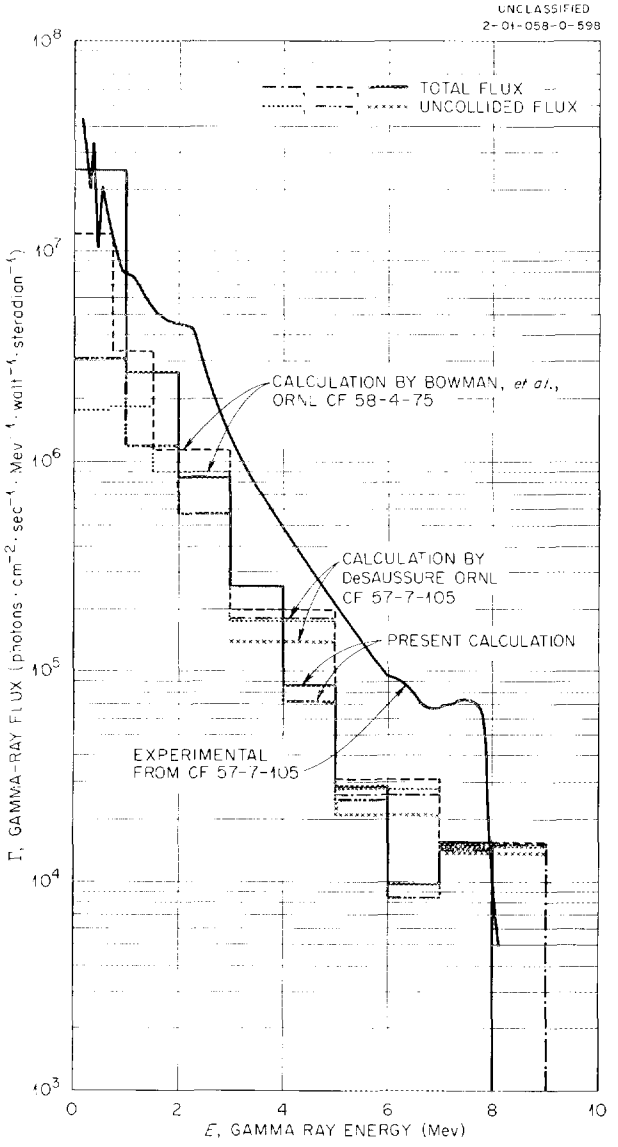

Fig. 7.6.2. Comparison of Calculated and Experimental Gamma-Ray Spectra from the Surface of the BSR-I.

7.7. EXPERIMENTAL VERIFICATION OF A GEOMETRICAL SHIELDING TRANSFORMATION

L. Jung, F. J. Muckenthaler, J. M. Miller, and J. K. Grant[1]

The "point kernel" concept of shielding theory is widely used. By definition, the kernel represents the response of a nondirectional detector, recording biological dose, to a unit point source of radiation at a given distance R. The specifications attached to the use of the kernel require an isotropically emitting source located in a homogeneous, isotropic, attenuating medium.[2]

[1]On loan from Lockheed Aircraft Corp., Marietta, Georgia.

[2]E. P. Blizard, *Introduction to Shield Design, Part I, Revised,* ORNL-CF-51-10-70 (Jan. 30, 1952).

Much of the data used in shielding calculations, however, derived from experiments at the Lid Tank Shielding Facility, where neither the source nor the shielding medium conform to all of the exacting conditions prescribed for the point kernel. It is thus of value to determine to what degree the theoretical calculations agree with results of experiment. The proposition under test in the present experiment states that the dose rate due to a large disk source can be determined from measurements using a smaller source disk, the two being related by the point kernel concept. Experimental data has been obtained from several sizes of source plates, and is now being analyzed. Preliminary checks indicate good agreement between calculation and experiment.

Theory

Figure 7.7.1 shows the source-detector geometry pertinent to the present discussion. Let $G(R)$ represent the response of an isotropic detector located a distance R from a unit point-isotropic source situated in an infinite, homogeneous medium. The function $G(R)$ then is the attenuation kernel, and the dose rate at R from a disk source of unit strength S and the radius A is obtained by integration over the disk:

$$D(R) = 2\pi S \int_0^A G(R)\rho \, d\rho \, . \tag{1}$$

Since, from the figure, $R^2 = \rho^2 + z^2$, and $R\, dR = \rho\, d\rho$ for constant z, Eq. 1 can be rewritten as

$$D(R) = 2\pi S \int_z^{\sqrt{z^2+A^2}} G(R)\, R\, dR \, . \tag{2}$$

By letting

$$D(R) = D(z, A) \, , \tag{3}$$

where $D(z, A)$ is defined as the dose rate at a distance z along the axis of a disk of radius A, and setting $A = \sqrt{m}\, a$, where a is the radius of a smaller disk source and m is an integer, Eq. 2 becomes

$$D(z, \sqrt{m}\, a) = 2\pi S \int_z^{\sqrt{z^2+ma^2}} G(R)\, R\, dR \tag{4}$$

or

$$D(z, A) = 2\pi S \left[\int_z^{\sqrt{z^2+a^2}} G(R)\, R\, dR + \int_{\sqrt{z^2+a^2}}^{\sqrt{z^2+2a^2}} G(R) R\, dR + \ldots + \int_{\sqrt{z^2+(m-1)a^2}}^{\sqrt{z^2+ma^2}} G(R) R\, dR \right] . \tag{5}$$

By rewriting the second integral of Eq. 4 as

$$\int_{\sqrt{z^2+a^2}}^{\sqrt{z^2+2a^2}} G(R) R\, dR = \int_{\sqrt{z^2+a^2}}^{\sqrt{(z^2+a^2)+a^2}} G(R) R\, dR \tag{6}$$

UNCLASSIFIED
DWG 17071 R1

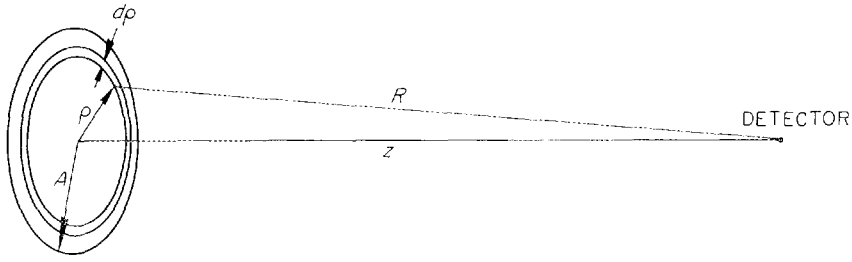

Fig. 7.7.1. Geometry for Disk Source and Homogeneous Shield.

and recalling the definition accompanying Eq. 3, it becomes clear that

$$2\pi S \int_{\sqrt{z^2+a^2}}^{\sqrt{z^2+2a^2}} G(R)\,R\,dR = D(\sqrt{z^2+a^2}\,,a)\,. \tag{7}$$

Equation 5 can then be written in the notation

$$D(z\,,A) = D(z\,,a) + D(\sqrt{z^2+a^2}\,,a) + D(\sqrt{z^2+2a^2}\,,a) + \ldots + D(\sqrt{z^2+(n-1)a^2}\,,a)\,, \tag{8}$$

or

$$D(z\,,A) = \sum_{n=1}^{m} \left[D\left(\sqrt{z^2+\frac{(n-1)a^2}{n}}\,,\ \frac{a}{\sqrt{m}}\right)\right], \tag{9}$$

where m and n are integers.

In this fashion the dose rates along the axis of a disk source can be calculated from axial dose-rate measurements from a smaller disk source.

Experimental Procedure

The values of the integer m used in this experiment were chosen as 16, 9, 4, and 2, which, from the relation $A = \sqrt{m}\,a$, where A is the diameter of the LTSF source plate and is equal to 28 in., gave source plate diameters of 7, 9.33, 14, and 19.80 in. These choices not only permitted a study of a reasonable range of diameters, but also will allow a cross-check between the 7- and 14-in.-dia source plates.

Since time and cost precluded fabrication of individual small source plates, they were simulated by placing a neutron-absorbing iris between the thermal-neutron beam from the Oak Ridge Graphite Reactor and the existing LTSF source plate. Both boral and cadmium irises were tried, but results of gold-foil mappings indicated that a much sharper definition of the iris was obtained by using cadmium. Neutrons scattered from the core hole wall or the lead gamma-ray suppressor and entering the source plate area at

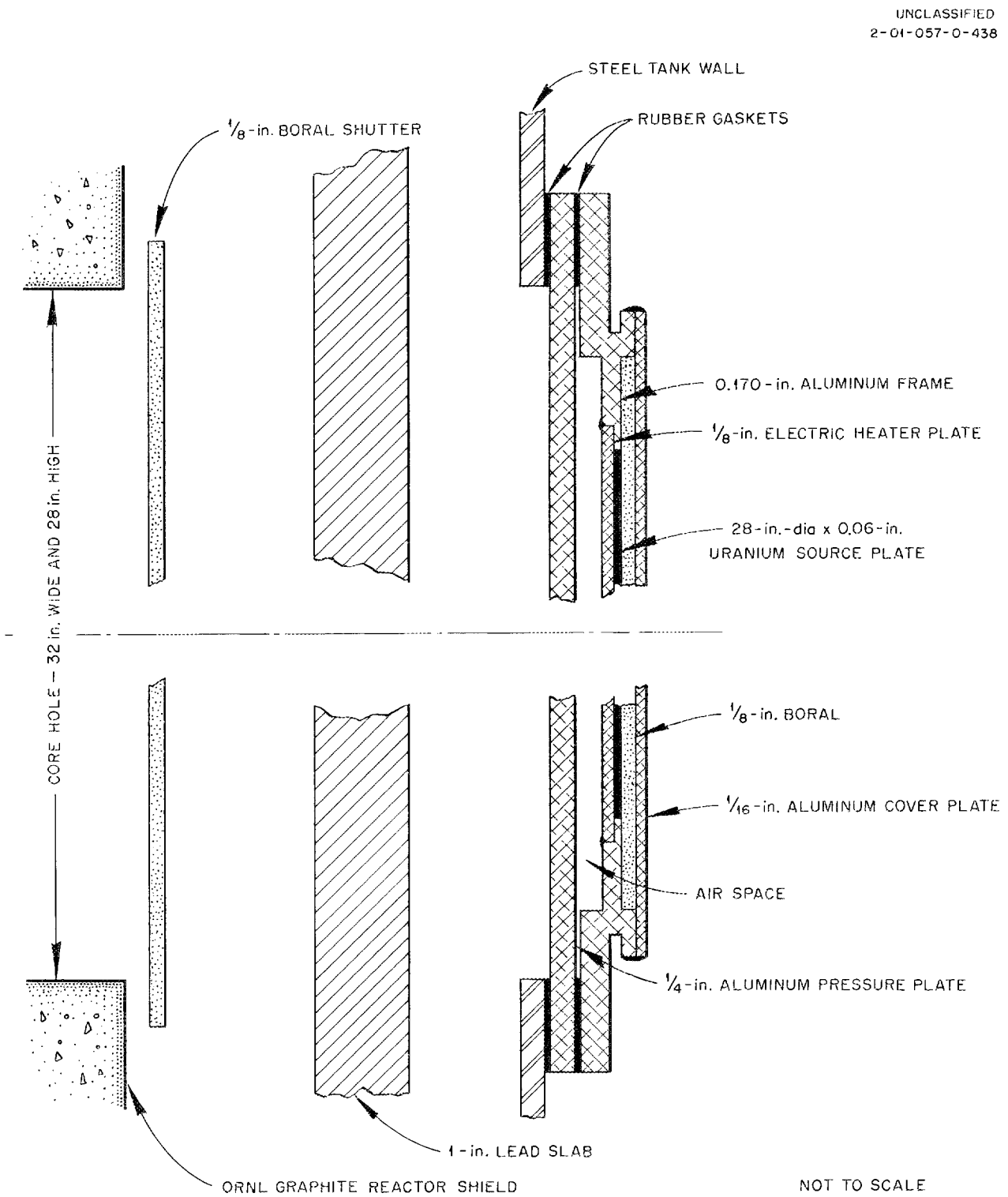

Fig. 7.7.2. Sectional View of the LTSF Source Plate Showing Its Position Relative to the ORNL Graphite Reactor.

angles other than normal were attenuated by the much thicker ($\frac{1}{2}$ in. vs 25 mils) edge of the boral iris. Final measurements were made with the cadmium iris in position and the gamma-ray suppressor removed from the beam in order to eliminate as much scattering as possible.

As shown in Fig. 7.7.2, it was impossible to place the cadmium iris directly in contact with the source plate. At least a $\frac{3}{8}$-in. thickness of aluminum and an air space separated the uranium disk from the iris during all measurements. The effect of this separation was evaluated by interposing more aluminum between the source and iris, and a correction will be applied to the final data.

Gamma-ray dose measurements early in the experiment indicated that thermal-neutron captures in the cadmium iris resulted in a secondary gamma-ray component from the source area, thus making the gamma-ray data suspect for use in verification of the theory. The resulting increase in gamma-ray-to-neutron ratio also made operation of the Hurst-type fast-neutron dosimeter impractical. Final analysis of the experiment and comparison with theory will therefore be made solely on the basis of the thermal-neutron flux measurements. This analysis is now in progress.

7.8. A GENERAL-PURPOSE MONTE CARLO GAMMA-RAY CODE

S. K. Penny

A general Monte Carlo code is being written for the purpose of studying the transport of gamma rays. The code is primarily for research with Monte Carlo methods; however, it will be readily adaptable for data production. It is presently being "debugged" on the IBM-7090 computer.

The code will handle a general source, heterogeneous media, importance sampling, and various geometries. It will operate much like the O5R Neutron Code[1] in that gamma-ray histories will be written on magnetic tapes, which may then be processed as needed.

[1]R. R. Coveyou, J. G. Sullivan, and H. P. Carter, *Neutron Phys. Ann. Prog. Rep. Sept. 1, 1958*, ORNL-2609, p. 87

7.9. THE DIFFERENTIAL ENERGY AND ANGULAR SPECTRA OF NEUTRONS FROM A POINT ISOTROPIC SOURCE IN INFINITE GEOMETRY

H. E. Stern,* R. E. Maerker, and D. K. Trubey

An attractive aspect of the application of the method of random sampling, or Monte Carlo, to radiation shielding problems has long been recognized to lie in its adaptability to a variety of geometries. The prohibitive cost in computing time, however, of solutions to practical problems obtained by the direct or analog method has led to the development of a variety of sampling or biasing schemes intended to focus attention upon the particles which will contribute to the final answer. In order to obtain insight into the usefulness of one of these methods, the technique of "statistical estimation,"

*On assignment from Lockheed Aircraft Corp., Marietta.

calculations have been performed to determine the differential energy and angular spectra of neutrons from an 8-Mev point isotropic source in an infinite medium of hydrogen. The choice of an infinite hydrogen medium permits the results to be directly compared to existing results from moments method calculations.

The neutron histories used in this calculation were generated by the O5R Code.[1] Two different schemes have been tried. The first employed point detectors and tabulated flux contributions in four concentric, contiguous spherical intervals about each detector. The purpose of the tabulation was to provide a means of discriminating against high flux contributions due to unusual collisions near the detector. Test results obtained with this scheme were not satisfactory for two reasons. First, for the number of neutrons considered (three batches of 480 neutrons each) an unrealistically high contribution to the flux resulted from collisions occurring in the spherical intervals closest to the detector. Second, it was uneconomical of neutrons, since a large fraction of collisions occurred at points where a scatter toward the detector regions was physically impossible in hydrogen.

The second scheme computes the neutron current, and from this the neutron flux, at various spherical surfaces centered on the point source. The neutron direction after collision given by the O5R Code is used directly, but any neutron whose projected path intersects one of the specified spherical surfaces is forced to cross that surface irrespective of the location of a subsequent collision. Differential angular and energy fluxes and currents are computed for 20 equal energy intervals and for as many as 20 arbitrary angular intervals. In addition, summations over energy and over angle are performed to give differential energy fluxes and currents, differential angular dose rates and currents, total current, and total dose rate.

For the test calculation of the second scheme, a total of 11 batches of 480 neutrons each was run. The hydrogen density used was 0.111 g/cm^3 (that of hydrogen in water) for which the scattering mean free path was about 13.2 cm.

The collided differential energy fluxes are shown in Table 7.9.1, together with the computed mean standard deviations. The data for source-detector separation distances of 20, 60, and 90 cm are compared in Fig. 7.9.1 with the moments method results of Krumbein.[2] The sharp rise in the moments method data at 8 Mev is due to the inclusion of uncollided 8-Mev source neutrons which are spread over a small energy interval, rather than being precisely monoenergetic. The agreement of the statistical estimation results with moments method values seems to be reasonably satisfactory out to a distance of 60 cm, and the data at 90 cm might be used in some applications if appropriate smoothing techniques were to be applied.

Angular collided dose rates are presented in Table 7.9.2, and total dose rates are compared to moments method results in Table 7.9.3. For consistency with the moments method results, flux-to-dose conversion factors from NDA 2092-9 (Ref. 3) have been applied to the present results.

---

[1] R. R. Coveyou and J. G. Sullivan, *Neutron Phys. Ann. Prog. Rep., Sept. 1, 1960*, ORNL-3016, p. 193.

[2] A. D. Krumbein, *Summary of NDA Unclassified Results of Moments Method Calculations for the Penetration of Neutrons Through Various Materials*, NDA 92-2 (Aug. 30, 1957).

[3] H. Goldstein and H. Mechanic, *Penetration of Neutrons from a Point Fission Source Through Beryllium and Beryllium Oxide*, NDA 2092-9 (June 23, 1958).

Table 7.9.1. Differential Energy Flux (Collided Only) from a Point Isotropic Source of 8-Mev Neutrons in an Infinite Hydrogen Medium

Lower Bound of Energy Interval (Mev)	Differential Energy Flux* ($4\pi R^2 \cdot$ neutrons $\cdot$ cm$^{-2} \cdot$ sec$^{-1} \cdot$ Mev^{-1})				
	10 cm from Source	20 cm from Source	30 cm from Source	60 cm from Source	90 cm from Source
	$\times 10^{-2}$	$\times 10^{-2}$	$\times 10^{-2}$	$\times 10^{-3}$	$\times 10^{-3}$
0.0094	25.6 ± 2.15	27.4 ± 2.12	21.1 ± 1.40	54.2 ± 7.73	8.26 ± 2.32
0.4089	10.7 ± 1.20	12.8 ± 1.82	10.2 ± 0.506	22.4 ± 5.78	2.66 ± 1.08
0.8085	9.61 ± 0.660	10.0 ± 0.616	8.99 ± 0.856	10.2 ± 1.78	0.800 ± 0.428
1.2080	7.65 ± 0.521	7.88 ± 0.577	5.39 ± 0.453	15.5 ± 4.93	3.87 ± 1.25
1.6075	7.19 ± 0.425	7.28 ± 0.631	5.63 ± 0.453	13.3 ± 2.18	1.11 ± 0.338
2.0071	6.31 ± 0.530	6.75 ± 0.465	4.70 ± 0.212	9.82 ± 1.45	1.62 ± 0.825
2.4066	5.79 ± 0.307	5.72 ± 0.395	4.13 ± 0.412	8.46 ± 1.70	0.937 ± 0.313
2.8061	5.95 ± 0.536	5.87 ± 0.579	4.42 ± 0.337	8.66 ± 1.70	1.15 ± 0.504
3.2057	5.24 ± 0.437	5.29 ± 0.392	3.66 ± 0.487	8.51 ± 1.23	0.907 ± 0.307
3.6052	4.46 ± 0.562	5.22 ± 0.292	3.52 ± 0.267	7.12 ± 1.00	0.768 ± 0.167
4.0047	5.81 ± 0.345	5.45 ± 0.312	3.73 ± 0.422	6.23 ± 0.991	1.11 ± 0.330
4.4042	5.05 ± 0.424	4.89 ± 0.523	3.06 ± 0.332	7.13 ± 1.21	1.18 ± 0.667
4.8038	5.02 ± 0.577	4.51 ± 0.470	3.07 ± 0.281	6.80 ± 1.01	0.543 ± 0.130
5.2033	4.46 ± 0.320	3.94 ± 0.376	3.10 ± 0.234	8.85 ± 1.05	0.770 ± 0.183
5.6028	4.59 ± 0.366	4.13 ± 0.368	3.00 ± 0.204	7.33 ± 1.36	1.48 ± 0.577
6.0024	4.87 ± 0.324	4.33 ± 0.350	3.09 ± 0.152	6.09 ± 0.933	1.34 ± 0.539
6.4019	4.40 ± 0.452	4.81 ± 0.489	3.53 ± 0.244	7.94 ± 1.40	1.02 ± 0.299
6.8014	5.18 ± 0.292	5.03 ± 0.448	3.42 ± 0.231	6.94 ± 0.955	0.681 ± 0.0746
7.2010	4.38 ± 0.503	3.99 ± 0.417	2.98 ± 0.368	6.20 ± 0.533	1.11 ± 0.388
7.6005	4.64 ± 0.332	4.39 ± 0.246	3.27 ± 0.199	7.11 ± 0.973	0.925 ± 0.173

*Normalized to one source neutron per second. The errors quoted are the standard deviation of the mean of batch averages (11 batches of 480 neutrons each).

Table 7.9.2. Differential Angular Dose Rate (Collided Only) from a Point Isotropic Source of 8-Mev Neutrons in an Infinite Hydrogen Medium

Cosine of Lower Bound of Angular Interval	Differential Angular Dose Rate* ($4\pi R^2 \cdot$ mrep $\cdot$ hr^{-1})				
	10 cm from Source	20 cm from Source	30 cm from Source	60 cm from Source	90 cm from Source
	$\times 10^{-5}$	$\times 10^{-5}$	$\times 10^{-5}$	$\times 10^{-5}$	$\times 10^{-6}$
0.80	461 ± 7.19	427 ± 5.30	302 ± 8.38	64.6 ± 3.99	87.3 ± 10.7
0.60	95.2 ± 6.00	109 ± 3.04	78.8 ± 4.80	15.8 ± 1.55	23.1 ± 5.69
0.40	39.4 ± 2.71	49.4 ± 3.21	38.2 ± 2.51	7.03 ± 1.20	14.4 ± 4.57
0.20	19.9 ± 3.20	15.2 ± 1.83	19.4 ± 2.12	4.25 ± 1.07	7.19 ± 3.31
0.00	4.31 ± 1.24	11.8 ± 2.96	10.4 ± 2.05	1.49 ± 0.633	0.204 ± 0.168
−0.20	2.97 ± 0.818	6.56 ± 2.58	4.80 ± 1.30	3.32 ± 1.83	0.760 ± 0.726
−0.40	4.54 ± 0.966	6.87 ± 1.02	2.99 ± 0.652	1.61 ± 0.487	2.14 ± 1.40
−0.60	2.76 ± 0.627	3.55 ± 0.335	2.90 ± 0.685	1.15 ± 0.276	3.13 ± 1.95
−0.80	2.33 ± 0.823	2.15 ± 0.449	1.43 ± 0.344	0.581 ± 0.232	0.911 ± 0.730
−1.00	1.39 ± 0.310	1.47 ± 0.343	1.31 ± 0.330	0.585 ± 0.242	1.09 ± 0.643

*Normalized to one source neutron per second. The errors quoted are the standard deviation of the mean of batch averages (11 batches of 480 neutrons each).

Table 7.9.3. Fast-Neutron Dose Rate (Collided Only) from a Point Isotropic Source of 8-Mev Neutrons in an Infinite Hydrogen Medium

Distance from Source (cm)	Fast-Neutron Dose Rate ($4\pi R^2 D \cdot$ mrep $\cdot$ hr$^{-1} \cdot$ cm^2)	
	Moments Method	Statistical Estimation
	$\times 10^{-4}$	$\times 10^{-4}$
10	133	138
20	90.5	98.3
30	55.2	62.7
60	9.24	11.7
90	1.25	1.57

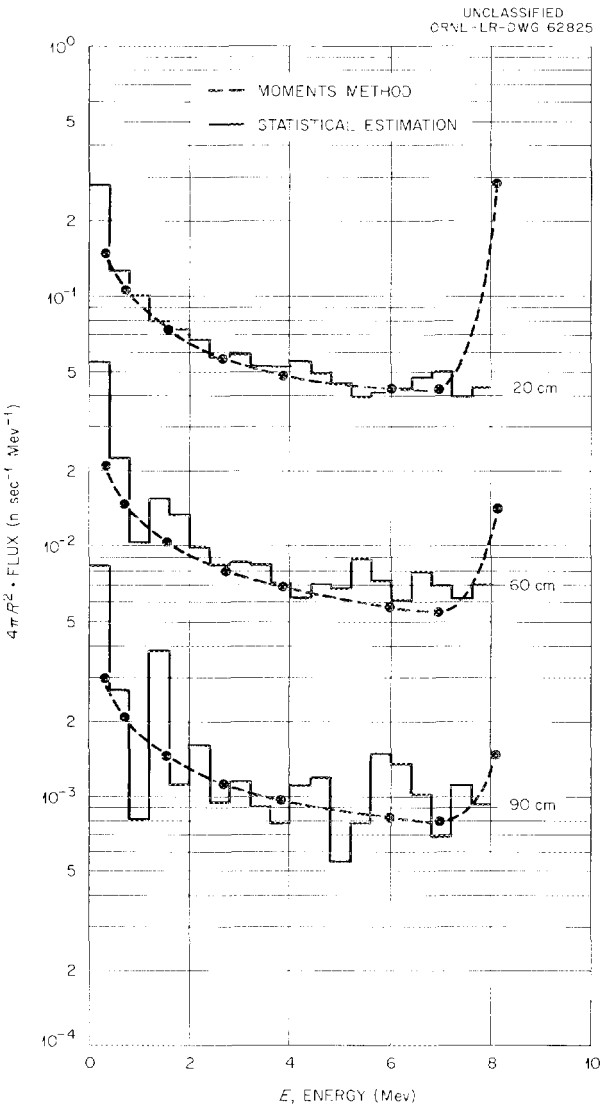

Fig. 7.9.1. Neutron Flux from an 8-Mev Point Isotropic Source in an Infinite Hydrogen Medium as a Function of Energy for Various Source-Detector Separation Distances. Moments method results include uncollided source neutrons; statistical estimation does not.

7.10. DESIGN OF A WINDOW FOR A HOT CELL

J. M. Miller F. J. Muckenthaler

The Transuranium Processing Facility now being designed by the Chemical Technology Division is to include a hot cell capable of containing point sources spontaneously fissioning at a maximum rate of 7.8×10^{11} fissions per sec. The window in this cell is required to have approximately the same shielding value for these sources as would magnetite concrete. The experimental work required in the design of the window is being performed by the Lid Tank Shielding Facility (LTSF) and preliminary studies have been completed.

The preliminary work has consisted of two phases. In the first the effective neutron removal cross sections of commercially available glasses of various densities have been measured and compared with calculations based upon manufacturers' analyses of the glasses. The results of this work are shown in Table 7.10.1.

The proposed design of the hot cell window envisages the use of various thicknesses of three types of glass separated by thicknesses of oil. The glasses to be used are a nonbrowning glass of density 2.7 g/cm^3, a lead-silicate glass of density 3.3 g/cm^3, and a lead-silicate glass of density 6.2 g/cm^3. In the second phase of the present study, ordinary plate glass and lead slabs were laminated to mock up the removal cross sections of the various high-density glasses and combined in various configurations with water to obtain the optimum arrangement for the most effective attenuation of both neutrons and (prompt and capture) gamma rays. Final analysis of this data has not been completed.

Based upon the experimental data obtained, a 4.5-ft-thick window has been designed. This window consists of appropriate laminations of three 1-in.-thick pieces of cover plate glass, one 8-in.-thick piece of 3.3-g/cm^3 glass, two 6-in.-thick pieces of 6.2-g/cm^3 glass, and 31 in. of oil. A full-scale mockup of this window is currently under test in the LTSF.

Table 7.10.1. Measured and Calculated Neutron Removal Cross Sections for Various Glasses

Type	Density (g/cm^3)	Removal Cross Section, Σ_R (cm^{-1})	
		Measured	Calculated*
Pittsburgh Plate Glass No. 4966	3.30	0.076 ± 0.004	0.080 ± 0.008
Corning No. 8362	3.30	0.080 ± 0.004	0.081 ± 0.008
Corning No. 8363	6.20	0.095 ± 0.005	0.101 ± 0.010

*The formulae for these glasses are proprietary and therefore are not given in this report.

Part 8

SHIELDING AGAINST HIGH-ENERGY RADIATIONS

8.1. INTRANUCLEAR CASCADE CALCULATION

H. Bertini

For the prediction of the shielding requirements of space vehicles and ultrahigh-energy particle accelerators, a large volume of cross-section data difficult or impossible to obtain by experiment is required. The initiation of a program to calculate some of this data was previously reported in considerable detail.[1] For convenience, however, a brief review of the initial assumptions will be given.

In the nuclear model it is assumed that the reactions of high-energy particles incident on complex nuclei can adequately be described as a series of individual particle-particle collisions inside the nucleus. The nucleus itself is assumed to consist of three concentric spherical shells, each with a uniform density of nucleons. This is done to approximate the actual continuous change of nucleon density with the nuclear radius. The momentum distribution of the nucleons in each of the shells is taken to be that of a zero-temperature Fermi gas, with the zero-temperature Fermi energy given by the nucleon density in each shell. There is a potential well associated with each shell, and the depth of each well is given by the sum of the binding energy per nucleon and the zero-temperature Fermi energy.

A Monte Carlo method is used for the calculation, in which every incident particle, the collision products of each particle, succeeding collision particles, etc. are traced within the nucleus. The problem is coded for the IBM-7090 computer.

The output of the calculation consists of a complete record of the types, energies, and direction cosines of the escaping collision products (cascade particles). This output will be written on magnetic tape. From it can be computed the average number, per incident particle, of each of the cascade products considered: protons, neutrons, and each of the three pi-mesons. In addition, their energy and angular distributions as well as the excitation energy and angular and momentum distributions of the recoil complex nucleus can be calculated.

The progress of the calculation has been agonizingly slow. Late in 1960 the low-energy portion (incident particle energy <350 Mev) was coded for the IBM-704 computer, and the code was found to be too big for the 704 memory. The code was then modified so that the calculation could be done in two steps, with one-half the code in the memory at any given time and the other half stored on tape. When the IBM-704 was replaced by the IBM-7090, the code then had to be modified for the new machine. Recently it was found that a different Monte Carlo sampling technique[2] which would eliminate the need for using estimated average cross sections, a weak point in the calculation, could be used. This modification, hopefully the last, is at present in flow diagram form and is being coded. In addition, a rather general output data analysis code is nearing completion. This code will analyze the cascade particle output and calculate cascade cross sections for the emission of any combination of emitted particles, provided that the total number is less than 10 emitted particles per incident particle. It will also calculate all the quantities (energies, angular distributions, etc.) listed previously.

---

[1] H. Bertini and C. D. Zerby, *Neutron Phys. Ann. Prog. Rep., Sept. 1, 1961*, ORNL-3016, p. 235.

[2] The method was suggested by C. D. Zerby.

Since additional coding assistance is now available for the IBM-7090, it is expected that the entire problem, which will include incident particle energies to 30 Bev, can be completed in about 12 months.

Before the most recent sampling modification was initiated, some problems were run in order to roughly evaluate the effectiveness of the three-region nucleus model. Previously reported work[3] had not accounted for (p,pn) cross sections very well. To properly compute this cross section it is necessary to use both an evaporation calculation and a cascade calculation. The evaporation calculation used here was coded by Dresner.[4] The results of the present calculation are compared with experiment and with previous calculations in Table 8.1.1.

Table 8.1.1. Comparison of Computed and Experimental (p,pn) Cross Sections

Target	Incident Proton Energy (Mev)	$\sigma_{(p,pn)}$ (mb)		
		Experiment*	Computed (Present Work)	Computed (Previous Work)**
F^{19}	82	46.0 ± 1.5	25	38
	225	24.3 ± 0.8	24	27
	426	23.1 ± 0.8	31	29
Cu^{65}	82	108.4 ± 4.2	30	48
	196	64.3 ± 2.5	24	38
	426	51.6 ± 2.0	28	35
Au^{197}	82	121.6 ± 9.8	63	28
	282	71.0 ± 5.7	37	24
	426	70.5 ± 5.7	46	24

*H. P. Yule and A. Turkevich, *Phys. Rev.* 118, 1591 (1961).
**Estimated from graphs.

The comparison indicates a rather poor agreement with experiment, and, in fact, is in poorer agreement than previous calculations in the case of a copper target. It was expected that the use of the three-region nucleus model would improve the calculational results. Although the results shown are hardly encouraging, it would be premature to conclude that improvement will not be made. The calculated value is highly sensitive to the spectrum of excitation energies of the complex residual nucleus. It is over only very narrow ranges of this spectrum that the required evaporation of two, one, or no particles to the final state is likely, and over these ranges the spectrum varies quite rapidly. The number of input histories for the cases run was not statistically sufficient to define the shape of the excitation energy spectra to any degree of satisfaction. Some of the cases will be repeated with a greater number of histories.

[3]N. Metropolis *et al.*, *Phys. Rev.* 110, 185 (1958).
[4]Section 6.8, this report.

8.2. EXPERIMENTAL SPACE VEHICLE SHIELDING PROGRAM*

W. A. Gibson, W. R. Burrus, and T. A. Love

With the discovery of proton and electron radiation belts around the earth by Van Allen in 1958[1] and the observance of the intense proton radiation arising from the sun,[2,3] radiation shielding on space vehicles became a major concern. The Van Allen protons range in energy from a few Mev up to hundreds of Mev, with intensities as high as about 4×10^4 protons/cm^2·sec. The energies of solar protons are also high, and while the maximum energy found in most solar proton events is 300 Mev, energies as great as 20 Bev have been observed in some cases. Thus, except for low orbital flights and short probes into space, considerable shielding[4] will be necessary to protect an astronaut from this lethal proton radiation. The problem will be further complicated by the fact that the protons will produce secondary radiations within the shield materials which can penetrate the shields and contribute significantly to the radiation dose. These secondary radiations are expected to be composed mainly of gamma rays, protons, and neutrons, with the neutron intensity considerably greater than the intensity of either the gamma rays or the protons. (The Van Allen electrons are not expected to create a problem if the proper proton shielding is employed.)

If the range of the incident protons is greater than the thickness of the shield, the primary protons will represent a large fraction of the radiation penetrating the shield. In principle at least, their energies can be determined from range calculations. The calculations for secondary radiations are less straightforward, however, and in any case will require experimental confirmation. For this reason, an experimental program has been initiated which will have as its primary goal the measurement of secondary radiations emerging from shields which have been bombarded by monoenergetic protons from cyclotrons. A primary proton energy range of from 50 to 700 Mev will be covered by employing cyclotrons at several different laboratories.

The experiments will consist of bombarding one side of a flat slab of shielding material with a collimated beam of monoenergetic protons from the cyclotron, keeping the area of illumination as small as practicable with the particular cyclotron used. A typical beam might have an area of 1 sq in. Counters to measure the radiation will be placed on the exit side of the shield.

In general, the shield will be of simple composition, for example, carbon, aluminum, or lead, but it may prove interesting to investigate a sandwich shield which has a slab of material with a large neutron cross section on the exit side. Several thicknesses will be used beginning with a thickness equal to the range of the primary protons in order to eliminate these particles from the penetrating radiation. Measurements with thinner shields will also be attempted, but the large number of primary protons that will

---

*Work performed for the National Aeronautics and Space Administration.

[1] James A. Van Allen, *J. Geophys. Research* 64, 1683 (1959).

[2] J. R. Winckler, *Proceedings of Conference on Radiation Problems in Manned Space Flight, June 1960, Washington*, NASA TN-D-588, p. 72.

[3] S. Biswas and P. S. Freier, *J. Geophys. Research* 66, 1029 (1961).

[4] R. I. Allen, A. J. Dessler, J. F. Perkins, and H. C. Price, "Shielding Problems in Manned Space Vehicles," *Semiannual Technical Summary Report (December 31, 1959–June 30, 1960)*, NR-104, Lockheed Aircraft Corp., Georgia.

penetrate is expected to dominate the picture, making measurements of the secondary radiations difficult.

As currently envisaged, the experimental program includes studies of the three major secondary radiation components (neutrons, protons, and gamma rays) and also dosimeter measurements to determine the gross effects of the radiation. Thus far, however, only the neutron measurements have been considered in detail. These measurements will determine the intensity, the energy spectra, and the angular distribution of the emerging neutrons through the use of a spectrometer of known efficiency. It is hoped that neutron spectral measurements can be made with a 15 per cent energy resolution. The angular distributions will be obtained by measuring the energy spectrum at several angles with respect to the incident beam (for example, at 15-deg intervals from 0 to 60 deg).

In order to obtain some estimate of the neutron spectra which will be encountered, a rough estimate of the energy spectrum of neutrons emerging from a 60-g/cm^2 copper slab bombarded by 240-Mev protons was made by simple extrapolation of experimental data[5] and calculations on nucleon cascade[6,7] and evaporation[8] processes. The resulting spectrum is shown in Fig. 8.2.1. For an estimate of the neutron intensity it was assumed that 7×10^7 protons/sec were incident on the shield.

The estimate of the energy spectrum shown in Fig. 8.2.1 was made without regard to the angular dependence of secondary neutrons. However, it is to be pointed out that a strong angular dependence is expected in the high-energy tail with a peak appearing in the forward direction near the primary proton energy.[9] At large scattering angles the high-energy neutrons will disappear almost entirely.

In view of the low intensity and wide range of neutron energies indicated by Fig. 8.2.1, the spectral measurements in this investigation will be divided into three energy regions, each region measured by a different type of spectrometer. The factors considered in choosing the spectrometers were efficiency, proton and neutron background rejection, simplicity, and ease of collecting data. Although actual experimental conditions may necessitate modifications, the three energy regions and the spectrometers which will probably be used are as follows:

(1) Thermal to 15 Mev – measured by a method described by Bonner[10] in which the neutron intensities inside solid polyethylene spheres of various diameters are determined. From these measurements it is possible to deduce an energy spectrum. The advantages of the method are its relative high efficiency and insensitivity to backgrounds. The main disadvantage is the difficulty in determining the energy spectrum from the data.

---

[5] E. Gross, *Absolute Yield of Low-Energy Neutrons from 190-Mev Proton Bombardment of Gold, Silver, Nickel, Aluminum, and Carbon*, UCRL-3330 (1956).

[6] N. Metropolis, R. Bivins, M. Storm, A. Turkevich, J. M. Miller, and G. Friedlander, *Phys. Rev.* **110**, 185 (1958).

[7] N. Metropolis, R. Bivins, M. Storm, J. M. Miller, G. Friedlander, and A. Turkevich, *Phys. Rev.* **110**, 204 (1958).

[8] I. Dostrovsky *et al.*, *Phys. Rev.* **116**, 683 (1959); *Phys. Rev.* **118**, 781 (1960).

[9] R. T. Seigel, "Nuclear Instrumentation II," *Encyclopedia of Physics*, S. Flügge, Editor, Vol. XLV, p. 487, Springer, Berlin, 1958.

[10] R. L. Bramblett, R. I. Ewing, and T. W. Bonner, *Nuclear Instr. and Methods* **9**, 1 (1960).

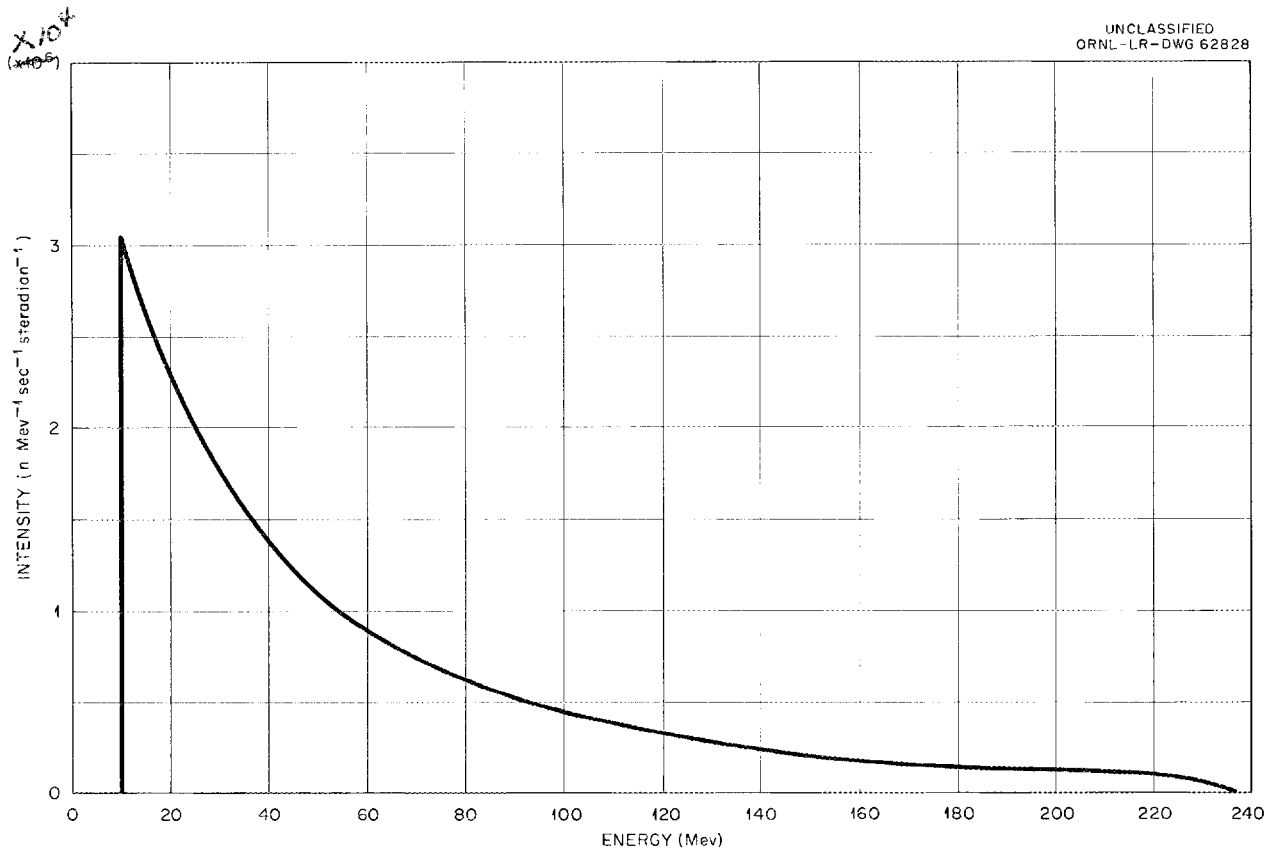

Fig. 8.2.1. Differential Energy Spectrum of Secondary Neutrons Resulting from the Bombardment of a 60-g/cm^2 Copper Shield by 240-Mev Protons. Normalized from 10–240 Mev to a primary proton beam of 7×10^7 protons/sec.

(2) 8 Mev to 50 Mev – covered with a proton-recoil telescope[11,12] with two proportional counters in coincidence with a scintillating crystal to measure the proton energy. Figure 8.2.2 is the efficiency of such a recoil telescope with 10% energy resolution plotted against energy. Although the *n-p* cross section drops as the energy increases, the over-all efficiency increases with energy because the increase in radiator thickness more than offsets the decrease in the *n-p* cross section. The dotted lines indicate the efficiency with a particular radiator thickness, and the solid line is the efficiency with a continual increase in the thickness of the radiator. Figure 8.2.3 is the differential counting rate from a point neutron source with the intensity and energy spectrum described by Fig. 8.2.1. For measurements in this region the proton background problem is expected to be severe and effective background rates are expected to be as high as 5×10^4 counts/sec. Thus it will be necessary to exercise care to prevent jamming of counters.

[11] C. H. Johnson, *Fast Neutron Physics*, J. B. Marion and J. L. Fowler, Editors, Interscience Publisher, Inc., New York, 1960.

[12] S. J. Bame, Jr., E. Haddad, J. E. Perry, Jr., and R. K. Smith, *Rev. Sci. Instr.* **28**, 997 (1957).

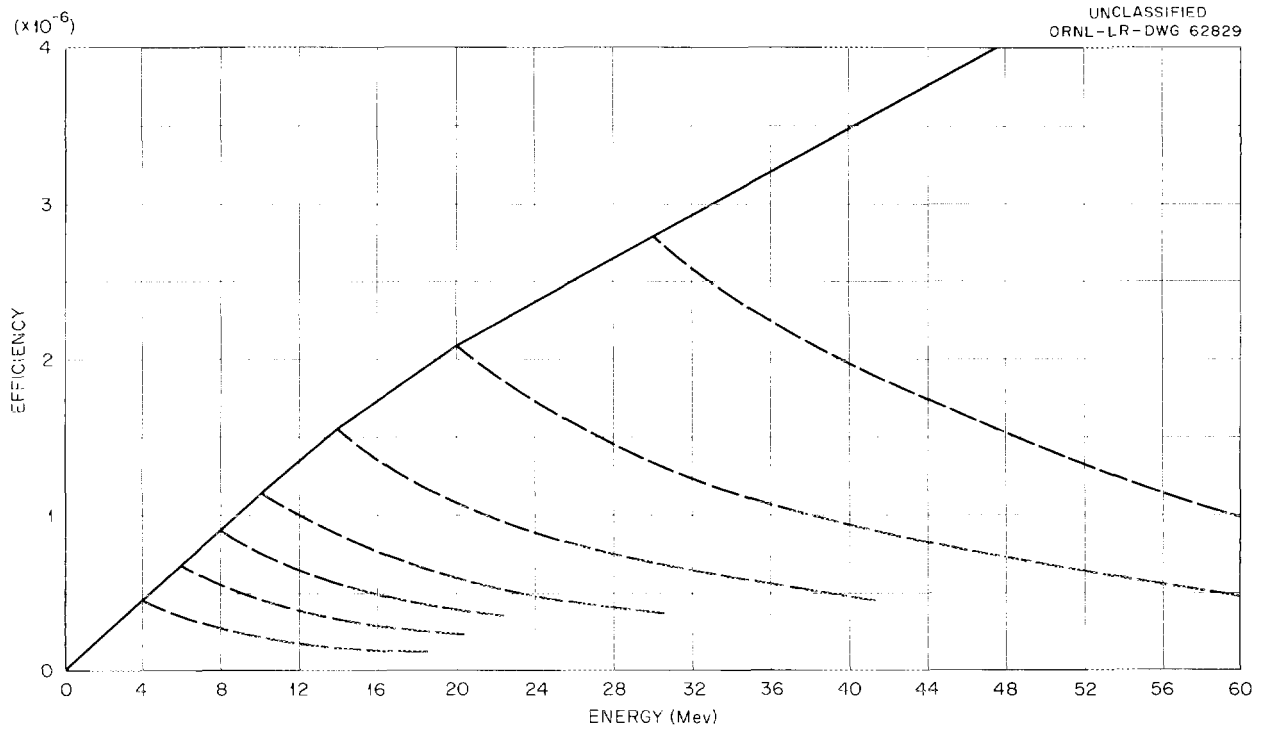

Fig. 8.2.2. Efficiency of Recoil Telescope with 10% Energy Resolution. Dotted lines indicate efficiency with particular radiator thicknesses; solid line shows efficiency for a continual increase in the thickness of the radiator.

(3) 50 Mev to maximum energy -- measured with a recoil telescope which will use organic scintillators to detect the proton recoils. The resolving time of organic scintillators is much shorter than proportional counters; hence, the background is not expected to be troublesome.

In addition to the above, if it proves to be feasible, measurements will also be made with threshold counters to furnish a rough check on the neutron spectral and intensity measurements.

Measurements for the secondary gamma radiation will be less extensive than for the neutrons since the gamma rays are not expected to pose an important biological problem. Rough spectral and intensity measurements are planned to indicate their importance, however.

The measurements for protons will be similar to those for the neutrons, although the instrumentation is expected to be much simpler.

It is to be understood that the experimental program is in its infancy and ideas concerning the interesting quantities to be studied and the counters to perform these studies may prove to be incorrect under actual experimental conditions. It is expected that modifications will be necessary as the program progresses.

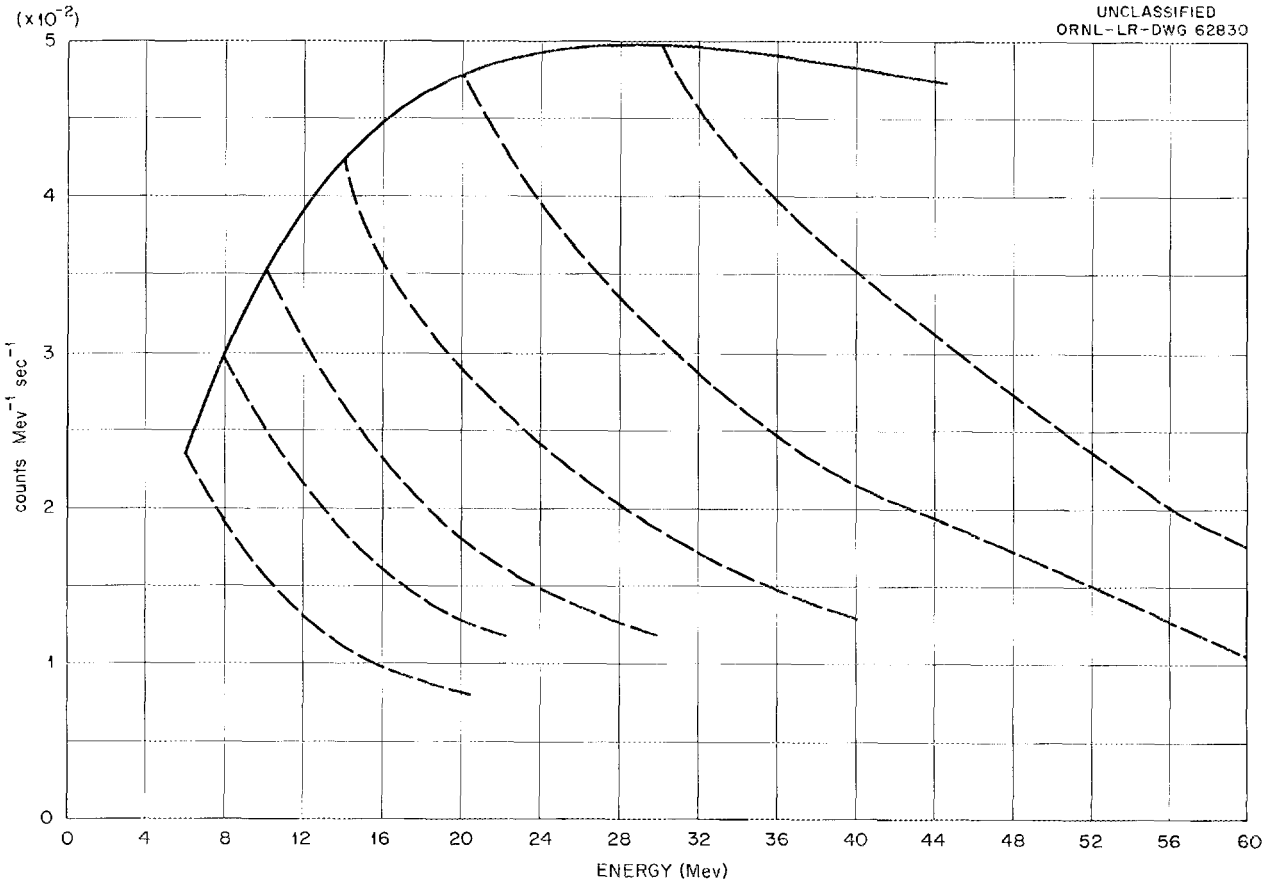

Fig. 8.2.3. Differential Counting Rate for Recoil Telescope with 10% Energy Resolution. Source is point neutron source described in Fig. 8.2.1.

8.3. ELECTRON-PHOTON CASCADE SHOWERS

C. D. Zerby and H. S. Moran

As a result of the many problems that arise during the design of high-energy electron accelerators which require detailed information about electron-initiated cascade showers, a general-purpose electron-photon cascade calculation which can provide some of the required data has been programmed for computation on the IBM-7090 data-processing machine. The Monte Carlo technique is used. The present version of the calculation was designed to study the longitudinal development of photon- or electron-initiated showers, and to this extent is similar to a calculation recently reported by Butcher and Messel.[1]

[1] J. C. Butcher and H. Messel, *Nuclear Phys.* 20, 15 (1960).

However, the two calculations differ in detail and to the amount of data that is computed. The IBM-7090, having a larger fast memory capacity than the machine used by Butcher and Messel, makes it possible to calculate and tabulate considerably more useful data on both the photon and electron cascade particles for each run on the computer.

In the first two sections of this paper some of the details of this calculation are described. They are followed by a section consisting of a description of all the data that result from one cascade calculation. The two final sections present part of the results obtained from calculations which have already been completed.

Simulation of the Physical Processes

Since the calculation was designed for the investigation of cascade showers in the energy range from 6.5 Mev to 50 Gev, only interaction processes of importance in that energy range were retained. Thus, for photons only Compton scattering and pair production processes were retained, and for charged particles only bremsstrahlung and ionization collisions were considered.

The Klein-Nishina expression for the Compton cross section[2] was used for determining the probability of scattering of the photons, and the relativistic form of the Bethe-Heitler expression for the pair production cross section was used for production events. The differential form of the latter expression, which includes the effects of screening, is given by[2]

$$d\sigma_p = \alpha r_0^2 Z(Z+1)\frac{dE_+}{k^3}\left\{(E_+^2+E_-^2)\left[\phi_1(y)-\frac{4}{3}V(Z)\right]+\frac{2}{3}E_+E_-\left[\phi_2(y)-\frac{4}{3}V(Z)\right]\right\}, \tag{1}$$

where k, E_+ and E_- are the energies of the photon, positron, and electron, respectively. The quantities α, r_0, and Z are the fine structure constant, classical electron radius, and atomic number, respectively. The function as used in Eq. 1 differs slightly from the form originally given by Bethe. An empirical correction term has been added to compensate for the deficiencies of the theory when applied to materials of high atomic number.[3] With the empirical correction included, $V(Z)$ is given by

$$V(Z) = \log Z + 3f(Z)\left(1-\frac{6\,mc^2}{0.511k}\right), \tag{2}$$

where

$$f(Z) = a^2\left(\frac{1}{1+a^2}+0.20206-0.0369a^2+0.0083a^4-0.002a^6\right).$$

The remaining functions $\phi_1(y)$ and $\phi_2(y)$ were tabulated[2] as a function of $y = 100k\,mc^2/E_+E_-Z^{1/3}$ for $y < 10$. For $y > 10$ they were represented by $\phi_1(y) = \phi_2(y) = 4\log(200/y) - 2$.

For bremsstrahlung events the following expression was used for the differential cross section:[2]

$$d\sigma_b = \alpha r_0^2 Z(Z+1)\frac{dk}{k}\left\{\left(1+\frac{E^2}{E_0^2}\right)\left[\phi_1(y)-\frac{4}{3}\log Z\right]-\frac{2}{3}\frac{E}{E_0}\left[\phi_2(y)-\frac{4}{3}\log Z\right]\right\}, \tag{3}$$

[2]H. A. Bethe and J. Ashkin, "Passage of Radiation Through Matter," *Experimental Nuclear Physics*, Edited by E. Segré, Vol. I, p. 166, John Wiley and Sons, Inc., New York, 1953.

where E_0 and E are the energies of the electron or positron before and after the radiative collision, respectively. It will be noted that an empirical correction term is not required in Eq. 3 as it is in the pair production equation.[3] The functions $\phi_1(y)$ and $\phi_2(y)$ are the same as described above except that the argument of the function is now given by $y = 100k\, mc^2/E_0 EZ^{1/3}$. In both Eqs. 1 and 3 the usual factor of Z^2, which expresses the dependence of the cross sections on the nuclear charge has been replaced by the factor $Z(Z+1)$ to approximately account for the interactions in the electrostatic field of the atomic electrons.

The ionization collisions of the electrons and positrons were treated as a continuous energy degradation process in which the energy change per unit path length traveled is given by the stopping power expression,[4]

$$S(E) = \frac{dE}{dx} = -2\pi r_0^2 NZ\, mc^2 \left(\log \frac{E^3}{2I^2\, mc^2} + B \right) . \tag{4}$$

In Eq. 4, B is set equal to $\frac{1}{8}$ for electrons and equal to $\log 4 - (\frac{23}{12})$ for positrons. The quantity N is the nuclear density, and I is the average ionization energy which can be obtained from a tabulation given by Bethe and Ashkin.[2] For mixtures it was assumed that the stopping power formulas were additive.[2] No account is taken of the shielding effect of the polarization of the medium in Eq. 4 or in the calculation. This is not likely to introduce a serious error since the density effect does not affect the stopping power formula except at high electron energies where energy losses by radiative collisions dominate the energy degradation problem.

The Monte Carlo Procedure

The Monte Carlo calculation was carried out in a straightforward manner which will be described very briefly in this section.

For photons that appeared in the cascade, the total interaction cross section, Σ, which is the sum of the Compton cross section and the total pair production cross section, was calculated first. The distance traveled by the photons between interactions, x, was then randomly selected from the exponential distribution $\Sigma \exp(-\Sigma x)$. At the point of interaction, the choice between a Compton event and a pair production event was made in a random way according to the relative probability of the events. If a Compton event was allowed to take place, the energy and angle after the scattering were randomly selected from the Klein-Nishina distribution function. The recoil electron was then added to the cascade after its energy and momentum had been calculated from the kinematics of the collision. If a pair production event was allowed to take place, the energy of one of the pair was randomly selected from a distribution which is proportional to the function given in Eq. 1. The energy of the other member of the pair was obtained from the energy conservation equations. Both these charged particles were assumed to go straight ahead and were added to the cascade.

---

[3] H. A. Bethe and L. C. Maximon, *Phys. Rev.* 93, 768 (1954); also H. Davies, H. A. Bethe, and L. C. Maximon, *Phys. Rev.* 93, 788 (1954).

[4] E. A. Uehlnig, *Ann. Rev. Nuclear Sci.* 4, 315 (1956).

The treatment of the charged particles in the shower was slightly more complicated than that of the photons. This occurs for two reasons: (1) the differential cross section for bremsstrahlung given in Eq. 3 has a singularity at $k = 0$; and (2) the charged particles continuously change energy according to the model that has been selected. The singularity was most easily avoided by arbitrarily setting the bremsstrahlung cross section equal to zero in the photon energy range from zero to ϵE_0 and using Eq. 3 for the remainder of the range. The approximation leads to an underestimate of the energy loss by radiative collisions by approximately ϵE_0, which corresponds to a fractional underestimate equal to ϵ. In the calculation it was convenient to choose ϵ to be constant and equal to 2×10^{-4}, so that the error introduced by the approximation was small.

Surprisingly enough, the integral of the altered bremsstrahlung equation, $\Sigma_{B'}$ is very nearly constant for any medium in the energy range of interest in this problem. This convenient fact leads to a simplification which allows the path lengths between radiative collisions to be selected from an exponential distribution. The procedure was to first select the distance, x, traveled between radiative collisions from the exponential distribution $\Sigma_B \exp(-\Sigma_B x)$. This distance was then compared with the path length, y, required by the charged particle to be degraded to 6 Mev by ionization collisions. The distance y was determined from range-energy relationships obtained with the use of the stopping power formula given in Eq. 4. If $x \geq y$, the charged particle was assumed to be stopped at the distance y, and 6 Mev of energy was deposited at that point. If $x < y$, the energy of the charged particle at the collision point was first determined from the appropriate range-energy relationship and a photon was then selected from the spectral distribution given by the modified bremsstrahlung differential cross section. Both the photon and the degraded charged particle were directed straight ahead after the collision.

The Computer Program

The present version of the computer program will develop cascades in slabs of a homogeneous material with mixtures of up to 20 elements. The slab can be infinitely thick or have a finite thickness. The cascades can be initiated by normally incident positrons, electrons, or photons at any incident energy up to 50 Gev.

Another feature of the program is the variable nature of the energy bounds for the spectral data of the cascade. It is possible to arbitrarily select up to 15 such bounds other than the source energy which automatically divides the spectral data into the corresponding number of intervals.

The results of a single cascade calculation include such information as the track length[5] in each energy interval for each half radiation length of thickness for both photons and charged particles. In addition, the flux for each energy interval integrated over the entire plane at each half radiation length depth is obtained for both photons and charged particles; this quantity is normalized to one incident particle per second. A third set of data gives the probability of finding exactly n particles with energy above each of the energy bounds at each half radiation length depth out to a maximum of 10 radiation

[5] Track length is equivalent to the flux which has been normalized to one source particle per second and integrated over a volume element. The units of track length are, for example, cm per Mev per source particle. Track length times the macroscopic cross section (cm^{-1}) gives the total number of reactions in the volume element per Mev.

lengths; these probabilities are for $n = 0, 1, \ldots, 9$ and greater than 9 for charged particles and for photons.

The last set of data obtained from the calculation gives the energy deposited in the slab as a function of depth for charged particles and for photons. The data for the charged particles was calculated by storing the energy deposited in each spatial interval by ionization collisions before the particles were degraded below some selected lower energy bound. Since the charged particles were not followed when their energy was degraded below the lower energy bound, the kinetic energy of each electron or the total energy of each positron plus one rest mass unit of energy to account for annihilation was deposited at the position where the charged particle was no longer followed. The energy deposited by the photons was calculated by assuming that photons degraded below the lower energy bound or created in the energy region below the lower energy bound by bremsstrahlung collisions were totally absorbed at the position of the event.

Electrons Incident on Copper

A series of calculations were run to study the cascades that develop when electrons are incident on an infinitely thick slab of copper. Incident energies of 50, 100, 200, 400, and 700 Mev and of 1.4, 3, 5, 10, 20, and 45 Gev were selected. The 20- and 45-Gev cases were run with 400 source electrons each, and the remaining cases were run with 1000 source electrons each. The total running time on the IBM-7090 was 60 hr.

The track lengths[5] for photons and charged particles in the entire volume of the slab are presented in Figs. 8.3.1 through 8.3.4. The dashed line in each case represents the analytic results under "Approximation A" from cascade theory.[6] They were calculated from the equations[7]

$$T(E) = 0.437 \frac{E_0 X_0}{E^2} \text{ for charged particles} \tag{5}$$

and

$$T(E) = 0.572 \frac{E_0 X_0}{E^2} \text{ for photons ,} \tag{6}$$

where E_0 is the source energy, E the degraded energy, and X_0 the radiation length (for copper $X_0 = 1.43$ cm). These equations are expected to hold when $E_c \ll E \ll E_0$, where E_c is the critical energy (for copper $E_c = 21.8$ Mev) and, indeed, it is easy to see from Figs. 8.3.1 and 8.3.2 that the analytic solutions do fit the Monte Carlo results rather well for photons in the energy range below approximately $0.6E_0$ and above the critical energy. The comparison between the approximate analytic results and the Monte Carlo solutions is not nearly so good for the charged particles, as is shown in Figs. 8.3.3 and 8.3.4.

---

[6] "Approximation A" neglects all processes but pair production and bremsstrahlung and uses the asymptotic expressions to describe these interactions.

[7] B. B. Rossi, *High Energy Particles*, Prentice-Hall, Inc., New York, 1952.

It can be shown that the value for the track length for the charged particles at the source energy for the case of incident charged particles is given by

$$T(E) = \frac{1}{-S(E_0)} , \tag{7}$$

where $S(E_0)$ is the stopping power formula given in Eq. 4 and evaluated with $E = E_0$. The derivative of Eq. 7 at the source energy is

$$\frac{d}{dE}[T(E)] = \frac{\Sigma_B}{2[-S(E_0)]^2} , \tag{8}$$

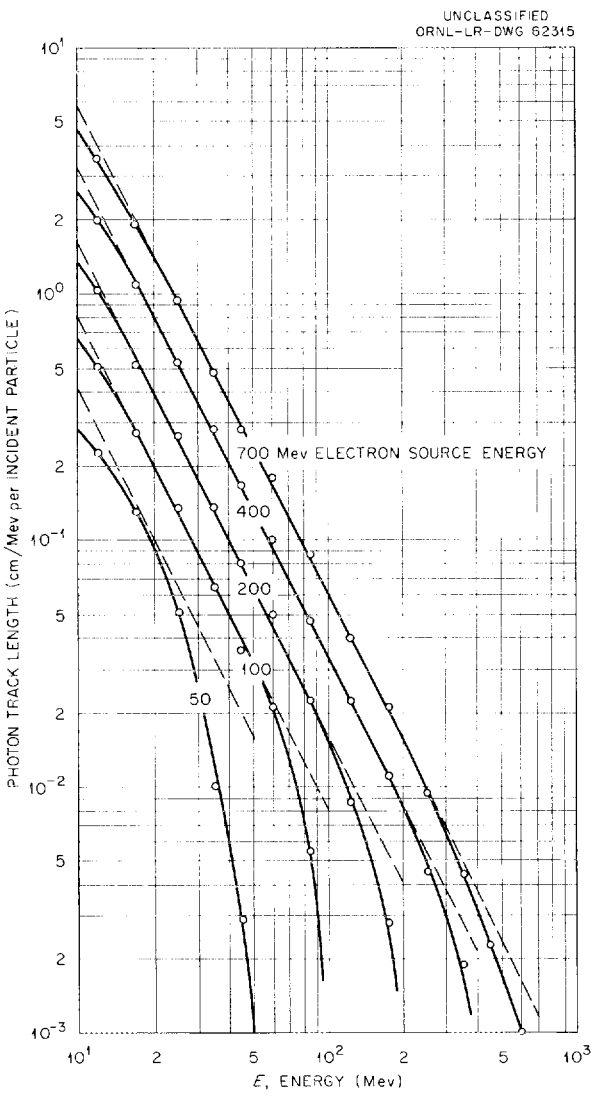

Fig. 8.3.1. Photon Track Lengths in Cascade Showers Initiated by 50- to 700-Mev Electrons Incident on an Infinite Slab of Copper. Dashed lines are from the track length formula using Approximation A; data points are from the Monte Carlo calculation.

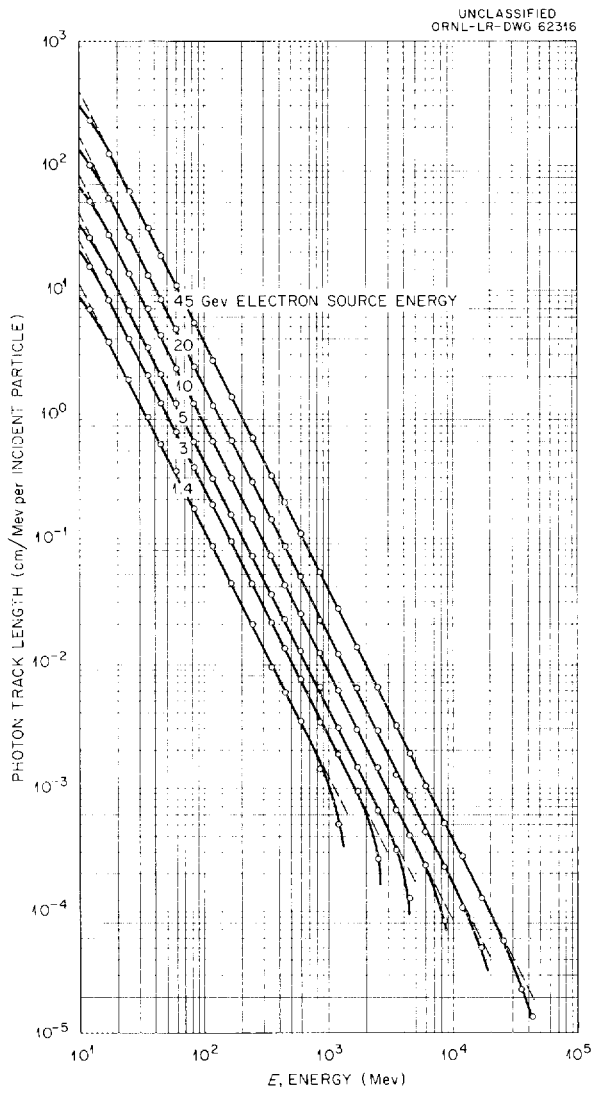

Fig. 8.3.2. Photon Track Lengths in Cascade Showers Initiated by 1.4- to 45-Gev Electrons Incident on an Infinite Slab of Copper. Dashed lines are from the track length formula using Approximation A; data points are from the Monte Carlo calculation.

where Σ_B is obtained from Eq. 3 by multiplying by the nuclear density and integrating over all photon energies from ϵE_0 to $E_0 - mc^2$.

The energy deposition data are presented in Figs. 8.3.5 and 8.3.6. These data represent the sum of the energy deposited by both charged particles and photons using a lower energy bound of 10 Mev as discussed above. The fraction of the energy deposited which was contributed by photons was less than 25% in all cases.

The energy deposition curves should be very accurate, although there might be some concern about the fact that the photons can travel a considerable distance after they are degraded below 10 Mev. The

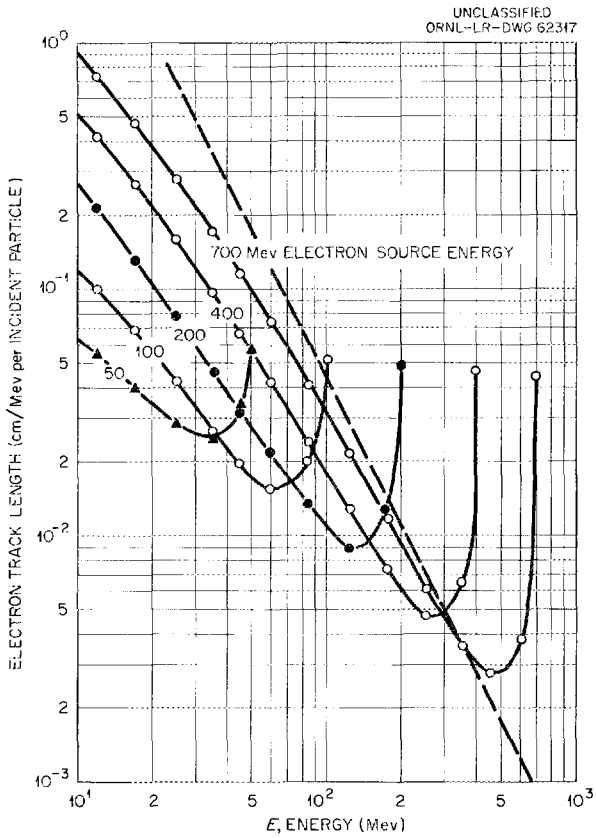

Fig. 8.3.3. Electron Track Lengths in Cascade Showers Initiated by 50- to 700-Mev Electrons Incident on an Infinite Slab of Copper. Dashed lines are from the track length formula using Approximation A; data points are from the Monte Carlo calculation.

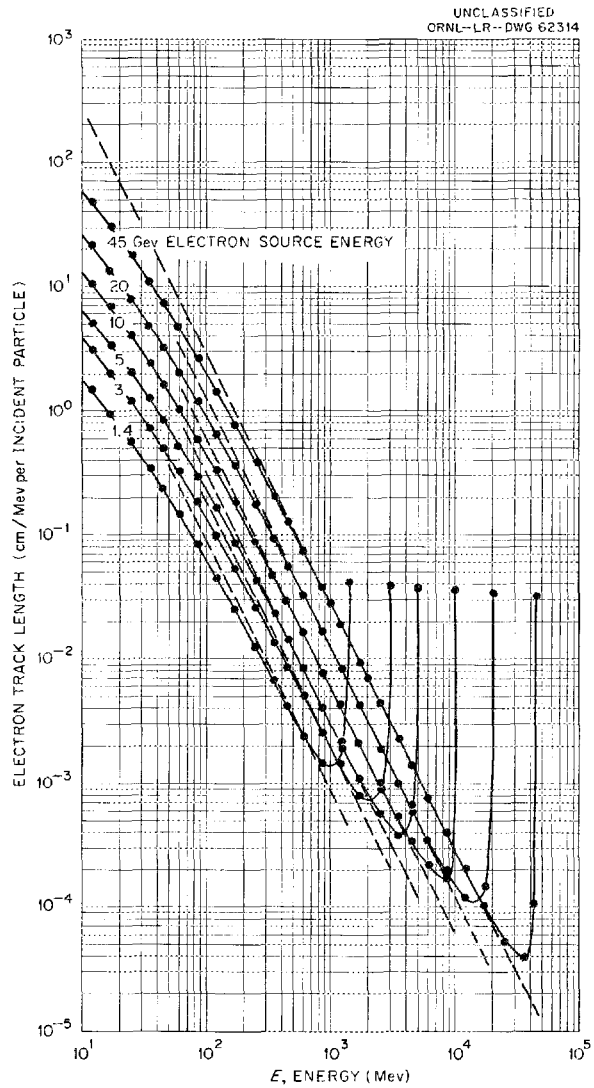

Fig. 8.3.4. Electron Track Lengths in Cascade Showers Initiated by 1.4- to 45-Gev Electrons Incident on an Infinite Slab of Copper. Dashed lines are from the track length formula using Approximation A; data points are from the Monte Carlo calculation.

fact is that most of the photons which make a contribution to the energy deposition are bremsstrahlung photons that are created in the very-low-energy region where the mean free path is very short because of

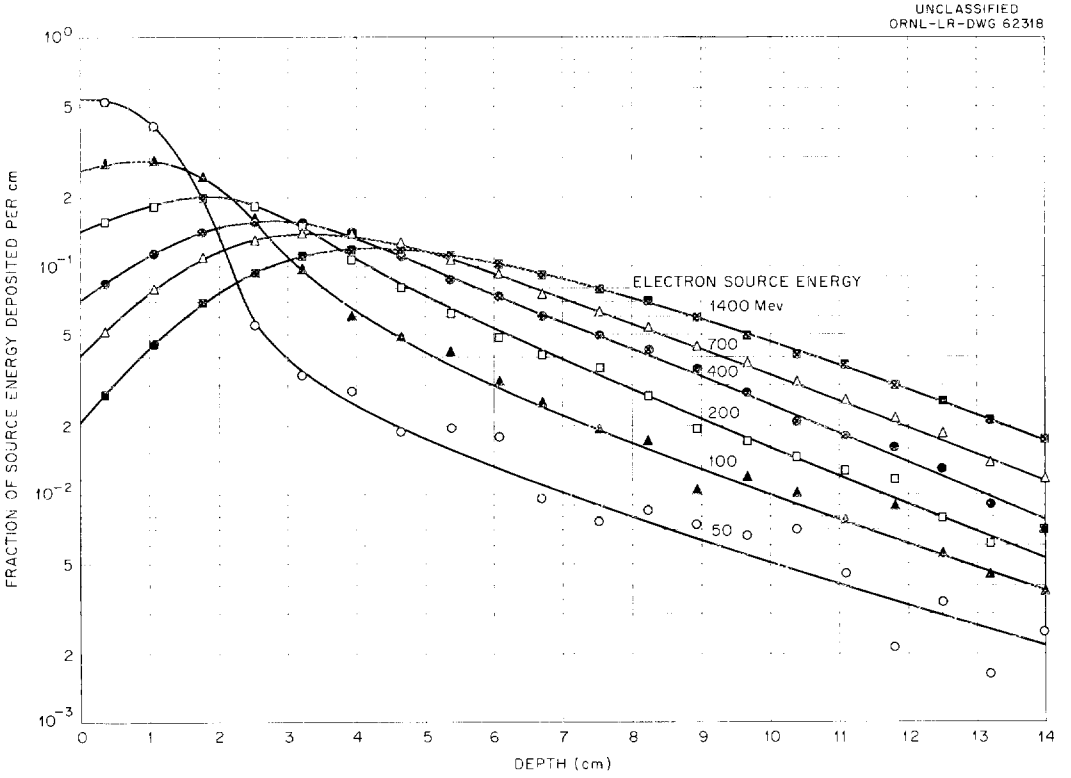

Fig. 8.3.5. Energy Deposition in a Copper Slab by Photon-Electron Cascades Initiated by Normally Incident 50- to 1400-Mev Electrons.

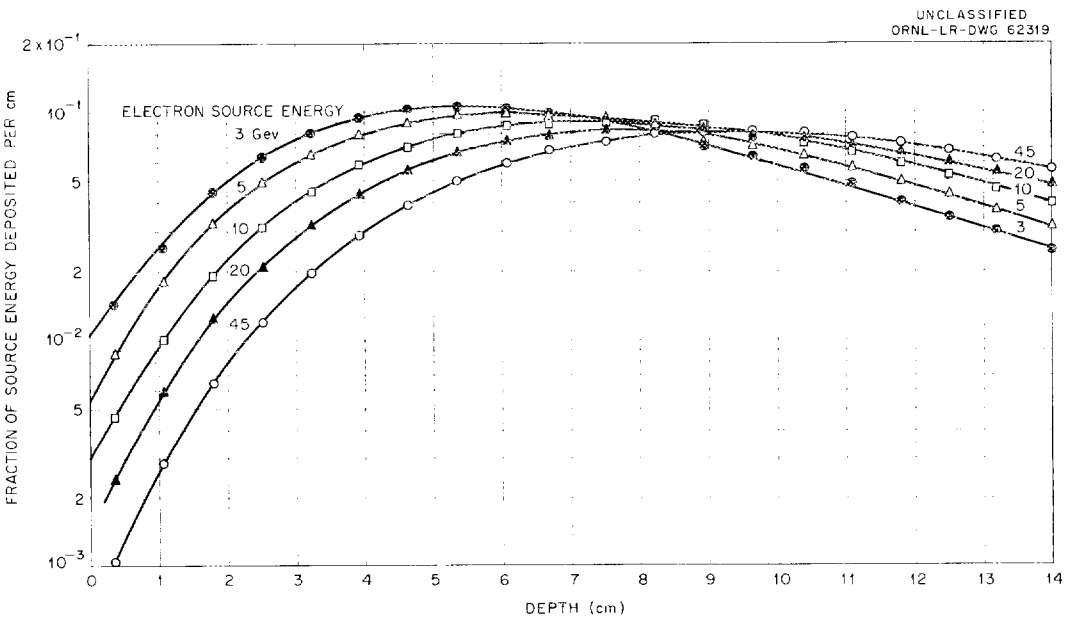

Fig. 8.3.6. Energy Deposition in a Copper Slab by Photon-Electron Cascades Initiated by Normally Incident 3- to 45-Gev Electrons.

the high photoelectric cross section, and calculations show that over 50% of the photon energy is dissipated within 1 mean free path in typical materials for low-energy photons.[8] Thus the approximation used for the deposition of the photon energy should be very accurate.

The buildup of intensity at the very low energy by the bremsstrahlung that was referred to above is obvious from plots of the differential cross section (see Eq. 3). These plots indicate that the intensity curve is an increasing function toward lower photon energies as a result of a single radiative collision; thus, after many such collisions in which the charged particles lose energy, the compounded intensity curve must be a very steeply increasing function toward the lower photon energies.

Target Heating Data

In order to provide data which would be useful for the design of the cooling channels in electron beam targets for machines of about 75 Mev, several energy deposition curves were obtained for water, iron, and

[8] L. A. Bowman and D. K. Trubey, *Deposition of Gamma-Ray Heating in Stratified Lead and Water Slabs*, ORNL-CF-58-7-99 (1958).

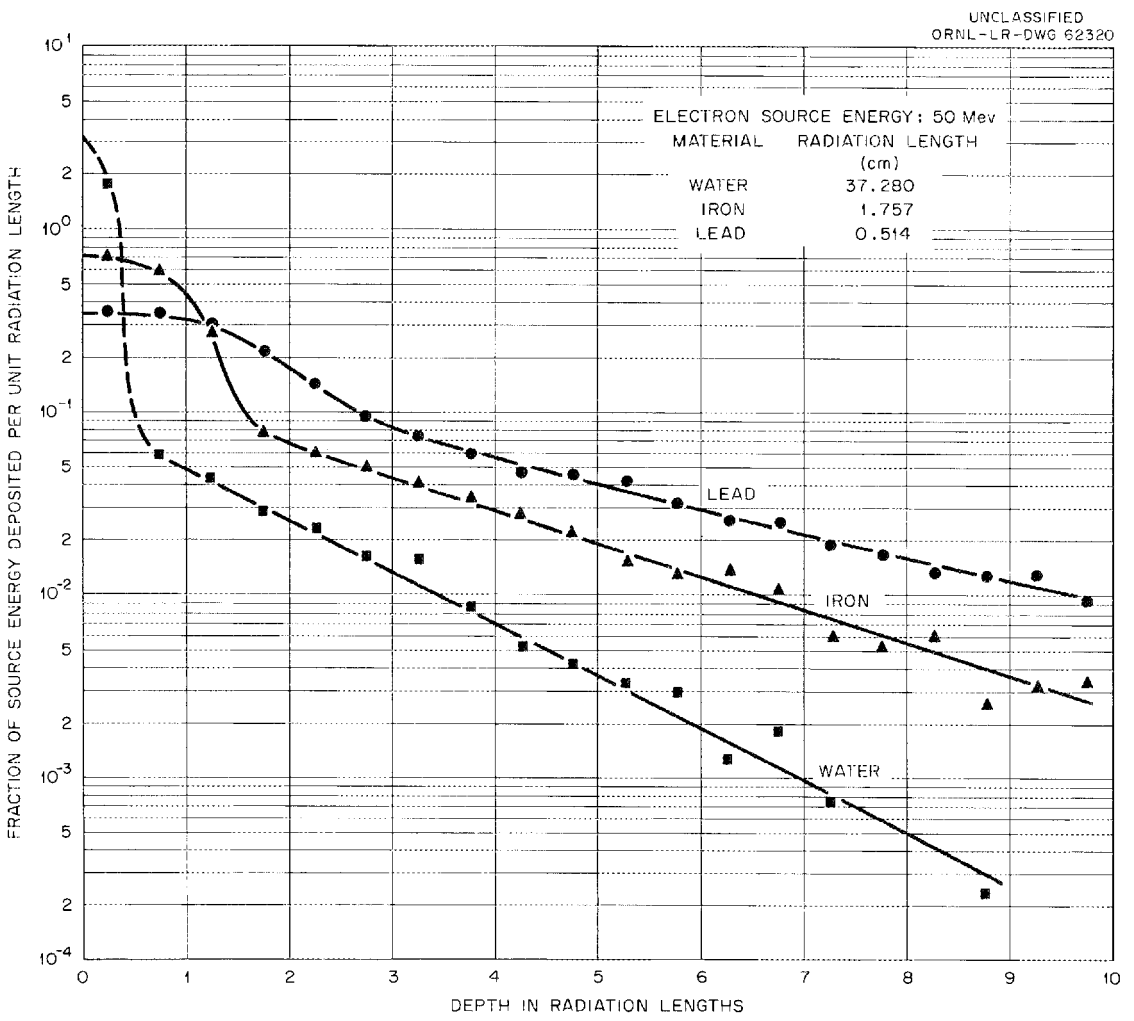

Fig. 8.3.7. Energy Deposition in Water, Iron, and Lead Slabs by Cascade Showers Initiated by Normally Incident 50-Mev Electrons.

lead which are representative of low, medium, and high atomic number materials. Electron beam energies of 50, 75, and 100 Mev were investigated for each material. The results of these calculations are presented in Figs. 8.3.7 through 8.3.9. The energy deposition is presented as a function of depth in radiation lengths in order to make interpolation easier for intermediate materials. The lower energy bound in these cases was 6.5 Mev. Each run was the result of 2000 source electrons. The total running time for the nine cases was $1\frac{1}{2}$ hr.

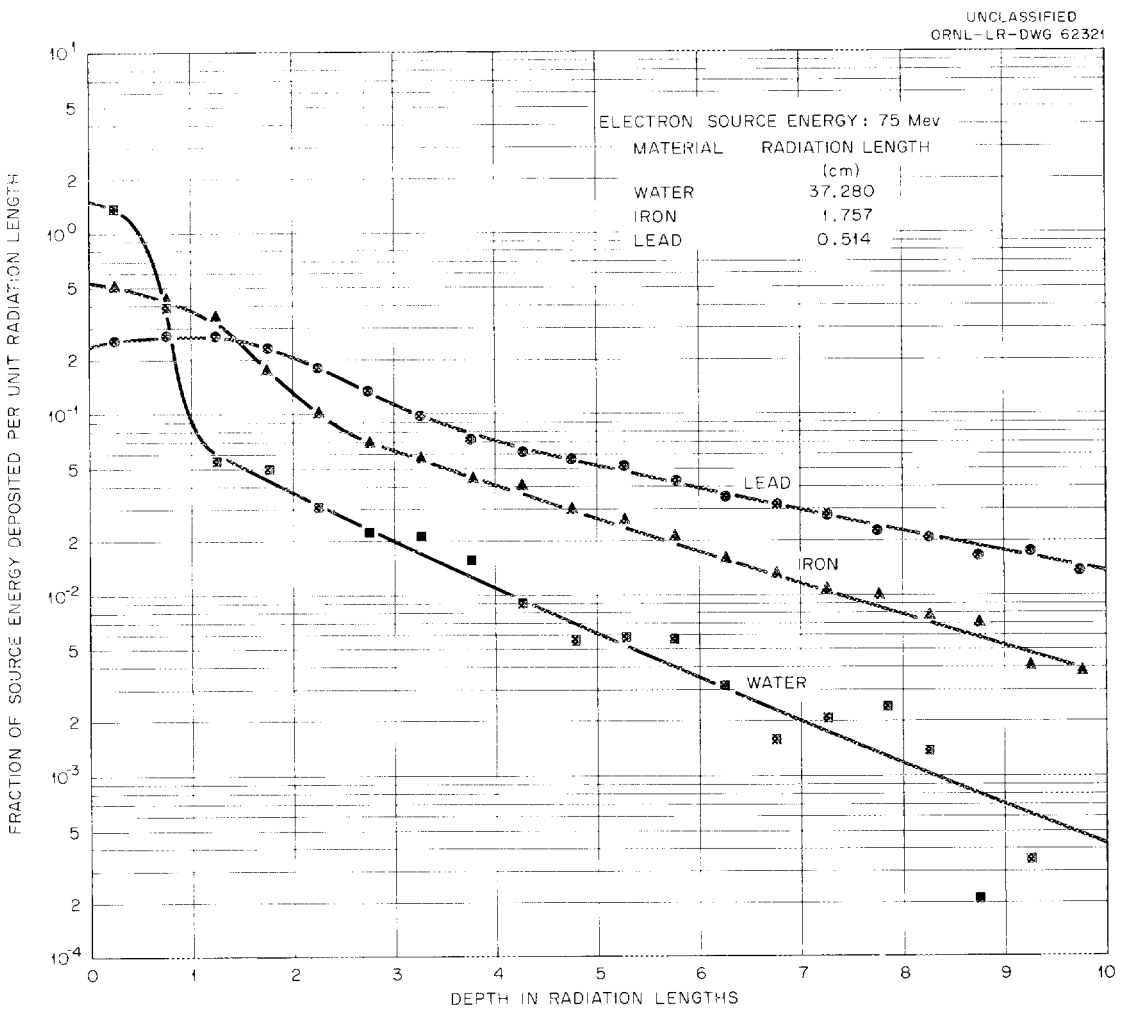

Fig. 8.3.8. Energy Deposition in Water, Iron, and Lead Slabs by Cascade Showers Initiated by Normally Incident 75-Mev Electrons.

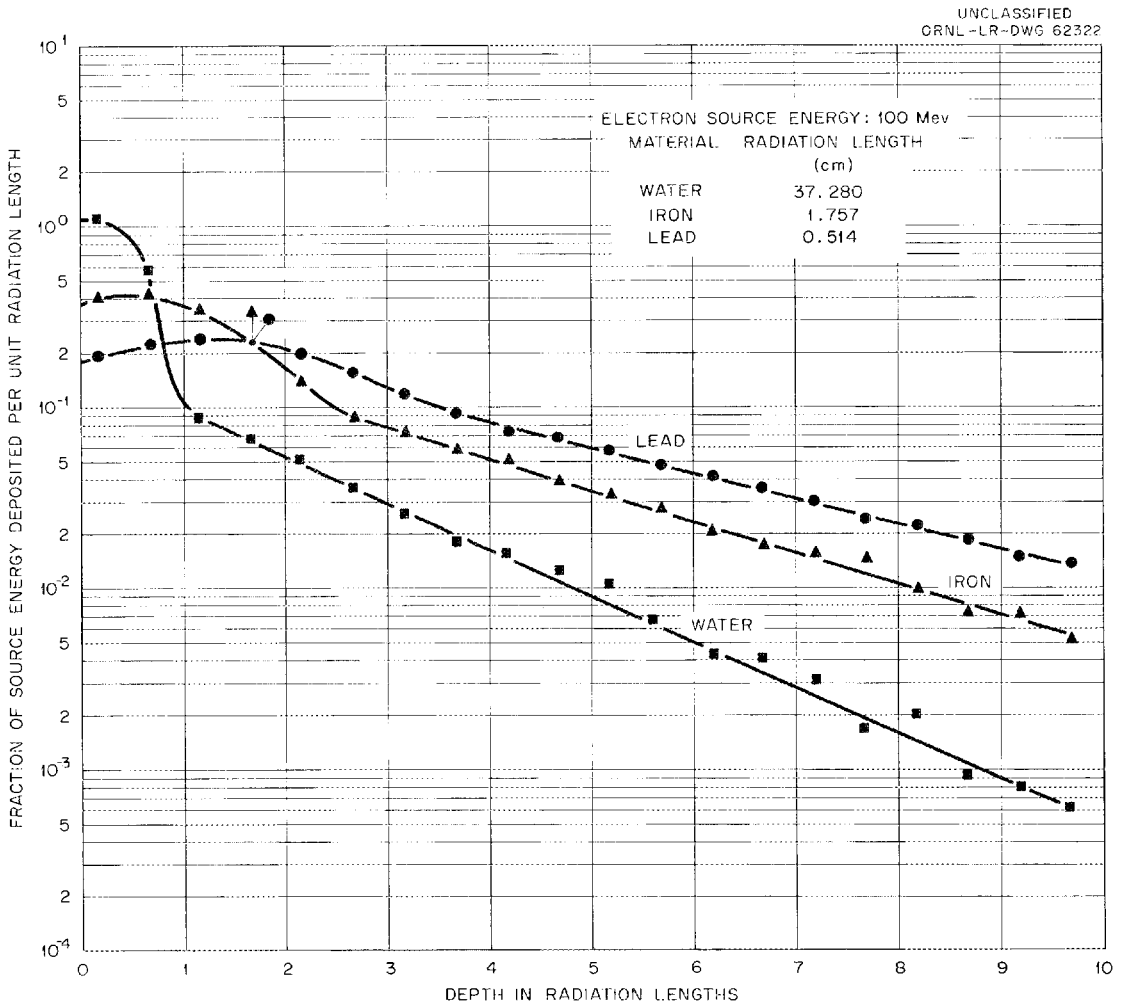

Fig. 8.3.9. Energy Deposition in Water, Iron, and Lead Slabs by Cascade Showers Initiated by Normally Incident 100-Mev Electrons.

8.4. TRANSVERSE SHIELDING CALCULATION FOR A 45-Bev ELECTRON ACCELERATOR

R. G. Alsmiller, Jr. and F. S. Alsmiller

In the proposed Stanford 45-Bev electron accelerator it is expected that some electrons will strike the walls of the accelerator tube and give rise to penetrating photonucleons and photopions. The accelerator

tube will be surrounded by an earth shield; estimates of the shielding thickness required have been made by the Stanford group.[1,2] An approximate cascade calculation to provide a check on these estimates is being carried out and is described here.

The energy and angular distributions of photonucleons and photopions which arise when a high-energy electron strikes a copper target have been calculated by Dedrick.[3,4,5] Since the electron stops in a very short distance compared to the shielding thicknesses in which we are interested, we assume that the photonucleons and photopions all emanate from a point. The point sources are located on the axis of a cylinder (we neglect the accelerator tube), and the various particle fluxes are calculated as a function of energy and distance.

The composition of earth is approximated by using a single "average" element. In the present calculation this average element is taken to be aluminum.

Using the straight-ahead approximation, i.e., assuming that a particle and all of the secondaries, tertiaries, etc. produced by this particle travel in the same straight line, a set of coupled integro-differential transport equations which give the neutron, proton, charged pion, and muon fluxes as functions of energy and distance is obtained. (The neutral pions are not included in the equation; see discussion below.) Because there is very little experimental information about high-energy interactions, the equations include many quantities, e.g., cross sections, multiplicities, etc., which are known only very approximately. In obtaining the necessary input information we have relied in so far as possible on cosmic-ray data,[6] but even so, many interpolations, extrapolations and *ad hoc* assumptions were required.

An IBM-7090 code has been written to solve the equations numerically.* Because of the approximations involved the equations are valid only at reasonably high energies, and the code is written in such a manner that only the particle fluxes at energies above 30 Mev are obtained. Of course, from the point of view of shielding, the lower-energy particles are quite important. To obtain the low-energy neutrons, we plan to normalize the measured cosmic-ray neutron flux[7] to our calculated flux above 30 Mev and use this renormalized cosmic-ray flux as an estimate of the neutron flux in the shield below 30 Mev. This procedure will be valid only in so far as our calculated flux has the same energy dependence as the measured cosmic-ray flux in an energy region above 30 Mev.

---

[1] *Proposal for a Two-Mile Linear Electron Accelerator*, Stanford University, Stanford, California (1957).

[2] H. C. DeStaebler, Jr., *A Review of Transverse Shielding Requirements for the Stanford Two-Mile Accelerator*, W. W. Hansen Laboratories of Physics M-262 (1961).

[3] K. G. Dedrick, *Deuteron Model Calculation of Photonucleon Yields*, W. W. Hansen Laboratories of Physics M-227 (1960).

[4] K. G. Dedrick, *Calculation of Pion Photoproduction from Electron Accelerators According to the Statistical Model*, W. W. Hansen Laboratories of Physics M-228 (1960).

[5] K. G. Deadrick, *More Calculations of Photopion Yields*, W. W. Hansen Laboratories of Physics M-229 (1960).

*This code and the numerical analyses involved were executed by J. E. Murphy, R. G. Edwards, and R. G. Mashburn at the Central Data Processing Facility of the Oak Ridge Gaseous Diffusion Plant.

[6] U. Camerini, W. O. Lock, and D. H. Perkins, "The Analysis of Energetic Nuclear Encounters Occurring in Photographic Emulsions," *Progress in Cosmic Ray Physics*, vol. 1, chap. 1, North Holland Publishing Co., 1952.

[7] W. N. Hess *et al.*, *Phys. Rev.* 116, 2 (1959).

This method cannot be used to obtain the low-energy charged-particle fluxes because there are no measured cosmic-ray fluxes for these particles. However, because these particles are charged they will be stopped efficiently, and it is expected that their contribution will be negligible, compared with that of the neutrons.

Because the equations are to be used only above 30 Mev, we have not included the neutral pions. The neutral pion decays very rapidly into two gamma rays; and thus, the primary effect of these pions will come from the photoneutrons produced by the decay gamma rays. These photoneutrons will be of sufficiently low energy that they will contribute little to the neutron flux above 30 Mev, and by using the cosmic-ray spectrum below 30 Mev these photoneutrons should automatically be included in our flux estimate.

The equations which are employed and the IBM code which solves them are in no way special to the Stanford problem, and it is hoped that they will be useful in solving other high-energy shielding problems in the future.

Part 9

PLASMA PHYSICS THEORY

9.1. INSTABILITIES IN A HOMOGENEOUS, ANISOTROPIC PLASMA

Y. Shima

It is well known that a homogeneous (in x space) plasma which is situated in a constant magnetic field and whose distribution function in velocity space is Maxwellian is stable against small perturbations. More generally, it was shown by Rosenbluth[1] that a sufficient condition for stability is that the distribution function be isotropic and a decreasing function of v^2.

It has been conjectured that all anisotropic plasmas are unstable, but no general proof has yet been given. A somewhat general investigation of the problem of homogeneous anisotropic plasmas has now been made. For the sake of simplicity, only systems with no initial electric or magnetic fields were considered. The results show that some general classes of such plasmas are indeed unstable. In addition, a sufficient condition for instability is derived.

This topic is discussed in detail elsewhere.[2]

---

[1]M. N. Rosenbluth, Lecture in the Infernational Summer Course in Plasma Physics, Denmark, August 1960.

[2]Y. Shima, *Instabilities in a Homogeneous, Anisotropic Plasma,* ORNL CF-61-7-69 (July 31, 1961).

9.2. A RECALCULATION OF THE H^3 BREEDING RATIO IN A STELLARATOR BLANKET

W. E. Kinney

Multigroup diffusion theory calculations have been made of the H^3 breeding ratio resulting from the introduction of (D,T) neutrons into a stellarator blanket which multiplies them by $Be(n,2n)$ reactions, moderates them, and finally captures them in the $Li^6(n,\alpha)H^3$ reaction. Two homogeneous blankets, the second having a Be density ten times the first, and one heterogeneous blanket were considered. Breeding ratios as high as 1.45 were computed for the heterogeneous blanket. Details have been published elsewhere.[1]

---

[1]W. E. Kinney, *A Recalculation of the H^3 Breeding Ratio in a Stellarator Blanket,* ORNL CF-61-6-63 (1961).

9.3. PLASMA STABILITY ANALYSIS EMPLOYING EQUILIBRIUM CONSTANTS OF MOTION

T. K. Fowler

By first transforming to equilibirum constants of motion as variables, a Green's function has been found by means of which the linearized Vlasov equation governing hot plasmas of low density may be solved for the perturbed space and velocity distributions in terms of the perturbed electric and magnetic fields. The second step in stability analysis, that of introducing the result into the field equations and

determining the dispersion relation, has been carried out for two examples. Details have been published elsewhere.[1]

[1] T. K. Fowler, *Plasma Stability Analysis Employing Equilibrium Constants of Motion*, ORNL-3123 (May 26, 1961).

9.4. "NEGATIVE MASS" INSTABILITY IN DCX-1

T. K. Fowler

The threshold for an instability by which space charge accumulates in a ring of ions circulating in a magnetic field with negative radial gradient has been calculated for DCX-1, using a model due to the MURA accelerator group. With present low densities, the energy spread necessary to quench the instability is of the order of a few tens of kev. Details have been published elsewhere.[1]

[1] T. K. Fowler, *Calculation of the "Negative Mass" Instability for DCX-1*, ORNL CF-61-7-1 (July 3, 1961).

9.5. ENERGY DISTRIBUTIONS OF PARTICLES IN DCX

T. K. Fowler and M. Rankin[1]

A code has been completed which calculates from Fokker-Planck equations the energy distributions of ions and electrons in DCX in steady state. The d-c plasma potential which develops to impede electron escape is also determined. It has been found that, because most of the electron distribution is energetically incapable of escaping over the potential barrier, electrons achieve a Maxwellian distribution. Ions do not. Details appear elsewhere.[2]

[1] Thermonuclear Division.

[2] T. K. Fowler and M. Rankin, *Energy Distribution of Ions and Electrons in DCX after Burnout: Oracle Code EDDIE*, ORNL-3161 (August, 1961).

9.6. EFFECT OF ENERGY DEGRADATION ON THE CRITICAL CURRENT IN AN OGRA-TYPE DEVICE

T. K. Fowler

The relation between the trapped-ion density achieved in machines like OGRA and DCX-2 and the molecular-ion injection current required, the "S-curve" calculated by Simon, has been recalculated to

include the effect of energy transfer from trapped ions to the continuous flux of cold electrons released in the ionization of the neutral background. The revised value for the critical current is more than twice the previous result. Details have been published elsewhere.[1]

[1]T. K. Fowler, *Effect of Energy Degradation on the Critical Current in an OGRA-Type Device*, ORNL-3037 (Dec. 28, 1960).

9.7. STABILITY OF PLASMAS AGAINST ELECTROSTATIC PERTURBATIONS

T. K. Fowler

With the notation $\partial f/\partial t + Vf = 0$ for the linearized Vlasov equation including electrostatic perturbations only, it has been shown that it is sufficient for stability that the operator V factor into a product of an anti-Hermitian operator and an Hermitian positive definite operator. By using this criterion, a class of stable functions has been found which includes spatially confined distributions isotropic in velocity. It has also been shown that electrostatic instability in "mirror" machines requires perturbations lacking the azimuthal symmetry of the magnetic field. Details have been published elsewhere.[1]

[1]T. K. Fowler, *Stability of Plasmas Against Electrostatic Perturbations*, ORNL-3162 (July 27, 1961); also accepted for publication in November 1961 issue of *Physics of Fluids*.

9.8. DISSOCIATION OF THE H_2^+ MOLECULE BY ELECTRONS AND PROTONS

R. G. Alsmiller, Jr.

In a recent publication M. Gryzinski[1] has introduced a formalism for calculating the ionization and excitation of atomic systems by charged-particle impact. Since the theory appears to give reliable results in the low-energy region where the Born approximation is not accurate, it has been used to calculate the total cross section for the dissociation of the H_2^+ molecule by electrons and protons for comparison with the Born approximation results.[2,3]

In making the calculation, the velocity distribution of the bound electron was obtained from the usual L.C.A.O. wave function for the ground state of the H_2^+ molecule,[4] the molecular protons were considered to be fixed force centers, and a classical average was taken over molecular orientations. It was further

[1]M. Gryzinski, *Phys. Rev.* 113, 2 (1959).

[2]E. V. Ivash, *Phys. Rev.* 112, 1 (1958).

[3]R. G. Alsmiller, Jr., *Cross Sections for the Dissociation of H_2^+ and D_2^+ by a Vacuum Arc*, ORNL-2766 (Oct. 6, 1959).

[4]L. Pauling and E. B. Wilson, *Introduction to Quantum Mechanics*, McGraw-Hill Book Co., Inc., New York, 1955.

assumed that all excitations of the molecule would lead to dissociation. In the case of dissociation by electrons, electron-electron exchange was not included.*

The total cross section for dissociation by electrons is shown in Fig. 9.8.1 and by protons in Fig. 9.8.2.** Also shown are the Born approximation results. The two Born curves in Fig. 9.8.1 correspond to including no electron-electron exchange and to including the prior-exchange terms. The use of the postexchange terms gives a peak which is considerably larger than those shown in the figure.

*M. Gryzinski has calculated the ionization of the H_2 molecule by electrons and obtained very good results without the inclusion of exchange.[1]

**An algebraic error in the published work of Gryzinski was corrected before the proton calculation was done.

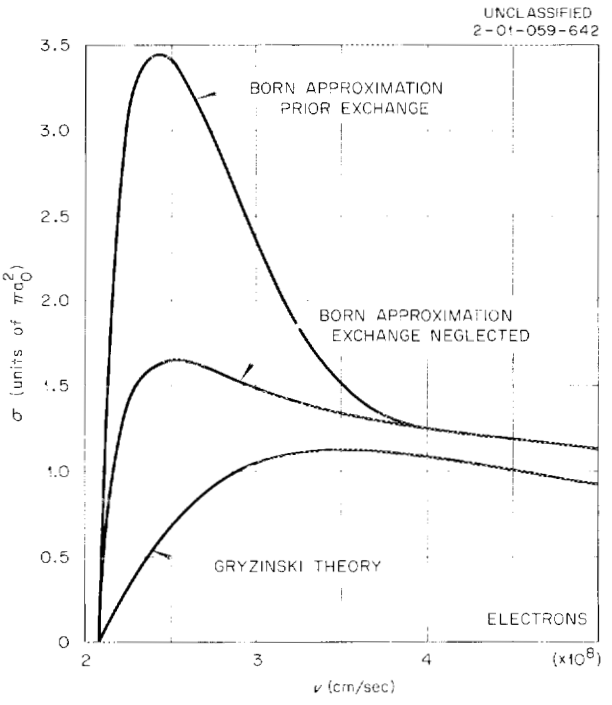

Fig. 9.8.1. Dissociation of H_2^+ by Electrons.

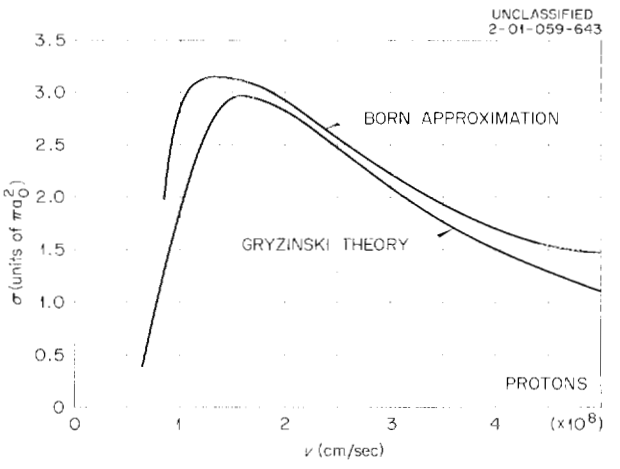

Fig. 9.8.2. Dissociation of H_2^+ by Protons.

9.9. FOKKER-PLANCK COEFFICIENTS FOR A PLASMA INCLUDING CYCLOTRON RADIATION[1]

Albert Simon[2] and Norman Rostoker[2]

Kinetic equations for a plasma have previously been obtained by starting with the Liouville equation and making an expansion in powers of the discreteness parameters.[3] To the lowest order in this expansion the Vlasov equations are obtained. In first order a Fokker-Planck equation is obtained where the coefficients come from the time-asymptotic solutions of integro-differential equations for the pair correlation functions.

Solutions have been published previously for an infinite plasma with Coulomb forces,[4] for a plasma with Coulomb forces and a constant magnetic field,[5] and for a plasma with the complete electromagnetic field and no constant magnetic field.[6] The problem has now been treated with both the complete electromagnetic field and a constant magnetic field. The new feature of this problem is the inclusion of the electromagnetic radiation whereas it was absent in all of the cases previously treated.

At the outset the system consists of a large number of "bare" particles that interact with each other and a denumerably infinite number of vacuum oscillators. The present statistical treatment leads to a kinetic equation for the one-body function that has a physical interpretation in terms of "dressed" particles and renormalized oscillators. A shield cloud of charge and current density envelopes a particle and the radiation takes place in terms of oscillators that satisfy the plasma dispersion relation instead of the vacuum dispersion relation.

In the low-density limit, or when $k >> \omega_p/c$, the result agrees with the vacuum radiation formula employed by Trubnikov.[7] If terms of order $(\omega_p/kc)^2$ are retained, the principal effect is the renormalization of the oscillators. In the exact radiation formula longitudinal and transverse waves are coupled, i.e., the normal modes do not have a simple polarization. The virtue of the present treatment is that it indicates the terms that represent electromagnetic radiation and the proper particle dressing under those circumstances.

---

[1]Abstract of paper submitted to Conference on Plasma Physics and Controlled Nuclear Fission Research, Salzburg, Austria, September 4–8, 1961.

[2]General Atomic, San Diego, California.

[3]N. Rostoker and M. N. Rosenbluth, *Phys. Fluids* 3, 1 (1960); A. Simon and E. G. Harris, *Phys. Fluids* 3, 245 (1960).

[4]A. Lenard, *Ann. Phys. (N.Y.)* 10, 390 (1960); R. Balescu, *Phys. Fluids* 3, 52 (1960).

[5]N. Rostoker, *Phys. Fluids* 3, 922 (1960).

[6]A. Simon, *Phys. Fluids* 4, 586 (1961).

[7]B. Trubnikov and V. Kudryavtsev, *Proc. U.N. Intern. Conf. Peaceful Uses Atomic Energy 2d, Geneva, 1958*, 31, p 93.

9.10. CONCERNING A POSSIBLE APPROACH TO THE MODE I-MODE II TRANSITION PROBLEM

G. Guest[1] and A. Simon[2]

An attempt has been made, following the method of Kadomtsev and Nedospasov,[3] to analyze the Mode I-Mode II instability[4] in terms of a simple model of the gaseous arc discharge in a uniform longitudinal magnetic field. The essential features of the model are the inclusion of streaming effects to the end walls as utilized by Simon[5] and the neglect of lower order terms in the transverse motion of charged particles due to electrostatic fields. Transverse motion of the ions and electrons is attributed entirely to diffusion processes and to Hall currents arising from $\vec{j} \times \vec{B}$ terms in the equations of motion.

The theory leads to a dispersion relation which predicts instability of the plasma for magnetic fields greater than a critical value, B_c, given by

$$B_i \sim 1.5 \times 10^{13}\, n_0 A \sigma_i \frac{T_i}{T_e} \sqrt{\kappa T_e m_e C^2}\,,$$

where T_e and T_i are the electron and ion temperatures respectively, σ_i is the ion-neutral atom collision cross section, A is the ion mass number and n_0 is the neutral atom number density.

[1]Research participant from Department of Physics, North Texas State University, Denton, Texas.

[2]Now at General Atomic, San Diego, California.

[3]B. B. Kadomtsev and A. V. Nedospasov, *J. Nucl. Energy, Part C: Plasma Physics* 1, 230 (1960).

[4]R. V. Neidigh, *The Effect of a Pressure Gradient on a Magnetically Collimated Arc*, ORNL-2288 (May 27, 1957).

[5]A. Simon, *An Introduction to Thermonuclear Research*, Chapter IX, Pergamon Press, New York (1959).

9.11. ELECTROSTATIC ION-CYCLOTRON PLASMA INSTABILITIES IN A TWO-FLUID HYDRODYNAMIC THEORY

H. K. Wimmel

It has been deduced by E. G. Harris[1] from the Vlasov equations (= self-consistent collisionless Boltzmann plus Maxwell equations) that a static homogeneous plasma in a uniform magnetic field $\vec{B}_0$ may exhibit unstable longitudinal plasma oscillations with $\omega' = \pm n\Omega_c$ [$\omega' = Re(\omega)$, Ω_c = ion cyclotron

[1]E. G. Harris, *Unstable Plasma Oscillations in a Magnetic Field*, ORNL-2728 (June 5, 1959); *Proceedings of a Conference on the Theoretical Aspects of Controlled Fusion Research, Gatlinburg, Tennessee, April 27–28, 1959*, TID-7582 (ORNL-2805), p 131; *J. Nucl. Energy, Part C: Plasma Physics*, 2, 138 (1961). Compare also: P. B. Burt and E. G. Harris, *Bull. Am. Phys. Soc.* 6, 300 (1961).

frequency, n = integer]. These electrostatic ion-cyclotron instabilities occur for $\omega_p > n\Omega_c$ (ω_p = electron plasma frequency) and for an ion pressure anisotropy ($P_\perp/P_\parallel$) greater than 8 or 9 (Ref. 2). There is experimental evidence that such instabilities may exist in the Oak Ridge DCX mirror machine.[3]

A theoretical analysis of these instabilities for a mirror configuration on the basis of the Vlasov equations seems difficult to accomplish; therefore, the possibility of using the moments method for an approximate treatment of certain Harris instabilities was examined. The method works only for the lowest harmonics of the ion-cyclotron frequency and generally predicts greater stability than the Vlasov equations.

The details of this calculation have been published.[4]

---

[2]W. E. Drummond, M. N. Rosenbluth, M. L. Johnson, *Bull. Am. Phys. Soc.* **6**, 185 (1961).

[3]C. F. Barnett, *Bull. Am. Phys. Soc.* **6**, 196 (1961).

[4]H. K. Wimmel, *Electrostatic Ion-Cyclotron Plasma Instabilities in a Two-Fluid Hydrodynamic Theory*, ORNL-3170 (Aug. 18, 1961).

INTERNAL DISTRIBUTION

1. C. E. Larson
2. Biology Library
3-5. Central Research Library
6. Reactor Division Library
7-50. Laboratory Records Department
51. Laboratory Records, ORNL R.C.
52. A. M. Weinberg
53. R. G. Jordan (Y-12)
54. J. P. Murray (K-25)
55. J. A. Swartout
56. G. E. Boyd
57. W. H. Jordan
58. A. H. Snell
59. C. E. Winters
60. D. S. Billington
61-85. E. P. Blizard
86. F. L. Culler
87. J. L. Fowler
88. J. H. Frye, Jr.
89. C. S. Harrill
90. A. Hollaender
91. A. S. Householder
92. M. T. Kelley
93. S. C. Lind
94. R. S. Livingston
95. K. Z. Morgan
96. M. L. Nelson
97. H. E. Seagren
98. E. D. Shipley
99. E. H. Taylor
100. E. Guth
101. P. F. Kasten
102. A. J. Miller
103. L. C. Oakes
104. G. D. O'Kelley
105. V. K. Pare
106. D. Phillips
107. W. M. Good
108. M. J. Skinner
109. R. O. Chester
110. L. S. Abbott
111. M. N. Alam
112. F. S. Alsmiller
113. R. G. Alsmiller, Jr.
114. H. Bertini
115. T. V. Blosser
116. B. Buck
117. W. R. Burrus
118. V. R. Cain
119. A. D. Callihan
120. G. T. Chapman
121. R. R. Coveyou
122. G. deSaussure
123. L. Dresner
124. J. F. Ellis
125. T. K. Fowler
126. J. K. Fox
127. R. M. Freestone
128. T. Fuse
129. F. Gibbons
130. W. A. Gibson
131. L. W. Gilley
132. J. K. Grant
133. R. Gwin
134. K. M. Henry
135. Roy Henry
136. L. B. Holland
137. J. L. Hull
138. L. Jung
139. E. B. Johnson
140. F. B. K. Kam
141. N. King
142. J. D. Kington
143. W. E. Kinney
144. J. Lewin
145. T. A. Love
146. J. J. Lynn
147. R. E. Maerker
148. D. W. Magnuson
149-151. F. C. Maienschein
152. J. J. Manning
153. J. T. Mihalczo
154. J. M. Miller
155. H. S. Moran
156. F. J. Muckenthaler
157. R. B. Murray

158. A. Meyer
159. R. W. Peelle
160. S. K. Penny
161. F. Perey
162. E. R. Rohrer
163. Y. Shima
164. E. G. Silver
165. H. E. Stern
166. J. G. Sullivan
167. J. T. Thomas
168. D. K. Trubey
169. W. C. Tunnell
170. E. Vander Spuy
171. V. V. Verbinski
172. D. R. Ward
173. J. H. Wilson
174. L. W. Weston
175. C. D. Zerby
176. W. Zobel
177. R. C. Block
178. H. G. MacPherson
179. F. C. VonderLage
180. G. E. Whitesides
181. E. G. Harris
182. R. L. Macklin
183. W. S. Lyon
184. R. D. Smiddie
185. C. A. Preskitt
186. R. A. Charpie (consultant)
187. P. F. Gast (consultant)
188. R. F. Taschek (consultant)
189. T. J. Thompson (consultant)
190. Gale Young (consultant)
191. ORNL – Y-12 Technical Library, Document Reference Section

EXTERNAL DISTRIBUTION

192. Division of Research and Development, AEC, ORO
193-826. Given distribution as shown in TID-4500 (16th ed. Rev.) under Physics category (75 copies – OTS)